

Biomechanics and Bioengineering of Orthopaedic and Cardiovascular Rehabilitation

Lead Guest Editor: Lizhen Wang

Guest Editors: Chia-Ying Lin, Wei Yao, Duo Wai-Chi Wong, and Rui Zhu





Biomechanics and Bioengineering of Orthopaedic and Cardiovascular Rehabilitation

Journal of Healthcare Engineering

**Biomechanics and Bioengineering of Orthopaedic
and Cardiovascular Rehabilitation**

Lead Guest Editor: Lizhen Wang

Guest Editors: Chia-Ying Lin, Wei Yao, Duo Wai-Chi Wong,
and Rui Zhu



Copyright © 2018 Hindawi. All rights reserved.

This is a special issue published in “Journal of Healthcare Engineering.” All articles are open access articles distributed under the Creative Commons Attribution License, which permits unrestricted use, distribution, and reproduction in any medium, provided the original work is properly cited.

Editorial Board

Saverio Affatato, Italy
Francesca Apollonio, Italy
Hasan Ayaz, USA
William Bertucci, France
Olivier Beuf, France
Patrick Boissy, Canada
Hongwei Chen, USA
Daniel H.K. Chow, Hong Kong
Gianluca Ciardelli, Italy
Elena De Momi, Italy
Costantino Del Gaudio, Italy
Tiago H. Falk, Canada
Mostafa Fatemi, USA
Jesus Favela, Mexico
David Dagan Feng, Australia
Joseph Finkelstein, USA
Jesus Fontecha, Spain
Jean-Luc Gennisson, France
Shahram M. Ghanaati, Germany
Luca Giancardo, USA
Antonio Gloria, Italy
Kheng-Lim Goh, Singapore
Pedro Gomes, Portugal
Carlos Gómez, Spain
Philippe Gorce, France
Sophia Z. Gu, Australia
Vincenzo Guarino, Italy

Valentina Hartwig, Italy
Andreas H. Hielscher, USA
Ernesto Iadanza, Italy
Norio Iriguchi, Japan
Jingfeng Jiang, USA
Zhongwei Jiang, Japan
Rashed Karim, UK
Pasi A. Karjalainen, Finland
Chandan Karmakar, Australia
John S. Katsanis, Greece
Terry K.K. Koo, USA
Panagiotis Kosmas, UK
Michel Labrosse, Canada
Jui-Yang Lai, Taiwan
Xiang Li, USA
Feng-Huei Lin, Taiwan
Yuan-Pin Lin, Taiwan
Maria Lindén, Sweden
Dongfei Liu, Finland
Francisco Lopez-Valdes, Spain
Zufu Lu, Australia
Ilias Maglogiannis, Greece
Andreas Maier, Germany
Mehran Moazen, UK
Rafael Morales, Spain
David Moratal, Spain
Angkoon Phinyomark, Canada

Vincenzo Positano, Italy
Alessandro Ramalli, Italy
Alessandro Reali, Italy
Lei Ren, UK
Jose Joaquin Rieta, Spain
Emanuele Rizzuto, Italy
Sébastien Roth, France
Simo Saarakkala, Finland
Hélder A. Santos, Finland
Emiliano Schena, Italy
Maurizio Schmid, Italy
Jiann-Shing Shieh, Taiwan
Tiago H. Silva, Portugal
Redha Taiar, France
Jinshan Tang, USA
Vinoy Thomas, USA
Ioannis G. Tollis, Greece
Kazunori Uemura, Japan
Uche Wejinya, USA
Damon W.K. Wong, Singapore
Ying Yang, UK
Ping Yu, Australia
Haihong Zhang, Singapore
Hongbo Zhang, Finland
Ping Zhou, USA
Loredana Zollo, Italy

Contents

Biomechanics and Bioengineering of Orthopedic and Cardiovascular Rehabilitation

Lizhen Wang , Chia-Ying Lin, Wei Yao , Duo Wai-Chi Wong , and Rui Zhu 
Editorial (2 pages), Article ID 1716809, Volume 2018 (2018)

Effect of Dropping Height on the Forces of Lower Extremity Joints and Muscles during Landing: A Musculoskeletal Modeling

Wenxin Niu , Lejun Wang , Chenghua Jiang, and Ming Zhang 
Research Article (8 pages), Article ID 2632603, Volume 2018 (2018)

Analysis of Bone Mineral Density/Content of Paratroopers and Hoopsters

Yixue Luo, Chenyu Luo, Yuhui Cai, Tianyun Jiang, Tianhong Chen, Wenyue Xiao, Junchao Guo, and Yubo Fan 
Research Article (8 pages), Article ID 6030624, Volume 2018 (2018)

Effect of Constraint Loading on the Lower Limb Muscle Forces in Weightless Treadmill Exercise

Ning Guo , Xingyu Fan, Yuting Wu , Zhili Li , Shujuan Liu , Linjie Wang , Jie Yao , and Yinghui Li 
Research Article (9 pages), Article ID 8487308, Volume 2018 (2018)

The Computational Fluid Dynamics Analyses on Hemodynamic Characteristics in Stenosed Arterial Models

Yue Zhou , Chunhian Lee , and Jingying Wang 
Research Article (6 pages), Article ID 4312415, Volume 2018 (2018)

A Comprehensive Method for Accurate Strain Distribution Measurement of Cell Substrate Subjected to Large Deformation

Hong He , Rong Zhou , Yuanwen Zou , Xuejin Huang, and Jinchuan Li
Research Article (10 pages), Article ID 8504273, Volume 2018 (2018)

An Approach to Developing Customized Total Knee Replacement Implants

Xinyu Li, Changjiang Wang, Yuan Guo, and Weiyi Chen
Research Article (8 pages), Article ID 9298061, Volume 2017 (2018)

Design and Interaction Control of a New Bilateral Upper-Limb Rehabilitation Device

Qing Miao, Mingming Zhang, Yupu Wang, and Sheng Q. Xie
Research Article (9 pages), Article ID 7640325, Volume 2017 (2018)

A Feasibility Study of SSVEP-Based Passive Training on an Ankle Rehabilitation Robot

Xiangfeng Zeng, Guoli Zhu, Lan Yue, Mingming Zhang, and Shane Xie
Research Article (9 pages), Article ID 6819056, Volume 2017 (2018)

Effect on Chest Deformation of Simultaneous Correction of Pectus Excavatum with Scoliosis

Jin-Duo Ye, Guang-Pu Lu, Jing-Jing Feng, and Wei-Hong Zhong
Research Article (10 pages), Article ID 8318694, Volume 2017 (2018)

Static Progressive Orthoses for Elbow Contracture: A Systematic Review

Bin Chen, Jianhua Lin, Lifen Liu, and Wenxin Niu

Review Article (8 pages), Article ID 7498094, Volume 2017 (2018)

The Effects of Physiological Biomechanical Loading on Intradiscal Pressure and Annulus Stress in Lumbar Spine: A Finite Element Analysis

Siti Nurfaezah Zahari, Mohd Juzaila Abd Latif, Nor Raihanah Abdull Rahim, Mohammed Rafiq Abdul Kadir, and Tunku Kamarul

Research Article (8 pages), Article ID 9618940, Volume 2017 (2018)

The Influence of Natural Head Position on the Cervical Sagittal Alignment

Kuan Wang, Zhen Deng, Zhengyan Li, Huihao Wang, and Hongsheng Zhan

Research Article (7 pages), Article ID 2941048, Volume 2017 (2018)

Novel Passive Two-Stage Magnetic Targeting Devices for Distal Locking of Interlocking Nails

Tze-Hong Wong, Meng-Shiue Lee, Sung-Yueh Wu, Wensyang Hsu, Tien-Kan Chung, Chia-Pei Wu, Pei-Jung Hsu, and Yuh-Shyong Yang

Research Article (11 pages), Article ID 3619403, Volume 2017 (2018)

Hollow Abutment Screw Design for Easy Retrieval in Case of Screw Fracture in Dental Implant System

Bo Kyun Sim, Bongju Kim, Min Jeong Kim, Guk Hyun Jeong, Kyung Won Ju, Yoo Jin Shin, Man Yong Kim, and Jong-Ho Lee

Research Article (6 pages), Article ID 4842072, Volume 2017 (2018)

Antagonist Muscle Prefatigue Increases the Intracortical Communication between Contralateral Motor Cortices during Elbow Extension Contraction

Lejun Wang, Aidi Ma, Yuting Wang, Songhui You, and Aiyun Lu

Research Article (6 pages), Article ID 8121976, Volume 2017 (2018)

Morphological and Microstructural Alterations of the Articular Cartilage and Bones during Treadmill Exercises with Different Additional Weight-Bearing Levels

Jiazi Gao, Juan Fang, He Gong, and Bingzhao Gao

Research Article (8 pages), Article ID 8696921, Volume 2017 (2018)

Biomechanical Effects of Various Bone-Implant Interfaces on the Stability of Orthodontic Miniscrews: A Finite Element Study

Fabing Tan, Chao Wang, Chongshi Yang, Yuanding Huang, and Yubo Fan

Research Article (10 pages), Article ID 7495606, Volume 2017 (2018)

Development and Implementation of an End-Effector Upper Limb Rehabilitation Robot for Hemiplegic Patients with Line and Circle Tracking Training

Yali Liu, Chong Li, Linhong Ji, Sheng Bi, Xuemin Zhang, Jianfei Huo, and Run Ji

Research Article (11 pages), Article ID 4931217, Volume 2017 (2018)

The Effect of Arch Height and Material Hardness of Personalized Insole on Correction and Tissues of Flatfoot

Shonglun Su, Zhongjun Mo, Junchao Guo, and Yubo Fan
Research Article (9 pages), Article ID 8614341, Volume 2017 (2018)

Experimental Study on the Mechanical Properties of Porcine Cartilage with Microdefect under Rolling Load

Yu-tao Men, Xiao-ming Li, Ling Chen, and Hu Fu
Research Article (9 pages), Article ID 2306160, Volume 2017 (2018)

User-Centric Feedback for the Development and Review of a Unique Robotic Glove Prototype to Be Used in Therapy

Stuart James Biggar, Wei Yao, Lizhen Wang, and Yubo Fan
Research Article (8 pages), Article ID 3896089, Volume 2017 (2018)

Effects of Scan Resolutions and Element Sizes on Bovine Vertebral Mechanical Parameters from Quantitative Computed Tomography-Based Finite Element Analysis

Meng Zhang, Jiazi Gao, Xu Huang, He Gong, Min Zhang, and Bei Liu
Research Article (14 pages), Article ID 5707568, Volume 2017 (2018)

Comparison of Morphologic Parameters of Temporomandibular Joint for Asymptomatic Subjects Using the Two-Dimensional and Three-Dimensional Measuring Methods

Yuanli Zhang, Xianchao Xu, and Zhan Liu
Research Article (8 pages), Article ID 5680708, Volume 2017 (2018)

Editorial

Biomechanics and Bioengineering of Orthopedic and Cardiovascular Rehabilitation

Lizhen Wang ¹, Chia-Ying Lin,^{2,3,4} Wei Yao ⁵, Duo Wai-Chi Wong ⁶ and Rui Zhu ⁷

¹Key Laboratory for Biomechanics and Mechanobiology of Ministry of Education, School of Biological Science and Medical Engineering, Beijing Advanced Innovation Centre for Biomedical Engineering, Beihang University, Beijing, China

²Department of Biomedical, Chemical & Environmental Engineering, University of Cincinnati, Cincinnati, OH, USA

³Department of Orthopaedic Surgery, University of Cincinnati, Cincinnati, OH, USA

⁴Department of Neurosurgery, University of Cincinnati, Cincinnati, OH, USA

⁵Department of Biomedical Engineering, University of Strathclyde, Glasgow, UK

⁶Department of Biomedical Engineering, Faculty of Engineering, The Hong Kong Polytechnic University, Kowloon, Hong Kong, China

⁷Spine Division of Orthopaedic Department, Tongji Hospital, Tongji University School of Medicine, Shanghai, China

Correspondence should be addressed to Lizhen Wang; lizhenwang@buaa.edu.cn

Received 12 July 2018; Accepted 12 July 2018; Published 19 August 2018

Copyright © 2018 Lizhen Wang et al. This is an open access article distributed under the Creative Commons Attribution License, which permits unrestricted use, distribution, and reproduction in any medium, provided the original work is properly cited.

Musculoskeletal problem, such as traumatic injury, osteoporosis, and osteoarthritis, is one of the leading causes of disability worldwide and is therefore a crucial branch of public health. Biomechanics has been proven to play a critical role in musculoskeletal pathology, treatment, and rehabilitation. Rehabilitation describes specialized healthcare dedicated to improving, maintaining, or restoring physiological strength, cognition, and mobility with maximized results. It helps an individual achieve the highest level of function or greatest independence and quality of life possible after illness, injury, or surgery using physical training, instruments, devices, or other methods. Advances in rehabilitation, including the theory, paradigm, protocol, modality, invention, and engineering, can improve the development of modern medicine and also the quality of life especially for the disabled and elderly people. The main focus of this special issue is on innovative theory and application of biomechanics to understand musculoskeletal pathology and to improve the techniques for the treatment and rehabilitation.

As the variety of topics presented in this special issue suggests, there are still many difficulties related to the mechanism of human injury and its rehabilitation and invention or development of the rehabilitation device. M. Zhang et al.

explored the effects of scan resolutions and element sizes on QCT/FEA outcomes. They showed scan resolution and element size should be chosen optimally to improve the accuracy of QCT/FEA. To characterize treadmill exercise, N. Guo et al. calculated muscle forces in full gait cycle by inverse dynamic analysis. They found the constraint loading mode had an impact on the muscle forces in treadmill exercise, thus could be manipulated to enhance the effect of the muscle training in spaceflight. J. Gao et al. concluded that effects of treadmill exercise on joints may be associated with different additional weight-bearing levels, and exercise intensities during joint growth and maturation should be selected reasonably. Some new cutting-edge technologies such as robotics, wear devices, and Artificial Intelligence have been applied for the treatment and rehabilitation. S. J. Biggar et al. have developed and evaluated a wearable robotic glove for hand rehabilitation. Regarding the effect of design parameters of personalized orthopedic insole, S. Su et al. showed insole material and support design is positively affecting the correction of orthopedic insole, but negatively resulting unreasonable stress on the stress in the joint and ligaments.

Rehabilitation to stroke patients has been constantly receiving close review. Two research teams came up with cutting edge rehabilitation devices for stroke patients to

regain, respectively, upper and lower limb motor functions. Q. Miao and colleagues designed a compact and user-friendly robotic exoskeleton for upper limb rehabilitation, which featured a real-time kinematic and dynamic-based system, and allowed both passive and interactive training. Their study demonstrated satisfactory positioning as well as force tracking performance and will head for field study for poststroke patients. Besides, X. Zeng et al. integrated the motion intention of stroke patients via steady-state visual evoked potential with virtual reality technology to develop a rehabilitation robot for the ankle joint. The motion intention-directed passive training was conducted on five subjects with a high success rate. The strategy enabled active engagement for subjects without the ability to conduct active training.

The complex interactions between neuromuscular pre-fatigue and brain control were investigated by L. Wang and colleagues. The research team induced antagonist muscle pre-fatigue by isometric elbow flexion. The influence of the fatigue on the cortico-cortical coupling and central modulation was assessed through the technique of EEG-EEG phase synchronization index. Their findings revealed an enhanced intracortical signal which could be an indication for the compensation for the pre-fatigued-induced joint instability. On the other contrary, Y. Men et al. concerned the microdefect behavior of articular cartilage which implicates the problem of osteoarthritis. Precisely, Y. Men et al. applied a rolling load on porcine articular cartilage and observed the strain of the samples. They identified that the shear strain could be the main factor in cartilage destruction, while rolling velocity also played an important role on the destruction of the superficial and middle layers.

Furthermore, recent criteria for orthopedic and cardiovascular rehabilitation affect not only the diagnosis but also the treatment and possibly involves the innovation of supportive or protective devices. This is the reason why, not only will future research focus on mechanism and criteria but also it will increasingly include therapies with rehabilitation and its effects.

*Lizhen Wang
Chia-Ying Lin
Wei Yao
Duo Wai-Chi Wong
Rui Zhu*

Research Article

Effect of Dropping Height on the Forces of Lower Extremity Joints and Muscles during Landing: A Musculoskeletal Modeling

Wenxin Niu ^{1,2}, Lejun Wang ³, Chenghua Jiang² and Ming Zhang ⁴

¹Yangzhi Rehabilitation Hospital, Shanghai Sunshine Rehabilitation Centre, Tongji University School of Medicine, Shanghai 201619, China

²Department of Rehabilitation Sciences, Tongji University School of Medicine, Shanghai 201619, China

³Sport and Health Research Center, Physical Education Department, Tongji University, Shanghai 200092, China

⁴Department of Biomedical Engineering, The Hong Kong Polytechnic University, Hong Kong

Correspondence should be addressed to Wenxin Niu; niu@tongji.edu.cn and Lejun Wang; wlj0523@163.com

Received 26 July 2017; Revised 18 March 2018; Accepted 10 May 2018; Published 2 July 2018

Academic Editor: John S. Katsanis

Copyright © 2018 Wenxin Niu et al. This is an open access article distributed under the Creative Commons Attribution License, which permits unrestricted use, distribution, and reproduction in any medium, provided the original work is properly cited.

The objective of this study was to investigate the effect of dropping height on the forces of joints and muscles in lower extremities during landing. A total of 10 adult subjects were required to land from three different heights (32 cm, 52 cm, and 72 cm), and the ground reaction force and kinematics of lower extremities were measured. Then, the experimental data were input into the AnyBody Modeling System, in which software the musculoskeletal system of each subject was modeled. The reverse dynamic analysis was done to calculate the joint and muscle forces for each landing trial, and the effect of dropping-landing on the results was evaluated. The computational simulation showed that, with increasing of dropping height, the vertical forces of all the hip, knee, and ankle joints, and the forces of rectus femoris, gluteus maximus, gluteus medius, vastii, biceps femoris and adductor magnus were all significantly increased. The increased dropping height also resulted in earlier activation of the iliopsoas, rectus femoris, gluteus medius, gluteus minimus, and soleus, but latter activation of the tibialis anterior. The quantitative joint and muscle forces can be used as loading conditions in finite element analysis to calculate stress and strain and energy absorption processes in various tissues of the lower limbs.

1. Introduction

Landing is a common and important form of movement that is necessary in a variety of sports, dancing, and special occupations [1–5]. Landing is also very easy to cause injuries, especially on the lower limbs. About 49%–52% of the injuries in gymnastics training occur during the landing phase [1, 2]. The reasonable protection of landing injuries, as well as the clinical treatment and rehabilitation of patients after injury, requires a scientific understanding of the landing injuries.

Traditionally, some people thought that greater ground reaction force (GRF) or shorter time to peak vertical GRF (TPvGRF) would be more likely to incur damage [5, 6]. We found that, compared to women, men had significantly higher vGRF and rate of loading (ROL, i.e., vGRF/TPvGRF) [7–10]. In accordance with the above traditional notion, the

phenomenon of women more prone to landing injuries could not be explained [11, 12]. Based on previous studies, we concluded that (1) the relationship between the ankle joint activity and the risk of injury was insignificant, while the joint angular velocity is positively related to the risk of injury [7, 8, 13]; (2) compared with women, men were more adept at using the ankle dorsiflexor and had better explosive strength and cocontraction of the ankle plantarflexor and dorsiflexor, and then, these factors induced the higher injury rate for women [8, 9]; and (3) the ankle brace significantly improved GRF and the muscle forces and enhanced the proprioception of the lower limbs [9, 10]. During landing, if the joint range of motion (ROM) was controlled within the tolerance range through muscle forces, more kinetic energy would be converted through increasing GRF to avoid excessive joint motions. This mainly reflects the relationship of



FIGURE 1: A female subject was in the trial: (a) jumping; (b) prelanding; (c) postlanding.

muscle force, GRF, and joint kinematics. Therefore, the influence of muscle force must be considered in the research of landing biomechanics.

Electromyography (EMG) has been commonly used to reflect the muscle activity [7–9, 14, 15]. However, due to many influential factors, it is hard to accurately get the muscle force and torque based on EMG measurement. In recent years, the rapid development of computer technology brought about reverse dynamic analysis to a complex computational musculoskeletal model [16–18]. This provides a reasonable way for us to calculate muscle forces accurately.

Therefore, the purpose of this study was to evaluate effects of dropping height on muscle forces and force of the lower limb joints during landing using a computational musculoskeletal model and experimental data.

2. Materials and Methods

Based on our previous data [4, 7–9], a power analysis revealed that to achieve 80% statistical power, with an exploratory α level of 0.05, a minimum of 10 subjects were required. Thus, 10 subjects (6 women and 4 men) were recruited for this study. Their mean \pm SD age was 23.8 ± 3.9 years, and the height and body mass were 165 ± 5 cm and 57.8 ± 8.5 kg, respectively. All subjects were right-leg dominant, which was determined individually by asking which one leg they would use to kick a ball as far as possible [7]. All subjects were physically active and had never experienced surgery, had no trauma and neurological dysfunction at least 6 months before the test, and were free from any trouble with inner ear problems, vision, neuromuscular dysfunction, or any orthopedic conditions. All

subjects signed the University-approved informed consent before participating.

The subjects jumped from three different heights (32 cm, 52 cm, and 72 cm) and landed on a force plate (FP4060-08, Bertec Corp, Columbus, OH) with a half-squatting posture (Figure 1). These heights were determined according to our previous studies [4, 7–9, 13] and a study by McNitt-Gray [19]. The landing posture was also defined elsewhere as a simulated parachute landing in China [8, 9]. The subjects were instructed to takeoff and touch down with both feet, to lean forward with body at takeoff, to make a half-squatting posture with foot contact, and finally to break the fall smoothly. The trial order was random to avoid the order effect on the results.

The GRF data in three directions were collected at a sampling frequency of 1000 Hz. An Optotrak Certus motion capture system (Northern Digital Inc., Waterloo, Canada) was used to measure the limb kinematics during landing. Each body segment was registered using a plate with 4 noncollinear LED markers, which was tightly attached to the corresponding segment [8, 9]. These markers were captured, and the kinematic data were then analyzed using Visual3D (C-Motion Inc., Rockville, MD). The processed signals were synchronized by an analog-to-digital converter.

The anthropometric data (body weight, body height, pelvis width, thigh, shanks, and foot length) were measured from each subject and then were used to construct the musculoskeletal model in the AnyBody Modeling System version 5.0 (AnyBody Technology A/S, Aalborg, Denmark) [20]. The model was developed from the Twente Lower Extremity Model (TLEM) in AnyBody Managed Model

Repository [21]. This model is based on a comprehensive and consistent data set from one donor [22]. According to our anthropometric measurement, the model was then scaled with a mass-fat scaling algorithm to simulate each individual. The AnyBody Modeling System and the musculo-skeletal model have been validated to be useful for analyzing human movement [20]. The main input of the modeling is the kinematic and GRF data from the subjects while landing. The GRF was filtered using a Woltring filter that does not affect the timing and hardly affects the amplitude.

The inverse dynamic analysis calculated the force of each muscle bundle and the lower limb joints. Because the force directions were similar for the bundles in the same muscle, we combined them all for simplifying the analysis. The calculated forces of the hip, knee, and ankle joints were normalized to the body weight (BW) of each subject. The effect of dropping height on these force values was evaluated using the univariate analysis of variance (ANOVA) and Turkey's HSD post hoc analysis. The statistical analysis confidence interval was 95%, and the statistical analysis was performed using the free data analysis system VassarStats (<http://vassarstats.net/>) [8, 9].

3. Results and Discussion

3.1. GRF and Joint Force. As a critical factor during landing, the dropping height greatly affects the landing speed. When landing from three different heights of 32 cm, 52 cm, and 72 cm, the performer at initial contact had the average speed of 2.1 m/s, 2.3 m/s, and 3.0 m/s, respectively, with significant statistical differences ($P < 0.001$). As shown in Figure 2, with increase of the dropping height, peak vGRF increased significantly ($P < 0.001$).

We have found a linear relationship between the peak vGRF and root dropping height [10]. In the present study, we found that, with the increase of the dropping height, the GRF peak increased significantly in the vertical and anterior-posterior (A-P) directions, but the dropping height has no significant influence on the peak medial-lateral (M-L) GRF peak, TPvGRF, or ROL. This is consistent with the finding by Yeow et al. [23].

Effects of dropping height on GRF were further reflected in the similar effects on the contact force of lower limb joints. This would lead to injury risk of these joints during high-speed landing. As listed in Table 1, with increasing of the dropping height, the vertical force of each joint significantly increased. The influence of dropping height on the ankle joint in any horizontal direction was not significant. Though no significant influence was found in the dropping height on the knee joint force in the A-P direction, the force in the M-L direction was significantly higher while landing from higher positions. We also found significant influences of the dropping height on the force of the hip joint in all three directions.

This study showed that the force peaks of the ankle joint and the hip joint could reach more than 20 BW when subjects landed from 72 cm height. If the dropping height was even increased, higher joint force may lead to injuries. Therefore, the high peak joint force was reasonable in the current study. When subjects landed from low and medium

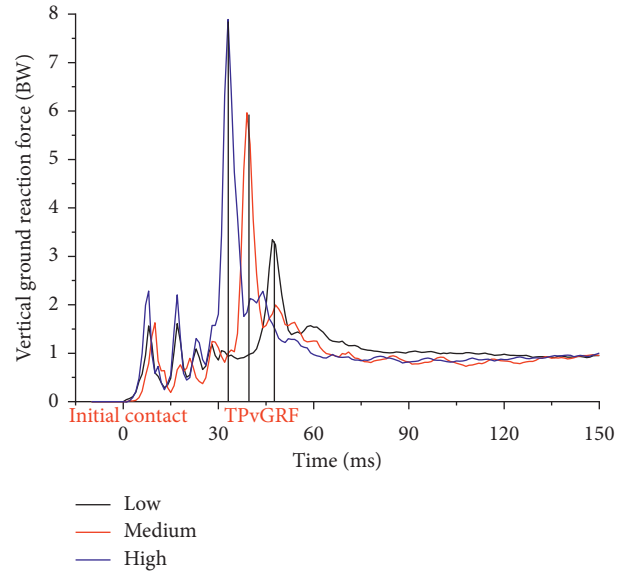


FIGURE 2: Vertical ground reaction forces when a representative subject landed from three different heights.

TABLE 1: Effects of dropping height on the forces of the ankle, knee, and hip joints (unit: body weight, BW).

Joint	Direction	Low (32 cm)	Medium (52 cm)	High (72 cm)	<i>F</i>	<i>P</i>
Ankle	Vertical	16.95 ± 2.59	18.88 ± 3.46	23.98 ± 4.21	8.815	<0.001
	A-P	4.87 ± 0.96	5.19 ± 1.04	5.18 ± 1.11	1.562	0.252
	M-L	4.17 ± 0.88	4.23 ± 1.06	5.83 ± 0.96	2.204	0.147
	Vertical	9.09 ± 2.09	11.5 ± 2.26	14.58 ± 2.17	6.895	0.004
Knee	A-P	2.86 ± 0.74	5.23 ± 1.09	4.98 ± 1.32	1.785	0.204
	M-L	0.72 ± 0.31	0.75 ± 0.24	0.88 ± 0.32	7.307	0.007
	Vertical	8.50 ± 2.53	9.49 ± 2.68	22.81 ± 4.69	10.208	<0.001
Hip	A-P	3.49 ± 1.15	4.08 ± 1.68	11.9 ± 2.96	8.024	0.003
	M-L	3.74 ± 0.69	4.76 ± 1.12	12.56 ± 3.36	8.749	0.004
	Vertical	8.50 ± 2.53	9.49 ± 2.68	22.81 ± 4.69	10.208	<0.001

A-P: anterior-posterior; M-L: medial-lateral.

heights, from the ankle to the knee and the hip joints, the peak forces in the vertical direction declined. However, when subjects landed from 72 cm height, the vertical force peak of the hip joint was significantly higher than that of the knee joint. It may be caused by higher muscle force of gluteus during landing from higher level.

3.2. Muscle Force. Because the joint force is directly related to the joint torque and the muscle force, the effect of the dropping height on the joint force is further reflected in the force of each muscle. In the current study, the same subject had similar musculation pattern even while landing from

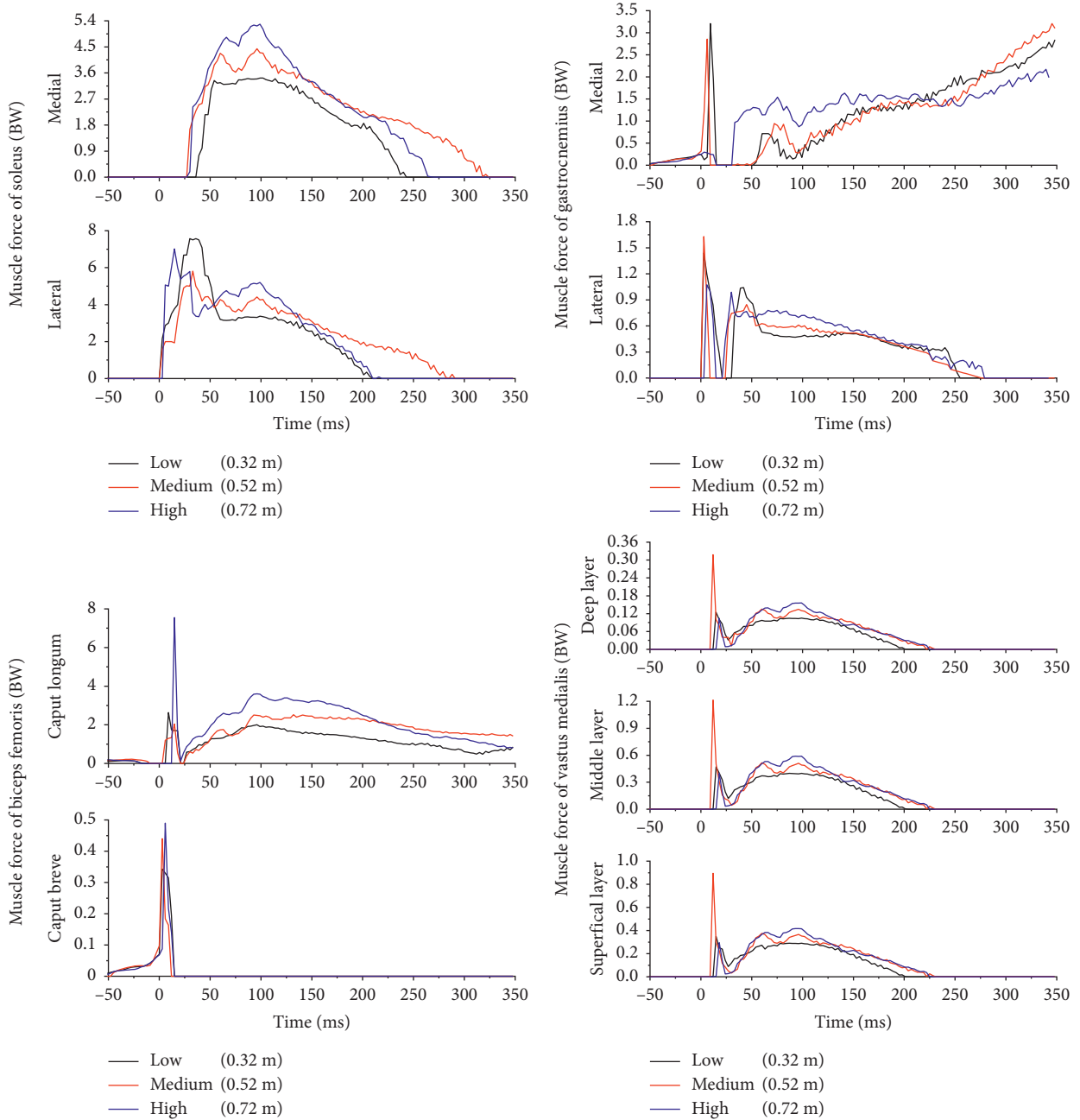


FIGURE 3: Continued.

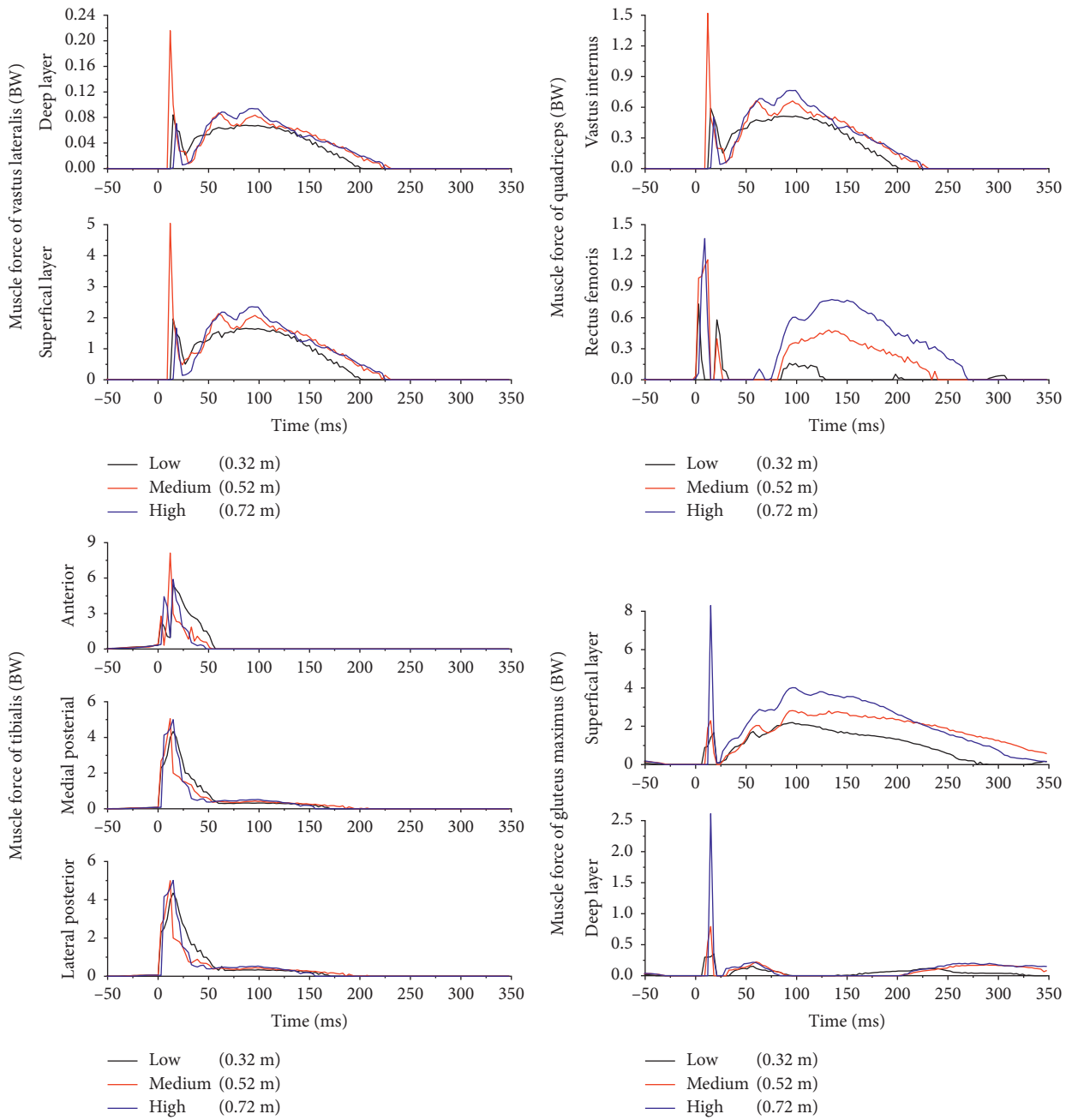


FIGURE 3: Continued.

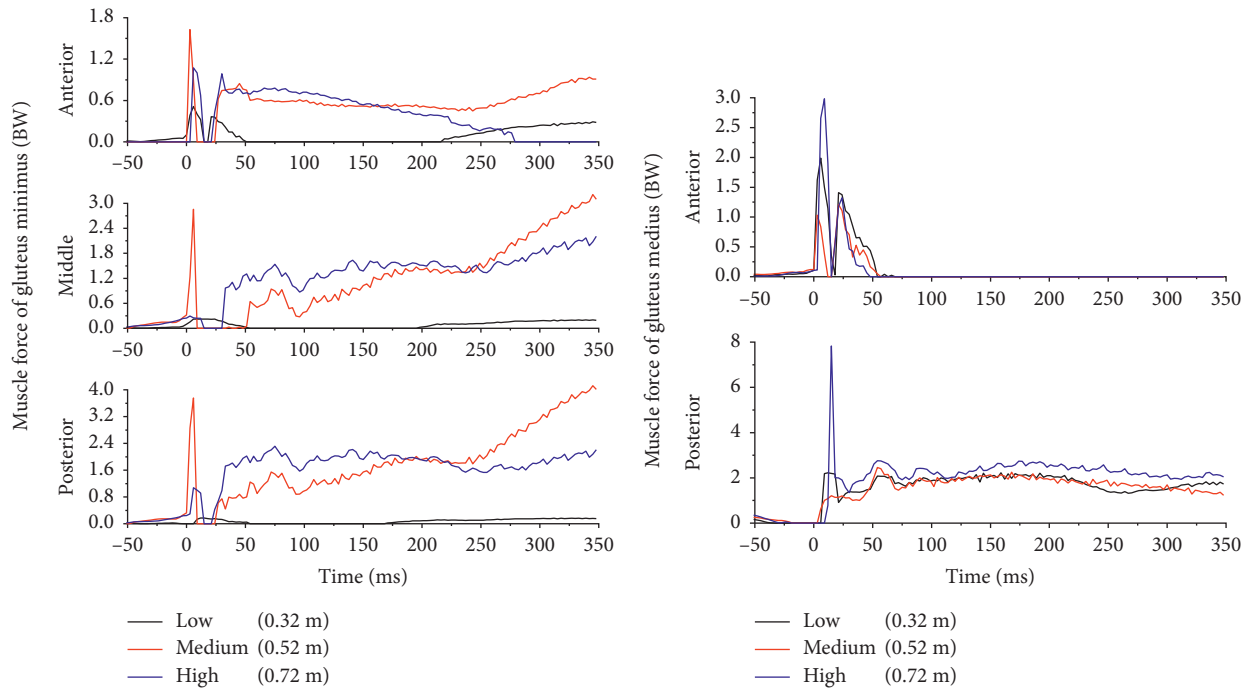


FIGURE 3: Forces of leg muscles when a representative subject landed from three different heights.

different heights, but certain difference of the sequence of muscle activation existed among different subjects.

Figure 3 showed the muscle activation of a representative subject landing from three heights. The peak forces of main muscles were statistically analyzed and shown in Table 2. With increasing of dropping height, the peak forces increased for most muscles in the lower limb, in which the rectus femoris (RF), GMax, gluteus medius (GMed), vastii, biceps femoris (BF), and adductor magnus all showed significant changes.

The increased dropping height also resulted in earlier activation of the iliopsoas, RF, GMed, gluteus minimus (GMin), and SOL, but latter activation of the tibialis anterior (TA). In addition, when subjects landed from higher positions, the time from initial contact to peak force of RF and SOL was significantly longer. The longer the duration of muscle activity, the longer and more durable the muscle force used to counter the impact.

As seen in Figure 1, we divided the entire landing process into three phases. Because the researcher instructed subjects not to jump higher than their initial level, the timing and amplitude of each muscle had consistent activity pattern and amplitude. The flying phase can also be called as the pre-landing phase, while the last phase can be called the post-landing phase. Some studies showed that, with increasing of dropping height, the EMG onset latency and duration would be longer in TA, soleus (SOL), RF, and BF, but the pre-landing EMG duration was less affected by the change of the dropping height [24, 25]. Our previous study also showed the similar phenomenon in TA and gastrocnemius (Gast) [7–9]. Because the landing is a high-intensity impact action, the requirement for muscle energy is high. Even during

a lower height landing, the muscle will be prepared with enough time. If the dropping height was increased, the accumulation of muscle power is not through the duration, but through the activity amplitude.

The calculated results showed that, with increasing dropping height, the maximum force of TA increased, but there was no significant difference between different heights. This was consistent with the experimental results. This also showed that ankle plantarflexor has a more important role on the landing movement than the dorsiflexor. In addition, the force of triceps muscle was up to 10 BW level and had a main role in changing the mechanics of the shank.

As for the effects of dropping height on the knee flexors and extensors, various experimental studies gave different findings [26–29]. This study showed that the knee flexors and extensors were all significantly activated to maintain the balance of the knee joint. As a result, when the dropping height was higher, the compressive force of the knee joint also increased because the larger muscle forces provided additional loads.

During landing, the muscle contraction mode is very complex, and the forces of some muscles or muscle groups are even beyond the level of ground reaction force. Because these muscle forces would be loaded on the skeleton around joints, they may have great impact on the stress or strain of bone and cartilage, energy absorption, and transmission in the lower limbs. Some authors have tried to get these data using finite element analysis [30], but it is necessary to understand the muscle contraction mode and force before modeling of local joints or organs. This study could provide more precise loading conditions for future finite element simulation of any phase of a typical landing movement.

TABLE 2: Effects of dropping height on the peak forces of main muscles in the lower limbs (unit: body weight, BW).

Muscles	Low (32 cm)	Medium (52 cm)	High (72 cm)	F	P
Gastrocnemius	5.3 ± 1.6	5.8 ± 1.7	5.5 ± 2.0	0.21	0.812
Soleus	9.9 ± 3.0	10.6 ± 3.7	11.8 ± 3.8	0.75	0.482
Tibialis posterior	4.1 ± 1.7	4.8 ± 2.5	3.5 ± 1.6	1.09	0.351
Tibialis anterior	7.2 ± 1.5	7.6 ± 1.7	7.6 ± 1.8	0.19	0.828
Biceps femoris	3.3 ± 1.2	4.0 ± 1.1	5.6 ± 1.9	6.75	0.004
Rectus femoris	0.5 ± 0.2	0.7 ± 0.3	1.0 ± 0.4	5.14	0.013
Vastus medialis	0.7 ± 0.2	0.9 ± 0.3	1.0 ± 0.3	4.99	0.014
Vastus lateralis	1.7 ± 0.5	2.7 ± 0.9	3.2 ± 1.1	7.84	0.002
Vastus internus	0.4 ± 0.1	0.7 ± 0.2	0.8 ± 0.3	6.36	0.005
Gluteus maximus	2.5 ± 0.8	5.1 ± 2.6	9.7 ± 2.5	28.78	<0.0001
Gluteus medius	3.8 ± 1.3	3.6 ± 1.6	8.5 ± 2.5	21.97	<0.0001
Gluteus minimus	0.7 ± 0.3	1.9 ± 0.9	2.8 ± 0.8	21.59	<0.0001
Iliacus	1.3 ± 0.4	1.4 ± 0.6	1.3 ± 0.5	0.40	0.67
Adductor magnus	1.6 ± 0.5	1.8 ± 0.6	2.8 ± 0.7	11.00	<0.001

4. Conclusion

Based on the experimental data, the inverse dynamic model of the human musculoskeletal system was established in this study. The force of the lower limb joints and the muscle groups was calculated while the subjects landed to evaluate the effects of dropping height on these parameters. The quantitative joint and muscle forces can be used as loading conditions in finite element analysis to calculate stress and strain and energy absorption processes in various tissues of the lower limbs. This would be useful for further understanding of the injury mechanism during landing.

Conflicts of Interest

The authors declare that there are no conflicts of interest regarding the publication of this paper.

Acknowledgments

This work was supported by the National Natural Science Foundation of China (Grant nos. 11732015 and 11672211) and the Fundamental Research Funds for the Central Universities.

References

- [1] J. W. O’Kane, M. R. Levy, K. E. Pietila, D. J. Caine, and M. A. Schiff, “Survey of injuries in Seattle area levels 4 to 10 female club gymnasts,” *Clinical Journal of Sport Medicine*, vol. 21, no. 6, pp. 486–492, 2011.
- [2] M. L. Harringe, P. Restom, and S. Werner, “Injury incidence, mechanism and diagnosis in top-level teamgym: a prospective study conducted over one season,” *Scandinavian Journal of Medicine & Science in Sports*, vol. 17, no. 2, pp. 115–119, 2007.
- [3] R. Xia, X. Zhang, X. Wang, X. Sun, and W. Fu, “Effects of two fatigue protocols on impact forces and lower extremity kinematics during drop landings: implications for non-contact anterior cruciate ligament injury,” *Journal of Healthcare Engineering*, vol. 2017, Article ID 5690519, 8 pages, 2017.
- [4] W. X. Niu, M. Zhang, Y. B. Fan, and Q. P. Zhao, “Dynamic postural stability for double-leg drop landing,” *Journal of Sports Sciences*, vol. 31, no. 10, pp. 1074–1081, 2013.
- [5] J. W. Whitting, J. R. Steele, M. Jaffrey, and B. J. Bunro, “Does foot pitch at ground contact affect parachute landing technique?,” *Military Medicine*, vol. 174, no. 8, pp. 832–837, 2009.
- [6] I. Janssen, J. M. Sheppard, A. A. Dingley, D. W. Chapman, and W. Spratford, “Lower extremity kinematics and kinetics when landing from unloaded and loaded jumps,” *Journal of Applied Biomechanics*, vol. 28, no. 6, pp. 687–693, 2012.
- [7] W. X. Niu, Y. Wang, Y. He, Y. B. Fan, and Q. P. Zhao, “Kinematics, kinetics, and electromyogram of ankle during drop landing: a comparison between dominant and non-dominant limb,” *Human Movement Science*, vol. 30, no. 3, pp. 614–623, 2011.
- [8] W. X. Niu, Y. Wang, Y. He, Y. B. Fan, and Q. P. Zhao, “Biomechanical gender differences of the ankle joint during simulated half-squat parachute landing,” *Aviation, Space, and Environmental Medicine*, vol. 81, no. 8, pp. 761–767, 2010.
- [9] W. X. Niu, Y. Wang, J. Yao, M. Zhang, Y. B. Fan, and Q. P. Zhao, “Consideration of gender differences in ankle stabilizer selection for half-squat parachute landing,” *Aviation, Space, and Environmental Medicine*, vol. 82, no. 12, pp. 1118–1124, 2011.
- [10] W. X. Niu, T. A. Feng, C. H. Jiang, and M. Zhang, “Peak vertical ground reaction force during two-leg landing: a systematic review and mathematical modeling,” *BioMed Research International*, vol. 2014, Article ID 126860, 10 pages, 2014.
- [11] E. Arendt and R. Dick, “Knee injury patterns among men and women in collegiate basketball and soccer: NCAA data and review of literature,” *American Journal of Sports Medicine*, vol. 23, no. 6, pp. 694–701, 1995.
- [12] A. Ekeland, “Injuries in military parachuting: a prospective study of 4499 jumps,” *Injury*, vol. 28, no. 3, pp. 219–222, 1997.
- [13] W. X. Niu and Y. B. Fan, “Terrain stiffness and ankle biomechanics during simulated half-squat parachute landing,” *Aviation, Space, and Environmental Medicine*, vol. 84, no. 12, pp. 1262–1267, 2013.
- [14] L. C. Tsai, S. McLean, P. M. Colletti, and C. M. Powers, “Greater muscle co-contraction results in increased tibiofemoral compressive forces in females who have undergone anterior cruciate ligament reconstruction,” *Journal of Orthopaedic Research*, vol. 30, no. 12, pp. 2007–2014, 2012.
- [15] L. C. Tsai and C. M. Powers, “Increased hip and knee flexion during landing decreases tibiofemoral compressive forces in women who have undergone anterior cruciate ligament reconstruction,” *American Journal of Sports Medicine*, vol. 41, no. 2, pp. 423–429, 2013.
- [16] N. Ali, M. S. Andersen, J. Rasmussen, D. G. Robertson, and G. Rouhi, “The application of musculoskeletal modeling to investigate gender bias in non-contact ACL injury rate during single-leg landings,” *Computer Methods in Biomechanics and Biomedical Engineering*, vol. 17, no. 14, pp. 1602–1616, 2014.
- [17] M. Adouni, A. Shirazi-Adl, and H. Marouane, “Role of gastrocnemius activation in knee joint biomechanics: gastrocnemius acts as an ACL antagonist,” *Computer Methods in*

- Biomechanics and Biomedical Engineering*, vol. 19, no. 4, pp. 376–385, 2016.
- [18] K. T. Kang, Y. G. Koh, M. Jung et al., “The effects of posterior cruciate ligament deficiency on posterolateral corner structures under gait- and squat-loading conditions,” *Bone and Joint Research*, vol. 6, no. 1, pp. 31–42, 2017.
- [19] J. L. McNitt-Gray, “Kinetics of the lower extremities during drop landings from three heights,” *Journal of Biomechanics*, vol. 26, no. 9, pp. 1037–1046, 1993.
- [20] M. Damsgaard, J. Rasmussen, S. T. Christensen, E. Christensen, E. Surma, and M. de Zee, “Analysis of musculoskeletal systems in the AnyBody Modeling System,” *Simulation Modelling Practice and Theory*, vol. 14, no. 8, pp. 1100–1111, 2006.
- [21] V. Carbone, R. Fluit, P. Pellikaan et al., “TLEM 2.0—a comprehensive musculoskeletal geometry dataset for subject-specific modeling of lower extremity,” *Journal of Biomechanics*, vol. 48, no. 5, pp. 734–741, 2015.
- [22] M. D. Klein Horsman, H. F. Koopman, F. C. van der Helm, L. P. Prosé, and H. E. Veeger, “Morphological muscle and joint parameters for musculoskeletal modelling of the lower extremity,” *Clinical Biomechanics*, vol. 22, no. 2, pp. 239–247, 2007.
- [23] C. H. Yeow, S. K. Rubab, P. V. S. Lee, and J. C. Goh, “Inhibition of anterior tibial translation or axial tibial rotation prevents anterior cruciate ligament failure during impact compression,” *American Journal of Sports Medicine*, vol. 37, no. 4, pp. 813–821, 2009.
- [24] M. Santello, M. J. McDonagh, and J. H. Challis, “Visual and non-visual control of landing movements in humans,” *Journal of Physiology*, vol. 537, no. 1, pp. 313–327, 2001.
- [25] M. Santello and M. J. McDonagh, “The control of timing and amplitude of EMG activity in landing movements in humans,” *Experimental Physiology*, vol. 83, no. 6, pp. 857–874, 1998.
- [26] S. Lee, J. Chang, and Y. Choi, “Low limb muscle activation and joint angle in the sagittal plane during drop landing from various heights,” *Journal of Physical Therapy Science*, vol. 23, no. 2, pp. 303–305, 2011.
- [27] J. S. Chang, Y. H. Kwon, C. S. Kim, S. H. Ahn, and S. H. Park, “Differences of ground reaction forces and kinematics of lower extremity according to landing height between flat and normal feet,” *Journal of Back and Musculoskeletal Rehabilitation*, vol. 25, no. 1, pp. 21–26, 2012.
- [28] H. T. Peng, “Changes in biomechanical properties during drop jumps of incremental height,” *Journal of Strength & Conditioning Research*, vol. 25, no. 9, pp. 2510–2518, 2011.
- [29] K. R. Ford, G. D. Myer, L. C. Schmitt, T. L. Uhl, and T. E. Hewett, “Preferential quadriceps activation in female athletes with incremental increases,” *Journal of Applied Biomechanics*, vol. 27, no. 3, pp. 215–222, 2011.
- [30] D. W. C. Wong, W. X. Niu, Y. Wang, and M. Zhang, “Finite element analysis of foot and ankle impact injury: risk evaluation of calcaneus and talus fracture,” *PloS One*, vol. 11, no. 4, Article ID e0154435, 2016.

Research Article

Analysis of Bone Mineral Density/Content of Paratroopers and Hoopsters

Yixue Luo,^{1,2} Chenyu Luo,^{1,2} Yuhui Cai,^{1,2} Tianyun Jiang,^{1,2} Tianhong Chen,^{1,2}
Wenyue Xiao,^{1,2} Junchao Guo,³ and Yubo Fan ^{1,2,3}

¹Key Laboratory for Biomechanics and Mechanobiology of Ministry of Education, Beijing Advanced Innovation Centre for Biomedical Engineering, School of Biological Science and Medical Engineering, Beihang University, Beijing 100191, China

²Beijing Advanced Innovation Centre for Biomedical Engineering, Beihang University, Beijing 102402, China

³Beijing Key Laboratory of Rehabilitation Technical Aids for Old-Age Disability, Key Laboratory of Technical Aids Analysis and Identification Key Laboratory of Ministry of Civil Affairs, National Research Centre for Rehabilitation Technical Aids, Beijing 100176, China

Correspondence should be addressed to Yubo Fan; yubofan@buaa.edu.cn

Received 29 November 2017; Revised 4 April 2018; Accepted 17 April 2018; Published 20 May 2018

Academic Editor: Rui Zhu

Copyright © 2018 Yixue Luo et al. This is an open access article distributed under the Creative Commons Attribution License, which permits unrestricted use, distribution, and reproduction in any medium, provided the original work is properly cited.

The different mechanical stimulus affects the bone mass and bone strength. The aim of this study was to investigate the effect of landing posture of the hoopster and paratrooper on the bone mass. In this study, 39 male participants were recruited including 13 paratroopers, 13 hoopsters, and 13 common students (control groups). Bone area (BA), BMD and BMC of calcaneus, and 1–5th of the metatarsus, hip, and lumbar spine (L₁–L₄) were measured by the dual-energy X-ray absorptiometry. Also, the vertical ground reaction forces (GRFs) of hoopsters and paratroopers were measured by the landing of 1.2 m 3D force platform. BA of hoopsters at the calcaneus, lumbar spine, and hip were significantly higher than the control group. The lumbar spine, hip, calcaneus, the 1st and 2nd metatarsals, BMC of paratroopers, and control groups were significantly lower than hoopsters. BMD of the lumbar spine, hip, and right and left femoral necks in hoopsters were significantly higher than the other participants. BMC and BMD of lower limb showed no significant difference between paratroopers and the control group. Besides, peak GRFs of paratroopers (11.06 times of BW) were significantly higher than hoopsters (6.49 times of BW). The higher GRF in the landing train is not always in accordance with higher BMD and BMC. Variable loads in hoopsters can improve bone remodeling and play an important role in bone expansions for trabecular bones. This will be considered by the method of training to prevent bone loss.

1. Introduction

Low bone mass, as one of the important factors for osteoporotic fractures, is usually measured with bone mineral content (BMC) and bone mineral density (BMD) [1]. Calcium deficiency, inadequate vitamin D intake, excessive drinking, low reproductive hormone levels, and lack of physical activity are main potential factors of bone loss [2, 3]. It was reported that physical exercise was usually a benefit to increase the bone mass and promote skeletal development [4]. Different loads contribute to bone formation and maintenance of bone metabolism, which also would improve the bone strength or microarchitecture [1, 5, 6]. The

mechanical loads of the adult rats showed the difference of intermittent and normal exercises [7].

The cyclic load on bones is generated in different exercises [8]. It was reported that BMD could be increased by duration exercise of more than two hours per week [9]. It was also found that the 2% BMD of the femoral neck was improved by the impact of exercise done for 6 months [10]. Continuous mechanical stimulus helps to maintain bone mass that is important to improve BMD and BMC [11–13]. Osteogenic responses are always produced at the specific loading sites [14, 15]. Basketball, volleyball, and gymnastics from the three times body weight (BW) or greater of reaction force are defined as high-impact exercises [16]. It was

beneficial to bone remodeling in high-impact exercises [17]. It was also shown that those high-impact exercises increased BMD and BMC of prepubertal girls [18]. BMD of the total body, lumbar spine (LS), femoral neck (FN), legs, and arms would be increased due to high-impact exercises such as basketball and volleyball exercise [14]. BMC and BMD of the lower limbs were not increased in no-impact or low-impact exercises (cycling and swimming) [19, 20], and there may be not enough stimuli against bones [17].

Basketball exercise included the various postures such as running, starts, stops, and shuffling. The multidirectional loads were produced during exercise. Basketball sport involves mainly jumping and landing [21]. They lean forward with the forefoot landing on the ground first, followed by the whole foot [22]. The twisting movement of the feet was found in balance training in basketball sport [23]. The triceps surae muscle in the musculoskeletal system mainly maintains the stability of ankle joints [24]. The ground reaction forces (GRFs) during the vertical jump-landing were generated in basketball exercise [25]. Meanwhile, parachuting was also a typical high-impact action [26]. Paratroopers perform half-squat parachute landing and keep their feet parallel to ground in the landing process [27]. Dynamic postures of hoopsters and paratroopers were quite different during the landing process. The mechanical loads acting on bones were also different. The effect of different dynamic landing postures on osteogenic responses still needs the quantified research method. In this study, BMD and BMC of hoopsters and paratroopers were investigated by the instruments and experiments, respectively. It would provide suggestion of training methods to prevent bone loss and osteoporotic fracture.

2. Methods

Thirty-nine males aged 20–25 years participated in this study (13 paratroopers, 13 hoopsters, and 13 normal men with less involvement in sports as the control group). They were divided into two subgroups: subgroup I with men 20–22 years old including 7 paratroopers, 7 hoopsters, and 7 controls, and the others were subgroup II aged 23–25 years. Volunteers were from the air force base, basketball sports team, and students in university, respectively. Paratroopers and hoopsters participated in training for more than 10 hours weekly compared to less than 1 hour of controls. Height, weight, and body mass index (BMI) of volunteers were shown in Table 1. Each volunteer has no disease of musculoskeletal disorders and bone metabolism.

Bone area (BA, cm^2), BMD (g/cm^2), and BMC (g) of the calcaneus, the 1st to the 5th metatarsus, hip (left hip and right hip), and lumbar spine (L_1 – L_4) were measured by dual-energy X-ray absorptiometry (DXA), respectively. The calcaneus and the metatarsus were placed at 90° inversion and 45° eversion by horizontal scanning of DXA, respectively. The informed consent including the measurement method and the potential risk were signed by volunteers. All measurements were performed in the same condition from March to May, 2016.

The statistical data of three groups (paratroopers, hoopsters, and controls) were compared by the one-way

TABLE 1: Characteristics of participations.

Variables	Paratroopers ^a	Hoopsters ^b	Controls ^c
<i>Subgroup I</i>			
Height (cm)	179.83 ± 4.02	184.29 ± 4.11 ^{a,c}	173.00 ± 6.73
Weight (kg)	70.03 ± 6.32	75.71 ± 8.01	70.66 ± 11.10
BMI ($\text{kg}\cdot\text{m}^{-2}$)	21.83 ± 1.99	22.29 ± 1.62	23.34 ± 2.68
<i>Subgroup II</i>			
Height (cm)	174.1 ± 3.70	181.17 ± 8.13 ^{a,c}	173.83 ± 2.14
Weight (kg)	68.72 ± 4.80	76.33 ± 8.45	64.33 ± 3.08
BMI ($\text{kg}\cdot\text{m}^{-2}$)	22.62 ± 2.32	23.18 ± 1.280	21.32 ± 1.23

Note. Data are means ± SD; ^asignificantly different with paratroopers, $P < 0.05$; ^bsignificantly different with hoopsters, $P < 0.05$; ^csignificantly different with controls, $P < 0.05$.

ANOVA test and nonparametric test. The significant differences of BA, BMC, and BMD are shown in Table 1.

Besides, hoopsters and paratroopers were required to jump from a 1.2 m platform. The height was consistent with the velocity of about 6 m/s of paratroopers landing [28]. Landing postures of hoopsters and paratroopers were captured by vidicon (Figures 1 and 2). The GRF was measured by a 3D force platform (1000 Hz, SMA-6, AMTI, USA).

3. Results

BA of the calcaneus, metatarsus, hip, femoral neck, and lumbar spine in both groups is shown in Tables 2 and 3. It was found that BA of the calcaneus in hoopsters was significantly larger than controls ($P < 0.05$). The difference of the metatarsal BA among hoopsters, paratroopers, and controls was less obvious. In subgroup I, BA of the lumbar spine and hip in hoopsters was significantly greater than controls ($P < 0.01$). Except for the BA of the left and right femoral neck and the fifth metatarsal, hoopsters were significantly greater than paratroopers ($P < 0.01$).

BMC values of the different bones in hoopsters, paratroopers and controls are listed in Tables 4 and 5. BMC of hoopsters' calcaneus and the 1st and 2nd metatarsals was significantly higher than that of paratroopers ($P < 0.05$) and controls ($P < 0.01$). BMC of hoopsters was also significantly higher than controls and paratroopers ($P < 0.05$) at the lumbar spine (L_1 , L_2 , L_3 , L_4 , and total lumbar spine) except for L_3 in subgroup II. BMC of hoopsters' total hip was the highest compared with controls and paratroopers ($P < 0.05$). However, there was no significant difference among all participants in BMC of the femoral neck.

BMD of the calcaneus in hoopsters was significantly higher than controls ($P < 0.05$) in both groups as shown in Tables 6 and 7. BMD of the first, second, and third metatarsals in hoopsters was significantly greater than controls ($P < 0.05$) in subgroup I. BMD of the third, fourth, and fifth metatarsals in paratroopers was significantly higher than controls ($P < 0.05$) in subgroup II. Higher BMD of the lumbar spine, hip, and femoral neck in hoopsters was obtained statistically compared to other bones ($P < 0.01$). However, paratroopers and controls had no significant difference in BMD at those anatomical locations.

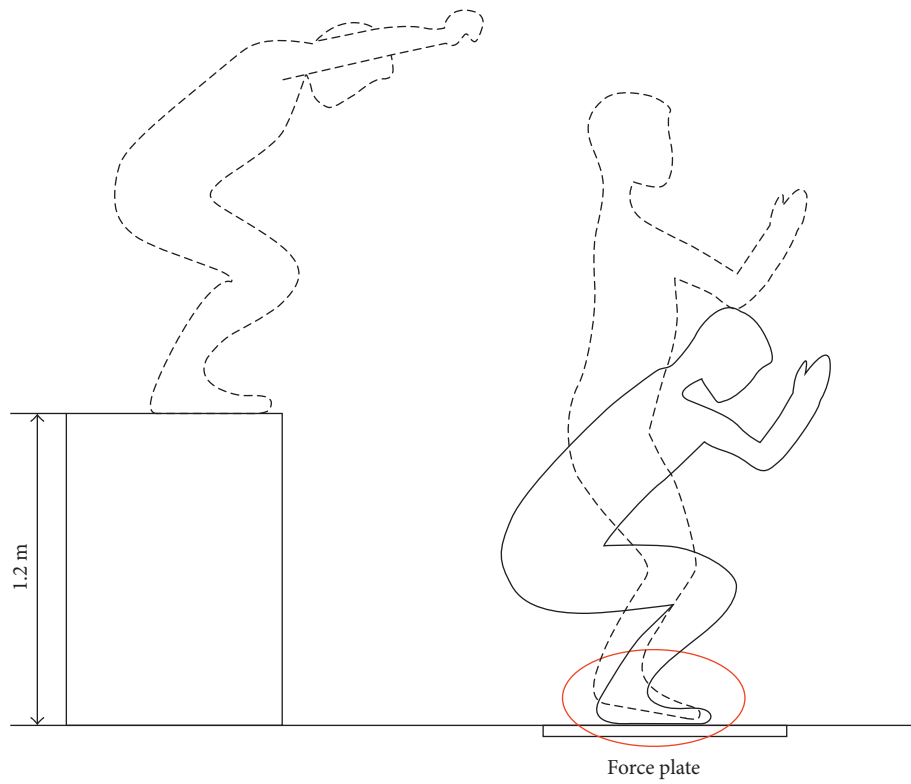


FIGURE 1: Landing posture of hoopsters.

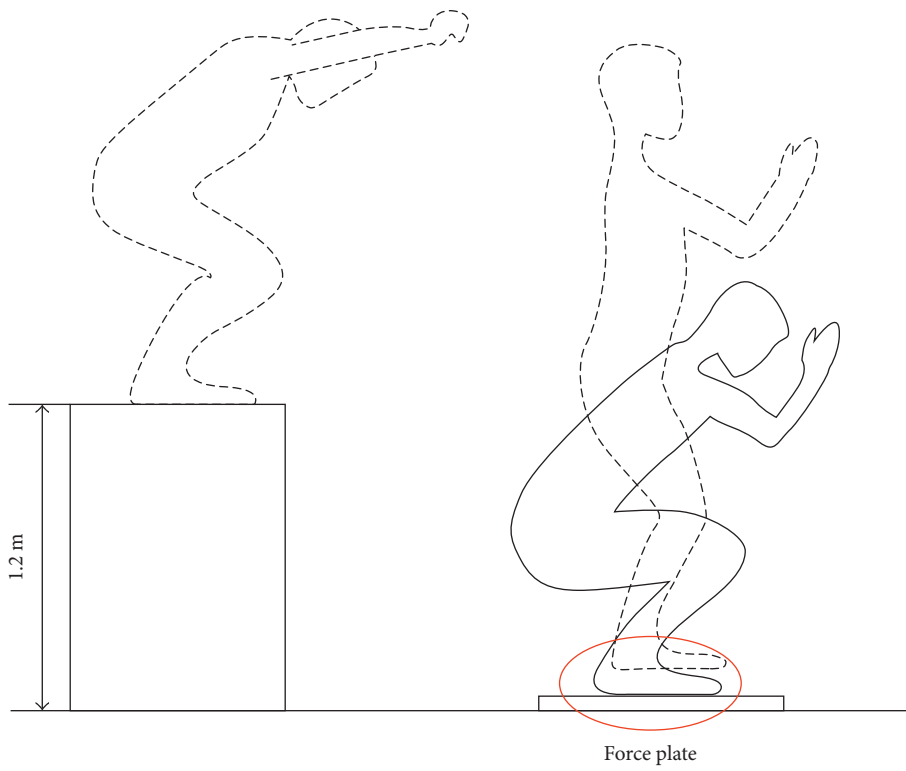


FIGURE 2: Landing posture of paratroopers.

TABLE 2: BA (cm²) of the different anatomical locations in subgroup I.

Variables	Paratroopers ^a (n = 7)	Hoopsters ^b (n = 7)	Controls ^c (n = 7)
Calcaneus	34.49 ± 3.83	36.66 ± 2.61 ^c	31.26 ± 3.32
First metatarsal	12.78 ± 0.88	13.54 ± 1.41	11.46 ± 0.74
Second metatarsal	8.37 ± 0.94	9.04 ± 1.28 ^c	7.76 ± 0.85
Third metatarsal	7.79 ± 1.13	8.27 ± 0.98	7.30 ± 0.70
Fourth metatarsal	7.95 ± 0.83	8.41 ± 1.15	7.42 ± 0.87
Fifth metatarsal	10.85 ± 1.14	10.24 ± 1.35	9.73 ± 1.28
Lumbar spine (L ₁ -L ₄) L ₁	13.97 ± 1.70	16.43 ± 1.05 ^{a,c}	13.96 ± 0.83
L ₂	15.39 ± 0.10	17.50 ± 2.06 ^{a,c}	14.84 ± 1.17
L ₃	17.16 ± 1.31	19.09 ± 2.74 ^c	16.54 ± 1.31
L ₄	18.67 ± 1.15	22.54 ± 2.39 ^{a,c}	18.17 ± 2.15
L _{total}	65.19 ± 4.40	75.56 ± 7.56 ^{a,c}	63.51 ± 4.52
Left femoral neck	6.10 ± 1.50	5.64 ± 0.38	5.64 ± 0.37
Left hip	40.78 ± 3.35	47.11 ± 4.14 ^{a,c}	39.64 ± 3.77
Right femoral neck	6.77 ± 1.30 ^{b,c}	5.46 ± 0.42	5.45 ± 0.43
Right hip	42.79 ± 3.0	46.53 ± 3.95 ^c	38.46 ± 4.89

Note. Data are means ± SD; ^asignificantly different with paratroopers, $P < 0.05$; ^bsignificantly different with hoopsters, $P < 0.05$; ^csignificantly different with controls, $P < 0.05$.

TABLE 3: BA (cm²) of the different anatomical locations in subgroup II.

Variables	Paratroopers ^a (n = 6)	Hoopsters ^b (n = 6)	Controls ^c (n = 6)
Calcaneus	32.00 ± 2.79	37.50 ± 4.71 ^{a,c}	31.95 ± 2.85
First metatarsal	12.59 ± 1.58	13.40 ± 2.88	11.55 ± 1.46
Second metatarsal	8.30 ± 0.81	8.86 ± 1.06	8.11 ± 0.51
Third metatarsal	6.91 ± 0.69	7.93 ± 1.10	7.22 ± 0.44
Fourth metatarsal	7.08 ± 0.49	7.94 ± 0.48	7.42 ± 0.77
Fifth metatarsal	9.54 ± 0.48	10.57 ± 1.01	9.17 ± 1.08
Lumbar spine (L ₁ -L ₄) L ₁	14.19 ± 0.95	15.38 ± 1.43	14.26 ± 1.19
L ₂	15.16 ± 1.18	16.36 ± 1.48	15.32 ± 0.49
L ₃	17.17 ± 2.12	18.12 ± 1.52	16.27 ± 1.63
L ₄	18.10 ± 0.98	19.78 ± 2.00 ^a	18.30 ± 0.63
L _{total}	64.61 ± 4.83	69.64 ± 6.27	64.15 ± 3.18
Left femoral neck	5.15 ± 1.32	5.27 ± 1.17	5.35 ± 0.26
Left hip	41.21 ± 4.19	44.07 ± 4.28	40.72 ± 2.17
Right femoral neck	5.21 ± 1.14	5.78 ± 0.76	4.99 ± 0.46
Right hip	41.57 ± 3.03	45.03 ± 4.12	40.91 ± 3.26

Note. Data are means ± SD; ^asignificantly different with paratroopers, $P < 0.05$; ^bsignificantly different with hoopsters, $P < 0.05$; ^csignificantly different with controls, $P < 0.05$.

TABLE 4: BMC (g) of the different anatomical locations in subgroup I.

Variables	Paratroopers ^a (n = 7)	Hoopsters ^b (n = 7)	Controls ^c (n = 7)
Calcaneus	27.84 ± 3.89	32.52 ± 5.12 ^{a,c}	24.58 ± 2.64
First metatarsal	6.19 ± 0.85	8.01 ± 1.84 ^{a,c}	5.68 ± 0.78
Second metatarsal	3.54 ± 0.36	4.60 ± 0.84 ^{a,c}	3.15 ± 0.58
Third metatarsal	3.09 ± 0.38	3.61 ± 1.15 ^c	2.41 ± 0.38
Fourth metatarsal	2.90 ± 0.60	2.96 ± 0.79	2.26 ± 0.48
Fifth metatarsal	3.82 ± 0.86	3.59 ± 0.81	3.06 ± 0.73
Lumbar spine (L ₁ -L ₄) L ₁	13.34 ± 1.68	17.29 ± 1.31 ^{a,c}	13.13 ± 1.87
L ₂	15.43 ± 1.43	19.70 ± 2.06 ^{a,c}	15.08 ± 2.52
L ₃	17.79 ± 1.48	23.03 ± 3.34 ^{a,c}	17.56 ± 2.26
L ₄	19.19 ± 0.93	25.31 ± 2.31 ^{a,c}	19.42 ± 2.49
L _{total}	65.75 ± 5.16	85.33 ± 8.38 ^{a,c}	65.19 ± 8.55
Left femoral neck	5.84 ± 1.33	6.86 ± 0.92	5.41 ± 0.78
Left hip	40.51 ± 5.09	58.94 ± 5.05 ^{a,c}	41.62 ± 3.00
Right femoral neck	6.46 ± 1.34	6.72 ± 0.72	5.18 ± 0.67 ^b
Right hip	41.96 ± 4.35	57.45 ± 4.61 ^{a,c}	40.36 ± 5.76

Note. Data are means ± SD; ^asignificantly different with paratroopers, $P < 0.05$; ^bsignificantly different with hoopsters, $P < 0.05$; ^csignificantly different with controls, $P < 0.05$.

TABLE 5: BMC (g) of the different anatomical locations in subgroup II.

Variables	Paratroopers ^a (n = 6)	Hoopsters ^b (n = 6)	Controls ^c (n = 6)
Calcaneus	23.85 ± 2.98	32.95 ± 9.03 ^{a,c}	22.82 ± 3.15
First metatarsal	6.46 ± 0.81	7.59 ± 1.88 ^{a,c}	5.64 ± 0.93
Second metatarsal	3.55 ± 0.43	4.22 ± 0.73 ^{a,c}	3.34 ± 0.36
Third metatarsal	2.67 ± 0.50	2.61 ± 0.88	2.17 ± 0.96
Fourth metatarsal	2.65 ± 0.39 ^c	2.50 ± 0.64	2.01 ± 0.29
Fifth metatarsal	3.43 ± 0.55	3.51 ± 0.89	2.57 ± 0.47
Lumbar spine (L ₁ -L ₄) L ₁	14.19 ± 1.06	17.20 ± 2.97 ^{a,c}	12.49 ± 1.47
L ₂	15.74 ± 1.02	19.84 ± 3.83 ^{a,c}	14.02 ± 1.01
L ₃	18.93 ± 2.27	22.50 ± 4.24 ^c	14.88 ± 1.95 ^{a,b}
L ₄	19.16 ± 2.57	23.70 ± 4.22 ^{a,c}	16.09 ± 1.45
L _{total}	68.02 ± 6.46	83.24 ± 14.95 ^{a,c}	57.47 ± 4.81
Left femoral neck	4.89 ± 1.73	6.29 ± 1.94	4.51 ± 0.67
Left hip	40.86 ± 7.54	53.28 ± 7.56 ^{a,c}	38.67 ± 5.12
Right femoral neck	5.36 ± 1.63	6.73 ± 1.51 ^c	4.14 ± 0.39
Right hip	42.96 ± 7.42	53.68 ± 7.50 ^{a,c}	38.44 ± 4.88

Note. Data are means ± SD; ^asignificantly different with paratroopers, $P < 0.05$; ^bsignificantly different with hoopsters, $P < 0.05$; ^csignificantly different with controls, $P < 0.05$.

TABLE 6: BMD (g/cm²) of the different anatomical locations in subgroup I.

Variables	Paratroopers ^a (n = 7)	Hoopsters ^b (n = 7)	Controls ^c (n = 7)
Calcaneus	0.81 ± 0.94	0.88 ± 0.92 ^c	0.79 ± 0.48
First metatarsal	0.49 ± 0.66	0.59 ± 0.85 ^{a,c}	0.50 ± 0.57
Second metatarsal	0.43 ± 0.44	0.51 ± 0.64 ^c	0.40 ± 0.47
Third metatarsal	0.40 ± 0.75	0.43 ± 0.95 ^c	0.33 ± 0.33
Fourth metatarsal	0.37 ± 0.08	0.35 ± 0.05	0.30 ± 0.05
Fifth metatarsal	0.36 ± 0.09	0.35 ± 0.04	0.31 ± 0.05
Lumbar spine (L ₁ -L ₄) L ₁	0.96 ± 0.04	1.05 ± 0.05	0.94 ± 0.10
L ₂	1.00 ± 0.05	1.13 ± 0.03	1.01 ± 0.10
L ₃	1.04 ± 0.06	1.21 ± 0.04 ^{a,c}	1.06 ± 0.10
L ₄	1.03 ± 0.04	1.13 ± 0.09	1.07 ± 0.06
L _{total}	1.01 ± 0.04	1.13 ± 0.04 ^{a,c}	1.02 ± 0.08
Left femoral neck	0.96 ± 0.08	1.21 ± 0.13 ^{a,c}	0.96 ± 0.10
Left hip	0.99 ± 0.08	1.25 ± 0.09 ^{a,c}	1.05 ± 0.09
Right femoral neck	0.95 ± 0.11	1.23 ± 0.08 ^{a,c}	0.95 ± 0.09
Right hip	0.98 ± 0.08	1.24 ± 0.07 ^{a,c}	1.05 ± 0.07

Note. Data are means ± SD; ^asignificantly different with paratroopers, $P < 0.05$; ^bsignificantly different with hoopsters, $P < 0.05$; ^csignificantly different with controls, $P < 0.05$.

TABLE 7: BMD (g/cm²) of the different anatomical locations in subgroup II.

Variables	Paratroopers ^a (n = 6)	Hoopsters ^b (n = 6)	Controls ^c (n = 6)
Calcaneus	0.75 ± 0.13	0.87 ± 0.14 ^c	0.71 ± 0.07
First metatarsal	0.52 ± 0.09	0.56 ± 0.03 ^c	0.49 ± 0.05
Second metatarsal	0.43 ± 0.08	0.47 ± 0.04	0.41 ± 0.02
Third metatarsal	0.39 ± 0.07	0.33 ± 0.08	0.30 ± 0.01 ^a
Fourth metatarsal	0.38 ± 0.06	0.31 ± 0.07	0.27 ± 0.03 ^a
Fifth metatarsal	0.36 ± 0.07	0.33 ± 0.07	0.28 ± 0.03 ^a
Lumbar spine (L ₁ -L ₄) L ₁	1.00 ± 0.08	1.11 ± 0.12	0.88 ± 0.07
L ₂	1.04 ± 0.11	1.20 ± 0.15 ^{a,c}	0.91 ± 0.04
L ₃	1.11 ± 0.13	1.23 ± 0.15	0.91 ± 0.06
L ₄	1.06 ± 0.15	1.19 ± 0.11	0.88 ± 0.08
L _{total}	1.06 ± 0.12	1.19 ± 0.13 ^{a,c}	0.90 ± 0.05
Left femoral neck	0.94 ± 0.15	1.18 ± 0.15 ^{a,c}	0.85 ± 0.14
Left hip	0.99 ± 0.14	1.21 ± 0.10 ^{a,c}	0.95 ± 0.10
Right femoral neck	1.02 ± 0.18	1.16 ± 0.15 ^{a,c}	0.84 ± 0.10
Right hip	1.03 ± 0.17	1.19 ± 0.09 ^{a,c}	0.94 ± 0.08

Note. Data are means ± SD; ^asignificantly different with paratroopers, $P < 0.05$; ^bsignificantly different with hoopsters, $P < 0.05$; ^csignificantly different with controls, $P < 0.05$.

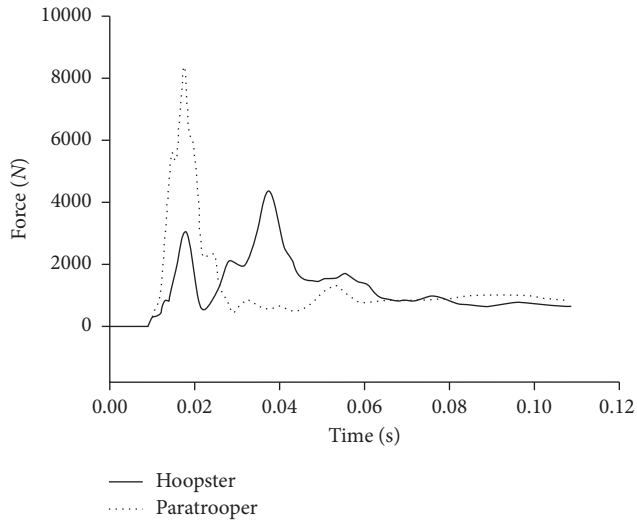


FIGURE 3: The vertical GRF of hoopsters and paratroopers.

Besides, peak vertical GRFs of paratroopers were 11.06 times of BW ($SD \pm 0.96$) compared to 6.49 times of BW in hoopsters ($SD \pm 1.19$). Compared with the forefoot of hoopsters, which first lands on the ground following the whole foot (Figure 1), the landing posture of paratroopers kept the feet parallel to ground (Figure 2). At the same time, the vertical GRF of both groups are shown in Figure 3. Only one peak value in paratroopers was obtained compared to two peaks of hoopsters.

4. Discussion

It was reported that different types of impact exercises including basketball, volleyball, swimming, gymnastics, handball, running, and cycling sports had different effects on BMC and BMD [11, 16, 17]. Basketball sport as a high-impact exercise had positive effect on BMC and BMD [29]. High ground reaction forces were also generated in half-squat parachute landing [26]. Paratroopers kept their feet parallel to ground in the landing process [27]. However, the landing posture of hoopsters was first landing on ground with forefoot, following the whole feet to jump [25]. Dynamic postures of hoopsters and paratroopers were quite different in the landing process. However, the effect of different dynamic landing postures on osteogenic responses still needs the quantified research method. So, the hoopsters and paratroopers as the typical impact subjects were recruited for landing postures to investigate BMD and BMC.

In this study, BMC of the first and second metatarsals in hoopsters was significantly higher than controls. This was consistent with studies that basketball exercising could enhance BMC of the bones [30]. Paratroopers in China perform half-squat parachute landing and keep their feet parallel to ground [27]. Compared with only a peak value of the paratrooper during landing, it was found that the first peak value of GRF was obtained during forefoot of the hoopster first landing on the ground, following the second peak value of the whole feet against ground (Figure 3). It indicated that in daily exercising, jumping of hoopsters with

two vertical GRF peaks more effectively generated mechanical loadings at the metatarsals than paratroopers, and this mechanical stimulus would promote local osteogenic responses at loading sites [14, 15]. Thus, land of hoopsters compared to paratroopers will improve BMC of the forefoot after frequent mechanical stimulus. However, it was further proof whether the higher BMC could help paratroopers to reduce injury.

BMC and BMD of the calcaneus and total hip in hoopsters were improved in contrast to controls in our study. It was consistent with previous study that BMC and BMD of the leg, hip, and pelvis were higher than controls [17]. Weight-bearing and high-impact exercises could stimulate bone mineral acquisition in children and adolescents [18, 31]. However, BMC and BMD of the calcaneus and total hip in paratroopers were not sensitive to daily training. It was found that training time of paratroopers in the questionnaire was about 40 to 50 hours weekly, which nearly included 70% of time for landing training. The peak GRF of paratroopers was nearly twice of hoopsters. In our study, it was clear that the high-impact exercising helped with bone formation and enhanced BMD [32]. The effect of the exercise posture on BMD and BMC has the different values for hoopsters' and paratroopers' bones. In Frost's mechanic stability theory, bone mass and bone strengthen were improved with the normal exercise [33]. The peak GRF of paratroopers was about 11 times of BW which would produce excessively large impact force. However, the cyclic loading from basketball exercising may be beneficial to increase BMC and BMD.

Waener et al. [34] found that BMD of all the bones in cyclists, mountain cyclists, was significantly higher. It was shown that the mountain cyclists had varying intensities and frequencies to stimulate osteogenic formation. Similarly, BMD of total lumbar spine and total hip in hoopsters were significantly higher than paratroopers. This was in accordance with the study that the variable velocities in basketball exercising could improve the bone mass and bone strength [22]. Thus, tension, compression, shear, and bending produced at different strain stimulus would act on lumbar spine and hip, which would induce bone formation and enhance BMD at weight-bearing regions [29, 32, 35]. It was also certified that the varying loads could be more benefit to positive osteogenic formation than constant loads [36, 37]. Thus, BMD of the lumbar spine and hip in basketball exercising was higher compared with parachuting. This was in accordance with the study by Platen et al. [38].

BA of the calcaneus, total lumbar spine, and total hip in hoopsters was also significantly higher than controls. This finding was consistent with previous conclusion that the basketball exercising enhanced BA of weight-bearing bones [29]. The BA of the left, right femoral necks and metatarsals in hoopsters was changed mildly compared to controls. It was shown that the mechanical stress of the cortical bone was less sensitive than the trabecular bone [39]. Besides, BA of paratroopers had no promotion compared with controls at measured anatomical locations. Although training of paratroopers was high-impact exercising, it could not generate bone expansions at loaded bones [40]. Different

exercise modalities induce variable mechanical stress at stimulated regions [41]. The different BA between paratroopers and hoopsters was caused from the different landing postures.

This study had several limitations. Firstly, the number of paratroopers was limited by air force base. Secondly, there was no dietary information, which may affect bone composition. Thirdly, lean tissue mass and degree of physical fitness were not considered due to the difficult quantitative methods.

5. Conclusions

The high-impact exercises have positive effect on osteogenic formation. BMC and BMD are not in accordance with magnitude of GRF. In this study, basketball exercise from the variable loads may be more effectively increasing BMC and BMD than parachuting with constant loads at loaded sites. Exercising like basketball with high acceleration and multidimensional directions needs further study on its positive effects of bone strength and prevention of osteoporotic fracture caused by bone loss.

Conflicts of Interest

The authors declare that they have no conflicts of interest.

Acknowledgments

This work was supported by the National Natural Science Foundation of China (nos. 11421202, 51372182, 61227902, and 11702068), Defense Industrial Technology Development Program (no. JCKY2016601B009), and the 111 Project (no. B13003).

References

- [1] I. Wolff, J. J. Van Croonenborg, H. C. G. Kemper, P. J. Kostense, and J. W. R. Twisk, "The effect of exercise training programs on bone mass: a meta-analysis of published controlled trials in pre- and postmenopausal women," *Osteoporosis International*, vol. 9, no. 1, pp. 1–12, 1999.
- [2] L. N. Bakhireva, E. Barrett-Connor, D. Kritiz-Silverstein, and D. J. Morton, "Modifiable predictors of bone loss in older men: a prospective study," *American Journal of Preventive Medicine*, vol. 26, no. 5, pp. 436–442, 2004.
- [3] W. P. Olszynski, K. S. Davison, J. D. Adachi et al., "Osteoporosis in men: epidemiology, diagnosis, prevention, and treatment," *Clinical Therapeutics*, vol. 26, no. 1, pp. 15–28, 2004.
- [4] R. Nikander, H. Sievänen, A. Heinonen et al., "Targeted exercise against osteoporosis: a systematic review and meta-analysis for optimising bone strength throughout life," *BMC Medicine*, vol. 8, no. 1, p. 47, 2010.
- [5] S. L. Francis, E. M. Letuchy, S. M. Levy, and K. F. Janz, "Sustained effects of physical activity on bone health: Iowa Bone Development Study," *Bone*, vol. 63, pp. 95–100, 2014.
- [6] K. T. Borer, "Physical activity in the prevention and amelioration of osteoporosis in women," *Sports Medicine*, vol. 35, no. 9, pp. 779–830, 2005.
- [7] Y. Shirazi-Fard, C. E. Metzger, A. T. Kwaczala, S. Judex, S. A. Bloomfield, and H. A. Hogan, "Moderate intensity resistive exercise improves metaphyseal cancellous bone recovery following an initial disuse period, but does not mitigate decrements during a subsequent disuse period in adult rats," *Bone*, vol. 66, pp. 296–305, 2014.
- [8] E. A. Marques, F. Wanderley, L. Machado et al., "Effects of resistance and aerobic exercise on physical function, bone mineral density, OPG and RANKL in older women," *Experimental Gerontology*, vol. 46, no. 7, pp. 524–532, 2011.
- [9] H. A. McKay, M. A. Petit, R. W. Schutz, J. C. Prior, S. I. Barr, and K. M. Khan, "Augmented trochanteric bone mineral density after modified physical education classes: a randomized school-based exercise intervention study in prepubescent and early pubescent children," *Journal of Pediatrics*, vol. 136, no. 2, pp. 156–162, 2000.
- [10] C. A. Bailey and K. Brooke-Wavell, "Optimum frequency of exercise for bone health: randomised controlled trial of a high-impact unilateral intervention," *Bone*, vol. 46, no. 4, pp. 1043–1049, 2010.
- [11] R. S. Rector, R. Rogers, M. Ruebel, and P. S. Hinton, "Participation in road cycling vs running is associated with lower bone mineral density in men," *Metabolism*, vol. 57, no. 2, pp. 226–232, 2008.
- [12] S. J. Allison, J. P. Folland, W. J. Rennie, G. D. Summers, and K. Brooke-Wavell, "High impact exercise increased femoral neck bone mineral density in older men: a randomised unilateral intervention," *Bone*, vol. 53, no. 2, pp. 321–328, 2013.
- [13] G. A. Kelley, K. S. Kelley, and W. M. Kohrt, "Exercise and bone mineral density in men: a meta-analysis of randomized controlled trials," *Bone*, vol. 53, no. 1, pp. 103–111, 2013.
- [14] C. S. Duncan, C. J. Blimkie, C. T. Cowell, S. T. Burke, J. N. Briody, and R. Howman-Giles, "Bone mineral density in adolescent female athletes: relationship to exercise type and muscle strength," *Medicine and Science in Sports and Exercise*, vol. 34, no. 2, pp. 286–294, 2002.
- [15] J. A. Nurmi-Lawton, A. D. Baxter-Jones, R. L. Mirwald et al., "Evidence of sustained skeletal benefits from impact-loading exercise in young females: a 3-year longitudinal study," *Journal of Bone and Mineral Research*, vol. 19, no. 2, pp. 314–322, 2004.
- [16] C. Milanese, F. Piscitelli, V. Cavedon, and C. Zancanaro, "Effect of distinct impact loading sports on body composition in pre-menarcheal girls," *Science & Sports*, vol. 29, no. 1, pp. 10–19, 2014.
- [17] E. Ubago-Guisado, A. Gómez-Cabello, J. Sánchez-Sánchez, J. García-Unanue, and L. Gallardo, "Influence of different sports on bone mass in growing girls," *Journal of Sports Sciences*, vol. 33, no. 16, pp. 1710–1718, 2015.
- [18] D. Courteix, E. Lespessailles, S. L. Peres, P. Obert, P. Germain, and C. L. Benhamou, "Effect of physical training on bone mineral density in prepubertal girls: a comparative study between impact-loading and non-impact-loading sports," *Osteoporosis International*, vol. 8, no. 2, pp. 152–158, 1998.
- [19] R. Rizzoli, M. L. Bianchi, M. Garabedian, H. A. McKay, and L. A. Moreno, "Maximizing bone mineral mass gain during growth for the prevention of fractures in the adolescents and the elderly," *Bone*, vol. 46, no. 2, pp. 294–305, 2010.
- [20] L. Maïmoun, O. Coste, P. Philibert et al., "Peripubertal female athletes in high-impact sports show improved bone mass acquisition and bone geometry," *Metabolism*, vol. 62, no. 8, pp. 1088–1098, 2013.
- [21] G. Ziv and R. Lidor, "Vertical jump in female and male volleyball players: a review of observational and experimental studies," *Scandinavian Journal of Medicine & Science in Sports*, vol. 20, no. 4, pp. 556–567, 2010.

- [22] A. Crisafulli, F. Melis, F. Tocco, P. Laconi, C. Lai, and A. Concu, "External mechanical work versus oxidative energy consumption ratio during a basketball field test," *Journal of Sports Medicine and Physical Fitness*, vol. 42, no. 4, pp. 409–417, 2002.
- [23] T. A. McGuine and J. S. Keene, "The effect of a balance training program on the risk of ankle sprains in high school athletes," *American Journal of Sports Medicine*, vol. 34, no. 7, pp. 1103–1111, 2006.
- [24] A. Zech, M. Hubscher, L. Vogt, W. Banzer, F. Hänsel, and K. Pfeifer, "Balance training for neuromuscular control and performance enhancement: a systematic review," *Journal of Athletic Training*, vol. 45, pp. 392–403, 2010.
- [25] J. E. Dook, C. James, N. K. Henderson, and R. I. Price, "Exercise and bone mineral density in mature female athletes," *Medicine and Science in Sports and Exercise*, vol. 29, no. 3, pp. 291–296, 1997.
- [26] J. W. Whitting, J. R. Steele, M. A. Jaffrey, and B. J. Munro, "Parachute landing fall characteristics at three realistic vertical descent velocities," *Aviation, Space, and Environmental Medicine*, vol. 78, no. 12, pp. 1135–1142, 2007.
- [27] W. Niu, Y. Wang, Y. He, Y. Fan, and Q. Zhao, "Biomechanical gender differences of the ankle joint during simulated half-squat parachute landing," *Aviation, Space, and Environmental Medicine*, vol. 81, no. 8, pp. 761–767, 2010.
- [28] F. Cilli, M. Mahirogullar, M. Inan et al., "Parachuting injuries: a retrospective study of 43,690 military descents," *Balkan Military Medical Review*, vol. 9, no. 4, pp. 144–147, 2006.
- [29] M. J. Falcai, A. Zamarioli, R. Okubo, F. J. A. de Paula, and J. B. Volpon, "The osteogenic effects of swimming, jumping, and vibration on the protection of bone quality from disuse bone loss," *Scandinavian Journal of Medicine & Science in Sports*, vol. 25, no. 3, pp. 390–397, 2015.
- [30] A. Zribi, M. Zouch, H. Chaari et al., "Enhanced bone mass and physical fitness in prepubescent basketball players," *Journal of Clinical Densitometry*, vol. 17, no. 1, pp. 156–162, 2014.
- [31] K. Hind and M. Burrows, "Weight-bearing exercise and bone mineral accrual in children and adolescents: a review of controlled trials," *Bone*, vol. 40, no. 1, pp. 14–27, 2007.
- [32] D. L. Creighton, A. L. Morgan, D. Boardley, and P. Gunnar Brolinson, "Weight-bearing exercise and markers of bone turnover in female athletes," *Journal of Applied Physiology*, vol. 90, no. 2, pp. 565–570, 2001.
- [33] H. M. Frost, "Skeletal structural adaptations to mechanical usage (SATMU): 1. Redefining Wolff's law: the bone modeling problem," *The Anatomical Record*, vol. 226, no. 4, pp. 403–413, 1990.
- [34] S. E. Warner, J. M. Shaw, and G. P. Dalsky, "Bone mineral density of competitive male mountain and road cyclists," *Bone*, vol. 30, no. 1, pp. 281–286, 2002.
- [35] P. Yang, G. P. Brüggemann, and J. Rittweger, "What do we currently know from in vivo bone strain measurements in humans?," *Journal of Musculoskeletal and Neuronal Interactions*, vol. 11, no. 1, pp. 8–20, 2011.
- [36] M. L. Hull, "Analysis of road induced loads in bicycle frames," *Journal of Mechanisms, Transmissions, and Automation in Design*, vol. 138, 1983.
- [37] E. L. Wang and M. L. Hull, "A dynamic system model of an off-road cyclist," *Journal of Biomechanical Engineering*, vol. 119, no. 3, pp. 248–253, 1997.
- [38] P. Platen, E. Chae, R. Antz, R. Lehmann, J. Kühlmorgen, and B. Alolio, "Bone mineral density in top level male athletes of different sports," *European Journal of Sport Science*, vol. 1, no. 5, pp. 1–15, 2001.
- [39] H. Chaari, M. Zouch, A. Zribi, E. Bouajina, M. Zaouali, and Z. Tabka, "Specific sites of bone expansion depend on the level of volleyball practice in prepubescent boys," *Biology of Sport*, vol. 30, no. 3, pp. 227–234, 2013.
- [40] M. Zouch, C. Jaffré, T. Thomas et al., "Long-term soccer practice increases bone mineral content gain in prepubescent boys," *Joint Bone Spine*, vol. 75, no. 1, pp. 41–49, 2008.
- [41] M. Zouch, H. Chaari, A. Zribi et al., "Volleyball and basketball enhanced bone mass in prepubescent boys," *Journal of Clinical Densitometry*, vol. 19, no. 3, pp. 396–403, 2016.

Research Article

Effect of Constraint Loading on the Lower Limb Muscle Forces in Weightless Treadmill Exercise

Ning Guo ¹, Xingyu Fan,² Yuting Wu ¹, Zhili Li ³, Shujuan Liu ³, Linjie Wang ³,
Jie Yao ¹ and Yinghui Li ³

¹Key Laboratory for Biomechanics and Mechanobiology of Ministry of Education, School of Biological Science and Medical Engineering, Beijing Advanced Innovation Centre for Biomedical Engineering, Beihang University, Beijing 100191, China

²College of Bioengineering, Chongqing University, Chongqing 400044, China

³State Key Laboratory of Space Medicine Fundamentals and Application, China Astronaut Research and Training Center, Beijing 100094, China

Correspondence should be addressed to Jie Yao; yaojie@buaa.edu.cn and Yinghui Li; yinghuidd@vip.sina.com

Received 27 November 2017; Accepted 21 February 2018; Published 3 April 2018

Academic Editor: Rui Zhu

Copyright © 2018 Ning Guo et al. This is an open access article distributed under the Creative Commons Attribution License, which permits unrestricted use, distribution, and reproduction in any medium, provided the original work is properly cited.

Long exposure to the microgravity will lead to muscle atrophy and bone loss. Treadmill exercise could mitigate the musculoskeletal decline. But muscle atrophy remains inevitable. The constraint loading applied on astronauts could affect the muscle force and its atrophy severity. However, the quantitative correlation between constraint loading mode and muscle forces remains unclear. This study aimed to characterize the influence of constraint loading mode on the lower limb muscle forces in weightless treadmill exercise. The muscle forces in the full gait cycle were calculated with the inverse dynamic model of human musculoskeletal system. The calculated muscle forces at gravity were validated with the EMG data. Muscle forces increased at weightlessness compared with those at the earth's gravity. The increasing percentage from high to low is as follows: biceps femoris, gastrocnemius, soleus, vastus, and rectus femoris, which was in agreement with the muscle atrophy observed in astronauts. The constraint loading mode had an impact on the muscle forces in treadmill exercise and thus could be manipulated to enhance the effect of the muscle training in spaceflight. The findings could provide biomechanical basis for the optimization of treadmill constraint system and training program and improve the countermeasure efficiency in spaceflight.

1. Introduction

Long exposure to the microgravity will lead to the decline of musculoskeletal system, including muscle atrophy and bone loss [1]. The decrement of muscle volume and performance significantly occurs in the lower limbs [2, 3]. Previous studies have reported an 8.8% to 15.9% reduction of plantar flexor muscle volume [4], a 35%–40% reduction of neuromuscular activity, and a 17% reduction of maximal isometric torque after spaceflight [5]. The decrease of muscle force will subsequently aggravate bone loss in microgravity [6, 7]. Long duration of spaceflight will further lead to musculoskeletal injuries including bone fracture, muscle tears, and back pain [2, 8–10]. Molecular and cellular studies revealed that mechanical environment is a critical factor to maintain the

musculoskeletal function [11–13]. Therefore, a properly designed loading stimulation, such as exercise, could help counteract the negative effect of microgravity.

Treadmill exercise could mitigate the musculoskeletal weakening to some extent. Currently, the used exercise devices in the International Space Station (ISS) include treadmill, bicycle ergometer, and resistance exercise device. Among these countermeasures, a significant correlation between treadmill training intensity and the muscle mass maintenance was observed, and muscle losses of astronauts with high-volume treadmill exercise were about 59% less than those with low-volume treadmill exercise [3, 14]. During the training, astronauts have to be restrained with bungee cords, which provide the vertical loading instead of the gravity effect. Increasing the constraint force may

mitigate the musculoskeletal decline but can cause discomfort and local injury at the harness contact regions [15]. Constraint force of 70% to 80% body weight was usually applied according to individual experience, which may limit the efficiency of the treadmill countermeasure [3, 15]. An optimal constraint system is desired to reduce the risk of local discomfort and increase the mechanical stimulation on the musculoskeletal system. However, the quantitative relationship between treadmill constraint system and in situ force in bones and muscles remains unclear.

Numeric musculoskeletal model combined with motion capture equipment could be used to estimate the in situ load on the bone and muscle during treadmill exercise. The muscle force and joint kinetics could be calculated from kinematical data with the inverse dynamic analysis. Then, the stress of the bone under muscle forces could be calculated with the finite element simulation [16, 17]. The methodology has been applied in sport, rehabilitation, and exoskeleton design [18–21]. Quantification of musculoskeletal loading in treadmill exercise could provide biomechanical basis for the optimization of training system and improve the countermeasure efficiency.

This study aims to investigate the influence of the constraint loading mode on the lower limb muscle force in treadmill training at weightlessness. An inverse dynamic musculoskeletal model was applied to simulate the treadmill exercise. Five loading modes of the constraint system were analyzed. Due to the lack of kinematical data at weightlessness, the kinematical data of treadmill exercise at gravity was used. To minimize the result deviation caused by this simplification, the sum of the constraint loadings was assumed to be equal to the body weight.

2. Materials and Methods

2.1. Participants. Eight healthy and physically active participants volunteered to take part into the study (5 males and 3 females, age 20 ± 2 , height 1.74 ± 0.16 m, and weight 63.5 ± 20 kg). Volunteers were recruited among university students. The study was approved by the local ethics board and every subject signed an informed consent before performing the trials.

2.2. Motion Capture Experiment. The subjects' kinematical information was recorded with the motion capture system, Vicon (Vicon, Oxford Metrics Ltd., UK). 34 reflective markers were attached to the bony landmarks of the subject (Figure 1). The markers' spatial coordinates were captured by 8 cameras with the sampling frequency of 100 Hz. Cameras were fixed on the wall to avoid vibration interference. Subjects were required to run on the treadmill with the speed of 1.5 m/s, which was a routine speed in the astronaut training program [10]. After the subject adapted to the treadmill speed (30 seconds), the motion information was recorded for 30 seconds. 10 stable full gait cycles were extracted from each measurement for muscle analysis. In the present study, one gait cycle was defined as the period between two adjacent left foot landings. Each subject was measured for 3 times, with one-minute interval. To eliminate the influence of the shoes

on the gait, subjects were required to wear the same type of shoes with proper sizes.

2.3. Inverse Dynamic Model of Human Musculoskeletal System. A human musculoskeletal model was developed with the inverse dynamic software, AnyBody Managed Model Repository (AnyBody Technology, Denmark). The lower limbs of the model contain 6 joints and 318 muscles. The accuracy of the muscle force prediction model was validated in the previous study. Compared with the *in vivo*-measured maximal voluntary moment, the calculated data was within the 95% confidence interval [22]. The weight, height, thigh length, shank length, foot length, and pelvis width of the model were set according to the subject. The model was driven by the motion information of the markers from motion capture experiment (Figure 2(a)). The ground reaction force (GRF) during running was calculated with a GRF prediction module [23, 24].

2.4. Constraint Methods. In the weightless condition, bungee cords were applied instead of gravity to constrain the body on the treadmill during exercise. Previous studies have suggested that providing a constraint force equal to gravity could better prevent musculoskeletal decline in spaceflight [14, 25]. Therefore, in the present study, the resultant force of the bungee cords was assumed to be constantly equal to gravity. The constraint forces of eight loading modes were applied on the shoulder (bilateral acromion) and waist (bilateral anterior superior spine) (Figure 2(b)). The influence of the constraint loading modes on lower limb muscle forces was analyzed. Eight loading modes of constraint system were analyzed (Table 1).

In the weightless musculoskeletal model, the gravity was set to zero. The experiment on NASA KC-135 research aircraft had reported that the gait at weightlessness approached to the gait at gravity when the resultant constraint force increased to body weight on earth [26]. Therefore, the kinematical data of treadmill exercise at gravity was also used to drive the musculoskeletal model at weightlessness. A quadratic muscle recruitment method was implemented in the present study.

2.5. Muscle Force and Data Processing. The following muscles were analyzed in the present study: biceps femoris, gastrocnemius, vastus, soleus, and rectus femoris, which were primary active muscles in treadmill exercise. The muscle forces in the full gait cycle were calculated. To normalize the data for each trail, the muscle force was divided by the subject's body weight. Then, the normalized muscle forces of all subjects' trails were averaged. A Two-way random average measure intraclass correlation coefficient (ICC (2, k)) was used to assess the reliability of the motion capture and muscle force calculation. Values greater than 0.75 indicate desirable repeatability of the methodology. Statistical software SPSS (IMB, US) was used for the data analysis.

2.6. Comparison with Electromyography (EMG). To evaluate the reliability of the muscle force calculation, the calculated muscle forces in treadmill exercise at gravity were compared with the muscle EMG data in the literature [27]. The

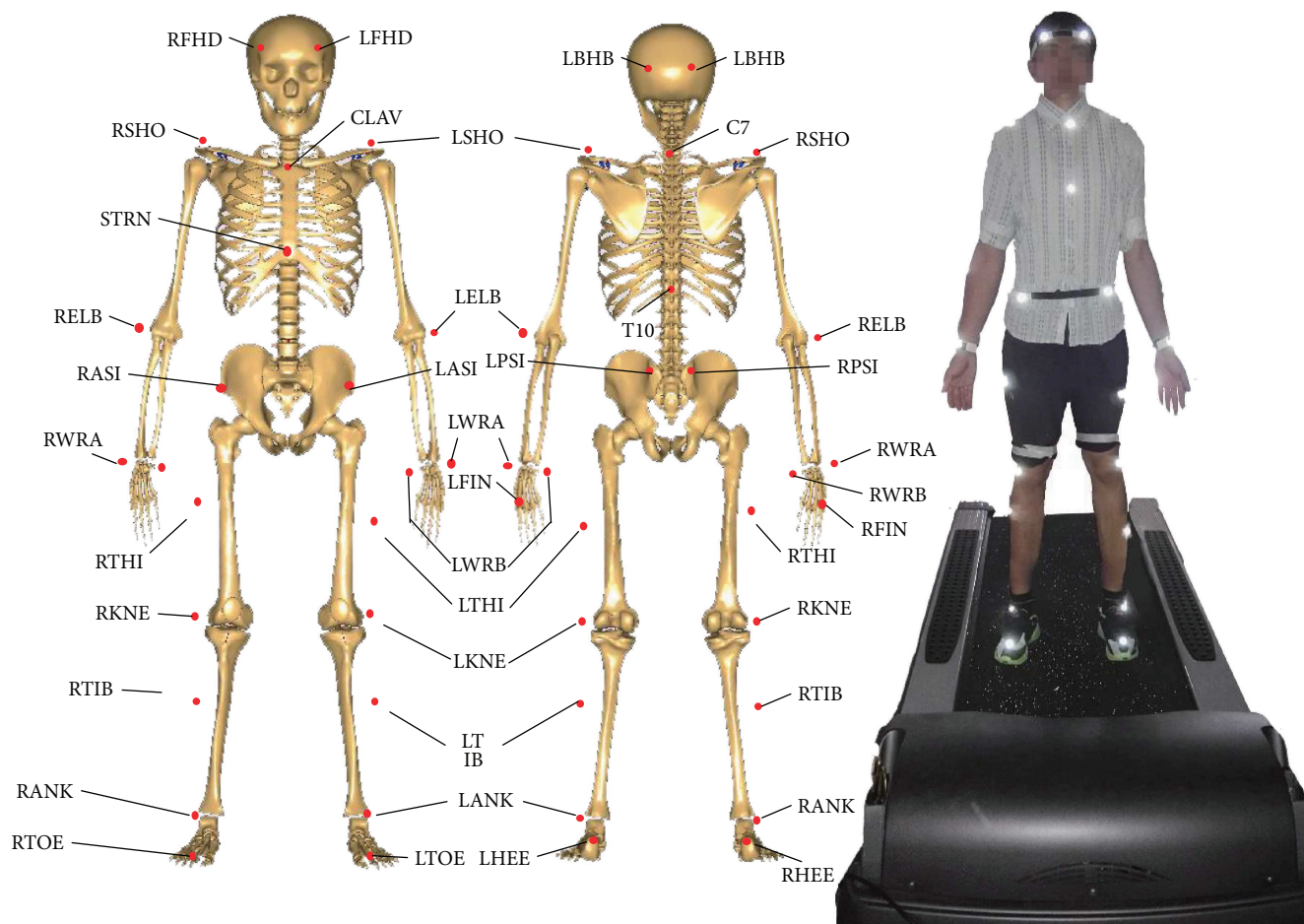


FIGURE 1: The locations of markers for motion capture experiment. Totally, 34 markers were fixed on the body during the treadmill exercise. The following is the meanings of the abbreviation for the markers' anatomic locations. R(L)FHD: right (left) front head; R(L)BHD: right (left) back head; R(L)SHO: right (left) shoulder; C7: 7th cervical; T10: 10th thoracic; CLAV: clavicle; STRN: sternum; R(L)ASI: right (left) anterior superior iliac; R(L)PSI: right (left) posterior superior iliac; R(L)ELB: right left elbow; R(L)WRA(B): right (left) wrist A(B); R(L)FIN: right (left) finger; R(L)THI: right (left) thigh; R(L)KNE: right (left) knee; R(L)TIB: right (left) tibia; R(L)ANK: right (left) ankle; R(L)TOE: right (left) toe; R(L)HEE: right (left) heel.

magnitude of the EMG could not sensitively reflect the muscle force in different muscles and action types; therefore, the correlation between the timing of peak EMG and the timing of peak muscle force in the full gait cycle was calculated to evaluate the validity of the muscle force calculation with the statistical software SPSS (IMB, US). The Spearman correlation factor was calculated. A correlation coefficient different from 0 and a significant level (p value) < 0.05 indicates a considerable correlation.

3. Result

3.1. Relationship between Muscle Force and EMG. The normalized force and EMG of the biceps femoris, gastrocnemius, vastus, soleus, and rectus femoris in the full gait cycle were shown in Figure 3. The timing of the peak muscle force was positively correlated with the timing of the peak EMG ($r = 0.757^*$, $p = 0.049$), which provided the validity of the muscle force calculation (Table 2). Furthermore, the ICC (2, k) results of the muscle forces in gravity and each

loading mode were greater than 0.75, which indicate desirable repeatability of the methodology (Supplementary Material, Tables S1 and S2).

3.2. Influence of Loading Mode on Muscle Force. Although the resultant constraint loading was constantly equal to the body weight at gravity, the maximum forces of biceps femoris, gastrocnemius, and vastus at weightlessness (all five modes) were greater than those at gravity (paired-samples t -test, $p < 0.01$). Furthermore, the muscle forces changed with the constraint modes. The average and the deviation of all normalized muscle forces were contained in Supplementary Material (Figures S1–S5, Tables S3–S7).

The biceps femoris was activated in both stance and swing phases; a larger peak muscle force occurred in the stance phase, and a smaller peak muscle force occurred in the swing phase (Figure 4(a)). With the constraint loading migrating from shoulder to waist, the maximum muscle force firstly increased and then decreased, ranging from 115% to 128% of body weight.

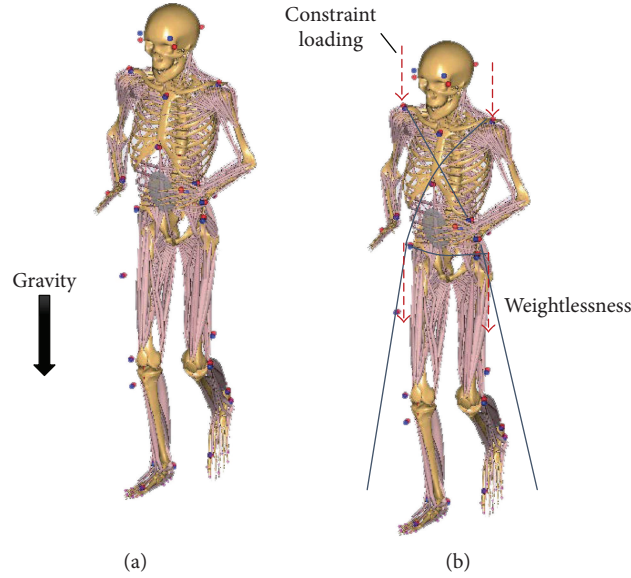


FIGURE 2: Inverse dynamic model of human musculoskeletal system and the diagram of loading conditions. The lower limbs of the model contain 6 joints and 318 muscles. (a) The model was in the condition of normal gravity. (b) The model was in the condition of weightlessness; the body was restrained with the bungee cords, which provide the vertical loading instead of the gravity effect.

TABLE 1: The constraint loading applied on the shoulder and waist.

	Mode 1	Mode 2	Mode 3	Mode 4	Mode 5
Shoulder loading	1 BW	2/3 BW	1/2 BW	1/3 BW	0 BW
Waist loading	0 BW	1/3 BW	1/2 BW	2/3 BW	1 BW

BW: body weight.

Gastrocnemius was activated at the end of the stance phase and the beginning of the swing phase, which was a result of flexion of the knee when lifting the leg. Only one peak was observed in the gastrocnemius force curve (Figure 4(b)). With the constraint loading migrating from shoulder to waist, the peak muscle forces of loading modes 1 to 4 were similar, while minimum peak muscle force occurred at loading mode 5 (shoulder load was 0% of body weight; waist load was 100% of body weight).

The trends of vastus and soleus forces in the gait cycle were similar. The vastus force was lower than soleus. The peak muscle forces occurred in the stance phase (Figures 5(c) and 5(d)). With the constraint loading migrating from shoulder to waist, the peak muscle forces of loading modes 1 to 4 were similar, while minimum peak muscle force occurred at loading mode 5.

In the rectus femoris, the peak muscle force occurred in the swing phase (Figure 4(e)). With the constraint loading migrating from shoulder to waist, the maximum muscle force changed slightly in loading modes 1 to 4 and decreased in loading mode 5.

3.3. Influence of Loading Mode on GRF. The GRF occurred only in stance phase because there is no contact with the ground during the swing phase. Only one peak of GRF was observed in the stance phase, inferring the non-heel-strike running in the present study (Figure 5(a)). The peak GRF at

gravity was 188% of body weight, which was lower than that at weightlessness (paired-samples t -test, $p < 0.01$). Among the loading modes at weightlessness, the minimum peak GRF occurred at loading mode 5. Peak GRFs at loading modes 1 to 4 were similar (Figure 5(b), Supplementary Material, Table S8).

4. Discussion

In the present study, a significant correlation ($r = 0.757^*$, $p = 0.049$) between the timings of peak muscle force and EMG was observed in the full gait cycle. These results provided the validity of the muscle force calculation. Previous studies on the treadmill constraint system mainly focused on the relationship between the resultant constraint loading and GRF, and the GRF was often regarded as an index of exercise strength. However, the present results indicated that although the resultant constraint loading was constantly equal to body weight, the GRF changed with the constraint loading modes. Minimum GRF occurred at loading mode 5 (shoulder load was 0% of body weight; waist load was 100% of body weight). Furthermore, although the GRF changed slightly in constraint loading modes 1 to 4, the muscle forces also changed with the constraint loading modes. These findings implied that resultant constraint force and GRF could not precisely reflect the muscle activity strength. The positions of the constraint loadings will influence the muscle forces in treadmill exercise, thus should be carefully considered in the optimization of exercise and the device design.

The forces of vastus and soleus had the similar trends as the GRF in the stance phase of the gait cycle, since they were all activated in this phase (Figure 4). The biceps femoris had the peaks in both the stance phase and swing phase, which correspond to its function; extension of hip joint in the stance phase; and flexion of knee joint in the swing phase. Half of

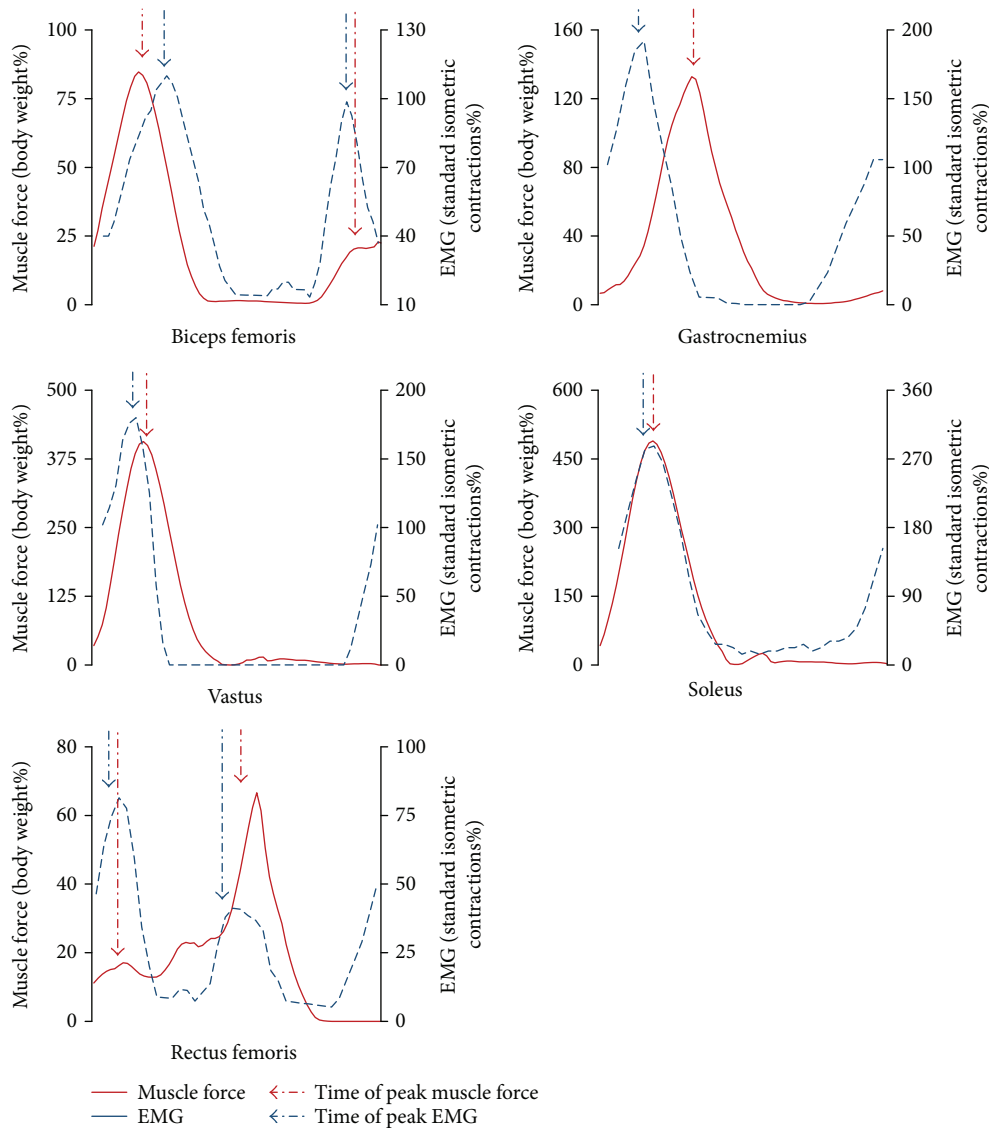


FIGURE 3: The force and EMG of the biceps femoris, gastrocnemius, rectus femoris, soleus, and vastus in a full gait cycle. The muscle forces were normalized with body weight; the EMG magnitudes were normalized with the standard isometric contractions. Since EMG magnitude could not sensitively reflect the muscle force, the correlation between the timing of peak EMG and the timing of peak muscle force was calculated to evaluate the validity of the muscle force calculation.

TABLE 2: The timings of the peak muscle forces and the peak EMGs in the full gait cycle.

	Biceps femoris (1st peak)	Biceps femoris (2nd peak)	Gastrocnemius	Rectus femoris (1st peak)	Rectus femoris (2nd peak)	Soleus	Vastus
Force	15%	90%	32%	10%	55%	18%	17%
EMG	17%	86%	12%	7%	49%	10%	7%

the gastrocnemius muscle force was in the stance phase, and the other half was in the swing phase, which were a result of flexion of the knee when lifting the leg. Rectus femoris force was quite different among the subjects. This phenomenon may be related to the personalized exercise habits and needs to be further studied.

Under the constraint loadings at weightlessness, the maximum forces of the biceps femoris, gastrocnemius, and vastus at weightlessness (all five modes) were significantly greater than those at gravity ($p < 0.01$). Take constraint loading mode 3, for example, the peak muscle forces from high to low is as follows: soleus, vastus, gastrocnemius, biceps

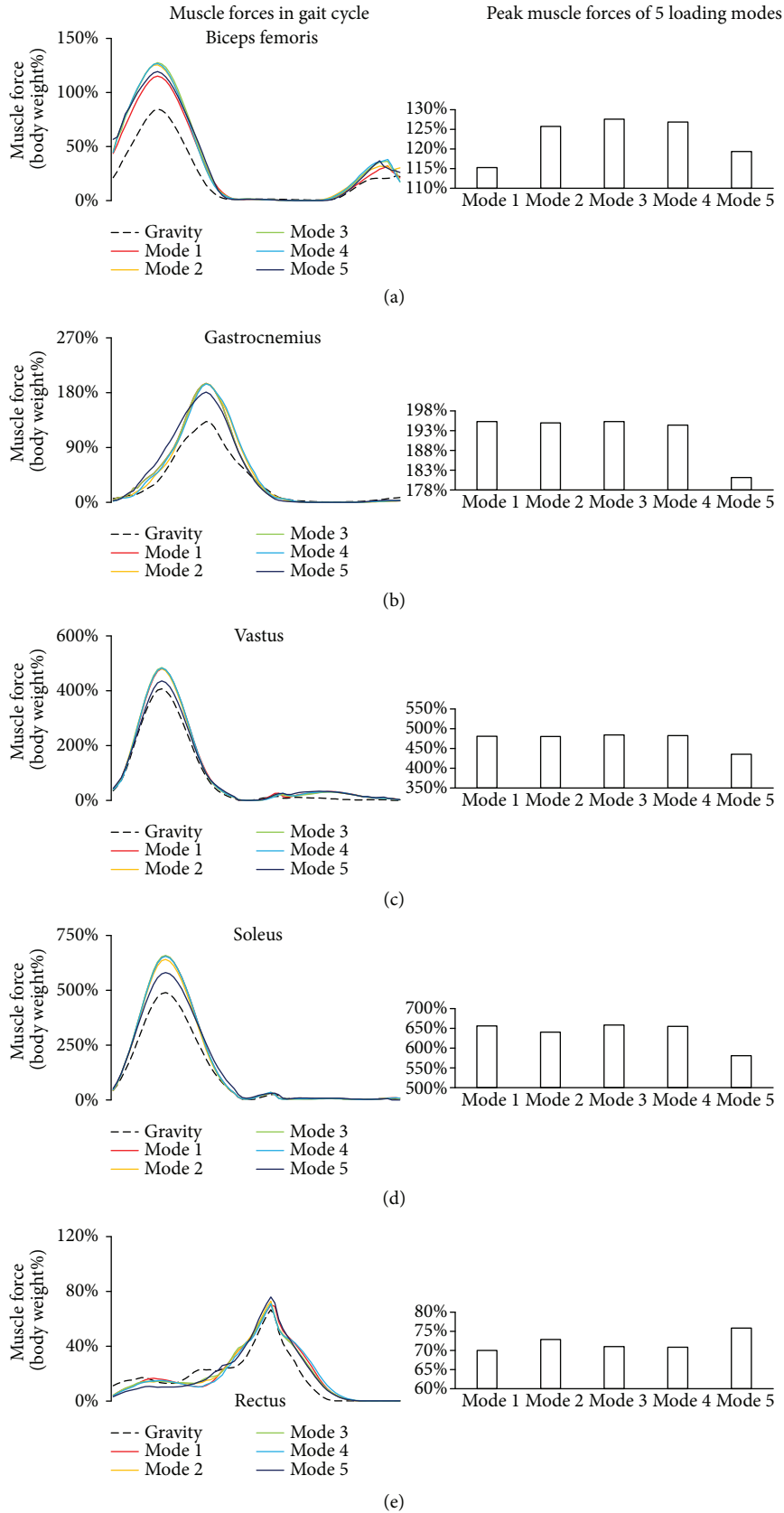


FIGURE 4: Muscle forces at gravity and five loading modes at weightlessness. The muscle forces were normalized with the body weight. For each muscle, the curve of the forces in the full gait cycle under 6 loading conditions was compared. Muscle forces at weightless condition were greater than those at gravity. (a) Biceps femoris; (b) gastrocnemius; (c) vastus; (d) soleus; (e) rectus femoris.

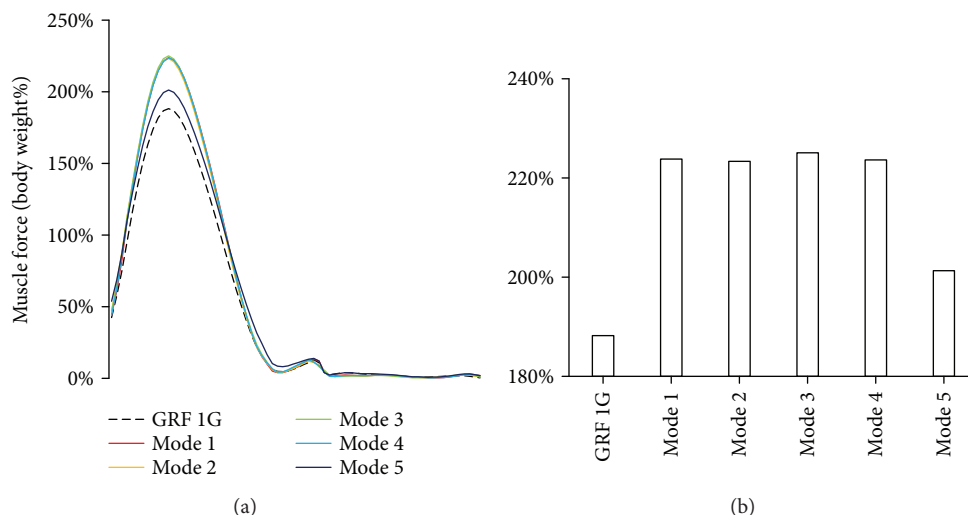


FIGURE 5: GRFs at gravity and five loading modes at weightlessness. The GRF was normalized with the body weight. The maximum GRFs at weightless condition were greater than those at gravity. (a) GRF curves in the full gait cycle under different loading conditions. (b) The maximum GRFs under different loading conditions.

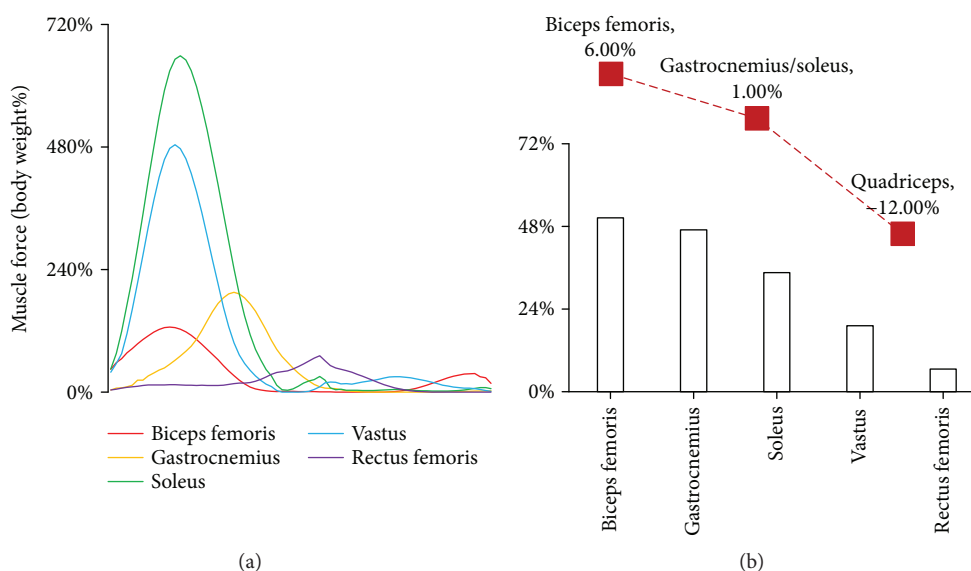


FIGURE 6: Muscle forces at weightlessness compared with those at gravity. (a) The curves of the five muscle forces at constraint loading mode 3; (b) the percent change in muscle forces based on the forces at gravity. The red curve is the postflight muscle concentric strengths compared with the preflight from NASA report [28]. The results were in agreement with the muscle atrophy observed in the astronaut.

femoris, and rectus femoris (Figure 6(a)). However, based on the muscle force at gravity, the percent change in muscle forces from high to low is as follows: biceps femoris, gastrocnemius, soleus, vastus, and rectus femoris. The results were consistent with the muscle strength change after spaceflight (Figure 6(b)) [28]. In the biceps femoris, gastrocnemius, soleus, and vastus, maximum muscle force occurred at constraint loading mode 3 (loadings applied on the shoulder and waist were 50% of the body weight). While in the rectus femoris, maximum muscle force occurred at constraint loading mode 5 (waist load was 100% of the body weight). The findings indicated that the constraint loading mode

could be manipulated to enhance the effect of muscle training at spaceflight.

The calculated curve of GRF in the gait cycle was consistent with the experimental data in the literature [29], which also provided a validation for the model calculation. Previous study has reported that the running speed had an impact on the GRF. The curve of GRF had two peaks in the stance phase when running at low speed, corresponding to heel strike and toe off. With increasing the speed, the GRF peak of heel strike will disappear [30]. A relatively high speed was applied in the treadmill countermeasure, which may lead to non-heel-striking running. Therefore, both the running

speed and constraint loading mode can affect the muscle forces during treadmill exercise. The loading configuration (loading magnitude, direction, loading positions, etc.) should be adaptive to the running speed in the future design of constraint system.

The present study has some limitations. First, the resultant constraint loading was constantly equal to the body weight. The current constraint bungee cord in space flight is an elastic material, implying that the constraint loading changes linearly with the body height during running. However, previous studies proposed that a constant constraint loading may better prevent the musculoskeletal decline in spaceflight [14, 25], which could be achieved by manipulating the loading devices. Second, the kinematical data of treadmill exercise at gravity was also used to drive the musculoskeletal model at weightlessness, because weightless experiment has reported that the gait at weightlessness approached to the gait at gravity when the resultant constraint force increased to body weight on earth. And the influence of the constraint loading on the body kinematics would be investigated with the supine treadmill experiment in our future study.

5. Conclusion

The study indicated that maximum forces of the biceps femoris, gastrocnemius, and vastus under five loading modes at weightlessness were significantly greater than those at gravity ($p < 0.01$). The percentage changes in different muscle forces were in agreement with the muscle atrophy observed in astronauts. The results further revealed that the resultant constraint force and GRF could not precisely reflect the muscle activity strength. The constraint loading mode had an impact on the muscle forces in treadmill exercise, thus could be manipulated to enhance the effect of the muscle training at spaceflight.

Disclosure

The sponsor had no role in any aspect of the study, including data collection and analysis, manuscript preparation, or authorization for publication.

Conflicts of Interest

There are no conflicts of interest for this study.

Authors' Contributions

Ning Guo and Xingyu Fan are co-first authors.

Acknowledgments

This study was supported by The Open Foundation of State Key Laboratory (SMFA16K01), the National Natural Science Foundation of China (no. 11502014, 11421202), the Young Elite Scientist Sponsorship Program by CAST (YESS 2015QNRC001), the National Key Lab of Virtual

Reality Technology, and the 111 Project (B13003). The authors thanked all the participants in this study.

Supplementary Materials

Figure S1: average and deviation of biceps femoris force in gait cycle in gravity and 5 loading modes. Figure S2: average and deviation of gastrocnemius force in gait cycle in gravity and 5 loading modes. Figure S3: average and deviation of vastus force in gait cycle in gravity and 5 loading modes. Figure S4: average and deviation of soleus force in gait cycle in gravity and 5 loading modes. Figure S5: average and deviation of rectus force in gait cycle in gravity and 5 loading modes. Table S1: ICC analysis in gait cycles. The table shows ICC analysis of each subject and five muscle force and GRF in gravity and 5 modes. Table S2: ICC analysis in 8 subjects. The table shows ICC analysis of 5 modes and gravity and 5 muscle force and GRF. Table S3: paired-samples *t*-test matrix of max biceps femoris force between different loading conditions. Table S4: paired-samples *t*-test matrix of max gastrocnemius force between different loading conditions. Table S5: paired-samples *t*-test matrix of max vastus force between different loading conditions. Table S6: paired-samples *t*-test matrix of max soleus force between different loading conditions. Table S7: paired-samples *t*-test matrix of max rectus femoris force between different loading conditions. Table S8: paired-samples *t*-test matrix of max GRF between different loading conditions. (*Supplementary Materials*)

References

- [1] G. C. Demontis, M. M. Germani, E. G. Caiani, I. Barravecchia, C. Passino, and D. Angeloni, "Human pathophysiological adaptations to the space environment," *Frontiers in Physiology*, vol. 8, p. 547, 2017.
- [2] T. Lang, J. J. W. A. van Loon, S. Bloomfield et al., "Towards human exploration of space: the THESEUS review series on muscle and bone research priorities," *npj Microgravity*, vol. 3, no. 1, p. 8, 2017.
- [3] S. Trappe, D. Costill, P. Gallagher et al., "Exercise in space: human skeletal muscle after 6 months aboard the International Space Station," *Journal of Applied Physiology*, vol. 106, no. 4, pp. 1159–1168, 2009.
- [4] H. Akima, Y. Kawakami, K. Kubo et al., "Effect of short-duration spaceflight on thigh and leg muscle volume," *Medicine and Science in Sports and Exercise*, vol. 32, no. 10, pp. 1743–1747, 2000.
- [5] D. Lambertz, C. Pérot, R. Kaspranski, and F. Goubel, "Effects of long-term spaceflight on mechanical properties of muscles in humans," *Journal of Applied Physiology*, vol. 90, no. 1, pp. 179–188, 2001.
- [6] L. W. Sun, D. Blottner, H. Q. Luan et al., "Bone and muscle structure and quality preserved by active versus passive muscle exercise on a new stepper device in 21 days tail-suspended rats," *Journal of Musculoskeletal & Neuronal Interactions*, vol. 13, no. 2, pp. 166–177, 2013.
- [7] A. LeBlanc, V. Schneider, L. Shackelford et al., "Bone mineral and lean tissue loss after long duration space flight," *Journal of Musculoskeletal & Neuronal Interactions*, vol. 1, no. 2, pp. 157–160, 2000.

- [8] D. L. Belavy, M. Adams, H. Brisby et al., "Disc herniations in astronauts: what causes them, and what does it tell us about herniation on earth?," *European Spine Journal*, vol. 25, no. 1, pp. 144–154, 2016.
- [9] M. D. de Boer, O. R. Seynnes, P. E. di Prampero et al., "Effect of 5 weeks horizontal bed rest on human muscle thickness and architecture of weight bearing and non-weight bearing muscles," *European Journal of Applied Physiology*, vol. 104, no. 2, pp. 401–407, 2008.
- [10] T. F. Lang, A. D. Leblanc, H. J. Evans, and Y. Lu, "Adaptation of the proximal femur to skeletal reloading after long-duration spaceflight," *Journal of Bone and Mineral Research*, vol. 21, no. 8, pp. 1224–1230, 2006.
- [11] T. Hosoyama, S. Ichida, M. Kanno et al., "Microgravity influences maintenance of the human muscle stem/progenitor cell pool," *Biochemical and Biophysical Research Communications*, vol. 493, no. 2, pp. 998–1003, 2017.
- [12] D. Shiba, H. Mizuno, A. Yumoto et al., "Development of new experimental platform 'MARS'-Multiple Artificial-gravity Research System-to elucidate the impacts of micro/partial gravity on mice," *Scientific Reports*, vol. 7, no. 1, article 10837, 2017.
- [13] Y. Huang, H. Luan, L. Sun, J. Bi, Y. Wang, and Y. Fan, "Local vibration enhanced the efficacy of passive exercise on mitigating bone loss in hindlimb unloading rats," *Acta Astronautica*, vol. 137, pp. 373–381, 2017.
- [14] S. M. Schneider, S. M. C. Lee, A. H. Feiveson, D. E. Watenpaugh, B. R. Macias, and A. R. Hargens, "Treadmill exercise within lower body negative pressure protects leg lean tissue mass and extensor strength and endurance during bed rest," *Physiological Reports*, vol. 4, no. 15, article e12892, 2016.
- [15] N. Petersen, P. Jaekel, A. Rosenberger et al., "Exercise in space: the European Space Agency approach to in-flight exercise countermeasures for long-duration missions on ISS," *Extreme Physiology & Medicine*, vol. 5, no. 1, p. 9, 2016.
- [16] T. M. Guess, A. P. Stylianou, and M. Kia, "Concurrent prediction of muscle and tibiofemoral contact forces during treadmill gait," *Journal of Biomechanical Engineering*, vol. 136, no. 2, article 021032, 2014.
- [17] X. Liu, J. Ouyang, Y. Fan, and M. Zhang, "A footwear-foot-knee computational platform for exploring footwear effects on knee joint biomechanics," *Journal of Medical and Biological Engineering*, vol. 36, no. 2, pp. 245–256, 2016.
- [18] J. Z. Wu, S. S. Chiou, and C. S. Pan, "Analysis of musculoskeletal loadings in lower limbs during stilts walking in occupational activity," *Annals of Biomedical Engineering*, vol. 37, no. 6, pp. 1177–1189, 2009.
- [19] N. E. Bezodis, A. I. T. Salo, and G. Trewartha, "Lower limb joint kinetics during the first stance phase in athletics sprinting: three elite athlete case studies," *Journal of Sports Sciences*, vol. 32, no. 8, pp. 738–746, 2014.
- [20] K.-Y. Wang, S. Wang, W.-Y. Zhao, P.-C. Yin, and X.-Q. Tang, "Effect of robot driving mode on lower limbs rehabilitative training," *Advances in Engineering Research*, vol. 105, pp. 622–627, 2016.
- [21] D. J. Farris, B. D. Robertson, and G. S. Sawicki, "Elastic ankle exoskeletons reduce soleus muscle force but not work in human hopping," *Journal of Applied Physiology*, vol. 115, no. 5, pp. 579–585, 2013.
- [22] M. D. K. Horsman, *The Twente Lower Extremity Model*, TMS International, Enschede, The Netherlands, 2007.
- [23] Y. Jung, M. Jung, K. Lee, and S. Koo, "Ground reaction force estimation using an insole-type pressure mat and joint kinematics during walking," *Journal of Biomechanics*, vol. 47, no. 11, pp. 2693–2699, 2014.
- [24] R. Fluit, M. S. Andersen, S. Kolk, N. Verdonchot, and H. F. J. M. Koopman, "Prediction of ground reaction forces and moments during various activities of daily living," *Journal of Biomechanics*, vol. 47, no. 10, pp. 2321–2329, 2014.
- [25] K. O. Genc, V. E. Mandes, and P. R. Cavanagh, "Gravity replacement during running in simulated microgravity," *Aviation, Space, and Environmental Medicine*, vol. 77, no. 11, pp. 1117–1124, 2006.
- [26] G. Schaffner, J. DeWitt, J. Bentley, E. Yarmanova, I. Kozlovskaya, and D. Hagan, *Effect of Load Levels of Subject Loading Device on Gait, Ground Reaction Force, and Kinematics during Human Treadmill Locomotion in a Weightless Environment*, National Aeronautics and Space Administration: Johnson Space Center, Houston, TX, USA, 2005.
- [27] S. C. Swanson and G. E. Caldwell, "An integrated biomechanical analysis of high speed incline and level treadmill running," *Medicine & Science in Sports & Exercise*, vol. 32, no. 6, pp. 1146–1155, 2000.
- [28] Institute of Medicine (U.S.), *Review of NASA's Evidence Reports on Human Health Risks: 2014 Letter Report*, The National Academies Press, Washington, DC, USA, 2015.
- [29] B. Kluitenberg, S. W. Bredeweg, S. Zijlstra, W. Zijlstra, and I. Buist, "Comparison of vertical ground reaction forces during overground and treadmill running. A validation study," *BMC Musculoskeletal Disorders*, vol. 13, no. 1, p. 235, 2012.
- [30] Y. Jung, M. Jung, J. Ryu, S. Yoon, S. K. Park, and S. Koo, "Dynamically adjustable foot-ground contact model to estimate ground reaction force during walking and running," *Gait & Posture*, vol. 45, pp. 62–68, 2016.

Research Article

The Computational Fluid Dynamics Analyses on Hemodynamic Characteristics in Stenosed Arterial Models

Yue Zhou ¹, Chunhian Lee ¹, and Jingying Wang ²

¹School of Aeronautic Science and Engineering, Beihang University, Beijing 100191, China

²School of Energy and Power Engineering, Shandong University, Jinan 250061, China

Correspondence should be addressed to Yue Zhou; yz_buaa@126.com

Received 30 November 2017; Revised 19 January 2018; Accepted 31 January 2018; Published 14 March 2018

Academic Editor: Rui Zhu

Copyright © 2018 Yue Zhou et al. This is an open access article distributed under the Creative Commons Attribution License, which permits unrestricted use, distribution, and reproduction in any medium, provided the original work is properly cited.

Arterial stenosis plays an important role in the progressions of thrombosis and stroke. In the present study, a standard axisymmetric tube model of the stenotic artery is introduced and the degree of stenosis η is evaluated by the area ratio of the blockage to the normal vessel. A normal case ($\eta=0$) and four stenotic cases of $\eta=0.25, 0.5, 0.625,$ and 0.75 with a constant Reynolds number of 300 are simulated by computational fluid dynamics (CFD), respectively, with the Newtonian and Carreau models for comparison. Results show that for both models, the poststenotic separation vortex length increases exponentially with the growth of stenosis degree. However, the vortex length of the Carreau model is shorter than that of the Newtonian model. The artery narrowing accelerates blood flow, which causes high blood pressure and wall shear stress (WSS). The pressure drop of the $\eta=0.75$ case is nearly 8 times that of the normal value, while the WSS peak at the stenosis region of $\eta=0.75$ case even reaches up to 15 times that of the normal value. The present conclusions are of generality and contribute to the understanding of the dynamic mechanisms of artery stenosis diseases.

1. Introduction

At present, arterial stenosis has been clinically regarded as playing a key role in some cardiovascular or cerebrovascular diseases, such as atherosclerotic plaque, thrombosis, and stroke [1, 2]. As the artery narrows, blood flow patterns and the vessel wall shear stress (WSS) will change greatly, which contributes to both thrombus formation and plaque cap rupture. However, it is difficult to directly measure hemodynamic factors of the diseased artery *in vivo*. CFD has become a very useful technique for predicting detailed information on human blood flows including flow patterns, pressures, and WSS [3].

Steinman et al. [4] simulated blood flows in both concentric and eccentric stenosed carotid bifurcation models to study geometrical effects on flow patterns. They proposed that the stenosed carotid bifurcation geometry may provide more specific indicators for vulnerable plaques. Long et al. [5] calculated blood flows in both axisymmetrical and asymmetrical stenosis models with three different area reductions and found that in axisymmetrical models, the poststenotic

blood flow is more sensitive to variations of the stenosis degree than in asymmetrical cases. Khader et al. [6] used CFD to study the blood flow in a simple vessel model of 66% eccentric stenosis generated from Doppler scan and demonstrated that blood flows changed dramatically with the increase in the severity of stenosis at throat region, which can cause a growth in velocity and WSS. Sui et al. [7] employed CFD to investigate the WSS, velocity, and pressure distributions in areas near carotid artery plaques and analyzed the relative change of hemodynamic parameters with different stenosis degrees.

Although many arterial stenosis cases have been investigated by the CFD technique, there remain several problems. On one hand, in some previous simulation works, the blood was treated to be Newtonian, while the real blood is non-Newtonian with rheological effects [8, 9]. On the other hand, most stenosis models used in prior CFD studies were always patient specific [10, 11], which could illustrate some unique flow characteristics in diseased arteries, but the conclusions may be lacking in theoretical generalization. Therefore, the present study introduces a standard axisymmetrical

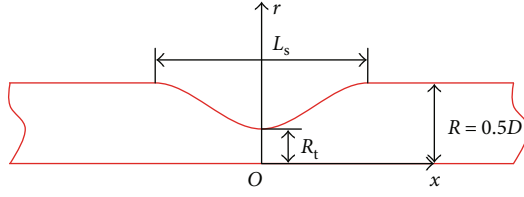


FIGURE 1: Axisymmetrical tube model of the stenosis artery.

cylindrical tube model as the stenosed artery and defines the corresponding degree of stenosis. Then, the blood flows through arterial models of different stenosis degrees are solved by CFD, respectively, with the Newtonian and a non-Newtonian constitutive model (the Carreau model [12]) for comparison. Finally, the hemodynamic characteristics of flow patterns, pressure drops, and WSS distributions are investigated quantitatively.

2. Stenosed Artery Model

The stenosed artery is simplified into a parameterized cylindrical tube model and currently only the axisymmetric stenosis case is investigated for preliminary study. As shown in Figure 1, x and r represent axial and radial coordinates, respectively; R and D are the tube radius and diameter, respectively; R_t is the radius of the stenosis throat; and L_s is the length of the stenosis region. A cosine curve is selected to describe the stenosis shape. The degree of stenosis η is defined as the ratio of the blockage area to the normal vessel cross-sectional area and is as follows:

$$\eta = \frac{\pi R^2 - \pi R_t^2}{\pi R^2} = 1 - \left(\frac{R_t}{R}\right)^2. \quad (1)$$

3. Numerical Schemes and Validation

Assuming laminar flow and neglecting the influence of body force, the arterial blood flow can be described by the incompressible viscous Navier-Stokes (N-S) equations as follows:

$$\begin{aligned} \nabla \cdot \mathbf{U} &= 0, \\ \frac{\partial \rho \mathbf{U}}{\partial t} + \nabla \cdot (\rho \mathbf{U} \mathbf{U}) &= -\nabla p + \nabla \cdot \boldsymbol{\tau}, \end{aligned} \quad (2)$$

where \mathbf{U} is the flow velocity vector; ρ is the blood density, with a value of 1050 kg/m^3 ; and p is the pressure. $\boldsymbol{\tau}$ is the viscous stress tensor and is expressed as follows:

$$\boldsymbol{\tau} = \mu \left[\nabla \mathbf{U} + (\nabla \mathbf{U})^T \right], \quad (3)$$

where μ is the dynamic viscosity. If the blood is treated as a Newtonian fluid, the viscosity μ will be a constant. However, the real blood is a multicomponent mixture consisting of blood cells and plasma, which behaves rheologically [13]. In this paper, the non-Newtonian effects of blood are calculated by the Carreau model as follows:

$$\mu = \mu_\infty + (\mu_0 - \mu_\infty) \left[1 + (\lambda \gamma)^2 \right]^{(n-1)/2}. \quad (4)$$

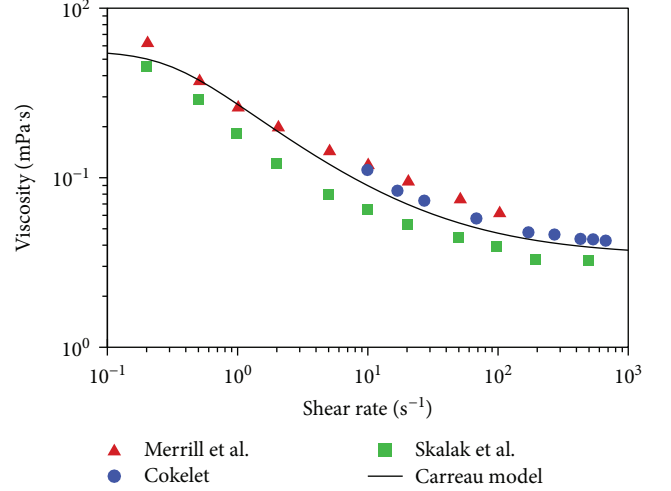


FIGURE 2: Comparison of blood viscosity given by the Carreau model with experimental data.

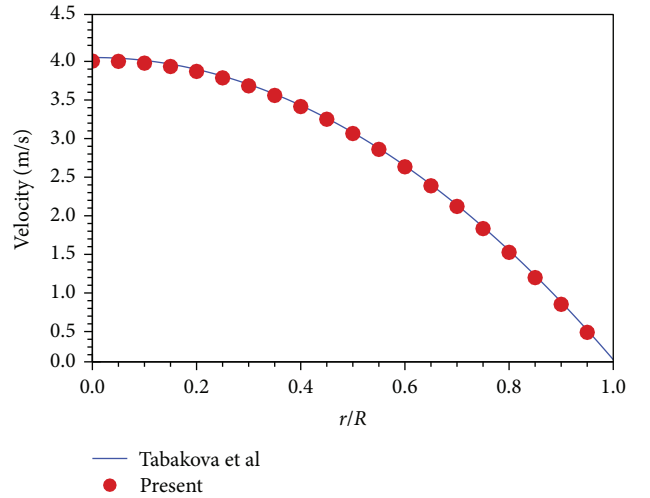


FIGURE 3: Validation of the present numerical scheme.

Equation (4) is an empirical expression, and γ is the local shear rate. There are $\mu_\infty = 0.00345 \text{ Pa} \cdot \text{s}$ (the plasma viscosity), $\mu_0 = 0.056 \text{ Pa} \cdot \text{s}$, $\lambda = 3.313 \text{ s}$, and $n = 0.3568$. Figure 2 compares the blood viscosity calculated by the Carreau model with experimental data from various sources (Merrill et al. [14]; Cokelet [15]; Skalak et al. [16]), which demonstrate that the Carreau model used in this work has a reasonable accuracy.

When implementing CFD simulations, (2), (3), and (4) are solved by the semi-implicit method for pressure-linked equations (SIMPLE) [17], which has been widely used to compute incompressible viscous flow problems. In the SIMPLE algorithm, the pressure and momentum equations are both discretized in second-order schemes to give accurate viscous blood flow results. A case of non-Newtonian tube blood flow calculated by Tabakova et al. [18] is employed to validate the present numerical scheme with the Carreau

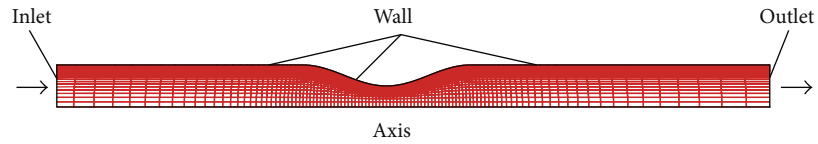


FIGURE 4: Computational grids and boundary conditions of the $\eta = 0.75$ case.

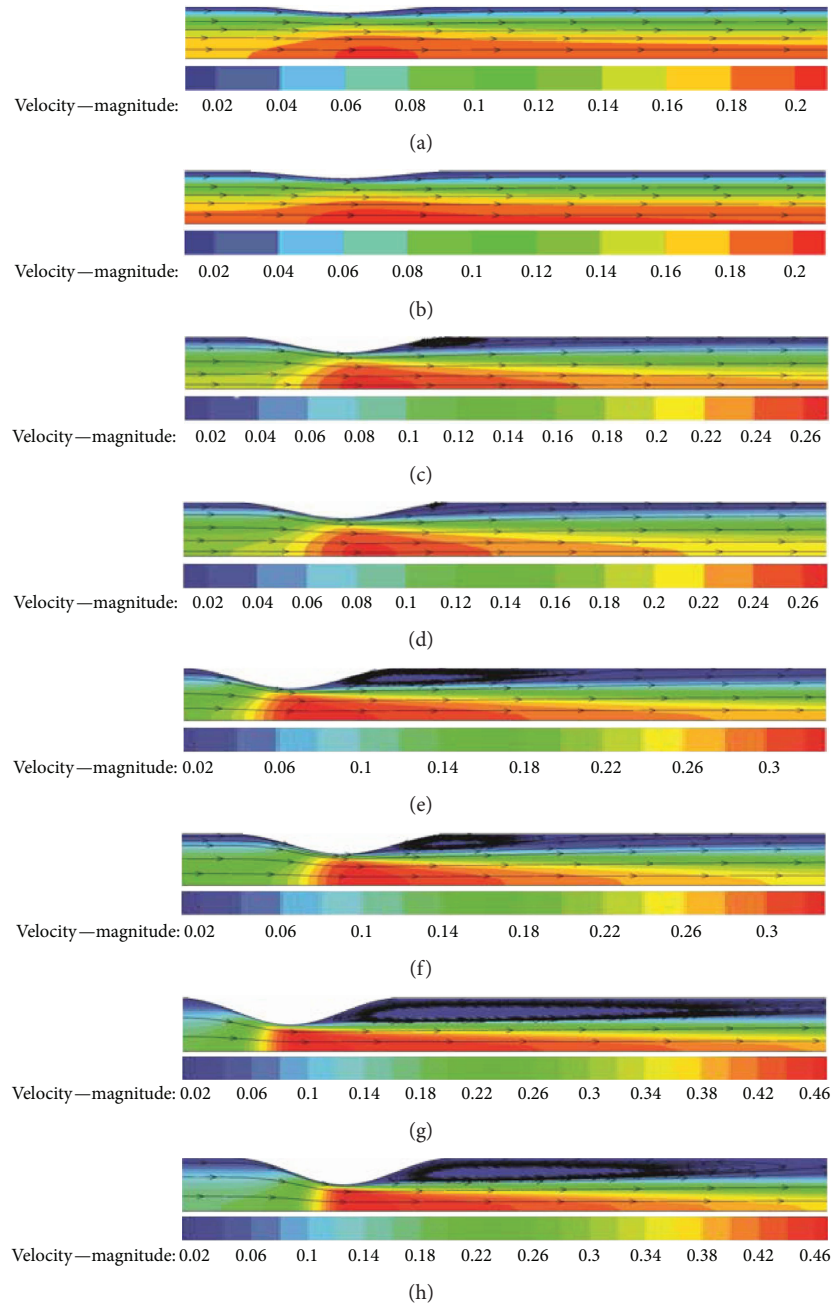


FIGURE 5: Flow patterns: (a) Newtonian, $\eta = 0.25$; (b) Carreau, $\eta = 0.25$; (c) Newtonian, $\eta = 0.5$; (d) Carreau, $\eta = 0.5$; (e) Newtonian, $\eta = 0.625$; (f) Carreau, $\eta = 0.625$; (g) Newtonian, $\eta = 0.75$; (h) Carreau, $\eta = 0.75$.

model. In this case, the tube radius is $R = 0.0031$ m, and the flow rate is $Q = 5.98 \times 10^{-5} \text{ m}^3/\text{s}$. The blood density is set to be $\rho = 1000 \text{ kg/m}^3$. Figure 3 shows that the present results

are very consistent with the data of Tabakova et al., which validate that the present numerical scheme can solve the tube blood flow accurately by the Carreau model.

4. Grids and Boundary Conditions

Five cases with different stenosis degrees, $\eta = 0, 0.25, 0.5, 0.625,$ and $0.75,$ are simulated, respectively, by using the Newtonian and Carreau models for comparison in this paper, where $\eta = 0$ represents the normal vessel without stenosis as the base case. For all cases, the radius of the arterial vessel is fixed at $R = 5 \text{ mm}$ ($D = 10 \text{ mm}$) and $L_s = 4R$. Computational grids of all cases are structural quadrangle elements and distributed nonuniformly. Close to the vessel wall and the stenosis, grid nodes are denser than other regions, so that the simulation can capture and recognize the flow patterns and hemodynamic characteristics clearly. Figure 4 shows the computational grids of the $\eta = 0.75$ case.

For all cases, boundary condition settings are the same. As illustrated in Figure 4, the left boundary is set to be the blood flow inlet, the top is the wall, the bottom is the axis, and the right is outlet. The blood flow rate of the inlet is constant with a value of $Q_b = 0.465 \text{ L/min}$ (the mean velocity $U_m = 0.0986 \text{ m/s}$). Under this flow rate, the Reynolds number is 300, which is calculated by using the vessel diameter and plasma viscosity.

5. Results and Discussions

This work focuses on analyzing the CFD results of flow patterns, pressure drops, and WSS distributions, which have the profound influence on the progression and diagnosis of artery stenosis in clinical settings.

5.1. Flow Patterns. Blood flow patterns have been considered to be specific indicators of vulnerable plaques [4]. Once stenosis happens in the artery, flow patterns can change greatly. A very important phenomenon is that there will be flow separation vortices in the poststenotic regions of severe stenosis cases, which is validated by the present CFD results. Figure 5 demonstrates that for both the Newtonian and Carreau models, the more severe the stenosis is, the bigger the separation vortex becomes. When the stenosis degree relieves to 0.25, the vortex disappears completely. Another notable phenomenon in Figure 5 is that for all cases, there is a poststenotic slow velocity region (blue-colored region) and this region enlarges as the stenosis becomes severe. In this region, the mass transportation is weak and the WSS is also small, where thrombosis is most likely to happen in clinical settings.

Figure 6 plots the vortex lengths nondimensionalized by the vessel radius R for cases of different stenosis degrees. As the vessel narrows gradually, the separation vortex lengths of the Newtonian and Carreau models both increase exponentially. When $\eta = 0.75$, the non-Newtonian vortex length can reach up to nine times that of the vessel radius. Figure 6 also shows that the vortex length of the Newtonian model is longer than that of the Carreau model, which substantiates that the Carreau model predict higher viscous dissipation than the Newtonian model. Therefore, the use of the Newtonian model for blood flow simulation should be cautious.

5.2. Pressure. Figure 7 shows the axial wall pressure (WP) distributions of all cases from $x = -3R$ to $x = 9R$ predicted,

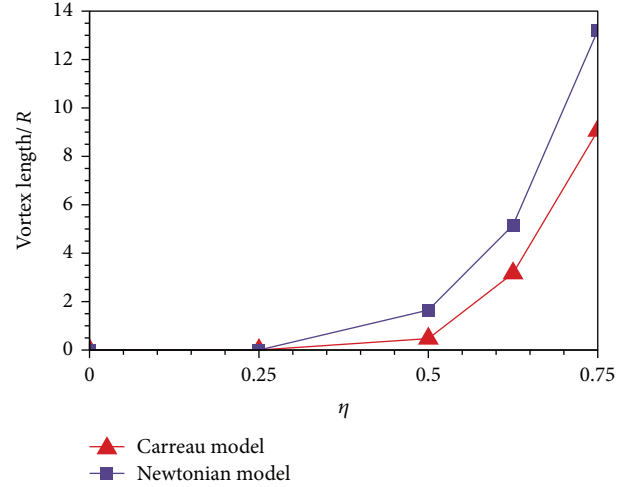


FIGURE 6: Separation vortex length.

respectively, by the Newtonian and Carreau models. The zero pressure point is set at $x = 9R$. For both models, the axial WP reduces linearly without stenosis, while it varies tortuously around the stenosis. The trend can be elucidated with the variation of the blood flow velocity. For the normal case ($\eta = 0$), the blood flow is fully developed with the unchanged velocity profile and the pressure gradient only needs to balance with the constant WSS along the axis. Therefore, the axial pressure reduces linearly. Once the stenosis happens, the velocity increases and the pressure decreases with the stenosis severity by the Bernoulli's theorem. Figure 8 illustrates that for both models, the pressure drop of $\eta = 0.75$ case is nearly 8 times that of the normal case. Therefore, artery stenosis can cause high blood pressure, which has been explained in [19]. For the Newtonian flow, if the flow rate Q is constant, there is

$$\frac{\delta(\Delta p)}{\Delta p} = -4 \frac{\delta D}{D}, \quad (5)$$

where δ is the differential operator, Δp is the pressure drop, and D is the tube radius. Equation (5) means that the variations of pressure drop and radius have opposite trends. According to (5), when the radius decreases, the pressure drop necessarily rises. The present CFD results validate the same for the non-Newtonian blood flow.

5.3. WSS. Existing studies always focus on analyzing the WSS characteristics of stenosis diseases. High WSS in the partially occluded vessel has been known to activate platelet-platelet binding events that play a very important role in thrombosis [4]. This work also predicts the WSS distributions of all stenosis and normal cases, respectively, by the Newtonian and Carreau models. Figure 9 displays the WSS distributions from $x = -3R$ to $x = 9R$ along the axis of the normal ($\eta = 0$), $\eta = 0.5$, and $\eta = 0.75$ cases for both models. Under each stenosis degree, the WSS of the Carreau model is a little greater than that of the Newtonian model but both have similar trends. For two models, at the stenosis region ($x = -2R$ to $x = 2R$), the stenosis WSS is remarkably higher than that

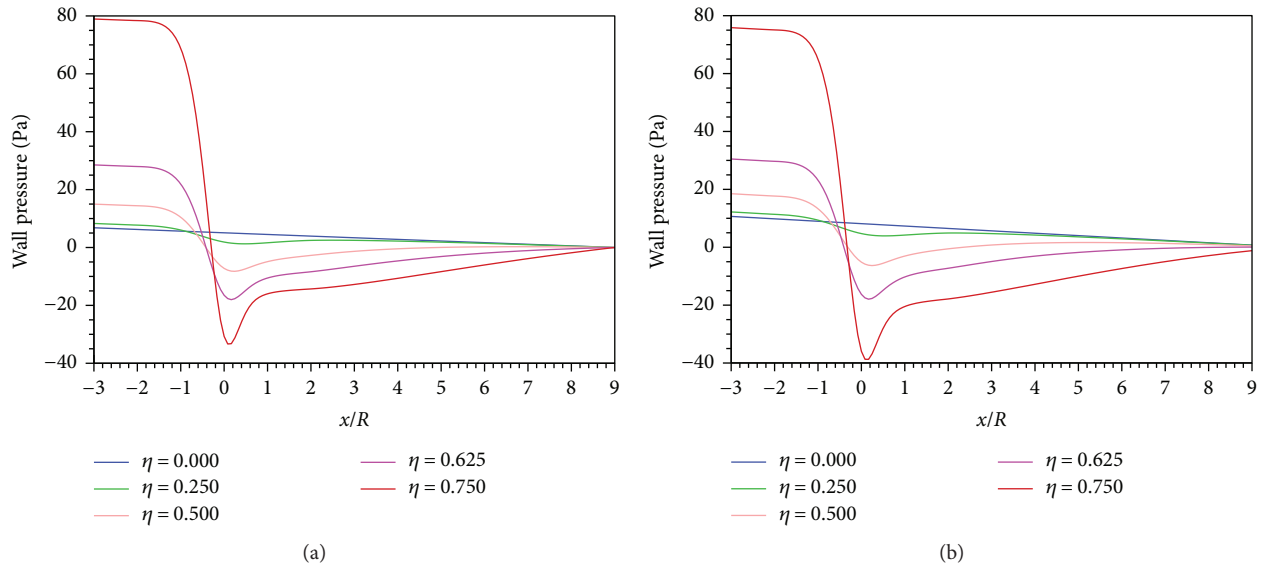


FIGURE 7: Axial wall pressure distributions of all stenosis cases: (a) Newtonian; (b) Carreau.

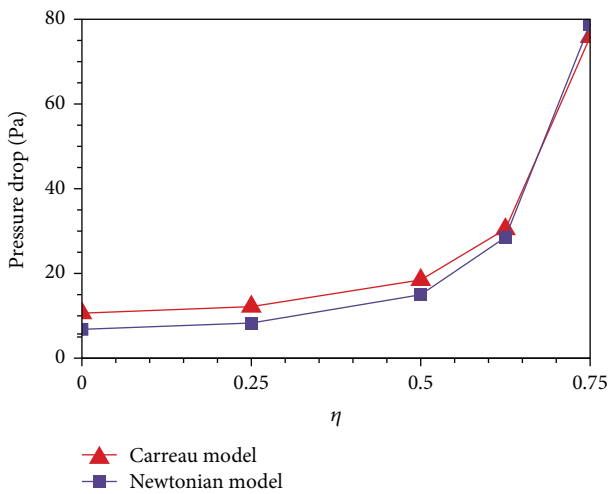


FIGURE 8: Pressure drops from $x = -3R$ to $x = 9R$ of all stenosis cases.

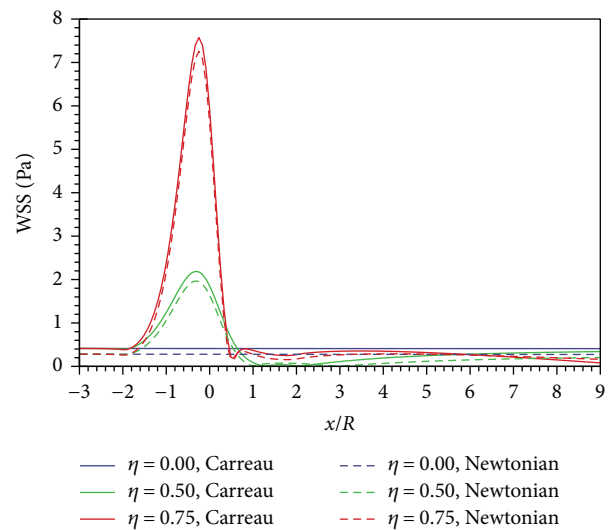


FIGURE 9: WSS distributions along the axis of all cases.

of the normal case and WSS peaks both appear around the stenosed centre ($x = 0$). The WSS peak increases dramatically with the growth of the stenosis degree. When the stenosis degree rises to $\eta = 0.75$, the WSS peaks of both models reach up to about 7.5 Pa, almost 15 times that of the normal value (about 0.5 Pa). Therefore, artery stenosis indeed causes a remarkable WSS increase. In fact, according to Figure 5 and (3), the high-speed flow at the stenosis region results in a high WSS, and clinically, this region may be the fibrous cap in the vessel. The corresponding mechanical stress can contribute to plaque rupture and dislodged material [20].

6. Conclusions

Although the CFD technique has been widely used to investigate arterial stenosis, many previous studies solved the blood flows through unique patient-specific artery models,

the conclusions of which may be the lack of generalization. In addition, some research employed only the Newtonian constitutive model for CFD simulation, which cannot reflect the rheological behaviour of blood. Therefore, the current study introduces a standard tube model of arterial stenosis and simulates tube blood flows, respectively, by the Newtonian and (non-Newtonian) Carreau models for comparison.

A normal ($\eta = 0$) and four diseased cases of different stenosis degrees, $\eta = 0.25, 0.5, 0.625,$ and 0.75 , are all computed with a constant Reynolds number, $Re = 300$. For the Newtonian and Carreau models, both results quantitatively show that the severe narrowing can cause the remarkable poststenotic flow separation and the length of separation vortex elongates exponentially as the tube contracts. However, the non-Newtonian vortex is shorter than the Newtonian vortex, because the viscous dissipation of the Carreau model

is higher than that of the Newtonian model. The arterial stenosis accelerates the blood flow and causes the high blood pressure drop. For both models, the pressure drop of $\eta = 0.75$ case is nearly 8 times that of the normal value. The WSS of the Carreau model is a little greater than that of the Newtonian model. The artery narrowing leads to a high WSS increase at the stenosis region. For both models, the WSS peak of $\eta = 0.75$ case even reaches up to 15 times that of the normal.

Conflicts of Interest

The authors declare that they have no conflicts of interest.

References

- [1] W. Rosamond, K. Flegal, G. Friday et al., "Heart disease and stroke statistics—2007 update," *Circulation*, vol. 115, no. 5, pp. e69–e171, 2007.
- [2] R. Shadman, M. H. Criqui, W. P. Bundens et al., "Subclavian artery stenosis: prevalence, risk factors, and association with cardiovascular diseases," *Journal of the American College of Cardiology*, vol. 44, no. 3, pp. 618–623, 2004.
- [3] J. Wu, G. Liu, W. Huang, D. N. Ghista, and K. K. L. Wong, "Transient blood flow in elastic coronary arteries with varying degrees of stenosis and dilatations: CFD modelling and parametric study," *Computer Methods in Biomechanics and Biomedical Engineering*, vol. 18, no. 16, pp. 1835–1845, 2014.
- [4] D. A. Steinman, T. L. Poepping, M. Tambasco, R. N. Rankin, and D. W. Holdsworth, "Flow patterns at the stenosed carotid bifurcation: effect of concentric versus eccentric stenosis," *Annals of Biomedical Engineering*, vol. 28, no. 4, pp. 415–423, 2000.
- [5] Q. Long, X. Y. Xu, K. V. Ramnarine, and P. Hoskins, "Numerical investigation of physiologically realistic pulsatile flow through arterial stenosis," *Journal of Biomechanics*, vol. 34, no. 10, pp. 1229–1242, 2001.
- [6] A. S. M. Khader, S. B. Shenoy, R. B. Pai, S. Ganesh Kamath, N. M. Sharif, and V. R. K. Rao, "Effect of increased severity in patient specific stenosis of common carotid artery using CFD—a case study," *World Journal of Modelling and Simulation*, vol. 7, pp. 113–122, 2011.
- [7] B. Sui, P. Gao, Y. Lin, L. Jing, S. Sun, and H. Qin, "Hemodynamic parameters distribution of upstream, stenosis center, and downstream sides of plaques in carotid artery with different stenosis: a MRI and CFD study," *Acta Radiologica*, vol. 56, no. 3, pp. 347–354, 2015.
- [8] Y. Zhang, T. Furusawa, S. F. Sia, M. Umezue, and Y. Qian, "Proposition of an outflow boundary approach for carotid artery stenosis CFD simulation," *Computer Methods in Biomechanics and Biomedical Engineering*, vol. 16, no. 5, pp. 488–494, 2013.
- [9] T. Frauenfelder, E. Boutsianis, T. Schertler et al., "In-vivo flow simulation in coronary arteries based on computed tomography datasets: feasibility and initial results," *European Radiology*, vol. 17, no. 5, pp. 1291–1300, 2007.
- [10] J. R. Cebal, M. A. Castro, J. E. Burgess, R. S. Pergolizzi, M. J. Sheridan, and C. M. Putman, "Characterization of cerebral aneurysms for assessing risk of rupture by using patient-specific computational hemodynamics models," *American Journal of Neuroradiology*, vol. 26, no. 10, pp. 2550–2559, 2005.
- [11] K. Pekkan, B. Whited, K. Kanter et al., "Patient-specific surgical planning and hemodynamic computational fluid dynamics optimization through free-form haptic anatomy editing tool (SURGEM)," *Medical & Biological Engineering & Computing*, vol. 46, no. 11, pp. 1139–1152, 2008.
- [12] Y. I. Cho and K. R. Kensey, "Effects of the non-Newtonian viscosity of blood on flows in a diseased arterial vessel. Part 1: steady flows," *Biorheology*, vol. 28, no. 3-4, pp. 241–262, 1991.
- [13] O. K. Baskurt and H. J. Meiselman, "Blood rheology and hemodynamics," *Seminars in Thrombosis and Hemostasis*, vol. 29, no. 5, pp. 435–450, 2003.
- [14] E. W. Merrill, E. R. Gilliland, G. Cokelet, H. Shin, A. Britten, and R. E. Wells Jr, "Rheology of human blood, near and at zero flow: effects of temperature and hematocrit level," *Biophysical Journal*, vol. 3, no. 3, pp. 199–213, 1963.
- [15] G. Cokelet, *Biomechanics: Its Foundation and Objectives*, Prentice-Hall, Englewood Cliffs, 1972.
- [16] R. Skalak, S. R. Keller, and T. W. Secomb, "Mechanics of blood flow," *Journal of Biomechanical Engineering*, vol. 103, no. 2, pp. 102–115, 1981.
- [17] S. V. Patankar and D. B. Spalding, "A calculation procedure for heat, mass and momentum transfer in three-dimensional parabolic flows," *International Journal of Heat and Mass Transfer*, vol. 15, no. 10, pp. 1787–1806, 1972.
- [18] S. Tabakova, E. Nikolova, and S. Radev, "Carreau model for oscillatory blood flow in a tube," *AIP Conference Proceedings*, vol. 1629, no. 1, pp. 336–343, 2014.
- [19] Y. C. Fung, *Biomechanics: Circulation*, Springer Science & Business Media LLC, New York, NY, USA, 1984.
- [20] G. J. Hademenos and T. F. Massoud, "Biophysical mechanisms of stroke," *Stroke*, vol. 28, no. 10, pp. 2067–2077, 1997.

Research Article

A Comprehensive Method for Accurate Strain Distribution Measurement of Cell Substrate Subjected to Large Deformation

Hong He ¹, Rong Zhou ¹, Yuanwen Zou ¹, Xuejin Huang,² and Jinchuan Li²

¹College of Materials Science and Engineering, Sichuan University, Chengdu 610065, China

²College of Architecture and Environment, Sichuan University, Chengdu 610065, China

Correspondence should be addressed to Yuanwen Zou; zyw@scu.edu.cn

Received 26 July 2017; Revised 11 October 2017; Accepted 23 October 2017; Published 8 January 2018

Academic Editor: Wei Yao

Copyright © 2018 Hong He et al. This is an open access article distributed under the Creative Commons Attribution License, which permits unrestricted use, distribution, and reproduction in any medium, provided the original work is properly cited.

Cell mechanical stretching *in vitro* is a fundamental technique commonly used in cardiovascular mechanobiology research. Accordingly, it is crucial to measure the accurate strain field of cell substrate under different strains. Digital image correlation (DIC) is a widely used measurement technique, which is able to obtain the accurate displacement and strain distribution. However, the traditional DIC algorithm used in digital image correlation engine (DICE) cannot obtain accurate result when utilized in large strain measurement. In this paper, an improved method aiming to acquire accurate strain distribution of substrate in large deformation was proposed, to evaluate the effect and accuracy, based on numerical experiments. The results showed that this method was effective and highly accurate. Then, we carried out uniaxial substrate stretching experiments and applied our method to measure strain distribution of the substrate. The proposed method could obtain accurate strain distribution of substrate film during large stretching, which would allow researchers to adequately describe the response of cells to different strains of substrate.

1. Introduction

Cardiovascular mechanobiology [1–5] is a discipline that focuses on the effects of the mechanical environment on the cardiovascular system and elucidates how mechanical factors produce biological effects that lead to vascular remodeling. Cardiovascular mechanobiology aims to provide biomechanical solutions for the diagnosis, prevention, and rehabilitation of cardiovascular disease. Cell mechanical stretching *in vitro*, vascular stretching *in vitro*, an animal model of stress changes in blood vessel *in vivo*, and numerical simulation method are commonly used in cardiovascular mechanobiology experiments. Cell-substrate stretching technique, extensively used *in vitro* cell mechanical experiments, is an effective method of force transduction [6–8]. Riehl et al. [9] summarized the methods of mechanical stretching in cell-substrate stretching experiments and showed that most of the strain loaded on substrate was large, with the maximum value up to 33%. Besides, strain distribution varies from region to region within a substrate. Thus, it is of great importance to analyze the accurate strain field of substrate under large deformation.

Some commonly used methods for measuring substrate strain include the direct calculation method, the resistance strain gauge measuring method, the phase shift shadow moiré method, and the finite element analysis. In the direct calculation method [10], several marks should be drawn first on the surface of substrate, so that the displacement and strain can be calculated by analyzing the difference of those marks between the images captured before and after deformation. The accuracy of this method is heavily dependent on the distribution of marks. Therefore, the direct calculation method is a rough measurement. The resistance strain gauge measurement method [11] attaches strain sensors to the surface of substrate for strain measurement. However, the use of any contact-type sensor would obstruct the stretching of substrate especially under large deformation and lead to unexpected results. The phase shift shadow moiré method [12] requires complex operation, resulting in large systematic errors, since its accuracy would be influenced by light intensity. The finite element analysis [13, 14] is a computational simulation method, which can investigate many mechanical properties such as displacement and strain by

setting material parameters and environmental parameters. However, the finite element analysis is usually based on models under ideal assumptions and cannot replace the actual experiment.

Digital image correlation (DIC) is a contactless full-field displacement and strain measurement technique. Since it was first proposed in the 1980s [15, 16], DIC is now extensively applied in many experimental mechanics researches [17, 18]. Digital image correlation engine (DICE) [19], developed by the Sandia National Laboratory, is an open-source library of DIC. With DICE, DIC would become a convenient and user friendly tool so that users can pay more attention to their researches rather than repeatedly programming the basic and complex procedures of DIC. To the best of our knowledge, to date, DICE has not been used to obtain accurate strain field of substrate in cell-substrate stretching experiments under large strain. The Newton-Raphson (NR) algorithm was used in DICE to calculate the desired deformation. However, in NR algorithm, the calculation result of the previous step is regarded as the start value of iteration for the next step. So the initial guess is of great importance in calculating strain field, especially under large deformation. An unreliable initial guess would seriously impact the results of strain measurement. Pan et al. [20] developed an incremental reliability-guided DIC technique (RG-DIC) for large deformation measurement, in which the recently developed robust RG-DIC technique was combined with an automatic reference image updating scheme, and the reference image for DIC analysis is automatically updated according to the seed point's zero-mean normalized cross-correlation (ZNCC) coefficient. This method could deal with specimens with irregular geometric shape and/or subjected to discontinuous deformation as well as minimize the accumulated errors in finally estimated displacements. Zhou et al. [21] proposed a fully automated method. In this method, the computer vision technique was used to extract image feature points and to match them between reference and deformed images. The deformation parameters of the seed point are initialized from the affine transform, and then the refined parameters are automatically transferred to adjacent points using a modified quality-guided initial guess propagation scheme. This method can accurately initialize all points of interest for the deformed images even in the presence of large rotation and/or heterogeneous deformation. Zhao et al. [22] proposed the utilization of three well-known population-based intelligent algorithms (PIAs), that is, genetic algorithm (GA), differential evolution (DE), and particle swarm optimization (PSO), and then incorporated standard PIAs with three improving strategies, including Q-stage evolutionary (T), parameter control (C), and space expanding (E) strategies, finally derived of a total of eighteen PIA-based algorithms. They tested these algorithms and found that DE-TCE performed best. Another large deformation measurement scheme, combining improved coarse search method and updating reference image scheme, was proposed by Tang et al. [23]. With this method, not only extremely large deformation can be

measured successfully but also the accumulated error introduced by updating reference image could be controlled. Pan et al. [24] proposed an integrated scheme which combined the Fourier–Mellin transform-based cross-correlation (FMT-CC) for seed point initiation with a reliability-guided displacement tracking (RGDT) strategy for the remaining points. This method can provide an accurate initial guess for DIC calculation, even in the presence of large rotations. In order to obtain reliable initial values and then calculate accurate strain field of cell substrate under large strain, a simple method was proposed in this study and was combined with DICE. Compared with methods described above, without the use of feature detection, feature point matching, and other techniques, our method can accurately obtain the initial guess of the NR iteration for large deformation.

2. Materials and Methods

2.1. DIC Principles

2.1.1. Basic Principles. DIC is an optical-numerical full-field displacement measuring technique with subpixel accuracy. In its basic principle, the measurement is performed by tracking or matching the same points (or pixels) between the two images recorded before and after deformation [17, 25]. The image recorded before and after motion is called reference image and deformed image, respectively. In general, the calculation area, also called the region of interest (ROI), should be specified or defined in the reference image, which is further divided into evenly spaced virtual grids. Moreover, each intersection point of virtual grids is selected as the center of a subset. The subset is the matching unit within the ROI, usually a square of $(2M + 1) \times (2M + 1)$ pixels. Then, a correlation criterion should be defined to evaluate the degree of similarity between reference and deformed subsets. The matching procedure is completed through searching the peak position of the distribution of correlation coefficient. Once the correlation coefficient extremum is detected, the position of the deformed subset is determined. The differences in the positions of the reference subset center and the target subset center yield the in-plane displacement vector at the calculate point.

2.1.2. Shape Function. Based on the assumption of deformation continuity of a deformed solid object, a set of neighboring points in a reference subset remains as neighboring points in the target subset. The coordinate of points around the subset center in the reference subset can be mapped to points in the target subset according to the shape function. The first-order shape function that allows translation, rotation, shear, normal strains, and their combinations of the subset is most commonly used.

$$x'_i = x_i + u + u_x \Delta x + u_y \Delta y, \quad (1)$$

$$y'_j = y_j + v + v_x \Delta x + v_y \Delta y, \quad (2)$$

where x_i, y_j is the local coordinate of each pixel point in reference subset, x'_i, y'_j is the coordinate in the deformed subset,

u and v are the displacement components, and $u_x, u_y, v_x,$ and v_y are the displacement gradient components.

2.1.3. Correlation Criterion. To evaluate the similarity degree between the reference and deformed subsets, a correlation criterion should be defined in advance before correlation analysis. It is concluded that the zero-normalized cross-correlation (ZNCC) or zero-normalized sum of squared differences (ZNSSD) correlation criterion offers the most robust noise-proof performance and is insensitive to the offset and linear scale in illumination lighting [17].

2.1.4. Subpixel Registration Algorithm. As shown in (1) and (2), the coordinate of points in the deformed subset may locate between pixels. Thus, before evaluating the similarity between reference and deformed subsets using the correlation criterion, the reference image and deformed image must be reconstructed by a certain kind of subpixel registration algorithm to further improve the accuracy of DIC.

2.1.5. DICE. DICE is an open-source library of DIC, which can be used as a module in an external application or as a standalone analysis code. With DICE, DIC would become a more convenient tool and decrease the complexity when users apply it to their researches.

In DICE, the ZNSSD [17] is applied as the correlation criterion for its insensitivity to offset and linear scale in illumination lighting.

$$C_{\text{ZNSSD}} = \sum_{i=-N}^N \sum_{j=-N}^N \left[\frac{f(x_i, y_j) - f_m}{\sqrt{\sum_{i=-N}^N \sum_{j=-N}^N [f(x_i, y_j) - f_m]^2}} - \frac{g(x'_p, y'_j) - g_m}{\sqrt{\sum_{i=-N}^N \sum_{j=-N}^N [g(x'_p, y'_j) - g_m]^2}} \right]^2, \quad (3)$$

where $f(x_i, y_j)$ and $g(x'_p, y'_j)$ denote the grayscale level of each point in the reference and deformed images, respectively, and f_m and g_m are the mean intensity value of two subsets. x_i, y_j is the local coordinate of each pixel point in reference subset, and x'_p, y'_j is the coordinate in the deformed subset.

As a classic algorithm in DIC, the NR algorithm is utilized in DICE as the iterative spatial domain cross-correlation algorithm. In the first-order shape function, the desired mapping parameter vector is $\mathbf{p} = (u, v, u_x, u_y, v_x, v_y)^T$, where u, v denotes the displacement components and u_x, u_y, v_x, v_y is the strain of subset. To acquire the desired deformation vector by the NR iteration method, the solution can be written as [17]

$$\mathbf{p} = \mathbf{p}_0 - \frac{\nabla C(\mathbf{p}_0)}{\nabla \nabla C(\mathbf{p}_0)}, \quad (4)$$

where \mathbf{p}_0 is the initial guess of the solution, \mathbf{p} is the next iterative approximation solution, $\nabla C(\mathbf{p}_0)$ is the gradients of

correlation criteria, and $\nabla \nabla C(\mathbf{p}_0)$ is the second-order derivation of correlation criteria.

2.2. Improved DIC Scheme. As described above, the NR algorithm was used in DICE to calculate the desired deformation vector. However, when it is applied to large strain measurement directly, the iteration divergence would appear, so that the accurate strain cannot be obtained. Figures 1 and 2 show the calculation results of DICE under small and large strain, respectively. Figure 1 is under 0.1% strain and Figure 2 is under 10% strain. As shown in Figure 1, the displacement distribution is continuous and the strain field is uniform. The strain distribution is very close to its setting value 0.1%, suggesting that the DICE calculation is valid and accurate. Nevertheless, as shown in Figure 2, the displacement distribution is not continuous which cannot happen in the actual, indicating that these results are invalid.

In traditional DICE, the coordinate (0,0) was used as the default NR iteration initial value of displacement (u_0, v_0), which is only suitable in small deformation situation. The iteration would not satisfy the converge condition when applied to calculating large strain. Therefore, the result in Figure 2 is caused by the default iterative initial value. Vendroux and Knauss [26] found that convergence range of the NR iteration is generally within 7 pixels through experimental results. However, the large deformation is common in many cardiovascular mechanobiology cell mechanical stretching experiments. Therefore, searching a reliable initial value is of great importance under large strain. In order to get the reliable initial guess, we proposed a comprehensive method and combined it with DICE.

To illustrate the proposed method, a schematic drawing is shown in Figure 3. Conventional correlation calculation generally starts with the upper-left point of the ROI, so the $P(x_0, y_0)$ point in Figure 3(a) is the first calculation point. After a uniaxial loading, $P(x_0, y_0)$ has moved to a new position called $P'(x'_0, y'_0)$ as shown in Figure 3(b).

In order to get the reliable initial guess, a searching area along the deformation direction should be set. Then, the similarity degree between the first subset in the reference image and all subsets of the searching area in the deformed image should be calculated by the chosen correlation criterion. The subset with the optimal similarity degree and the first subset is the target subset.

$$C(p) = C(u, v) = \sum_{i=1}^M \sum_{j=1}^M \left[\frac{f(x_i, y_j) - f_m}{\sqrt{\sum_{i=1}^M \sum_{j=1}^M [f(x_i, y_j) - f_m]^2}} - \frac{g(x_i + u, y_j + v) - g_m}{\sqrt{\sum_{i=1}^M \sum_{j=1}^M [g(x_i + u, y_j + v) - g_m]^2}} \right]^2, \quad (5)$$

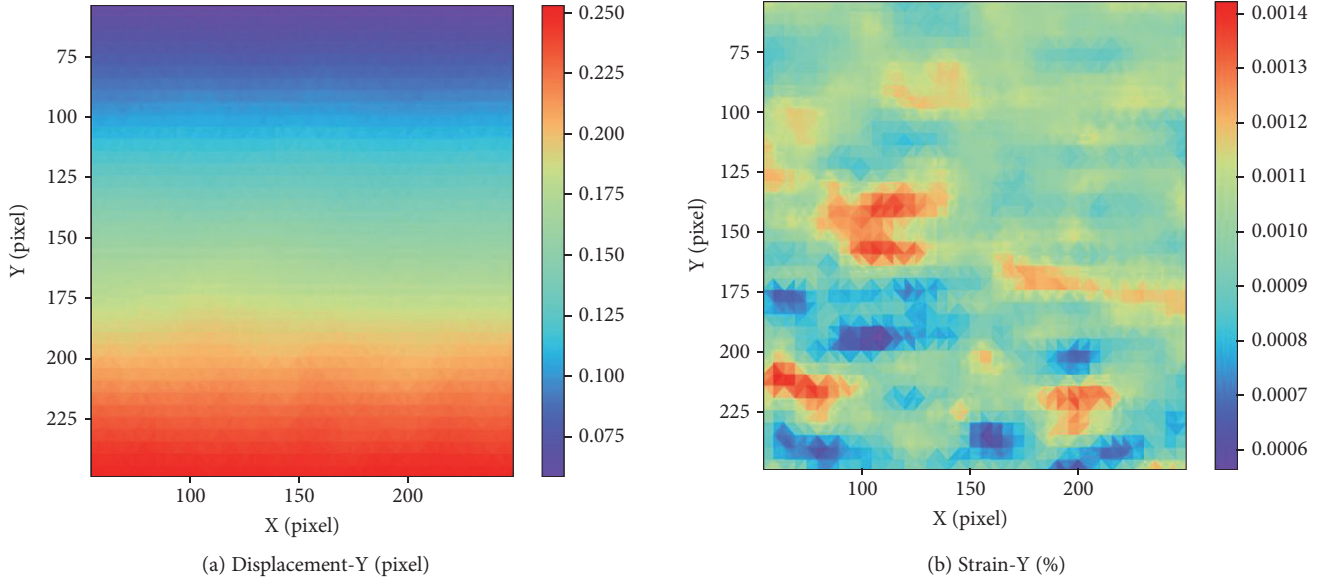


FIGURE 1: Calculation results by DICe under 0.1% strain: (a) displacement distribution along y-axis; (b) strain distribution along y-axis.

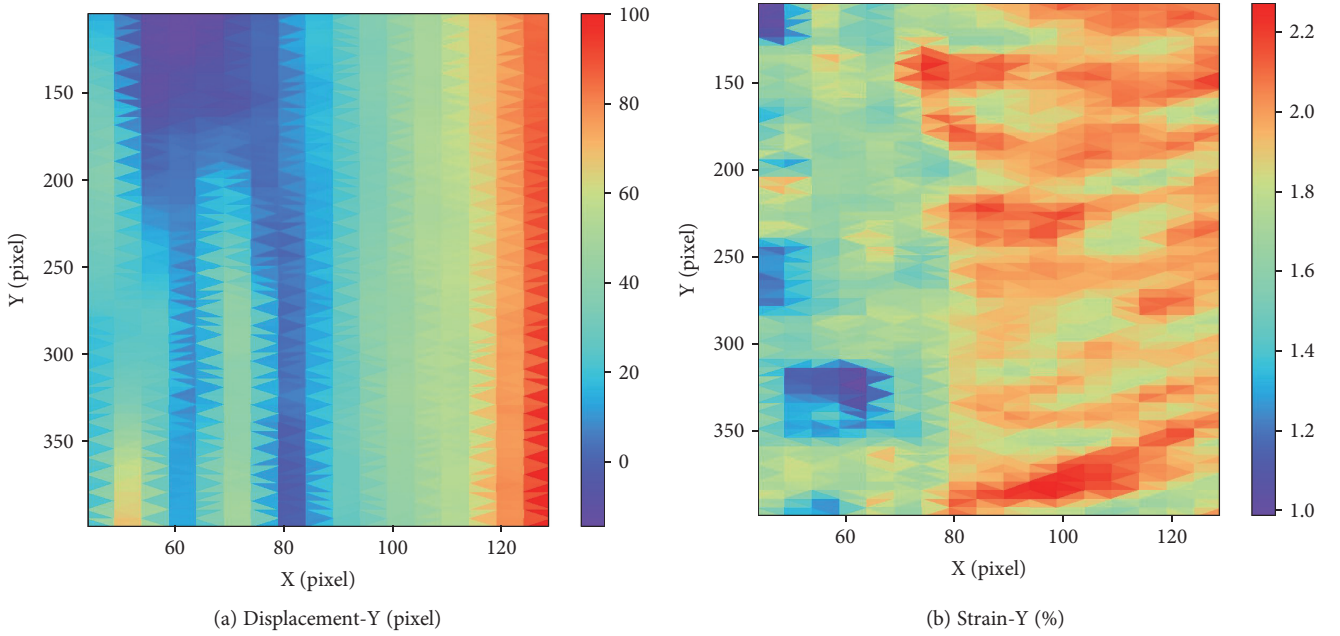


FIGURE 2: Calculation results by DICe under 10% strain: (a) displacement distribution along y-axis; (b) strain distribution along y-axis.

where u, v denotes the displacement components, and f_m and g_m are the mean intensity value of two subsets, respectively. M is the size of the first subset, $\mathbf{p} = (u, v)^T$ is the displacement parameter vector, and x_i, y_j is the coordinate of each pixel point in the first subset. It is worth noting that the points $(x_i + u, y_j + v)$ in the deformed image should be located in the searching area. Then, the maximum value of $C(u, v)$ would be calculated.

$$C(\mathbf{p}') = \max(C(u, v)), \quad (6)$$

where \mathbf{p}' is the displacement parameter vector corresponding to the maximum value. The parameters u and v in \mathbf{p}' are the initial guess for NR iteration.

The detailed process of the proposed method is as follows:

Step 1. In the reference image, define the ROI and divide it into evenly spaced virtual grids. Each intersection point of virtual grids is selected as the center of a subset.

Step 2. Reconstruct the deformed image. Choose fourth-order Keys interpolant (Keys4) algorithm as the subpixel registration algorithm.

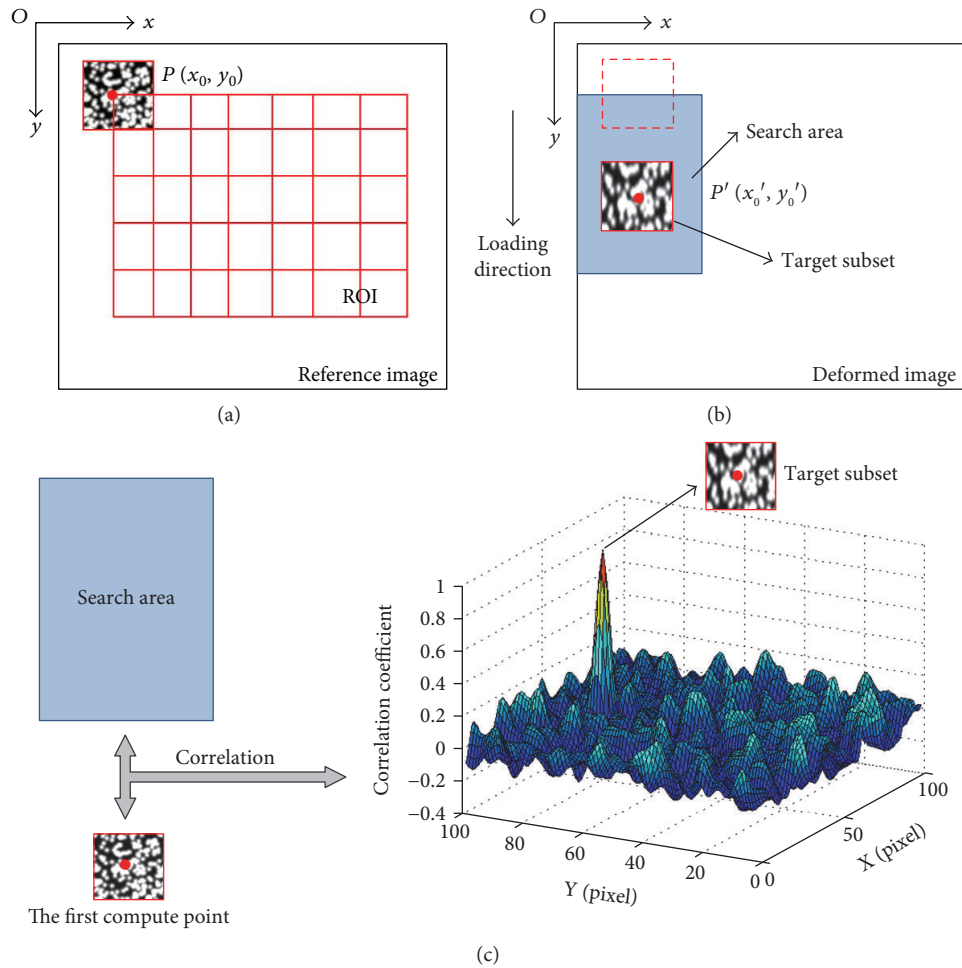


FIGURE 3: Schematic illustration of the proposed method: (a) reference image; (b) deformed image; (c) matching results.

Step 3. Set deformation direction, the size of the searching area. Obtain the reliable initial guess for NR iteration with the method described above. The calculated (u, v) is the initial guess for NR iteration in the next step.

Step 4. Choose the next calculate point and calculate its displacement and strain. The displacement and strain suppose to be calculated by NR iteration using the initial guess obtained in the last step. It is worth noting that the number of NR iterations should not exceed the given threshold. If it exceeds, set another searching area along the deformation direction and calculate the displacement and strain of the current calculate point by the method in Step 3.

Step 5. Repeat Step 4 until the displacement and strain of all calculate points are acquired.

The flowchart of the proposed method is shown in Figure 4. D is the deformation direction, S is the size of the searching area, and ϵ , a very small value, is the precision variable to calculate the reliable displacement and strain for NR iteration. If the difference between the calculated displacement/strain values twice in succession is less than ϵ in an

iteration, the convergence conditions of Newton iteration are satisfied. Then, we take the calculated displacement/strain value as the displacement/strain of the current calculate point. N represents the number of NR iterations, N_{th} represents the threshold of NR iteration number, $Count$ represents the number of points whose displacement has been calculated, and $Count_{th}$ represents the total of the calculate points.

It is worth noting that the threshold for the NR iteration number N_{th} may impact the results. In our method, the NR iteration stops when the number of iterations reaches the threshold or the convergence condition satisfies. If the threshold for the NR iteration number is too small, the NR iteration may stop because of reaching the threshold rather than the iteration convergence, so that the calculated result of the calculate point may be not the best value or not the correct result at all, which would affect the correctness of the next calculate point in turn. So it is necessary to set a suitable value as the threshold for the NR iteration number. Experiments show that when the strain is less than 20%, the NR iteration of each calculate point would satisfy the convergence condition within 20–50 iterations. In this situation, it is proper to set the threshold to 50. When the strain value is between 20%

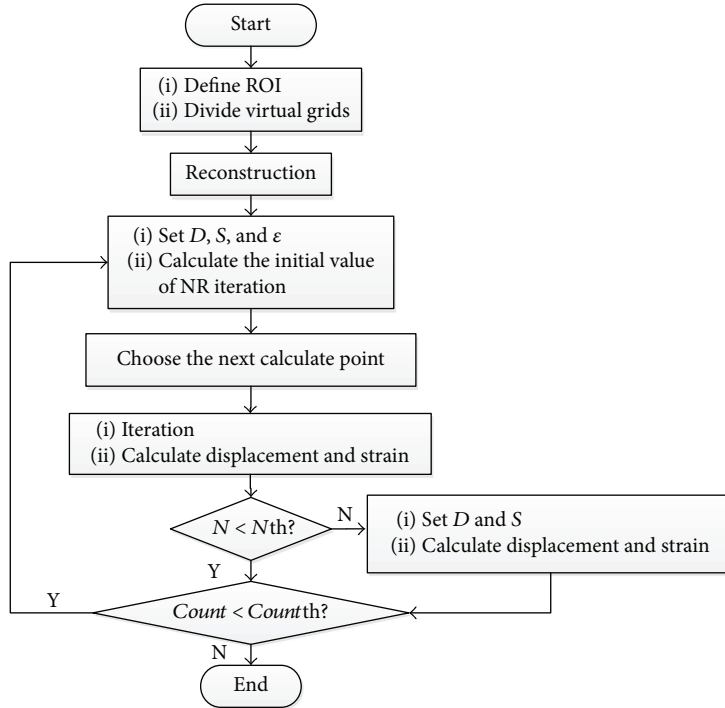


FIGURE 4: Flowchart of the proposed method process.

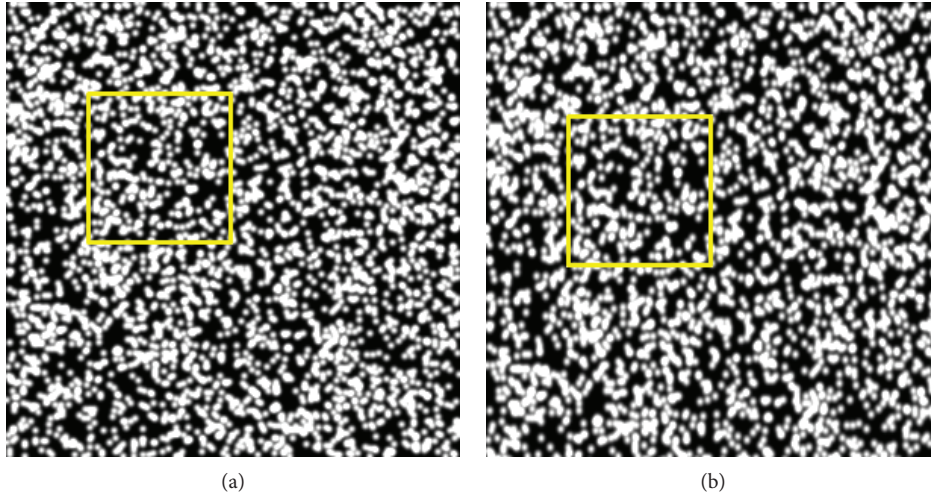


FIGURE 5: Simulated speckle patterns: (a) reference image; (b) deformed image at the strain of 20%. The imposed yellow rectangle shows the obvious deformation.



FIGURE 6: Artificial speckle pattern.

and 50%, the NR iteration of each calculate point would converge within 50–100 iterations. It is more appropriate to set the threshold to 100 under this circumstance. Because the strain values in our experiments range from

0 to 50%, we choose 100 as the threshold for the NR iteration number.

2.3. Experiments

2.3.1. Numerical Verification Experiments. Computer-simulated images can provide well-controlled image features and deformation information and are therefore used in our study to verify the accuracy and precision of the proposed method.

Zhou and Goodson [27] proposed an approach to generate simulated speckle images. Speckle patterns before and after deformation are assumed to be the sum of individual Gaussian speckles with random distribution.

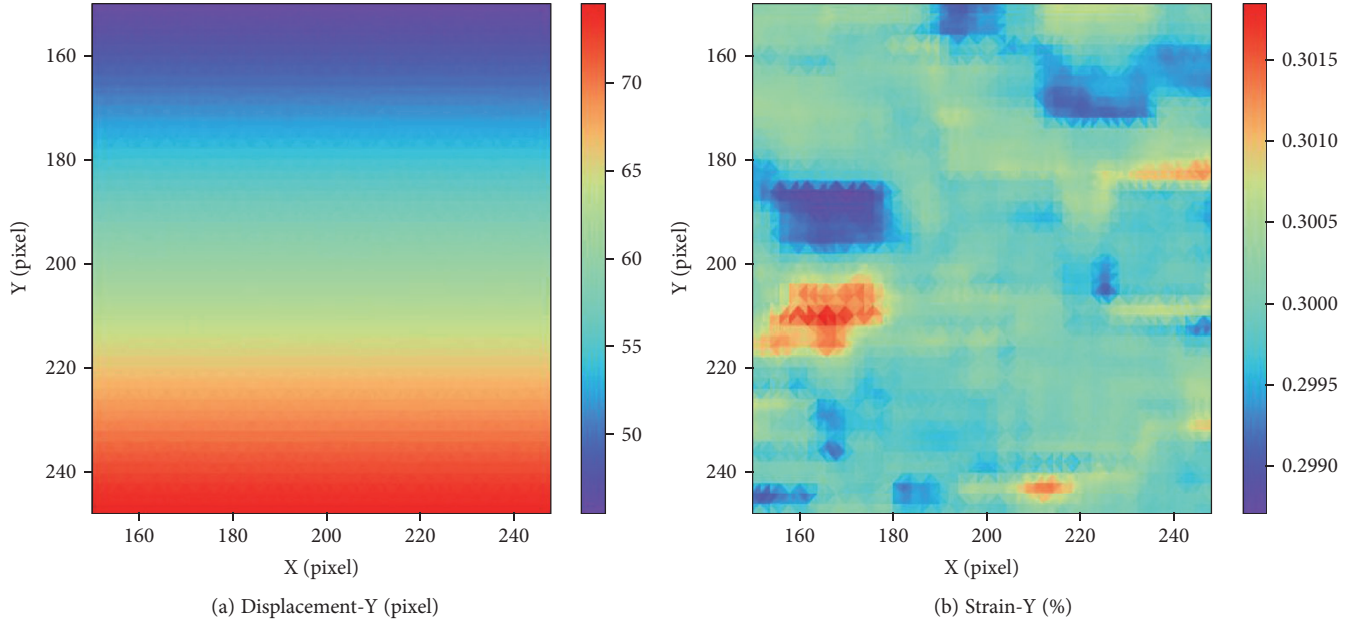


FIGURE 7: The result of simulated speckle experiment in 30% strain: (a) displacement distribution along y -axis; (b) strain distribution along y -axis.

TABLE 1: Comparison between setting strain and computing strain.

Setting strain (10^{-2})	Computing strain (10^{-2})	Bias error
5	5.001 ± 0.037	$1.0 e-05$
10	10.002 ± 0.038	$2.0 e-05$
15	15.002 ± 0.047	$2.0 e-05$
20	20.004 ± 0.047	$4.0 e-05$
25	24.999 ± 0.045	$1.0 e-05$
30	30.001 ± 0.044	$1.0 e-05$
35	35.003 ± 0.044	$3.0 e-05$
40	40.000 ± 0.039	0
45	45.004 ± 0.041	$4.0 e-05$
50	49.998 ± 0.044	$2.0 e-05$

$$I_1(\mathbf{r}) = \sum_{k=1}^s I_0 \exp\left(-\frac{|\mathbf{r} - \mathbf{r}_k|^2}{a^2}\right), \quad (7)$$

$$I_2(\mathbf{r}) = \sum_{k=1}^s I_0 \exp\left(-\frac{|\mathbf{r} - \mathbf{U}(\mathbf{r}) - \mathbf{r}_k|^2}{a^2}\right), \quad (8)$$

$$\mathbf{U}(\mathbf{r}) = \mathbf{U}_0 + \nabla \mathbf{U}_0 \mathbf{r} = \begin{pmatrix} u_0 + u_x x + u_y y \\ v_0 + v_x x + v_y y \end{pmatrix}, \quad (9)$$

where I_1 and I_2 denote the reference image and the deformed image, respectively. s is the total number of speckles, I_0 is the peak intensity of each speckle, $\mathbf{r}_k = (x_k, y_k)^T$ is the position of each speckle with a random distribution, and a is the speckle size. $\mathbf{U}(\mathbf{r})$ in (9) is the displacement field calculated to describe deformation.

In this paper, we used this method to generate ten different strains of speckle patterns, ranging from 5% to 50%, with the increment of 5%. Figure 5 shows the simulated speckle patterns at the setting strain of 20%. We utilized our proposed method to calculate the strain by reference image and the deformed image and then compared the strain to the setting value to verify the accuracy of our method.

2.3.2. Uniaxial Substrate Stretching Experiments. At present, there are three methods widely used *in vitro* cell-substrate tensile stress experiments: rectangular substrate stretching method, 4-point bending beam loading method, and circular substrate deformation method. The rectangular substrate stretching method is a uniaxial stretching method, which can approximate the mechanical environment of the blood vessel in human body maximally and achieve a more uniform strain [28, 29]. Therefore, uniaxial substrate stretching experiments were performed and our method was applied to measure the strain distribution of the substrate.

In these experiments, we used medical silica gel film as stretching substrate specimen, which is colorless and transparent. Therefore, the speckle pattern must be artificially made firstly. In this study, black and white quick-drying paints were sprayed on the film (see Figure 6). The size of the substrate specimen was $25 \text{ mm} \times 80 \text{ mm}$ (thickness of 0.4 mm).

The stretching device is as Zhou et al. [30] depicted. The substrate was placed between two stainless steel clamps and imaged using an industrial camera (JHSM1400f, Shenzhen Jinghang Technology Co. Ltd.). The images were captured at the selected resolution of 2048×1536 pixels. Two stepper motors fixed on an optical platform were used to perform uniaxial stretching. A self-designed multichannel motor control module was used to control these stepper motors. A

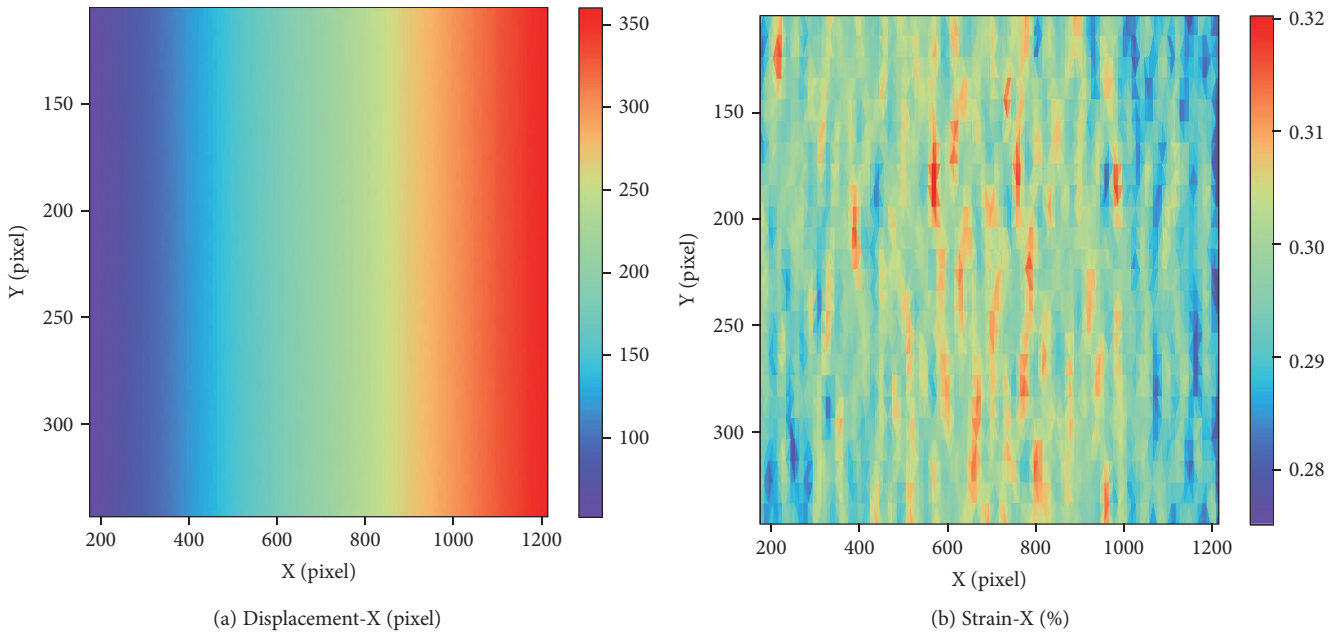


FIGURE 8: The result of uniaxial substrate stretching experiments at the tension of 30%: (a) displacement distribution along x -axis; (b) strain distribution along x direction.

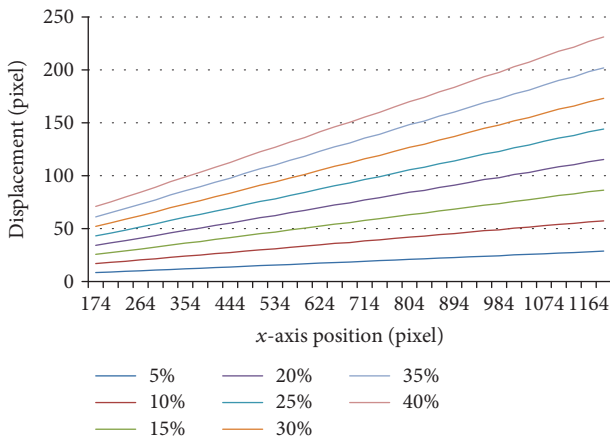


FIGURE 9: The distribution of displacement under different tension along y direction.

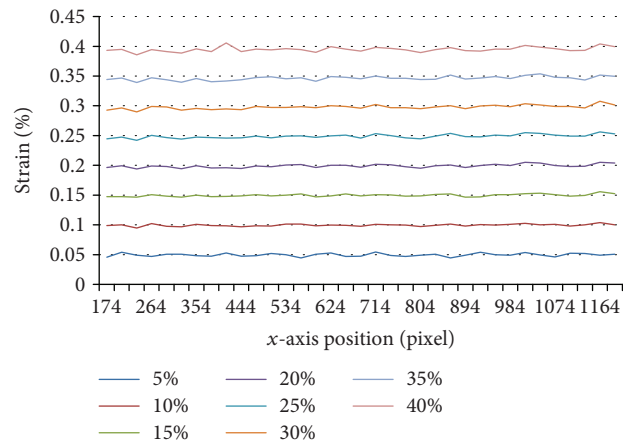


FIGURE 10: The distribution of strain under different tension along y direction.

computer equipped with a 4-port RS-232 USB-to-serial converter (UPort 1450, MOXA) was programmed to provide the accurate synchrony of stepper motors via RS-232 serial ports and the image capture via USB. A series of tension, ranging from 5% to 40% with the increment of 5%, was applied as constant tension. Afterwards, the acquired images were processed with the proposed method to calculate the displacement and strain distribution of the substrate. In these experiments, the central region of substrate, usually as the cell culture area, was selected as the ROI.

3. Results and Discussion

3.1. Numerical Verification Experiments. In the simulation experiment, normal strain was exerted in y direction in the value of 5%, 10%, 15%, 20%, 25%, 30%, 35%, 40%, 45%,

and 50%. In our method, the displacement and strain distribution can be acquired. Figure 7 shows the calculation result at the strain of 30%. The horizontal coordinate is the position in x direction, and the vertical coordinate is the position in y direction. Different colors in legend represent different displacement values or strain values. As shown in Figure 7, the displacement field is continuous and the strain distribution is generally uniform with small standard deviations. The average of measuring strain is 30.00083%, which is very close to the setting value 30%, demonstrating that the proposed method can measure the large strain accurately.

All results of these simulated speckle experiments are displayed in Table 1. Setting strain is the parameter used to generate deformed images. Computing strain, presented as

TABLE 2: Comparison between the proposed method and stretching equipment.

Reference strain (%)	Measured strain (%)	Relative error (%)
5	4.95 ± 0.59	1.00
10	9.97 ± 0.52	0.30
15	15.0 ± 0.58	0.00
20	19.9 ± 0.67	0.50
25	24.9 ± 0.73	0.40
30	29.8 ± 0.78	0.67
35	34.6 ± 0.85	1.14
40	39.3 ± 1.13	1.75

mean \pm standard deviation, denotes the calculation value by our proposed method. According to Table 1, the computing strains in all images are very close to the setting strains with small bias error. Additionally, each computing strain has small standard deviation. These results suggest that the proposed method is highly accurate and can be used in calculating the strain distribution under large deformation.

3.2. Uniaxial Substrate Stretching Experiments. Figure 8 shows the calculation results at the tension of 30% by the proposed method. The horizontal and vertical coordinate is the position in x direction and y direction, respectively. Different colors in legend represent different displacement value or strain value. The displacement is continuous and changes along x direction as expected. The strain values are ranging from 28% to 32% and concentrate at 30%.

As the tension was loaded in the x direction, we evaluated the component of the displacement and strain vector in the x direction, and the results can be seen in Figures 9 and 10. Figure 9 shows the distribution of displacement under different tension along x -axis. The horizontal axis represents the position in x direction, and the vertical axis represents the displacement of substrate calculated by the proposed method along x direction under different tension. Different colors represent different strain group. The displacement along x -axis appears the same rising tendency at every step and also increased with tension. Figure 10 shows the distribution of strain under different tension along x -axis. The horizontal axis represents the position in x direction, and the vertical axis represents the strain of substrate calculated by the proposed method along x direction under different tension. Different colors represent different strain group. The strains along x -axis remain stable and appear small fluctuation in each tension, indicating that the substrate is homogeneous.

We compared the strains calculated by the proposed method with which obtained from the stretching equipment, the result is shown in Table 2. Reference strain is the strain calculated by the displacement from the stretching equipment and the initial length of the substrate. Measured strain, presented as mean \pm standard deviation, is calculated by the proposed method in this paper, which is the average value of strain field in the central region of substrate sized 1050×250 pixels. The relative error equals the ratio of the difference between the reference strain and the measured strain to the reference strain.

According to Table 2, the measured strain is always very close to the reference strain. The differences between the reference strains and the calculated strains are tiny, and the maximum of relative errors is 1.75%, which shows that the proposed method can be used for large strain measurement in the actual tensile experiments. Moreover, every measured strain appears small standard deviation, demonstrating that the strain distribution of the substrate is uniform and the substrate is homogeneous.

4. Conclusions

In order to obtain accurate strain distribution *in vitro* mechanical stretching of cell culture, an improved method is proposed in this paper and combined with DICe. The proposed method successfully solved the problem that DICe could not be used directly to compute the large strain. To evaluate the effect and accuracy of the proposed method, numerical experiments were performed. The results demonstrated that accurate displacement and strain field could be acquired by the proposed method. Moreover, uniaxial substrate stretching experiments were performed and the proposed method was used for strain distribution measurement of the substrate, large strain in the actual tensile experiments to obtain accurate strain distribution. In addition, our method can be applied to measure strain in a wide range, especially in strain distribution measurement of soft tissues. Combining our method with 3D DIC technique, the 3D displacement field and surface strain field of 3D object can be measured. It can be applied to soft tissue deformation measurement (e.g., muscles and skin) in mechanobiology and sports medicine experiments. Thus, it could allow experimenters to adequately research the response of cells and soft tissues to different strains.

Conflicts of Interest

The authors declare that there is no conflict of interests regarding the publication of this paper.

References

- [1] Z. Jiang, "Research on cardiovascular mechanobiology and medical engineering: a review," *Journal of Medical Biomechanics*, vol. 20, no. 2, pp. 65-66, 2005.
- [2] J. S. Park, N. F. Huang, K. T. Kurpinski, S. Patel, S. Hsu, and S. Li, "Mechanobiology of mesenchymal stem cells and their use in cardiovascular repair," *Frontiers in Bioscience*, vol. 12, no. 12, pp. 5098-5116, 2007.
- [3] S. Arjunon, S. Rathan, H. Jo, and A. P. Yoganathan, "Aortic valve: mechanical environment and mechanobiology," *Annals of Biomedical Engineering*, vol. 41, no. 7, pp. 1331-1346, 2013.
- [4] D. G. Simpson, W. W. Sharp, T. K. Borg, R. L. Price, A. M. Samarel, and L. Terracio, "Mechanical regulation of cardiac myofibrillar structure," *Annals of New York Academy of Sciences*, vol. 752, pp. 131-140, 1995.
- [5] Z. Jiang, "Recent advances in cardiovascular biomechanics," *Journal of Medical Biomechanics*, vol. 25, no. 5, pp. 313-315, 2010.

- [6] P. R. Standley, A. Cammarata, B. P. Nolan, C. T. Purgason, and M. A. Stanley, "Cyclic stretch induces vascular smooth muscle cell alignment via NO signaling," *American Journal of Physiology - Heart and Circulatory Physiology*, vol. 283, no. 5, pp. H1907–H1914, 2002.
- [7] J. H. C. Wang, P. Goldschmidt-Clermont, and F. C. P. Yin, "Contractility affects stress fiber remodeling and reorientation of endothelial cells subjected to cyclic mechanical stretching," *Annals of Biomedical Engineering*, vol. 28, no. 10, pp. 1165–1171, 2000.
- [8] J. H. Haga, Y. S. Li, and S. Chien, "Molecular basis of the effects of mechanical stretch on vascular smooth muscle cells," *Journal of Biomechanics*, vol. 40, no. 5, pp. 947–960, 2007.
- [9] B. D. Riehl, J. H. Park, I. K. Kwon, and J. Y. Lim, "Mechanical stretching for tissue engineering: two-dimensional and three-dimensional constructs," *Tissue Engineering Part B: Reviews*, vol. 18, no. 4, pp. 288–300, 2012.
- [10] A. Colombo, P. A. Cahill, and C. Lally, "An analysis of the strain field in biaxial Flexcell membranes for different waveforms and frequencies," *Proceedings of the Institution of Mechanical Engineers, Part H: Journal of Engineering in Medicine*, vol. 222, no. 8, pp. 1235–1245, 2008.
- [11] H. Zhang, *The Study on the Biological Effects of Cyclic Substrate Strain on Human Pulmonary Epithelial Cells*, College of Bioengineering, [Ph.D. thesis], Chongqing University, China, 2002.
- [12] H. L. Mi and C. Xu, "Mechanical property of elastic culture membrane using phase-shift shadow moiré method," *Journal of Clinical Rehabilitative Tissue Engineering Research*, vol. 13, no. 12, pp. 2378–2382, 2009.
- [13] J. P. V. Geest, E. S. D. Martino, and D. A. Vorp, "An analysis of the complete strain field within Flexercell™ membranes," *Journal of Biomechanics*, vol. 37, no. 12, pp. 1923–1928, 2004.
- [14] T. Tang, J. Qiu, and Z. Zhuang, "Theoretical model and numerical simulation of cardiac myocyte reorientation during cyclic substrate stretch," *Journal of Tsinghua University (Science and Technology)*, vol. 50, no. 5, pp. 660–664, 2010.
- [15] I. Yamaguchi, "A laser-speckle strain gauge," *Journal of Physics E: Scientific Instruments*, vol. 14, no. 11, pp. 1270–1273, 1981.
- [16] W. H. Peters and W. F. Ranson, "Digital imaging techniques in experimental stress analysis," *Optical Engineering*, vol. 21, no. 3, article 213427, 1982.
- [17] B. Pan, K. Qian, H. Xie, and A. Asundi, "Two-dimensional digital image correlation for in-plane displacement and strain measurement: a review," *Measurement Science and Technology*, vol. 20, no. 6, article 062001, 2009.
- [18] Y.-t. Men, X.-m. Li, L. Chen, and H. Fu, "Experimental study on the mechanical properties of porcine cartilage with micro-defect under rolling load," *Journal of Healthcare Engineering*, vol. 2017, Article ID 2306160, 9 pages, 2017.
- [19] D. Turner, *Digital Image Correlation Engine (DICE) Reference Manual*, Sandia Report, SAND2015 - 10606 O, 2015.
- [20] B. Pan, W. DF, and Y. Xia, "Incremental calculation for large deformation measurement using reliability-guided digital image correlation," *Optics and Lasers in Engineering*, vol. 50, no. 4, pp. 586–592, 2012.
- [21] Y. H. Zhou, B. Pan, and Y. Q. Chen, "Large deformation measurement using digital image correlation: a fully automated approach," *Applied Optics*, vol. 51, no. 31, pp. 7674–7683, 2012.
- [22] J.-q. Zhao, P. Zeng, L.-p. Lei, and Y. Ma, "Initial guess by improved population-based intelligent algorithms for large inter-frame deformation measurement using digital image correlation," *Optics and Lasers in Engineering*, vol. 50, no. 3, pp. 473–490, 2012.
- [23] Z. Tang, J. Liang, Z. Xiao, and C. Guo, "Large deformation measurement scheme for 3D digital image correlation method," *Optics and Lasers in Engineering*, vol. 50, no. 2, pp. 122–130, 2012.
- [24] B. Pan, Y. Wang, and L. Tian, "Automated initial guess in digital image correlation aided by Fourier–Mellin transform," *Optical Engineering*, vol. 56, article 014103, 2017.
- [25] T. C. Chu, W. F. Ranson, and M. A. Sutton, "Applications of digital-image-correlation techniques to experimental mechanics," *Experimental Mechanics*, vol. 25, no. 3, pp. 232–244, 1985.
- [26] G. Vendroux and W. G. Knauss, "Submicron deformation field measurements: part 2. Improved digital image correlation," *Experimental Mechanics*, vol. 38, no. 2, pp. 86–92, 1998.
- [27] P. Zhou and K. E. Goodson, "Subpixel displacement and deformation gradient measurement using digital image/speckle correlation," *Optical Engineering*, vol. 40, no. 8, pp. 1613–1620, 2001.
- [28] J. Imsirovic, K. Derricks, J. A. Buczek-Thomas, C. B. Rich, M. A. Nugent, and B. Suki, "A novel device to stretch multiple tissue samples with variable patterns: application for mRNA regulation in tissue-engineered constructs," *Biomatter*, vol. 3, no. 3, article e24650, 2013.
- [29] Y. Yung, H. Vandenburg, and D. J. Mooney, "Cellular strain assessment tool (CSAT): precision-controlled cyclic uniaxial tensile loading," *Journal of Biomechanics*, vol. 42, no. 2, pp. 178–182, 2009.
- [30] R. Zhou, Y. Yang, W. Zhang, and Y. Zou, "A strain feedback compensation method during cell tensile experiments," *Journal of Healthcare Engineering*, vol. 2017, Article ID 1587670, 6 pages, 2017.

Research Article

An Approach to Developing Customized Total Knee Replacement Implants

Xinyu Li,¹ Changjiang Wang,^{1,2} Yuan Guo,¹ and Weiyi Chen¹

¹*Institute of Applied Mechanics and Biomedical Engineering, Taiyuan University of Technology, Taiyuan, Shanxi 030024, China*

²*School of Engineering and Informatics, University of Sussex, Brighton BN1 9QJ, UK*

Correspondence should be addressed to Weiyi Chen; chenweiyi211@163.com

Received 25 July 2017; Accepted 9 October 2017; Published 7 November 2017

Academic Editor: Lizhen Wang

Copyright © 2017 Xinyu Li et al. This is an open access article distributed under the Creative Commons Attribution License, which permits unrestricted use, distribution, and reproduction in any medium, provided the original work is properly cited.

Total knee replacement (TKR) has been performed for patients with end-stage knee joint arthritis to relieve pain and gain functions. Most knee replacement patients can gain satisfactory knee functions; however, the range of motion of the implanted knee is variable. There are many designs of TKR implants; it has been suggested by some researchers that customized implants could offer a better option for patients. Currently, the 3-dimensional knee model of a patient can be created from magnetic resonance imaging (MRI) or computed tomography (CT) data using image processing techniques. The knee models can be used for patient-specific implant design, biomechanical analysis, and creating bone cutting guide blocks. Researchers have developed patient-specific musculoskeletal lower limb model with total knee replacement, and the models can be used to predict muscle forces, joint forces on knee condyles, and wear of tibial polyethylene insert. These available techniques make it feasible to create customized implants for individual patients. Methods and a workflow of creating a customized total knee replacement implant for improving TKR kinematics and functions are discussed and presented in this paper.

1. Introduction

Total knee replacement (TKR) has been widely used to relieve osteoarthritis pain, and it has been established as a successful treatment for advanced degenerative joint disease. TKR is expected to rise due to the aging population, obesity, and public expectations. A typical TKR implant has a metal femoral component, a metal tibial tray, a polyethylene insert, and a polyethylene button. One of the main aims of TKR is for a patient to walk postoperatively; however, Milner [1] showed that some patients remain walking abnormally following TKR. The altered gait patterns do not necessarily mean that the TKR has failed, but it may have an impact on the patient's functional capacity in everyday life. For example, more pain, joint stiffness, not able to walk, instability, longer leg, and loose of implanted knee have been reported by patients. Bonnefoy-Mazure et al. [2] presented their research on the evolution of the knee gait kinematic in patients with knee osteoarthritis before and three months after TKR; they pointed out that the disability is still significant for most patients three months after TKR. They

suggested that a better understanding of the impairments and functional limitations following surgery would help clinicians design rehabilitation programs. Rahman et al. [3] showed that even 12 months after surgery, many TKR patients have not improved their gait relative to preoperative states. With the abnormal kinematics, the TKR can reduce efficiency of the quadriceps and change patella mechanics, and patients would not have the feeling of a normal knee. The demands in a higher range of motion such as squatting and kneeling require the total knee replacement to provide better function. Lavernia et al. [4] also pointed out that the mean bone mineral density (BMD) in the anterior femoral condylar zone in TKR specimens was significantly lower than that in normal specimens without arthroplasty, most likely due to stress shielding.

In the past decades, there have been attempts to create a more natural feeling and anatomical TKR. The objective of this paper was to review the latest development on TKR, then propose an approach to making customized total knee replacement implants which can function as close as possible to the normal knee of the patient.

1.1. Review Methods. Literature review was conducted related to TKR using PUBMED database (US National Library of Medicine and National Institute of Health). There are 336 papers available through a PUBMED search (revised September 25, 2017) using the query “Total knee replacement/arthroplasty” and “patient specific instrumentation.” However, there are 68 papers available through a PUBMED search (revised September 25, 2017) using the query “Total knee replacement/arthroplasty” and “customized.” Among these 68 papers, 28 papers are relevant to the knee replacement and patient-specific instrumentation (PSI) or implant designs. There were recent review papers on PSI by Rodrigues and Gutierrez [5] and Alcelik et al. [6]; therefore, this paper will focus on customized TKR implants and musculoskeletal (MSK) modelling of knee joint. Relevant papers searched from ScienceDirect (Elsevier) were also reviewed for the development of customized TKR.

2. Design of Total Knee Replacement

There are many TKR implants available in the market; each of them has its design rationale. Different designs of implant aim to enhance the satisfaction of patients by providing close to normal kinematics. The femoral condyle in sagittal plane may be circular shaped as shown in Figure 1(a) or has multicircles as shown in Figure 1(b), and the J-curve designs are also adopted in femoral component. An oval-shaped design is shown in Figure 1(c). Some of the implants are designed with the same medial and lateral articular surfaces as shown in Figure 2(a); however, asymmetrical articular surfaces have been also designed for achieving close to natural knee kinematics as shown in Figure 2(b).

The motion of the medial compartment in TKR is normally simplified into a ball-and-socket; however, the lateral converged femoral condyle in a surface-guided knee implant has been designed to control the motion of the joint. The lateral condyle may be designed to produce a constant or variable bearing distance between the medial condyle and lateral condyle. To achieve close to normal kinematics in TKR, Walker [7] showed that a knee implant which has medial stability and lateral mobility characteristics should be designed. For example, the SAIPH™ knee (MatOrtho, UK) has been designed to have a medial pivot knee kinematic pattern and an asymmetric posterior translation of the lateral femoral condyle to mimic the natural knee motion. Shimmin et al. [8] studied the stability of the SAIPH knee by video-fluoroscopy during four different weight-bearing activities. They concluded that the medially conforming total knee shows a medial pivot motion with tibial internal rotation. However, Warth et al. [9] showed that a medial pivot pattern may not significantly govern clinical success after TKR based on intraoperative kinematics and modern outcome measures. They pointed out that further research is warranted to determine if a particular kinematic pattern promotes optimal clinical outcomes.

Kim et al. [10] compared high-flexion TKR implant with other implants and concluded that there was no improvement with regard to range of motion, clinical outcomes, and the incidence of radiolucent lines despite theoretical

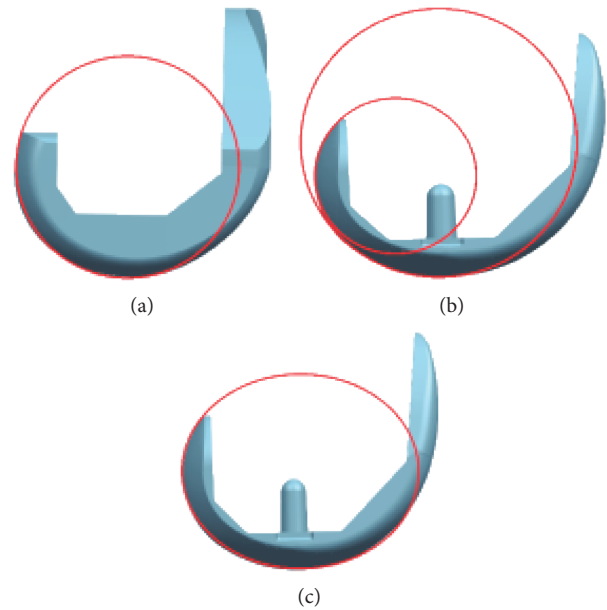


FIGURE 1: Curvatures of sagittal plane, (a) single circle, (b) multicircle, and (c) ellipse.

range of motion advantages of high-flexion prosthesis. Li et al. [11] studied the kinematics of knee joint with TKR and concluded that the clinical outcome after TKR may be affected by factors such as preoperative range of motion, flexion space balancing, posterior tibiofemoral articular contact stability, and quadriceps contraction.

With regard to implant wear, Abdelgaied et al. [12] investigated the effect of tibial insert conformity and material on total knee replacement wear; they concluded that the expected TKR lifetime might be increased by less conforming TKR implant. However, due to the noncongruent and sometimes unstable form of the TKR, wear is a constant issue. Massin [13] reported that wear can be reduced by improving techniques such as choice of implant size, component alignment, and adapted balancing.

Culler et al. [14] compared the outcomes of 126 customized individually made implant and 122 standard off-the-shelf implant patients undergoing TKR. They found that patients treated with customized individually made implant had significantly lower transfusion rates and fewer adverse event rates without increasing costs. White and Ranawat [15] evaluated manipulation rates and clinical outcomes of 21 patient-specific TKRs and off-the-shelf TKRs. They found that the patient-specific knee accurately restored the anatomical joint line and posterior condylar offset; however, patient-specific TKRs were associated with higher manipulation rate and lower satisfaction scores compared to off-the-shelf implants. Research on the comparison of customized cruciate-retaining TKR and asymmetric condylar cruciate-retaining TKA was carried out by Zeller et al. [16], and they concluded that the customized cruciate-retaining TKR demonstrated kinematics more similar to a normal knee.

Many researches showed that women had significantly narrower distal femoral condyle width than men. Wise et al. [17] showed that distal femoral and proximal tibial knee

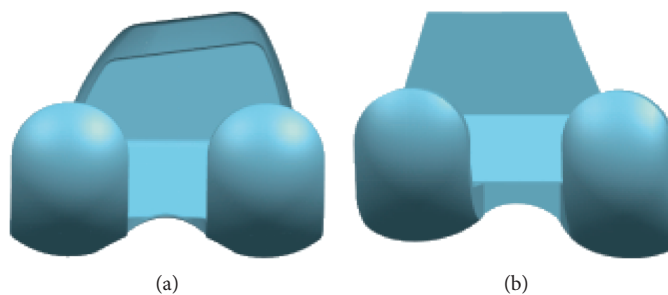


FIGURE 2: Femoral condyles (a) symmetrical and (b) asymmetrical.

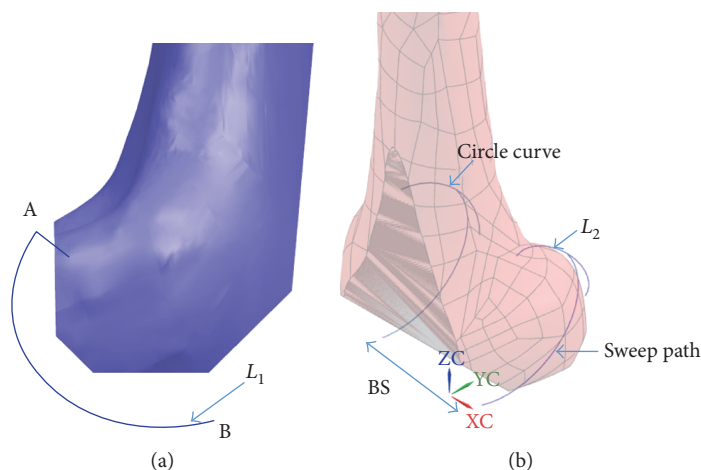


FIGURE 3: Oval curves derived from the femoral bone model, (a) sagittal view and (b) isometric view.

shapes differ by sex and recommended further study to understand the effect of shape modes on the development of osteoarthritis. Li et al. [18] used 3D anatomic models which showed that the shape and the peak positions of anterior condyle groove have gender difference, and they pointed out that the shape of the trochlear groove and the height of medial anterior condyle need to be designed gender specific.

Customized TKR implant has been developed based on the patient's MRI/CT data. Figure 3(a) shows a curve L_1 in the sagittal plane; this curve is a condyle profile that matches a patient's knee shape. The circular curve and the other curve L_2 are created based on a patient knee model. The curve L_2 sweeps along the curve L_1 from point A to point B and creates a condylar articular surface. BS is the distance between two condyle profiles, and it is determined from a patient knee model.

Carr and Goswami [19] reviewed knee replacements and biomechanics; they pointed out that issues such as wear and fixation had become more critical with prolonged use of knee implants. Knee implant recipients are more active today than ever; therefore, designing implants that mimic the natural knee is essential to the patients' long-term satisfaction and survival.

3. 3D Printed Patient-Specific Instrumentation

Lower limb mechanical axis restoration is very important for long-term survivorship of TKR. Recently, patient-specific

instrumentation or patient-specific cutting block/guide has been developed to help improve mechanical axis alignment. Medical images can be processed to create 3D models, along with the development of 3D printing technologies. There has been an increased use of 3D printing techniques in patient-specific treatments. 3D printing can be used mostly to create patient-specific anatomical models, customized moulds, surgical guides, and implants. It has been reported that patient-specific guide or cutting block can provide guidance to surgeons during surgery, and this can minimize tissue loss and optimize the positioning of implants. A distal femoral cutting guide is shown in Figure 4(a), and it is used to insert guide pins for cutting block during TKR. A tibial cutting guide is shown in Figure 4(b).

Both MRI and CT imaging have been used for creation of patient-specific guides. MRI is able to account for residual articular cartilage; therefore, the cutting guide can cover a broad contact area and can be directly placed on bone and residual cartilage of knee joint. CT is unable to account for residual cartilage; the corresponding cutting guide has to rely on multiple bony sites. Frye et al. [20] concluded that an MRI-generated template is better than CT-based guides.

Patient knee shapes are well known to be different; the surface geometry of TKR implant affects joint congruence and contact mechanics. It has been suggested by Pati et al. [21] that customized knee replacement from CT scan to 3D printing, customized cutting measures, and customized fitting templates could reduce operation time and assure

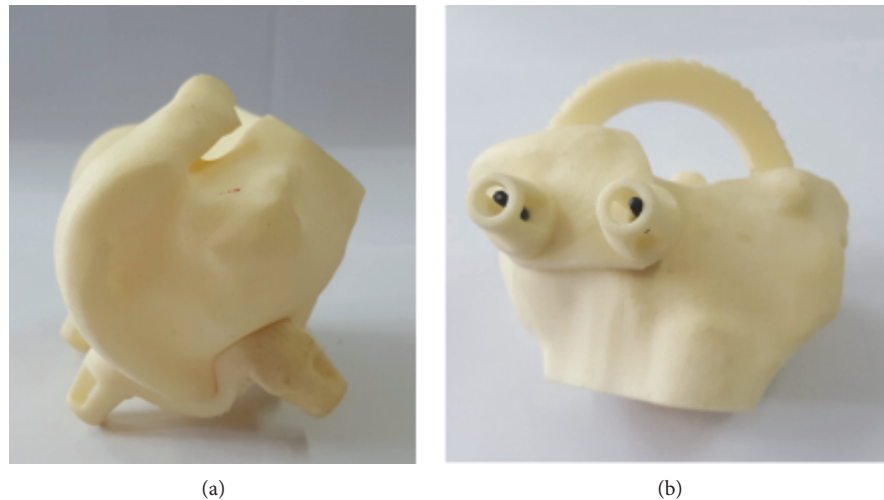


FIGURE 4: Cutting guide (a) distal femur and (b) tibia.

good alignment. Ganapathi [22] discussed using the technique of patient-specific guides (PSG) to perform TKR; the PSG replaces traditional jigs. To produce PSG, computerized 3D models of the distal femur and proximal tibia are created and the models are used to plan the operation and generate negative moulds of the patient's distal femur and proximal tibia. The operative time may be saved depending on a surgeon's experience and proficiency with the PSG technique. Ganapathi [22] concluded that the advantage of PSG is notable in terms of adequate fit and accuracy of the PSG.

Goyal and Tripathy [23] have surveyed the functional outcomes of total knee replacement using PSI. They pointed out that the PSI is not a patient-matched implant, and the main focus of implant design should be creating the patient-matched implant. Goyal et al. [24] studied the effect of implant design on PSI accuracy, and they concluded that differences in implant design can influence the accuracy of bone resection and component alignment for a given PSI design system.

However, Rodrigues and Gutierrez [5] reviewed comparison studies between patient-specific instrumentation (PSI) and standard instruments in TKR, and they noted that PSI had not consistently been shown to be cost-effective or to offer any clinical benefit with regard to functional scores. More studies and longer follow-up period are needed to make definitive conclusions about the PSI efficacy and the potential applicability of PSI to special situations. A similar study by Alcelik et al. [6] showed that PSI is not superior to ST instrumentation in primary total knee arthroplasty.

4. Lower Limb Musculoskeletal Model with Total Knee Replacement

Park et al. [25] investigated the relationship of lower limb muscle with pain, function, and frontal plane gait kinematics in patients with osteoarthritis. They confirmed that patients have knee osteoarthritis, reduced hip rotation, knee extension, and ankle inversion strength, but increased peak knee adduction during gait. Also, muscle strength played a

significant role in the self-reported function and gait in patient with osteoarthritis.

Musculoskeletal models can be created using software such as AnyBody and Opensim. A lower limb musculoskeletal model with a TKR implant is shown in Figure 5(a), and it includes main muscles in the lower limb. A normal lower limb musculoskeletal model is shown in Figure 5(b), and the knee joint is simplified as a pin joint that has a rational degree of freedom.

Knowledge of muscle and joint loading is important for evaluating the performance of TKR implant. If the knee is assumed as a pin joint in MSK models, it will produce erroneous results in knee muscle forces and moments acting in the frontal and transverse planes. Walter and Pandy [26] simulated the knee joint articular contact loading during level walking and stair descent, and they integrate a six degree of freedom tibiofemoral joint model into a forward dynamics simulation framework. Medial and lateral tibiofemoral joint contact loads were predicted with good agreement with the experimental data of knee joint loads for level walking.

Lower limb musculoskeletal model has been used in the analysis of joint mechanics and kinematics. Many researchers have tried different methods to create musculoskeletal models. Knarr and Higginson [27] proposed a practical approach to subject-specific estimation of knee joint contact force. A statistical finite element model of knee accounting for shape and alignment variability was developed by Rao et al. [28], and this model can be used to investigate knee joint mechanics and implant design. Belvedere et al. [29] discussed the importance of accurate muscle geometry for musculoskeletal models for subject-specific simulations. They combined a nonlinear scaling technique with a procedure to reconstruct bones from incomplete or scattered geometry data; this method can predict muscle geometries based on bone shapes. During total knee replacement, neutral mechanical alignment is generally targeted. Nolte et al. [30] pointed out that kinematic alignment which is based on the alignment of the prearthritic lower limb can allow better restoration of knee physiological function. Ullrich et al.

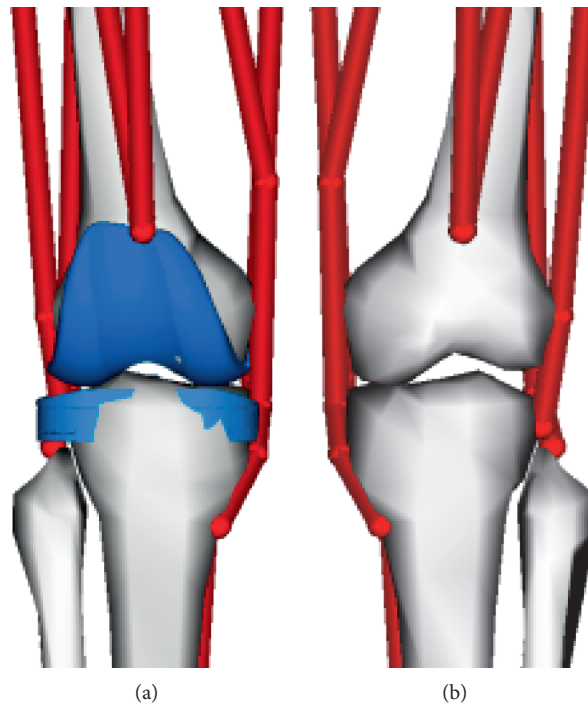


FIGURE 5: Lower limb musculoskeletal model, (a) knee implant model and (b) knee pin joint model.

[31] studied the long-term data of gait characteristics and moment-knee angle relations in female total knee replacement patients, and they found that the patients showed significant gait deficits during constant and self-selected walking speeds and lower average absolute values in the moment-knee angle relations of the knee extensors and flexors. Baldwin et al. [32] developed subject-specific finite element models from imaging data. They demonstrated an integrated approach to facilitate finite element analysis and statistical shape modelling of knee structures.

Musculoskeletal models can be used for implant wear analysis. TKR implant has traditionally been tested in knee wear simulator to determine its ability to resist wear. The computational models can be used to predict wear of implant as did by Zhang et al. [33], and they created a patient-specific wear prediction framework for TKR implant combined musculoskeletal multibody dynamics and finite element analysis. An interesting research was carried out by Chen et al. [34], and they created a full lower limb subject-specific musculoskeletal model that is scaled from a generic MSK model according to patient's CT images and gait dataset. In this model, a total knee replacement implant was modelled. Contact and ligament forces were predicted using a force-dependent kinematics method. This approach is very useful for design-customized TKR implants. Shi et al. [35] used computational models to predict stresses in TKR implant; the model was used to compare the performance of implants. Pejhan et al. [36] evaluated the kinematic performance of a customized surface-guided TKR implant using virtual simulation and load-controlled knee wear simulator. They concluded that virtual simulation is a valid tool for future evaluations of the customized surface-guided TKR implants.

Wang et al. [37] evaluated knee strength and mechanics during walking for patients with either a modern off-the-shelf TKR or a customized bicompartamental knee replacement after one year postsurgery. They concluded that the patients with bicompartamental knee replacement exhibit better strength and mechanics while performing daily activities.

Patient's gait dataset was used in the modelling, and this may raise the question of obtaining the gait data. The evolution of the knee gait kinematics in patients with knee osteoarthritis before and several months after a total knee replacement has been researched and presented by Bonnefoy-Mazure et al. [2] and Rahman et al. [3]. Kramers-de Quervain et al. [38] reported that two years after TKR there were significant improvements in gait velocity, cadence, and most of the ground reaction parameters; however, forces during loading and unloading remained lower for the operated leg than for the contralateral leg. Therefore, a patient's two-year postoperative gait could be predicted if a patient's preoperative gait is measured. With the patient's own gait data, a customized TKR implant could be developed.

5. Discussion

Based on the progress described in the previous sections, a new approach which is different from the current customized knee implant design is proposed in this paper. The focus of this approach is using patient-specific loading and gait dataset for knee implant designs in addition to the knee joint anatomical features. The procedure of creating a customized TKR implant is shown in Figure 6.

To design a customized TKR implant, 3D computer models from CT scans or MRI should be created firstly.

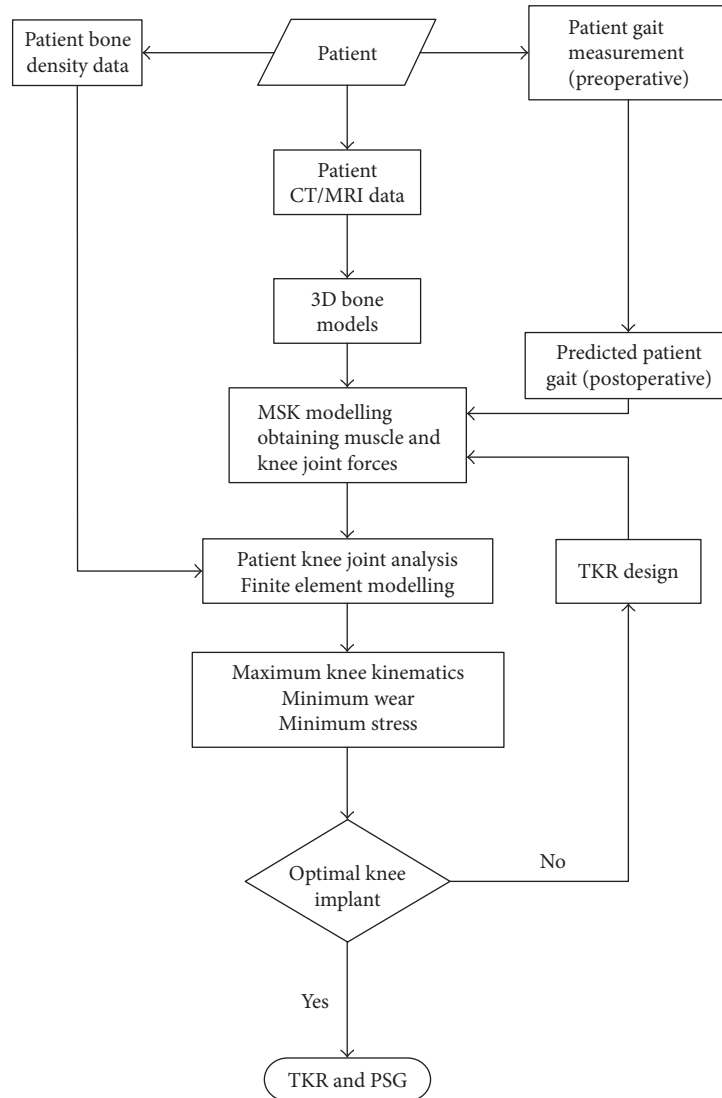


FIGURE 6: A schematic flow of designing a customized TKR implant.

The gait and foot reaction forces of the patient will be measured preoperatively and used for the prediction of load and kinematics of knee joint. Postoperative gait characteristics of patient can be predicted using the derived relationship between measured preoperative and postoperative gait datasets; then, the predicted patient gait is used in the MSK modelling. The interaction between TKR implant and knee joint dynamics will be evaluated using MSK models. The optimal TKR implant should reproduce knee function, maintain bone-implant interface integrity, and resist wear. The kinematics and loads on the TKR implant are very important to the success of TKR. To create a customized TKR implant, an iteration procedure is required to optimise stress, material wear, and knee kinematics.

Customized TKR implant has the potential to greatly improve knee kinematics and patient knee functions compared to off-the-shelf TKR implant. However, further studies need to be carried out to make the customized TKR implant available for patients.

6. Conclusion

Customized total knee replacement implant has been previously designed considering knee anatomical shape; however, with the latest development on lower limb musculoskeletal models, force dependent kinematics, and wear simulations, a customized total knee replacement implant could be developed to enhance patient satisfaction. The workflow of the approach to making customized TKR implant is presented in this paper. The customized total knee replacement implant will not only replicate the shape of the knee joint but also to restore normal gait of the patient postoperatively.

Conflicts of Interest

The authors declare that there are no competing interests regarding the publication of this paper.

Acknowledgments

This work was supported by grants from the Natural Science Foundation of China (nos. 11472185 and 11772214).

References

- [1] C. E. Milner, "Is gait normal after total knee arthroplasty? Systematic review of the literature," *Journal of Orthopaedic Science*, vol. 14, no. 1, pp. 114–120, 2009.
- [2] A. Bonnefoy-Mazure, S. Armand, J. Y. Sagawa et al., "Evolution of knee kinematics three months after total knee replacement," *Gait & Posture*, vol. 41, pp. 624–629, 2015.
- [3] J. Rahman, Q. Tang, M. Monda, J. Miles, and I. McCarthy, "Gait assessment as a functional outcome measure in total knee arthroplasty: a cross-sectional study," *BMC Musculoskeletal Disorders*, vol. 16, no. 1, p. 66, 2015.
- [4] C. J. Lavernia, J. A. Rodriguez, D. A. Iacobelli, D. S. Hungerford, and K. A. Krackow, "Bone mineral density of the femur in autopsy retrieved total knee arthroplasties," *The Journal of Arthroplasty*, vol. 29, no. 8, pp. 1681–1686, 2014.
- [5] A. S. T. Rodrigues and M. A. P. Gutierrez, "Patient-specific instrumentation in total knee arthroplasty. Should we adopt it?," *Revista Brasileira de Ortopedia*, vol. 52, no. 3, pp. 242–250, 2017.
- [6] I. Alcelik, M. Blomfield, C. Ozturk, A. Soni, and R. Charity, "A comparison of short term radiological alignment outcomes of the patient specific and standard instrumentation for primary total knee arthroplasty: a systematic review and meta-analysis," *Acta Orthopaedica et Traumatologica Turcica*, vol. 51, no. 3, pp. 215–222, 2017.
- [7] P. S. Walker, "Application of a novel design method for knee replacements to achieve normal mechanics," *The Knee*, vol. 21, no. 2, pp. 353–358, 2014.
- [8] A. Shimmin, S. Martinez-Martos, J. Owens, A. D. Iorgulescu, and S. Banks, "Fluoroscopic motion study confirming the stability of a medial pivot design total knee arthroplasty," *The Knee*, vol. 22, no. 6, pp. 522–526, 2015.
- [9] L. C. Warth, M. K. Ishmael, E. R. Deckard, M. Ziemba-Davis, and R. M. Meneghini, "Do medial pivot kinematics correlate with patient-reported outcomes after total knee arthroplasty?," *The Journal of Arthroplasty*, vol. 32, no. 8, pp. 2411–2416, 2017.
- [10] M. S. Kim, J. H. Kim, and I. J. Koh, S. W. Jang, D. H. Jeong, and Y. In, "Is high-flexion total knee arthroplasty a valid concept? Bilateral comparison with standard total knee arthroplasty," *The Journal of Arthroplasty*, vol. 31, no. 4, pp. 802–808, 2016.
- [11] G. Li, E. Mos, P. G. Sultan et al., "Flexion posterior stabilized total knee prosthesis, an in vitro robotic experimental investigation," *The Journal of Bone and Joint*, vol. 86, no. 8, pp. 1721–1729, 2004.
- [12] A. Abdelgaied, C. L. Brockett, F. Liu, L. M. Jennings, Z. Jin, and J. Fisher, "The effect of insert conformity and material on total knee replacement wear," *Proceedings of the Institution of Mechanical Engineers, Part H: Journal of Engineering in Medicine*, vol. 228, no. 1, pp. 98–106, 2014.
- [13] P. Massin, "How does total knee replacement technique influence polyethylene wear?," *Orthopaedics & Traumatology: Surgery & Research*, vol. 103, pp. s21–s27, 2017.
- [14] S. D. Culler, G. M. Martin, and A. Swearingen, "Comparison of adverse events rates and hospital cost between customized individually made implants and standard off-the-shelf implants for total knee arthroplasty," *Arthroplasty Today*, In press.
- [15] P. B. White and A. S. Ranawat, "Patient-specific total knees demonstrate a higher manipulation rate compared to "off-the-shelf implants"," *The Journal of Arthroplasty*, vol. 31, no. 1, pp. 107–111, 2016.
- [16] I. M. Zeller, A. Sharma, W. B. Kurtz, M. R. Anderle, and R. D. Komistek, "Customized versus patient-sized cruciate-retaining total knee arthroplasty: an in vivo kinematics study using mobile fluoroscopy," *The Journal of Arthroplasty*, vol. 32, no. 4, pp. 1344–1350, 2017.
- [17] B. L. Wise, F. Liu, L. Kritikos et al., "The association of distal femur and proximal tibia shape with sex: the osteoarthritis initiative," *Seminars in Arthritis & Rheumatism*, vol. 46, no. 1, pp. 20–26, 2016.
- [18] P. Li, T.-Y. Tsai, J.-S. Li et al., "Gender analysis of the anterior femoral condyle geometry of the knee," *The Knee*, vol. 21, no. 2, pp. 529–533, 2014.
- [19] B. C. Carr and T. Goswami, "Knee implants – review of models and biomechanics," *Materials & Design*, vol. 30, pp. 398–413, 2009.
- [20] B. M. Frye, A. A. Najim, J. B. Adams, K. R. Berend, and A. V. Lombardi Jr., "MRI is more accurate than CT for patient-specific total knee arthroplasty," *The Knee*, vol. 22, no. 6, pp. 609–612, 2015.
- [21] S. Patil, A. Bunn, W. D. Bugbee, C. W. Colwell Jr, and D. D. D'Lima, "Patient-specific implants with custom cutting blocks better approximate natural knee kinematics than standard TKA without custom cutting blocks," *The Knee*, vol. 22, pp. 624–629, 2015.
- [22] M. Ganapathi, "Patient specific guides for total knee replacements – a review," *Orthopaedics and Trauma*, vol. 28, no. 5, pp. 315–321, 2014.
- [23] T. Goyal and S. K. Tripathy, "Does patient-specific instrumentations improve short-term functional outcomes after total knee arthroplasty? A systematic review and meta-analysis," *The Journal of Arthroplasty*, vol. 31, no. 10, pp. 2173–2180, 2016.
- [24] N. Goyal, A. R. Patel, M. A. Yaffe, M. Y. Luo, and S. D. Stulberg, "Does implant design influence the accuracy of patient specific instrumentation in total knee arthroplasty?," *The Journal of Arthroplasty*, vol. 30, no. 9, pp. 1526–1530, 2015.
- [25] S.-K. Park, D. Kobsar, and R. Ferber, "Relationship between lower limb muscle strength, self-reported pain and function, and frontal plane gait kinematics in knee osteoarthritis," *Clinical Biomechanics*, vol. 38, pp. 68–74, 2016.
- [26] J. P. Walter and M. G. Pandy, "Dynamic simulation of knee-joint loading during gait using force-feedback control and surrogate contact modelling," *Medical Engineering & Physics*, vol. 48, pp. 196–205, 2017.
- [27] B. A. Knarr and J. S. Higginson, "Practical approach to subject-specific estimation of knee joint contact force," *Journal of Biomechanics*, vol. 48, no. 11, pp. 2897–2902, 2015.
- [28] C. Rao, C. K. Fitzpatrick, P. J. Rullkoetter, L. P. Maletsky, R. H. Kim, and P. J. Laz, "A statistical finite element model of the knee accounting for shape and alignment variability," *Medical Engineering & Physics*, vol. 35, no. 10, pp. 1450–1456, 2013.
- [29] C. Belvedere, S. Tamarri, A. Ensini et al., "Better joint motion and muscle activity are achieved using kinematic alignment

- than neutral mechanical alignment in total knee replacement,” *Gait & Posture*, vol. 42, Supplement 2, pp. S19–S20, 2015.
- [30] D. Nolte, C. K. Tsang, K. Y. Zhang, Z. Ding, and A. E. Kedgley, “Non-linear scaling of a musculoskeletal model of the lower limb using statistical shape models,” *Journal of Biomechanics*, vol. 49, no. 14, pp. 3576–3581, 2016.
- [31] B. Ullrich, J. Stening, T. Pelzer, and J. Raab, “Long-term data of gait characteristics and moment–knee angle relations in female total knee arthroplasty patients,” *Clinical Biomechanics*, vol. 30, no. 5, pp. 462–468, 2015.
- [32] M. A. Baldwin, J. E. Langenderfer, P. J. Rullkoetter, and P. J. Laz, “Development of subject-specific and statistical shape models of the knee using an efficient segmentation and mesh-morphing approach,” *Computer Methods and Programs in Biomedicine*, vol. 97, no. 3, pp. 232–240, 2010.
- [33] J. Zhang, Z. Chen, L. Wang, D. Li, and Z. Jin, “A patient-specific wear prediction framework for an artificial knee joint with coupled musculoskeletal multibody-dynamics and finite element analysis,” *Tribology International*, vol. 109, pp. 382–389, 2017.
- [34] Z. Chen, Z. Zhang, L. Wang, D. Li, Y. Zhang, and Z. Jin, “Evaluation of a subject-specific musculoskeletal modelling framework for load prediction in total knee arthroplasty,” *Medical Engineering & Physics*, vol. 38, no. 8, pp. 708–716, 2016.
- [35] J. F. Shi, C. J. Wang, T. Laoui, W. Hart, and R. Hall, “A dynamic model of simulating stress distribution in the distal femur after total knee replacement,” *Proceedings of the Institution of Mechanical Engineers, Part H: Journal of Engineering in Medicine*, vol. 221, no. 8, pp. 903–912, 2007.
- [36] S. Pejhan, E. Bohm, J.-M. Brandt, T. Gascoyne, and U. Wyss, “Kinematic behavior of a customized surface-guided knee implant during simulated knee-bending,” *Medical Engineering & Physics*, vol. 48, pp. 168–175, 2017.
- [37] H. Wang, J. Foster, N. Franksen, J. Estes, and L. Rolston, “Gait analysis of patients with an off-the-shelf total knee replacement versus customized bi-compartmental knee replacement,” *International Orthopaedics*, pp. 1–6, 2017.
- [38] I. A. Kramers-de Quervain, S. Kampfen, U. Munzinger, and A. F. Mannion, “Prospective study of gait function before and 2 years after total knee arthroplasty,” *The Knee*, vol. 19, no. 5, pp. 622–627, 2012.

Research Article

Design and Interaction Control of a New Bilateral Upper-Limb Rehabilitation Device

Qing Miao,¹ Mingming Zhang,^{2,3} Yupu Wang,² and Sheng Q. Xie²

¹*School of Mechanical and Electrical Engineering, Wuhan University of Technology, Wuhan, China*

²*Department of Mechanical Engineering, The University of Auckland, Auckland, New Zealand*

³*Medical & Rehabilitation Equipment Research Centre, Tongji Zhejiang College, Jiaxing, China*

Correspondence should be addressed to Mingming Zhang; mzha130@aucklanduni.ac.nz

Received 5 May 2017; Accepted 13 July 2017; Published 20 September 2017

Academic Editor: Duo Wai-Chi Wong

Copyright © 2017 Qing Miao et al. This is an open access article distributed under the Creative Commons Attribution License, which permits unrestricted use, distribution, and reproduction in any medium, provided the original work is properly cited.

This paper proposed a bilateral upper-limb rehabilitation device (BULReD) with two degrees of freedom (DOFs). The BULReD is portable for both hospital and home environment, easy to use for therapists and patients, and safer with respect to upper-limb robotic exoskeletons. It was implemented to be able to conduct both passive and interactive training, based on system kinematics and dynamics, as well as the identification of real-time movement intention of human users. Preliminary results demonstrate the potential of the BULReD for clinical applications, with satisfactory position and interaction force tracking performance. Future work will focus on the clinical evaluation of the BULReD on a large sample of poststroke patients.

1. Introduction

In the United States, more than 700,000 people suffer from stroke each year, and approximately two-thirds of these individuals survive and require rehabilitation [1]. In New Zealand (NZ), there are an estimated 60,000 stroke survivors, and many of them have mobility impairments [2]. Stroke is the third reason for health loss and takes the proportion of 3.9 percent, especially for the group starting on middle age, suffering the stroke as a nonfatal disease in NZ [3]. Professor Caplan who studies Neurology at Harvard Medical School describes stroke as a term which is a kind of brain impairment as a result of abnormal blood supply in a portion of the brain [4]. The brain injury is most likely leading to dysfunctions and disabilities. These survivors normally have difficulties in activities of daily living, such as walking, speaking, and understanding, and paralysis or numbness of the human limbs. The goals of rehabilitation are to help survivors become as independent as possible and to attain the best possible quality of life.

Physical therapy is conventionally delivered by the therapist. While this has been demonstrated as an effective way for motor rehabilitation [5], it is time-consuming and costly.

Treatments manually provided by therapists require to take place in a specific environment (in a hospital or rehabilitation center) and may last several months for enhanced rehabilitation efficacy [6]. A study by Kleim et al. [7] has shown that physical therapy like regular exercises can improve plasticity of a nervous system and then benefits motor enrichment procedures in promoting rehabilitation of brain functional models. It is a truth that physical therapy should be a preferable way to take patients into regular exercises and guided by a physical therapist, but Chang et al. [8] showed that it is a money-consuming scheme. Robot-assisted rehabilitation solutions, as therapeutic adjuncts to facilitate clinical practice, have been actively researched in the past few decades and provide an overdue transformation of the rehabilitation center from labor-intensive operations to technology-assisted operations [9]. The robot could also provide a rich stream of data from built-in sensors to facilitate patient diagnosis, customization of the therapy, and maintenance of patient records. As a popular neurorehabilitation technique, Liao et al. [10] indicated that robot-assisted therapy presents market potential due to quantification and individuation in the therapy session. The quantification of robot-assisted therapy refers that a robot can provide consistent training



FIGURE 1: The BULReD on a lab table.

pattern without fatigue with the given parameter. The characterization of individuation allows therapists to customize a specific training scheme for an individual.

Many robotic devices have been developed in recent years for stroke rehabilitation and show great potential for clinical applications [11, 12]. Typical upper-limb rehabilitation devices are MIME, MIT-Manus, ARM Guide, NeReBot, and ARMin [5, 13–21]. Relevant evidences demonstrated that these robots are effective for upper-limb rehabilitation but mostly for the one side of the human body. Further, upper-limb rehabilitation devices can be unilateral or bilateral [22–24]. Despite the argument between these two design strategies, bilateral activities are more common than unilateral activities in daily living. Liu et al. [25] pointed that the central nervous system dominates the human movement with coordinating bilateral limb to act in one unit instead of independent unilateral actions. From this point, bilateral robots are expected to be more potential than unilateral devices. Robotic devices for upper-limb rehabilitation can be also divided into two categories in terms of structure: the exoskeleton and the end-effector device [26]. Two examples of upper-limb exoskeletons are the arm exoskeleton [27] and the RUPERT IV [28]. In addition, Lum et al. [13] incorporated a PUMA 560 robot (Staubli Unimation Inc., Duncan, South Carolina) to apply forces to the paretic limbs in the MIME system. This robotic device can be made for both unilateral and bilateral movements in a three-dimensional space. To summarize, existing robotic exoskeletons for upper-limb rehabilitation are mostly for unilateral training.

There are some devices that have been specially designed for bilateral upper-limb training for poststroke rehabilitation. van Delden et al. [29] conducted a systematic review to provide an overview and qualitative evaluation of the clinical applications of bilateral upper-limb training devices. A systematic search found a total of six mechanical devices and 14 robotic bilateral upper-limb training devices, with a comparative analysis in terms of mechanical and electromechanical characteristics, movement patterns, targeted part, and active involvement of the upper limb, training protocols, outcomes of clinical trials, and commercial availability. Obviously, these mechanical devices require the human limbs to actively move for training, while the robotic ones can be operated in both passive and active modes. However, few of these robotic bilateral upper-limb training devices

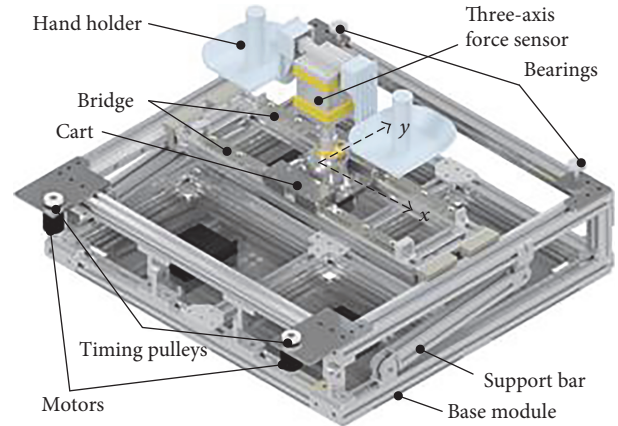


FIGURE 2: A three-dimensional model of the BULReD designed in Solidwork.

have been commercially available with current technology. For example, the exoskeleton presented in [30] requires the development of higher power-to-weight motors and structural materials to make it mobile and more compact.

The University of Auckland developed an end-effector ReachHab device to assist bilateral upper-limb functional recovery [31]. However, this device suffered from some limitations, such as deformation of the frame leading to significant vibration, also hard to achieve satisfactory control performance. This paper presents the design and interaction control of an improved bilateral upper-limb rehabilitation device (BULReD). This device is portable for both hospital and home environment, easy to use for therapists and patients, and safer with respect to upper-limb robotic exoskeletons. This paper is organized as follows. Following Introduction, a detailed description of the BULReD is given, including mechanical design, electrical design, kinematics, and dynamics. Then, the control design is presented for both passive training and interactive training, as well as the fuzzy-based adaptive training. Experiments and Results is introduced next and the last is Conclusion.

2. Bilateral Upper-Limb Rehabilitation Device (BULReD)

2.1. Mechanical Design. The BULReD aims to deliver bilateral upper-limb exercises to stroke patients. Overview of the BULReD is shown in Figure 1. This device has two DOFs for the planar exercises of human upper limbs.

To make the structural design clear to the readers, a three-dimensional model design in Solidwork is also given in Figure 2. The BULReD mainly consists of three components (the base module, the motion module, and the hand holder). The base module acts as a foundation to support the whole motion module and also a container for some electronic components. There is a support bar in the base module, which can be used to adjust the angle of inclination of the BULReD. The motion module consists of two mutually perpendicular linear slide systems, the bridge and the cart. The linear slide systems are used to transfer the rotatory motion of motors to the linear motion of the sliders by using

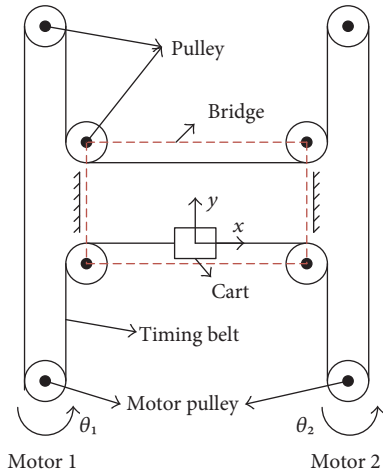


FIGURE 3: The schematic mechanism of the BULReD.

two timing belts. The bridge moves along the y -axis rail, and the cart is along the x -axis rail. The hand holder is rigidly connected with the cart through a three-axis force sensor. Some bearings are also set to allow low friction motion transmission.

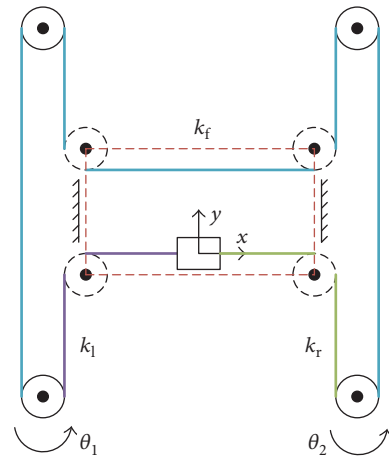
The inclination angle of the BULReD is considered to be 0° when the motion module is parallel to the bottom base. By moving the attachment position of the support bar, the angle of inclination can be adjusted up to 60° . Such a design can make patients have a larger workspace for upper-limb rehabilitation exercises. The hand holder is designed based on anthropometry. Kaya et al. [32] suggested that the shoulder breadth has the mean measurement of 355.8 mm (female) and 389.4 mm (male) at age 17. In the prototype of the BULReD, the designed shoulder breadth is set at 38 cm. Fransson and Winkel [33] indicated that hand size measurements have the maximum finger length and handbreadth between women's and men's mean values of 72 mm and 90 mm, respectively. In the prototype, the handle height is set at 90 mm. However, these two parameters can be easily made to be adjustable to allow the use on patients with different sizes.

2.2. Electrical Design. The electrical component of the BULReD consists of two Maxon DC motors (each has one brushless motor and one gearbox), two motor controllers (Maxon ESCON 50/5), a three-axis force sensor (FUTEK MTA400), three amplifiers (FUTEK CSG110), and an embedded controller (NI myRIO-1900). Predefined data and those from the motor controller communicate with the embedded controller through digital input/output (DI/O), analog input (AI), and analog output (AO). Specifically, the myRIO outputs signals to drive servo motors and obtains feedback inputs of the position. The servo system provides speed feedback based on the built-in encoder with 2048 counts per turn. The position feedback is implemented by the computation of the speed feedback. The motor controller provides a stable power supply for DC motor and internally realizes closed loop speed control. The three-axis force sensor is used to measure real-time human-robot interaction to

TABLE 1: The qualitative description of the motion transmission of the BULReD.

Motion pattern	Motor pulley angular displacement		End-effector direction
	Motor 1	Motor 2	
1	+	·	\nearrow
2	+	+	\rightarrow
3	+	-	\uparrow
4	-	·	\swarrow
5	-	+	\downarrow
6	-	-	\leftarrow
7	·	+	\searrow
8	·	-	\nwarrow

Note: + means anticlockwise rotation, - means clockwise rotation, and · represents the motor being still.

FIGURE 4: The simplified dynamic model of the BULReD (k_f , k_l , and k_r represent the stiffness of the forward section, the left section, and the right section of the motion module, resp.).

facilitate the implementation of the interactive training. For training safety, four limit switches are also set up, located at the corner of the workbench. They are also used as a reference to set the starting point.

2.3. Kinematics. H-Bot (also known as H-gantry or H-frame) is a kind of XY positioning system which is commonly used in industries. It can place a part or carry a tool in a planar space. A model of the H-Bot consists of two mutually perpendicular linear slide systems and connects with the power source by timing belts [34]. It is driven by two independent motors in the cooperative work and results in planar motions. Figure 3 presents the schematic mechanism of the BULReD, where the bridge moves along the y -axis and the cart moves along the x -axis. The hand holder is rigidly connected with the cart and forms a planar motion area.

The planar displacement of the cart is obtained from two rotational motors (motor 1 and motor 2 in Figure 3). Forward kinematics can be used to derive the linear displacement ΔX and ΔY of the cart from two angular displacements

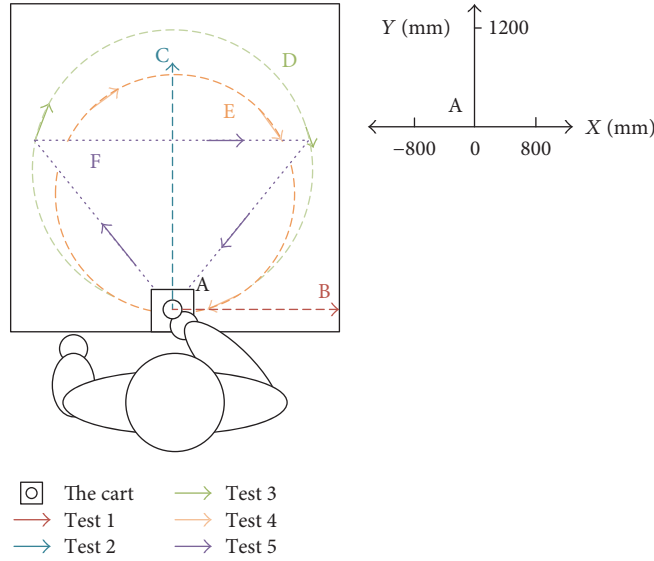


FIGURE 7: The predefined training trajectories on the BULReD. Training exercises along trajectories 1, 2, 3, 4, and 5 are denoted as tests 1, 2, 3, 4, and 5, respectively.

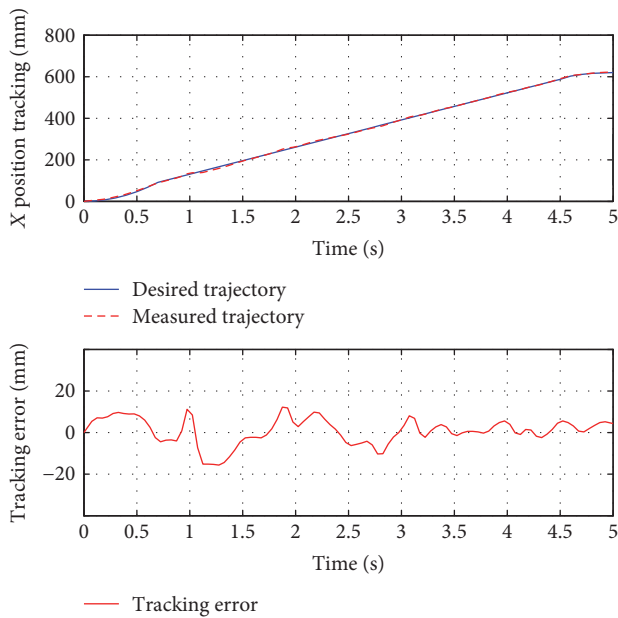


FIGURE 8: The position tracking responses of test 1.

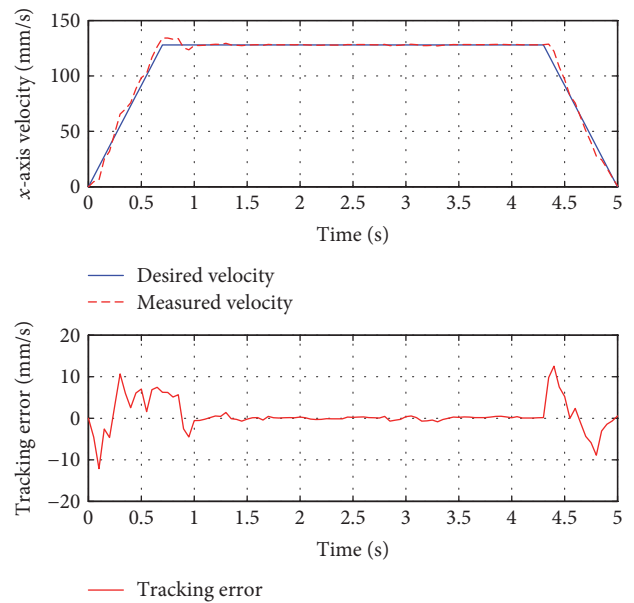


FIGURE 9: The velocity tracking responses of test 1.

divided into three sections with different colors, the left section (purple), the right section (green), and the forward section (blue).

The dynamic energy of each section in the simplified system can be written as

$$T_x = \frac{1}{2} m_{\text{cart}} \dot{x}^2, \quad (6)$$

$$T_y = \frac{1}{2} m_{\text{bridge}} \dot{y}^2, \quad (7)$$

$$T_i = \frac{1}{2} J_i \dot{\theta}_i^2 \quad (i = 1, 2). \quad (8)$$

The potential energy of the simplified system is stored in the three sections and shown in the following:

$$V_f = \frac{1}{2} k_f (\theta_1 r - \theta_2 r - 2y)^2, \quad (9)$$

$$V_l = \frac{1}{2} k_l (-\theta_1 r + x + y)^2, \quad (10)$$

$$V_r = \frac{1}{2} k_r (\theta_2 r - x + y)^2. \quad (11)$$

The Lagrange equation is applied to build the dynamic model and is shown in (12). Combining the virtual work theory as well, (13) is obtained.

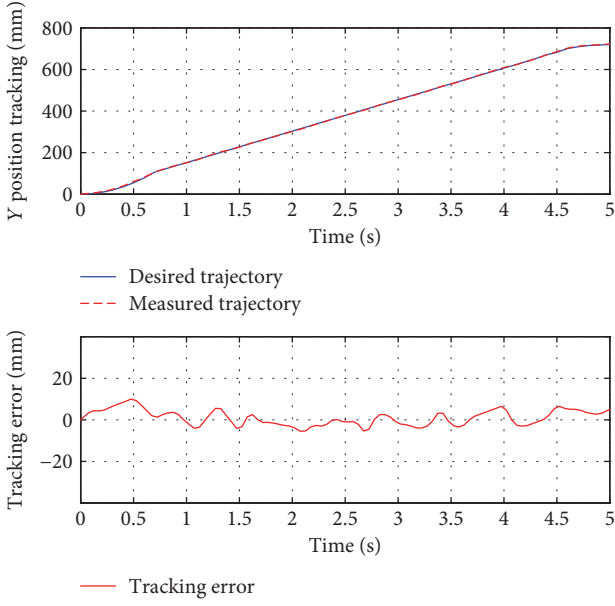


FIGURE 10: The position tracking responses of test 2.

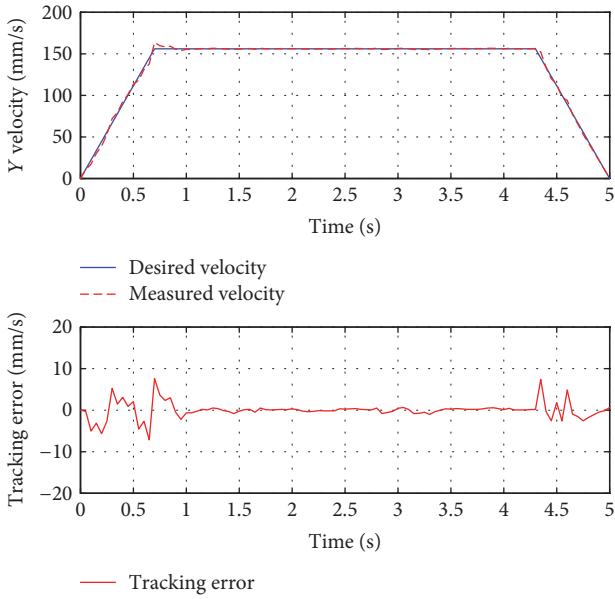


FIGURE 11: The velocity tracking responses of test 2.

$$L = \frac{1}{2} m_{\text{cart}} \dot{x}^2 + \frac{1}{2} m_{\text{bridge}} \dot{y}^2 + \frac{1}{2} J_1 \dot{\theta}_1^2 + \frac{1}{2} J_2 \dot{\theta}_2^2 - \frac{1}{2} k_f (\theta_1 r - \theta_2 r - 2y)^2 - \frac{1}{2} k_l (-\theta_1 r + x + y)^2 - \frac{1}{2} k_r (\theta_2 r - x + y)^2, \quad (12)$$

$$\delta W^{\text{NC}} = -c_{\text{cart}} \dot{x} \delta x - c_{\text{bridge}} \dot{y} \delta y + (\tau_1 - c_1 \dot{\theta}_1) \delta \theta_1 + (\tau_2 - c_2 \dot{\theta}_2) \delta \theta_2. \quad (13)$$

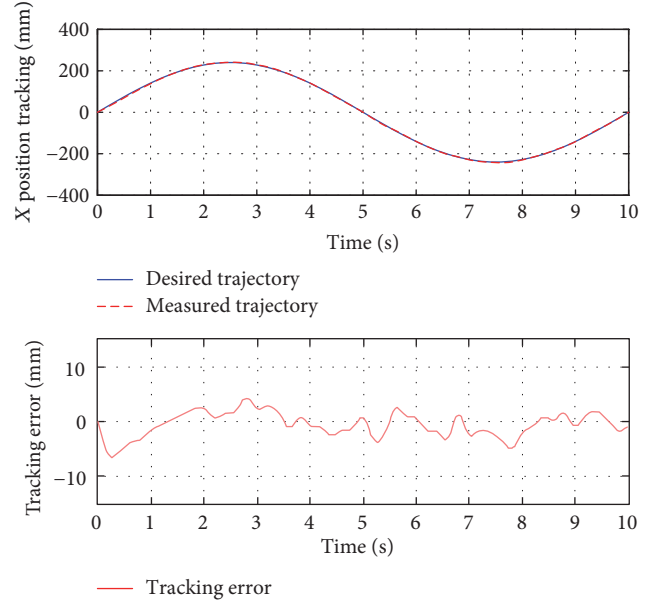


FIGURE 12: The x-axis position tracking responses of test 3.

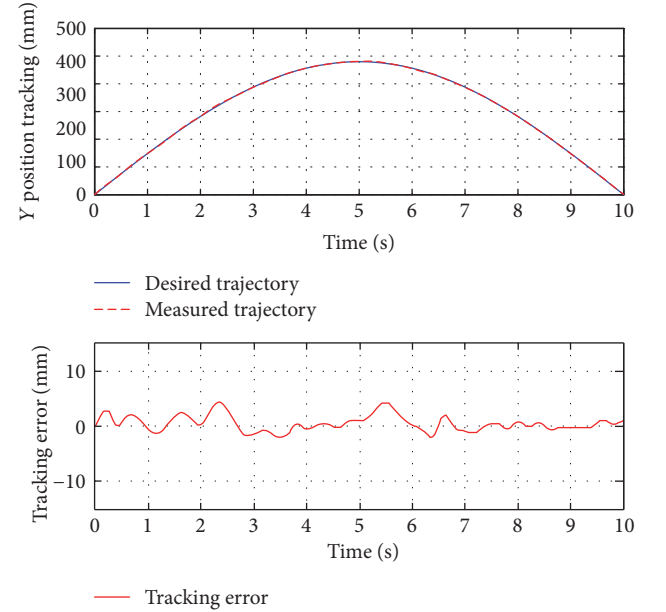


FIGURE 13: The y-axis position tracking responses of test 3.

Substituting Lagrange's equation given, the simplified dynamic system can be represented using

$$\ddot{x} = \frac{1}{m_{\text{cart}}} \left[-(k_l + k_r)x - c_{\text{cart}} \dot{x} - (k_l - k_r)y + k_l r \theta_1 + k_r r \theta_2 \right], \quad (14)$$

$$\ddot{y} = \frac{1}{m_{\text{bridge}}} \left[-(k_l - k_r)x - (4k_f + k_l + k_r)y - c_{\text{bridge}} \dot{y} + (2k_f + k_l)r\theta_1 - (2k_f + k_l)r\theta_2 \right], \quad (15)$$

TABLE 3: Statistical results of the tracking responses of all tests.

Error type		x -axis position (mm)	y -axis position (mm)	x -axis velocity (mm/s)	y -axis velocity (mm/s)	Force (N)
RMSE						
Mode						
Passive mode	Test 1	4.0558	N\A	3.3779	N\A	N\A
	Test 2	N\A	3.7781	N\A	2.0551	N\A
	Test 3	1.8324	1.2391	N\A	N\A	N\A
Assistive mode	Test 4	N\A	N\A	N\A	N\A	1.0051
	Test 5	N\A	N\A	N\A	N\A	0.9012

RMSE: root-mean-square error; N\A: not available.

$$\ddot{\theta}_1 = \frac{1}{J_1} \left[k_1 r x + (2k_f + k_1) r y - (k_f + k_1) r^2 \theta_1 - c_1 \dot{\theta}_1 + k_f r^2 \theta_2 + \gamma \eta k_t I_1 \right] - \frac{1}{2} k_1 (-\theta_1 r + x + y)^2 - \frac{1}{2} k_t (\theta_2 r - x + y)^2, \quad (16)$$

$$\ddot{\theta}_2 = \frac{1}{J_2} \left[k_1 r x - (2k_f + k_1) r y - (k_f + k_t) r^2 \theta_2 - c_2 \dot{\theta}_2 + k_f r^2 \theta_1 + \gamma \eta k_t I_2 \right]. \quad (17)$$

3. Control Design of the BULReD

3.1. Trajectory Tracking Control. The trajectory tracking control of the BULReD is the basis of a variety of robot-assisted rehabilitation exercises. It can be directly used for passive training on stroke patients who has week active motor ability. However, tracking desired trajectories is not only a simple but also an effective method for rehabilitation applications [35]. For passive training, patients totally follow the predefined motion trajectory of the BULReD. The proposed control techniques are presented in Figure 5.

3.2. Interaction Control. To ensure active participation from patients during the robotic training, and hence enhance the training efficacy, a fuzzy adaptive-based variable impedance (FABVI) controller has been given to modify parameters of stiffness and damping according to desired force with detected user's force. The proposed control techniques are presented in Figure 6. Considering the impaired limb, the desired impedance property between robot and impaired limb can be given in

$$M\ddot{X} + B(\dot{X}_d - \dot{X}) + K(X_d - X) = f - f_e, \quad (18)$$

where M , B , and K are variable inertia, damping, and stiffness matrix, respectively; X_d is the 2×1 vector of the desired position of device end-effector; and X is the 2×1 vector of the current location; \dot{X}_d , \dot{X} , and \ddot{X} are first and second derivatives individually; f is the end-effector input force; and f_e represents limb applying force on the device. The fuzzy inference rules are shown in Table 2.

The fuzzy subsets are defined as follows:

$$e_p = X_d - X = \{\text{NB, NM, NS, O, PS, PM, PB}\}, \quad (19)$$

$$e_v = \dot{X}_d - \dot{X} = \{\text{NB, NM, NS, O, PS, PM, PB}\}, \quad (20)$$

$$e_f = f - f_e = \{\text{NB, NM, NS, O, PS, PM, PB}\}. \quad (21)$$

e_p , e_v , e_f , and b , k all follow Gaussian distributions.

4. Experiments and Results

To preliminarily estimate the performance of the BULReD and its control system, two healthy subjects participated in the test in the lab environment. Subject A has the age of 20 years old, with 178 cm height. Subject B is a 28-year-old male, with the height of 174 cm. The max force of both pulling and pushing is 200 N. The predefined training trajectories are presented in Figure 7.

4.1. Trajectory Tracking Responses. For passive training, subject A was guided to finish three training trajectories (A-B, A-C, and D, also denoted as test 1, test 2, and test 3, resp.). During the whole process, the subject was encouraged to relax and did not apply intentional active force on the hand holder. Figure 8 presents the position tracking responses of test 1, and the corresponding velocity tracking is shown in Figure 9. Both show satisfactory tracking accuracy, with the root-mean-square error (RMSE) values being 4.0558 mm for position tracking and 3.3779 mm/s for velocity tracking. Test 2 is a trajectory along the y -axis, and experimental results are presented in Figures 10 and 11. The achieved position tracking accuracy is an RMSE of 3.7781 mm, and for velocity tracking, it is 2.0551 mm/s. To conduct a combined motion along both x - and y -axes, test 3 was designed where the BULReD took the limbs for a circle within the workspace. The position tracking responses are presented in Figures 12 and 13 for x - and y -axes, respectively. The RMSE values are 1.8324 mm and 1.2391 mm, respectively. These statistical results are summarized in Table 3.

4.2. Interaction Control Responses. With respect to the FABVI controller, the initial desired impedance control parameters M , B , and K were chosen as 1.5, 20, and 100, respectively. Domains of the input and output variables in the fuzzy adaptive algorithm were defined as $e_p \in [-1, 1]$, $e_v \in [-1, 1]$, $e_f \in [-1, 1]$, $b \in [-6, 6]$, $k \in [-6, 6]$. The desired force between the BULReD and the human limbs was set at 10 N.

For interactive training, subject B was guided to finish two training trajectories (E and F, also denoted as test 4 and test 5, resp.). In the case of this situation, people are

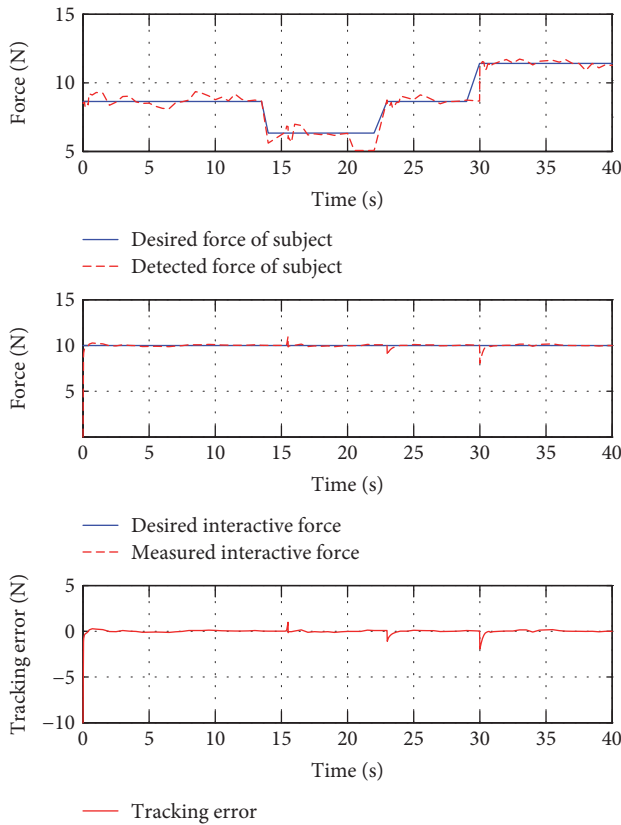


FIGURE 14: The force tracking responses of test 4.

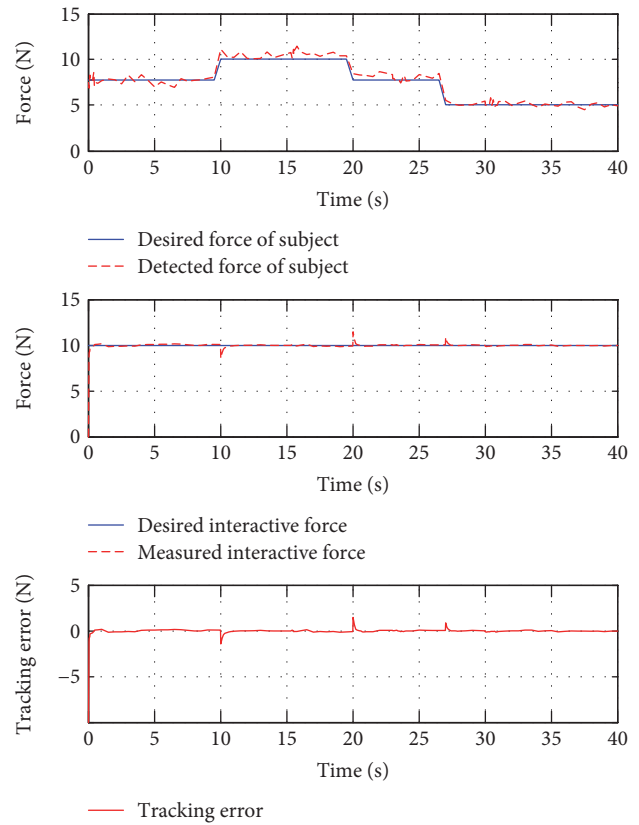


FIGURE 15: The force tracking responses of test 5.

demanding to use changing force to simulate stiffness or spasticity. In test 4, the subject applied an initial force 8 N, then reduced to 6 N at around the 14th second and got back to 8 N at the 23rd second, and finally changed to 11 N at the 28th second. In test 5, the initial force was also 8 N, it turned to 10 N at the 10th second, back to 8 N at the 19th second, and decreased to 5 N at the 27th second. These data are presented in the top plots of Figures 14 and 15.

Figure 14 also presents the force tracking responses of test 4 (middle plot). It is shown that the controller can achieve the reference constant force with the presence of the user's variable force applying, with the RMSE value being 1.0051 N. Similarly, Figure 15 also shows satisfactory force tracking performance, with the RMSE value at 0.9012 N. These statistical results are also included in Table 3.

5. Conclusions

This paper proposed a two-DOF end-effector device for bilateral upper-limb rehabilitation training. The BULReD is portable for both hospital and home environment, easy to use for therapists and patients, and safer with respect to upper-limb robotic exoskeletons. It was implemented to be able to conduct both passive and interactive trainings, based on system kinematics and dynamics, as well as the identification of real-time movement intention of human users. Preliminary results demonstrate the potential of the BULReD

for clinical applications, with satisfactory position and interaction force tracking performance. Future work will focus on the clinical evaluation of the BULReD on a large sample of poststroke patients.

Conflicts of Interest

The authors declare that they have no competing interests.

References

- [1] D. Mozaffarian, E. J. Benjamin, A. S. Go et al., "Heart disease and stroke statistics—2015 update," *Circulation*, vol. 131, pp. e29–e322, 2015.
- [2] "Facts about stroke in New Zealand," 2014, <http://www.stroke.org.nz/stroke-facts-and-fallacies>.
- [3] M. Turley and New Zealand, *Ministry of M. Turley Health, Health Loss in New Zealand: A Report from the New Zealand Burden of Diseases, Injuries and Risk Factors Study, 2006–2016*, Ministry of Health, 2013, Wellington, NZ, 2013.
- [4] L. R. Caplan, *Stroke*, AAN Press, American Academy of Neurology c2006, New York: Saint Paul, MN: New York: Demos; Saint Paul, MN, 2006.
- [5] P. S. Lum, C. G. Burgar, P. C. Shor, M. Majmundar, and M. Van der Loos, "Robot-assisted movement training compared with conventional therapy techniques for the rehabilitation of upper-limb motor function after stroke," *Archives of Physical Medicine and Rehabilitation*, vol. 83, pp. 952–959, 2002.

- [6] R. Loureiro, F. Amirabdollahian, M. Topping, B. Driessen, and W. Harwin, "Upper limb robot mediated stroke therapy—GENTLE/s approach," *Autonomous Robots*, vol. 15, pp. 35–51, 2003.
- [7] J. A. Kleim, T. A. Jones, and T. Schallert, "Motor enrichment and the induction of plasticity before or after brain injury," *Neurochemical Research*, vol. 28, pp. 1757–1769, 2003.
- [8] Y.-J. Chang, W.-Y. Han, and Y.-C. Tsai, "A Kinect-based upper limb rehabilitation system to assist people with cerebral palsy," *Research in Developmental Disabilities*, vol. 34, pp. 3654–3659, 2013.
- [9] H. I. Krebs, J. J. Palazzolo, L. Dipietro et al., "Rehabilitation robotics: performance-based progressive robot-assisted therapy," *Autonomous Robots*, vol. 15, pp. 7–20, 2003.
- [10] W. W. Liao, C. Y. Wu, Y. W. Hsieh, K. C. Lin, and W. Y. Chang, "Effects of robot-assisted upper limb rehabilitation on daily function and real-world arm activity in patients with chronic stroke: a randomized controlled trial," *Clinical Rehabilitation*, vol. 26, pp. 111–120, 2012.
- [11] G. Kwakkel, B. J. Kollen, and H. I. Krebs, "Effects of robot-assisted therapy on upper limb recovery after stroke: a systematic review," *Neurorehabilitation and Neural Repair*, vol. 22, pp. 111–121, 2008.
- [12] J. Stein, H. I. Krebs, W. R. Frontera, S. E. Fasoli, R. Hughes, and N. Hogan, "Comparison of two techniques of robot-aided upper limb exercise training after stroke," *American Journal of Physical Medicine & Rehabilitation*, vol. 83, pp. 720–728, 2004.
- [13] P. S. Lum, C. G. Burgar, M. Van der Loos, and P. C. Shor, "MIME robotic device for upper-limb neurorehabilitation in subacute stroke subjects: a follow-up study," *Journal of Rehabilitation Research and Development*, vol. 43, pp. 631–642, 2006.
- [14] H. Krebs, N. Hogan, B. Volpe, M. Aisen, L. Edelstein, and C. Diels, "Overview of clinical trials with MIT-MANUS: a robot-aided neuro-rehabilitation facility," *Technology and Health Care*, vol. 7, pp. 419–423, 1999.
- [15] C. Fanin, P. Gallina, A. Rossi, U. Zanatta, and S. Masiero, "Nerebot: a wire-based robot for neurorehabilitation," in *Proceedings of the 8th International Conference on Rehabilitation Robotics*, pp. 23–25, 2003.
- [16] M. Mihelj, T. Nef, and R. Riener, "ARMin-toward a six DoF upper limb rehabilitation robot," in *BioRob 2006. The First IEEE/RAS-EMBS International Conference on Biomedical Robotics and Biomechatronics, 2006*, pp. 1154–1159, Pisa, Italy, 2006.
- [17] Interactive Motion Technologies, "InMotion ARM™ Interactive Therapy System," August 2015, <http://interactive-motion.com/healthcarereform/upper-extremity-rehabilitation/inmotion2-arm/>.
- [18] K. Baur, "Arm rehabilitation (ARMin)," August 2015, <http://www.sms.hest.ethz.ch/research/current-research-projects/armin-robot.html>.
- [19] G. Rosati, P. Gallina, and S. Masiero, "Design, implementation and clinical tests of a wire-based robot for neurorehabilitation," *IEEE Transactions on Neural Systems and Rehabilitation Engineering*, vol. 15, pp. 560–569, 2007.
- [20] C. G. Burgar, P. S. Lum, A. M. Scremin et al., "Robot-assisted upper-limb therapy in acute rehabilitation setting following stroke: Department of Veterans Affairs multisite clinical trial," *Journal of Rehabilitation Research and Development*, vol. 48, pp. 445–458, 2011.
- [21] L. E. Kahn, M. L. Zygman, W. Z. Rymer, and D. J. Reinkensmeyer, "Robot-assisted reaching exercise promotes arm movement recovery in chronic hemiparetic stroke: a randomized controlled pilot study," *Journal of Neuroengineering and Rehabilitation*, vol. 3, p. 12, 2006.
- [22] J. Mehrholz and M. Pohl, "Electromechanical-assisted gait training after stroke: a systematic review comparing end-effector and exoskeleton devices," *Journal of Rehabilitation Medicine*, vol. 44, pp. 193–199, 2012.
- [23] J. J. Summers, F. A. Kagerer, M. I. Garry, C. Y. Hiraga, A. Loftus, and J. H. Cauraugh, "Bilateral and unilateral movement training on upper limb function in chronic stroke patients: a TMS study," *Journal of the Neurological Sciences*, vol. 252, pp. 76–82, 2007.
- [24] J. H. Morris, F. van Wijck, S. Joice, S. A. Ogston, I. Cole, and R. S. MacWalter, "A comparison of bilateral and unilateral upper-limb task training in early poststroke rehabilitation: a randomized controlled trial," *Archives of Physical Medicine and Rehabilitation*, vol. 89, pp. 1237–1245, 2008.
- [25] W. Liu, S. M. Waller, T. Kepple, and J. Whittall, "Compensatory arm reaching strategies after stroke: induced position analysis," *Journal of Rehabilitation Research and Development*, vol. 50, pp. 71–84, 2013.
- [26] H. S. Lo and S. Q. Xie, "Exoskeleton robots for upper-limb rehabilitation: state of the art and future prospects," *Medical Engineering & Physics*, vol. 34, no. 3, pp. 261–268, 2012.
- [27] D. G. Caldwell, N. G. Tsagarakis, S. Kousidou, N. Costa, and I. Sarakoglou, "'Soft' exoskeletons for upper and lower body rehabilitation—design, control and testing," *International Journal of Humanoid Robotics*, vol. 4, pp. 549–573, 2007.
- [28] S. Balasubramanian, W. Ruihua, M. Perez et al., "RUPERT: an exoskeleton robot for assisting rehabilitation of arm functions," in *2008 Virtual Rehabilitation*, pp. 163–167, 2008.
- [29] A. E. Q. van Delden, C. E. Peper, G. Kwakkel, and P. J. Beek, "A systematic review of bilateral upper limb training devices for poststroke rehabilitation," *Stroke Research and Treatment*, vol. 2012, Article ID 972069, 17 pages, 2012.
- [30] J. C. Perry, J. Rosen, and S. Burns, "Upper-limb powered exoskeleton design," *IEEE/ASME Transactions on Mechatronics*, vol. 12, pp. 408–417, 2007.
- [31] H. Sheahan and E. Maxwell, "ReachHab: a bilateral upper limb rehabilitation device for stroke," *UoAA*, p. 8, 2013.
- [32] M. D. Kaya, A. S. Hasiloglu, M. Bayramoglu, H. Yesilyurt, and A. F. Ozok, "A new approach to estimate anthropometric measurements by adaptive neuro-fuzzy inference system," *International Journal of Industrial Ergonomics*, vol. 32, pp. 105–114, 2003.
- [33] C. Fransson and J. Winkel, "Hand strength: the influence of grip span and grip type," *Ergonomics*, vol. 34, pp. 881–892, 1991.
- [34] S. Weikert, R. Ratnaweera, O. Zirn, and K. Wegener, *Modeling and Measurement of H-Bot Kinematic Systems*, American Society for Precision Engineering, Denver, CO, 2011.
- [35] T. Proietti, V. Crocher, A. Roby-Brami, and N. Jarrassé, "Upper-limb robotic exoskeletons for neurorehabilitation: a review on control strategies," *IEEE Reviews in Biomedical Engineering*, vol. 9, pp. 4–14, 2016.

Research Article

A Feasibility Study of SSVEP-Based Passive Training on an Ankle Rehabilitation Robot

Xiangfeng Zeng,¹ Guoli Zhu,¹ Lan Yue,¹ Mingming Zhang,² and Shane Xie³

¹School of Mechanical Science and Engineering, Huazhong University of Science and Technology, Luoyu Road 1037, Wuhan, China

²Department of Mechanical Engineering, University of Auckland, Auckland 1142, New Zealand

³School of Mechanical Engineering, School of Electronic and Electrical Engineering, University of Leeds, Leeds LS2 9JT, UK

Correspondence should be addressed to Guoli Zhu; glzhu_wh@163.com

Received 5 May 2017; Revised 5 July 2017; Accepted 1 August 2017; Published 17 September 2017

Academic Editor: Duo Wai-Chi Wong

Copyright © 2017 Xiangfeng Zeng et al. This is an open access article distributed under the Creative Commons Attribution License, which permits unrestricted use, distribution, and reproduction in any medium, provided the original work is properly cited.

Objective. This study aims to establish a steady-state visual evoked potential- (SSVEP-) based passive training protocol on an ankle rehabilitation robot and validate its feasibility. **Method.** This paper combines SSVEP signals and the virtual reality circumstance through constructing information transmission loops between brains and ankle robots. The robot can judge motion intentions of subjects and trigger the training when subjects pay their attention on one of the four flickering circles. The virtual reality training circumstance provides real-time visual feedback of ankle rotation. **Result.** All five subjects succeeded in conducting ankle training based on the SSVEP-triggered training strategy following their motion intentions. The lowest success rate is 80%, and the highest one is 100%. The lowest information transfer rate (ITR) is 11.5 bits/min when the biggest one of the robots for this proposed training is set as 24 bits/min. **Conclusion.** The proposed training strategy is feasible and promising to be combined with a robot for ankle rehabilitation. Future work will focus on adopting more advanced data process techniques to improve the reliability of intention detection and investigating how patients respond to such a training strategy.

1. Introduction

Stroke is one of the main root causes leading patients unable to comfortably control their muscles and bodies in the daily living, and even lose the ability [1–3]. The ability of body controlling is inversely proportional to the distance between brains and limbs, which means that the longer the distance is, the lower the ability is [4]. Motor function of injured ankles will be recovered more difficult than one of the hands with a similar disability.

For early stage rehabilitation of injured ankles, if without sufficient rotations, ankle joints could gradually become stiff, and finally, foot drop will be generated [5, 6]. In order to avoid being stiff, muscle stretching and joint rotating are regarded as one of the important methods in traditional therapy of injured ankle joints. Traditional physical therapy is usually operated manually by therapists. It has a unique advantage, which therapists can observe real-time feedback from patients through their body reaction and communication and thus adjust the process accordingly. However, it also

has several limitations: (1) therapists can feel weary for long-time operation; (2) operating strength cannot be kept uniformly during the whole process; (3) mental state of therapists is one of the key factors to affect therapy effect [7].

In order to release manpower and address those limitations, robots have been invented to substitute partial functions of traditional therapy [8, 9]. For ankle rehabilitation, there are two kinds of robots invented, one of which is platform-based robots, and the other is wearable devices [3]. When training on platform-based robots, subjects are normally in a sitting position to train their physical function of muscle stretching and joint rotating [8, 10]. When training on wearable ankle robots, subjects are required to be in a standing position to improve their ability on walking [1]. Therefore, platform-based robots can provide better rehabilitation for subjects with weak motion ability of ankle joints, while targeted subjects of wearable ankle robots are those whose motion ability of ankle joints is strong enough to walk, but gait needs to be rebuilt and improved further recovery [11].

Passive training is one of the basic functions of platform-based robots. Different with common passive stretching with constant speed, Zhang et al. [12] proposed an intelligent passive stretching strategy in ankle dorsiflexion/plantarflexion (DF/PF) for safety. During intelligent passive stretching, rotating speed of the robot was inversely proportional to resistance torque. As soon as predefined maximum resistance torque was reached, ankle joints would be held at the extreme position for a period of time to allow stress relaxation. For robot-assisted passive ankle training, subjects are requested to keep relaxed to follow up trajectories of robots [3, 10]. After experiencing passive training, physic function of ankle joints can be kept to a certain degree and foot drop can be alleviated correspondingly [5, 8, 12].

Active training is another function of platform-based robots, where subjects are requested to actuate robots to track targets by allowing the foot to follow visual or auditory instructions [1, 10, 13, 14]. Visual reality circumstance has been widely applied in robot-assisted active ankle training. Girone et al. [15] proposed a virtual reality exercise library on the Rutgers Ankle. Subjects could conduct simulation exercise of strength, flexibility, and balance with haptic and visual feedback. Burdea et al. [14] proposed rehabilitation games including the airplane game and breakout 3D game. Michmizos et al. [16] proposed three goal-directed serious games especially for children. In this study, visual reality circumstance is set as a game of whack-a-mole, which four hamsters are arranged in four directions as targets, and a hammer is initially located in the center as the movable cursor. The vertical trajectory of hammer is projected to DF/PF, while the horizontal one is corresponded to inversion/eversion (INV/EV).

For passive training, subjects do not need to exert active effort, and thus few information transmission loops between brains and ankles exist [17]. A prerequisite of conducting active training is that subjects should have enough motion ability of ankle joints to trigger robots [10]. Therefore, for subjects whose motion intentions of ankle joints cannot be detected by built-in force sensors of robots, solving the problem of how they can actively conduct ankle training is a big challenge. This study aims to construct an information transmission loop between brains and ankle robots and enable subjects with weak motion ability of ankle joints to actively conduct robot-assisted ankle training.

When subjects focus their attention on a flickering source with frequency above 6 Hz, electroencephalography (EEG) signals originated from their visual cortex are named SSVEP, spectrum of which shows peak at the flickering frequency and its harmonics [18]. SSVEP signals have been extracted and applied in many fields, such as controlling the robotic wheelchair [19], the humanoid robot navigation [20, 21], the semiautonomous mobile robotic car operation [22], and the artificial upper limb [23].

In this study, SSVEP signals are introduced and used for passive training on an ankle rehabilitation robot, in which motion intentions of subjects can be extracted to trigger related passive training. Four flickering circles with the diameter of 22 mm are arranged in four directions. Flickering

frequencies are set as 10 Hz for the upper, 12 Hz for the bottom, 8.6 Hz for the left, and 15 Hz for the right [24]. For subjects, gazing at the upper flickering circle represents the motion intention for DF, the bottom for PF, the left for INV, and the right for EV.

To enable subjects with weak motion ability of ankle joints to conduct motion intention-directed passive training, this study develops a SSVEP-based passive training strategy through combining SSVEP signals and virtual reality circumstance on an ankle robot. To verify its feasibility, this study recruited five healthy subjects for preliminary evaluation.

2. Methods

2.1. Ankle Rehabilitation Robot. The ankle rehabilitation robot applied in this study is an improved version of the one used in [11] by adding adjustable robot structure and was briefly introduced as in Figure 1(a). The footplate of the ankle robot could move with three degrees of freedom, which are corresponding to ankle DF/PF, INV/EV, and adduction/abduction (AA). The robot is actuated in parallel by four FFMs (FESTO DMSP-20-400N), pressure control of which is regulated by four proportional pressure regulators (FESTO VPPM-6L-L-1-G18-0L6H). Three magnetic rotary encoders (AMS AS5048A) are installed along each axis to measure angular positions forming a three-dimensional coordinate system of the footplate. Four single-axis load cells (FUTEK LCM 300) are installed to measure contraction forces generated by FFMs. A six-axis load cell (SRI M3715C) is installed below the footplate to measure interaction forces and torques between human feet and the footplate.

The position control of this robot can be achieved by controlling individual FFM length in joint space, as shown in Figure 2. The desired individual FFM length is calculated by inverse kinematics based on the desired position of the end effector, while, as the feedback to the PID controller, the actual individual FFM length is obtained by inverse kinematics based on the measured position of the end effector. This joint space position controller outputs four pressure values that directly go to four proportional pressure regulators for the actuation of the robot.

2.2. Information Transmission Loop. An information transmission loop between brains and ankle robots is constructed through combining SSVEP signals and virtual reality circumstance for passive training on the ankle rehabilitation robot, as shown in Figure 3. SSVEP signals are evoked in brains when subjects pay their attention on one of the flickering sources, which represents motion intentions of subjects in the training. The robot can recognize motion intentions of subjects by analyzing the flickering source of SSVEP signals and immediately trigger the robot to conduct predefined training. Real-time visual feedback of ankle rotation ascends to brains immediately when the hammer in virtual reality training circumstance moves, as in Figure 4.

2.2.1. Virtual Reality Training Circumstance. The virtual reality training circumstance is set as a game of whack-a-mole,

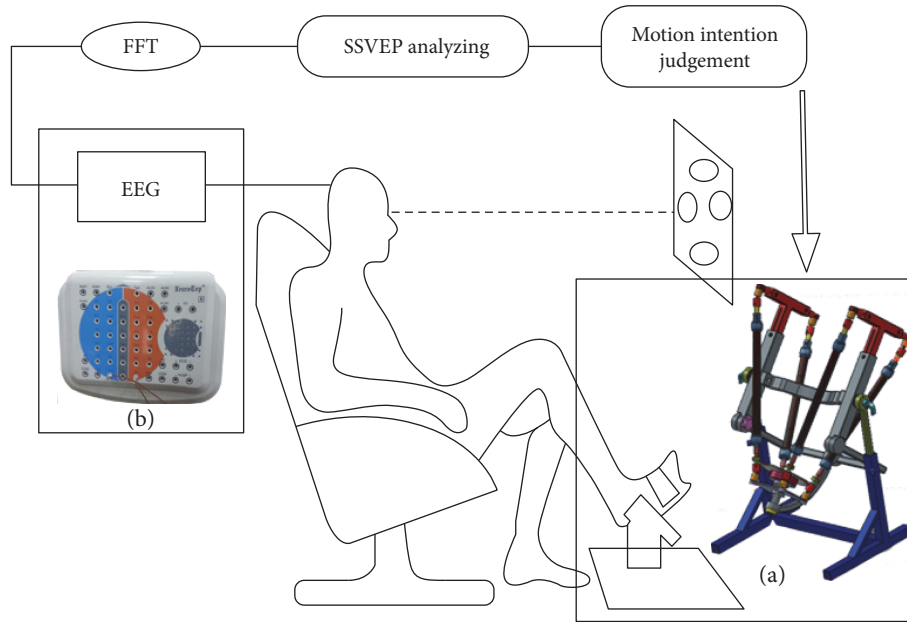


FIGURE 1: SSVEP-based passive training on an ankle rehabilitation robot. Subjects sit on a comfortable chair and are requested to gaze at one of the flickering circles. Motion intentions are detected through analyzing SSVEP signals. Each detection would immediately trigger the ankle robot to conduct a predefined passive stretching. (a) An ankle rehabilitation robot is applied to provide passive and active ankle training along DF/PF, INV/EV, and AA trajectories. (b) An EEG system (NT9200, symtop) is applied to acquire and amplify EEG signals.

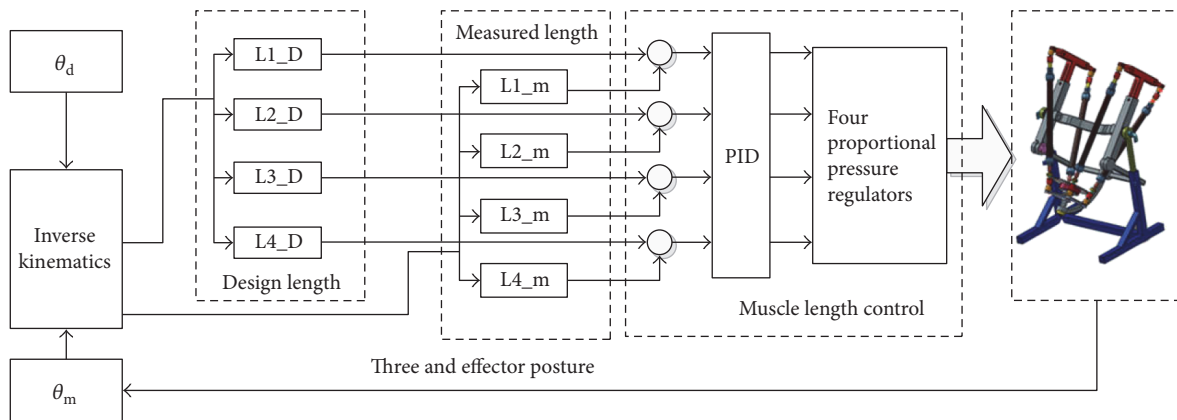


FIGURE 2: The flowchart of individual muscle length control in joint space.

which consists of a black background wall, a vertical rail, a horizontal rail, a hammer, a tent, four Hamsters, and four flickering circles (Figure 4). The vertical rail is projected to DF/PF trajectory, and the horizontal rail is corresponding to INV/EV trajectory. There are four hamsters located at the end of the vertical and horizontal rail, nearby which four circles with a diameter of 22 mm are flickering with frequency of 10 Hz for the upper, 12 Hz for the bottom, 8.6 Hz for the left, and 15 Hz for the right [24]. The tent is located at the cross point between the vertical and horizontal rail, corresponding to the neutral position of ankle joints. The hammer can move freely along with the vertical or horizontal rail, and its position represents the posture of the footplate or the human ankle during the training.

At the beginning of the game, four hamsters and four flickering circles appear on the computer screen, which the upper represents the target for subjects to conduct the training of DF, the bottom for PF, the left for INV, and the right for EV. When subjects focus their attention on one of the flicking circles about 5 seconds, the robot will be triggered to rotate the footplate based on its judgment of motion intention of subjects through analyzing SSVEP signals. Meanwhile, accompanying with the targeted vertical or horizontal rail appearing and the tent disappearing, the hammer will start to move toward the targeted hamster. Once the hammer reaches the end of rails, the targeted hamster will disappear, and then it will return back to the cross point. Tent and hamsters will reappear as soon

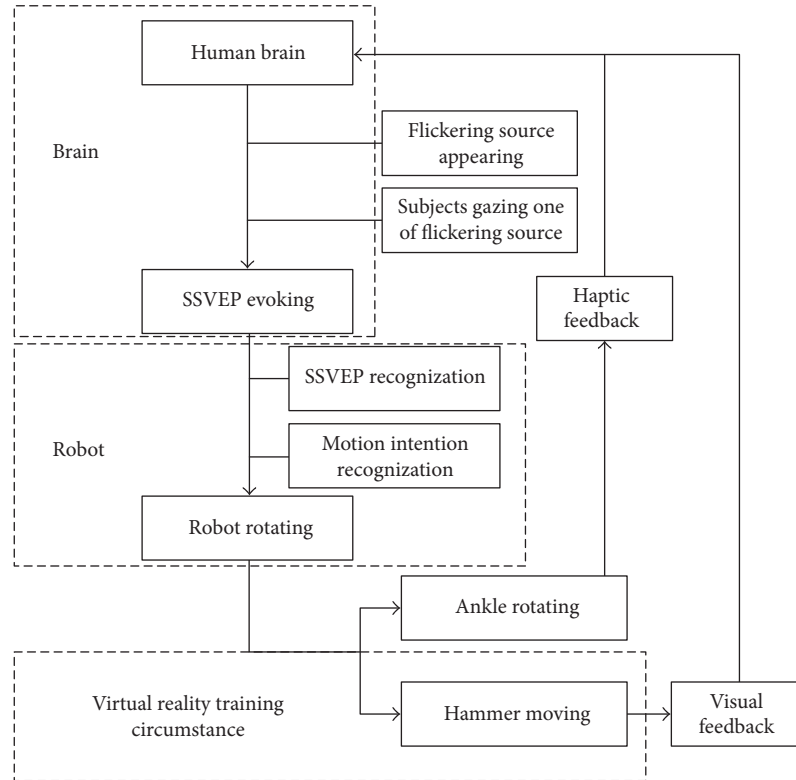


FIGURE 3: Information transmission loop. SSVEP signals are evoked in brains when subjects pay their attentions to one of the flickering circles. The robot judges motion intentions of subjects through recognizing the flickering source of SSVEP signals and is triggered to deliver predefined training. Haptic feedback ascends to brains when ankles rotate following the robot, and visual feedback of ankle rotation ascends to brains when the hammer moves in virtual reality training circumstance.

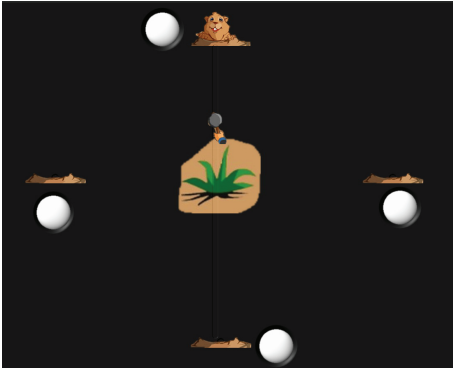


FIGURE 4: Virtual reality circumstance. Hamsters are set as targets and will disappear when ankle joints rotate to a predefined maximum position. SSVEP signals will be evoked when subjects gaze at one of the flickering circles. Rails of the hammer are mapped to the trajectories of ankle joints.

as the hammer arrives at the cross point, representing that preparation for the next cycle of training is ready.

2.2.2. SSVEP Recognition. EEG signals are acquired and amplified by a video EEG system (NT9200, symtop) that can provide 41 Ag/AgCl electrodes, which are positioned according to international 10/20 system as in Figure 1(b)

[25]. Prior to data acquisition, impedance inspection of the EEG system is conducted to verify whether contact resistance among electrodes and scalps can meet design specification after conductive gel is injected to fill up the gap between working electrodes and head of subjects. The signals from Oz is applied to extract motion intentions of subjects, while the reference electrode is placed on earlobe A2 and the ground electrode is placed on Fpz. EEG signals are digitalized and processed through Labview software (National Instruments, Austin, USA), the sampling frequency of which is set up to 500 Hz, and the duration for robot to judge motion intention of subjects is set to 5 seconds. EEG recordings are band-pass filtered from 6 Hz to 30 Hz through the application of the Butterworth filter.

Fast Fourier transform (FFT) [26] is applied to those epochs, which contain 2500 data points for every electrode. According to generation mechanism of SSVEP signals, the peak of amplitude will occur at the flickering frequency and its harmonic when subjects focus their attention on a flickering source [23]. But off-line analysis indicates that it has a slight shift of frequencies for the peak amplitude occasionally, caused possibly by displaying characteristics of LCD. Therefore, it can partially eliminate deviation caused by frequency shift when the maximum amplitude of five adjacent frequencies centered on a flickering frequency is designated as the amplitude of that flickering frequency, which is expressed as in (1), where X_{ij} is the amplitude of five adjacent

frequencies centered on the flickering frequency, j is the serial number of five adjacent frequencies, and i is the serial number of flickering circles.

$$A_i = \max(X_{ij}), (i = 1, \dots, 4; j = 1, \dots, 5). \quad (1)$$

After amplitudes of flickering frequencies are ascertained, the dominant frequency in the SSVEP signals will be identified as the flickering frequency with the maximum amplitude, in (2).

$$f_{\text{target}} = \arg \max(A_i), (i = 1, \dots, 4). \quad (2)$$

2.3. Subjects. Five healthy subjects with ages at 24 ± 3 years participated in this study. One of them is female, and others are male. Inclusion criteria are subjects with (i) normal vision, (ii) corrected-to-normal vision, and (iii) no history of clinical visual impairment. Subjects who can be easily distracted will be excluded. All subjects are right-handed. All of subjects are the first time to conduct SSVEP-triggered passive training on the ankle robot. During the training, blinking is not prohibited. The whole experiment was conducted in a laboratory with a floor space of approximately 43 square meter. It is quiet in the surrounding, and light illumination is weak.

2.4. Training Protocol. Each subject was requested to sit calmly 50 cm in front of LCD, looking straightly at the virtual reality circumstance, and put the right leg in the ankle rehabilitation robot, with the right foot fixed on the footplate. The electrode cap is placed on the head of subjects following up the regulation of international 10/20 system [25], and electrode gel is applied. Before the training, subjects are informed (i) gazing at the upper flickering circle represents the motion intention for DF, the bottom for PF, the left for INV, and the right for EV; (ii) gazing at the intended flickering circle once the tent appears, and giving up the gazing when the tent disappears or ankle joints begin to rotate; (iii) during stretching of the robot, subjects need to observe moving situation of the hammer and imagine rotation situation of related ankle joints; (iv) if actual stretching of the robot is not consistent with their motion intention, subjects merely follow up the rotation without any resistance against the movement.

Subjects were requested to conduct two kinds of combined ankle movement tasks through focusing on one of the four flicking sources to trigger the robot. One kind of task combines ankle DF training with PF training together, and no time interval exists between them. A total five tasks are set in the training. The other kind of task is the combination of INV and EV training, without time interval among them, and a total of five tasks are set. There is 1 minute for free between both tasks, and SSVEP signals of subjects will not be extracted to judge motion intentions of subjects until the footplate of the robot returns back to the neutral position.

2.5. Evaluation Procedures. In this study, the performance of motion intention detection is evaluated by a success rate and information transfer rate (ITR). The success rate is defined as the percentage of output that actual movements of the robot are consistent with motion intentions of subjects. Therefore,

TABLE 1: Result of conducting combined ankle movement tasks.

Subject	S1	S2	S3	S4	S5
Number of accordant task	20	18	16	17	18
Success rate	100%	90%	80%	85%	90%
ITR (bits/min)	24	16.5	11.5	13.8	16.5

Note. Two kinds of tasks, one for combined DF and PF training, and the other for combined INV and EV training. The total number of motion intentions requested to identify for every subject is 20. The duration for robot to judge the motion intention of subjects is 5 s. The number of flickering circles representing the motion intention of subjects was 4.

the success rate is described as in (3), where A denotes the quantity of motion intentions which are correctly recognized and B denotes the total quantity of motion intentions which are requested to identify.

$$\text{Success Rate} = \frac{A}{B} \times 100\%. \quad (3)$$

The ITR [27] under the unit of bits/min is expressed as in (4), where N is the number of flickering circles, which is set to 4 in this study. P is the success rate, and T is the time during which SSVEP signals are extracted to determine the motion intention of a subject.

$$B = \left\{ \log_2 N + P \log_2 P + (1 - P) \log_2 \left[\frac{1 - P}{N - 1} \right] \right\} \times \frac{60}{T}. \quad (4)$$

3. Results

The results of combined ankle rotation tasks are shown in Table 1. All five subjects can trigger the ankle rehabilitation robot. Subject 1 conducts a total of 20 tasks without any discordance with his motion intentions, and subject 3 achieved 16 accordant tasks with the lowest success rate of 80% (Figure 5).

The biggest ITR of the robot for this training is set as 24 bits/min, and only subject 1 achieved it. The lowest ITR in this study is 11.5 bits/min when subject 3 achieved the success rate of 80% (Figure 6).

Tracking responses in joint space of combined DF/PF trajectory during ankle stretching are plotted in Figure 7. All subjects can trigger the robot to conduct the training. During conducting combined DF/PF tasks, subject 1 controls the training entirely following up his motion intention. Subjects 2, 4, and 5 have one inconsistent PF or DF training, and subject 3 has three inconsistent trainings.

4. Discussion

All five subjects succeeded in conducting training on the SSVEP-triggered robot following their motion intentions. The lowest success rate is 80%, and the highest one is 100%. The lowest ITR is 11.5 bits/min when the biggest one of the robots for this proposed training is set as 24 bits/min. The training is safe even when motion intentions of subjects are not consistent with real trajectories of ankle rotation.

This study introduces SSVEP signals to an ankle rehabilitation robot and combines partial characteristics of

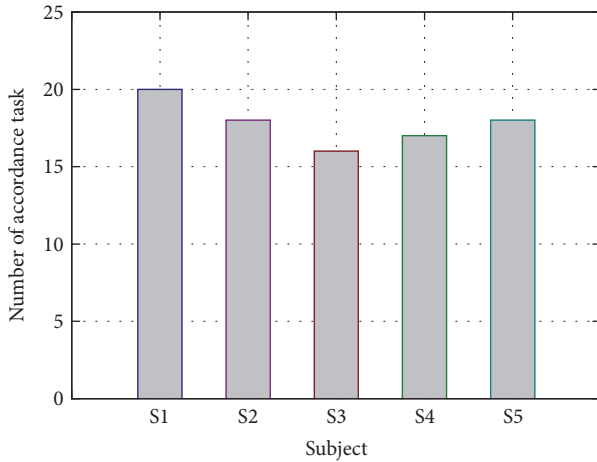


FIGURE 5: Number of accordance tasks for five subjects. A total of 20 tasks are set for subjects to trigger ankle robot based on clarification of SSVEP signals. Accordance task indicates that motion intention of subjects in that task is in accordance with actual stretching.

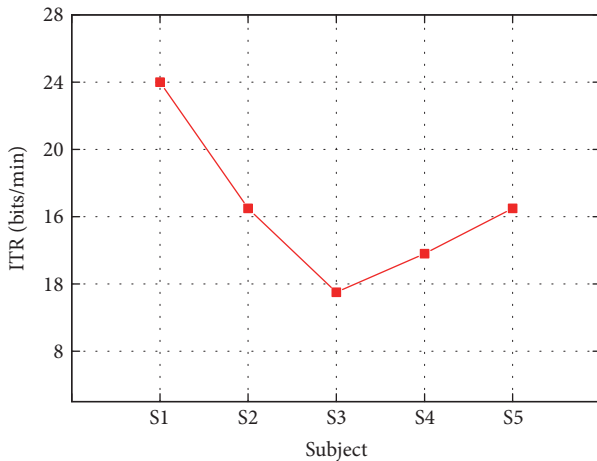


FIGURE 6: ITR for five subjects. The time applied to extract SSVEP signals is set as 5 seconds. A total of four targets are set in the SSVEP-triggered ankle training.

active ankle training with passive training. An information transmission loop between brains and ankle robots is proposed by combining SSVEP signals and virtual reality training circumstance on the ankle rehabilitation robot. This training strategy extends those active characteristics to subjects without ability to conduct active training. The feasibility study will be discussed from aspects of feasibility, motion intention-directed passive training, mechanism, and limitations.

4.1. Feasibility. In this study, five healthy subjects participated in the ankle training through gazing one of the four flickering sources to trigger passive ankle stretching on an ankle rehabilitation robot. One subject completely conducted the ankle training without any discordance between his motion intentions and actual rotation of the robot. Other subjects conducted the training with no less than 80% success

rate. For subjects with weak motion ability of ankle joints, many of them still maintain a normal vision and can focus their attention on one of their interested things or objects over a period of time. Subjects with stroke even can achieve higher classification accuracy of extracting SSVEP signals from online experiments than normal subjects [28]. For subjects with weak motion ability of ankle joints, their confidence to recover health can be enhanced in further training when they actively conduct ankle training with 80% success rate through their own efforts, albeit with the assistance of a robot. Even if a judgment of the motion intention is wrong, the passive training will still be conducted following up the trajectory based on judgment of the robot. This definition can keep the integrity and continuity of the whole training and further improve efficiency of the training. During the training inconsistent with motion intention of subjects, ankle joints will still rotate following up trajectories of robot, which can maintain the whole quantity of ankle stretching motion.

The maximum ITR is 24 bits/min in this study, and the least ITR is 11.5 bits/min. Although the value of ITR is less than recordings in many other literature [27–29], it is suitable to apply in this study. Based on the definition of ITR expressed in (4), its value is computed based on the value of T and N , which is proportional to the value of N , and reversely proportional to the value of T . Although the ankle robot is designed with three rotational degrees of freedom, when combining the robot with virtual reality circumstance, the proposed SSVEP-based therapy retains two degrees of freedom; therefore, the value of N is set to 4. As mentioned in [11], in the passive training mode, the combined DF/PF trajectory is a sine wave with frequency of 0.02 Hz; therefore, the duration conducting single DF or PF trajectory will be approximately 25 seconds. In this study, it is suitable to set the value of T as 5 seconds, because subjects can have 5 seconds to prepare in mind to generate SSVEP signals, and at the same time, to accumulate energy in the body to conduct the judged training. Adding extra 5 seconds of motion intention judgment to 25 seconds of passive ankle training does not damage integrity of the whole training because its time compared to the total training is less. Subjects with weak motion ability of ankle joints might spend more than 5 seconds to prepare in their mind and accumulate energy in their body in advance before they can rotate ankles based on their own efforts. Therefore, extra 5 seconds of motion intention judgment applied to trigger passive training are comparable to their actual movement pattern of ankle joints.

4.2. Motion Intention-Directed Passive Training. For motion intention-directed passive training, virtual reality circumstance transfers rotation of ankle joints to trajectories of the cursor, which are requested to touch the target to complete the training [1, 13, 14]. Through observing the distance between the target and the cursor, human brains estimate which direction and how fast ankle joints should move and how much effort ankle joints should exert. Then, through neural pathways of the body, brains transfer the motion command to ankles. At the same time, trajectories of the cursor in virtual reality circumstance display the motion situation of ankle joints. After several loops of information transferring,

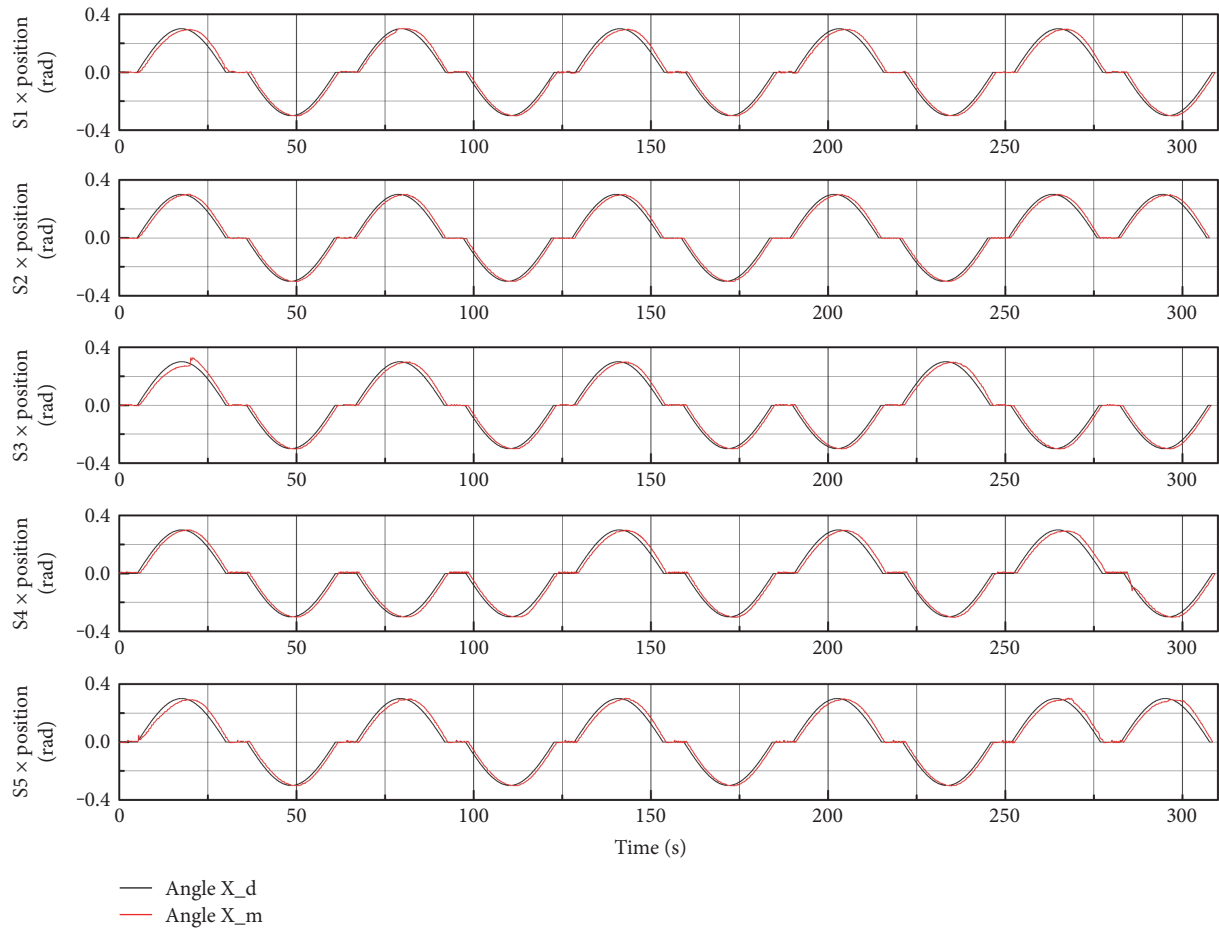


FIGURE 7: Tracking responses in joint space of DF/PF trajectory during ankle stretching conducted by five subjects. The red curve denotes actual moving trajectory, and the blue one represents the predefined ones. The amplitude of ankle rotation is 0.3 degree, and frequency is 0.02 Hz.

the motion intention-directed passive training is accomplished when the target is reached by the cursor.

For pure passive training, subjects are requested to relax completely by tracking predefined trajectories of the robot [12]. Comparing with motion intention-directed passive training, the biggest difference of pure passive training is that brains of subjects might be in an idle state [11]. Relaxation of the whole body indicates that the brain does not respond to any body motion. If their neural pathways are not blocked, internal feedback of ankle motion along nervous system should be maintained, which means that brains can feel the situation of ankle motion in their mind [17].

In this study, virtual reality circumstance is combined with passive training. Movement of the hammer on the rail can exactly display the rotation of the robot footplate. Therefore, subjects can get real-time visual feedback from movement of the hammer to know what trajectories ankle joints follow up and the real-time ankle position during the training. Once the hammer touches the targeted hamster, the hamster disappears immediately, and subjects can know that ankle joints have rotated to predefined maximum position. To summarize, the motion intention-directed passive training requires part of active engagement from subjects.

4.3. Mechanism. When subjects prepare or deliver ankle movements, EEG oscillatory activity at α -band (8–12 Hz) and β -band (12–30 Hz) decreases over the premotor and primary sensorimotor areas. This phenomenon is so called event-related desynchronization (ERD), representing increased activation of the corresponding cortical area. Event-related synchronization (ERS) is the phenomenon that power recovers to the resting condition at the end of movement [30]. Voluntary active movement, passive robot-assisted movement, and motor imagery all associate with ERD and ERS, and their oscillatory amplitude change is successively from big to small [31]. When a stroke patient was requested to repeatedly attempt DF of a paretic ankle joint at a comfortable pace, ERD-modulated functional electrical stimulation (FES) system could achieve short-term functional improvement comparing with FES alone [32]. To some extent, this supports the potential of the intention-directed passive training with respect to pure passive mode.

The proposed SSVEP-based training strategy extends partial characteristics of active training into passive training. Firstly, subjects with weak motion ability of ankle joints can actively trigger training. They can intentionally select certain training plan through gazing one of the flickering circles in

virtual reality circumstance. Secondly, subjects with weak motion ability of ankle joints can pay more attention to their training. When in passive training, subjects are always requested to keep relax, and only follow up predefined trajectories of the robot [3, 10]. In general, the proposed intention-directed passive training strategy requires subjects to keep their attention on virtual reality circumstance to get visual feedback. In this way, subjects can not only know actual rotating position of ankle joints but also devote more efforts to the training.

4.4. Limitations. While preliminary experiments support the feasibility and promise of the proposed intention-based passive training on an ankle rehabilitation robot, this study still has some limitations. Firstly, EEG signal processing is performed simply through FFT which is a very basic algorithm. More advanced data process techniques should be involved to improve the reliability. Second, the proposed training strategy only involves very limited active engagement from participants. It can be a good idea to combine SSVEP signals with the whole training process for enhanced rehabilitation efficacy. The third one is that future experiments should recruit a large sample of patients with ankle disabilities. The question that how patients perform with such a training should be also investigated.

5. Conclusion

This study proposed a steady-state visual evoked potential (SSVEP-) based passive training protocol on an ankle rehabilitation robot and validated its feasibility and promise on five healthy subjects. By combining SSVEP signals and the virtual reality circumstance, the ankle rehabilitation robot was found to be able to trigger the training based on their motion intentions. The virtual reality training circumstance also provides real-time visual feedback of ankle rotation. Experiments showed that subjects could succeed in conducting ankle training based on the SSVEP-triggered training strategy. Future work will focus on adopting more advanced data process techniques to improve the reliability of motion intention detection. The question that how patients perform with such a training strategy should be also investigated.

Conflicts of Interest

The authors declare that there is no conflict of interest regarding the publication of this paper.

References

- [1] R. N. Goodman, J. C. Rietschel, A. Roy et al., "Increased reward in ankle robotics training enhances motor control and cortical efficiency in stroke," *Journal of Rehabilitation Research and Development*, vol. 51, pp. 213–227, 2014.
- [2] N. Hogan, H. I. Krebs, B. Rohrer et al., "Motions or muscles? Some behavioral factors underlying robotic assistance of motor recovery," *The Journal of Rehabilitation Research and Development*, vol. 43, pp. 605–618, 2006.

- [3] Z. Zhou, Y. Zhou, N. Wang, F. Gao, K. Wei, and Q. Wang, "A proprioceptive neuromuscular facilitation integrated robotic ankle-foot system for post stroke rehabilitation," *Robotics and Autonomous Systems*, vol. 73, pp. 111–122, 2015.
- [4] J. T. Gwin and D. P. Ferris, "Beta- and gamma-range human lower limb corticomuscular coherence," *Frontiers in Human Neuroscience*, vol. 6, 2012.
- [5] A. Roy, H. I. Krebs, D. J. Williams et al., "Robot-aided neurorehabilitation: a novel robot for ankle rehabilitation," *IEEE Transactions on Robotics*, vol. 25, pp. 569–582, 2009.
- [6] C. M. McCrimmon, C. E. King, P. T. Wang, S. C. Cramer, Z. Nenadic, and A. H. Do, "Brain-controlled functional electrical stimulation therapy for gait rehabilitation after stroke: a safety study," *Journal of Neuroengineering and Rehabilitation*, vol. 12, 2015.
- [7] S. Pittaccio, F. Zappasodi, S. Viscuso et al., "Primary sensory and motor cortex activities during voluntary and passive ankle mobilization by the SHADE orthosis," *Human Brain Mapping*, vol. 32, pp. 60–70, 2011.
- [8] R. W. Selles, X. Li, F. Lin, S. G. Chung, E. J. Roth, and L. Q. Zhang, "Feedback-controlled and programmed stretching of the ankle plantarflexors and dorsiflexors in stroke: effects of a 4-week intervention program," *Archives of Physical Medicine and Rehabilitation*, vol. 86, pp. 2330–2336, 2005.
- [9] A. Roy, H. I. Krebs, C. T. Bever, L. W. Forrester, R. F. Macko, and N. Hogan, "Measurement of passive ankle stiffness in subjects with chronic hemiparesis using a novel ankle robot," *Journal of Neurophysiology*, vol. 105, pp. 2132–2149, 2011.
- [10] L. W. Forrester, A. Roy, A. Krywonis, G. Kehs, H. I. Krebs, and R. F. Macko, "Modular ankle robotics training in early subacute stroke: a randomized controlled pilot study," *Neurorehabilitation and Neural Repair*, vol. 28, pp. 678–687, 2014.
- [11] M. Zhang, *Improving Effectiveness of Robot-Assisted Ankle Rehabilitation via Biomechanical Assessment and Interaction Control*, [Ph.D. thesis], Department of Mechanical Engineering, The University of Auckland, Auckland 1142, New Zealand, 2016.
- [12] L. Q. Zhang, S. G. Chung, Z. Bai et al., "Intelligent stretching of ankle joints with contracture/spasticity," *IEEE Transactions on Neural Systems and Rehabilitation Engineering*, vol. 10, pp. 149–157, 2002.
- [13] T. Sukal-Moulton, T. Clancy, L. Q. Zhang, and D. Gaebler-Spira, "Clinical application of a robotic ankle training program for cerebral palsy compared to the research laboratory application: does it translate to practice?," *Archives of Physical Medicine and Rehabilitation*, vol. 95, pp. 1433–1440, 2014.
- [14] G. C. Burdea, D. Cioi, A. Kale, W. E. Janes, S. A. Ross, and J. R. Engsborg, "Robotics and gaming to improve ankle strength, motor control and function in children with cerebral palsy—a case study series," *IEEE Transaction on Neural System and Rehabilitation Engineering*, vol. 21, no. 2, pp. 165–173, 2013.
- [15] M. Girone, G. Burdea, and M. Bouzit, "The 'Rutgers ankle' orthopedic rehabilitation interface," in *Proceedings of the ASME Haptics Symposium*, vol. DSC-67, pp. 305–312, 1999.
- [16] K. P. Michmizos, S. Rossi, E. Castelli, P. Cappa, and H. I. Krebs, "Robot-aided neurorehabilitation: a pediatric robot for ankle rehabilitation," *IEEE Transactions on Neural Systems and Rehabilitation Engineering*, vol. 23, pp. 1056–1067, 2015.
- [17] Y. J. Chang, J. N. Liang, M. J. Hsu, H. Y. Lien, C. Y. Fang, and C. H. Lin, "Effects of continuous passive motion on reversing

- the adapted spinal circuit in humans with chronic spinal cord injury,” *Archives of Physical Medicine and Rehabilitation*, vol. 94, pp. 822–828, 2013.
- [18] Z. Lin, C. Zhang, W. Wu, and X. Gao, “Frequency recognition based on canonical correlation analysis for SSVEP-based BCIs,” *IEEE Transactions on Biomedical Engineering*, vol. 54, pp. 1172–1176, 2007.
- [19] P. F. Diez, S. M. Torres Müller, V. A. Mut et al., “Commanding a robotic wheelchair with a high-frequency steady-state visual evoked potential based brain-computer interface,” *Medical Engineering & Physics*, vol. 35, pp. 1155–1164, 2013.
- [20] J. Zhao, W. Li, and M. Li, “Comparative study of SSVEP- and P300-based models for the telepresence control of humanoid robots,” *PLoS One*, vol. 10, article e0142168, 2015.
- [21] B. Choi and S. Jo, “A low-cost EEG system-based hybrid brain-computer interface for humanoid robot navigation and recognition,” *PLoS One*, vol. 8, article e74583, 2013.
- [22] P. Stawicki, F. Gembler, and I. Volosyak, “Driving a semiautonomous mobile robotic car controlled by an SSVEP-based BCI,” *Computational Intelligence and Neuroscience*, vol. 2016, Article ID 4909685, 14 pages, 2016.
- [23] P. Horki, T. Solis-Escalante, C. Neuper, and G. Müller-Putz, “Combined motor imagery and SSVEP based BCI control of a 2 DoF artificial upper limb,” *Medical & Biological Engineering & Computing*, vol. 49, pp. 567–577, 2011.
- [24] I. Volosyak, H. Cecotti, and A. Graser, “Optimal visual stimuli on LCD screens for SSVEP based brain-computer interfaces,” in *International IEEE/EMBS Conference on Neural Engineering*, pp. 447–450, Antalya, Turkey, 2009.
- [25] T. D. Lagerlund, F. W. Sharbrough, C. R. Jack Jr. et al., “Determination of 10–20 system electrode locations using magnetic resonance image scanning with markers,” *Electroencephalography and Clinical Neurophysiology*, vol. 86, pp. 7–14, 1993.
- [26] C. Lu, J. W. Cooley, and R. Tolimieri, “FFT algorithms for prime transform sizes and their implementations on VAX, IBM3090VF, and IBM RS/6000,” *IEEE Transactions on Signal Processing*, vol. 41, pp. 638–648, 1993.
- [27] J. R. Wolpaw, N. Birbaumer, W. J. Heetderks et al., “Brain-computer interface technology: a review of the first international meeting,” *IEEE Transactions on Rehabilitation Engineering*, vol. 8, p. 164, 2000.
- [28] X. Chen, Z. Chen, S. Gao, and X. Gao, “Brain-computer interface based on intermodulation frequency,” *Journal of Neural Engineering*, vol. 10, article 066009, 2013.
- [29] M. Cheng, X. Gao, S. Gao, and D. Xu, “Design and implementation of a brain-computer interface with high transfer rates,” *IEEE Transactions on Biomedical Engineering*, vol. 49, pp. 1181–1186, 2002.
- [30] J. T. Gwin and D. P. Ferris, “An EEG-based study of discrete isometric and isotonic human lower limb muscle contractions,” *Journal of Neuroengineering and Rehabilitation*, vol. 9, 2012.
- [31] E. Formaggio, S. F. Storti, I. Boscolo Galazzo et al., “Modulation of event-related desynchronization in robot-assisted hand performance: brain oscillatory changes in active, passive and imagined movements,” *Journal of Neuroengineering and Rehabilitation*, vol. 10, 2013.
- [32] M. Takahashi, K. Takeda, Y. Otaka et al., “Event related desynchronization-modulated functional electrical stimulation system for stroke rehabilitation: a feasibility study,” *Journal of Neuroengineering and Rehabilitation*, vol. 9, 2012.

Research Article

Effect on Chest Deformation of Simultaneous Correction of Pectus Excavatum with Scoliosis

Jin-Duo Ye,^{1,2} Guang-Pu Lu,^{1,2} Jing-Jing Feng,^{1,2} and Wei-Hong Zhong^{1,2}

¹Tianjin Key Laboratory of the Design and Intelligent Control of the Advanced Mechatronic System, Tianjin University of Technology, Binshuixi Road, No. 391, Tianjin 300384, China

²National Demonstration Center for Experimental Mechanical and Electrical Engineering Education, Tianjin University of Technology, Binshuixi Road, No. 391, Tianjin 300384, China

Correspondence should be addressed to Wei-Hong Zhong; zhong426@126.com

Received 5 May 2017; Revised 20 July 2017; Accepted 6 August 2017; Published 12 September 2017

Academic Editor: Lizhen Wang

Copyright © 2017 Jin-Duo Ye et al. This is an open access article distributed under the Creative Commons Attribution License, which permits unrestricted use, distribution, and reproduction in any medium, provided the original work is properly cited.

Objective. This paper is to understand the effect of simultaneous correction of pectus excavatum with scoliosis and to provide some useful information for clinical orthopedic surgery design. **Methods.** The method of a three-dimensional reconstruction has been used to the reconstruction of the chest model of pectus excavatum with scoliosis, and the numerical stimulation has been conducted to the process of minimally invasive correction. Three kinds of correction methods have been considered in the numerical simulation, stretch spine, stretch spine and minimally invasive correction at the same time, and release stretch spine after stretch spine and minimally invasive correction of pectus excavatum at the same time. **Results.** It is found that stretch spine may help to correction of scoliosis but aggravate the sternum collapse, and release stretch spine after stretch spine and minimally invasive correction at the same time could not only be good at scoliosis but also improve the collapse of the sternum, which could help to improve the heartbeat and breath of the patients. **Conclusion.** Among the three kinds of correction methods, release stretch spine after stretch spine and minimally invasive correction at the same time could help to improve both the scoliosis and the collapse of the sternum.

1. Introduction

Pectus excavatum (PE) is a common disease with chest wall deformity in adolescents. The incidence in newborns is about 1/300~1/1000, the prevalence rate of male and female is approximately 4:1, and some patients may be accompanied with scoliosis [1]. The typical symptom of pectus excavatum was sunken sternum. The symptom can lead to respiratory and circulatory system dysfunction, palpitation, shortness of breath after fatigue, exercise intolerance, and other diseases [2, 3]. The current clinical treatment for pectus excavatum is commonly minimally invasive correction surgery, which replaces the traditional Wada Stern turnover and Ravitch sternal elevation [4]. Its advantages are without osteotomy, shorter operation time, less bleeding, quick recovery, and small and hidden incision [5–7]. The Nuss procedure changed the mechanical environment of the thorax. It also has a pulling effect on the spine

which causes the lateral deformation of the spine and is the main cause of postoperative pain. Because of the difference of patients, the operation plan is lack of the support of the numerical results and the Nuss procedure has to rely on the experience of the doctors.

Scoliosis refers to one or several spinal segments deviate from midline bend to side and form a radian. Cobb angle is used to judge the degree of scoliosis deformity. When the angle is $30^\circ < \text{Cobb} < 40^\circ$ [8–10], the patient needs to be treated in hospital. If not promptly treated, it could develop into a serious deformity and will affect the heart and lung function. There are two kinds of treatments of scoliosis, one is nonsurgical treatment and the other is surgical treatment. At present, there are two kinds of effective methods: Boston-type brace [11] and electric stimulation therapy [12]. They are good for the treatment of mild idiopathic scoliosis with Cobb angle less than 15° , which needs no treatment but careful observation. In recent years, there

are various methods of surgical treatment; the emergence of new technology, such as Luque method [13], Zieker method, and C-D operation [14, 15], has good effect, but the surgical treatment is easy to injure the spinal cord nerve and cause permanent damage [16, 17]. Pectus excavatum patients are often associated with scoliosis symptoms. According to clinical experience, for patients whose chest wall deformity is not serious, the doctor could perform spine correction and then correct pectus excavatum; a case of right convex of thoracic spine with pectus excavatum was reported in 2005 for the treatment of first spinal traction and then the pectus excavatum correction. For serious pectus excavatum and scoliosis, patients first underwent Nuss procedure and then correction of scoliosis. In 2008, Blane et al. from the University of Michigan first performed a Nuss procedure for a child with scoliosis and then corrected the scoliosis.

At present, there are great progresses for the Nuss procedure research in the field of biomechanics in the world. In 2007, Qiren Zhang from Chang Gung University, Taiwan, made a mechanical analysis of the Nuss minimally invasive correction procedure in three patients with symmetrical funnel chest, but the model did not take into account the spine and did not give the results of stress and strain after correction [18]. In 2010, Nagasao T, a Japanese scholar, created the thorax model by the beam element and compared the postoperative thorax stress distribution between children and adults, in which there were some differences between numerical simulation and clinical results of funnel chest with scoliosis minimally invasive correction process; the numerical simulations predicted the improvement of scoliosis, and scoliosis postoperatively were aggravating [19]. Since 2010, Jin-Duo Ye, from Tianjin University of Technology, has carried out the numerical simulation of the pectus excavatum with scoliosis orthopedic process by using the three-dimensional solid-assembled model and the beam element model. The numerical results of the three-dimensional solid model are consistent with the clinical results. However, in the results of the beam element model, the predicted scoliosis results were significantly different from the clinical results. In 2016, Jin-Duo Ye et al., from Tianjin University of Technology, conducted an experiment on the goat thorax model by using the method of electrical measurement and the strain distribution of the thorax model was obtained [20].

Now, there is less research work on both effects of scoliosis correction on thorax deformation of pectus excavatum and simultaneous correction of pectus excavatum and scoliosis. The author carried out the biomechanics study of simultaneous correction of pectus excavatum and scoliosis by the numerical simulation of minimally invasive correction surgery and scoliosis stretching process and compared the distribution of both the displacement field and stress field of simultaneous correction on thorax deformity.

2. Methods

2.1. Construction of Finite Element Model. Computed tomography (CT) images of thorax of the patient with pectus

excavatum with scoliosis were provided by General Hospital of Beijing Command. In the patient with pectus excavatum with scoliosis, the sternum concaves inward to the right side with a depth of 40.3 mm, and the spine bows to the left with a Cobb angle of 20°. The 3-D solid model of the deformed thorax was reconstructed in Mimics. The model was imported into Geomagic for point cloud processing and finally imported into ANSYS to create the assembled solid model (Figure 1). Figure 1 was the thorax model with discs. It included two pieces of sternums, twelve pairs of ribs, and twelve section of thoracic vertebrae, and the coordinates of the model are in accordance with the previous CT default coordinate system. In the model, the method of coupling displacement has been used to link the vertebrae and the ribs and the ribs and the sternum. The intervertebral discs are obtained by Boolean operation between two vertebrae. Finally, the 3-D solid model of the thorax is shown in Figures 1(a) and 1(b).

For the pretreatment of the model, element type is set solid45 and material parameters are set linear isotropic. The elastic modulus of sternum, thoracic vertebrae, and ribs is set to $E=380$ MPa, Poisson's ratio is $\mu=0.3$, the elastic modulus of the intervertebral disc is set to $E=10$ MPa, and Poisson's ratio is $\mu=0.45$ [21].

The mesh is divided into 106,913 elements and 56,584 nodes. The finite element model is shown in Figure 2.

2.2. Correction of Scoliosis

2.2.1. Boundary Conditions. The lower surface of T_{12} of thoracic vertebrae is fully constrained, and the 11 mm displacement along the z -axis is applied to the upper surface of T_1 to simulate the correction of spine. The connection of clavicle and the manubrium sterni has been taken into account, and the influence of the restraint of the sternum on the deformation of the chest has been also taken into account in the paper. Considering the geometric nonlinearity, we set the appropriate load step, adopt the residual force convergence criterion, set the convergence precision to 0.001.

2.3. Simultaneous Correction of Pectus Excavatum with Scoliosis

2.3.1. Boundary Condition. In this section, the numerical simulation sets two load steps. In the first step, the T_{12} thorax bottom surface displacement is constrained. Tensile displacement along the axial is 8 mm on the upper thorax spine T_1 , which was to simulate the stretching of the spine. Minimally invasive orthopedic correction displacement of pectus excavatum applying on the second sternum is -40 mm of Y direction. In the second load step, the axial displacement of the T_1 segment of the thorax spine was released and the displacement of Y orientation was kept. Because of the large deformation of the ribs in the process of correction, the geometric nonlinearity has been considered. The last step is the option of nonlinear solution, such as step length, step number, calculation time, and calculation results of output frequency, and precision of residual force convergence criterion is set to 0.001.

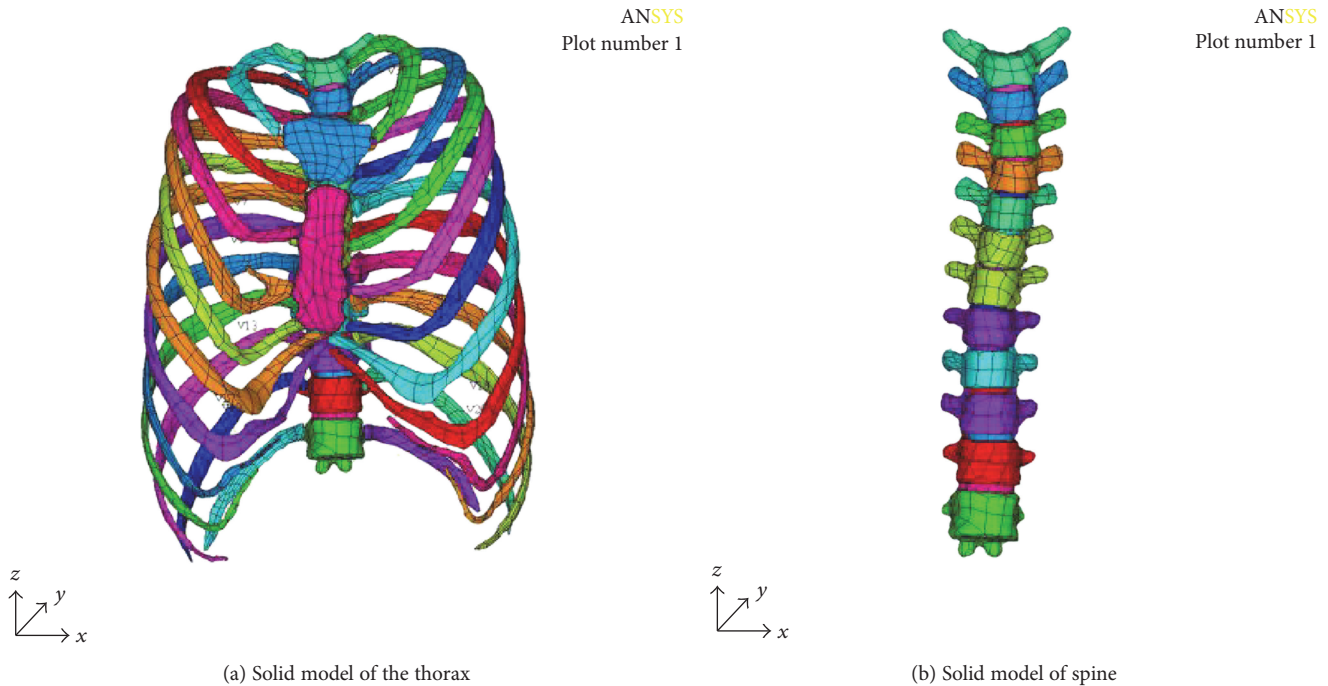


FIGURE 1: 3-D solid model of PE with scoliosis.

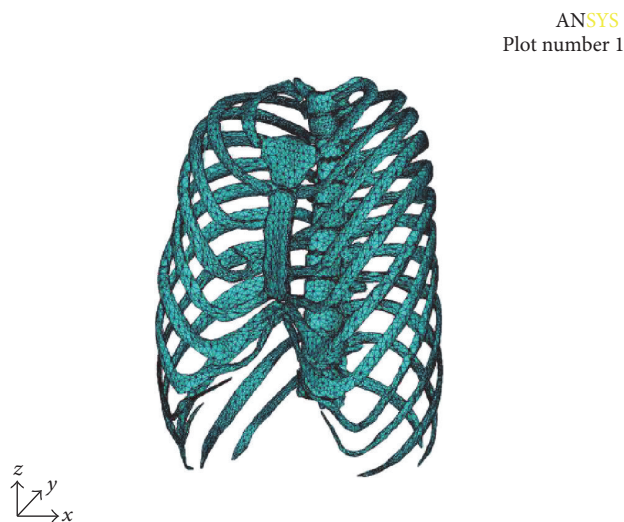


FIGURE 2: Finite element model.

3. Results

3.1. Spine Correction Displacement Analysis. Numerical results of displacement are shown in Figure 3. Figure 3(a) is the spine before correction; it shows that the thoracic vertebra T_3 - T_4 segment bends to the right (X positive direction, coronal plane), thoracic vertebra T_7 - T_9 segment bends to the left (X negative direction, coronal plane). From Figure 3(b), after correction, the maximum displacement of U_x is 3.313 mm in thoracic vertebra T_7 - T_9 , moved to left; the minimum displacement of U_x is -2.487 mm in thoracic vertebra T_3 - T_4 , moved to right. The results show that the spine has been corrected.

3.2. The Analysis of Thorax Displacement. The numerical results of the displacement are shown in Figure 4. It can be seen from Figure 4 (cross section) that the sternum depression is more serious after scoliosis correction, and the maximum value of displacement located on the first rib which is connected to the sternum is 13.879 mm. The displacement of the manubrium sterni is larger than that of sternum. The relationship between the displacement of the sternum and the correction displacement is plotted in Figure 5. Figure 5 shows the spine stretch displacement is less than 2 mm; the displacement of the sternum is smaller; after 2 mm, the subsidence displacement of the sternum increased rapidly; and when the displacement is more than 4 mm, there is a linear relationship between the displacement of the sternum and the spine stretch displacement.

Figure 6 shows the deformation vector of the thorax. It can be seen from Figure 6 that the displacements of the sternum, the first rib, the second rib, and the thoracic vertebra T_1 - T_2 segment are larger than those of others. In the process of stretching the spine, not only the scoliosis of the spine was corrected but also the normal physiological kyphosis of the spine was changed. It can be seen from Figure 3(c) that the displacement of T_1 - T_2 segment of thoracic vertebra is the largest in sagittal plane, and the maximum value is 6.216 mm. The first pair of ribs and the second pair of ribs connect to thoracic vertebra T_1 - T_2 , manubrium sterni, and sternum; the function of the ribs is like a rod, so when the thoracic vertebrae T_1 - T_2 segment move in the sagittal plane, it will drive the displacement of manubrium sterni and sternum and result in a further collapse of the thorax. The numerical results clearly explain the phenomenon of hypotension in patients; it is the correction of scoliosis that effected the breathing and heartbeat [22].

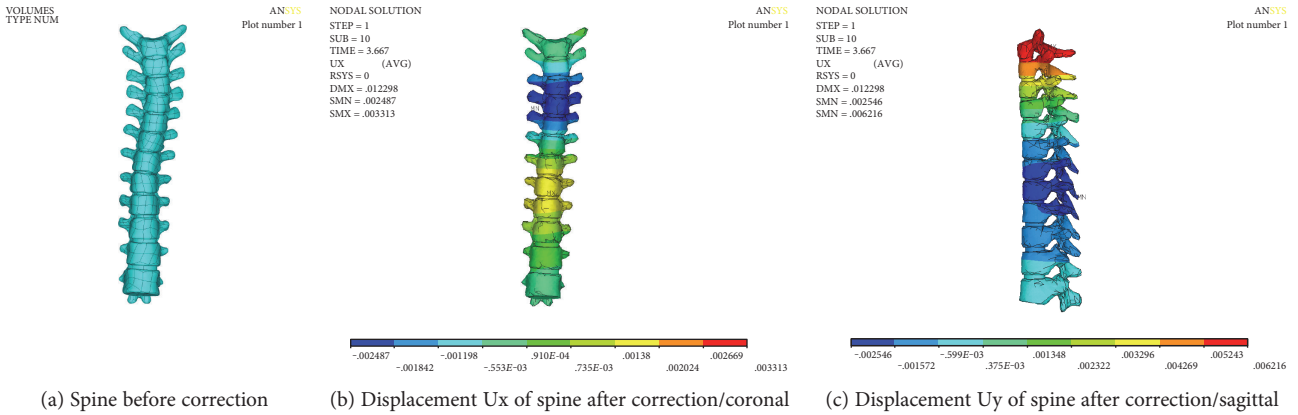


FIGURE 3: Displacement of spine.

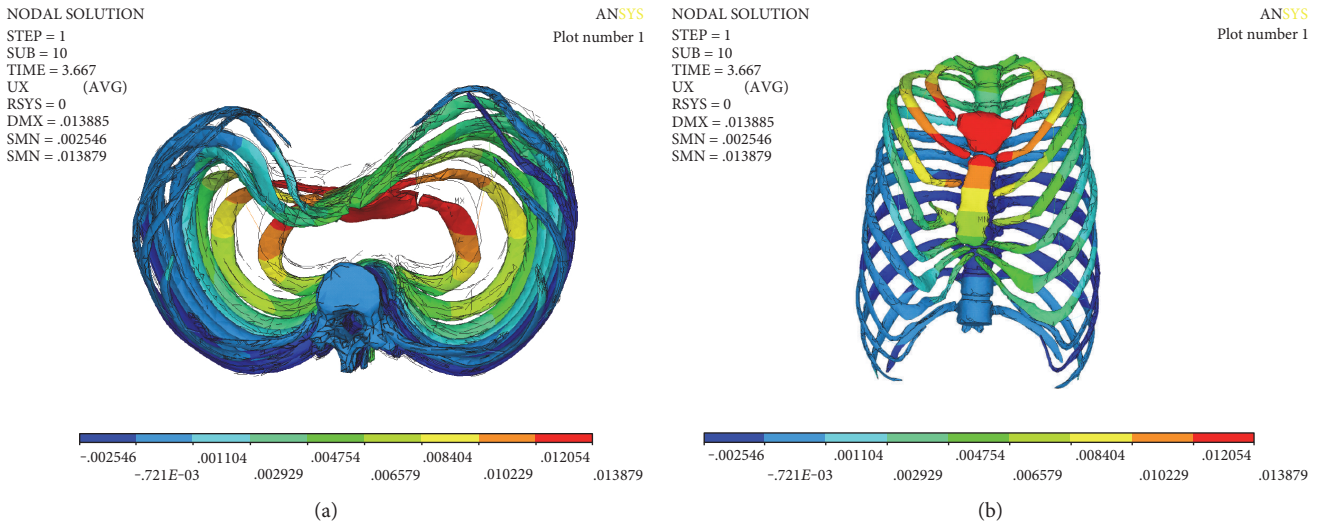


FIGURE 4: Displacement Uy of thorax ((a) cross, (b) coronal).

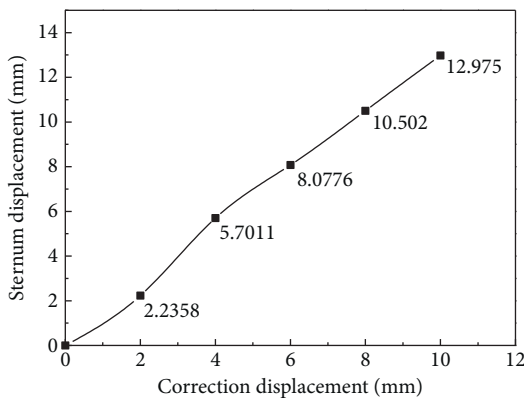


FIGURE 5: Displacement vector of thorax.

The numerical simulation results show that the displacement boundary condition at the connection of the clavicle and the manubrium sterni has a significant influence on the deformation of the thorax. The influence of the boundary

condition both in X direction (coronal plane) and in the axial direction of spine has relatively less influence on the deformation of the chest, but the boundary condition in sagittal plane has a great influence on the deformation of the chest. Once the sagittal displacement of the sternum is completely restrained, the sternum is no longer collapsing to the spine, which is not consistent with the appearance of hypotension in the patients of pectus excavatum with scoliosis treated in the literature [22].

3.3. *Stress Analysis of Correction of Spine.* The Mises stress of the spine is shown in Figure 7. The maximum stress of the spine was 30.2 MPa, which appeared in the thoracic vertebra T₁-T₂ segment. The rest of the stress is smaller. The Mises stress of the intervertebral disc is shown in Figure 8, and the maximum stress of the intervertebral disc is 7.03 MPa.

3.4. *Analysis of Correction Force of Spine.* The numerical results of the correction force are shown in Figure 9; correction force is proportional to correction displacement; with the increase of correction displacement, the correction

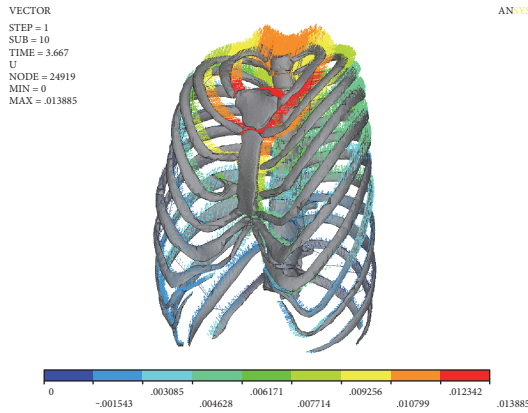


FIGURE 6: Displacement curve of sternum.

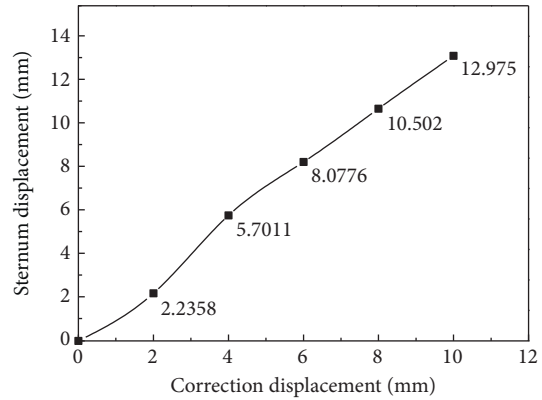


FIGURE 9: Curve of correction force displacement.

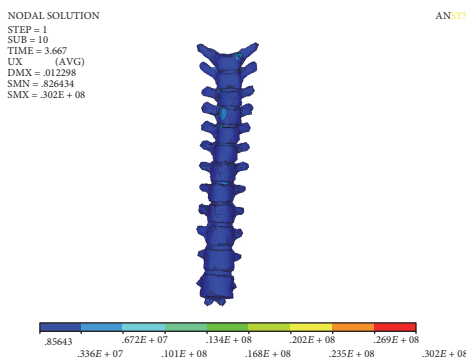


FIGURE 7: Mises stress of spine.

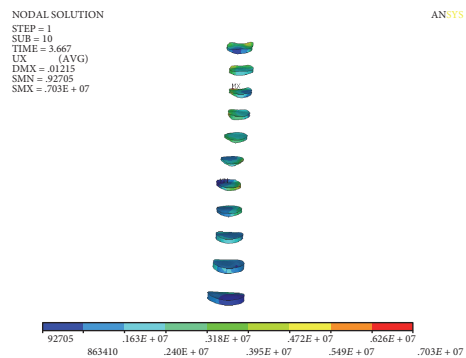


FIGURE 8: Mises stress of intervertebral discs.

force gradually increased. When the correction is completed, the maximum correction force reaches 467.9 N. With the increase of displacement correction, Cobb angle decreases, correction torque arm decreases, and correction torque depends on the correction force and correction arm. When the lateral bending angle decreases, the correction force increases.

3.5. Numerical Simulation Results of Nuss Procedure and Stretch of Spine. The displacement and stress of the thorax can be obtained through numerical simulation of minimally invasive surgery and stretch of spine. Figures 10 and 11 show the displacement of the chest in sagittal and coronal plane. It

can be seen that the sternum (sagittal plane) was raised to 41.953 mm, followed by the upward movement of the ribs. The collapse symptom of pectus excavatum was improved. The maximum value U_x of the displacement on the coronal plane is 2.19 mm, which is located on the T_7 - T_8 segment of the spine. The minimum value is -2.995 mm, which is located on the T_3 - T_4 segment of the spine. The maximum displacement of the spine is 8.176 mm; in the direction of axis of spine, the Cobb angle was significantly decreased. The numerical results have achieved the effect of simultaneous correction of pectus excavatum and scoliosis. The Mises stress is uniform; the maximum Mises stress is located on the sternum and thoracic vertebrae at T_1 - T_4 , and the maximum values were 76.6 MPa and 23.4 MPa, respectively. It may be the main reason of the pain of Nuss procedure and the correction of spine.

The correction force displacement of the numerical calculation is shown in Figure 12. The relation of correction force and the displacement of the correction are basically linear. The correction force is to increase along with the increase of the displacement. When the correction is completed, the maximum correction force reaches 319.52 N. At the beginning of correction, the correction force is small. With the increase of the displacement correction, the symptoms of scoliosis decreased, Cobb angle decreased, and correction force increased.

3.6. Numerical Simulation Results after Releasing of Stretch Correction. The axial displacement of the spine is removed, and only the minimally invasive correction displacement of pectus excavatum is kept. The displacement of the thorax on sagittal plane is shown in Figure 13(a); the numerical result shows that the maximum displacement of correction is -41.48 mm, occurred on the lower piece of the sternums, and the ribs of left four, left five, and left six and right three, right four, right five, and right six are significantly raised. The overall funnel chest symptoms improved significantly. Figure 13(b) shows Mises stress distribution of thorax after correction; we can see that the maximum stress position is on the sternum, which is consistent with the position of correction displacement. The maximum stress is 45.9 MPa.

Figure 13(c) shows the chest vector of displacement; it can be seen that the greater displacement is located on the

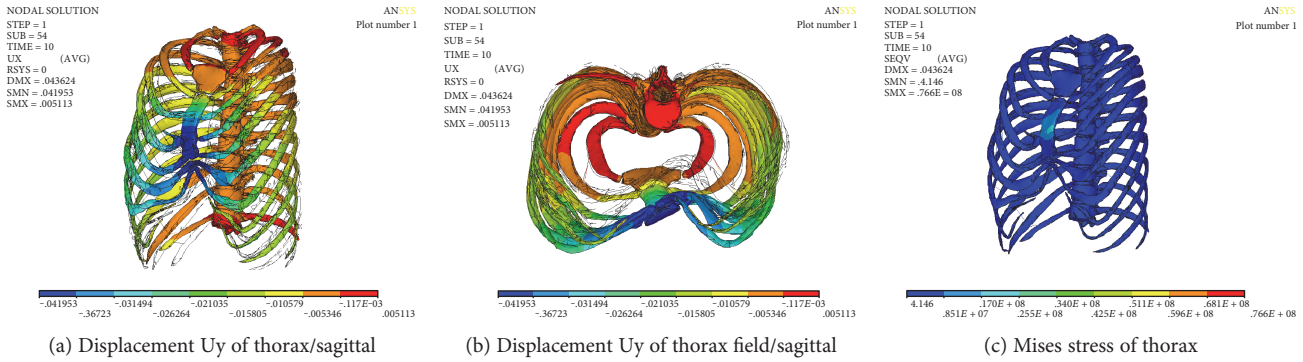


FIGURE 10: Numerical results of simultaneous correction of PE with scoliosis.

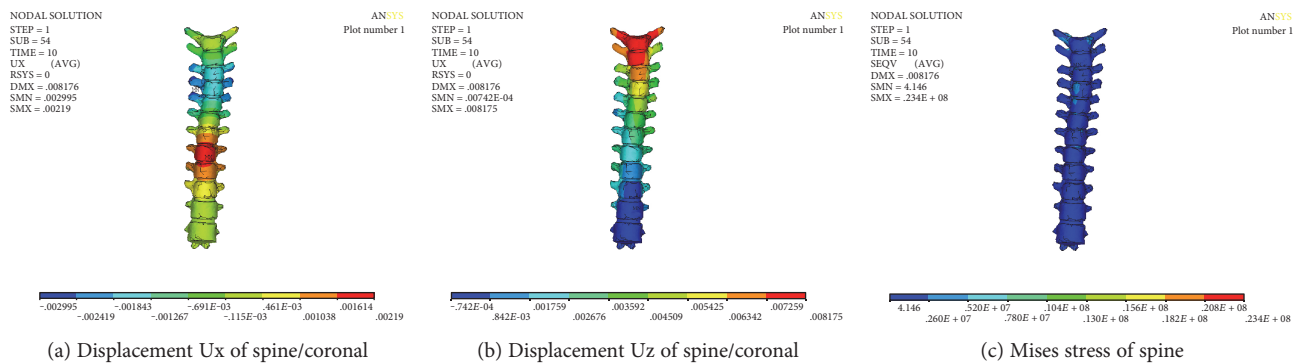


FIGURE 11: Numerical results of spine/simultaneous correction of PE with scoliosis.

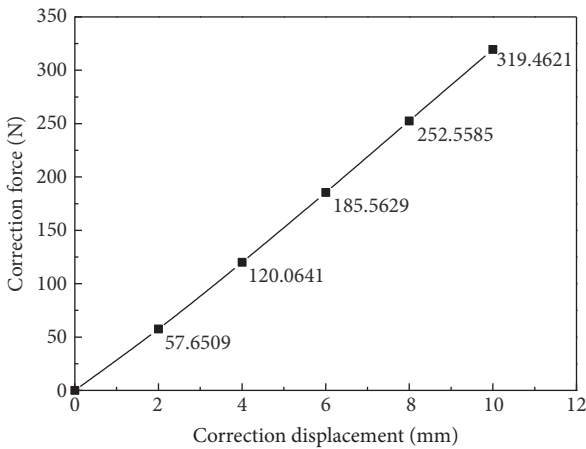


FIGURE 12: Correction force-displacement curve.

sternum. In addition to the correction of the lateral curvature of the spine, it also corrects the normal convex in the process of stretching the spine.

The numerical results of correction and Mises stress of the spine are shown in Figure 14; from the numerical results, it can be seen that T_3 - T_5 section of the thoracic spine on both sides of the transverse moves around 1 mm to the left (X direction), it indicates that the funnel chest and the spinal column side bending simultaneously could help to improve

the scoliosis and that the maximum stress of the spine is 22.6 MPa, which is located in the cross section of the T_1 segment of the thoracic spine. This may be related to the load way of displacement.

As shown in Figure 15, the displacement change of the sternum is gradient. The maximum displacement is located on the sternum. The maximum value is 40.502 mm. The minimum displacement of the upper manubrium sterni is 15.478 mm. The maximum stress of the sternum is 45.9 MPa.

Figure 16 shows the displacement and the Mises stress distribution along the sagittal plane after correction. A more serious collapse occurred on the ribs of left four and left five, and at same time, the ribs of right four and right five were significantly elevated; funnel chest symptom was improved. The maximum stress is 39.5 MPa, which is located on the right side of the rib. It may be the stress concentration caused by the load way of spine correction.

3.7. Comparison of Numerical Results of the Correction of Pectus Excavatum with Scoliosis. As seen from Table 1, there is less difference of the maximum displacements of the sternum except the stretching correction and there is much difference of the minimum displacements of the manubrium sterni. According to the results of removing the displacement of stretch spine, the result of release of the stretch spine is better than that of the Nuss procedure. The results show that simultaneous correction and release of the spine stretch is beneficial to the improvement of pectus excavatum.

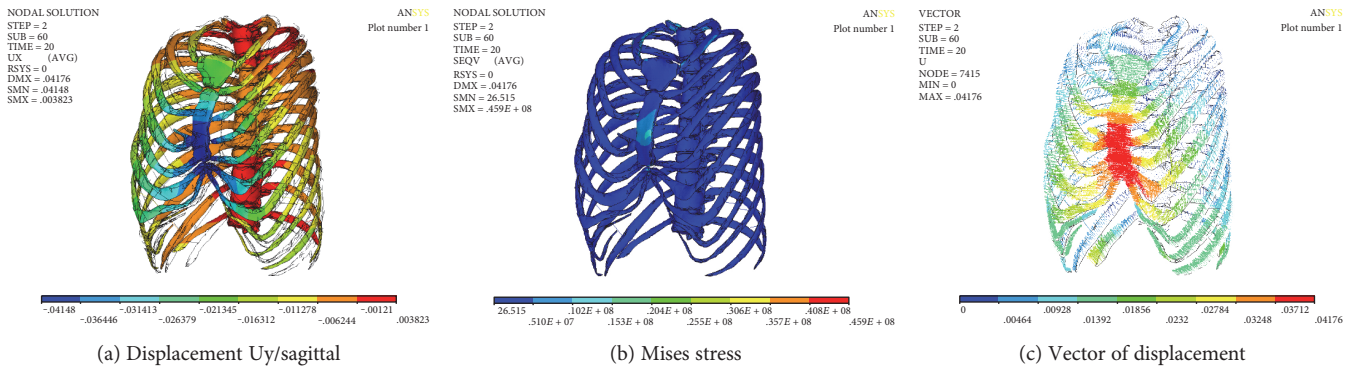


FIGURE 13: Numerical results of the release stretch of spine.

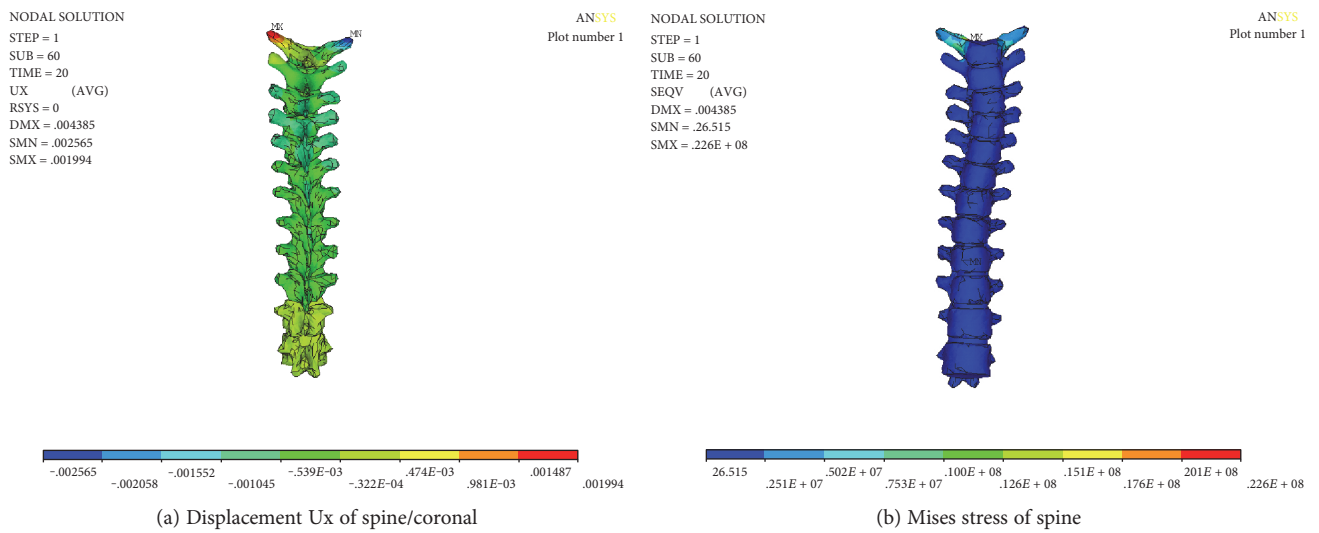


FIGURE 14: Numerical results of spine after stretching and releasing.

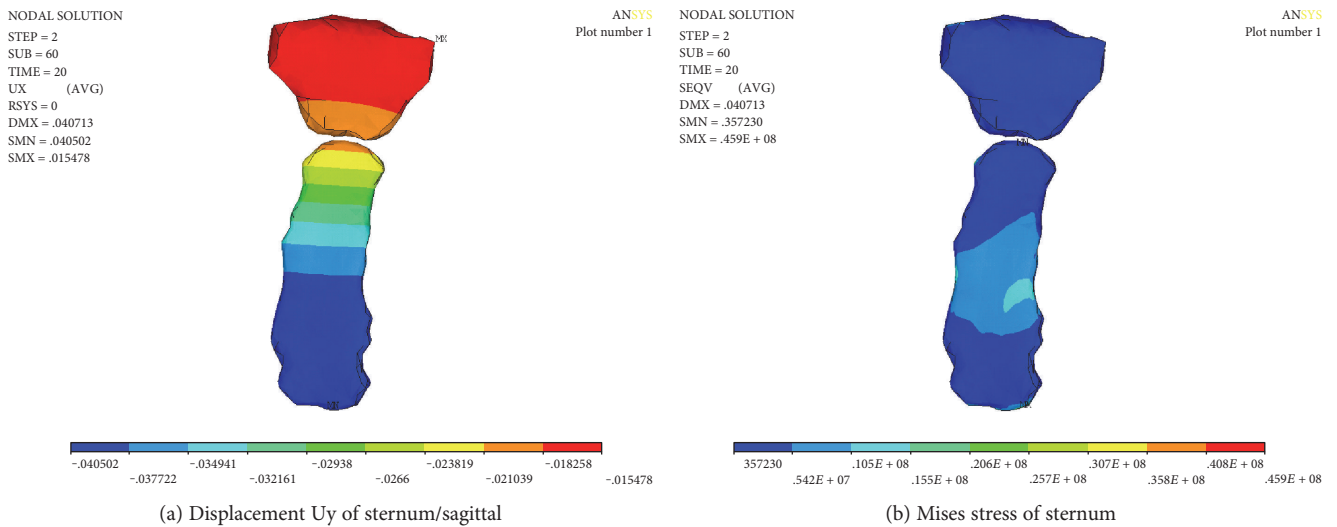


FIGURE 15: Numerical results of sternum after stretching and releasing.

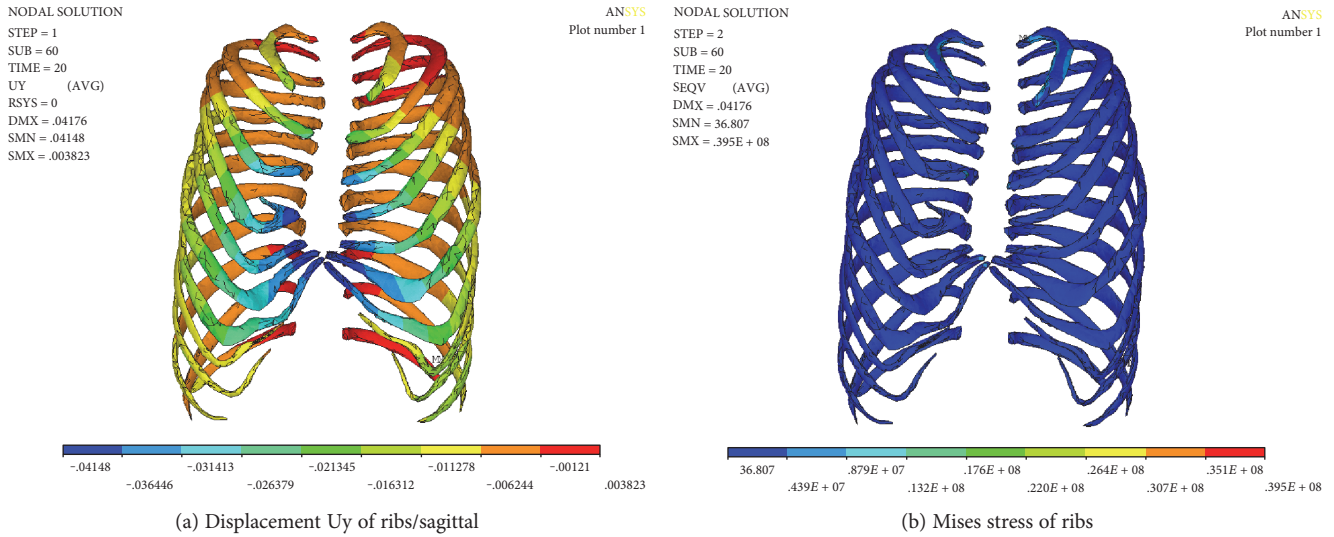


FIGURE 16: Numerical results of ribs after stretching and releasing.

TABLE 1: Comparison of the numerical results.

Method of correction	Maximum displacement/sternum (/mm)	Minimum displacement/manubrium sterni (/mm)	Mises stress of sternum (/MPa)
Simultaneous correction	40.502	15.478	45.9
Released correction of stretch spine	40.743	2.120	70.5
Stretch spine	-25.460	-13.879	30.2
Nuss procedure	40.737	0.210	70.3

Meanwhile, the maximum stress of releasing stretch scoliosis is close to that of the Nuss procedure.

4. Discussion

There are many factors influencing on the deformation of both thorax and spine. In this paper, we investigated the effect of stretching of the spine on the deformation of the chest from the biomechanical point of view. So far, there have been no definite conclusions about the correction order of pectus excavatum and scoliosis. Pectus excavatum patients are often associated with scoliosis symptoms. According to clinical experience, for patients whose chest wall deformity is not serious, the doctor could perform spine correction and then correct pectus excavatum; Huizhong Tian reported a case of right convex of thoracic spine with pectus excavatum for the treatment of first spinal traction and then the pectus excavatum correction in 2005, which achieved a satisfactory result [23]. However, for the patients with serious pectus excavatum and scoliosis, the treatment should first be the Nuss procedures and then scoliosis correction. In 2008, Blane et al. from the University of Michigan first performed a Nuss procedure for a child of pectus excavatum with scoliosis and then corrected the scoliosis [22]. The deformity of thorax in funnel chest with scoliosis is extremely complicated and varied. Many factors such as the location and depth of the funnel

chest and the lateral bending of the spine may affect the correction outcome. The purpose of this paper is to explore a surgical approach to reduce the risk of pain in patients and to improve the symptoms of funnel chest and scoliosis, providing a reference for the design of clinical surgery.

5. Conclusion

- (1) In this paper, numerical simulation method was used to simulate the process of the Nuss procedure and scoliosis-stretching correction simultaneously. It is found that stretch of spine did influence the deformation and stress of the thorax. The numerical results clearly explain the phenomenon of hypotension in patients; it is the correction of scoliosis that effected the breathing and heartbeat.
- (2) Numerical simulation results have shown that correction of both pectus excavatum and scoliosis simultaneously could help to improve of the symptom of both pectus excavatum and scoliosis. At the same time, releasing of stretch displacement after correction of spine could help to raise the sternum and is favorable to the Nuss procedure.
- (3) Comparing different correction method in the paper, it is found that the displacement of manubrium sterni

by releasing stretch of spine was greater than that of the Nuss procedure and the Mises stress of the sternum is close to that of the Nuss procedure. Comparing the results of simultaneous correction, the results of the Nuss procedure, and the results of released correction of stretch spine, it is found that the loading path affects the correction results, which suggests that not only the process of Nuss procedure but also the process of the stretch of spine are nonlinear rather than linear.

Abbreviations

PE:	Pectus excavatum
CT:	Computed tomography
DICOM:	Digital image and communication in medicine
DOF:	Degree of freedom.

Conflicts of Interest

The authors declare that they have no competing interests.

Authors' Contributions

Jin-Duo Ye designed the research, the methodology, and the technical route; Guang-Pu Lu and Jing-Jing Feng conducted numerical simulation; Wei-Hong Zhong analyzed results and wrote the manuscript. All authors read and approved the final manuscript.

Acknowledgments

This study was supported by the National Nature Science Foundation of China [11372221, 11432016]. Jifu Liu, the director of General Hospital of Beijing Command, provided the materials of the patient and finished the Nuss procedure.

References

- [1] M. J. Cartoski, D. Nuss, M. J. Goretsky et al., "Classification of the dysmorphology of pectus excavatum," *Journal of Pediatric Surgery*, vol. 41, no. 9, pp. 1573–1581, 2006.
- [2] D. Schaerer, J. Virbalas, E. Willis, B. Siegal, N. Gonik, and J. Bent, "Pectus excavatum in children with laryngomalacia," *International Journal of Pediatric Otorhinolaryngology*, vol. 77, no. 10, pp. 1721–1723, 2013.
- [3] E. Felts, J. L. Jouve, B. Blondel, F. Launay, F. Lacroix, and G. Bollini, "Child pectus excavatum: correction by minimally invasive surgery," *Orthopaedics & Traumatology Surgery & Research*, vol. 95, no. 3, pp. 190–195, 2009.
- [4] S. L. Frick, "Scoliosis in children with anterior chest wall deformities," *Chest Surgery Clinics of North America*, vol. 10, no. 2, pp. 427–436, 2000.
- [5] D. Nuss, R. E. Kelly Jr, D. P. Croitoru, and M. E. Katz, "A 10-year review of a minimally invasive technique for the correction of pectus excavatum," *Journal of Pediatric Surgery*, vol. 33, no. 4, pp. 545–552, 1998.
- [6] B. Binazzi, G. Innocenti Bruni, F. Gigliotti et al., "Effects of the Nuss procedure on chest wall kinematics in adolescents with pectus excavatum," *Respiratory Physiology & Neurobiology*, vol. 183, no. 2, pp. 122–127, 2012.
- [7] T. Belytschko, R. F. Kulak, A. B. Schultz, and J. O. Galante, "Finite element stress analysis of an intervertebral disc," *Journal of Biomechanics*, vol. 7, no. 3, pp. 277–285, 1974.
- [8] J. Cobb, "Outline for the study of scoliosis," *Instructional Course Lectures*, vol. 5, pp. 261–275, 1947.
- [9] S. L. Weinstein, L. A. Dolan, J. C. Cheng, A. Danielsson, and J. A. Morcuende, "Adolescent idiopathic scoliosis," *Lancet*, vol. 371, no. 9623, p. 1527, 2008.
- [10] S. Negrini, F. Negrini, C. Fusco, and F. Zaina, "Idiopathic scoliosis patients with curves more than 45 Cobb degrees refusing surgery can be effectively treated through bracing with curve improvements," *Spine Journal*, vol. 11, no. 5, pp. 369–380, 2011.
- [11] J. B. Emans, A. Kaelin, P. Bancel, J. E. Hall, and M. E. Miller, "The Boston bracing system for idiopathic scoliosis. Follow-up results in 295 patients," *Spine*, vol. 11, no. 8, pp. 792–801, 1986.
- [12] D. L. Skaggs, "Effectiveness of treatment with a brace in girl who have adolescent idiopathic scoliosis. A prospective, controlled study based on data from the brace study of the Scoliosis Research Society," *Journal of Bone & Joint Surgery American Volume*, vol. 7, no. 1, p. 151, 1996.
- [13] V. Seshadri and S. Mendelson, "Neuromuscular scoliosis: hybrid fixation and iliac screw modification of Luque-Galveston technique," *Operative Techniques in Orthopaedics*, vol. 19, no. 1, pp. 36–43, 2009.
- [14] D. J. Sucato, "Management of severe spinal deformity: scoliosis and kyphosis," *Spine*, vol. 35, no. 25, pp. 2186–2192, 2010.
- [15] R. Nowak, S. Mrozek, and W. Miecznikowski, "The radiometric analysis of the chest and spine deformity following surgical treatment of idiopathic scoliosis by the C-D method," *Ortopedia, Traumatologia, Rehabilitacja*, vol. 4, no. 5, pp. 559–566, 2002.
- [16] E. Nectoux, M. C. Giacomelli, C. Karger, B. Herbaux, and J. M. Clavert, "Complications of the Luque-Galveston scoliosis correction technique in paediatric cerebral palsy," *Orthopaedics & Traumatology Surgery & Research*, vol. 96, no. 4, pp. 354–361, 2010.
- [17] S. Charosky, P. Guigui, A. Blamoutier, P. Roussouly, D. Chopin, and Study Group on Scoliosis, "Complications and risk factors of primary adult scoliosis surgery: a multicenter study of 306 patients," *Spine*, vol. 37, no. 8, p. 693, 2012.
- [18] Y. C. Pei, Z. Y. Hsu, D. P. Chen, J. Y. Lai, and C. J. Wang, "Preliminary analysis of the forces on the thoracic cage of patients with pectus excavatum after the Nuss procedure," *Clinical Biomechanics*, vol. 23, no. 7, pp. 881–885, 2008.
- [19] T. Nagasao, M. Noguchi, and J. Miyamoto, "Dynamic effects of the Nuss procedure on the spine in asymmetric pectus excavatum," *Journal of Thoracic & Cardiovascular Surgery*, vol. 140, no. 6, pp. 1294–1299, 2010.
- [20] J. D. Ye, B. L. Liu, J. F. Liu, C. Y. Zhang, W. Zhong, and C. Zhang, "Research on electrical measurement experiment of deformation of artificial thorax model," *Journal of Mechanics in Medicine and Biology*, vol. 17, no. 3, 2017.
- [21] Z. C. Zhong, S. H. Wei, J. P. Wang, C. K. Feng, C. S. Chen, and C. H. Yu, "Finite element analysis of the lumbar spine with a new cage using a topology optimization method," *Medical Engineering & Physics*, vol. 28, no. 1, pp. 90–98, 2006.

- [22] B. T. Bafus, D. Chiravuri, M. E. Van der Velde, B. I. Chu, R. Hirshl, and F. A. Farley, "Severe hypotension associated with the prone position in a child with scoliosis and pectus excavatum undergoing posterior spinal fusion," *Journal of Spinal Disorders & Techniques*, vol. 21, no. 6, pp. 451-454, 2008.
- [23] H. Z. Tian, "Diagnosis and treatment of scoliosis with pectus excavatum," *Orthopedic Journal of China*, vol. 13, no. 5, pp. 393-394, 2005.

Review Article

Static Progressive Orthoses for Elbow Contracture: A Systematic Review

Bin Chen,¹ Jianhua Lin,¹ Lifen Liu,² and Wenxin Niu²

¹Department of Therapy, Shanghai Yangzhi Rehabilitation Hospital, Tongji University School of Medicine, Shanghai 201619, China

²Tongji University School of Medicine, Shanghai 200092, China

Correspondence should be addressed to Wenxin Niu; niu@tongji.edu.cn

Received 29 April 2017; Revised 7 July 2017; Accepted 3 August 2017; Published 7 September 2017

Academic Editor: Wei Yao

Copyright © 2017 Bin Chen et al. This is an open access article distributed under the Creative Commons Attribution License, which permits unrestricted use, distribution, and reproduction in any medium, provided the original work is properly cited.

Background. As one of the most common musculoskeletal complications following trauma, elbow contracture is a frequent source of disabled daily activities. Conventional interventions are inadequate to provide favorable outcome. The static progressive orthoses are getting popular in the treatment of this problem. **Objective.** The purpose of this review was to assess the effectiveness of static progressive orthoses for elbow contracture. **Methods.** Literatures when written in English published during 1 January 1997 and 31 January 2017 were searched in the following databases: Web of Science, Cochrane Library, PubMed, and EBSCOhost. Articles are quality-assessed by two assessors, each article was summarized in evidence tables, and a narrative synthesis was also performed. **Results.** Ten clinical trials were included. The study design and outcome measures used varied. Significant immediate improvement in the range of motion was reported by all studies, and those effects were still significant at follow-up. No significant difference was shown between static progressive and dynamic orthoses for elbow contracture in one randomized control trial. **Conclusions.** Current low-quality evidence suggested that static progressive orthoses provided assistance for elbow contracture through improving range of motion. Further research is recommended using high-quality randomized controlled trials.

1. Introduction

As one of the most common musculoskeletal complications following trauma, elbow contracture is a frequent source of disabled daily activities [1, 2]. Due to the multitude of etiologies, the incidence of elbow contracture after trauma and surgery which requires surgical treatment is up to 12% [3]. Posttraumatic elbow contracture may result from both intrinsic and extrinsic factors. The intrinsic causes include intra-articular adhesions, articular malalignment, loss of articular cartilage, and a combination of the above, while the extrinsic causes contain capsular and ligamentous contracture, heterotopic ossification, extra-articular malunions, and soft-tissue contractures following burns [4]. Among those factors, capsular and soft-tissue contractures are considered the main causes of elbow contracture [5]. Recent reviews, however, suggested that most of elbow contractures are caused by a combination of both intrinsic and extrinsic factors [4]. More importantly, pain and swelling after trauma or surgery play an essential role in promoting the formation of contracture [2, 6].

The most direct consequence of contracture is the decreased range of motion (ROM). Normally, the range of elbow flexion 100° (30°~100°) and forearm rotation between 50° of pronation and 50° of supination is required for most daily activities, with a loss 50° flexion leading to an 80% loss of functionality [7]. Currently, there are two types of interventions for elbow contracture: operative and nonoperative treatment. The operative treatment involves open or arthroscopic release, arthroplasty, and manipulation under anesthesia [4]. Although these are efficient treatments, surgery and manipulation under anesthesia are complex and tend to cause neurovascular complications as well as recurrence [8]. The nonoperative treatment mainly involves passive or assistant movement, continuous passive movement, serial bracing, and static and dynamic orthoses [9, 10].

However, these interventions still have some limitations, such as time-consuming, therapist reliance, and lack of solid evidence support [11]. Also, the dynamic orthoses tend to cause soft-tissue injury and inflammation under a constant load to the joint, which results in low compliance [9, 12, 13].

Nowadays, static progressive orthoses have been used for the treatment of severe joint contracture after trauma and/or surgery. The underlying mechanism of static progressive orthoses on contracture is based on creep and stress relaxation [14]. As reported previously, it is faster to achieve the elongation with the stress relaxation principle [8, 15, 16].

According to Schultz-Johnson [17], static progressive orthoses have many advantages: (1) adjustable ROM and force, they could be adjusted to the maximum tolerable intensity to avoid pain and to have minimal damage; (2) controllable load, the patient could adjust load according to the subjective feeling; (3) higher tolerance and compliance; (4) mobility, the patient could do active exercise after removing the orthoses easily; and (5) effective, efficient, and economic, it requires less money and time by using static progressive orthoses.

Although many studies have reported that static progressive orthoses significantly improved the disabilities of patients with elbow contracture, there is still no consensus on the effectiveness and the protocols of static progressive orthoses [8, 16, 18]. Therefore, the purpose of this systematic review was to assess the effectiveness of static progressive orthoses on the management of patients with elbow contracture.

2. Methods

2.1. Search Strategy. A comprehensive literature search was conducted in the following bibliographic electronic databases: Web of Science, Cochrane Library, PubMed, and EBS-COhost. Articles were included when written in English, published between the beginning of 1 January 1997 and 31 January 2017. The following key terms and their combinations were used for literature search: static progressive/splint/splinting/brace/bracing/orthosis/orthoses, elbow, and range of motion. Two independent authors retrieved and selected the papers to determine the appropriateness based on the titles and abstracts. Then, full texts of these articles were assessed according to the inclusion and exclusion criteria. Any differences in the results of identification were resolved by consulting the third author.

The inclusion criteria were as follows: (1) subjects are patients with elbow contracture, (2) interventions include a static progressive technique, (3) outcome measure involves ROM, and (4) study design includes a clinical randomized control trial and pre-post intervention design.

The exclusion criteria were as follows: (1) case reports, comments, protocols, and review papers; (2) employment of invalid outcome measures; and (3) no static progressive technique as interventions.

2.2. Data Extraction and Assessment. Two independent reviewers extracted the data from the included studies by using the Population Intervention Comparison Outcome (PICO) method [19]. The data extracted from the studies included study design, sample size, population characteristics, intervention protocols, and outcome measures. Narrative and tabulation were used to conclude the effect of

the static progressive orthoses. The included studies were qualitatively evaluated without attempting data synthesis.

All studies were assessed independently by two reviewers for methodological quality. The methodological index for nonrandomized studies (MINORS) was used to assess the articles without randomized design [20]. This appraisal tool consists of 8 items focused on stated aim, inclusion of patients, collection of data, outcome measure, unbiased assessment, follow-up, drop rate, and calculation of the study size. Each additional item is worth 2 points, for a maximum score of 16. Differences of the score were resolved by consensus between the two reviewers. The individual item scores and quality assessment score for each article are evaluated. Otherwise, level of evidence of the two controlled studies (randomized or nonrandomized controlled study) was used to assess the quality of the articles [21, 22]. The level of evidence ratings focused on patient enrollment, results, control group, study initiation, and outcomes. Higher levels of evidences could be more convincing to clinical practitioners [23].

3. Results

As shown in Figure 1, a total of 353 studies were identified from a comprehensive search. Firstly, the titles were read, and 297 articles were excluded for having no relevance to the primary objective of this review. Among the 56 trials left, 46 were excluded by reading abstracts and/or through full text. The reasons were displayed as follows: 22 studies were not clinical trials, 20 studies were excluded because they did not use the static progressive stretching in the method, and 4 studies were excluded for not treating elbow contracture. Thus, 10 clinical trials were included in this review (Table 1).

Of the ten studies included in this review, only two had controlled trials in the group [21, 22], whereas the remaining eight were of pre-post intervention design [9, 12, 15, 24–28]. The two controlled studies were scored as therapeutic evidence I and III, respectively [21, 22]. The individual item scores and total quality assessment score for the pre-post intervention study are summarized in Table 2. Only one study had a methodological score exceeding 60% [27], suggesting overall low methodological quality. All studies lost quality points for a lack of prospective collection of data. Only four studies explained the main outcome which should be in accordance with the question addressed by the study [12, 15, 27, 28]. Two studies did not report the inclusion and exclusion criteria [24, 28]. Assessors were not blinded in 7 studies [9, 12, 15, 24–26, 28], and four studies lacked appropriate follow-up [15, 24, 26, 27]. Another four studies were attributed to a high risk of bias in terms of high drop rate [9, 25, 26, 28]. Only two articles discussed their results on the basis of statistical significance, treating this equally to clinical relevance [25, 27].

In total, the included studies involved 289 patients (age: 8~77 years old), of which, 153 patients failed to improve by using standard physiotherapy [9, 12, 15, 21, 24, 27], whereas 89 patients received surgical release before static progressive stretching in other third studies [12, 22, 26].

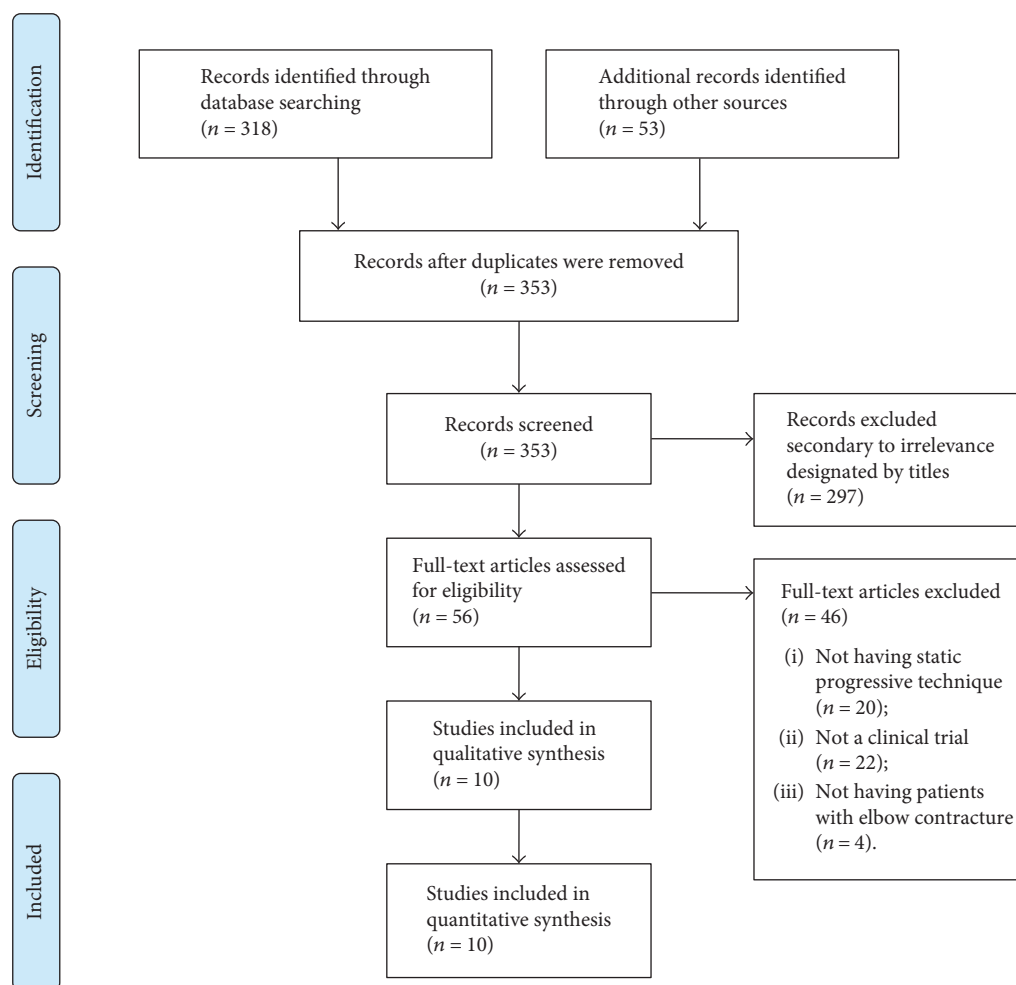


FIGURE 1: Flow chart of literature identification.

Types of device used in the involved studies varied. There were four studies that investigated splint [21, 24, 25, 28] and two studies that examined the effects of orthoses [9, 26]. All other studies used mobilization brace [12], hinged external fixation [22], and Joint Active System [15, 27]. Most devices were custom-made based on the clients' elbow shape [9, 12, 21, 25, 26, 28]. In these studies, various intervention protocols were studied. For instance, some studies performed the treatment 30 mins/time, 3 times/day [15, 21, 25, 27], while the other studies applied the intervention between 6 hours and 20 hours per day [9, 12, 21, 24, 27]. The duration of the treatment was varied between 1 week and 9 months. Most of the patients insisted on the intervention at least 4 weeks [9, 12, 22, 24–27]. Five articles set the intensity to the most discomfort but without pain [9, 15, 24, 26, 27]. In addition, patients in most studies were instructed to do active or assisted active exercise during each session of treatment to maintain the stretching effects [9, 12, 22, 24, 26, 28].

A majority of studies have long-term follow-up after treatment [9, 12, 21, 22, 25, 28]. Significant immediate improvement in the ROM was reported in all studies, and those effects were still significant at follow-up. Two studies examined the satisfaction of interventions with significant results [15, 27]. In addition, two studies found a significant

improvement in the upper limb function following the stretching intervention [21, 28]. The randomized control study found that both static progressive and dynamic orthoses could significantly improve posttraumatic elbow contracture, but the difference between the groups was not significant [21]. A slight increase in elbow motion in the group treated with static progressive orthoses than in the group not treated with static progressive orthoses was showed by another trial [22].

4. Discussion

This systematic review was aimed to appraise the effectiveness of static progressive orthoses on the elbow contracture. Despite the poor quality of included studies, this review suggested that static progressive orthoses could improve ROM for patients with elbow contracture. Although it is impossible to provide guidelines due to the diversity in therapy content and dosage, findings and suggestions are discussed in more detail within this discussion.

In these ten studies included, the subjects were reported to have experienced trauma, such as fracture and elbow dislocation. According to the reports, no study analyzed the outcome basing on the type or severity of the injury which

TABLE 1: Summary of evidence on splint for elbow contracture.

Reference	Study design	Subjects		Intervention	Duration	Evaluation		Results
		Number of subjects	Mean age			Outcome measures	Measurement schedule	
Ring et al. 2005 [22]	Nonrandomized control trial	Rx group: 23; C group: 19	39 (18–71)	Rx: hinged external fixation, active-assisted exercise; C: hinged external fixation (4–8 wks), active-assisted exercise; flexion and extension	Rx and C: 6 wks (4–8 wks)	ROM	Baseline, average of 39 mos	Between groups: ROM improvement with no significant difference ($p > 0.05$)
Parent-Weiss and King 2006 [26]	Pre-post intervention trial	28	41.2 (23–64)	3–4 hs/time, removed 3 times for 1–2 hs each day; point of strong stretching sensation	12–24 wks	ROM (goniometer)	Baseline, end of Rx	Within group: supination and pronation ROM ↑
Doornberg et al. 2006 [25]	Pre-post intervention trial	29	38	Static progressive splinting, flexion and extension	4 mos (1–9 mos)	ROM (goniometer)	Baseline, average of 11 mos	Within group: ROM ↑ ($p < 0.05$)
McGrath et al. 2009 [27]	Pre-post intervention trial	38	44 (20–77)	Static progressive splinting, supination and pronation	12 wks (4–8 wks)	ROM; Likert scale (satisfaction)	Baseline, end of Rx	Within group: supination and pronation ROM ↑, the mean satisfaction score: 8.1 points
Bhat et al. 2010 [9]	Pre-post intervention trial	28	32 (8–68)	Turnbuckle orthosis, multiple directions; exercise	5 mos	ROM (goniometer)	Baseline, end of Rx, average of 29 mos (follow-up)	Within group: flexion and extension group ROM ↑, rotation no effect
Ulrich et al. 2010 [15]	Pre-post intervention trial	37	45	Joint Active Systems (JAS); flexion and extension, when both required, larger deficit first 30 mins, then rest 15–30 mins, the other direction	10 wks (2–23 wks)	ROM (goniometer); 11-point ordinal Likert scale; analgesic use	Baseline, twice a week, until no ROM gains for 2 wks	Within group: ROM in flexion and extension ↑; 94% patients have satisfaction index scores; no patients require medication or an increase in the dosage

TABLE 1: Continued.

Reference	Study design	Subjects Number of subjects	Mean age	Type	Intervention Frequency	Duration	Evaluation Outcome measures	Measurement schedule	Results
Marinelli et al. 2010 [12]	Pre-post intervention trial	42	Group A: ≥ 18	Groups A & B: mobilization brace; self-assisted movement; extension direction; group C: mobilization brace; self-assisted movement; GPM	Group A: night + removed 4 times/day for 1 h for exercise; after 4-6 wks, 4 times/day, 1 h/time + night; group B: same; group C: night + 5 times/day, 1 h/time, alternating flexion and extension	Group A: 3.5 mos; Group B: 3 mos; group C: 2 mos	ROM (goniometer)	Baseline, at least 6 mo follow-up	Within group: 3 groups ROM \uparrow
R. Suksathien and Y. Suksathien 2010 [24]	Pre-post intervention trial	3	17	Splint + motion exercise; extension direction	20 hs/day + night + every 1-2 hs was taken off for exercise daytime; adjust to the point of discomfort, but no pain	14 wks (11-20 wks)	ROM (goniometer)	Baseline, 14 wks (end of Rx)	Within group: ROM \uparrow
Liu et al. 2011 [28]	Pre-post intervention trial	14	41 (16-77)	Custom-made progressive stretching, flexion and extension; ROM exercise		7 days	ROM (goniometer); Mayo Elbow Performance score (MEPS)	Baseline, average of 14 mos (follow-up)	Within group: flexion and extension ROM \uparrow ; mean MEPS score 92
Lindenhovius et al. 2012 [21]	Randomized control trial	Rx group: 35; C group: 31	≥ 18	Rx: static progressive splint; C: dynamic splint, multiple directions	3 times/day and 30 mins/time; 6-8 hs/day or night	Until no gains in AROM achieved in a thirty-day period	ROM (goniometer); Disabilities of the Arm, Shoulder and Hand (DASH)	Baseline, 3 mos, 6 mos, 9 mos, 12 mos; baseline, 6 mos, 9 mos, 12 mos	Both ROM and DASH \uparrow ; between groups: ROM at baseline, 3, 6, and 9 mos has no significant difference ($p > 0.05$); DASH at baseline and 12 mos has no significant difference ($p > 0.05$)

Rx: treatment; C: control; h(s): hour(s); wk(s): week(s); mo(s): month(s); BEO: before elbow orthosis treatment; DEO: during elbow orthosis treatment.

TABLE 2: Methodological quality ratings for each article.

Reference	Parent-Weiss and King 2006 [26]	Doornberg et al. 2006 [25]	McGrath et al. 2009 [27]	Bhat et al. 2010 [9]	Ulrich et al. 2010 [15]	Marinelli et al. 2010 [12]	R. Suksathien and Y. Suksathien 2010 [24]	Liu et al. 2011 [28]
A clearly stated aim	2	2	2	2	2	2	2	2
Inclusion of consecutive patients	2	2	2	2	2	2	0	0
Prospective collection of data	0	0	0	0	0	0	0	0
Endpoints appropriate to the aim of the study	0	0	2	0	2	1	0	2
Unbiased assessment of the study endpoint	0	0	2	0	0	0	0	0
Follow-up period appropriate to the aim of the study	0	2	0	2	0	2	0	2
Loss to follow-up less than 5%	0	0	2	0	2	2	2	0
Prospective calculation of the study size	0	2	2	0	0	0	0	0
Total score	4	8	12	6	8	9	4	6

MINORS (methodological index for nonrandomized studies) for 8 pre-post intervention design studies. The items are scored 0 (not reported), 1 (reported but inadequate), or 2 (reported and adequate).

could play a determinant role in the recovery process. If the injury occurred in the joint leading to the collapse of the joint surface, the prognosis could be limited when compared with that taking place in the ligament. A literature review concluded that orthoses could not provide an increase in joint motion due to intrinsic factors [29]. However, patients who had significant intrinsic factors did also have some degree of extrinsic factors that might respond to static progressive orthoses. This may suggest the demand of subgroup analysis to examine the specific effect on the dysfunction in different injured populations.

It is also noticed that the onset of the intervention varies among those studies. A few studies selected patients right after surgical treatment while other studies recruit patients who failed the 4-week to 11-week standard physiotherapy or had undergone elbow contracture between 52 days and 16.7 months. Although positive improvements have been reported in all these studies, for the studies that perform early intervention after surgery, the contribution of static progress orthoses to the improvement could be questionable as it is difficult to exclude the effects of other concurrent treatment.

As demonstrated in Table 1, the intervention protocols adopted in terms of the frequency, intensity, and duration of static progressive orthoses are discrepant among these studies. The treatment protocols were determined according to a physiotherapist's clinical experience or a manufacturers' suggestions, but the evidence was determined from the clinical study of high quality. Due to the discrepancy in intervention protocols, it is unable to synthesize the data to evaluate its effects on the elbow contracture. Muller et al. [8] suggested that the treatment should be 30 mins/time, about 3 times/day in each direction in consideration of the

patient's compliance. Since there is no rigid randomized clinical trial to confirm this suggestion, its reasonableness remains unclear. However, a recent study found that higher stretch intensity or duration might be necessary to achieve better outcomes based on the creep and stress relaxation properties of the soft tissue [30].

All the studies included in this review used the ROM as the outcome measure, while two studies also employed functional scales and three studies assess the satisfaction with the treatment. It is well known that the clinical outcome should not only limit to impairment level as the importance of functional, psychosocial, and environmental aspects has been recognized in the International Classification of Functioning, Disability and Health (ICF) model. From current research, Disabilities of the Arm, Shoulder and Hand (DASH), American Shoulder and Elbow Surgeons evaluation (ASES-e), and Patient-Rated Elbow Evaluation (PREE) could enhance the ability of clinical practitioners and researchers to evaluate the patients with elbow pathology [31]. In order to comprehensively explore the effects of static progressive orthoses, these instruments meeting reliability and validity criteria should be recommended.

Out of the ten studies, five studies did long-term follow-up ranging from 6 months to 29 months and found that all the positive improvement remained at the follow-up [9, 12, 21, 25, 28]. It is interesting to notice that the duration of follow-up covers such a long time range. It is generally known that self-exercise could maintain the elbow function in the follow-up as ROM improves [29]. Compared to the long-term follow-up, it may be more valuable to investigate the short-term effect as the change of the length and flexibility of soft tissue will not take a

long period if the patients kept doing appropriate range of motion exercise. Instead, the short-term measurement could reveal a more detailed time and range relationship of the elbow contracture which could provide a useful reference to optimize the treatment protocol.

Adverse events were mentioned in five studies [9, 12, 22, 26, 28]. The following complications are defined as adverse events in those studies: skin allergic reactions, scar breakdown, and nerve irritation. Only a few patients reported one of these complications during the treatment, but clinicians need to be aware of the risk of those complications and the measures to prevent or to deal with them when happened.

Another important finding was that all included articles were conducted between 2005 and 2012. It is somewhat surprising that no studies on static progressive orthoses for elbow contracture are performed in recent years. In contrast to our findings, however, a few studies confirmed the effectiveness of static progressive orthoses for shoulder and metacarpophalangeal joint contracture recently [14, 32]. This result may be explained by the fact that the effectiveness of static progressive orthoses for elbow contracture is generally confirmed.

Several methodological weaknesses may affect the strength of the evidence of these studies. Firstly, eight studies used pre-post intervention design without control groups, making it difficult to discriminate the real effect from the natural recovery or other factors. Secondly, in most of the studies, measurements were not conducted by independent assessors. Thirdly, the sample sizes of most of the studies in this review were not generally performed which could confound the efficacy of the program. As the drop rates were generally high, the clinical relevance of the effects often seems relatively small. Furthermore, there is a lack of a standardized treatment protocol of static progressive stretching, and it is impossible to synthesize the data for analysis.

This systematic review has the following strengths. Several databases were searched, and articles were selected independently. The methodological quality of the included pre- post intervention studies was assessed using the MINORS. It is considered that this article gives relevant additional information. More high-quality randomized control trials are required to increase the strength of evidence. The sample size should be calculated scientifically, and detailed intervention protocols are required for future studies. Future studies are also recommended to conduct a comprehensive outcome measurement with reasonable long-term follow-up to examine the effects of the static progressive orthoses for elbow contracture.

Finally, some factors may affect the outcomes of this review: (1) As the search strategy is limited to articles published in English, some studies may have been missed and (2) a meta-analysis is not appropriate due to study heterogeneity and low study quality.

5. Conclusion

To the author's knowledge, this is the first systematic review to consider the methodological quality for static progressive

orthoses. Current low-quality evidence suggests that static progressive orthoses provided assistance for elbow contracture through improving ROM. Further research is recommended to examine the effectiveness of this treatment using high-quality randomized controlled trials.

Conflicts of Interest

The authors declare that they have no conflicts of interest.

Authors' Contributions

Bin Chen and Jianhua Lin contributed equally to this work.

References

- [1] P. S. Issack and K. A. Egol, "Posttraumatic contracture of the elbow: current management issues," *Bulletin/Hospital for Joint Diseases*, vol. 63, no. 3-4, pp. 129-136, 2006.
- [2] R. J. Bruno, M. L. Lee, R. J. Strauch, and M. P. Rosenwasser, "Posttraumatic elbow stiffness: evaluation and management," *The Journal of the American Academy of Orthopaedic Surgeons*, vol. 10, no. 2, pp. 106-116, 2002.
- [3] C. Myden and K. Hildebrand, "Elbow joint contracture after traumatic injury," *Journal of Shoulder and Elbow Surgery*, vol. 20, no. 1, pp. 39-44, 2011.
- [4] C. P. Charalambous and B. F. Morrey, "Posttraumatic elbow stiffness," *The Journal of Bone and Joint Surgery*, vol. 94, no. 15, pp. 1428-1437, 2012.
- [5] G. Trudel and H. K. Uthoff, "Contractures secondary to immobility: is the restriction articular or muscular? An experimental longitudinal study in the rat knee," *Archives of Physical Medicine and Rehabilitation*, vol. 81, no. 1, pp. 6-13, 2000.
- [6] J. B. Jupiter, S. W. O'Driscoll, and M. S. Cohen, "The assessment and management of the stiff elbow," *Instructional Course Lectures*, vol. 52, pp. 93-111, 2003.
- [7] M. A. Schruppf, S. Lyman, H. Do et al., "Incidence of postoperative elbow contracture release in New York State," *The Journal of Hand Surgery*, vol. 38, no. 9, pp. 1746-1752, 2013.
- [8] A. M. Muller, P. Sadoghi, R. Lucas et al., "Effectiveness of bracing in the treatment of nonosseous restriction of elbow mobility: a systematic review and meta-analysis of 13 studies," *Journal of Shoulder and Elbow Surgery*, vol. 22, no. 8, pp. 1146-1152, 2013.
- [9] A. K. Bhat, K. Bhaskaranand, and S. G. Nair, "Static progressive stretching using a turnbuckle orthosis for elbow stiffness: a prospective study," *Journal of Orthopaedic Surgery (Hong Kong)*, vol. 18, no. 1, pp. 76-79, 2010.
- [10] A. L. Lindenhovius and J. B. Jupiter, "The posttraumatic stiff elbow: a review of the literature," *The Journal of Hand Surgery*, vol. 32, no. 10, pp. 1605-1623, 2007.
- [11] S. L. Michlovitz, B. A. Harris, and M. P. Watkins, "Therapy interventions for improving joint range of motion: a systematic review," *Journal of Hand Therapy*, vol. 17, no. 2, pp. 118-131, 2004.
- [12] A. Marinelli, G. Bettelli, E. Guerra, M. Nigrisoli, and R. Rotini, "Mobilization brace in post-traumatic elbow stiffness," *Musculoskeletal Surgery*, vol. 94, Supplement 1, pp. S37-S45, 2010.
- [13] J. Nakayama, M. Horiki, K. Denno, K. Ogawa, H. Oka, and K. Domen, "Pneumatic-type dynamic traction and flexion splint

- for treating patients with extension contracture of the metacarpophalangeal joint,” *Prosthetics Orthotics International*, vol. 40, no. 1, pp. 142–146, 2016.
- [14] M. Ibrahim, R. Donatelli, M. Hellman, and J. Echternach, “Efficacy of a static progressive stretch device as an adjunct to physical therapy in treating adhesive capsulitis of the shoulder: a prospective, randomised study,” *Physiotherapy*, vol. 100, no. 3, pp. 228–234, 2014.
- [15] S. D. Ulrich, P. M. Bounutti, T. M. Seyler, D. R. Marker, B. F. Morrey, and M. A. Mont, “Restoring range of motion via stress relaxation and static progressive stretch in posttraumatic elbow contractures,” *Journal of Shoulder and Elbow Surgery*, vol. 19, no. 2, pp. 196–201, 2010.
- [16] D. A. Schwartz, “Static progressive orthoses for the upper extremity: a comprehensive literature review,” *Hand (N Y)*, vol. 7, no. 1, pp. 10–17, 2012.
- [17] K. Schultz-Johnson, “Static progressive splinting,” *Journal of Hand Therapy*, vol. 15, no. 2, pp. 163–178, 2002.
- [18] J. M. Hijmans, K. Postema, and J. H. Geertzen, “Elbow orthoses: a review of literature,” *Prosthetics Orthotics International*, vol. 28, no. 3, pp. 263–272, 2004.
- [19] A. Sayers, “Tips and tricks in performing a systematic review,” *The British Journal of General Practice*, vol. 57, no. 545, p. 999, 2007.
- [20] K. Slim, E. Nini, D. Forestier, F. Kwiatkowski, Y. Panis, and J. Chipponi, “Methodological index for non-randomized studies (minors): development and validation of a new instrument,” *ANZ Journal of Surgery*, vol. 73, no. 9, pp. 712–716, 2003.
- [21] A. L. Lindenhovius, J. N. Doornberg, K. M. Brouwer, J. B. Jupiter, C. S. Mudgal, and D. Ring, “A prospective randomized controlled trial of dynamic versus static progressive elbow splinting for posttraumatic elbow stiffness,” *The Journal of Bone and Joint Surgery*, vol. 94, no. 8, pp. 694–700, 2012.
- [22] D. Ring, R. N. Hotchkiss, D. Guss, and J. B. Jupiter, “Hinged elbow external fixation for severe elbow contracture,” *The Journal of Bone and Joint Surgery*, vol. 87, no. 6, pp. 1293–1296, 2005.
- [23] J. G. Wright, M. F. Swiontkowski, and J. D. Heckman, “Introducing levels of evidence to the journal,” *The Journal of Bone and Joint Surgery*, vol. 85, no. 1, pp. 1–3, 2003.
- [24] R. Suksathien and Y. Suksathien, “A new static progressive splint for treatment of knee and elbow flexion contractures,” *Journal of Medicine Association of Thailand*, vol. 93, no. 7, pp. 799–804, 2010.
- [25] J. N. Doornberg, D. Ring, and J. B. Jupiter, “Static progressive splinting for posttraumatic elbow stiffness,” *Journal of Orthopaedic Trauma*, vol. 20, no. 6, pp. 400–404, 2006.
- [26] N. M. Parent-Weiss and J. C. King, “Static progressive forearm rotation contracture management orthosis design: a study of 28 patients,” *Journal of Prosthetics and Orthotics*, vol. 18, no. 3, pp. 63–67, 2006.
- [27] M. S. McGrath, S. D. Ulrich, P. M. Bonutti, D. R. Marker, H. R. Johanssen, and M. A. Mont, “Static progressive splinting for restoration of rotational motion of the forearm,” *Journal of Hand Therapy*, vol. 22, no. 1, pp. 3–9, 2009.
- [28] H. H. Liu, K. Wu, and C. H. Chang, “Treatment of complex elbow injuries with a postoperative custom-made progressive stretching static elbow splint,” *The Journal of Trauma*, vol. 70, no. 5, pp. 1268–1272, 2011.
- [29] S. A. Dávila and K. Johnston-Jones, “Managing the stiff elbow: operative, nonoperative, and postoperative techniques,” *Journal of Hand Therapy*, vol. 19, no. 2, pp. 268–281, 2006.
- [30] G. H. Peixoto, A. G. Andrade, H. J. Menzel, S. R. Araújo, A. E. Pertence, and M. H. Chagas, “Viscoelastic stress relaxation in the hamstrings before and after a 10-week stretching program,” *Muscle & Nerve*, vol. 51, no. 5, pp. 761–764, 2015.
- [31] J. C. MacDermid, “Outcome evaluation in patients with elbow pathology: issues in instrument development and evaluation,” *Journal of Hand Therapy*, vol. 14, no. 2, pp. 105–114, 2001.
- [32] J. Wang, G. Erlandsson, Y. J. Rui, and C. Li-Tsang, “Efficacy of static progressive splinting in the management of metacarpophalangeal joint stiffness: a pilot clinical trial,” *Hong Kong Journal of Occupational Therapy*, vol. 24, no. 2, pp. 45–50, 2014.

Research Article

The Effects of Physiological Biomechanical Loading on Intradiscal Pressure and Annulus Stress in Lumbar Spine: A Finite Element Analysis

Siti Nurfaezah Zahari,¹ Mohd Juzaila Abd Latif,^{1,2} Nor Raihanah Abdull Rahim,³ Mohammed Rafiq Abdul Kadir,³ and Tunku Kamarul⁴

¹Faculty of Mechanical Engineering, Universiti Teknikal Malaysia Melaka, Hang Tuah Jaya, 76100 Durian Tunggal, Melaka, Malaysia

²Center for Robotics and Industrial Automation (CeRIA), Universiti Teknikal Malaysia Melaka, Hang Tuah Jaya, 76100 Durian Tunggal, Melaka, Malaysia

³Medical Devices and Technology Group, Faculty of Biosciences and Medical Engineering, Universiti Teknologi Malaysia, 81310 Skudai, Johor, Malaysia

⁴Tissue Engineering Group (TEG), National Orthopaedic Centre of Excellence in Research and Learning (NOCERAL), Department of Orthopaedic Surgery, Faculty of Medicine, University of Malaya, Lembah Pantai, 50603 Kuala Lumpur, Malaysia

Correspondence should be addressed to Mohd Juzaila Abd Latif; juzaila@utem.edu.my

Received 5 May 2017; Revised 10 July 2017; Accepted 24 July 2017; Published 27 August 2017

Academic Editor: Lizhen Wang

Copyright © 2017 Siti Nurfaezah Zahari et al. This is an open access article distributed under the Creative Commons Attribution License, which permits unrestricted use, distribution, and reproduction in any medium, provided the original work is properly cited.

The present study was conducted to examine the effects of body weight on intradiscal pressure (IDP) and annulus stress of intervertebral discs at lumbar spine. Three-dimensional finite element model of osseoligamentous lumbar spine was developed subjected to follower load of 500 N, 800 N, and 1200 N which represent the loads for individuals who are normal and overweight with the pure moments at 7.5 Nm in flexion and extension motions. It was observed that the maximum IDP was 1.26 MPa at L1-L2 vertebral segment. However, the highest increment of IDP was found at L4-L5 segment where the IDP was increased to 30% in flexion and it was more severe at extension motion reaching to 80%. Furthermore, the maximum annulus stress also occurred at the L1-L2 segment with 3.9 MPa in extension motion. However, the highest increment was also found at L4-L5 where the annulus stress increased to 17% in extension motion. Based on these results, the increase of physiological loading could be an important factor to the increment of intradiscal pressure and annulus fibrosis stress at all intervertebral discs at the lumbar spine which may lead to early intervertebral disc damage.

1. Introduction

Obesity has been recognised as a factor that could lead to chronic low back pain (LBP). This problem is expected to further escalate in the near future with the current increasing numbers of overweight and obese population [1, 2]. It was demonstrated that the increase of body weight will increase the stress at the lumbar spine which leads to potential factor of intervertebral disc (IVD) degeneration [3–6]. Furthermore, excessive loading applied on the lumbar spine tends

to fracture the vertebral body endplate before damaging the IVD [7].

In computational studies, follower load applied to the lumbar spine could increase intradiscal pressure (IDP), intersegmental rotation and facet joint force [8, 9]. The compressive load on the spine reduces the disc height due to the decrease of the volume of mass gelatinous in nucleus pulposus. As the fluid is being squeeze out from the disc, the tissue will reorganize which caused the viscoelastic annulus collagen fibers to creep [10, 11]. Consequently, this increases the hydrostatic

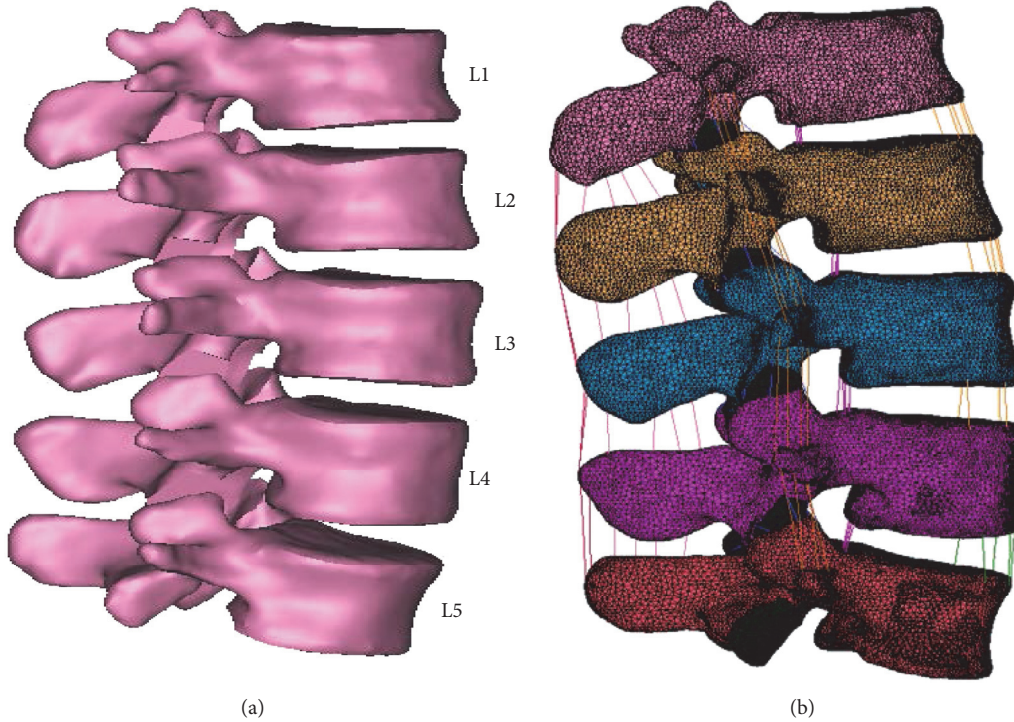


FIGURE 1: L1–L5 lumbar spine. (a) Three-dimensional model and (b) finite element model.

pressure and the outer annulus starts to bulge. Although these phenomena have been described in many computational and clinical studies, the fundamental understanding that underpins the biomechanics leading to disc damage has yet to be explored. Furthermore, the relationship between the increase in body weight to the stresses occurs at various vertebral segments of the lumbar spine when the body in different posture needs to be elucidated.

In the present study, the effects of physiological loading on the lumbar spine were studied at all vertebral segments to examine the IVD during flexion and extension motions using finite element method. The IDP at nucleus pulposus and the von Mises stress (VMS) at annulus fibrosis of the IVD were investigated.

2. Materials and Methods

2.1. Finite Element Modeling. The geometrical data of lumbar vertebrae were obtained from computed tomography (CT) scan of a healthy 21-year-old male with 1.73 m height and 70 kg weight. The CT scan images of 3 mm slice thickness in two-dimensional (2D) Standard Tessellation Language (STL) format were segmented to develop a three-dimensional (3D) model of human lumbar spine using Mimics 14.0 (Materialise, Leuven, Belgium) and Magics (Materialise, Leuven, Belgium) softwares as shown in Figure 1(a). Marc Mentat 2011 (MSC, Software, Santa Ana, CA) finite element (FE) software was then used to generate the FE model using linear first-order tetrahedral elements as shown in Figure 1(b).

TABLE 1: Geometrical parameters of the lumbar spine ligaments [15, 18].

Ligaments	Cross-sectional area (mm ²)
Posterior longitudinal ligament (PLL)	20.0
Anterior longitudinal ligament (ALL)	63.7
Ligamentum flavum (LF)	40.0
Capsular ligament (CL)	30.0
Intertransverse ligament (ITL)	1.8
Interspinous ligament (ISL)	40.0
Supraspinous ligament (SSL)	30.0

The vertebra was divided into hard cortical bone on the outside and less dense cancellous bone inside where linear isotropic material properties were imposed for both cortical and cancellous bones [12]. The thickness of cortical was set at 1 mm [13].

The 3D model of the IVD was created manually using SolidWorks (Dassault Systèmes SolidWorks Corporation) software where the volumetric ratio between the annulus and nucleus was set to 3:7 [14]. The top and the bottom surfaces of the disc were constructed such that the surfaces were in contact with the corresponding adjacent surfaces of the vertebral body using Mimics software. The IVD was composed of nucleus pulposus and annulus fibrosis which was modelled as hyperelastic using Mooney-Rivlin formulation [15, 16]. The annulus was constructed to be composite of a homogenous ground substance reinforced by collagen fibers. The fibers were represented by 3D truss element with

TABLE 2: Material properties of the components in the osseoligamentous lumbar spine model.

Element set	Element type	Material properties	Reference
Cortical bone	3D tetrahedron	$E = 12,000 \text{ MPa}$, $\nu = 0.3$	[16]
Cancellous bone	3D tetrahedron	$E = 100 \text{ MPa}$, $\nu = 0.2$	[16]
Articular cartilage	3D Herman formulation, lower order tetrahedron	$E = 35 \text{ MPa}$, $\nu = 0.4$	[15]
Nucleus pulposus	3D Herman formulation, lower order tetrahedron	Mooney-Rivlin: $C_1 = 0.12$, $C_2 = 0.03$	[12]
Annulus fibrosis	3D Herman formulation, lower order tetrahedron	Mooney-Rivlin: $C_1 = 0.18$, $C_2 = 0.045$	[12, 16]
PLL	3D truss	$E = 10.0 \text{ MPa}$ ($\epsilon < 11\%$), $E = 20 \text{ MPa}$ ($\epsilon > 11\%$)	[15, 18]
ALL	3D truss	$E = 7.8 \text{ MPa}$ ($\epsilon < 12\%$), $E = 20 \text{ MPa}$ ($\epsilon > 12\%$)	[15, 18]
LF	3D truss	$E = 15.0 \text{ MPa}$ ($\epsilon < 6.2\%$), $E = 19.5 \text{ MPa}$ ($\epsilon > 6.2\%$)	[15, 18]
CL	3D truss	$E = 7.5 \text{ MPa}$ ($\epsilon < 25\%$), $E = 32.9 \text{ MPa}$ ($\epsilon > 25\%$)	[15, 18]
ITL	3D truss	$E = 10.0 \text{ MPa}$ ($\epsilon < 18\%$), $E = 58.7 \text{ MPa}$ ($\epsilon > 18\%$)	[15, 18]
ISL	3D truss	$E = 10.0 \text{ MPa}$ ($\epsilon < 14\%$), $E = 11.6 \text{ MPa}$ ($\epsilon > 14\%$)	[15, 18]
SSL	3D truss	$E = 8.0 \text{ MPa}$ ($\epsilon < 20\%$), $E = 15.0 \text{ MPa}$ ($\epsilon > 20\%$)	[15, 18]

E : Young's modulus; ν : Poisson's ratio; ϵ : strain; C_1 and C_2 : material constant characterising the deviatoric deformation of material.

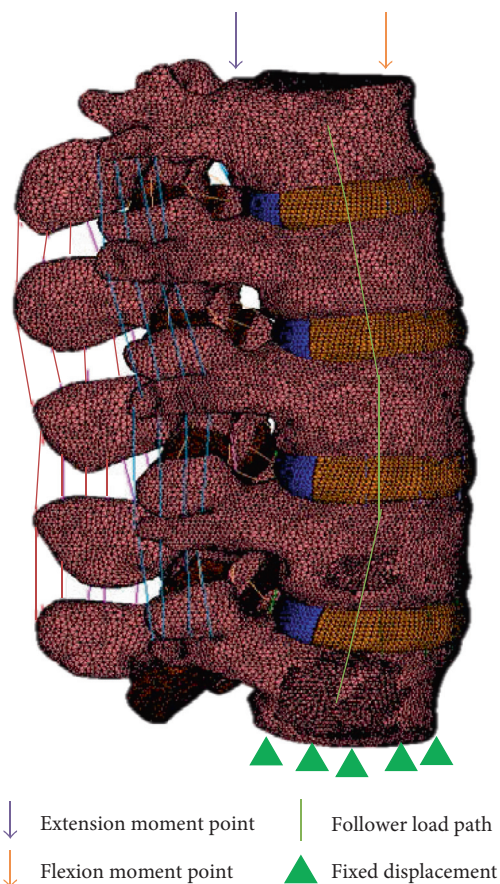


FIGURE 2: Loading and boundary condition of FE model of the lumbar spine.

nonlinear stress-strain curve material properties and the angle varied from $\pm 24^\circ$ to $\pm 46^\circ$ [12, 15].

The facet cartilage area was set as hyperelastic using the Mooney-Rivlin formulation with the thickness of 2 mm [12, 16]. The articulating facet surfaces were modelled as

TABLE 3: Magnitude of moment loading applied on the lumbar spine.

Loading direction	Flexion moment point		Extension moment point	
	F_y (N)	F_z (N)	F_y (N)	F_z (N)
Flexion	-98 N	-230 N	98 N	230 N
Extension	98 N	230 N	-98 N	-230 N

surface-to-surface contact with 0.5 mm initial gap where the normal contact stiffness was 200 N/mm and the friction coefficient is zero [15]. This will only allow the compressive force to be transmitted within the gap between the articulating facet surfaces [15, 17].

The ligaments were represented using truss elements. Table 1 shows the geometrical parameter of the lumbar spine ligaments [15, 18]. The complete list of the material properties imposed in the FE model of the osseoligamentous lumbar spine is presented in Table 2.

Mesh convergence analysis was performed in order to obtain an optimum FE model of the lumbar spine. Four FE models of L4-L5 lumbar segment were developed using 1.5 mm, 2.0 mm, 2.5 mm, and 3 mm mesh sizes. The analysis was based on the IDP results of the IVD where the optimum mesh size started at 2 mm as the IDP reached a plateau value. The 2.0 mm was then applied in FE model of L1-L5 lumbar spine [12].

2.2. Finite Element Analysis. The contact surfaces between the vertebral bodies and the IVD were set as perfectly connected to each other using segment to segment contact algorithm in Marc Mentat software. The FE model was subjected to follower load of 500 N, 800 N, and 1200 N which represent the typical human normal weight, overweight, and obesity based on 65% of upper body weight with an additional 200 N of local muscle force [19, 20]. Pure moment of 7.5 Nm was generated using force couple applied at flexion

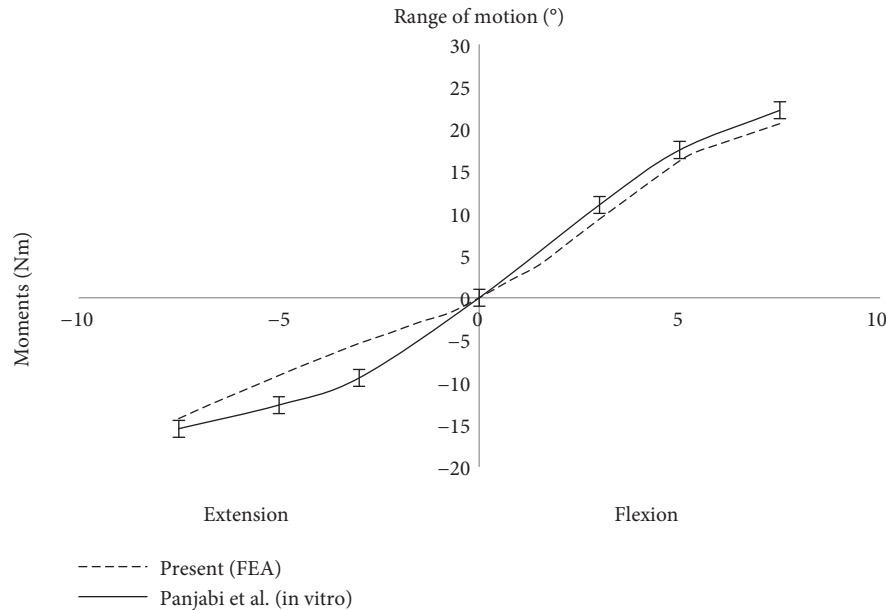


FIGURE 3: Comparison of ROM between present FE model and previous in vitro result under 7.5 Nm pure moments.

and extension moment points (Figure 2) to create either flexion or extension motions [21, 22]. The force couple consists of two equal and opposite forces as shown in Table 3 [23].

Eight spring elements were applied around the L1–L5 lateral vertebral body where the total load was divided equally to each of the spring element [24, 25]. This is to assure the uniformity of the applied follower load and to avoid any potential rotation of the intervertebral body. The inferior surface of the L5 vertebral body was completely fixed in all directions as shown in Figure 2.

3. Results

3.1. Verification of FE Model. The FE model of osseoligamentous lumbar spine was verified by comparing the range of motion (ROM) with previous in vitro study for flexion and extension motions at pure moment of 7.5 Nm. The present results of the intersegmental rotations of the lumbar spine follow similar trend to the previous in vitro results as shown in Figure 3 [21]. The percentage difference of the ROM between present and previous in vitro study in flexion was 7.5% at 7.5 Nm. Although notable difference was found between 2 Nm and 5 Nm in extension motion of the lumbar spine, the percentage difference of the ROM was decreased to 8.1% when reaching 7.5 Nm moments.

Further comparisons were also carried out to examine the axial displacement and IDP of IVD at L4–L5 vertebral segment. It was found that similar trends were observed in the previous in vitro studies as shown in Figure 4 [26, 27]. The differences between the present FEA results and previous in vitro study results for axial displacement and IDP of the IVD at 1200 N compression load were 7.1% and 6.9%, respectively. Based on these results, the developed FE model could produce appropriate and reliable results for further FE analysis.

3.2. The Effects of Human Weight on the Intradiscal Pressure. Figure 5 shows the comparison of the IDP of nucleus pulposus for each IVD vertebral segments in the lumbar spine. It was found that the IDP was increased as the human spine physiological loading increased in flexion motion where the highest pressure was 1.26 MPa at L1–L2 vertebral segment. The IDP was increased in flexion motion but an opposite trend was observed in extension motion. The effects of the human weight were observed to be more significant at the L4–L5 segment as shown in Figure 6. In flexion motion, the 1200 N load generated 30% higher pressure than the 500 N load, respectively, whereas in extension motion, the pressure decreased to 80%. At other vertebral levels, the difference of the IDP between 500 N and 1200 N loads ranges from 4% to 8% in flexion motion, whereas higher range was obtained between 18–60% in extension motion.

3.3. The Effects of Human Weight on Annulus Fibrosis. In general, the annulus stress increased as the human weight increased with the maximum annulus stress of 3.9 MPa for 1200 N load at L1–L2 lumbar segment as shown in Figure 7. The highest increment was observed at the L4–L5 where the annulus stress increased to 17% in extension motion, whereas in flexion motion, the annulus stress increased to 10%. At other vertebral levels, the increment of the annulus stress between 500 N and 1200 N loads was between 1.3–8% in extension and 1–8% in flexion motion.

4. Discussion

The present study demonstrates that physiological loading of body weight plays an important role of stress distribution at IVD in the lumbar spine. It was observed that increasing body weight will increase the pressure at nucleus pulposus and annulus fibrosis at all levels of the IVD. Furthermore, the position and direction of motion appears to affect these

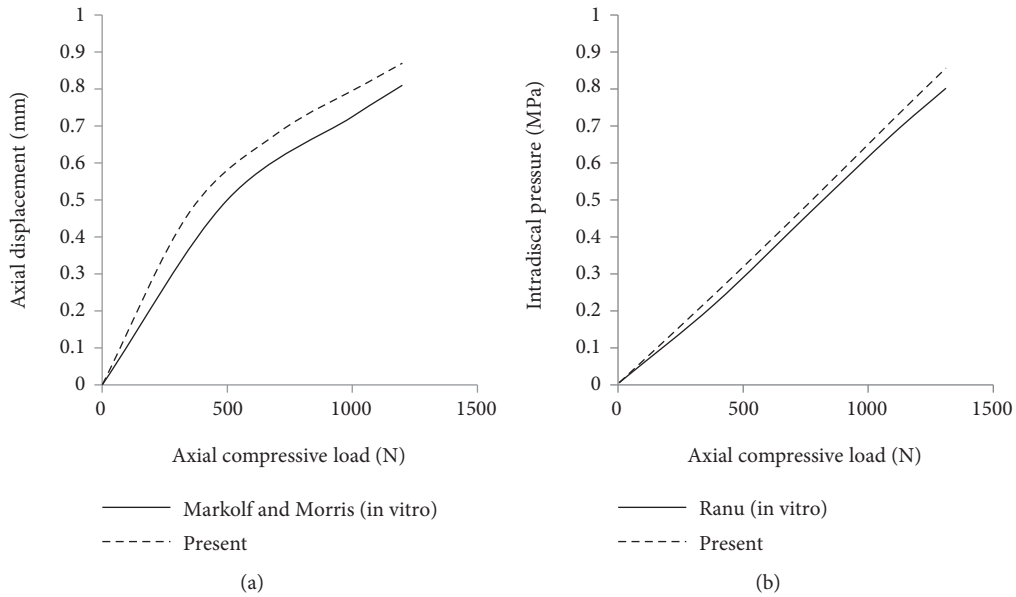


FIGURE 4: Comparison of present FEA and previous in vitro study of IVD results. (a) Axial displacement and (b) IDP under compressive load up to 1200 N.

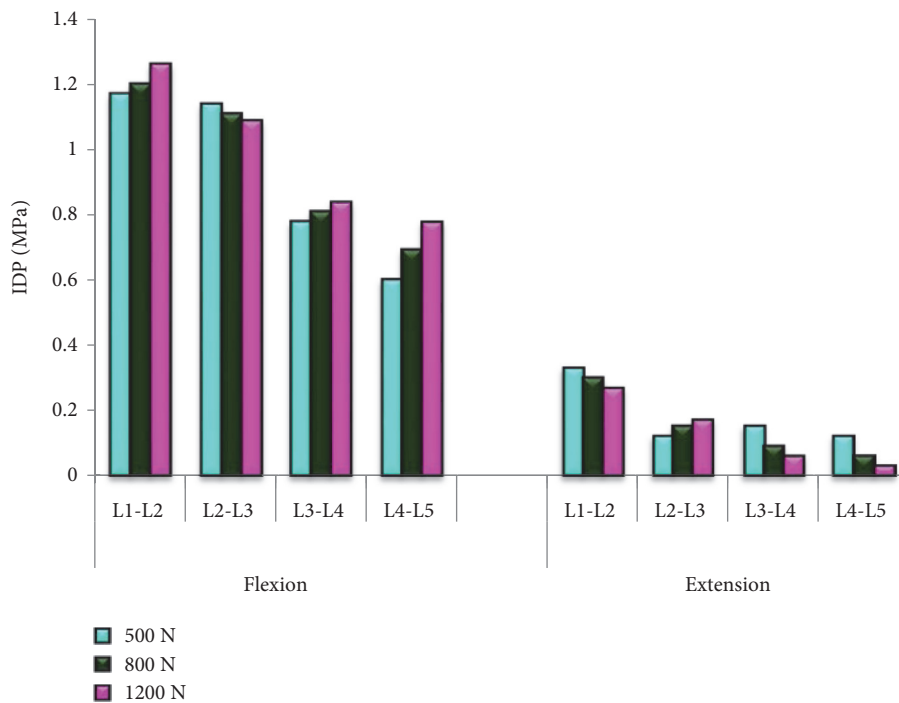


FIGURE 5: Comparison of the IDP of nucleus pulposus for each IVD vertebral segments in the lumbar spine.

results where the IDP was increased in flexion motion but an opposite trend was observed in extension motion. A severe effect was noticed when heavier individuals continue to experience increased stress and pressure on IVD at all vertebral segments in the lumbar spine particularly at L4-L5 segment in both flexion and extension motions.

The results of the present study show similar pattern to the IDP measured in *in vitro* study where the maximum IDP was found in flexion motion due to the load shift from the posterior

towards the anterior of the IVD in flexion motion [12, 28, 29]. The increase of nucleus pressure enhances the tensile stress on the annulus fibers which leads to the excessive stress on the IVD and stimulate the propagation of disc degeneration particularly in nucleus pulposus [21]. This will increase the stiffness of IVD and could reduce its height due to the outflow of fluid through the vertebral body endplates [30]. Subsequently, the fluid loss will increase the proteoglycan and osmotic pressure within the nucleus [30, 31].

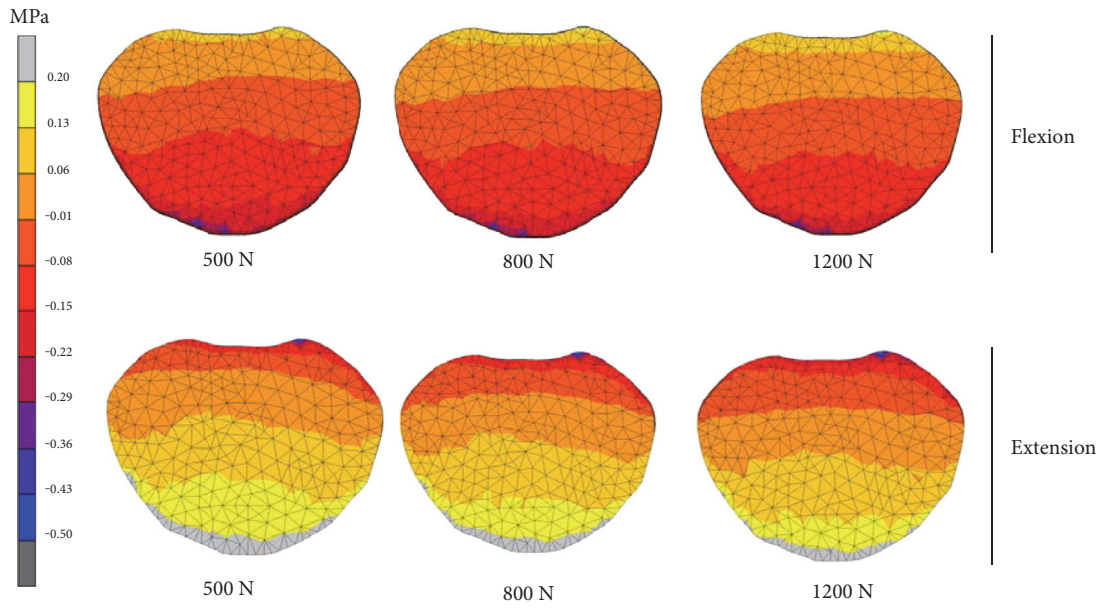


FIGURE 6: IDP contour plots of nucleus pulposus at L4-L5 vertebral segment.

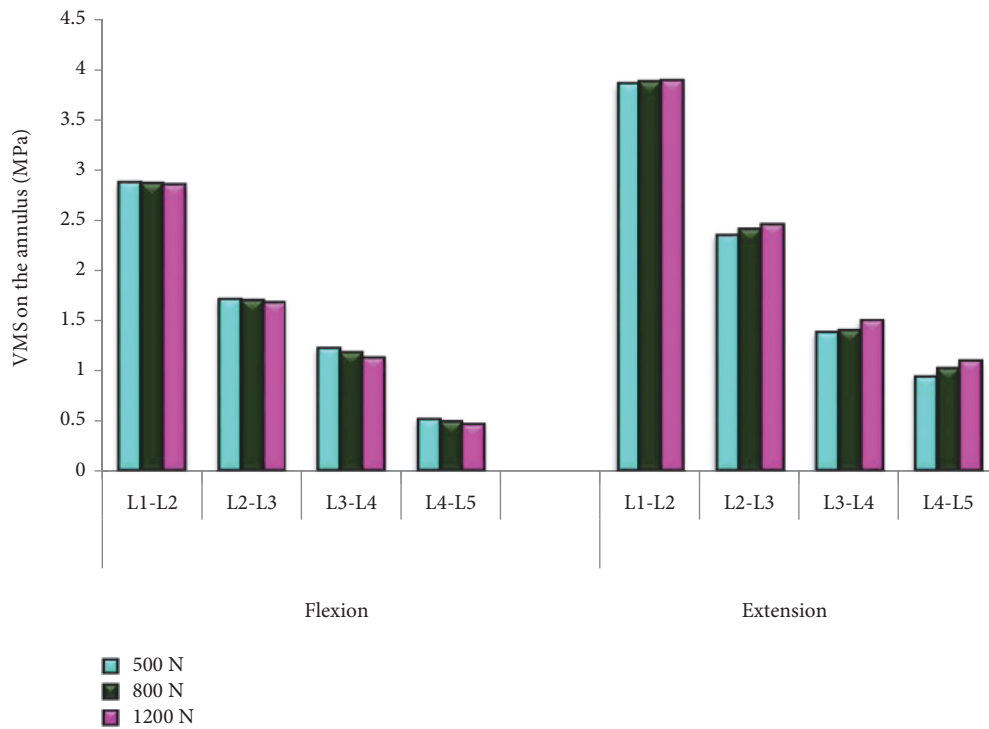


FIGURE 7: Annulus stress of 500 N, 800 N, and 1200 N loads in flexion and extension motions.

The maximum annulus stress was obtained in extension motion due to the load shift from the anterior towards the posterior of the IVD. This phenomenon was also observed in previous clinical study where the structural defect in the vertebral body endplate tends to distribute the load transferred from the nucleus to the posterior annulus. It has been shown that this can potentially lead to pain and could tear the annulus at the disc rim [32, 33].

5. Conclusion

Gaining body weight will increase stresses of IVD at all vertebral segments in the lumbar spine particularly the L4-L5 segment. Furthermore, the nucleus pulposus was more severely affected compared with the annulus fibrosus. Although flexion and extension motions of the lumbar spine appear to have different percentage effect on the IVD, it was

found that heavier individuals will continue to experience an increase in stress at IVD regardless of the position of the spine. This could be a factor that can lead to early intervertebral disc damage.

Conflicts of Interest

The authors declare that they have no conflicts of interest.

Acknowledgments

The authors would like to thank the Rehabilitation Engineering and Assistive Technology Research Group, Universiti Teknikal Malaysia Melaka (UTeM) and the Medical Devices and Technology Group, Faculty of Biosciences and Medical Engineering, Universiti Teknologi Malaysia for the valuable research facilities. This research is funded by the Ministry of Higher Education, Malaysia: ERGS/2012/FKM/TK01/02/3/E00005.

References

- [1] P. Gordon-Larsen, H. Wang, and B. M. Popkin, "Overweight dynamics in Chinese children and adults," *Obesity Reviews*, vol. 15, pp. 37–48, 2014.
- [2] M. Djurasovic, K. R. Bratcher, S. D. Glassman, J. R. Dimar, and L. Y. Carreon, "The effect of obesity on clinical outcomes after lumbar fusion," *Spine*, vol. 33, no. 16, pp. 1789–1792, 2008.
- [3] L. Vismara, F. Menegoni, F. Zaina, M. Galli, S. Negrini, and P. Capodaglio, "Effect of obesity and low back pain on spinal mobility: a cross sectional study in women," *Journal of NeuroEngineering and Rehabilitation*, vol. 7, no. 3, pp. 1–8, 2010.
- [4] H. C. D. Porto and C. M. Pechak, "Biomechanical effects of obesity on balance," *International Journal of Exercise Science*, vol. 5, no. 4, pp. 301–320, 2012.
- [5] G. Mellin, K. Harkapaa, H. Vanharanta, M. Hupli, R. Heinonen, and A. Jarvikoski, "Outcome of a multimodal treatment including intensive physical training of patients with chronic low back pain," *Spine*, vol. 18, no. 7, pp. 825–829, 1993.
- [6] K. Martin, K. Fontaine, B. J. Nicklas, K. E. Dennis, A. P. Goldberg, and M. C. Hochberg, "Weight loss and exercise walking reduce pain and improve physical functioning in overweight post-menopausal women with knee osteoarthritis," *Journal of Clinical Rheumatology*, vol. 7, no. 4, pp. 219–223, 2001.
- [7] M. A. Adams, "Biomechanics of back pain," *Acupuncture in Medicine*, vol. 22, no. 4, pp. 178–188, 2004.
- [8] A. Rohlmann, S. Neller, L. Claes, G. Bergmann, and H. J. Wilke, "Influence of a follower load on intradiscal pressure and intersegmental rotation of the lumbar spine," *Spine*, vol. 26, no. 24, pp. E557–E561, 2001.
- [9] C. F. Du, N. Yang, J. C. Guo, Y. P. Huang, and C. Zhang, "Biomechanical response of lumbar facet joints under follower preload: a finite element study," *BMC Musculoskeletal Disorders*, vol. 17, no. 1, p. 126, 2016.
- [10] F. Heuer, H. Schmidt, and H. J. Wilke, "Stepwise reduction of functional spinal structures increase disc bulge and surface strains," *Journal of Biomechanics*, vol. 41, pp. 1953–1960, 2008.
- [11] V. Palepu, M. Kodigudla, and V. K. Goel, "Biomechanics of disc degeneration," *Advances in Orthopedics*, vol. 2012, Article ID 726210, 17 pages, 2012.
- [12] H. Schmidt, A. Kettler, F. Heuer, U. Simon, L. Claes, and H. J. Wilke, "Intradiscal pressure, shear strain, and fiber strain in the intervertebral disc under combined loading," *Spine*, vol. 32, no. 7, pp. 748–755, 2007.
- [13] R. Eberlein, G. A. Holzapfel, and F. Markus, "Multi-segment FEA of the human lumbar spine including the heterogeneity of the annulus fibrosus," *Computational Mechanics*, vol. 34, no. 2, pp. 147–163, 2004.
- [14] V. Moramarco, A. P. D. Palamor, C. Pappalettere, and M. Doblare, "An accurate validation of a computational model of a human lumbosacral segment," *Journal of Biomechanics*, vol. 43, no. 2, pp. 334–342, 2010.
- [15] H. J. Kim, K. T. Kang, B. S. Chang, C. L. Lee, J. W. Kim, and J. S. Yeom, "Biomechanical analysis of fusion segment rigidity upon stress at both the fusion and adjacent segments: a comparison between unilateral and bilateral pedicle screw fixation," *Yonsei Medical Journal*, vol. 55, no. 5, pp. 1386–1394, 2014.
- [16] W. M. Park, K. Kim, and Y. H. Kim, "Effects of degenerated intervertebral discs on intersegmental rotations, intradiscal pressures, and facet joint forces of the whole lumbar spine," *Computers in Biology and Medicine*, vol. 43, no. 9, pp. 1234–1240, 2013.
- [17] H. Schmidt, F. Galbusera, A. Rohlmann, T. Zander, and H. J. Wilke, "Effect of multilevel lumbar disc arthroplasty on spine kinematics and facet joint loads in flexion and extension: a finite element analysis," *European Spine Journal*, vol. 21, Supplement 5, pp. S663–S674, 2012.
- [18] C. S. Chen, C. K. Cheng, C. L. Liu, and W. H. Lo, "Stress analysis of the disc adjacent to interbody fusion in lumbar spine," *Medical Engineering & Physics*, vol. 23, pp. 483–491, 2001.
- [19] A. Rohlmann, N. K. Burra, T. Zander, and G. Bergmann, "Comparison of the effects of bilateral posterior dynamic and rigid fixation devices on the loads in the lumbar spine: a finite element analysis," *European Spine Journal*, vol. 16, no. 8, pp. 1223–1231, 2007.
- [20] M. Kurutz and L. Oroszvary, "Finite element analysis of weightbath hydrotraction treatment of degenerated lumbar spine segments in elastic phase," *Journal of Biomechanics*, vol. 43, no. 3, pp. 433–441, 2010.
- [21] M. M. Panjabi, T. R. Oxland, I. Yamamoto, and J. J. Crisco, "Mechanical behavior of the human lumbar and lumbosacral spine as shown by three-dimensional load-displacement curves lumbosacral behavior spine of the human curves," *The Journal of Bone and Joint Surgery American Volume*, vol. 76, pp. 413–424, 1994.
- [22] S. M. Renner, R. N. Natarajan, A. G. Patwardhan et al., "Novel model to analyze the effect of a large compressive follower pre-load on range of motions in a lumbar spine," *Journal of Biomechanics*, vol. 40, no. 6, pp. 1326–1332, 2007.
- [23] M. Nordin and V. H. Frankel, *Basic Biomechanics of the Musculoskeletal System*, Lippincott Williams & Wilkins, Philadelphia, 3rd edition, 2001.
- [24] W. Wang, H. Zhang, K. Sadeghipour, and G. Baran, "Effect of posterolateral disc replacement on kinematics and stress distribution in the lumbar spine: a finite element study," *Medical Engineering & Physics*, vol. 35, no. 3, pp. 357–364, 2013.

- [25] A. G. Patwardhan, R. M. Havey, G. Carandang et al., "Effect of compressive follower preload on the flexion-extension response of the human lumbar spine," *Journal of Orthopaedic Research*, vol. 21, no. 3, pp. 540–546, 2003.
- [26] K. L. Markolf and J. M. Morris, "The structural components of the intervertebral disc: a study of their contributions to the ability of the disc to withstand compressive forces," *The Journal of Bone and Joint Surgery (American Volume)*, vol. 56, no. 4, pp. 675–687, 1974.
- [27] H. S. Ranu, "Measurement of pressures in the nucleus and within the annulus of the human spinal disc: due to extreme loading," *Proceedings of the Institution of Mechanical Engineers, Part H: Journal of Engineering in Medicine*, vol. 204, no. 3, pp. 141–146, 1990.
- [28] O. L. Osti, V. Roberts, R. Moore, and R. D. Fraser, "Annular tears and disc degeneration in the lumbar spine: a post-mortem study of 135 discs," *Journal of Bone and Joint Surgery*, vol. 74, no. 5, pp. 678–682, 1992.
- [29] H. Schmidt, A. Kettler, A. Rohlmann, L. Claes, and H. J. Wilke, "The risk of disc prolapses with complex loading in different degrees of disc degeneration: a finite element analysis," *Clinical biomechanics*, vol. 22, no. 9, pp. 988–998, 2007.
- [30] M. A. Adams, D. S. McNally, and P. Dolan, "'Stress' distribution inside intervertebral discs: the effects of age and degeneration," *The Journal of Bone and Joint Surgery American Volume*, vol. 78, no. 6, pp. 965–972, 1996.
- [31] M. A. Adams, S. May, B. J. C. Freeman, H. P. Morrison, and P. Dolan, "Effects of backward bending on lumbar intervertebral discs: relevance to physical therapy treatments for low back pain," *Spine*, vol. 25, no. 4, pp. 431–437, 2000.
- [32] G. Cinotti and F. Postacchini, *The Biomechanics. In Lumbar Disc Herniation*, Springer Vienna, Vienna, 1999.
- [33] B. Johnstone, J. Urban, S. Roberts, and J. Menage, "The fluid content of the human intervertebral disc: comparison between fluid content and swelling pressure profiles of discs removed at surgery and those taken postmortem," *Spine*, vol. 17, no. 4, pp. 412–416, 1992.

Research Article

The Influence of Natural Head Position on the Cervical Sagittal Alignment

Kuan Wang,^{1,2} Zhen Deng,^{1,3} Zhengyan Li,^{1,4} Huihao Wang,^{1,4} and Hongsheng Zhan^{1,4}

¹Shi's Center of Orthopedics and Traumatology, Shuguang Hospital Affiliated to Shanghai University of TCM, Shanghai 201203, China

²Tongji Hospital, Tongji University School of Medicine, Shanghai 200092, China

³Baoshan Branch, Shuguang Hospital Affiliated to Shanghai University of TCM, Shanghai 201900, China

⁴Institute of Traumatology & Orthopedics, Shanghai Academy of TCM, Shanghai 201203, China

Correspondence should be addressed to Huihao Wang; huihaowang@126.com and Hongsheng Zhan; zhanhongsheng2010@163.com

Received 24 March 2017; Revised 6 June 2017; Accepted 3 July 2017; Published 13 August 2017

Academic Editor: Wei Yao

Copyright © 2017 Kuan Wang et al. This is an open access article distributed under the Creative Commons Attribution License, which permits unrestricted use, distribution, and reproduction in any medium, provided the original work is properly cited.

Introduction. This study investigated the relationship between the parameters related to the natural head position and cervical segmental angles and alignment of patients with neck pain. **Material and Methods.** The lateral radiographs of the cervical spine were collected from 103 patients and were used to retrospectively analyze the correlation between the natural head position, cervical local sagittal angles, and alignment. Sagittal measurements were as follows: cervical curvature classification, slope of McGregor's line (McGS), local sagittal angles (C0–C2 angle, C2–C5 angle, C5–C7 angle, and C2–C7 angle), T1 slope, center of gravity of the head to sagittal vertical axis (CG–C7 SVA), and local sagittal alignment (C0–C2 SVA and C2–C7 SVA). **Results.** McGS was significantly correlated to C0–C2 angle ($r = 0.57$), C0–C2 SVA ($r = -0.53$), C2–C7 SVA ($r = -0.28$), and CG–C7 SVA ($r = -0.47$). CG–C7 SVA was also significantly correlated to curvature type ($r = 0.27$), C5–C7 angle ($r = -0.37$), and C2–C7 angle ($r = -0.39$). **Conclusions.** A backward shift with an extended head position may accompany a relatively normal curvature of the cervical spine. The effect of posture control in relieving abnormal mechanical state of the cervical spine needs to be further confirmed by biomechanical analysis.

1. Introduction

Cervical curvature is one of the clinical assessments which could reflect the mechanical state of the cervical spine. With a normal lordotic curvature, the least amount of energy is spent to maintain the horizontal gaze in the upright position [1]. Under this condition, tensile and compression loads on spinal structures are smallest compared to other cervical alignments [2, 3].

The cervical spine connects the skull and thoracic vertebrae and supports the mass of the head. It is a multijoint structure that allows complex movement of the neck. In recent years, many studies have used X-ray imaging to explore the relationship between parameters related to cervical sagittal alignment, involving the mass point of the head, C2 vertebral center, T1 slope, and other measurements [4].

Lee et al. found that T1 slope and C2–C7 Cobb angle were strongly correlated [5], whereas the cranial offset and C2–C7 Cobb angle were in moderate correlation. Nunez-Pereira et al. found that the occiput–C2 angle and C2–C7 Cobb angle also showed a moderate correlation [6]. Tang et al. found a close relationship between the C2–C7 sagittal vertical axis (C2–C7 SVA) and health-related quality of life in patients who underwent surgery of the cervical spine [7].

The above studies have shown that the segmental angle, alignment of the cervical spine, and the position of the first thoracic spine were interdependent and may contribute to the progression of cervical degeneration and quality of life. These studies focused a lot on the effect of cervicothoracic junction towards sagittal alignment of the cervical spine, but less attention was paid to the head position. As already known, the head position could be controlled freely by our

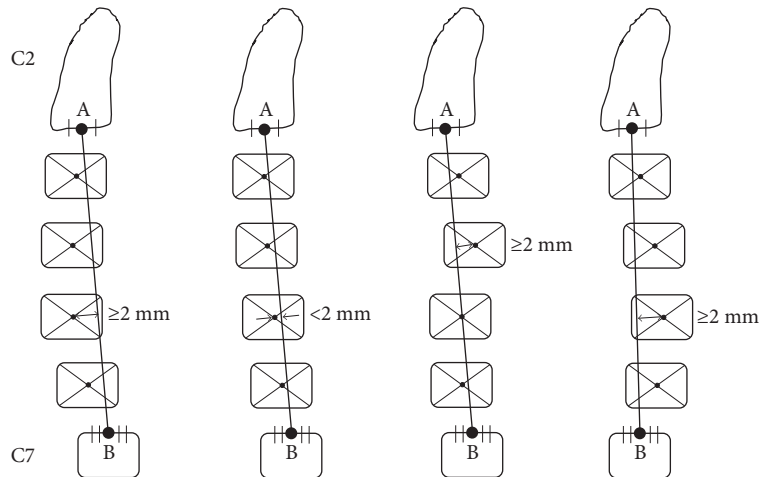


FIGURE 1: The cervical curvature types (from left to right: lordosis, straight, sigmoid, and kyphosis).

mind in a certain range of motion, and it needs a little moment to move the head in a neutral zone [8]. For a proper transmission of the head weight, there should be some relationship between the position of the head in the natural standing position, the local sagittal angles, and the alignment of the cervical spine. The natural head position in the sagittal plane may include the rotation and translation degrees of freedom, which could be represented by a head tilt and forward/backward head shift [9] or by McGregor slope (McGS) and C0–C7 sagittal vertical axis (CG–C7 SVA) [10, 11]. We hypothesized that these parameters of the head position have some impacts on the cervical segmental angles and alignment.

Therefore, the objective of this study was to investigate the relationship between the parameters related to the natural head position and the cervical alignment, through retrospectively analyzing the cervical lateral radiographs of 103 patients with neck pain.

2. Materials and Methods

2.1. Study Design. This study was a retrospective data analysis of consecutive patients who underwent sagittal plane cervical spine X-ray from January 2015 to January 2016. Inclusion criteria were adult neck pain patients (>18 years of age), with symptoms like neck stiffness, pain, and local tenderness, with or without limited cervical activity. Their X-ray examination can be normal or with mild degeneration. Exclusion criteria included patients with ankylosing spondylitis, tumor, cervical fracture or dislocation, diffuse idiopathic bone hypertrophy, and other specific diseases or mutations.

2.2. Radiographic Analysis. The lateral radiographs of the cervical spine were taken when patients were in the standing position. The measurements included cervical curvature classification (Figure 1) and parameters related to the head position and cervical alignment (Figure 2). The entire measurements included the following parameters:

- (1) Cervical curvature classification [12]: the cervical curvature was divided into three types including lordosis, straight/sigmoid, and kyphosis as types 1–3. To classify the curvature, a line was drawn to connect the midpoint of the C2 inferior end plate and C7 superior end plate. Then, the center of each vertebral body from C3 to C6 was located by connecting the diagonals of each vertebral body in the sagittal plane, and the distance from each center to line AB (see Figure 1) was measured. If all centers of vertebral bodies were in front of the line and the maximum distance was greater than 2 mm, the curvature was classified into the lordosis group; if the centers were in front of or behind the line but the maximum value of distance was no more than 2 mm, the curvature was classified into the straight group. For the sigmoid group, the centers were in front of or behind the line, but the maximum value of distance was greater than 2 mm. For the kyphosis group, the centers were all behind the line connecting the C2–C7 endplates, and the maximum value of distance was greater than 2 mm.
- (2) Slope of McGregor’s line (McGS) [13]: McGregor slope was defined as the slope of the line that connected the posterior margin of the hard palate and foramen magnum against the horizontal plane. This value was reported to be strongly correlated with the chin-brow vertical angle (CBVA) ($r = 0.862$) which was one measurement of horizontal gaze. So this value was used in the current study as an angular assessment of the natural head position. A positive value means that the head was in the extension position with ascending gaze, and a negative value means that the head was in the flexion position with descending gaze.
- (3) Local sagittal angles: local sagittal angles included C0–C2 angle, C2–C5 angle, C5–C7 angle, and C2–C7 Cobb angle. C0–C2 angle was defined as the angle between the inferior endplates of C2 and McGregor’s line [6]. C5–C7 angle denoted the angle between the C5 superior endplate and C7 inferior endplate [14].

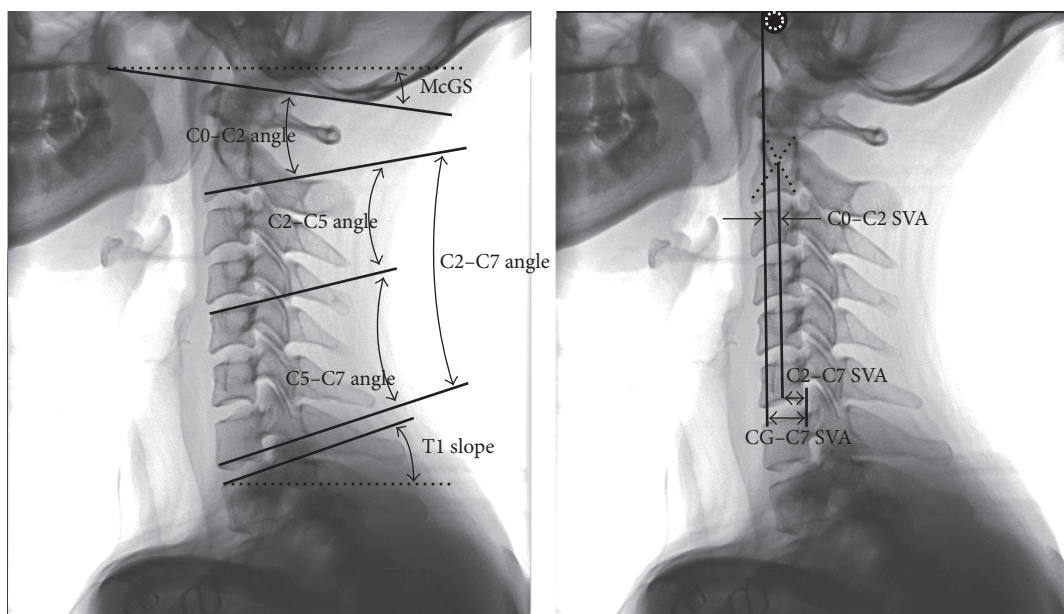


FIGURE 2: The measurement of parameters related to natural head position and cervical alignment (McGS, slope of McGregor's line; SVA, sagittal vertical axis).

C2–C7 Cobb angle denoted the angle between the C2 inferior endplate and C7 inferior endplate [5]. In the current study, to see the effect of the head position on the middle cervical spine, C2–C5 angle was defined as the value of C2–C7 Cobb angle subtracted by C5–C7 angle.

- (4) T1 slope [10]: T1 slope was defined as the angle between the line that was parallel to the superior end plate of T1 and the horizontal plane.
- (5) The center of gravity of the head to sagittal axis (CG–C7 SVA): CG–C7 SVA was defined as the distance between a plumb line dropped from the anterior margin of the external auditory canal and the posterior superior corner of C7. This value reflected relative translation of the head against the C7 vertebra [10].
- (6) Local sagittal alignment: C2–C7 sagittal vertical axis (C2–C7 SVA) was defined as the distance between a plumb line dropped from the centroid of C2 and the posterior superior corner of C7 [7]. This value reflected the relative translation of the C2 vertebra against the C7 vertebra. To see the effect of the head position on the sagittal alignment of the upper cervical spine, we defined the C0–C2 sagittal vertical axis (C0–C2 SVA) as the value of CG–C7 SVA subtracted by C2–C7 SVA.

The above parameters concerning the head position and cervical alignment have been widely used in previous studies with good reliability [10]. These measurements were processed independently by two experienced radiologists, and the measured values were averaged to produce the results.

The study protocol was approved by the medical ethics committee of our hospital.

To investigate the effect of the natural head position on the cervical alignment, the subjects were divided into four groups according to their CG–C7 SVA and McGS values. The median CG–C7 SVA was used for the division of the forward shift head position or backward shift head position. Lafage et al. reported the mean value of McGS and equations generated with linear regression between CBVA and McGS [13]. According to their results, 0.87° was the mean value of McGS, and this value was used for the division of the extended or flexed cranial position. Therefore, in terms of translation and rotation of the head position in the sagittal plane, four groups included forward shift with the extended head position (FE), backward shift with the extended head position (BE), forward shift with the flexed head position (FF), and backward shift with the flexed head position (BF).

2.3. Statistical Analysis. Data were analyzed by SPSS 20.0 software. Values were presented as mean \pm SD. Spearman's correlation analyses were performed to examine associations among the selected variables. The curvature type numbers 1–3 were treated as ordinal categorical variables in the current study. If the curvature type number is negatively correlated with a local segmental angle, an increase in the curvature type number is correlated with a decrease in the angle. This results should be interpreted as that the curvature type number would be more close to 1 (lordosis type) rather than 3 (kyphosis type), with a decrease in the local segmental angle. The comparison of each radiographic parameter among four head positions was determined by using one-way ANOVA with Bonferroni's post hoc test. A *P* value equal to or less than 0.05 was set up as threshold for statistical significance.

TABLE 1: Radiographic measurements related to natural head position and cervical alignment.

Variable	N	Min	Max	Mean	SD
McGS (°)	103	-12.00	20.90	6.14	6.10
C0-C2 angle (°)	103	0.80	34.80	16.61	7.39
C2-C5 angle (°)	103	-19.70	21.50	2.88	7.71
C5-C7 angle (°)	103	-11.80	17.30	4.52	6.61
C2-C7 angle (°)	103	-16.80	30.30	7.40	9.55
T1 slope (°)	103	8.70	43.40	23.31	6.64
C0-C2 SVA (mm)	103	-16.50	22.30	1.36	6.77
C2-C7 SVA (mm)	103	-4.60	49.80	17.91	8.54
CG-C7 SVA (mm)	103	-12.00	72.10	19.27	13.12

McGS: slope of McGregor's line; SVA: sagittal vertical axis.

3. Results

3.1. Demographic and Cervical Curvature Classification. There were 103 subjects included in this study. Among these subjects, 33 subjects were male and 70 were female. The mean age was 37.4 ± 12.3 years. There were 35 subjects allocated to the lordosis group, 56 subjects to the straight or sigmoid group (only one subject was classified as sigmoid curvature; thus, the two groups were combined), and 12 subjects to the kyphosis group. The mean age of each group was 39.4 ± 13.2 , 37.3 ± 11.4 , and 32.7 ± 13.6 years, respectively. There was no significant difference in age and gender between each group ($P > 0.05$).

3.2. Measurement of Parameters and Correlation Analysis. The results of radiographic measurements related to the head position and cervical alignment are shown in Table 1. The results of Spearman's correlation analyses are shown in Table 2. McGS was found to be significantly correlated to C0-C2 angle ($r = 0.57$), C0-C2 SVA ($r = -0.53$), C2-C7 SVA ($r = -0.28$), and CG-C7 SVA ($r = -0.47$) but not significantly correlated to curvature classification, C2-C5 angle, C5-C7 angle, and C2-C7 angle. CG-C7 SVA was also significantly correlated to curvature type ($r = 0.27$), C5-C7 angle ($r = -0.37$), and C2-C7 angle ($r = -0.39$).

3.3. The Influence of Different Head Positions. Figure 3 shows the distribution of cervical curvatures in different head positions. Among the four groups (FE, BE, BF, and FF groups), the proportion of subjects with lordosis curvature in the BE group was most compared to those in other groups, and the proportion of subjects with straight or sigmoid curvature was most in the FE group. In the FF group, the proportion of subjects with kyphosis curvature was most compared to those in other groups. There were only four subjects in the BF group, with three subjects classified with straight/sigmoid curvatures. Table 3 shows the comparison of each radiographic parameter among four head positions determined by one-way ANOVA with Bonferroni's post hoc test. C0-C2 angle, C5-C7 angle, C2-C7 angle, C0-C2 SVA, and C2-C7 SVA are significantly different among the four head positions. C2-

C5 angle and T1 slope are not significantly different among the four head positions.

4. Discussion

In this study, the lateral radiographs of the cervical spine were used to analyze the relationship between the natural head position and cervical alignment. The measured parameters related to cervical alignment (e.g., C2-C7 angle and T1 slope) were consistent with the reported data [5, 6, 12]. This study provides some insight into the effect of the head position on the cervical spine alignment.

Since T1 was the fixed end of the cervical spine and the cervical column is influenced by the weight of the head, it is expected that the T1 slope might play a determining role in the curvature of the cervical spine. In the current study, T1 slope was in positive correlation with C2-C7 angle. The results agreed with the data reported by Lee et al. [5].

The translation or rotation of the head is controlled by the nervous system to keep an economic posture [14]. Due to the large vision field, people could maintain a horizontal gaze with varying head positions within a certain range. In the current study, the CG-C7 SVA was found to be in negative correlation with curvature type. This means that it is more likely to be kyphotic of the cervical spine with the anterior translation of the head. Furthermore, the CG-C7 SVA was found to be negatively correlated with C5-C7 angle and C2-C7 angle but not significantly correlated with C2-C5 angle. This result suggested that a forward shift of the head in the natural head position might indicate a loss of lordosis in the lower cervical spine.

This study also found that the extended or flexed position of the head represented by McGS was not correlated with local sagittal angle except C0-C2 angle. This might be because most flexion and extension range of motion is found at C0-C2 compared to mid and lower cervical regions [8]. Thus, it has a great compensatory space for the flexion/extension of the head and minimizes the impact on the local segmental angle below C2. Additionally, the McGS was found to be in negative correlation with C0-C2 SVA, C2-C7 SVA, and CG-C7 SVA, which means that the mass point of the head moves posteriorly with the extension of the head. The results suggested that the rotation in the natural head position might be indirectly involved in the balance control of the cervical spine by adjusting the translation of the head. A study by Tang et al. found that patients who underwent posterior cervical fusion surgery reported a decrease in the quality of life with an increased value of C2-C7 SVA [7]. According to our results, the anterior translation of the head might accompany cranial flexion as well as a flattening of the cervical lordosis. To balance the extensor moment produced by the flexed head, the extensor muscles need to produce additional extension torque and the fatigue of these muscles might lead to neck or upper back symptoms. Therefore, it might be more appropriate to keep the head in a neutral position rather than a flexed position to prevent neck and back pain.

TABLE 2: The correlation analysis between parameters.

Variable	Curvature type	McGS	C0–C2 angle	C2–C5 angle	C5–C7 angle	C2–C7 angle	T1 slope	C0–C2 SVA	C2–C7 SVA	CG–C7 SVA	
Curvature type	<i>r</i>	1	–0.11	0.38	–0.61	–0.33	–0.73	–0.40	0.42	0.06	0.27
	<i>P</i>		0.29	<0.01	<0.01	<0.01	<0.01	<0.01	<0.01	0.55	0.01
McGS	<i>r</i>		1	0.57	0.05	0.08	0.12	–0.05	–0.53	–0.28	–0.47
	<i>P</i>			<0.01	0.63	0.42	0.24	0.59	<0.01	<0.01	<0.01
C0–C2 angle	<i>r</i>			1	–0.51	–0.17	–0.53	–0.07	0.12	0.18	0.18
	<i>P</i>				<0.01	0.08	<0.01	0.46	0.24	0.07	0.07
C2–C5 angle	<i>r</i>				1	–0.12	0.69	0.29	–0.46	0.14	–0.16
	<i>P</i>					0.24	<0.01	<0.01	<0.01	0.15	0.11
C5–C7 angle	<i>r</i>					1	0.58	0.48	–0.22	–0.38	–0.37
	<i>P</i>						<0.01	<0.01	0.03	<0.01	<0.01
C2–C7 angle	<i>r</i>						1	0.55	–0.53	–0.15	–0.39
	<i>P</i>							<0.01	<0.01	0.13	<0.01
T1 slope	<i>r</i>							1	–0.05	0.28	0.13
	<i>P</i>								0.61	<0.01	0.21
C0–C2 SVA	<i>r</i>								1	0.39	0.79
	<i>P</i>									<0.01	<0.01
C2–C7 SVA	<i>r</i>									1	0.85
	<i>P</i>										<0.01
CG–C7 SVA	<i>r</i>										1
	<i>P</i>										

Note: bold font indicates statistical significance ($P < 0.05$). McGS: slope of McGregor's line; SVA: sagittal vertical axis.

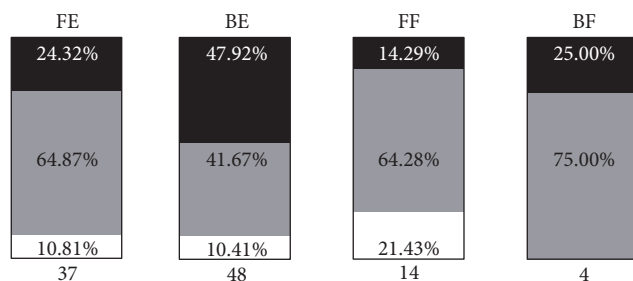


FIGURE 3: The proportion of each cervical curvature type and total number of subjects in different head position (FE, forward shift with extended head position; BE, backward shift with extended head position; FF, forward shift with flexed head position; BF, backward shift with flexed head position; black square, lordosis; gray square, straight or sigmoid; white square, kyphosis).

With the development of modern electronic devices, a forward head posture is common among people [15] and the forward head posture has been associated with musculoskeletal pain in previous studies [16, 17]. Although the total number of subjects with kyphosis curvature was small in the current study, the proportion of subjects with the kyphosis type curvature was most in the FF group. This result suggested that the forward shift with the flexed head position may be associated with cervical kyphosis thus leading to the unbalance of a mechanical state. In contrast, the proportion of the lordosis type was most in

the BE group, meaning that a backward shift with an extended head position was more likely to be accompanied with a normal cervical curvature. The cervical spine could be divided into three columns (one vertebral body and two facet joints on the same level) [10]. With the backward shift and the extended head position, the weight of the head would be more loaded on the posterior column of the cervical spine. Since we found that C2–C5 angle was not significantly different among the four head positions, this position (BE) might relieve the load on the intervertebral disc of C5–C7 segments and be helpful in compensating the additional load caused by nonphysiological cervical curvature like kyphosis and straight/sigmoid type. In the current study, some subjects with kyphotic curvature were found to have a forward shift and flexed position of the head. Whether posture control (e.g., keeping a backward shift and extended head position) is helpful to these subjects in relieving abnormal mechanical state of the cervical spine needs to be further confirmed by biomechanical analysis.

Some limitations existed in this study. Since this study was a retrospectively radiograph analysis, it could not accurately reflect the causal relationship between each parameter and no healthy subjects as the control group. Age is also an important factor affecting the curvature. In the current study, there is a trend that the age of subjects with nonphysiological cervical curvature (straight, sigmoid, and kyphosis) become younger. Also,

TABLE 3: ANOVA test for comparison of each radiographic parameter among four head positions.

Variable	Head position				P
	FE	BE	FF	BF	
C0–C2 angle	19.38 ± 8.05	16.38 ± 6.50	12.86 ± 4.92★	6.85 ± 5.09★	0.001
C2–C5 angle	1.13 ± 7.78	4.51 ± 7.97	2.51 ± 6.56	0.88 ± 5.19	0.227
C5–C7 angle	3.23 ± 6.05	6.39 ± 6.76	0.75 ± 5.62▲	7.15 ± 6.33	0.013
C2–C7 angle	4.36 ± 8.09	10.90 ± 9.82★	3.26 ± 8.61▲	8.03 ± 9.66	0.004
T1 slope	23.67 ± 6.02	23.10 ± 7.62	23.54 ± 5.29	21.70 ± 5.06	0.940
C0–C2 SVA	4.74 ± 5.47	−3.40 ± 4.74★	8.41 ± 4.75▲	2.65 ± 3.78	<0.001
C2–C7 SVA	22.21 ± 5.32	12.71 ± 6.39★	26.93 ± 8.98▲	9.10 ± 3.12★■	<0.001

Note: ★ indicates $P < 0.05$ in comparison with the FE group; ▲ indicates $P < 0.05$ in comparison with the BE group; ■ indicates $P < 0.05$ in comparison with the FF group.

the cervical curvature in male and female showed a different trend with increasing age [10]. Further prospective study including measurements of the quality of life and pain in terms of age, along with the neurological deficits and MRI images, which could accurately show the degeneration of intervertebral disc, would uncover the causal relationship of them.

5. Conclusions

The natural head position was related to local sagittal angle and alignment of the cervical spine. The mass point of the head moved posteriorly with the extension of the head. Backward shift with an extended head position may accompany a relatively normal curvature of the cervical spine. Some subjects with nonphysiological cervical curvature were in the forward shift and flexed head position. The effect of posture control in relieving abnormal mechanical state of the cervical spine needs to be further confirmed by biomechanical analysis.

Conflicts of Interest

The authors declare that there is no conflict of interest regarding the publication of this paper.

Acknowledgments

This work was supported by the National Natural Science Foundation of China (nos. 81473702, 81503596, 81202707, and 81001528) and the Shanghai Committee of Science and Technology (no. 15401934100).

References

- [1] E. Berthonnaud, J. Dimnet, P. Roussouly, and H. Labelle, “Analysis of the sagittal balance of the spine and pelvis using shape and orientation parameters,” *Journal of Spinal Disorders & Techniques*, vol. 18, no. 1, pp. 40–47, 2005.
- [2] T. J. Albert and A. Vacarro, “Postlaminectomy kyphosis,” *Spine (Phila Pa 1976)*, vol. 23, no. 24, pp. 2738–2745, 1998.
- [3] H. Deutsch, R. W. Haid, G. E. Rodts, and P. V. Mummaneni, “Postlaminectomy cervical deformity,” *Neurosurgical Focus*, vol. 15, no. 3, pp. 1–5, 2003.
- [4] C. P. Ames, B. Blondel, J. K. Scheer et al., “Cervical radiographical alignment: comprehensive assessment techniques and potential importance in cervical myelopathy,” *Spine (Phila Pa 1976)*, vol. 38, no. 22, Supplement 1, pp. S149–S160, 2013.
- [5] S. H. Lee, K. T. Kim, E. M. Seo, K. S. Suk, Y. H. Kwack, and E. S. Son, “The influence of thoracic inlet alignment on the craniocervical sagittal balance in asymptomatic adults,” *Journal of Spinal Disorders & Techniques*, vol. 25, no. 2, pp. E41–E47, 2011.
- [6] S. Nunez-Pereira, W. Hitzl, V. Bullmann, O. Meier, and H. Koller, “Sagittal balance of the cervical spine: an analysis of occipitocervical and spinopelvic interdependence, with C-7 slope as a marker of cervical and spinopelvic alignment,” *Journal of Neurosurgery Spine*, vol. 23, no. 1, pp. 16–23, 2015.
- [7] J. A. Tang, J. K. Scheer, J. S. Smith et al., “The impact of standing regional cervical sagittal alignment on outcomes in posterior cervical fusion surgery,” *Neurosurgery*, vol. 71, no. 3, pp. 662–669, 2012.
- [8] M. M. Panjabi, J. J. Crisco, A. Vasavada et al., “Mechanical properties of the human cervical spine as shown by three-dimensional load-displacement curves,” *Spine (Phila Pa 1976)*, vol. 26, no. 24, pp. 2692–2700, 2001.
- [9] X. Guan, G. Fan, X. Wu et al., “Photographic measurement of head and cervical posture when viewing mobile phone: a pilot study,” *European Spine Journal*, vol. 24, no. 12, pp. 2892–2898, 2015.
- [10] J. K. Scheer, J. A. Tang, J. S. Smith et al., “Cervical spine alignment, sagittal deformity, and clinical implications: a review,” *Journal of Neurosurgery Spine*, vol. 19, no. 2, pp. 141–159, 2013.
- [11] B. G. Diebo, V. Challier, J. K. Henry et al., “Predicting cervical alignment required to maintain horizontal gaze based on global spinal alignment,” *Spine (Phila Pa 1976)*, vol. 41, no. 23, pp. 1795–1800, 2016.
- [12] M. Yu, W. K. Zhao, M. Li et al., “Analysis of cervical and global spine alignment under Roussouly sagittal classification in Chinese cervical spondylotic patients and asymptomatic subjects,” *European Spine Journal*, vol. 24, no. 6, pp. 1265–1273, 2015.
- [13] R. Lafage, V. Challier, B. Liabaud et al., “Natural head posture in the setting of sagittal spinal deformity: validation of chin-brow vertical angle, slope of line of sight, and McGregor’s slope with health-related quality of life,” *Neurosurgery*, vol. 79, no. 1, pp. 108–115, 2016.
- [14] Y. Matsubayashi, H. Chikuda, Y. Oshima et al., “C7 sagittal vertical axis is the determinant of the C5–7 angle in cervical

- sagittal alignment,” *The Spine Journal*, vol. 17, no. 5, pp. 622–626, 2017.
- [15] Y. Brink, Q. Louw, K. Grimmer, and E. Jordaan, “The spinal posture of computing adolescents in a real-life setting,” *BMC Musculoskeletal Disorders*, vol. 15, p. 212, 2014.
- [16] G. P. Szeto, L. Straker, and S. Raine, “A field comparison of neck and shoulder postures in symptomatic and asymptomatic office workers,” *Applied Ergonomics*, vol. 33, no. 1, pp. 75–84, 2002.
- [17] K. T. Lau, K. Y. Cheung, K. B. Chan, M. H. Chan, K. Y. Lo, and T. T. Chiu, “Relationships between sagittal postures of thoracic and cervical spine, presence of neck pain, neck pain severity and disability,” *Manual Therapy*, vol. 15, no. 5, pp. 457–462, 2010.

Research Article

Novel Passive Two-Stage Magnetic Targeting Devices for Distal Locking of Interlocking Nails

Tze-Hong Wong,^{1,2} Meng-Shiue Lee,³ Sung-Yueh Wu,^{3,4} Wensyang Hsu,³ Tien-Kan Chung,³ Chia-Pei Wu,³ Pei-Jung Hsu,³ and Yuh-Shyong Yang¹

¹Department of Biological Science and Technology, National Chiao Tung University, Hsinchu 30010, Taiwan

²Department of Orthopedics, National Taiwan University Hospital Hsinchu Branch, Hsinchu 30059, Taiwan

³Department of Mechanical Engineering, National Chiao Tung University, Hsinchu 30010, Taiwan

⁴Additive Manufacturing and Laser Application Center, Additive Manufacturing Innovation Department, Industrial Technology Research Institute, Tainan 73445, Taiwan

Correspondence should be addressed to Wensyang Hsu; whsu@mail.nctu.edu.tw

Received 6 April 2017; Revised 22 June 2017; Accepted 9 July 2017; Published 13 August 2017

Academic Editor: Chia-Ying Lin

Copyright © 2017 Tze-Hong Wong et al. This is an open access article distributed under the Creative Commons Attribution License, which permits unrestricted use, distribution, and reproduction in any medium, provided the original work is properly cited.

Interlocking nailing is a common surgical operation to stabilize fractures in long bones. One of the difficult parts of the surgery is how to locate the position and direction of a screw hole on the interlocking nail, which is invisible to the naked eye after insertion of the nail into the medullary canal. Here, we propose a novel two-stage targeting process using two passive magnetic devices to locate the position and direction of the screw hole without radiation for the locking screw procedure. This involves a ring-shape positioning magnet inside the nail to generate a magnetic field for targeting. From the accuracy test results of these two-stage targeting devices, the search region can be identified in less than 20 seconds by the 1st-stage targeting device, while the total targeting time to locate the drilling position and direction takes less than 4 minutes, with 100% successful rate in 50 attempts. The drilling test further combines the two-stage targeting process and drilling process on the swine tibia, and it is shown that a 100% successful rate is achieved in all 10 attempts, where the total time needed is less than 5 minutes.

1. Introduction

Interlocking nailing, also known as intramedullary nailing, is a common surgical operation to stabilize fractures in long bones [1–5] and is one of the best methods for treating fractures of the lower extremities [6, 7]. The procedure involves the insertion of a hollow nail in the bone medullary canal, which is secured by screws at the proximal and distal ends to prevent the rotation or displacement of the bone after adequate reduction. One of the most difficult parts of the surgery is to find the accurate drilling position and screwing direction for the interlocking screw, which is invisible to the naked eye after the insertion of the nail into the long bone, as shown in Figure 1.

The target-aiming devices based on the parallel mechanism [4, 8–10] have been clinically used, but they often fail to provide an accurate drilling location due to nail distortion during insertion. X-ray imaging is a direct method to locate screw hole orientation through radiological imaging, so-called the free-hand method [11, 12]. Utilizing X-ray-imaging approach, however, exposes surgeons, medical teams, and patients to radioactivity hazard for a considerable dose. To avoid using X-rays, which are harmful to humans, transilluminating [13], sound-guided [10], ultrasonic [14], and magnetic [15, 16] methods were proposed to find the drilling position. However, these methods were unable to locate the exact drilling direction. A magnetic assistant system [17–19] with magnetic sensors was proposed for both

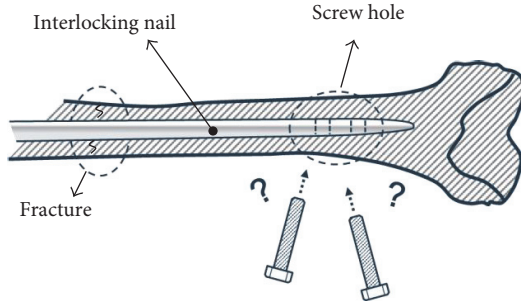


FIGURE 1: Distal locking of interlocking nail.

positioning and directional guidance, but it lacked accuracy and required complicated signal processing.

In this study, a novel two-stage magnetic targeting process with two passive targeting devices is proposed to provide a rapid and accurate method for the distal locking of interlocking nailing without radiation. The 1st-stage targeting device is used to focalize the screw hole area rapidly for the next targeting process. The 2nd-stage targeting device is used to identify accurately not only the position but also the direction of the screw hole of the interlocking nail. Furthermore, a light-based indicator is integrated with the 2nd-stage targeting device to indicate the alignment state during the targeting process in a more intuitive way.

2. Concept Design

To ensure a radiation-free method in the distal locking process for the interlocking nailing operation, passive magnetic sensing is chosen for targeting. It is known that the magnetic field can pass through human tissue without damaging the tissue or undergoing significant distortion, so it is suitable for biomedical applications [17]. To apply magnetic field targeting, the magnetic field from a permanent magnet inside the nail is used as a positioning magnet, where the position and magnetic field direction of the magnet are detected remotely through the magnetic guiding device outside the bone. The positioning magnet is made of neodymium iron boron (NdFeB), which is biocompatible and can provide a strong magnetic field for targeting. The proposed shape of the magnet is cylindrical with a hollow hole at the center, as shown in Figure 2(a); the magnetic field gradient is concentric and uniform around the magnet and the flux lines converge on the center of the magnet. Here, the positioning magnet is placed on the screw hole and the magnetic field direction is aligned with the drilling direction, after which the positioning magnet can determine the drilling position and direction.

2.1. The 1st-Stage Targeting. The 1st-stage targeting device consists of two permanent magnets and a flexible thin film. The two permanent magnets, called targeting magnets, are fixed on the flexible thin film in the same magnetic direction, as shown in Figure 2(b). When a positioning magnet is inside the cylindrical limbs, the targeting magnets are rapidly attracted to the skin surface by the positioning magnet, but two targeting magnets are also repelled each other in static

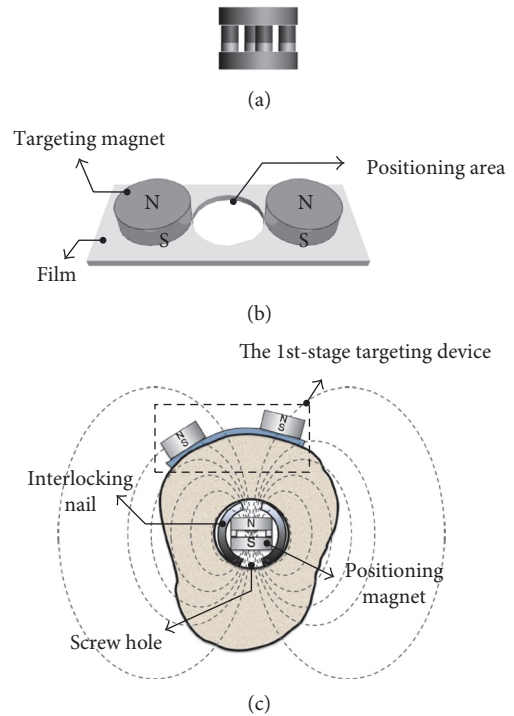


FIGURE 2: Schematic diagrams of (a) the positioning magnet, (b) the 1st-stage targeting device, and (c) the 1st-stage targeting device attracted by the positioning magnet.

equilibrium due to the cylindrical geometric condition, as shown in Figure 2(c). The screw hole area can then be focalized rapidly to a definitive region between the two targeting magnets. An opening between two targeting magnets on the film is designed so that the area can be easily marked for the next targeting stage.

2.2. The 2nd-Stage Targeting. The 2nd-stage targeting device consists of a transparent baseboard with three aligning lines, conductive rings, three magnetic pins with rotary joints, and an indicator, as shown in Figure 3(a). The three symmetrically placed magnetic pins can rotate freely and point to the positioning magnet inside the nail. The three magnetic pins act as three mechanical switches in operation, which are linked to the indicator by conductive rings and used to indicate alignment or misalignment by a light signal. Each magnetic pin can rotate to the strongest gradient direction of the nearby magnetic field from the positioning magnet inside the nail. The magnetic pin has two equal parts with a rotary joint in the middle to eliminate the gravity effect in operation, which can provide a flexible and unrestricted operation method in surgery. The transparent baseboard with three aligning lines provides a clear field of vision to observe the motion of the magnetic pins, which is used to guide the device to rapidly and accurately identify the alignment status. The indicator consists of two light-emitting diodes (LEDs) and a relay with DC voltage through a simple circuit, as shown in Figure 3(b), to indicate the alignment (green light) or misalignment (red light) state directly. The LED signal can help the user to determine alignment state in a more intuitive way.

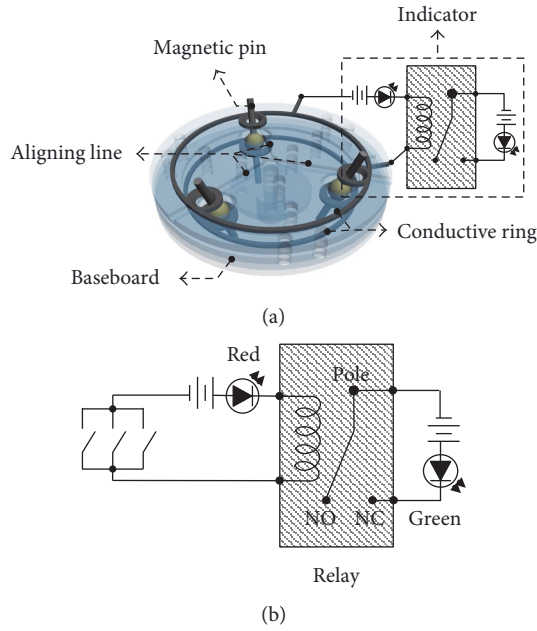


FIGURE 3: Schematic diagram of (a) the 2nd-stage targeting device and (b) equivalent circuit of the 2nd-stage targeting device.

In the proposed design, when the 2nd-stage targeting device misaligns with the positioning magnet either in position or direction, one or more pins will contact with the conductive ring on the transparent baseboard to turn on the red LED, as shown in Figures 4(a) and 4(b), respectively. By moving the guiding device around the positioning area identified by the 1st-stage targeting device, once three magnetic pins reach to symmetrical positions without contacting the conductive ring on the upper transparent baseboard, as shown in Figure 4(c), the green LED instead of red will be switched on. The 2nd-stage targeting device is considered to be aligned with the positioning magnet inside the nail. Then, the drilling process can be performed through the drilling hole at the center of the 2nd-stage targeting device.

The transparent baseboard with alignment lines can provide a clear field of vision to observe the motion of the magnetic pins. When the guiding device aligns with the invisible positioning magnet in the nail, the projection of the three magnetic pins should overlap the aligning lines, as shown in Figure 5(a). When the guiding device misaligns with the magnet either in position or direction, one or more pins will deviate from the aligning line on the transparent baseboard, as shown in Figure 5(b). Then, the adjustment of the device should be continued.

3. Detail Design

Due to the space limit of the interlocking nail, the positioning magnet made of NdFeB (N52, Asia Magnets Co. Ltd.) with a 9 mm outer diameter, a 5 mm inner diameter, and 7 mm high is designed to place into a commercial interlocking nail with inner radius of 10 mm and outer radius of 12 mm. The following designs and tests on the 1st-stage and the 2nd-stage

targeting devices are all based on this positioning magnet. However, the maximum operating temperature of the positioning magnet used in this work should be less than 140°C [20, 21]. Therefore, in the sterilization process of the positioning magnet, the operating temperature should be less than 140°C to main the strength of positioning magnet. For example, some clinical low-temperature sterilization processes, such as EO sterilization, activated glutaraldehyde sterilization, and plasma sterilization, are operating below 140°C.

3.1. The 1st-Stage Targeting Device. For the 1st-stage targeting device, two critical parameters need to be identified: the distance between two targeting magnets (d_m) and the radius of the positioning area (r_m), as shown in Figure 6(a). Here, these two parameters are decided experimentally. The experimental setup consists of the positioning magnet, two targeting magnets, and a semicylinder plate with a radius of 30 mm, as shown in Figure 6(b). The two targeting magnets, with radius of 4.5 mm and thickness of 2 mm, are also made of NdFeB. The semicylinder plate with radius of 30 mm is used to simulate the geometry of the limb. Since the minimum radius of the limb is 16 mm, the working distance between targeting magnet and the positioning magnet would be 16 mm at least. Then, the following steps are performed: (i) fixing the positioning magnet above the center of the semicylinder plate, (ii) placing two targeting magnets on the semicylinder plate, and (iii) measuring the distance between the two targeting magnets. For the working distance of 16 mm, the measured distance between two targeting magnets is in the range of 12 mm to 20 mm. Therefore, 20 mm is chosen to be the distance of two targeting magnets (d_m) on the flexible film. Also, the shortest distance between the edges of two targeting magnets is about 11 mm due to 9 mm diameter of the targeting magnet. Therefore, 5 mm is selected to be the radius of the hollow circle, r_m , for positioning area.

3.2. The 2nd-Stage Targeting Device. For the 2nd-stage targeting device, there will be three symmetrically placed magnetic pins on the transparent baseboard. Therefore, the critical parameter is the location of the pin on the baseboard, that is, the distance from the rotary joint of pin to the center of the board (R_m), as shown in Figure 7(a). Since these three magnetic pins without sufficient distance may rotate due to the magnetic repelling force from each other, the minimum distance between two pins (X_m) without causing rotation needs to be identified first. Once X_m is determined, R_m can be calculated from the basic trigonometry. The transparent baseboard has three layers, as shown in Figure 7(b), where the top layer has three aligning lines and the lower two layers can hold the rotary joint of pin. There is a conductive ring on each layer to form the circuit for the LED indicator. Definitions of other dimensional parameters on the board are also illustrated in Figure 7(b).

The experimental setup to determine X_m includes two magnetic pins on a sliding track. The two magnetic pins made of NdFeB are identical with a length of 25 mm and a radius of 1 mm. First, one of the magnetic pins is fixed on the sliding track and the other pin is also placed on the track but away from the fixed pin, as shown in Figure 8(a). Then,

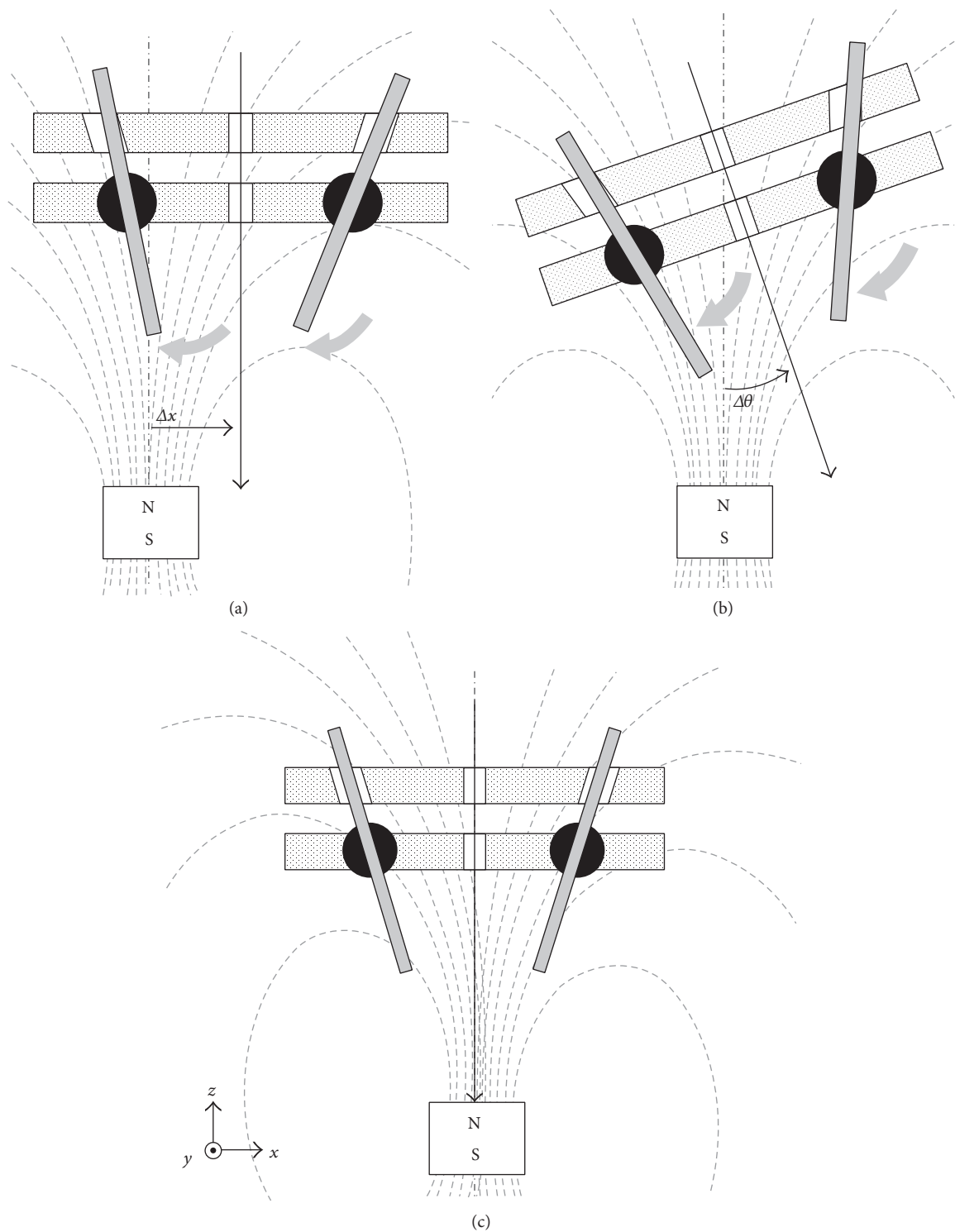


FIGURE 4: Illustrations of the 2nd-stage targeting device: (a) misalignment due to incorrect position for pins to contact with the conductive ring, (b) misalignment due to incorrect direction for pins to contact with the conductive ring, and (c) correct alignment.

the moving magnetic pin is pushed closer to the fixed one until the magnetic pins are affected by each other to have rotation, as shown in Figure 8(b). The measured maximum distance between two magnetic pins to have interference is found to be around 30 mm. Therefore, 31 mm is chosen as the lower limit of X_m . According to the trigonometric

function ($\sqrt{3}R_m = X_m$), 17.90 mm is the lower limit of R_m . Here, 18 mm is chosen to be the dimension of R_m . Other designed dimensions of parameters are listed in Table 1.

Moreover, some orthopedic instruments may contain ferromagnetism material, such as r316 stainless steel. Usually the magnetic strength in orthopedic instruments is lower

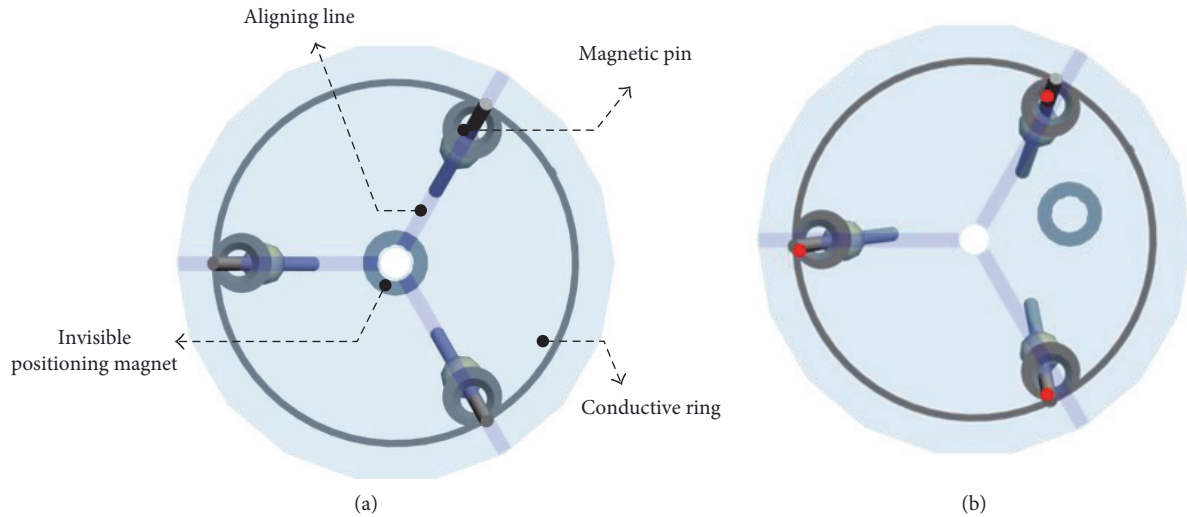


FIGURE 5: Alignment observation through deviation between pins and three aligning lines on the 2nd-stage targeting device: (a) correct alignment and (b) deviation between pins and aligning lines due to incorrect position or direction.

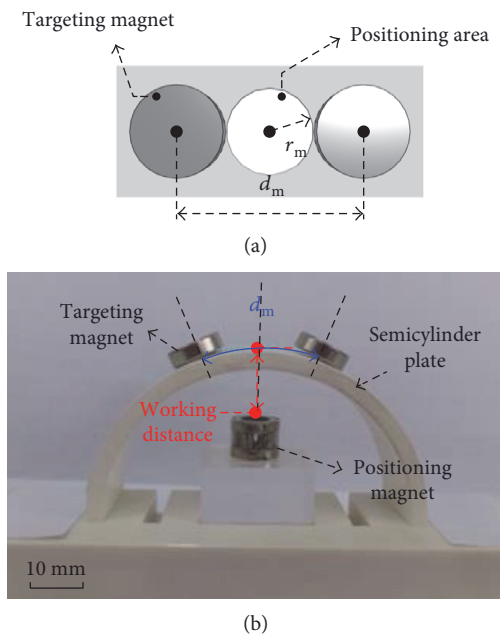


FIGURE 6: Critical dimensions of the 1st-stage targeting device: (a) the distance between two targeting magnets is d_m and the radius of the position area is r_m and (b) experimental setup for determining d_m .

than the permanent magnet. It is suggested that the orthopedic instrument should be away from the device at least 30 mm during the targeting process.

4. Fabrication

Figures 9(a) and 9(b) show the prototypes of the proposed 1st-stage and 2nd-stage targeting devices for this feasibility study, respectively. The 1st-stage targeting device consists of two targeting magnets on a flexible thin film with a hollow

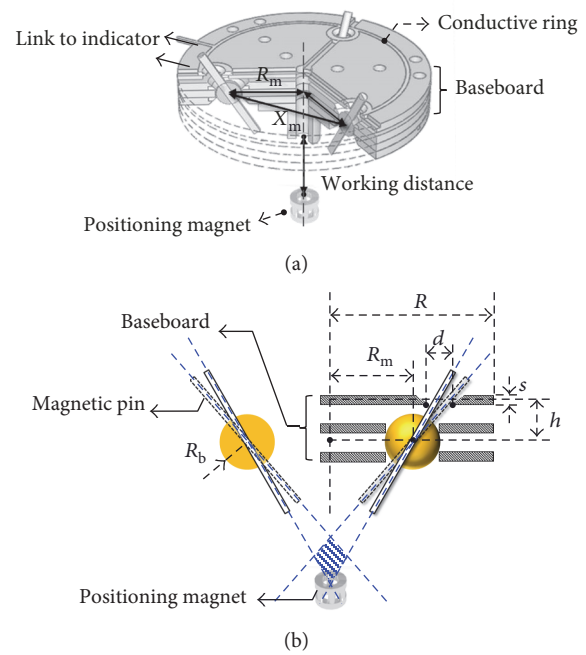


FIGURE 7: Illustrations of parameters in the 2nd-stage targeting device: (a) the distance from the board center to the rotary joint of magnetic pin (R_m) and the distance between two magnetic pins (X_m) and (b) other related parameters.

positioning area. The targeting magnets are made of NdFeB, and the flexible thin film is made of a 0.8 mm thick PET film. The 2nd-stage targeting device consists of three magnetic pins with rotary joints, a transparent baseboard with three conductive rings, and an indicator. The three layers to form the transparent baseboard are made of acrylic with a drilling hole and a conductive ring on each layer. On the top layer of the baseboard, there are three aligning lines, as shown in Figure 9(b). The three magnetic pins and rotary joints are

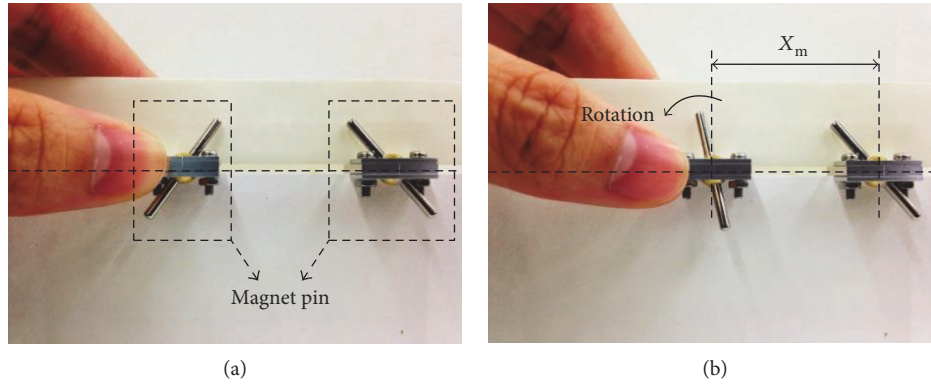


FIGURE 8: Experimental setup to determine X_m : (a) initial state and (b) insufficient distance between two magnetic pins to cause interference.

TABLE 1: Dimensions of the 2nd-stage targeting device.

Description	Parameter	Design size (mm)
The radius of the 2nd-stage targeting device	R	30
The thickness of each layer of the baseboard	s	2
The vertical distance between rotary joint and the baseboard	h	5
The radius of rotary joint of the magnetic pin	R_b	3
The distance from the rotary joint of pin to the center of the board	R_m	18
The diameter of the hole on the conductive ring	d	3.8

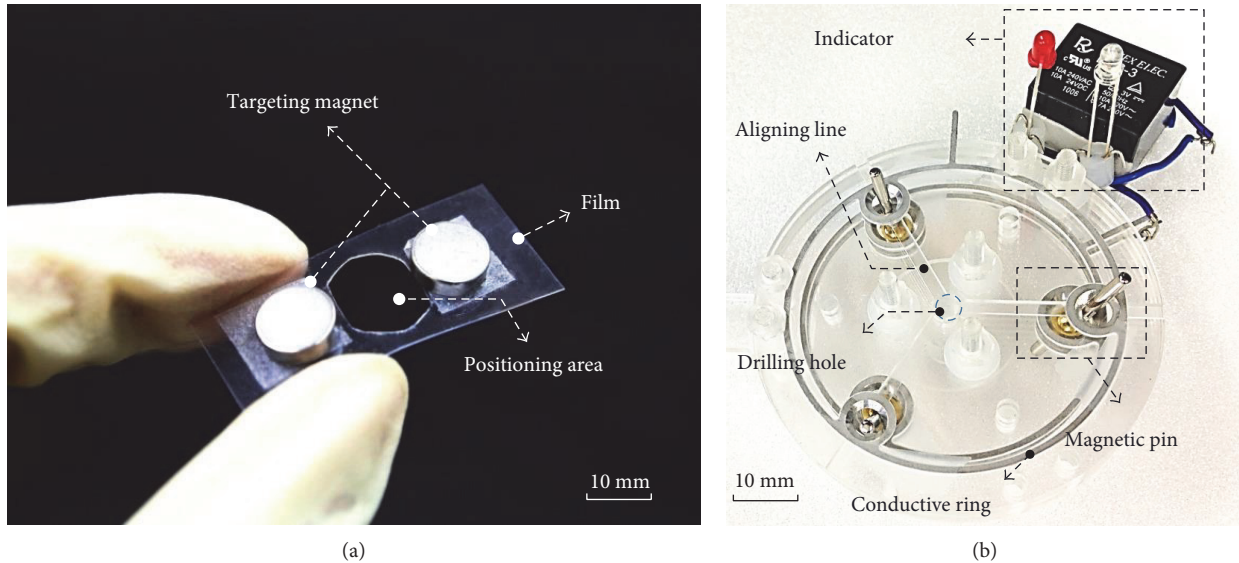


FIGURE 9: Photos of fabricated (a) 1st-stage targeting device and (b) 2nd-stage targeting device.

made of NdFeB and Cu, respectively, and the rotary joint is assembled at the center of the pins.

5. Testing Results and Discussion

5.1. Accuracy Test of the 1st-Stage Targeting Device. The measurement setup to test the accuracy of the 1st-stage targeting device is shown in Figure 10, where the 1st-stage targeting device is placed on a semicylinder plate with a graph paper

on it. The semicylinder plate having a 30 mm radius is used to simulate the curved shape of limbs. The positioning magnet is placed right beneath the middle of the curved plate. The test procedure involves the following three steps: (i) adjusting the working distance of the positioning magnet at a specified value, (ii) placing the 1st-stage targeting device on the semicylinder plate, and (iii) measuring the discrepancy distance between the center of the 1st-stage targeting device and the projected location of the positioning magnet

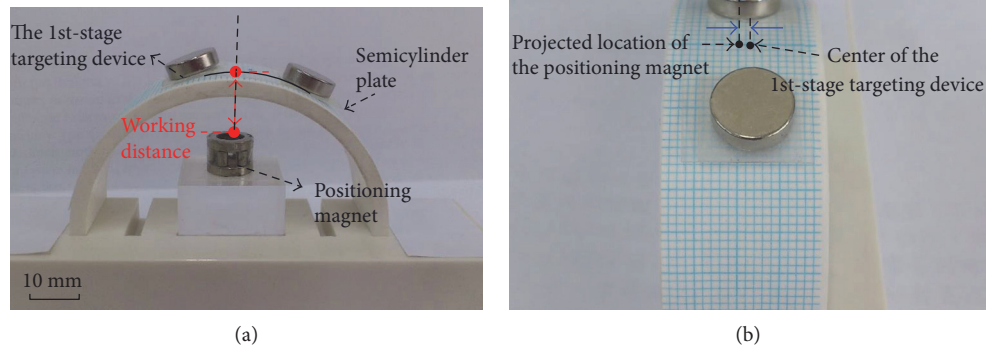


FIGURE 10: Measurement setup for the accuracy test of the 1st-stage targeting. (a) Side view and (b) top view.

on the graph paper, as shown in Figure 10(b). The working distance is tested at 16 mm, 17 mm, 18 mm, 19 mm, and 20 mm. At each working distance, the measurement is conducted three times, and the maximum discrepancy for different working distances is 1.9 mm, 2.5 mm, 1.8 mm, 2.0 mm, and 1.6 mm, respectively, as shown in Figure 11. The testing results show that the accuracy of the 1st-stage targeting is 2.5 mm, which confirms that a hollow positioning area with a 5 mm radius is sufficient.

5.2. Accuracy Test of the 2nd-Stage Targeting Device. There are two kinds of tests, translational and angular accuracy tests, to examine the guiding accuracy of the 2nd-stage targeting device on position and direction. The indicator with two LEDs is used to indicate the alignment (green light) or misalignment (red light) state directly. For the translational accuracy test, the positioning magnet is fixed on a ruler, as shown in Figure 12(a), where the 2nd-stage targeting device is placed opposite down and the ruler with the positioning magnet is above the 2nd-stage targeting device with different working distances. The translational accuracy test involves following three steps: (i) adjusting the working distance of the positioning magnet at a specified value, (ii) adjusting the horizontal distance (X_p) between the positioning magnet and the projection location of the 2nd-stage targeting device, and (iii) recoding the state of the 2nd-targeting device by the indicator in each locations. For the angular accuracy test, the positioning magnet is fixed on a rotation table, as shown in Figure 12(b), where the 2nd-stage targeting device is also placed opposite down and the rotation table with the positioning magnet is above the 2nd-stage targeting device. The test process involves following three steps: (i) adjusting the working distance of the positioning magnet at a specified value, (ii) adjusting the angle of the position magnet by turning the rotation table, and (iii) recoding the aligned or misaligned state of the 2nd-stage targeting device by the indicator at each angle.

The experimental results on translational and angular accuracy tests are shown in Figures 13(a) and 13(b), respectively. The working distance is also tested at 16 mm, 17 mm, 18 mm, 19 mm, and 20 mm. It is found that detection

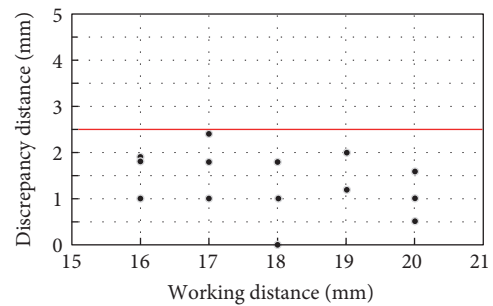


FIGURE 11: Accuracy test results on the 1st-stage targeting device.

accuracy for alignment in position is ± 2.1 mm and in direction is ± 7 degrees.

5.3. Two-Stage Targeting Test and Positioning Time Measurement. The two-stage targeting test combines the 1st-stage targeting process with the 2nd-stage targeting process to examine the successful rate and the time required for the whole targeting procedure. The positioning magnet is fixed on the screw hole of the nail to provide a magnetic field for targeting tests, as shown in Figure 14(a), and then, the nail with the positioning magnet is inserted into a transparent model bone. In the tests, the transparent model bone is covered by a paper barrier to ensure that the screw hole of the nail is invisible to the user. The 1st-stage targeting device then is placed on the barrier and moved around to find the location that the 1st-stage targeting device could be attracted on the paper barrier by the positioning magnet. After that, the positioning area is marked through the hollow circle on the 1st-stage target device, as shown in Figure 14(b). When the aiming direction is close to be horizontal, the 1st-stage targeting device may not stay on the surface due to the gravity. Therefore, the patient's pose needs to be adjusted to be more vertical in the 1st-stage targeting process. For the 2nd-stage targeting process, the 2nd-stage targeting device is moved around the positioning area identified by the 1st-stage targeting process. Before reaching the aligned state, the red LED is on, as shown in Figure 14(c). Once the device reached the aligned state, the green LED instead of the red

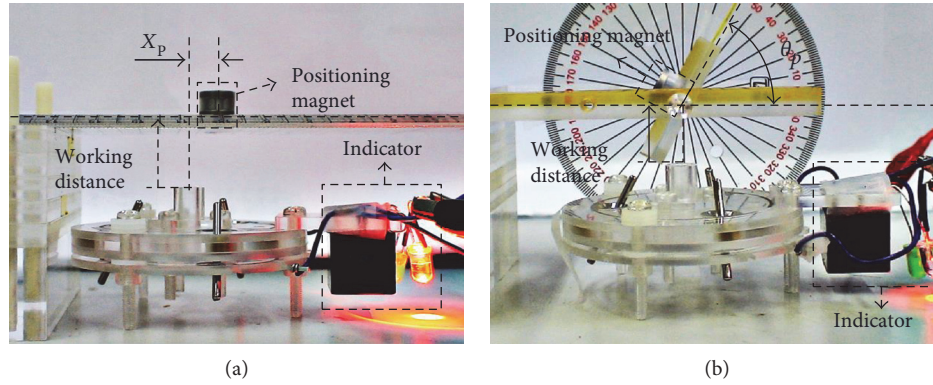


FIGURE 12: Measurement setup of the 2nd-stage targeting device for (a) translational and (b) angular accuracy tests.

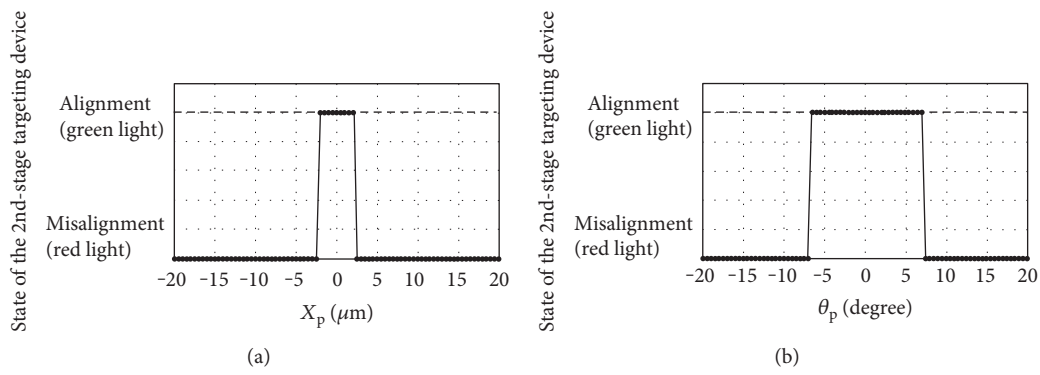


FIGURE 13: Experimental results of the 2nd-stage targeting device from the (a) translational and (b) angular accuracy tests.

one is on, as shown in Figure 14(d). In order to check the above targeting process is successful or not, a laser pointer is mounted on the drilling hole of the 2nd-stage targeting device. By moving the paper barrier away and turning on the laser pointer, when the alignment is truly achieved, the laser light should pass through the transparent model bone and the screw hole on the nail to the other side where a mirror is placed, as shown in Figure 14(e).

The two-stage targeting tests are conducted by two different persons with 25 attempts each, and 100% successful rate is achieved in all these 50 attempts. The time to finish the 1st-stage and the 2nd-stage targeting process is between 10–20 seconds and 29–215 seconds, respectively. The total time needed in the entire two-stage targeting process is between 43–230 seconds, less than 4 minutes.

Since the influence of gravity has been considered in the design of the 2nd-stage targeting device by using symmetrical magnetic pins with the rotary joints at the middle, the moment due to gravity on the magnetic pin can be balanced. Therefore, in the 2nd-stage targeting tests, even the aiming directions are randomly selected from horizontal to vertical directions, the successful rate still can reach 100% to verify that the gravity effect does not affect the accuracy at the 2nd-stage targeting process.

5.4. Drilling Test on a Swine Tibia. In order to further verify that the proposed targeting devices can successfully identify

the drilling position and direction, a drilling test on a swine tibia is also performed after the two-stage targeting process. The nail with the positioning magnet is inserted into the medullary cavity of the swine tibia, and the screw hole of the nail becomes invisible. The 1st-stage targeting is performed to find the positioning area for the 2nd-stage targeting process, as shown in Figure 15(a). In the 2nd-stage targeting process, before reaching the aligned state, the red LED is on, as shown in Figure 15(b). Once the aligned state is achieved, the green LED is on instead of red, as shown in Figure 15(c). Then, a powered drill with a 20 cm long drill bit is mounted on the drilling hole at the center of the transparent baseboard to successfully drill through the bone and the screw hole on the nail, as shown in Figure 15(d).

The two-stage targeting with drilling tests is conducted by two different persons with five attempts each, and 100% successful rate is achieved in all these 10 attempts. The time to finish the 1st-stage targeting process, the 2nd-stage targeting process, and the drilling process is between 7–11 seconds, 29–215 seconds, and 38–40 seconds, respectively, as listed in Table 2. The total time used in the entire process is between 95–300 seconds, less than 5 minutes.

6. Conclusions

Here, a novel two-stage magnetic targeting process with two passive targeting devices is proposed to provide a

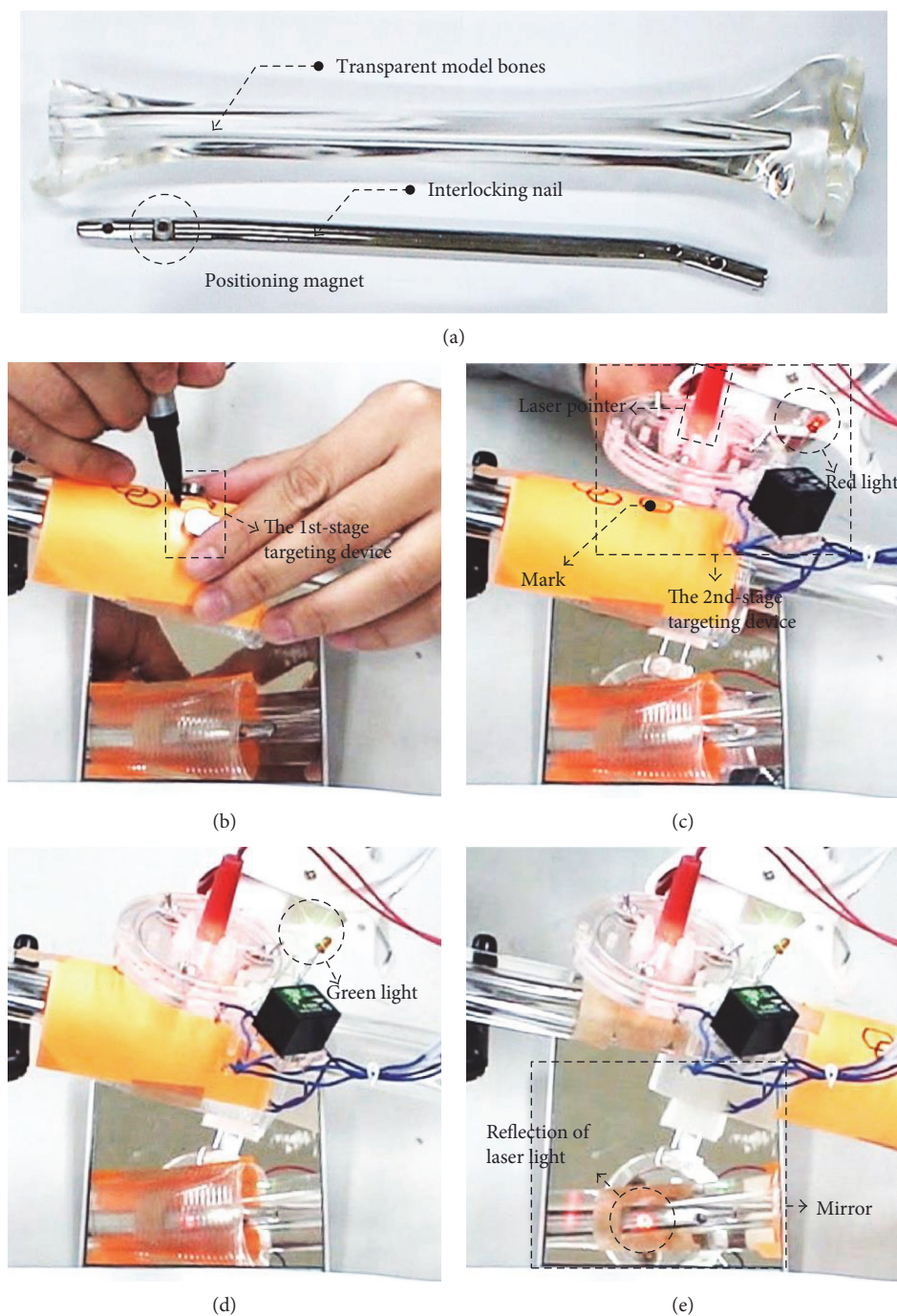


FIGURE 14: The two-stage targeting test on a transparent model bone. (a) A transparent model bone and a commercial interlocking nail with a positioning magnet fixed on the screw hole. (b) The 1st-stage targeting process. (c) The 2nd-stage targeting process in a misaligned state with red LED on. (d) The 2nd-stage targeting process in an aligned state with green LED on. (e) The paper barrier is moved away. Laser light successfully passes through the transparent model bone and the screw hole to the mirror to verify the success of the two-stage targeting process.

rapid, accurate, and secure method for the distal locking of interlocking nailing without radiation. The 1st-stage targeting device is used to focalize rapidly the screw hole area for the 2nd-stage targeting process. The 2nd-stage targeting device can accurately identify both the position and direction of the screw hole. From the accuracy tests, the experimental results show that alignment accuracy of the proposed 2nd-

stage targeting device in position is ± 2.1 mm and in direction is ± 7 degrees. The results from the two-stage targeting tests show that the successful rate is 100% in 50 attempts. The time to finish the 1st-stage and the 2nd-stage targeting process is between 10–20 seconds and 29–215 seconds, respectively. The total time in the entire targeting process is less than 4 minutes. From the results of the drilling test on the swine

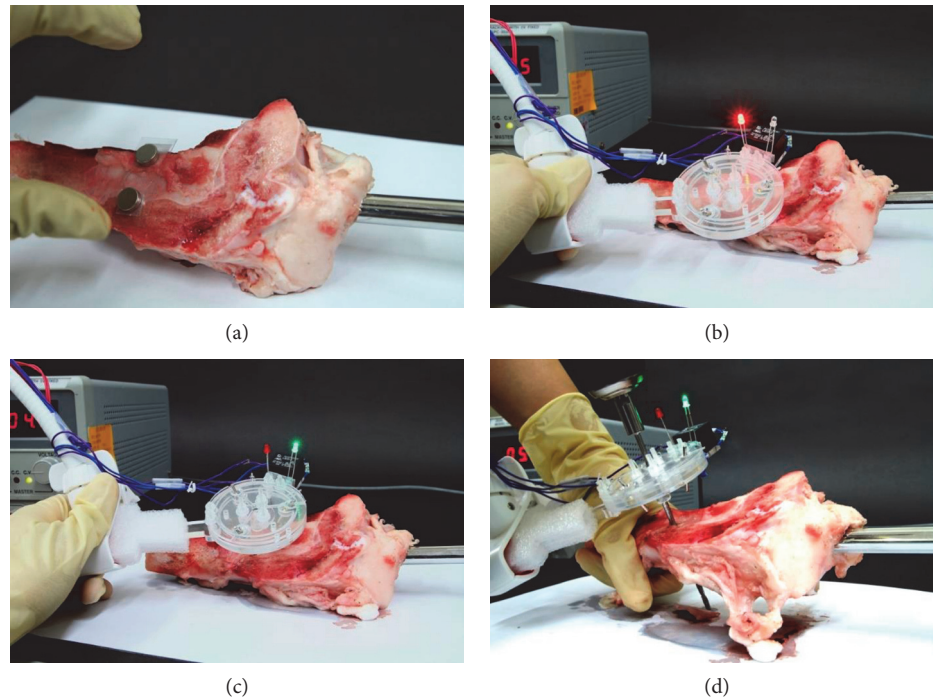


FIGURE 15: The drilling test with a swine tibia: (a) the 1st-stage targeting, (b) the 2nd-stage targeting process in misalignment state with red LED on, (c) the 2nd-stage targeting in alignment state with green LED on, and (d) successfully drilling through the screw hole of the interlocking nail inside the swine tibia.

TABLE 2: Time used in the drilling tests.

	The 1st-stage targeting	The 2nd-stage targeting	Drilling	Total
Time (seconds)	7–11	91–251	38–40	95–300

tibia, 100% successful rate is achieved in all 10 attempts. The total time to finish the 1st-stage targeting process, the 2nd-stage targeting process, and the drilling process is less than 5 minutes. With the proposed targeting process and devices, the user could easily identify the alignment state in an intuitive way by direct observation through the transparent baseboard and the light-based indicator. The feasibility of the proposed two-stage passive targeting procedure to locate the screw hole position and orientation is successfully demonstrated. It is shown to be a time-saving, accurate, and radioactivity-free method in interlocking nailing with great potential on clinical purposes.

However, the proposed devices can be further improved, such as the working distance. Currently, the maximum working distance is around 20 mm, which may be sufficient for nailing surgery with thin soft tissue, such as tibia nailing, but not enough for nailing surgery with thick soft tissue, such as femoral nailing. In order to cover all cases in lower limb intramedullary nailing, the working distance of device needs to be further enhanced, such as using a stronger position magnet (a bigger position magnet or a magnet with a better magnetic material) or reducing the friction at the joints of magnetic pins to allow smaller magnetic force to rotate the pins.

Conflicts of Interest

The authors declare that there are no conflicts of interest regarding the publication of this paper.

Acknowledgments

The authors would like to acknowledge the grant (HCH103-034) supported by the National Chiao Tung University and National Taiwan University Hospital Hsinchu Branch.

References

- [1] B. K. Moor, M. Ehlinger, and Y. Arlettaz, "Distal locking of femoral nails. Mathematical analysis of the appropriate targeting range," *Orthopaedics & Traumatology: Surgery & Research*, vol. 98, no. 1, pp. 85–89, 2012.
- [2] G. Anastopoulos, P. G. Ntagiopoulos, D. Chissas, A. Papaeliou, and A. Asimakopoulos, "Distal locking of tibial nails," *Clinical Orthopaedics and Related Research*, vol. 466, no. 1, pp. 216–220, 2008.
- [3] G. C. Babis, I. S. Benetos, A. B. Zoubos, and P. N. Soucacos, "The effectiveness of the external distal aiming device in intramedullary fixation of tibial shaft fractures," *Archives of Orthopaedic and Trauma Surgery*, vol. 127, no. 10, pp. 905–908, 2007.
- [4] Z. Gugala, A. Nana, and R. W. Lindsey, "Tibial intramedullary nail distal interlocking screw placement: comparison of the free-hand versus distally-based targeting device techniques," *Injury*, vol. 32, pp. 21–25, 2001.

- [5] A. Baltov, R. Mihail, and E. Dian, "Complications after interlocking intramedullary nailing of humeral shaft fractures," *Injury*, vol. 45, pp. S9–S15, 2014.
- [6] M. Bråten, P. Helland, T. Grøntvedt, A. Aamodt, P. Benum, and A. Mølster, "External fixation versus locked intramedullary nailing in tibial shaft fractures: a prospective, randomised study of 78 patients," *Archives of Orthopaedic and Trauma Surgery*, vol. 125, no. 1, pp. 21–26, 2005.
- [7] J. Christie and M. M. McQueen, "Closed intramedullary tibial nailing. Its use in closed and type I open fractures," *Bone & Joint Journal*, vol. 72, no. 4, pp. 605–611, 1990.
- [8] S. Tyropoulos and C. Garnavos, "A new distal targeting device for closed interlocking nailing," *Injury*, vol. 32, no. 9, pp. 732–735, 2001.
- [9] K. M. Abdslam and F. Bonnaire, "Experimental model for a new distal locking aiming device for solid intramedullary tibia nails," *Injury*, vol. 34, no. 5, pp. 363–366, 2003.
- [10] M. Y. Lee, C. H. Kuo, and S. S. Hung, "Implementation of a sound-guided navigation system for tibial closed interlocking nail fixations in orthopedics," *Journal of Medical and Biological Engineering*, vol. 24, pp. 147–154, 2004.
- [11] R. J. Medoff, "Insertion of the distal screws in interlocking nail fixation of femoral shaft fractures. Technical note," *The Journal of Bone and Joint Surgery (American Volume)*, vol. 68, no. 8, pp. 1275–1277, 1986.
- [12] D. Pennig and E. Brug, "Insertion of distal screws in interlocking nailing using a new free-hand control device," *Der Unfallchirurg*, vol. 92, no. 7, pp. 331–334, 1989.
- [13] W. Chu, J. Wang, S. T. Young, and W. C. Chu, "Reducing radiation exposure in intra-medullary nailing procedures: intra-medullary endo-transilluminating (iMET)," *Injury*, vol. 40, no. 10, pp. 1084–1087, 2009.
- [14] Y. Ikeda, S. Kobashi, K. Kondo, and Y. Hata, "Fuzzy ultrasonic array system for locating screw holes of intramedullary nail," in *2007 IEEE International Conference on Systems, Man and Cybernetics*, pp. 3428–3432, Montreal, Que., Canada, October 2007.
- [15] T. K. Chung, H. J. Chu, T. H. Wong et al., "An electromagnetic-induction approach for screw-hole targeting in interlocking-nail surgery," in *2012 IEEE Sensors*, pp. 1–4, Taipei, Taiwan, October 2012.
- [16] T. H. Wong, T. K. Chung, T. W. Liu et al., "Electromagnetic/magnetic-coupled targeting system for screw-hole locating in intramedullary interlocking-nail surgery," *IEEE Sensors Journal*, vol. 14, no. 12, pp. 4402–4410, 2014.
- [17] M. Rigoberto and M. Arturo, "Assistant system for locking intramedullary nails used to repair fractures of the long bones," in *2007 4th International Conference on Electrical and Electronics Engineering (ICEEE)*, pp. 65–67, Mexico City, Mexico, September 2007.
- [18] M. R. Martinez and M. A. Minor, "A system for distal fixation of intramedullary nails," *International Journal of Applied Electromagnetics and Mechanics*, vol. 32, no. 1, pp. 21–30, 2010.
- [19] M. S. Lee, S. Y. Wu, T. H. Wong, W. Hsu, and T. K. Chung, "A novel guiding device for distal locking of intramedullary nails," in *2012 IEEE Sensors*, pp. 1–4, Taipei, Taiwan, October 2012.
- [20] M. S. Walmer, C. H. Chen, and M. H. Walmer, "A new class of Sm-TM magnets for operating temperatures up to 550/spl deg/C," *IEEE Transactions on Magnetics*, vol. 36, no. 5, pp. 3376–3381, 2000.
- [21] O. Gutfleisch, M. A. Willard, E. Brück, C. H. Chen, S. G. Sankar, and J. P. Liu, "Magnetic materials and devices for the 21st century: stronger, lighter, and more energy efficient," *Advanced Materials*, vol. 23, no. 7, pp. 821–842, 2011.

Research Article

Hollow Abutment Screw Design for Easy Retrieval in Case of Screw Fracture in Dental Implant System

Bo Kyun Sim,¹ Bongju Kim,¹ Min Jeong Kim,¹ Guk Hyun Jeong,¹ Kyung Won Ju,¹
Yoo Jin Shin,¹ Man Yong Kim,¹ and Jong-Ho Lee²

¹Clinical Translational Research Center for Dental Science, Seoul National University Dental Hospital, Seoul, Republic of Korea

²Department of Oral and Maxillofacial Surgery, School of Dentistry, Seoul National University, Seoul, Republic of Korea

Correspondence should be addressed to Man Yong Kim; dentykim@gmail.com and Jong-Ho Lee; leejongh@snu.ac.kr

Received 3 March 2017; Revised 19 June 2017; Accepted 22 June 2017; Published 6 August 2017

Academic Editor: Rui Zhu

Copyright © 2017 Bo Kyun Sim et al. This is an open access article distributed under the Creative Commons Attribution License, which permits unrestricted use, distribution, and reproduction in any medium, provided the original work is properly cited.

The prosthetic component of dental implant is attached on the abutment which is connected to the fixture with an abutment screw. The abutment screw fracture is not frequent; however, the retrieval of the fractured screw is not easy, and it poses complications. A retrieval kit was developed which utilizes screw removal drills to make a hole on the fractured screw that provides an engaging drill to unscrew it. To minimize this process, the abutment screw is modified with a prefabricated access hole for easy retrieval. This study aimed to introduce this modified design of the abutment screw, the concept of easy retrieval, and to compare the mechanical strengths of the conventional and hollow abutment screws by finite element analysis (FEA) and mechanical test. In the FEA results, both types of abutment screws showed similar stress distribution in the single artificial tooth system. A maximum load difference of about 2% occurred in the vertical load by a mechanical test. This study showed that the hollow abutment screw may be an alternative to the conventional abutment screws because this is designed for easy retrieval and that both abutment screws showed no significant difference in the mechanical tests and in the FEA.

1. Introduction

Placement of dental implants has become the main treatment option for oral function recovery in partially or completely edentulous patients. The components of a dental implant consist of fixture, abutment, and abutment screws.

Despite the high success rate of implants, it is not free of complications and dental implants occasionally fail due to biological factors or technical complications [1, 2]. The technical problems of implant-based restoration components including abutment screw fracture and peri-implantitis are deeply related to dental implant system failure, and an increase in related complications are also being reported [3–5]. Many studies have reported that after osseointegration of the implant, abutment screw loosening and fracture are the most common problems, and

other mechanical problems involve prosthesis fracture and overdenture attachments [6, 7]. One study reported that the incidence rate of screw fracture is 3.9% which is normally due to overload or elevated torque [6, 8]. If the abutment screw fractures, the screw must be removed and replaced with a new one so that implant prosthesis may be fabricated again. Otherwise, it will compromise the long-term success of the implant [9].

Majority of implant failures nowadays are caused by mechanical factors rather than the implant itself, and so, there are alternative abutment systems that were developed. Only a few studies on the removal of fractured screw in the implant [10, 11] were reported. Many techniques and methods were shown through case reports which all concluded that removing the fractured screw from an implant can be difficult and that there is no

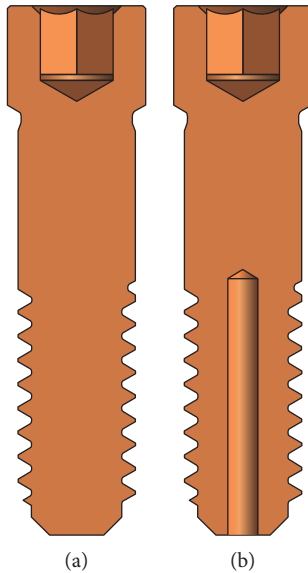


FIGURE 1: Abutment screw design. (a) Conventional type. (b) Hollow type.

universal method that can be applied. Therefore, the abutment screw was modified to have a prefabricated access hole for easy retrieval when the abutment screw fractures. The purpose of this study was to introduce this modified design of the abutment screw, the concept for easy retrieval with this new innovative design, and to compare the mechanical strengths of the conventional abutment screws and the modified version with prefabricated access holes.

2. Materials and Method

2.1. Hollow Abutment Screw Design for Easy Retrieval. Conventional abutment screw measures 2 mm in diameter, 7.8 mm in length, and 0.4 mm in screw thread pitch (Figure 1(a)), and the hollow abutment screw was made with the same system as the conventional abutment screw but modified by creating a hole of 0.5 mm in diameter from the lower end of the abutment screw up to the 1st thread (Figure 1(b)).

For easy retrieval of the fractured screw of the hollow type screw (modified with prefabricated access hole), the hole was fabricated with a reverse screw drill. The reversed screw was tightened with the screw driver allowing stabilization of the fractured portion, and the external thread would be unscrewed from the fixture.

2.2. Mechanical Test and Finite Element Analysis. 3D implant system models were constructed using Solidworks 2016 (Dassault Systèmes) for this study. Mechanical test was performed on the conventional abutment screw and the hollow abutment screw by fabricating 3D models, and finite element analysis (FEA) was implemented to the single artificial tooth system model.

MTS Bionix 370.02 (MTS Systems Co., USA) was used for the vertical load test to compare the mechanical strength of the conventional abutment screw and the hollow abutment screw. Before the vertical load test, the abutment screw was fixed on the jig vertically by applying 30 N·cm of insertion torque (Figure 2(a)) [12]. The experiment was performed with a load speed of 5 mm per minute where it was fixed on the equipment (Figure 2(b), $N = 3$, independent experiments).

IS II Active Implant System (NeoBiotech Co., Korea) was used in fabricating the 3D model of the single implant system design (Figure 1). The bone model height is 17 mm, the width is 30 mm, and bucco-lingual thickness is 13 mm and consisted of a 1.5 mm layer of the cortical region. The height of the crown is 9 mm with the diameter of 12 mm, and it was modeled in a flat form (Figure 3).

Hypermesh version 14 (Altair Engineering Inc., USA) was used to construct the model for FEA (Figure 3), and FEA was performed using Abaqus 6.16 (Dassault Systèmes, France).

The values assumed for the modulus of elasticity and Poisson's ratio are given in Table 1, and the nodes and elements are shown in Table 2. All materials used in the models were considered to be isotropic, homogenous, and linear elastic. Boundary fixation included restraints for all six degrees of freedom including rotation and translation in three coordinate axes for the correspondent nodes located at the bottom and both sides of the bone model including the cancellous bone. Various sizes of masticatory force are being reported; however, this study conducted FEA on two types of load (500 N vertical load and 142 N horizontal load) with the concentrated load on the center of the upper artificial prosthesis [13].

2.3. Statistical Analysis. Sample sizes were estimated for comparison of two groups based on previous study (total sample sizes = 7, [14]). The experimental result was based on three repeated measurements under the same loading condition independently (1 set, conventional, and hollow type, $n = 3$, resp.).

All data are presented as means \pm SD of independent recordings. Statistical analyses were performed by unpaired two-tailed t -test (SigmaPlot, Systat Software Inc., San Jose, CA, USA). $P < 0.05$ was considered significant.

3. Results and Discussion

Hollow abutment screw eliminates the usage of a commercially available screw retrieval kit which was developed to utilize screw removal drills to make a hole on the fractured screw which provides an engaging drill to unscrew it. Hence, the fractured screw could be easily removed using the H-file (Figure 4).

In the vertical load mechanical test, maximum compressive load did not show significant difference between the conventional and the hollow abutment screws



FIGURE 2: Example of mechanical test. (a) Fixed abutment screw on the jig by applying insertion torque. (b) Vertical loading.

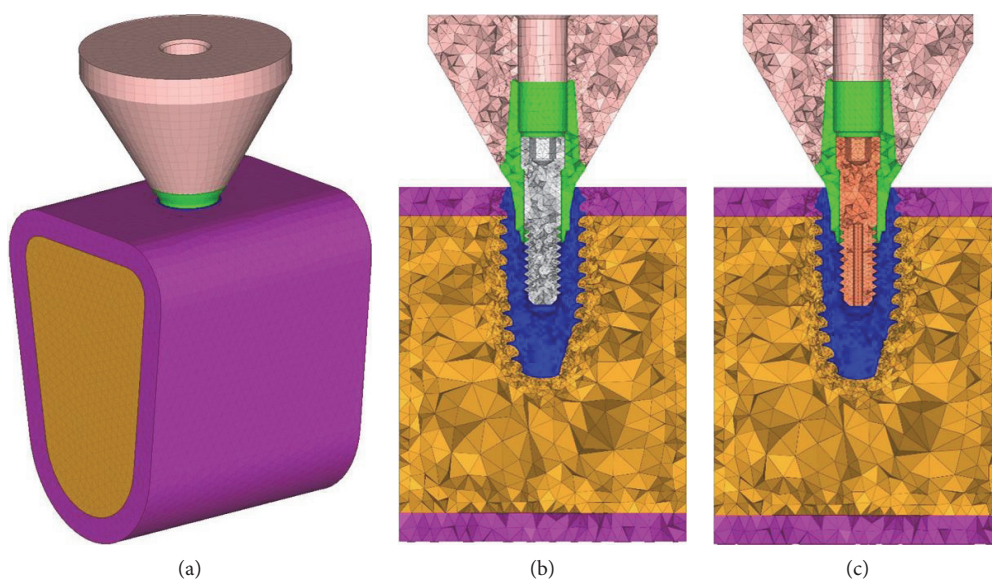


FIGURE 3: 3D finite element model. (a) Constructed 3D model, (b) conventional type, and (c) hollow type.

(Table 3, Figure 5). Table 4 shows the maximum von Mises stress occurred in the abutment screws of each type by vertical and horizontal load in a single artificial tooth system. For the vertical load, approximately 19.68 MPa higher von Mises stress value was observed in the conventional abutment screw, where the value was 116.16 MPa for the conventional type and 96.48 MPa for the hollow type. Both the conventional and hollow abutment screws showed similar stress distribution in the single artificial teeth system (Figure 6). For the horizontal load, von Mises stress value was higher in the hollow type screw by

approximately 4.66 MPa, where the value was 110.99 MPa for the conventional type screw and 106.33 MPa for the hollow type screw. Similar stress distribution was observed as well as for the horizontal load (Figure 7).

As this experiment does not provide a standard for strength evaluation of the abutment screw, it was performed according to the ASTM standard (ASTM F543—standard specification and test methods for metallic medical bone screws) on metallic bone screw, and the experiment was performed with only the abutment screw. Thereafter, strength evaluation of the conventional and the hollow abutment

TABLE 1: Material properties.

Components	Material	Elasticity (Gpa)	Poisson's ratio
Crown	Zirconia	260	0.28
Abutment			
Fixture	Ti alloy	113.8	0.342
Abutment screw			
Cortical bone	Cortical bone	14.0	0.3
Cancellous bone	Cancellous bone	1.5	0.45

TABLE 2: Number of elements and nodes.

Components	Elements		Nodes	
	Conventional	Hollow	Conventional	Hollow
Crown	29,614		6441	
Abutment	6242		1868	
Fixture	5441		13,307	
Cortical bone	32,916		8633	
Cancellous bone	149,721		31,303	
Abutment screw	26,792	14,513	5963	3667

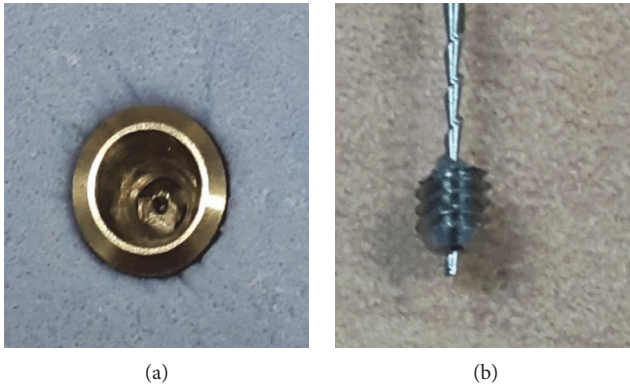


FIGURE 4: (a) Abutment screw fracture on the hollow abutment screw. (b) Hollow abutment screw is easily retrieved with the H-file.

TABLE 3: Mechanical test parameters of two different types of abutment screws, $n = 9$, respectively.

Direction	Type	Value	Max load (N)	Displacement at max load (mm)
Vertical	Conventional	Ave.	1452.27	0.25
		SD	256.10	0.04
	Hollow	Ave.	1480.37	0.35
		SD	137.90	0.05

No significant difference between the two groups ($P > 0.05$).

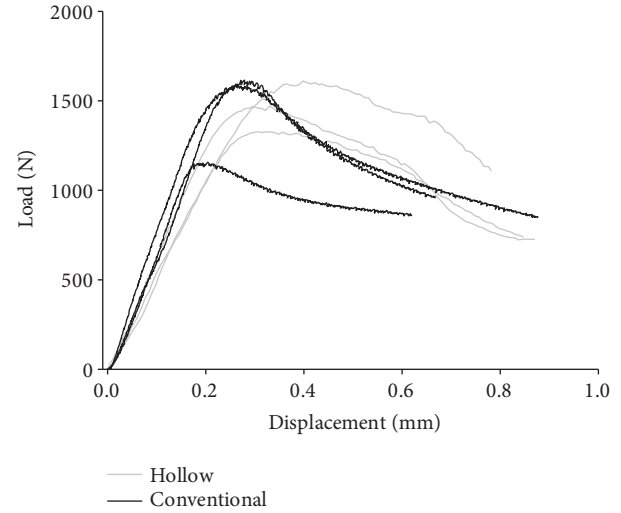


FIGURE 5: Load-displacement curve of abutment screws.

TABLE 4: Finite element analysis results of two different types of abutment screw forms: vertical load and horizontal load.

Load	Type	von Mises stress (MPa)
Vertical	Conventional	116.16
	Hollow	96.48
Horizontal	Conventional	110.99
	Hollow	106.33

screws was performed with a mechanical test, and the maximum load difference of about 2% occurred in the vertical load.

In the mechanical test of the three specimens, there were differences depending on the specimens' processing conditions. However, all three specimens showed similar load form, and it was considered that not much difference was observed in the conventional and hollow abutment screws.

In this study, the compressive strength test and FEA were performed to compare the physical performance of the conventional type and the hollow type abutment screws. However, since the physical performance on fatigue loading is important, it is necessary to test and verify the fatigue of the screw in future studies in the actual implant system.

4. Conclusion

Management of fractured abutment screw is clinically challenging and timely but it is necessary to provide an adequate rehabilitation plan. This study showed that the hollow abutment screw may be an alternative to the conventional abutment screws because this is designed for easy retrieval and that both abutment screws showed no significant difference in the mechanical tests and in FEA.

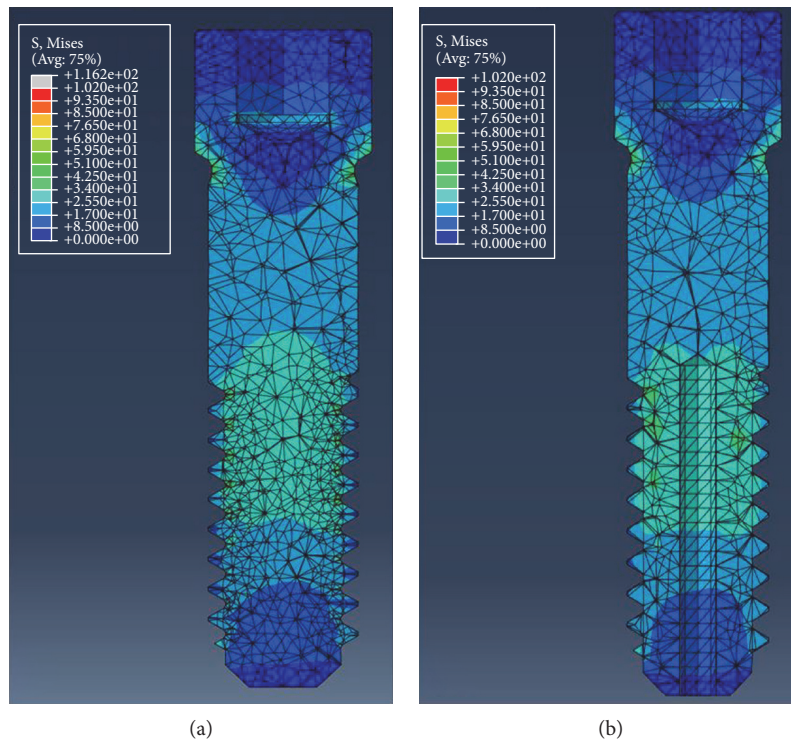


FIGURE 6: von Mises stress distribution under vertical loading condition. (a) Conventional abutment screw. (b) Hollow abutment screw.

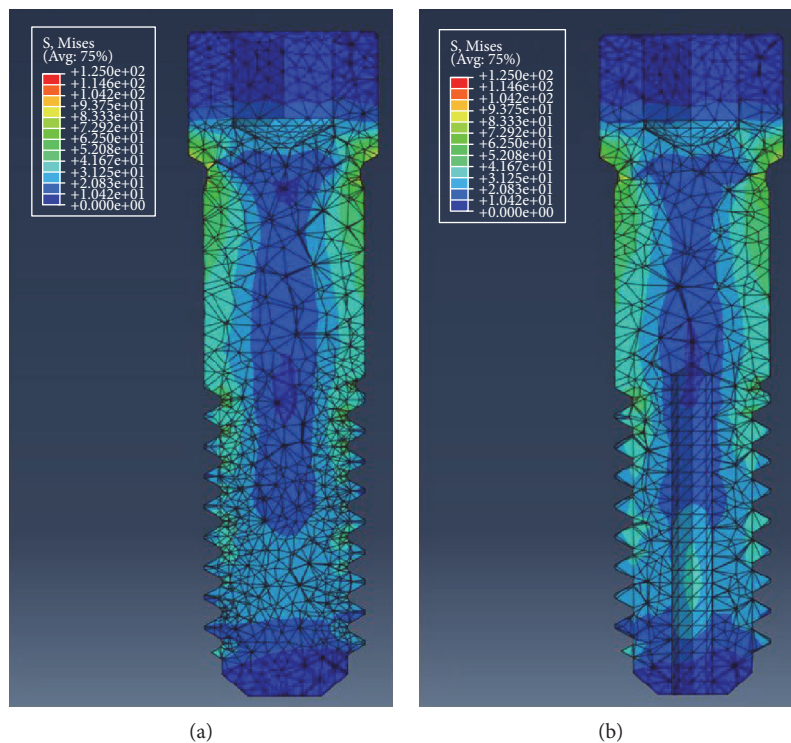


FIGURE 7: von Mises stress distribution under horizontal loading condition. (a) Conventional abutment screw. (b) Hollow abutment screw.

Conflicts of Interest

The authors declare that they have no conflicts of interest.

Authors' Contributions

Bo Kyun Sim and Bongju Kim contributed equally to the paper.

Acknowledgments

This research was supported by a grant from the Korea Health Technology R&D Project through the Korea Health Industry Development Institute (KHIDI), funded by the Ministry of Health and Welfare, Republic of Korea (Grant no. HI15C1535).

References

- [1] A. Reyhanian, S. Parker, J. Moshonov, and N. Fuhrman, "The use of Er:YAG in laser-assisted broken abutment screw treatment. Case report_Er:YAG," *Lasers*, vol. 3, pp. 6–11, 2010.
- [2] R. Adell, B. Eriksson, U. Lekholm, P. I. Branemark, and T. Jemt, "A long-term follow-up study of osseointegrated implants in the treatment of totally edentulous jaws," *The International Journal of Oral & Maxillofacial Implants*, vol. 5, pp. 347–358, 1990.
- [3] H. Wie, "Regitration of localization, occlusion and occluding materials for failing screw joints in the Brånemark implant system," *Clinical Oral Implants Research*, vol. 6, pp. 47–53, 1995.
- [4] M. S. Schwarz, "Mechanical complications of dental implants," *Clinical Oral Implants Research*, vol. 11, Supplement 1, pp. 156–158, 2000.
- [5] C. J. Goodacre, J. Y. Kan, and K. Rungcharassaeng, "Clinical complications of osseointegrated implants," *The Journal of Prosthetic Dentistry*, vol. 81, pp. 537–552, 1999.
- [6] A. Scarano, M. Quaranta, T. Traini, M. Piattelli, and A. Piattelli, "SEM and fractography analysis of screw thread loosening in dental implants," *International Journal of Immunopathology and Pharmacology*, vol. 20, pp. 19–22, 2007.
- [7] J. Satterthwaite and L. Rickman, "Retrieval of a fractured abutment screw thread from an implant: a case report," *British Dental Journal*, vol. 204, pp. 177–180, 2008.
- [8] R. E. Jung, B. E. Pjetursson, R. Glauser, A. Zembic, M. Zwahlen, and N. P. Lang, "A systematic review of the 5-year survival and complication rates of implant-supported single crowns," *Clinical Oral Implants Research*, vol. 19, no. 2, pp. 119–130, 2008.
- [9] P. Satwalekar, K. S. Chander, B. A. Reddy, N. Sandeep, N. Sandeep, and T. Satwalekar, "A simple and cost effective method used for removal of a fractured implant abutment screw: a case report," *Journal of International Oral Health*, vol. 5, no. 5, pp. 120–123, 2013.
- [10] I. Nergiz, P. Schmager, and R. Shahin, "Removal of a fractured implant abutment screw: a clinical report," *The Journal of Prosthetic Dentistry*, vol. 91, pp. 513–517, 2004.
- [11] A. Maalhage-Fard and L. C. Jabobs, "Retrieval of a stripped abutment screw: a clinical report," *The Journal of Prosthetic Dentistry*, vol. 104, pp. 212–215, 2010.
- [12] G. Siamos, S. Winkler, and K. G. Boberick, "Relationship between implant preload and screw loosening on implant-supported prostheses," *The Journal of Oral Implantology*, vol. 28, pp. 67–73, 2002.
- [13] Y. Çiftçi and S. Canay, "Stress distribution on the metal framework of the implant-supported fixed prosthesis using different veneering materials," *The International Journal of Prosthodontics*, vol. 14, pp. 406–411, 2001.
- [14] J. Eng, "Sample size estimation: how many individuals should be studied?" *Radiology*, vol. 227, no. 2, pp. 309–313, 2003.

Research Article

Antagonist Muscle Prefatigue Increases the Intracortical Communication between Contralateral Motor Cortices during Elbow Extension Contraction

Lejun Wang,^{1,2} Aidi Ma,¹ Yuting Wang,¹ Songhui You,¹ and Aiyun Lu²

¹*Sport and Health Research Center, Physical Education Department, Tongji University, Shanghai, China*

²*School of Kinesiology, Shanghai University of Sport, Shanghai, China*

Correspondence should be addressed to Lejun Wang; wlj0523@163.com

Received 27 March 2017; Accepted 27 June 2017; Published 31 July 2017

Academic Editor: Duo Wai-Chi Wong

Copyright © 2017 Lejun Wang et al. This is an open access article distributed under the Creative Commons Attribution License, which permits unrestricted use, distribution, and reproduction in any medium, provided the original work is properly cited.

To investigate the cortico-cortical coupling changes related to antagonist muscle prefatigue, we recorded EEG at FC3, C3, FC4, and C4 electrodes of twelve young male volunteers during a 30-second-long, nonfatiguing isometric elbow extension contraction with a target force level of 20% MVC before and after a sustained fatiguing elbow flexion contraction until task failure. EEG-EEG phase synchronization indices in alpha and beta frequency bands were calculated for the pre- and postfatigue elbow extension contractions. The phase synchronization index in the beta frequency band was found significantly increased between EEG of FC3-C3. The increased phase synchronization index may reflect an enhanced intracortical communication or integration of the signals between contralateral motor cortices with antagonist muscle prefatigue, which may be related to the central modulation so as to compensate for the antagonist muscle prefatigue-induced joint instability.

1. Introduction

Exercise-induced muscle fatigue is defined as a reversible reduction in the neuromuscular system's capacity to generate force or power [1]. It represents a complex phenomenon and encompasses a number of changes occurring at both the central and peripheral levels [2, 3]. Studies have revealed that during muscle fatigue, the activities of agonistic and antagonistic muscles are interrelated and can change in parallel with one another. Particularly, it has been interestingly found that the prefatigue of antagonist muscle may have significant influence on muscle activities, joint mechanical performance, and central voluntary activation [4, 5]. As previous researches have demonstrated the importance of the role of central mechanisms for the regulation of antagonistic muscle coactivation activities, the influence of antagonist muscle prefatigue may be closely related to the modulation of supraspinal mechanisms. However, the underlying neuromuscular control mechanism has rarely been concerned and still remains unclear.

The synchronization of neural activity across different frequencies may play an important role in the formation of neural representations [6]. Previous researchers have found the significant role of synchronization in the organization of distributed cortical activities, and the cortical control of movements involves complex facilitatory and inhibitory cortical interactions [7]. Phase synchronization analysis has been demonstrated to be a useful method to infer functional connectivity with multichannel neural signals, for example, electroencephalography (EEG) [8]. Particularly, based on EEG-EEG phase synchronization analysis method, a fatigue-induced increase in intracortical communication during cycling exercise has been found [9]. However, there is relatively little evidence that cortico-cortical coupling changes as antagonist muscle fatigued. Such evidence would provide further support for a role of synchronization across cortical regions in the organization of movement related to antagonist muscle prefatigue.

To this end, the present study aimed to examine changes of EEG-EEG phase synchronization index induced by

antagonistic muscle pre-fatigue and thus to explore the effects of antagonist fatigue on cortico-cortical coupling and central modulation. EEG signals were recorded, and the effect of antagonist pre-fatigue on functional cortico-cortical coupling was determined by comparing EEG-EEG phase synchronization index during isometric elbow flexion contraction before and immediately after antagonist muscle fatigue.

2. Materials and Methods

2.1. Participants. Twelve right-handed young male volunteers (age 23.75 ± 2.49 years, height 173.08 ± 5.37 cm, and weight 64.79 ± 7.53 kg) participated in this study, which was approved by the Ethics Committee of Shanghai University of Sport. The subjects were all healthy, with no known neuromuscular disorders or musculoskeletal injuries of the neuromuscular system.

2.2. Experimental Protocol. The maximal elbow flexion and voluntary extension contraction torques were determined for each subject using maximum voluntary isometric elbow flexion and extension contraction (MVC) tests. Then, each subject was instructed to perform a 30-second-long, non-fatiguing isometric elbow extension contraction with the target force level at 20% MVC (pre-fatigue elbow extension contraction). After a sufficient rest period of 2 minutes, the subjects performed a sustained elbow-flexion-fatiguing contraction at 20% MVC until task failure (fatiguing elbow flexion contraction). As soon as the fatiguing elbow flexion contraction task was complete, the subjects were instructed to perform another 30-second-long, non-fatiguing isometric elbow extension with the target force level at 20% MVC (post-fatigue elbow extension contraction).

In the experiment, the subjects sat with the upper arm vertically placed and the elbow angle kept at 90° . The right forearm was positioned parallel to the ground and supinated. When performing isometric elbow extension contraction task, the subjects were told to maintain the above posture while lifting a suitable weight from the distal part of the right forearm by means of a rope and pulley to produce a target force of 20% maximal elbow extension force. During the isometric elbow-flexion-fatiguing contraction task, a weight was suspended from the distal part of the right forearm to produce a target force of 20% maximal elbow flexion force, and the participants were told to maintain the posture by flexing the elbow with the elbow joint maintained at 90° until they felt exhausted and were no longer able to continue the contraction. The arm position was monitored by visual inspection, and feedback was given to the subjects by the same investigators for all experiments. The failure criteria for the position task were either an inability to maintain the elbow angle within 12° of the target for 5 s or displacement of the forearm from the neutral position for 5 s without correction [10]. The participants were verbally strongly encouraged to continue the sustained contraction for as long as possible. In the experiment, a self-made apparatus was used that could convert quickly between the elbow flexion and extension contraction tasks.

During the experiment, EEG signals were recorded. To reduce EEG artefacts, the experiment was conducted in a quiet, electrically shielded, dimly lit laboratory with a constant indoor temperature of approximately 24°C . The subjects were told to relax before the experiment and to gaze at a target point approximately 3 metres in front of them during the experiment session.

2.3. EEG Data Acquisition and Preprocessing. Using the international 10–20 electrode placement system, EEG recorded from both right and left motor cortex areas (C3, FC3, C4, and FC4) from the scalp using a 64-channel NeuroSoft SYNAMPS system (NeuroScan Labs, El Paso, TX). The scalp was cleaned with 70% ethanol before the electrode gaps were filled with conducting gel to connect the recording surface of each electrode with the scalp. The EEG data recording did not begin until the impedance for all electrodes settled below 5000Ω . All channels of the EEG signals were amplified ($\times 75,000$, NeuroScan SynAmps RT amplifier), band-pass filtered (0.01–100 Hz), digitized (2000 samples/s), and acquired using the NeuroScan system (NeuroScan Labs, El Paso, TX). The subjects were required to concentrate on the task performance and minimize distractions as much as possible. They were asked to maintain a stable body position and avoid eye blinks, teeth biting, and head movements during the pre- and post-fatigue 30-second isometric elbow extension contraction. Possible sources of distraction or noise, such as sound or light, were minimized. During offline preprocessing, EEG signals were re-referenced to the average value of the bilateral mastoids (M1 and M2), ocular artefacts were reduced, band pass filtering at 3–60 Hz was performed using an FIR zero-phase-shift filter, artefacts were rejected (based on the criteria of signals exceeding $\pm 100\mu\text{V}$ at any time point), and the results were visually inspected. Using the above procedure, data with apparent signal artefacts were excluded. Based on the above procedure, artefact-free 24.576-second length signals recorded during both pre- and post-fatigue elbow extension contractions were acquired for each subject for later analysis.

2.4. EEG Power Spectrum Analysis and Nonlinear Analysis. EEG power was computed and averaged across the appropriate frequencies to obtain the power values for alpha (8–12 Hz) and beta (15–35 Hz). All power estimates were subjected to a log transformation prior to analysis, to achieve the assumption of normality [11]. Nonlinear indices including fractal dimension and sample entropy of EEG were calculated. Fractal dimension was calculated with the box-counting method as previously reported [12] while sample entropy was calculated as reported by Richman and Moorman [13]. Besides, in order to observe and confirm that the antagonist muscle do fatigue, RMS and MF of BB and TB muscles were also calculated during fatiguing elbow flexion contraction (antagonist pre-fatigue-induced process).

2.5. Phase Synchronization Analysis. EEG signals recorded during pre- and post-fatigue elbow extension contractions were filtered for the frequency ranges 8–12 Hz (alpha band) and 15–35 Hz (beta band) using a 4th-order zero-phase-

shift Butterworth filter. Phase synchronization analysis was then conducted, and the phase synchronization index of FC3-C3, FC4-C4, C3-C4, and FC3-FC4 during pre- and postfatigue elbow extension contractions were calculated as [14]

$$\begin{aligned} &\text{Phase synchronization index} \\ &= \sqrt{\left\langle \cos \theta_{xy}^H(t) \right\rangle_t^2 + \left\langle \sin \theta_{xy}^H(t) \right\rangle_t^2}, \quad (1) \end{aligned}$$

where $\langle \cdot \rangle_t$ means the average of all the values, and

$$\theta_{xy}^H(t) = n\theta_x^H(t) - m\theta_y^H(t), \quad (2)$$

in which $\theta_x^H(t)$ is the phase angle calculated based on the Hilbert transformation of the EMG signals and $\theta_y^H(t)$ is calculated based on the EEG signals. In all cases, m and n were assigned a value of 1 according to relevant studies [14, 15].

Data processing was performed using MATLAB R2009a software (The MathWorks Inc., Natick, MA, USA).

2.6. Statistical Analysis. The statistical analysis was performed using SPSS 13.0 for Windows (SPSS, Inc., Chicago, IL, USA). Normality was tested using the Kolmogorov-Smirnov test. Phase synchronization index in the alpha (8~12 Hz) and beta (15~35 Hz) frequency bands, as well as power, fractal dimension, and sample entropy during pre- and postfatigue contractions were tested using paired sample t -tests. All significance thresholds were fixed at $\alpha = 0.05$.

3. Results

The fatiguing elbow flexion contractions lasted for an average of 400.2 ± 79.9 s (ranging 319~561 s). Examples of the raw EEG signals and power spectral density functions (PSDs) for the EEG are shown in Figure 1. It can be observed from the figure that during the antagonistic muscle postfatigue elbow extension contraction, EEG amplitude and power spectra of both C3 and C4 increased in 0–60 Hz compared with those during the prefatigue contraction.

Figure 2 shows the average EEG power in alpha and beta bands during pre- and postfatigue elbow extension contractions. The EEG power at C3 in the alpha band and FC3, C3, FC4, and C4 in the beta band was significantly increased during postfatigue contraction compared with that during prefatigue contraction (alpha band: C3: $P = 0.009$; beta bands: FC3: $P = 0.045$; C3: $P = 0.013$; FC4: $P = 0.013$; and C4: $P = 0.013$).

Figure 3 showed sample entropy and fractal dimension of EEG in pre- and postfatigue elbow extension contractions. Paired sample t -test results have revealed that sample entropy and fractal dimension of the EEG at FC3, C3, FC4, and C4 were all significantly increased during postfatigue contraction compared with those during prefatigue contraction (sample entropy: C3: $P = 0.017$, FC3: $P = 0.040$, C4: $P = 0.037$, and C4: $P = 0.013$; Fractal dimensions: C3: $P = 0.014$, FC3: $P = 0.032$, C4: $P = 0.011$, and C4: $P = 0.006$).

Figure 4 represents the EEG-EEG phase synchronization index during pre- and postfatigue elbow extension contractions. A paired sample t -test showed that the phase synchronization index in the beta frequency band between EEG of FC3-C3 electrodes was significantly increased during postfatigue elbow extension contraction compared with that during prefatigue contraction ($P = 0.015$).

4. Discussion

The main finding of this study is that EEG-EEG phase synchronization index in beta frequency band between contralateral primary motor cortex increased when the antagonistic muscle was prefatigued during isometric elbow extension contraction. To our knowledge, this is the first report to examine the effect of antagonistic muscle prefatigue on cortico-cortical coupling and the neural control mechanism.

It may be argued that the increase of phase synchronization index in this study may be related to the increase of EEG power in the relevant frequency band. However, no significant correlation between EEG-EEG phase synchronization index and EEG power has been discovered in previous researches [9, 16]. Besides, EEG power at FC3, C3, FC4, and C4 increased in the beta frequency band in this study while only phase synchronization index of EEG-EEG at C3 and FC3 has been found increased in the beta frequency band. All these results demonstrated that the increase of phase synchronization index cannot be explained by the enhancement of power in the corresponding frequency band.

In this study, EEG power in the beta frequency band as well as EEG sample entropy and fractal dimension of both left and right motor cortices shows a significant increase in postfatigue contraction than in prefatigue contraction. As movements of the right side of the body are mainly controlled by the left motor cortex of the brain and bilateral connection of upper limb movement [17, 18], the increase of EEG power, sample entropy, and fractal dimension in both left and right motor cortices can be easily expected. However, significant phase synchronization index changes were only found between C3 and FC3, indicating that elbow flexion muscle fatigue may only have significant influences on the functional connectivity of the contralateral motor cortex during elbow extension contraction.

EEG oscillation activity in beta rhythm is associated with motor cortical function [17, 19, 20], and a significant increase of EEG-EMG and EMG-EMG coupling in the beta frequency band induced by muscle fatigue has been revealed in many studies [15, 21, 22]. In this study, a significant increase of the phase synchronization index was found in the beta frequency band between contralateral primary motor cortices, which suggested a significant role for synchronization in the organization and regulation of elbow extension movement within the contralateral primary motor cortex when the antagonist muscle prefatigued.

It has been suggested that the central nervous system may control muscles around a joint acting synergistically as a functional unit [23]. Particularly, agonist and antagonist

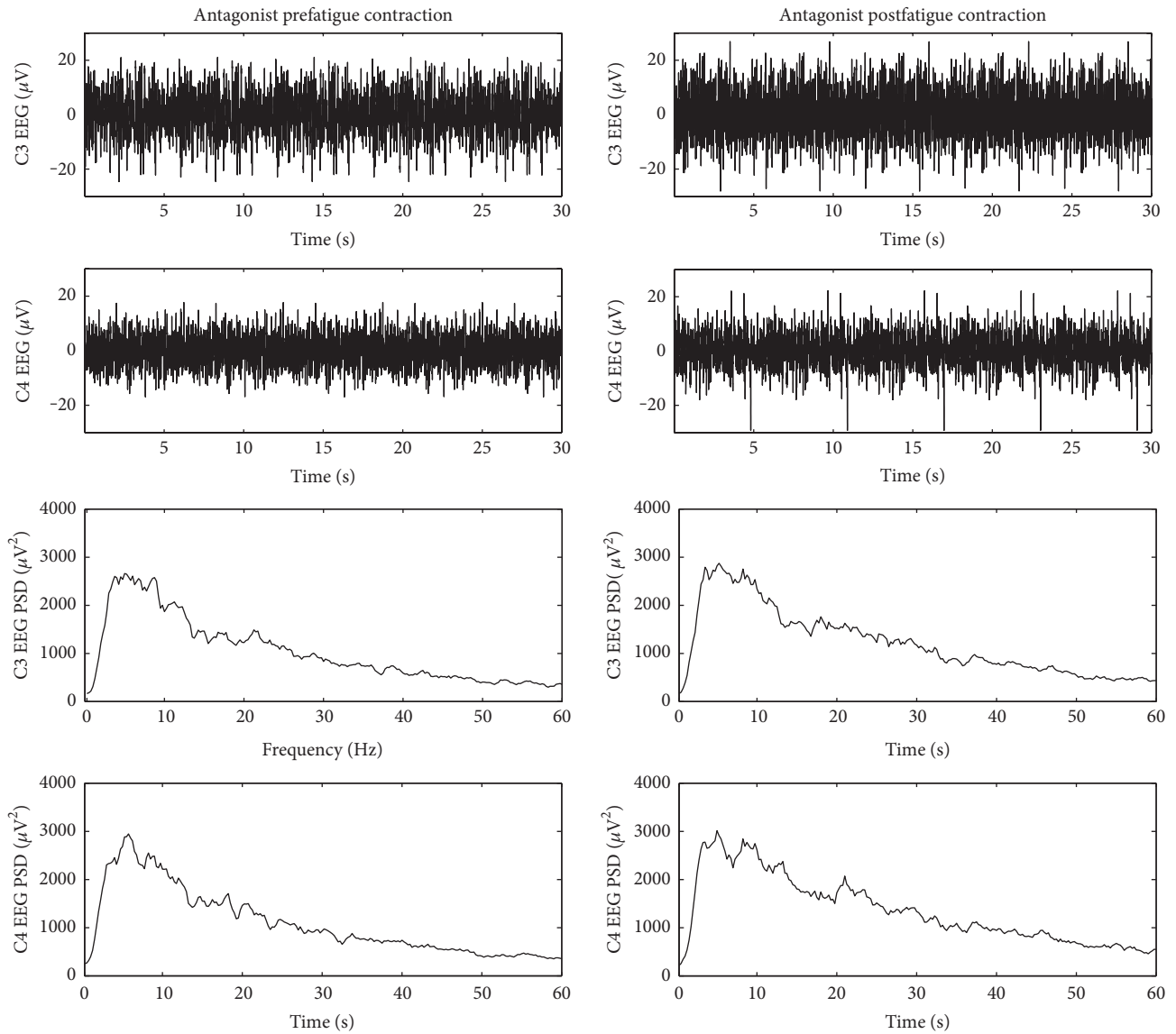


FIGURE 1: Typical examples of raw EEG signals and power spectral density function (PSD) for the EEG during pre- and postfatigue elbow extension contractions.

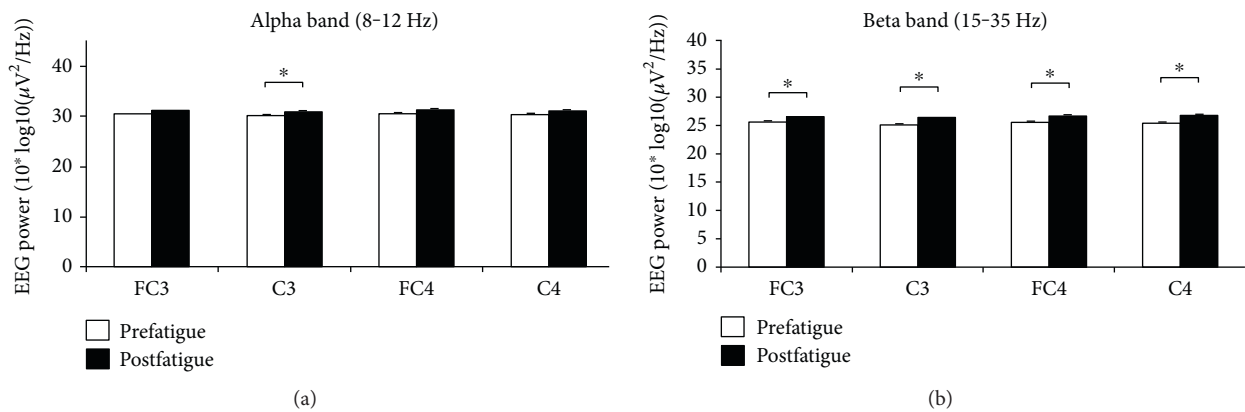


FIGURE 2: Average EEG power during pre- and postfatigue elbow extension contractions. The EEG power at C3 in the alpha band and FC3, C3, FC4, and C4 in the beta band was significantly increased during postfatigue contraction compared with that during prefatigue contraction. Data are mean \pm SE. Significant differences are indicated by asterisks ($P < 0.05$).

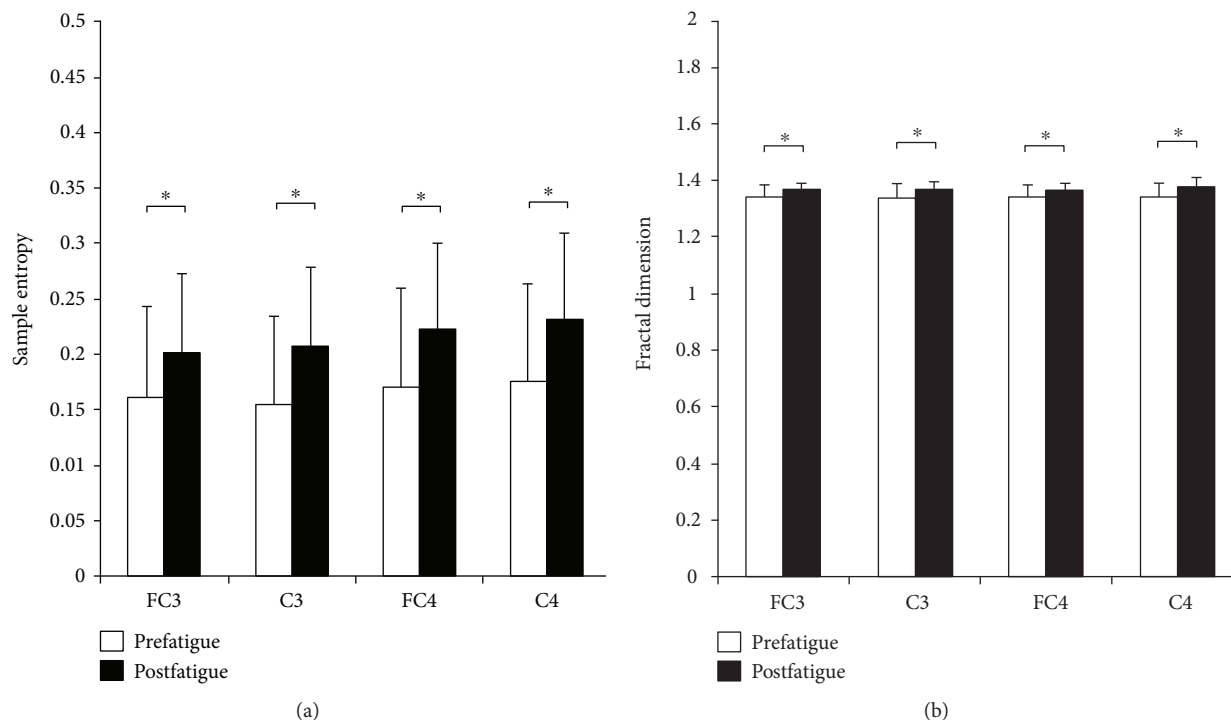


FIGURE 3: Sample entropy and fractal dimension of EEG in pre- and postfatigue elbow extension contractions. Sample entropy and fractal dimension of EEG at FC3, C3, FC4, and C4 were all found significantly increased in postfatigue contraction than in prefatigue contraction. Data are mean \pm SE. Significant differences are indicated by asterisks ($P < 0.05$).

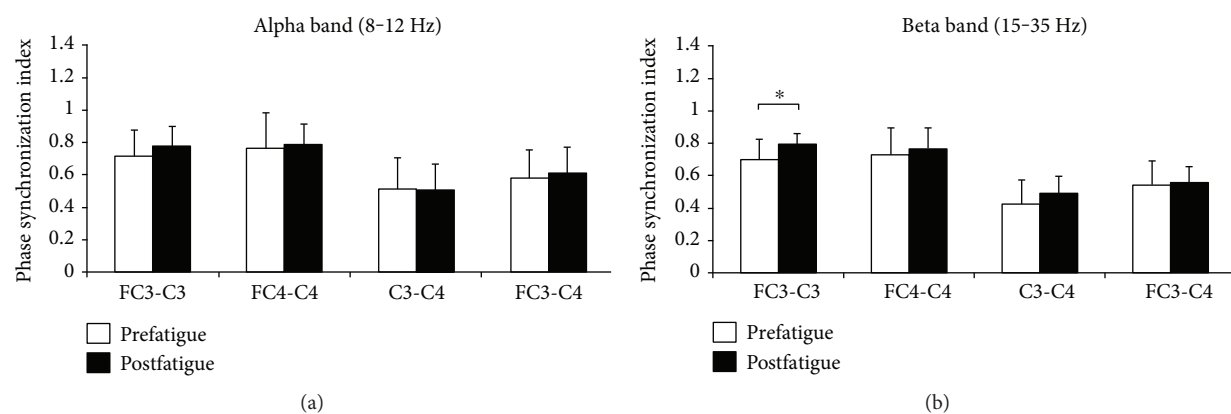


FIGURE 4: Comparisons of the phase synchronization index between EEG-EEG signals during pre- and postfatigue elbow extension contractions. The phase synchronization index in the beta frequency band between EEG of FC3-C3 electrodes was significantly increased during postfatigue elbow extension contraction compared with that during prefatigue contraction. Data are mean \pm SE. Significant differences are indicated by asterisks ($P < 0.05$).

muscles seem to cooperate with each other as a task group in which the main task of the agonist muscle is to produce force or power while the antagonist muscle is to maintain joint stability [15]. As a result of elbow flexor prefatigue, a series of changes in peripheral and central sites related to elbow flexor and extensor muscles happens, which may influence the joint stability of motor task during the later elbow extension contraction [24]. Therefore, the increase of the phase synchronization index between contralateral motor cortices may be related to the modulation of the central nervous system so as to compensate for the antagonistic muscle prefatigue-induced joint instability, although the extent to

which the intracortical physiological relationship between the researched motor areas during elbow extension task is still not fully understood.

In conclusion, phase synchronization indices in the beta frequency band were found significantly increased between contralateral motor cortices. The increased EEG-EEG phase synchronization index may reflect an enhanced intracortical communication or integration of the signals between contralateral motor cortices with antagonist muscle prefatigue, which may be related to the central modulation so as to compensate for the antagonistic muscle prefatigue-induced joint instability.

Conflicts of Interest

The authors declare that there is no conflict of interest regarding the publication of this paper.

Acknowledgments

This work was supported by the National Natural Science Foundation of China (11672211/11302154) and Science & Technology Project Foundation of Shanghai Sports Bureau (16Z013).

References

- [1] N. K. Vollestad, "Measurement of human muscle fatigue," *Journal of Neuroscience Methods*, vol. 74, no. 2, pp. 219–227, 1997.
- [2] S. C. Gandevia, "Spinal and supraspinal factors in human muscle fatigue," *Physiological Reviews*, vol. 81, no. 4, pp. 1725–1789, 2001.
- [3] R. M. Enoka, S. Baudry, T. Rudroff, D. Farina, M. Klass, and J. Duchateau, "Unraveling the neurophysiology of muscle fatigue," *Journal of Electromyography and Kinesiology*, vol. 21, no. 2, pp. 208–219, 2011.
- [4] J. Beltman, A. J. Sargeant, D. Ball, C. N. Maganaris, and A. D. Haan, "Effect of antagonist muscle fatigue on knee extension torque," *Pflügers Archiv European Journal of Physiology*, vol. 446, no. 6, pp. 735–741, 2003.
- [5] E. Kellis and V. Kouveliod, "Agonist versus antagonist muscle fatigue effects on thigh muscle activity and vertical ground reaction during drop landing," *Journal of Electromyography and Kinesiology*, vol. 19, no. 1, pp. 55–64, 2009.
- [6] D. J. Serrien and P. Brown, "Changes in functional coupling patterns during bimanual task performance," *Neuroreport*, vol. 15, no. 9, pp. 1387–1390, 2004.
- [7] M. Muthuraman, K. Arning, R. B. Govindan, U. Heute, G. Deuschl, and J. Raethjen, "Cortical representation of different motor rhythms during bimanual movements," *Experimental Brain Research*, vol. 223, no. 4, pp. 489–504, 2012.
- [8] J. Sun, X. Hong, and S. Tong, "Phase synchronization analysis of EEG signals: an evaluation based on surrogate tests," *IEEE Transactions on Biomedical Engineering*, vol. 59, no. 8, pp. 2254–2263, 2012.
- [9] L. Hilty, N. Langer, R. Pascual-Marqui, U. Boutellier, and K. Lutz, "Fatigue-induced increase in intracortical communication between mid/anterior insular and motor cortex during cycling exercise," *European Journal of Neuroscience*, vol. 34, no. 12, pp. 2035–2042, 2011.
- [10] T. Rudroff, J. N. Justice, M. R. Holmes, S. D. Matthews, and R. M. Enoka, "Muscle activity and time to task failure differ with load compliance and target force for elbow flexor muscles," *Journal of Applied Physiology*, vol. 110, no. 1, pp. 125–136, 2011.
- [11] F. F. Zhu, J. P. Maxwell, Y. Hu et al., "EEG activity during the verbal-cognitive stage of motor skill acquisition," *Biological Psychology*, vol. 84, no. 2, pp. 221–227, 2010.
- [12] G. Boccia, D. Dardanillo, M. Beretta-Piccoli et al., "Muscle fiber conduction velocity and fractal dimension of EMG during fatiguing contraction of young and elderly active men," *Physiological Measurement*, vol. 37, no. 1, pp. 162–174, 2016.
- [13] J. S. Richman and J. R. Moorman, "Physiological time-series analysis using approximate entropy and sample entropy," *American Journal of Physiology Heart & Circulatory Physiology*, vol. 278, no. 6, pp. H2039–H2049, 2000.
- [14] R. Q. Quiroga, A. Kraskov, T. Kreuz, and P. Grassberger, "Performance of different synchronization measures in real data: a case study on electroencephalographic signals," *Physical Review E Statistical Nonlinear & Soft Matter Physics*, vol. 65, article 041903, 2002.
- [15] L. Wang, A. Lu, S. Zhang, W. Niu, F. Zheng, and M. Gong, "Fatigue-related electromyographic coherence and phase synchronization analysis between antagonistic elbow muscles," *Experimental Brain Research*, vol. 233, no. 3, pp. 971–982, 2015.
- [16] T. P. Jung, S. Makeig, A. J. Bell, and T. J. Sejnowski, "Independent component analysis of electroencephalographic and event-related potential data," *Advances in Neural Information Processing Systems*, no. 8, pp. 1548–1551, 1996.
- [17] J. Long, T. Tazoe, D. S. Soteropoulos, and M. A. Perez, "Inter-hemispheric connectivity during bimanual isometric force generation," *Journal of Neurophysiology*, vol. 115, no. 3, pp. 1196–1207, 2016.
- [18] G. Todd, N. T. Petersen, J. L. Taylor, and S. C. Gandevia, "The effect of a contralateral contraction on maximal voluntary activation and central fatigue in elbow flexor muscles," *Experimental Brain Research*, vol. 150, no. 3, pp. 308–313, 2003.
- [19] P. Brown, "Cortical drives to human muscle: the piper and related rhythms," *Progress in Neurobiology*, vol. 60, no. 1, pp. 97–108, 2000.
- [20] S. N. Baker, "Oscillatory interactions between sensorimotor cortex and the periphery," *Current Opinion in Neurobiology*, vol. 17, no. 6, pp. 649–655, 2007.
- [21] V. Siemionow, V. Sahgal, and G. H. Yue, "Single-trial EEG-EMG coherence analysis reveals muscle fatigue-related progressive alterations in corticomuscular coupling," *IEEE Transactions on Neural Systems & Rehabilitation Engineering*, vol. 18, no. 2, pp. 97–106, 2010.
- [22] J. Ushiyama, M. Katsu, Y. Masakado, A. Kimura, M. Liu, and J. Ushiba, "Muscle fatigue-induced enhancement of corticomuscular coherence following sustained submaximal isometric contraction of the tibialis anterior muscle," *Journal of Applied Physiology*, vol. 110, no. 5, pp. 1233–1240, 2011.
- [23] C. J. D. Luca and Z. Erim, "Common drive in motor units of a synergistic muscle pair," *Journal of Neurophysiology*, vol. 87, no. 4, pp. 2200–2204, 2002.
- [24] B. Andersen, B. Westlund, and C. Krarup, "Failure of activation of spinal motoneurons after muscle fatigue in healthy subjects studied by transcranial magnetic stimulation," *Journal of Physiology-LONDON*, vol. 551, no. 1, pp. 345–356, 2003.

Research Article

Morphological and Microstructural Alterations of the Articular Cartilage and Bones during Treadmill Exercises with Different Additional Weight-Bearing Levels

Jiazi Gao,^{1,2} Juan Fang,² He Gong,^{1,2} and Bingzhao Gao¹

¹State Key Laboratory of Automotive Simulation and Control, Jilin University, Changchun, China

²Department of Engineering Mechanics, Nanling Campus, Jilin University, Changchun, China

Correspondence should be addressed to He Gong; gonghe@jlu.edu.cn

Received 28 February 2017; Revised 16 June 2017; Accepted 19 June 2017; Published 11 July 2017

Academic Editor: Rui Zhu

Copyright © 2017 Jiazi Gao et al. This is an open access article distributed under the Creative Commons Attribution License, which permits unrestricted use, distribution, and reproduction in any medium, provided the original work is properly cited.

The aim of this study was to investigate the morphological and microstructural alterations of the articular cartilage and bones during treadmill exercises with different exercise intensities. Sixty 5-week-old female rats were randomly divided into 10 groups: five additional weight-bearing groups (WBx) and five additional weight-bearing with treadmill exercise groups (EBx), which were subjected to additional weight bearing of $x\%$ ($x=0, 5, 12, 19,$ and 26) of the corresponding body weight of each rat for 15 min/day. After 8 weeks of experiment, the rats were humanely sacrificed and their bilateral intact knee joints were harvested. Morphological analysis of the cartilages and microcomputed tomography evaluation of bones were subsequently performed. Results showed that increased additional weight bearing may lead to cartilage damage. No significant difference was observed among the subchondral cortical thicknesses of the groups. The microstructure of subchondral trabecular bone of 12% and 19% additional weight-bearing groups was significantly improved; however, the WB26 and EB26 groups showed low bone mineral density and bone volume fraction as well as high structure model index. In conclusion, effects of treadmill exercise on joints may be associated with different additional weight-bearing levels, and exercise intensities during joint growth and maturation should be selected reasonably.

1. Introduction

Osteoporosis and its consequential fragility fractures are among the leading causes of morbidity, thereby causing considerable and growing social and economic burden [1–3]. Bone mass is considered to be a key determinant of fracture risk [1], and peak bone mass is suggested to be the most important factor in the development of osteoporosis [1]. Maximizing bone mass during childhood and adolescence may contribute to the reduction of fracture risk in the elderly [1]. In addition, physical activities may be an important contributor to the increase in bone mass [4–10]. A study on 4-week-old female Sprague-Dawley rats showed that 8 and 12 weeks of exercise (treadmill running at 24 m/min, 1 hr per day, 5 days a week) substantially increased the mineral apposition and bone formation rates in the proximal and distal tibial metaphyses and increased the cancellous bone

volume in the proximal tibial metaphyses [4]. In another study that subjected 4-week-old male Wistar rats to treadmill running exercises (30 m/min, 1 hr per day, 5 days a week for 10 weeks), the increase in bone strength induced by exercise was mediated by the changes in the trabecular bone microarchitecture, as well as in the density and cortical geometry [10].

Moreover, increasing evidence showed that the effects of physical activities on the bones of growing rats persisted after exercise cessation [8, 9, 11, 12]. For example, 4-week-old male Wistar rats that underwent treadmill training for 10 weeks (35 m/min, +5-degree inclination, 1 hr per day, 5 days a week) had greater bone mineral content and longer bones than the rats in the control group, and the increased bone mass due to training was retained after the cessation of training [11]. Furthermore, the forearm axial compression loading for 3 days a week for 7 weeks on 5-week-old Sprague-Dawley rats significantly improved

TABLE 1: Groups' information and experimental design.

Groups	Number	Experimental design
WBx ($x=0, 5, 12, 19, 26$)	6×5 groups	Additional weight-bearing groups with additional weight bearing at $x\%$ of the individual body weight, backpack for 15 min/day with no weight bearing or treadmill exercise at other times.
EBx ($x=0, 5, 12, 19, 26$)	6×5 groups	Exercise groups combined with additional weight bearing at $x\%$ of the individual body weight, treadmill exercise with backpack for 15 min/day with no weight bearing or treadmill exercise at other times.

bone mineral content, areal density, and strength. These improvements remained until the rats were two years of age [12]. These findings suggest that exercise at a young age provides lifelong benefits to bone structure and strength. These benefits are expected to increase the peak bone mass and reduce the risk of fracture due to aging in the later years; in addition, the prepubertal period is also suggested to be the most effective stage for physical activity interventions [8, 13].

In prepubertal rats, although weight-bearing physical activities play an important role in the accrual of bone mass and maintenance of bone quality, the effects of exercise on other tissues, such as articular cartilage and subchondral bone, should not be disregarded, especially when the bones and cartilages are growing at a fast rate. The biomechanical environment can initiate degenerative changes on immature articular cartilage during joint growth and maturation [14]. Excessive running exercises (15 km within 3 weeks or 30 km within 6 weeks) in 13- to 14-week-old male Wistar rats induced knee osteoarthritis [15]. Furthermore, 16- to 18-week-old Wistar rats forced to run 30 km on a treadmill platform for 6 weeks also suffered from osteoarthritis [16]. In another study, an *in vivo* tibial loading model was used to assess the influence of mechanical load on articular cartilage and bone; the results showed that *in vivo* cyclic compression of 4.5 and 9.0 N peak loads via the knee joint (1200 cycles, 4 Hz, 5 days a week) caused cartilage degeneration and subchondral bone changes in 10- and 26-week-old mice [17].

Overall, these studies verified the following assumptions: (1) physical activities can improve bone quality and prevent osteoporosis due to aging, (2) physical activities at a young age may enhance bone quality and the prolong exercise-induced benefits until old age, and (3) improper (e.g., excessive) physical activities may increase the risk of osteoarthritis to the joints.

Most studies on physical activities at a young age focused on bone tissues and paid little attention to the joints. Therefore, in this study, we focused on the influence of physical activities on the articular cartilages and bones (including subchondral bone and proximal tibial trabecular bone) of growing rats. In the present study, growing rats were subjected to continuous treadmill running. A morphological analysis of the cartilages and microcomputed tomography (micro-CT) evaluation of the bones were then performed. The peak strain during exercise can be increased by adding weights [18], and thus, exercise intensity was regulated by adjusting the addition of weights during exercise in this study.

2. Materials and Methods

2.1. Animals. All the experimental procedures were approved by the Ethics Committee of The First Hospital of Jilin University (number 2013-145).

A week before the experiment, 85 female Wistar rats, aged 4 weeks, were purchased and brought to the laboratory so that they can acclimate to the new environment. All the rats were housed in cages (6 rats in each cage) under local vivarium conditions (temperature $24 \pm 2^\circ\text{C}$ and 12 hr on/off light cycle). Free cage movement was allowed. The rats were provided with standard pelleted chow diet and water in the entire experimental period, and no dietary adjustments were made.

2.2. Experimental Design. According to previous studies, 12 m/min was considered to be a "gentle" running (walking) speed on account of the onset of blood lactate accumulation [19], which was confirmed in the present study. On the last day of acclimation, 25 rats were selected and randomly divided into either the sedentary group ($n=5$) or the exercise group ($n=20$). The rats in the exercise group were subjected to treadmill exercise at speeds of 8, 10, 12, and 14 m/min ($n=5$ for each speed) for 15 min; they were then sacrificed immediately after exercise. Blood samples from the rats were collected via the abdominal aorta before death and then centrifuged at 3000 rpm for 15 min. The serums were separated, and the blood lactate concentrations were determined.

No significant blood lactate accumulation was observed until the running speed increased to 14 m/min (the median value of the blood lactate concentration was 4.5 mmol/L). Therefore, 12 m/min (the median value of the blood lactate concentration was 2.5 mmol/L, which was significantly lower than that at 14 m/min, $P < 0.05$) showed only a slight blood lactate accumulation and thus can be regarded as the highest threshold level of gentle running. As such, 12 m/min was selected in the present study.

Subsequently, the other 60 rats were randomized into 10 groups with 6 rats each (Table 1). Additional weight bearing was carried out by allowing the rats to carry a backpack filled with leaden strips [18]. All the rats in the exercise groups were subjected to running exercise on a rodent treadmill platform. The speed of the treadmill and the weight-bearing of each rat were gradually increased during the first 14 days. That is, the running speed was increased from 8 m/min, with 3% increment, to 12 m/min. The weight of the backpack was increased from 0% of the individual weight until the targeted additional weight in increments of 7% of the experimental

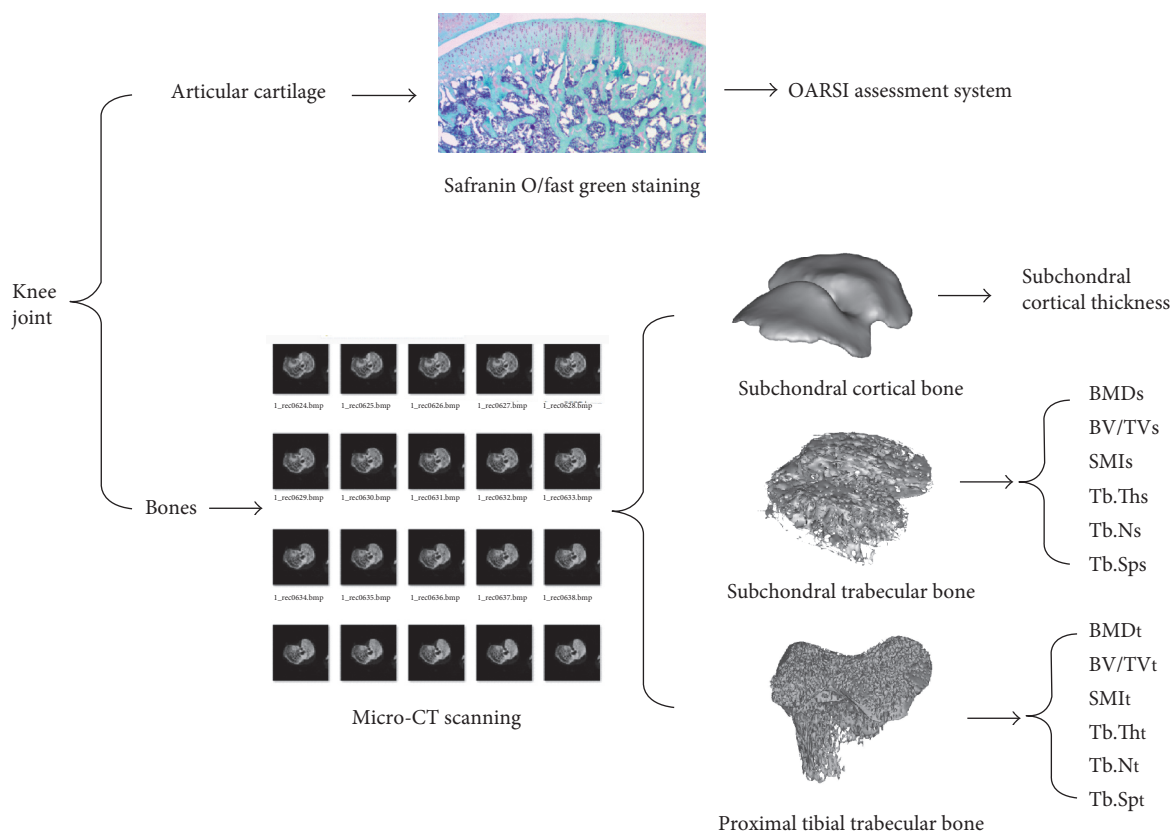


FIGURE 1: Assessment of morphological and microstructural alterations of the articular cartilage and bones.

requisite weight. All the experimental groups were maintained for an additional 8 weeks (7 days per week) as an experimental period. The additional loads in the backpack were adjusted in accordance with the change in the body weights of the rats per week. After the experiment, the rats were humanely killed under general anesthesia using sodium pentobarbital. Bilateral intact knee joints were harvested and fixed in 10% formalin for 24 hr. Morphological analysis of the articular cartilage and micro-CT evaluation of the bones were then performed (Figure 1).

2.3. Morphological Analysis on the Articular Cartilage. After tissue fixation, the right knee joints were decalcified in ethylenediaminetetraacetic acid for 2 weeks, and then dehydrated in a series of alcohol baths, and finally embedded in paraffin. Serial sagittal sections ($6\ \mu\text{m}$ thick) were obtained using a rotary microtome. Safranin O/fast green staining was performed to assess the articular cartilage morphology. Articular cartilage degeneration was assessed in tibial plateau using the OARSI osteoarthritis cartilage histopathology assessment system [20].

2.4. Microstructural Analysis on Bones. After the tissues were fixed, the left knee joints were scanned by a high-resolution micro-CT scanner (Skyscan 1076, Skyscan, Belgium) set at $18\ \mu\text{m}$ resolution, 70 kV, $142\ \mu\text{A}$, and an Al 1.0 mm filter. Quantitative microstructural analysis of bones was then performed.

Subchondral bone includes subchondral cortical bone and subchondral trabecular bone. Thus, the subchondral cortical thickness and microstructural parameters of the subchondral trabecular bone, including bone mineral density (BMD_s), bone volume fraction (BV/TV_s), structure model index (SMI_s), trabecular thickness (Tb.Th_s), trabecular number (Tb.N_s), and trabecular separation (Tb.Sp_s), were calculated. In addition, microstructural parameters of the proximal tibial trabecular bone under growth plate (BMD_t , BV/TV_t , SMI_t , Tb.Th_t , Tb.N_t , and Tb.Sp_t) were also quantified to compare with those of the subchondral trabecular bone.

2.5. Statistical Analysis. Given that the data were nonnormally distributed, nonparametric tests of significance were performed. Two independent variables (exercise and additional weight bearing) with different levels (exercise or not; additional weight bearing of 0%, 5%, 12%, 19%, and 26%) were analyzed using the nonparametric two-way analysis of variance (Scheirer-Ray-Hare test). The Mann-Whitney U test was then used to compare the morphological and microstructural parameters between every two groups. A P value < 0.05 was considered statistically significant [21, 22].

3. Results

3.1. Evaluation of Articular Cartilage Degeneration in the Tibial Plateau. The results of the OARSI assessment are shown in Table 2. No change in the cartilages of WB0, EB0,

TABLE 2: OARSI grades of cartilage (the numbers of cartilages in each grade).

Grade	WB0	EB0	WB5	EB5	WB12	EB12	WB19	EB19	WB26	EB26
Grade 0	6	6	6	6	5	4	4	4	4	3
Grade 1	0	0	0	0	1	2	1	1	1	1
Grade 2	0	0	0	0	0	0	1	1	1	1
Grade 3	0	0	0	0	0	0	0	0	0	1

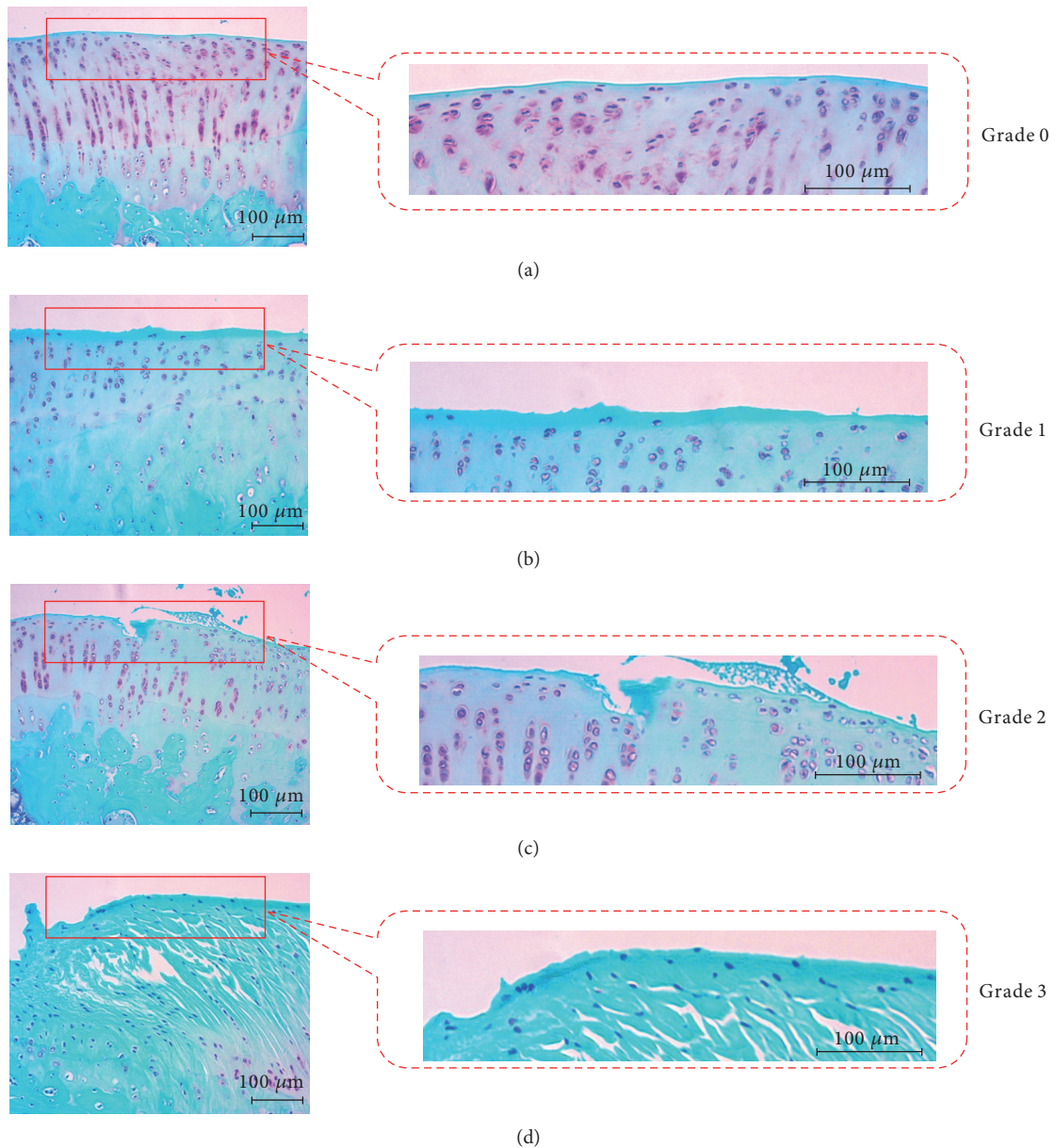


FIGURE 2: OARSI assessment of articular cartilage ((a) grade 0: cartilage surface is smooth; (b) grade 1: surface intact with uneven articular surface is observed; (c) grade 2: discontinuity of surface is destroyed; and (d) grade 3: cartilage degeneration is observed with obvious cracks extension).

WB5, and EB5 were observed. WB12 and EB12 showed minimal surface discontinuities (Figure 2(a)). WB19, EB19, and WB26 had same sample distribution in terms of their OARSI

grades (Figures 2(b) and 2(c)). However, EB26 showed obvious cartilage damage. In this group, only 3 of 6 samples were in grade 0, and 1 of 6 samples was in grades 1, 2, and 3.

TABLE 3: Microstructural parameters of subchondral bone.

Groups	Subchondral cortical thickness (mm)	Subchondral trabecular bone					
		BMD _S (g/cm ³)	BV/TV _S (%)	SMI _S	Tb.N _S (1/mm)	Tb.Th _S (mm)	Tb.Sp _S (mm)
WB0	0.1840	0.6145	36.6019	1.1143	2.6330	0.1365	0.2727
EB0	0.1849	0.6106	35.9493	1.1867	2.6300	0.1378	0.2844
WB5	0.2017	0.6147	41.1165	1.0059	2.7910	0.1395	0.2841
EB5	0.1978	0.6131	43.2750*	1.0251	2.9930	0.1427	0.2662 [#]
WB12	0.1840	0.6231 [#]	41.4677*	0.9902	2.7920	0.1457 [#]	0.2611 [#]
EB12	0.1893	0.6260 [#]	44.0822* [#]	0.9188*	2.8620	0.1534 [#]	0.2452* [#]
WB19	0.2045	0.6190	41.4688*	0.9976	2.9990	0.1488 [#]	0.2585
EB19	0.1860	0.6185	41.6078*	1.0281	2.8290	0.1506 [#]	0.2588 [#]
WB26	0.1952	0.6065	39.3952	1.2407	2.8670	0.1367	0.2764
EB26	0.1971	0.5997	39.8096	1.3481	2.6430	0.1346	0.2895

*Significantly different from the WB0 group; $P < 0.05$. [#]Significantly different from the EB0 group; $P < 0.05$.

TABLE 4: Microstructural parameters of the proximal tibial trabecular bone.

Groups	BMD _t (g/cm ³)	BV/TV _t (%)	SMI _t	Tb.N _t (1/mm)	Tb.Th _t (mm)	Tb.Sp _t (mm)
WB0	0.5583	25.3438	1.8431	2.2250	116.9828	242.2194
EB0	0.5528	23.6330	1.7450	2.0890	111.1648	264.1477
WB5	0.5767 [#]	30.1409	1.6501	2.2050	130.5708	265.4428
EB5	0.5713 [#]	29.1304	1.7560	2.1260	127.7959	233.0518
WB12	0.5747* [#]	30.9775	1.8210	1.8530	131.9947	262.4064
EB12	0.5950* [#]	44.9278* [#]	0.9834 [#]	2.4910	163.0242 [#]	228.0384
WB19	0.5688 [#]	32.2411	1.6022	2.0080	128.8975	212.6581
EB19	0.5740* [#]	38.3036	1.1095	2.0800	143.4085	225.0497
WB26	0.5645	21.2810	1.9553	1.8500	119.9064	287.3870
EB26	0.5603	21.7358	2.1625	1.8030	122.8960	272.5016

*Significantly different from the WB0 group; $P < 0.05$. [#]Significantly different from the EB0 group; $P < 0.05$.

Visualized Safranin O staining loss and cartilage thinning were observed in EB26 (Figure 2(d)).

3.2. Microstructural Evaluation of Subchondral Bone. The microstructural parameters of the subchondral bone were analyzed, and the results are shown in Table 3.

No significant difference in subchondral cortical thickness was observed among groups.

Statistical analysis results show that exercise or the interaction between exercise and weight-bearing level had no significant effect on any parameter of the subchondral trabecular bone (Scheirer-Ray-Hare test: exercise or not, $P > 0.05$; interaction between exercise and weight-bearing level, $P > 0.05$). Subchondral trabecular bone changes in the BMD_S, BV/TV_S, SMI_S, Tb.Th_S, and Tb.Sp_S were mainly dependent on the weight-bearing level (Scheirer-Ray-Hare test: weight-bearing level, $P < 0.05$). High BMD_S was observed in the 12% additional weight-bearing groups (WB12 and EB12), which had significantly higher BMD_S than EB0. For BV/TV_S, both 12% and 19% additional weight-bearing groups and EB5 showed higher values than WB0 ($P < 0.05$). EB12 had the highest BV/TV_S (higher than WB0 and EB0, $P < 0.05$). Although the 12% and 19% additional weight-bearing groups showed low SMI_S, a significant

difference was only observed from EB12 and WB0 ($P < 0.05$). No difference among the groups was observed with respect to Tb.N_S. The 12% and 19% additional weight-bearing groups showed higher Tb.Th_S than EB0 ($P < 0.05$). EB5, WB12, EB12, and EB19 showed significantly lower values than EB0 in terms of Tb.Sp_S. Among the groups, EB12 had the lowest Tb.Sp_S (significantly different from WB0 and EB0, $P < 0.05$).

3.3. Microstructural Evaluation of Proximal Tibial Trabecular Bone. The microstructural parameters of the proximal tibial trabecular bone are shown in Table 4.

Results of proximal tibial trabecular bone show the similar trend with the subchondral trabecular bone. That is, exercise or the interaction between exercise and weight-bearing level had no significant effect on any parameter of the proximal tibial trabecular bone (Scheirer-Ray-Hare test: exercise or not, $P > 0.05$; interaction between exercise and weight-bearing level, $P > 0.05$). Microstructural parameters (BMD_t, BV/TV_t, SMI_t, Tb.Th_t, and Tb.Sp_t) were mainly dependent on the weight-bearing level (Scheirer-Ray-Hare test: weight-bearing level, $P < 0.05$). The 0% additional weight-bearing groups (WB0 and EB0) showed lower BMD_t than other groups, with the highest value observed in EB12. For other microstructural parameters, EB12 showed the

highest BV/TV_t (significantly higher than WB0 and EB0, $P < 0.05$), $Tb.N_t$, and $Tb.Th_t$ (significantly higher than EB0, $P < 0.05$) and the lowest SMI_t and $Tb.Sp_t$ (significantly lower than EB0, $P < 0.05$).

4. Discussion

The influence of different exercise intensities on the articular cartilage and bones of growing rats was investigated in this study. The rats were subjected to continuous treadmill running with different additional weight bearings. The cartilages and bones were then subjected to morphological analysis and micro-CT evaluation, respectively.

With regard to the running speed, 12 m/min corresponded to a moderate level by evaluating blood lactate accumulation in the present study. Apparent blood lactate concentration was observed when the running speed increased to 14 m/min, which means the intensity of the exercise has exceeded our expectations. Besides, lower speeds (such as 8 m/min or 10 m/min) were still rejected to avoid confusion with voluntary exercise. Accordingly, the speed of 12 m/min was selected in the current study.

Although treadmill running could enhance bone quality [4, 10, 11], the influence of running on cartilage should not be ignored. Moderate mechanical loading could maintain the integrity of the cartilage and prevent the progression of cartilage-subchondral bone lesions [23, 24]. However, overuse of joints may result in cartilage degradation [15, 16, 25]. In this study, articular cartilage degeneration was clearly observed in the 26% additional weight-bearing groups (WB26 and EB26). The 12% and 19% additional weight-bearing groups showed different grades of cartilage changes. The results of the assessment of cartilage in the tibial plateau indicated that the increase in additional weight bearing exacerbated cartilage damage. This effect may be related to the immature cartilage in growing rats and thus imply the importance of selecting beneficial exercise intensity during the growing period of cartilage and bones.

Subchondral bone, which plays an important role in load distribution and support in joints, is closely associated with osteoarthritis and thus is a tissue of great interest [26–34]. Whether the onset of osteoarthritis occurs in the bone or articular cartilage remains controversial. Several studies suggested that changes in the subchondral bone occur following the degeneration of the cartilage [26, 27]. However, many researchers speculated that changes in the bone occur simultaneously with cartilage degradation or even before cartilage degradation [28, 29]. Mechanical factors play a significant role in the physiologic imbalance of osteoarthritis. The health and integrity of the overlying articular cartilage depend on the mechanical properties of its bony bed [30]. The mechanical effects of loading not only influence the bone mass but also alter the subchondral bone [34]. Although no significant change in the subchondral cortical bone was observed in the current study, the subchondral trabecular bone exhibited substantial changes. The results of this study showed that the 12% and 19% additional weight-bearing groups considerably improved the microstructure of the subchondral trabecular bone, but the positive results were not observed

in the 26% additional weight-bearing groups. In addition, although no significant difference was found between WB26 and EB26, they showed low BMD_s and BV/TV_s , as well as high SMI_s , thus indicating that the 26% additional weight bearing failed to improve bone quality. Therefore, increased exercise intensity cannot improve further exercise-induced positive effects, especially in growing joints, which may be associated with the ability of bone adaption especially that of growing bones. Though this study provided a proper additional weight-bearing level (19% additional weight bearing) for the growing bones and joints, a further study is still needed to explore the reasonable exercise intensities more precisely.

Microstructural parameters of the proximal tibial trabecular bone under the growth plate showed similar changes with the subchondral trabecular bone. However, the changes of BMD_t seemed more sensitive; that is, not only 12% and 19% additional weight-bearing groups but also 5% additional weight-bearing groups showed significant higher values than 0% additional weight-bearing groups. Though those results may not be helpful to understand the load transduction with regard to bones and joints under treadmill exercises with different additional weight-bearings levels in growing individuals, they still suggested that the proper exercise intensities could improve bone quality for the growing individuals.

The current results should be considered in light of several limitations. First, no additional weight bearing heavier than 26% of the individual body weight was used in this study because the adaptability of the rats was considered. Thus, the effects of additional weight bearing heavier than 26% on articular cartilage and subchondral bone were not discussed. However, articular cartilage degeneration was clearly observed in the 26% additional weight-bearing groups, which means it is unnecessary to enlarge the range of an additional weight-bearing value. Second, the models used in this study lacked exact evaluation of the strains produced by different exercise intensities in the joints. The relationship between mechanical stimulation (strain) and changes in the joint (articular cartilage and subchondral bone) was not discussed, which should be improved in the future studies to conduct a quantitative and comprehensive research. Third, the results obtained in the paper were based on female rats, which means that the conclusion might not be applicable to the male rats. The differences between genders should be investigated deeply in the future to extend the conclusion of this study. Although restricted by these limitations, the influence of physical activity (treadmill running) on articular cartilage and subchondral bone were investigated, and the results may provide insights into the means of enhancing bone quality.

In conclusion, different exercise intensities did not considerably affect the subchondral cortical thickness but influenced the articular cartilage structure, as well as the microstructural parameters of subchondral trabecular bone and proximal tibial trabecular bone. The results of this study suggested that the exercise intensities during joint growth and maturation should be selected reasonably to improve bone quality and avoid the risk of osteoarthritis due to aging.

Conflicts of Interest

The authors have declared that no competing interest exists.

Acknowledgments

This work is supported by the National Natural Science Foundation of China (nos. 81471753, 11432016, and 11322223), the Natural Science Foundation of Jilin Province (nos. 20160101297JC, 20170519008JH, and 20170520093JH), and the China Postdoctoral Science Foundation (2016M591477).

References

- [1] R. Rizzoli, M. L. Bianchi, M. Garabédian, H. A. McKay, and L. A. Moreno, "Maximizing bone mineral mass gain during growth for the prevention of fractures in the adolescents and the elderly," *Bone*, vol. 46, no. 2, pp. 294–305, 2010.
- [2] O. Johnell and J. A. Kanis, "An estimate of the worldwide prevalence, mortality and disability associated with hip fracture," *Osteoporosis International*, vol. 15, no. 11, pp. 897–902, 2004.
- [3] J. Y. Reginster and N. Burlet, "Osteoporosis: a still increasing prevalence," *Bone*, vol. 38, pp. S4–S9, 2006.
- [4] J. Iwamoto, J. K. Yeh, and J. F. Aloia, "Differential effect of treadmill exercise on three cancellous bone sites in the young growing rat," *Bone*, vol. 24, no. 3, pp. 163–169, 1999.
- [5] J. Iwamoto, J. K. Yeh, and J. F. Aloia, "Effect of deconditioning on cortical and cancellous bone growth in the exercise trained young rats," *Journal of Bone and Mineral Research*, vol. 15, no. 9, pp. 1842–1849, 2000.
- [6] I. Pajamäki, P. Kannus, T. Vuohelainen et al., "The bone gain induced by exercise in puberty is not preserved through a virtually life-long deconditioning: a randomized controlled experimental study in male rats," *Journal of Bone and Mineral Research*, vol. 18, no. 3, pp. 544–552, 2003.
- [7] K. J. MacKelvie, K. M. Khan, and H. A. McKay, "Is there a critical period for bone response to weight-bearing exercise in children and adolescents? A systematic review," *British Journal of Sports Medicine*, vol. 36, no. 4, pp. 250–257, 2002.
- [8] K. Gunter, A. D. Baxter-Jones, R. L. Mirwald et al., "Impact exercise increases BMC during growth: an 8-year longitudinal study," *Journal of Bone and Mineral Research*, vol. 23, no. 7, pp. 986–993, 2008.
- [9] K. Gunter, A. D. Baxter-Jones, R. L. Mirwald et al., "Jump starting skeletal health: a 4-year longitudinal study assessing the effects of jumping on skeletal development in pre and circum pubertal children," *Bone*, vol. 42, no. 4, pp. 710–718, 2008.
- [10] Y. I. Joo, T. Sone, M. Fukunaga, S. G. Lim, and S. Onodera, "Effects of endurance exercise on three-dimensional trabecular bone microarchitecture in young growing rats," *Bone*, vol. 33, no. 4, pp. 485–493, 2003.
- [11] A. Kiuchi, Y. Arai, and S. Katsuta, "Detraining effects on bone mass in young male rats," *International Journal of Sports Medicine*, vol. 19, no. 4, pp. 254–259, 1998.
- [12] S. J. Warden, R. K. Fuchs, A. B. Castillo, I. R. Nelson, and C. H. Turner, "Exercise when young provides lifelong benefits to bone structure and strength," *Journal of Bone and Mineral Research*, vol. 22, no. 2, pp. 251–259, 2007.
- [13] P. Kannus, H. Haapasalo, M. Sankelo et al., "Effect of starting age of physical activity on bone mass in the dominant arm of tennis and squash players," *Annals of Internal Medicine*, vol. 123, no. 1, pp. 27–31, 1995.
- [14] G. E. Nugent, A. W. Law, E. G. Wong et al., "Site- and exercise-related variation in structure and function of cartilage from equine distal metacarpal condyle," *Osteoarthritis and Cartilage*, vol. 12, no. 10, pp. 826–833, 2004.
- [15] G. Pap, R. Eberhardt, I. Stürmer et al., "Development of osteoarthritis in the knee joints of Wistar rats after strenuous running exercise in a running wheel by intracranial self-stimulation," *Pathology, Research and Practice*, vol. 194, no. 1, pp. 41–47, 1998.
- [16] T. Tang, T. Muneta, Y. J. Ju et al., "Serum keratan sulfate transiently increases in the early stage of osteoarthritis during strenuous running of rats: protective effect of intraarticular hyaluronan injection," *Arthritis Research & Therapy*, vol. 10, no. 1, p. R13, 2008.
- [17] F. C. Ko, C. Dragomir, D. A. Plumb et al., "In vivo cyclic compression causes cartilage degeneration and subchondral bone changes in mouse tibiae," *Arthritis and Rheumatism*, vol. 65, no. 6, pp. 1569–1578, 2013.
- [18] H. E. v. d. Wiel, P. Lips, W. C. Graafmans et al., "Additional weight-bearing during exercise is more important than duration of exercise for anabolic stimulus of bone: a study of running exercise in female rats," *Bone*, vol. 16, no. 1, pp. 73–80, 1995.
- [19] J. Iwamoto, T. Takeda, and S. Ichimura, "Effects of exercise on bone mineral density in mature osteopenic rats," *Journal of Bone and Mineral Research*, vol. 13, no. 8, pp. 1308–1317, 1998.
- [20] K. P. Pritzker, S. Gay, S. A. Jimenez et al., "Osteoarthritis cartilage histopathology: grading and staging," *Osteoarthritis and Cartilage*, vol. 14, no. 1, pp. 13–29, 2006.
- [21] E. G. Vajda and R. D. Bloebaum, "Age-related hypermineralization in the female proximal human femur," *Anatomical Record*, vol. 255, no. 2, pp. 202–211, 1999.
- [22] C. J. Scheirer, W. S. Ray, and N. Hare, "The analysis of ranked data derived from completely randomized factorial designs," *Biometrics*, vol. 32, no. 2, pp. 429–434, 1976.
- [23] H. Iijima, T. Aoyama, A. Ito et al., "Exercise intervention increases expression of bone morphogenetic proteins and prevents the progression of cartilage-subchondral bone lesions in a post-traumatic rat knee model," *Osteoarthritis and Cartilage*, vol. 24, no. 6, pp. 1092–1102, 2016.
- [24] H. Iijima, T. Aoyama, A. Ito et al., "Effects of short-term gentle treadmill walking on subchondral bone in a rat model of instability-induced osteoarthritis," *Osteoarthritis and Cartilage*, vol. 23, no. 9, pp. 1563–1574, 2015.
- [25] J. Beckett, W. Jin, M. Schultz et al., "Excessive running induces cartilage degeneration in knee joints and alters gait of rats," *Journal of Orthopaedic Research*, vol. 30, no. 10, pp. 1604–1610, 2012.
- [26] E. Calvo, I. Palacios, E. Delgado et al., "High-resolution MRI detects cartilage swelling at the early stages of experimental osteoarthritis," *Osteoarthritis and Cartilage*, vol. 9, no. 5, pp. 463–472, 2001.
- [27] Y. Song, J. M. Greve, D. R. Carter, and N. J. Giori, "Meniscectomy alters the dynamic deformational behavior and cumulative strain of tibial articular cartilage in knee joints subjected to cyclic loads," *Osteoarthritis and Cartilage*, vol. 16, no. 12, pp. 1545–1554, 2008.
- [28] J. L. Huebner, M. A. Hanes, B. Beekman, J. M. TeKoppele, and V. B. Kraus, "A comparative analysis of bone and cartilage

- metabolism in two strains of guinea-pig with varying degrees of naturally occurring osteoarthritis," *Osteoarthritis and Cartilage*, vol. 10, no. 10, pp. 758–767, 2002.
- [29] C. S. Carlson, R. F. Loeser, M. J. Jayo, D. S. Weaver, M. R. Adams, and C. P. Jerome, "Osteoarthritis in cynomolgus macaques: a primate model of naturally occurring disease," *Journal of Orthopaedic Research*, vol. 12, no. 3, pp. 331–339, 1994.
- [30] E. L. Radin and R. M. Rose, "Role of subchondral bone in the initiation and progression of cartilage damage," *Clinical Orthopaedics and Related Research*, vol. 213, pp. 34–40, 1986.
- [31] E. Hargrave-Thomas, F. van Sloun, M. Dickinson, N. Broom, and A. Thambyah, "Multi-scalar mechanical testing of the calcified cartilage and subchondral bone comparing healthy vs earlydegenerative states," *Osteoarthritis and Cartilage*, vol. 23, no. 10, pp. 1755–1762, 2015.
- [32] A. J. Barr, T. M. Campbell, D. Hopkinson, S. R. Kingsbury, M. A. Bowes, and P. G. Conaghan, "A systematic review of the relationship between subchondral bone features, pain and structural pathology in peripheral joint osteoarthritis," *Arthritis Research & Therapy*, vol. 17, p. 228, 2015.
- [33] J. L. Huebner, A. C. Bay-Jensen, K. M. Huffman et al., "Alpha C-telopeptide of type I collagen is associated with subchondral bone turnover and predicts progression of joint space narrowing and osteophytes in osteoarthritis," *Arthritis & Rheumatology*, vol. 66, no. 9, pp. 2440–2449, 2014.
- [34] S. R. Goldring, "Alterations in periarticular bone and cross talk between subchondral bone and articular cartilage in osteoarthritis," *Therapeutic Advances in Musculoskeletal Disease*, vol. 4, no. 4, pp. 249–258, 2012.

Research Article

Biomechanical Effects of Various Bone-Implant Interfaces on the Stability of Orthodontic Miniscrews: A Finite Element Study

Fabing Tan,¹ Chao Wang,^{1,2} Chongshi Yang,³ Yuanding Huang,^{1,2} and Yubo Fan¹

¹College of Stomatology, Chongqing Medical University, Chongqing, China

²Chongqing Key Laboratory of Oral Diseases and Biomedical Sciences, Chongqing, China

³Chongqing Municipal Key Laboratory of Oral Biomedical Engineering of Higher Education, Chongqing, China

Correspondence should be addressed to Chao Wang; wangchao_buaa@163.com

Received 9 February 2017; Revised 26 April 2017; Accepted 3 May 2017; Published 19 June 2017

Academic Editor: Wei Yao

Copyright © 2017 Chao Wang et al. This is an open access article distributed under the Creative Commons Attribution License, which permits unrestricted use, distribution, and reproduction in any medium, provided the original work is properly cited.

Introduction. Osseointegration is required for prosthetic implant, but the various bone-implant interfaces of orthodontic miniscrews would be a great interest for the orthodontist. There is no clear consensus regarding the minimum amount of bone-implant osseointegration required for a stable miniscrew. The objective of this study was to investigate the influence of different bone-implant interfaces on the miniscrew and its surrounding tissue. *Methods.* Using finite element analysis, an advanced approach representing the bone-implant interface is adopted herein, and different degrees of bone-implant osseointegration were implemented in the FE models. A total of 26 different FE analyses were performed. The stress/strain patterns were calculated and compared, and the displacement of miniscrews was also evaluated. *Results.* The stress/strain distributions are changing with the various bone-implant interfaces. In the scenario of 0% osseointegration, a rather homogeneous distribution was predicted. After 15% osseointegration, the stress/strains were gradually concentrated on the cortical bone region. The miniscrew experienced the largest displacement under the no osseointegration condition. The maximum displacement decreases sharply from 0% to 3% and tends to become stable. *Conclusion.* From a biomechanical perspective, it can be suggested that orthodontic loading could be applied on miniscrews after about 15% osseointegration without any loss of stability.

1. Introduction

Miniscrew has been extensively applied in orthodontic treatment as a temporary anchorage device because of its ease of placement, low cost, minimal anatomic limitations, and enhanced patient comfort. The existing evidence suggests a success rate of more than 80% for miniscrews [1]. Likewise, Albogha and Takahashi have stated a success rate ranging from 77.7% to 93.43% in their study [2]. However, the failure of miniscrew may have dramatic consequences and remain difficult to be anticipated by orthodontists [3]. Since the failure of miniscrew necessitates additional surgical interventions and prolonged treatment time, investigating the mechanical stability of miniscrew becomes imperative.

The biomechanical properties of bone to implant interface are the key determinants for miniscrew stability. Initially, when the miniscrew is placed into bone, the retention

of the implant is provided by mechanical locking. Later, with the progression of bone formation around the implant, bioactive retention can be achieved via physicochemical bonding. It is clinically evident that full osseointegration is a prerequisite for successful prosthetic (or dental) implants [4, 5]. Nevertheless, some fibrous tissue formation at the bone-implant interface would be acceptable because orthodontic loading has to be applied as early as possible and also the miniscrew at the end of treatment must be easily removable [3]. That is to say, partial bone-implant osseointegration of the miniscrew might be permitted for orthodontic treatment. Therefore, the effect of the different degrees of bone-implant osseointegration on the stability will be of great interest from the orthodontist's point of view.

The objective of this study was to investigate the influence of the different implant-bone interface conditions on the biomechanics of an orthodontic miniscrew and its

surrounding tissue with the use of finite element analysis (FEA). FEA is particularly suitable for a biological structure analysis as it allows great flexibility in dealing with geometric complex domains composed of multiple materials [2, 6–8]. In the present study, an advanced approach representing the bone implant interfaces was adopted wherein [9] different percentages of bone-implant osseointegration were implemented in the FE models and the biomechanical behavior of miniscrew and the supporting tissue with the various bone-implant interfaces was predicted and compared.

2. Materials and Methods

The geometry of the partial maxilla, including both premolar and molar, was obtained from the dental hospital, and computed tomography images captured at 0.5 mm intervals were disposed with Mimics software (Materialise NV, Leuven, Belgium) and Geomagic Studio software (Geomagic Company, NC, USA). Maxillary trabecular bone was modeled as a solid structure in the cortical bone with an average thickness of 2 mm based on the CT images. Likewise, the periodontal ligament (PDL) was modeled based on the external geometry of teeth roots with a thickness of 0.20 mm. The implant was structured as a threaded endosseous miniscrew (8 mm length, 1.3 mm diameter, 0.1 mm thread ridge, 60 degrees screw top angle, and 0.5 mm thread pitch) by using a commercial CAD software SolidWorks (SolidWorks Corp., Dassault Systemes, Concord, MA, USA). The miniscrew was inserted into maxillary bone between the premolar and molar at a distance of 3 mm from the alveolar crest, as shown in Figure 1.

The entire model was imported to the finite element package ANSYS Workbench (Swanson Analysis System Co., Houston, TX, USA). The finite element model was meshed using 10-node solid tetrahedral elements (Figure 2(a)). Following a convergence test [7], 0.5 mm was determined to be the appropriate element mesh size for bone and tooth, and even a miniature size (0.2 mm) was selected to accommodate the small feature in the model (e.g., PDL and miniscrew). The detailed element assignment is listed in Table 1. The contacts among the tooth, the related bones, tissue, and ligaments are defined in Table 2.

For the realistic presentation, different amounts of bone-implant osseointegration were implemented, ranging from 0% to 100% (Figure 3). In the existing studies, it was found that there should be a small gap between the implant and peri-implant bone [9, 10]. To evaluate the effect of different bone implant interfaces, a simulation method has already been developed by Lian et al. [9], which was used in the present study. Hence, based on the histological image (Figure 2(c)) [11], it can be suggested that 0.1 mm (100 μ m) thick mixed tissue exists around the miniscrew, constituting a blend of bony tissue and soft tissue to simulate varying bone-implant contact (Figure 2(b)). An ad hoc APDL (ANSYS Parametric Design Language) routine was developed to set the different bone-implant osseointegration. As shown in Figure 3, a certain percentage of mixed tissue elements were selected randomly and assigned the properties of bony tissue. The remaining elements within the mixed

tissue were designated as soft tissue. In this study, a total of 13 different percentages of bone-implant osseointegration were considered (0%, 1%, 2%, 3%, 4%, 5%, 10%, 15%, 20%, 25%, 50%, 75%, and 100%).

Mesial and superior maxillary bone surfaces were fixed in all directions as the boundary conditions (Figure 1(b)). To consider the loading effect of different clinical applications [9, 12], two different kinds of orthodontic load (traction force and revolving torque) were applied at the head of the screw (Figures 1(c) and 1(d)). The direction of the traction force applied was 30 degrees declination to the occlusal plane (Figure 1(c)), and the revolving torque was applied in the clockwise direction (Figure 1(d)).

Fully anisotropic elastic components were used for both cortical and trabecular bones [13, 14], as listed in Table 3. A nonlinear elastic stress-strain behavior of PDL was employed and inputted into FE models, following the approach proposed by Toms et al. [14]. Miniscrew and dentin were considered homogeneous, isotropic, and linearly elastic (Table 4).

3. Results

In the present study, a total of 26 analyses were performed, including the 13 different degrees (from 0% to 100%) of bone-implant osseointegration models with two different kinds of orthodontic load applications (traction force and revolving torque).

The FE simulated results for the force and torque load in the peri-implant tissue (mixed tissue region) are shown in Figures 4 and 5, respectively. For the ease of observation, equivalent stresses/strains in the cross section of the FE models are displayed. As shown in the figures, the stress and strain distributions in the mixed tissue are changing with the various bone-implant interfaces. Initially, in the scenario of 0% osseointegration, a rather homogeneous equivalent stress/strain distribution was predicted. And then, remarkable stress/strain concentrations could be seen in the peri-implant tissue with the 1% osseointegration interface. After the 15% osseointegration, the stress and strains were gradually concentrated on the cortical bone region rather than in the trabecular bone region. It is worth noting that, whatever kind of the orthodontic loads are subjected, there is a significant change in the first 7 degrees (0%~10%), but the variation range reduced obviously after the 15% osseointegration.

Figures 6 and 7 show the equivalent stress and strain on the surrounding bone under the application of traction force and revolving torque, respectively. As evident from Figure 6, under the application of traction force, the stress induced in the cortical bone was much higher as compared to that in the trabecular bone. With the change in bone-implant interfaces, the stress distribution gradually concentrated on the bone around the neck of miniscrew. The strain distribution also showed a trend similar to the stress. However, in the initial phase (0%~15%), the maximum strain was located in the trabecular bone rather than the cortical bone. Furthermore, the equivalent stress and strain distributions with revolving torque application are shown in Figure 7. The changing trend of equivalent stress and strain is much similar to that of traction force application. At the beginning

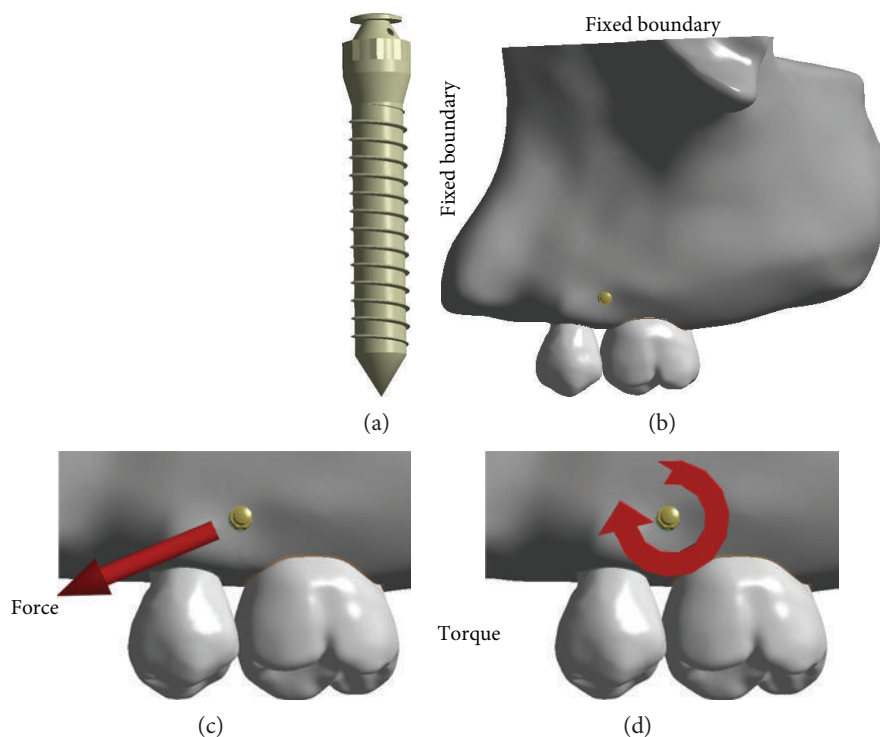


FIGURE 1: (a) Microimplant. (b) Geometry models with fixed boundary conditions (buccal side). (c) The traction force and (d) revolving torque employed during orthodontic loading.

(0% osseointegration), the stress was longitudinally distributed along the whole miniscrew. With the integration of the bone and implant, the stress was highly concentrated in the neck of the miniscrew. Similarly, the strain distribution was concentrated on the trabecular bone initially, which later on shifted towards the neck of the miniscrew with the change in bone-implant osseointegration percentages.

Figure 8 illustrates quantitatively the relationship between the degree of bone-implant osseointegration and biomechanical characteristics of bone-implant complex. Figures 8(a) and 8(b) represent the change in average equivalent stress and strain in the mixed (peri-implant) tissue, respectively. It is evident from Figure 8(a) that the stress increases progressively before the 10% osseointegration, followed by a slight decrease, and then increases again. As shown in Figure 8(b), the strain decreases significantly at the beginning, and then tends towards stability until the 100% osseointegration is achieved. From Figures 8(c) and 8(d), it can be seen that the equivalent stress changes with the increase in the osseointegration degrees in the cortical bone and trabecular bone region, respectively. Besides, initially the stress increases sharply, and then drops down followed by a gradual increase again after the 15% osseointegration. As shown in Figure 8(d), it can be seen that the graph exhibits similar patterns to those presented in Figure 8(c), but a turning point is not observed at the 15% osseointegration in the trabecular bone. Relative to the displacement (Figure 8(e)), the miniscrew experienced the largest displacement under the condition of no osseointegration (0%). The maximum displacement decreases sharply from

0% to 3% and tends to become stable after completion of approximately 3~4% osseointegration.

4. Discussion

In this study, finite element models were generated to investigate the effect of different implant-bone interface conditions on the mechanical stability of miniscrew. From 0% to 100%, 13 different degrees of bone-implant interfaces were simulated. The stress/strain patterns generated by the miniscrews at the surrounding tissue were calculated and compared, and the displacement of miniscrew was also evaluated.

In dental biomechanics, almost all the FE models generated currently simulated different bone to implant interfaces by employing frictional contact analysis [2]. In a typical FE model built by Yang and Xiang [15], three different contact types were used to represent the integration quality at the implant-bone interface. The “bonded” type simulates a full osseointegration; the “no separation” type indicates an imperfect osseointegration, and the “frictionless” contact implies no osseointegration. As a progressive technology of simulating partial contact, a random algorithm was developed by Gracco et al. to set a part of the nodes localized at the bone/implant interface as the tie constraint, and the remaining part of the interface was set as frictional contact [16]. However, although contact analyses with different frictional coefficients can be used to assess the biomechanical effects of many different implant-bone complex, the specific frictional coefficients is still difficult to determine by an

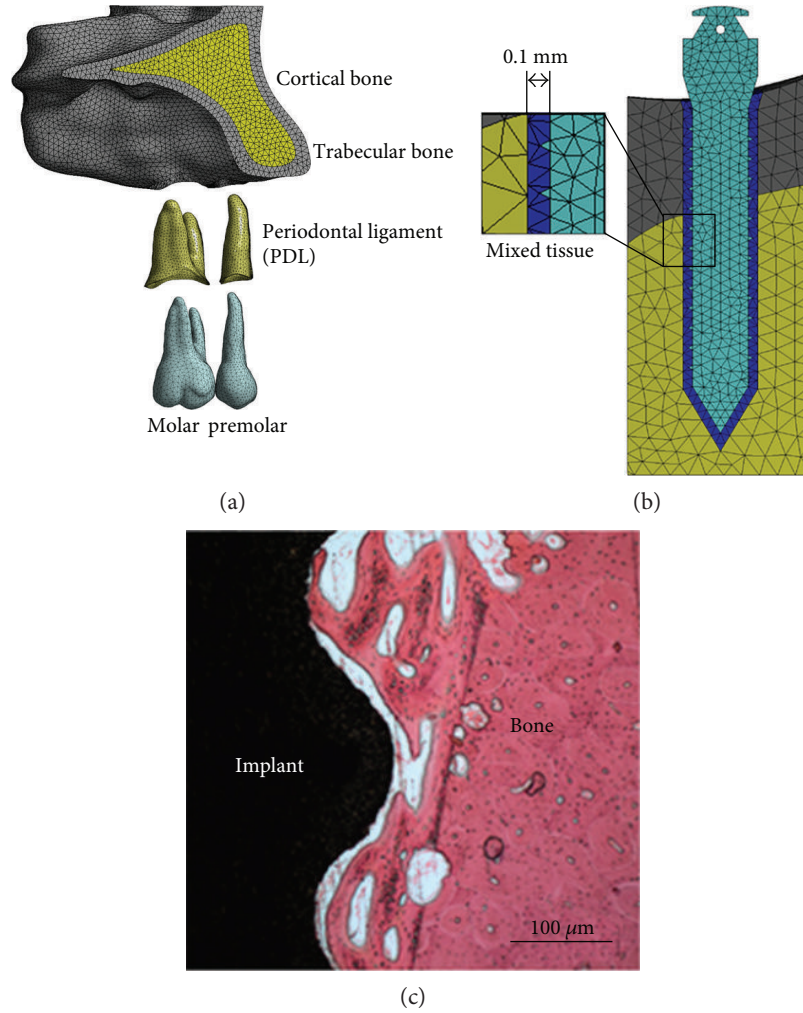


FIGURE 2: (a) Finite element models of cortical bone, trabecular bone, periodontal ligament (PDL), and premolar and molar (palatal side). (b) The 0.1 mm ($100\ \mu\text{m}$) thick mixed tissue around microimplant. (c) The histological image showing the bone-implant interface (courtesy of Professor Shicheng Wei).

TABLE 1: The number of nodes and elements of FE model.

	Nodes	Elements
Cortical bone	150,450	94,395
Trabecular bone	161,301	107,895
Microimplant	7563	4000
PDL	28,913	14,332
Teeth	16,793	9384
Mixed tissue	56,068	29,579
Total	421,088	259,585

existing biomechanical testing [17]. In order to overcome the limitations of the existing methodologies, an alternative method was proposed by Lian et al. [9]. In this method, an assumption was made that a small part of tissue surrounding the implant was constituted as a mix of hard and soft tissue. According to the observation of previous histological studies [18, 19], this assumption has been proved to be reasonable. Therefore, considering the progressive change of the

TABLE 2: Contact types set in the FE models.

Contact bodies		Contact type
Tooth	Tooth	Frictionless
Tooth	PDL	Bonded
PDL	Bone	Bonded
Microimplant	Mixed tissue	Bonded
Mixed issue	Bone	Bonded

surrounding tissue around the miniscrew, this alternative method was advanced from a 2D simulation to 3D, to reproduce the different bone-implant interfaces in our FE models.

Till date, the minimum level of bone-implant osseointegration for clinical success in orthodontics has not been clearly described. From the biomechanical viewpoint, the minimum amount of bone-implant osseointegration required can be inferred from our analytical results. For the equivalent stress and strain (Figures 4–7), the implant-bone interface conditions significantly affected the stress/strain distributions

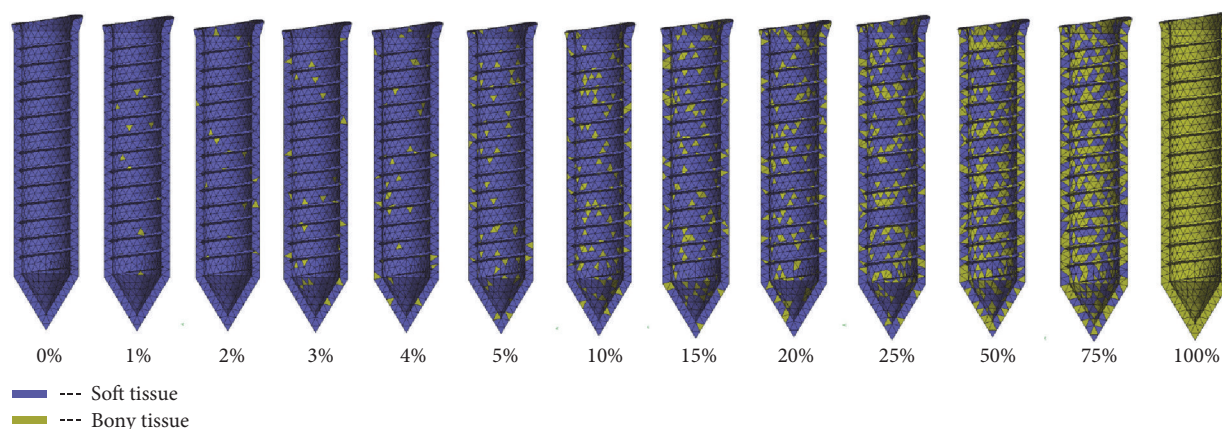


FIGURE 3: Different degrees of the bone-implant osseointegration interfaces implemented in the FE models, varying from 0% to 100%.

TABLE 3: Anisotropy elastic coefficients for cortical and trabecular bone^a.

	E1	E2	E3	G12	G13	G23	ν_{12}	ν_{13}	ν_{23}
Cortical bone ^b	12.5	17.9	26.6	4.5	5.3	7.1	0.18	0.31	0.28
Trabecular bone ^c	0.21	1.148	1.148	0.068	0.068	0.434	0.055	0.055	0.322

^a E_i represents Young's modulus (GPa); G_{ij} represents shear modulus (GPa); ν_{ij} represents Poisson's ratio; the 1-direction is radial, the 2-direction is tangential (circumferential), and the 3-direction is axial (longitudinal); the 1-direction is inferosuperior (the axis of transverse isotropy symmetry with the smallest of Young's modulus value), the 2-direction is mediolateral, and the 3-direction is anteroposterior.

TABLE 4: Material elastic modulus parameter employed in the FE models.

	Elastic modulus (GPa)	Poisson's ratio	References
Tooth	22.0	0.31	Holberg et al., 2013
Microimplant	113.4	0.342	Alrbata et al., 2014
Bony tissue	2.4	0.3	Lian et al., 2010
Soft tissue	0.07	0.3	Lian et al., 2010

on the surrounding tissue when the osseointegration was less than 15%. Further analysis (15%~100%) reveals that, even though the stress/strain concentration appears around the implant neck region, the overall changes in the stress/strain distributions from 15% to 100% osseointegration can be neglected. Besides, according to the progressive biomechanical characteristics of bone-implant complex (Figure 8), the minimum amount of bone-implant osseointegration may vary between 2% and 10%. Some of the previous findings are also in support of our results. Deguchi et al. implied that implants with as little as 5% bone osseointegration at the bone-implant interface can successfully withstand orthodontic force [20], and also the study by Woods suggested that 2.2 percent BIC may be sufficient for light force [21]. However, during the low degrees of bone-implant osseointegration (0~15%), our results show that the presence of connective tissue (soft tissue) at the implant-bone interface might result in an increase of stress/strain magnitudes in the trabecular bone as compared with full osseointegration conditions.

Because of the occurrence of fibrous tissue, miniscrew cannot be tightly held by alveolar bone, leading to miniscrew instability. The surrounding trabecular bone might be damaged due to the changing mechanical environment induced by the miniscrew, and excessive implant displacement may cause loosening, dislocation, or even loss of the implant. Therefore, it can be inferred that orthodontic loading can be applied over the miniscrew after completion of 15% osseointegration without a compromise of stability. That is to say, less than 15% osseointegration might be a risk factor in terms of implant stability, and hence should be avoided.

Now, a critical question arises, that is, what should be the latency period to achieve the minimum percentage of bone-implant osseointegration during an orthodontic treatment? In reference to previous animal/ histological studies, several investigations have been done on the healing time of orthodontic miniscrew. However, no study has been conducted specifically to solve this problem. Even more, the existing results are inconclusive about the proper timing of orthodontic force application. A histological study done by Ramazanzadeh et al. concluded that healing time has no significant effect on miniscrew stability, but only a comparison of bone-implant contact between 4 weeks and 8 weeks was made in his study [22]. In another study by Oltramari-Navarro et al., similar histomorphometric results were observed for the immediate and the delayed orthodontic loads groups, but it is important to note that the immediate group presented higher failure rate (50%) than the delayed group [18]. Likewise, the results of an animal study by Zhao et al. indicated that early loading may decrease the osseointegration of miniscrews, and the same investigators

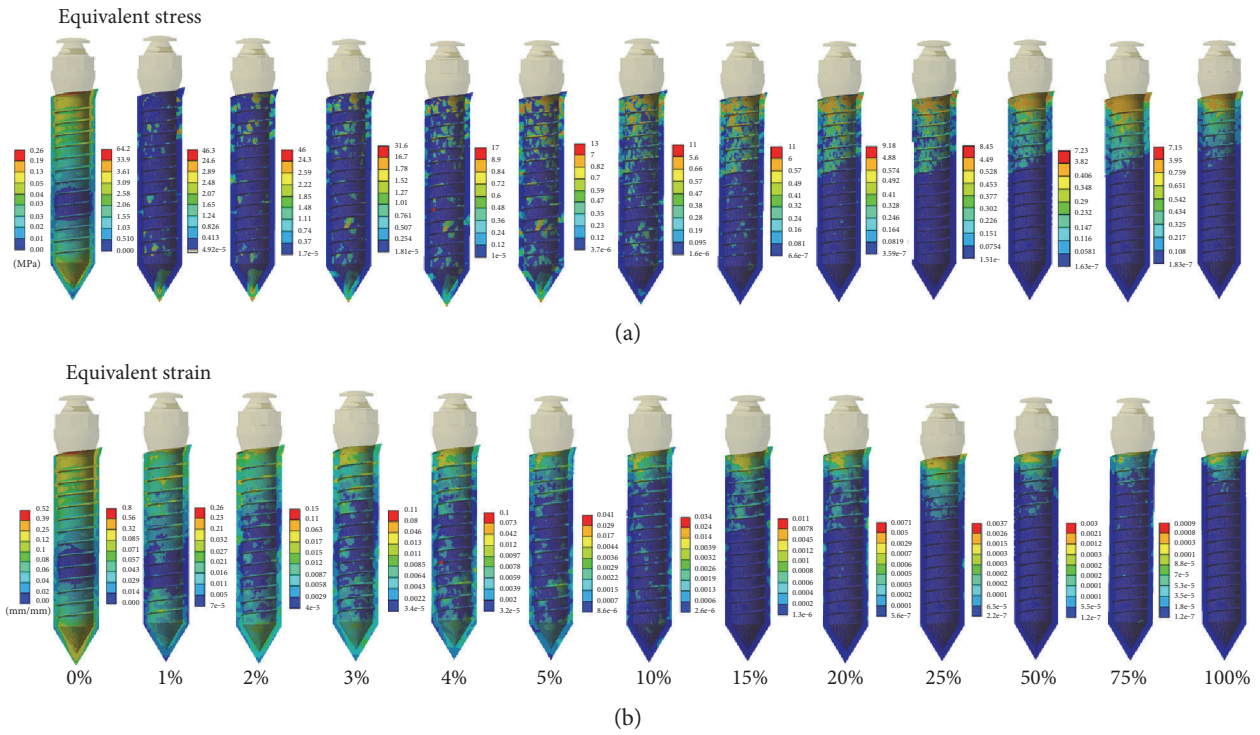


FIGURE 4: Progressive alteration of (a) equivalent stress and (b) strain distributions in peri-implant tissue under the application of traction force.

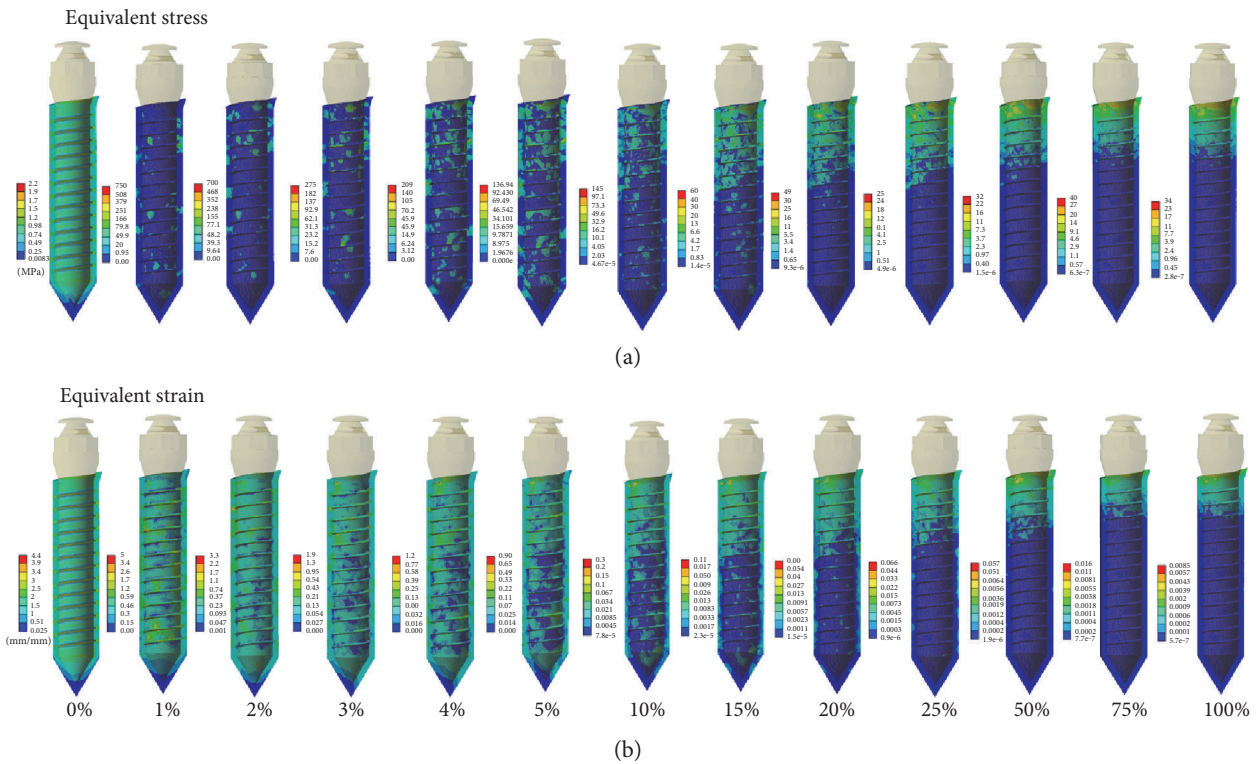


FIGURE 5: Progressive alteration of (a) equivalent stress and (b) strain distributions in peri-implant tissue under the application of revolving torque.

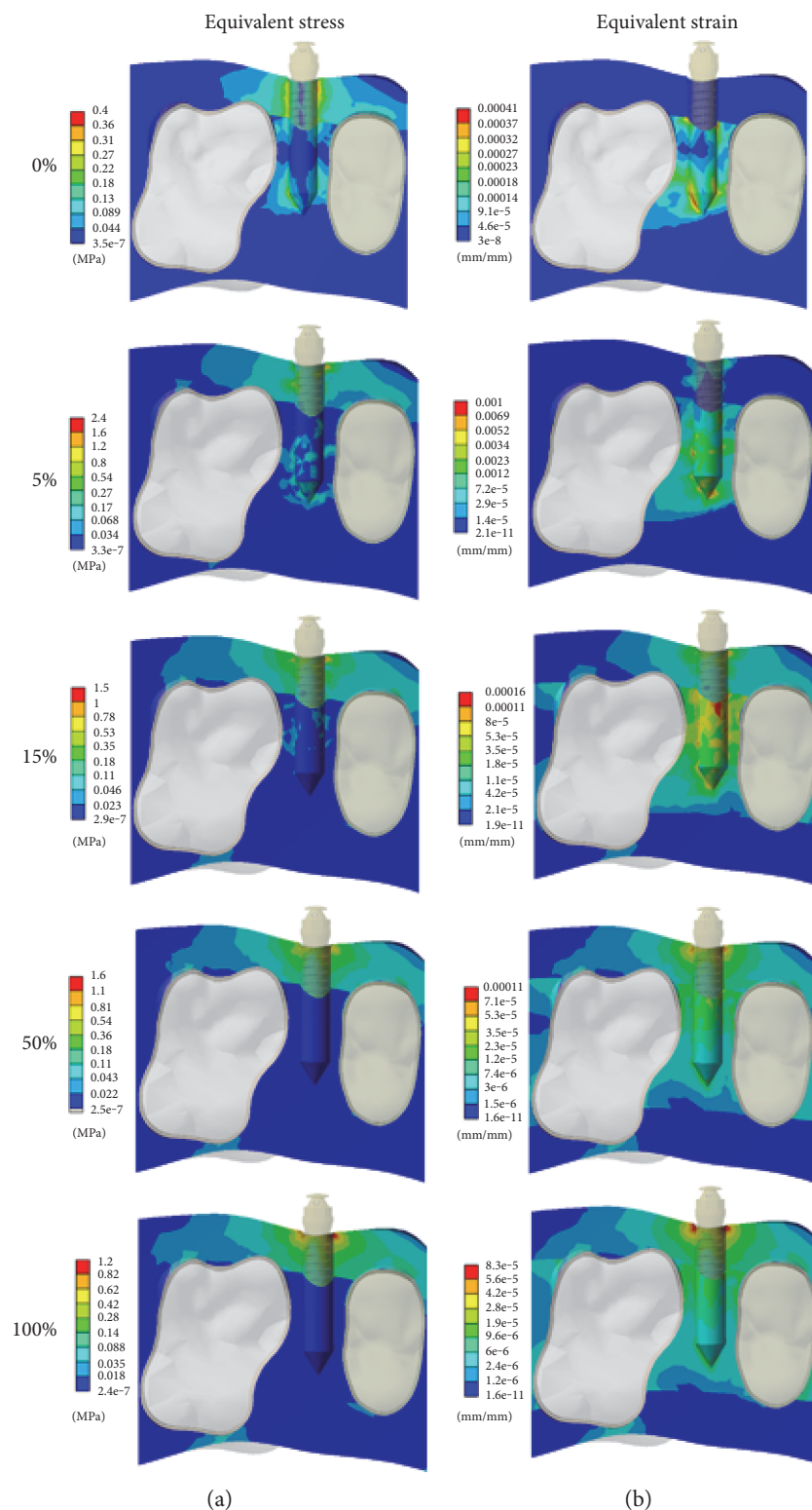


FIGURE 6: Progressive alteration of (a) equivalent stress and (b) strain distributions in the surrounding bone under the application of traction force.

suggested that a 4-week healing time is recommended before orthodontic loading [23]. Deguchi et al. also concluded that a minimal healing period of 3 weeks is required for orthodontic loading [20]. Above all, the existing animal

experiments presented some useful conclusion; however, their results remain limited when it comes to understanding the various conditions of bone-implant interfaces playing a role in miniscrew stability.

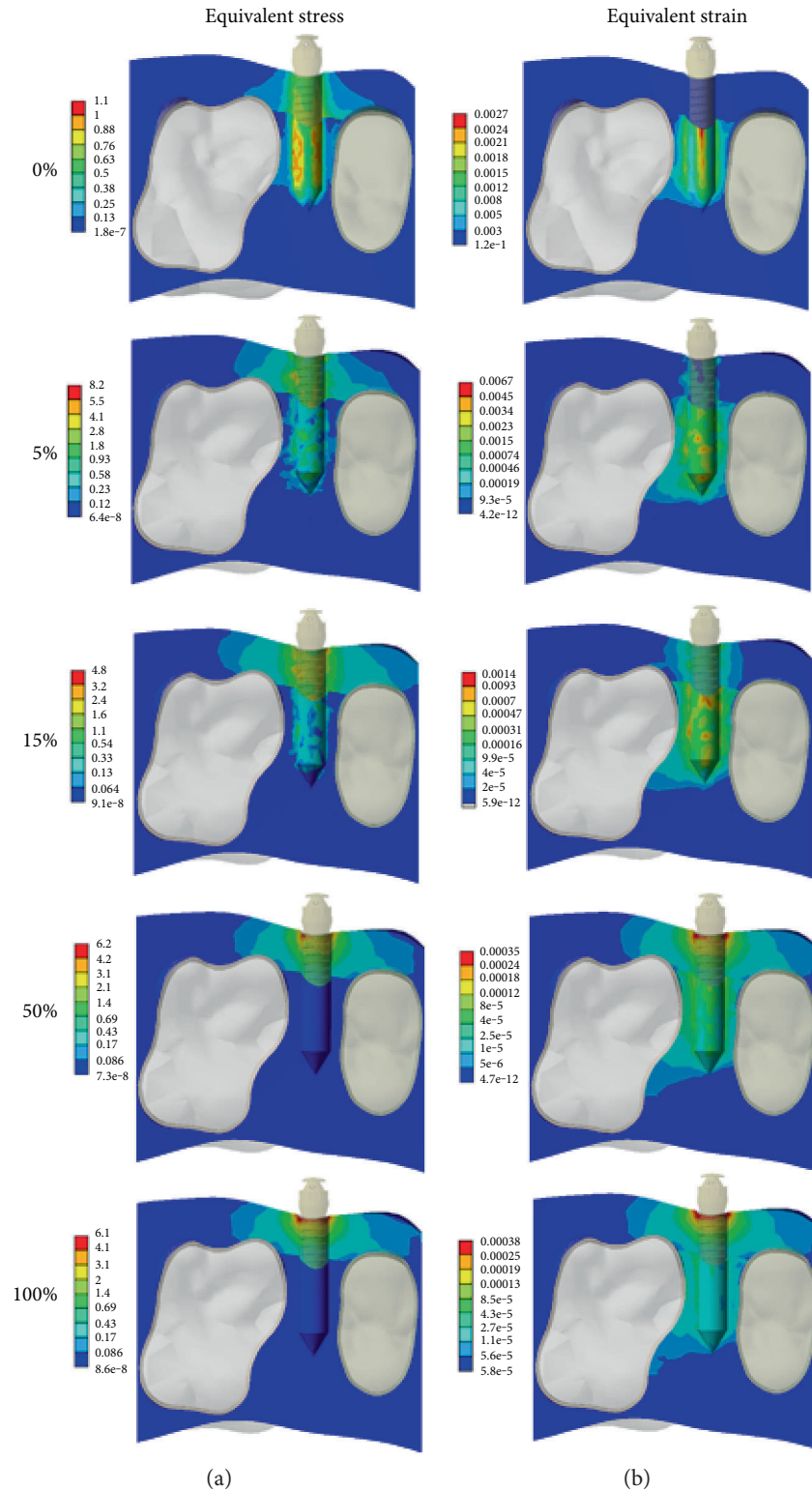


FIGURE 7: Progressive alteration of (a) equivalent stress and (b) strain distributions in the surrounding bone under the application of revolving torque.

The research limitations and suggestions for future research should be pointed out. Firstly, additional animal research is required to answer the above-mentioned question. If the exact time for achieving 15% osseointegration of

miniscrew could be confirmed, the appropriate time of miniscrew loading can be effectively ensured for orthodontists. Secondly, the bone remodeling process was not considered in the simulation. In fact, the bone remodeling occurs around

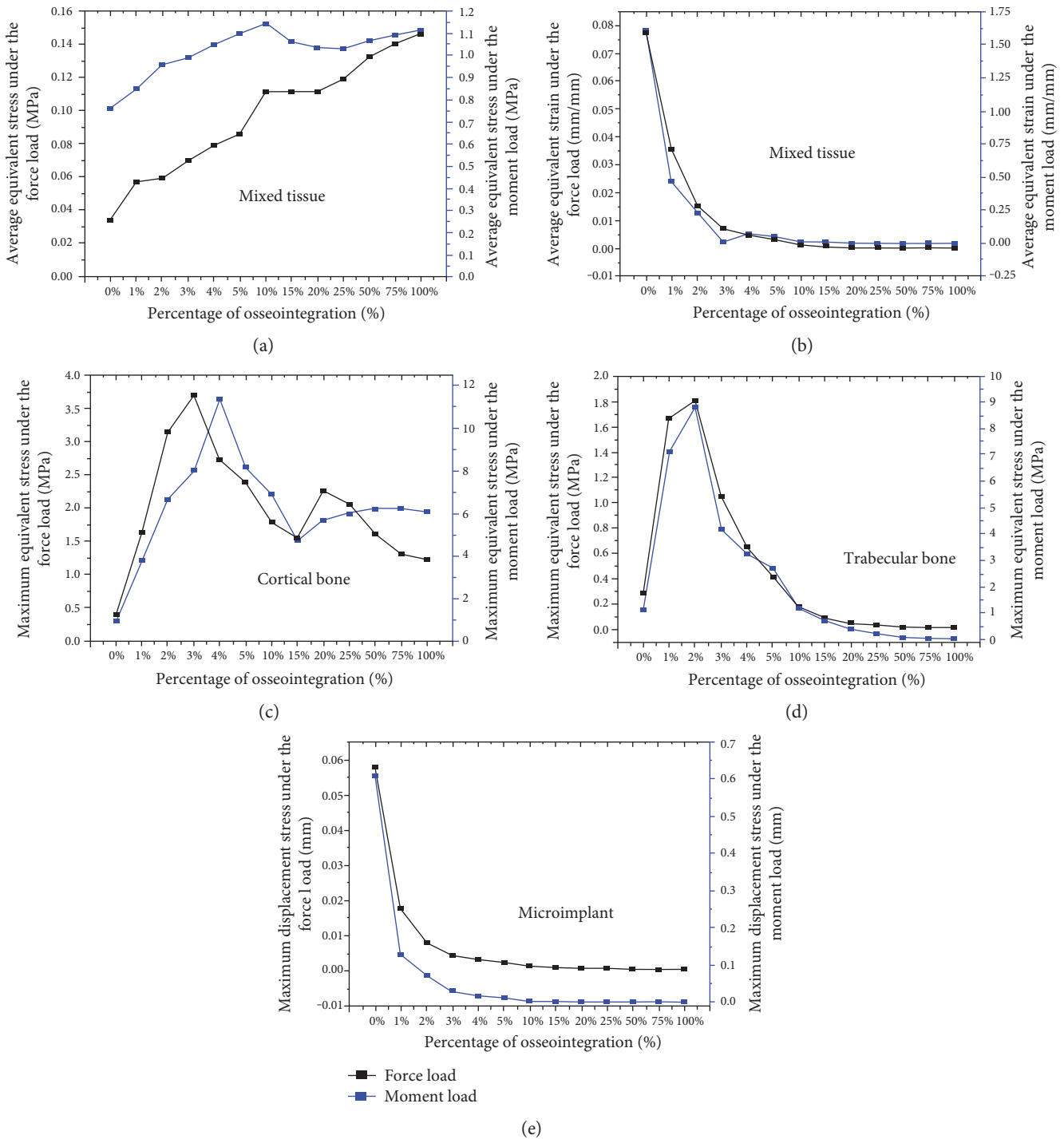


FIGURE 8: Change in biomechanical characteristics of microimplant and supporting oral tissues with the different bone-implant osseointegration interfaces. (a) The average equivalent stress in the peri-implant mixed tissue. (b) The average equivalent strain in the peri-implant tissue. (c) The maximum equivalent stress in cortical bone. (d) The maximum equivalent stress in trabecular bone. (e) The maximum displacement of microimplant.

the implant during the healing period. So the progressive process of bone remodeling should be included in further simulation to investigate mechanical stability of orthodontic miniscrew. Finally, the material nonlinear properties of the mixed tissue (hard and soft tissue) should be considered in the FE analysis. Because large deformation can be observed during this simulation, the incorporation of nonlinear properties can provide more accurate and reliable results.

5. Conclusions

Within the limitation of this study, it can be suggested that the orthodontic force can be applied at the miniscrew after completion of approximately 15% osseointegration which is the more beneficial for the mechanical stability of the miniscrew. Under this condition, the miniscrew can be tightly held in place by the surrounding tissue and employed as

orthodontic anchorage without compromising implant stability. For clinical application of the results simulated in our study, a specifically designed study is required to confirm the appropriate time of orthodontic loading in the future.

Conflicts of Interest

The authors declare that there is no conflict of interest regarding the publication of this paper.

Acknowledgments

The work was supported by the National Natural Science Foundation of China (Grant no. 11402042), the Medical Scientific Research Foundation of Health and Family Planning Commission of Chongqing (major project, Grant no. 20141012) and the Program for Innovation Team Building at Institutions of Higher Education in Chongqing in 2013. Special thanks are to Professor Shicheng Wei of Peking University at Beijing for his assistance during this study.

References

- [1] R. Reynders, L. Ronchi, and S. Bipat, "Mini-implants in orthodontics: a systematic review of the literature," *American Journal of Orthodontics and Dentofacial Orthopedics*, vol. 135, no. 5, pp. 564.e1–564.e19, 2009.
- [2] M. H. Albogha and I. Takahashi, "Generic finite element models of orthodontic mini-implants: are they reliable?" *Journal of Biomechanics*, vol. 48, no. 14, pp. 3751–3756, 2015.
- [3] J. C. Rodriguez, F. Suarez, H. L. Chan, M. Padial-Molina, and H. L. Wang, "Implants for orthodontic anchorage: success rates and reasons of failures," *Implant Dentistry*, vol. 23, no. 2, pp. 155–161, 2014.
- [4] P. I. Branemark, "Osseointegration and its experimental background," *The Journal of Prosthetic Dentistry*, vol. 50, no. 3, pp. 399–410, 1983.
- [5] T. Albrektsson and G. A. Zarb, "Current interpretations of the osseointegrated response: clinical significance," *The International Journal of Prosthodontics*, vol. 6, no. 2, pp. 95–105, 1993.
- [6] R. H. Alrbata, W. Yu, and H. M. Kyung, "Biomechanical effectiveness of cortical bone thickness on orthodontic microimplant stability: an evaluation based on the load share between cortical and cancellous bone," *American Journal of Orthodontics and Dentofacial Orthopedics*, vol. 146, no. 2, pp. 175–182, 2014.
- [7] C. Wang, W. Zhang, D. H. Ajmera, Z. Yun, Y. Fan, and J. Ping, "Simulated bone remodeling around tilted dental implants in the anterior maxilla," *Biomechanics and Modeling in Mechanobiology*, vol. 15, no. 3, pp. 701–712, 2016.
- [8] Y.-S. Lin, J.-H. Yu, Y.-Z. Chang, and C.-L. Lin, "Biomechanical evaluation of an orthodontic miniimplant used with revolving (translation and rotation) temporary anchorage device by finite element analysis and experimental testing," *Implant Dentistry*, vol. 22, no. 1, pp. 77–82, 2013.
- [9] Z. Lian, H. Guan, S. Ivanovski, Y. C. Loo, N. W. Johnson, and H. Zhang, "Effect of bone to implant contact percentage on bone remodelling surrounding a dental implant," *International Journal of Oral and Maxillofacial Surgery*, vol. 39, no. 7, pp. 690–698, 2010.
- [10] P. Trisi, D. Berardi, M. Paolantonio, G. Spoto, A. D'Addona, and G. Perfetti, "Primary stability, insertion torque, and bone density of conical implants with internal hexagon: is there a relationship?" *The Journal of Craniofacial Surgery*, vol. 24, no. 3, pp. 841–844, 2013.
- [11] A. Xu, "The research of osteogenic modification with BFP-1 peptide via polydopamine on surface of polyetheretherketone nano composites," *Chongqing Medical University*, 2015.
- [12] C. Holberg, P. Winterhalder, N. Holberg, I. Rudzki-Janson, and A. Wichelhaus, "Direct versus indirect loading of orthodontic miniscrew implants-an FEM analysis," *Clinical Oral Investigations*, vol. 17, no. 8, pp. 1821–1827, 2013.
- [13] S. H. Liao, R. F. Tong, and J. X. Dong, "Influence of anisotropy on peri-implant stress and strain in complete mandible model from CT," *Computerized Medical Imaging and Graphics*, vol. 32, no. 1, pp. 53–60, 2008.
- [14] S. R. Toms, G. J. Dakin, J. E. Lemons, and A. W. Eberhardt, "Quasi-linear viscoelastic behavior of the human periodontal ligament," *Journal of Biomechanics*, vol. 35, no. 10, pp. 1411–1415, 2002.
- [15] J. Yang and H. J. Xiang, "A three-dimensional finite element study on the biomechanical behavior of an FGBM dental implant in surrounding bone," *Journal of Biomechanics*, vol. 40, no. 11, pp. 2377–2385, 2007.
- [16] A. Gracco, A. Cirignaco, M. Cozzani, A. Boccaccio, C. Pappalettere, and G. Vitale, "Numerical/experimental analysis of the stress field around miniscrews for orthodontic anchorage," *European Journal of Orthodontics*, vol. 31, no. 1, pp. 12–20, 2009.
- [17] N. B. Damm, M. M. Morlock, and N. E. Bishop, "Friction coefficient and effective interference at the implant-bone interface," *Journal of Biomechanics*, vol. 48, no. 12, pp. 3517–3521, 2015.
- [18] V. P. Oltramari-Navarro Paula, R. L. Navarro, J. F. C. Henriques et al., "The impact of healing time before loading on orthodontic mini-implant stability: a histomorphometric study in minipigs," *Archives of Oral Biology*, vol. 58, no. 7, pp. 806–812, 2013.
- [19] B. Melsen and N. P. Lang, "Biological reactions of alveolar bone to orthodontic loading of oral implants," *Clinical Oral Implants Research*, vol. 12, no. 2, pp. 144–152, 2001.
- [20] T. Deguchi, T. Takano-Yamamoto, R. Kanomi, J. K. Hartsfield, W. E. Roberts, and L. P. Garetto, "The use of small titanium screws for orthodontic anchorage," *Journal of Dental Research*, vol. 82, no. 5, pp. 377–381, 2003.
- [21] P. W. Woods, P. H. Buschang, S. E. Owens, P. E. Rossouw, and L. A. Opperman, "The effect of force, timing, and location on bone-to-implant contact of miniscrew implants," *European Journal of Orthodontics*, vol. 31, no. 3, pp. 232–240, 2009.
- [22] R. B. Ali, K. Fatemi, M. Dehghani, N. Mohtasham, A. Jahanbin, and H. Sadeghian, "Effect of healing time on bone-implant contact of orthodontic micro-implants: a histologic study," *ISRN Dentistry*, vol. 2014, no. 1, pp. 1–7, 2014.
- [23] Z. Lixing, Z. Xu, Z. Yang, X. Wei, T. Tang, and Z. Zhao, "Orthodontic mini-implant stability in different healing times before loading: a microscopic computerized tomographic and biomechanical analysis," *Oral Surgery, Oral Medicine, Oral Pathology, Oral Radiology, and Endodontology*, vol. 108, no. 2, pp. 196–202, 2009.

Research Article

Development and Implementation of an End-Effector Upper Limb Rehabilitation Robot for Hemiplegic Patients with Line and Circle Tracking Training

Yali Liu,¹ Chong Li,¹ Linhong Ji,¹ Sheng Bi,² Xuemin Zhang,² Jianfei Huo,² and Run Ji³

¹Division of Intelligent and Biomechanical System, State Key Laboratory of Tribology, Tsinghua University, Haidian, Beijing, China

²Rehabilitation Medical Center, Affiliated Hospital of National Research Center for Rehabilitation Technical Aids, Haidian, Beijing, China

³Human Biomechanics Laboratory, National Research Center for Rehabilitation Technical Aids, Beijing, China

Correspondence should be addressed to Linhong Ji; jilh@tsinghua.edu.cn

Received 3 March 2017; Accepted 23 April 2017; Published 15 June 2017

Academic Editor: Lizhen Wang

Copyright © 2017 Yali Liu et al. This is an open access article distributed under the Creative Commons Attribution License, which permits unrestricted use, distribution, and reproduction in any medium, provided the original work is properly cited.

Numerous robots have been widely used to deliver rehabilitative training for hemiplegic patients to improve their functional ability. Because of the complexity and diversity of upper limb motion, customization of training patterns is one key factor during upper limb rehabilitation training. Most of the current rehabilitation robots cannot intelligently provide adaptive training parameters, and they have not been widely used in clinical rehabilitation. This article proposes a new end-effector upper limb rehabilitation robot, which is a two-link robotic arm with two active degrees of freedom. This work investigated the kinematics and dynamics of the robot system, the control system, and the realization of different rehabilitation therapies. We also explored the influence of constraint in rehabilitation therapies on interaction force and muscle activation. The deviation of the trajectory of the end effector and the required trajectory was less than 1 mm during the tasks, which demonstrated the movement accuracy of the robot. Besides, results also demonstrated the constraint exerted by the robot provided benefits for hemiplegic patients by changing muscle activation in the way similar to the movement pattern of the healthy subjects, which indicated that the robot can improve the patient's functional ability by training the normal movement pattern.

1. Introduction

Stroke is a leading cause of physical impairments, with symptoms of spasticity, weakness, and hemiplegia [1, 2]. Functional disability of upper limb is a common impairment among hemiplegic patients, which causes difficulties and inconvenience in activities of daily life [3, 4]. It has been reported that the repetitive interventions, such as constraint-induced movement therapy and variable task-oriented repetitive therapy, can improve movement coordination in patients with hemiplegic disabilities [5, 6]. Robots with its good repeatability and movement accuracy have been widely used in hemiplegic patients' physical therapy researches [6–9].

Although many robot rehabilitation therapies have been designed, such as the passive-guided mode, the active as needed, and the resistant mode [10–14], the clinical experiment with rehabilitation robots has not demonstrated expected effects, which may be caused by the patients' individual difference [15]. Researchers are paying more and more attention to improve the adaptation of rehabilitation robots to individual difference. Many researches have reported that researchers determine the equivalent impedance parameters of human upper limb online and offline by intelligent control algorithm to increase the adaptation of the robot system and improve the participants' experience [16–19]. Demir et al. [19] analyzed the patients' mechanical impedance parameters by neural network algorithm while training with their

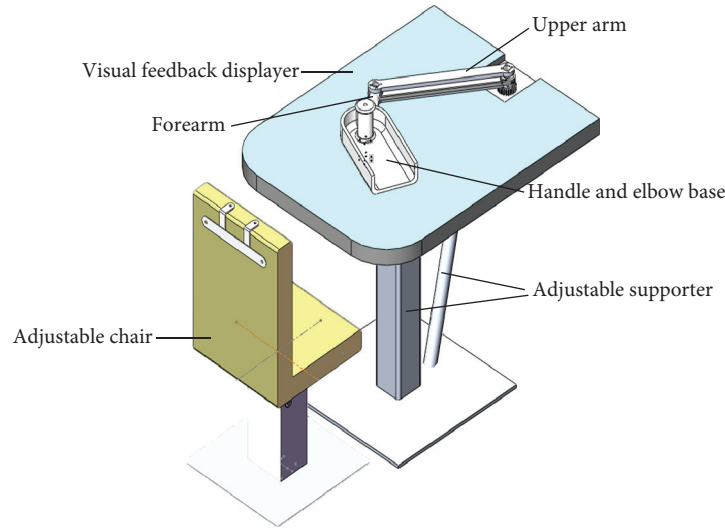


FIGURE 1: The Solidworks model of EEULRobot system.

therapist and then used the parameters to activate the robot to imitate the interaction. Song et al. [20] developed an adaptive motion control for a 4-DOF end-effector upper limb robot based on impedance identification and confirmed that the control strategy can realize the adaption of the system among five healthy subjects' experiment. The intelligent control strategies have been considered as an effective method to improve the adaption of rehabilitation robot system during clinical experiment.

The parameters of movement therapy in most rehabilitation robots cannot be intelligently changed to individual difference. Because of the complex and diversity of upper limb movement during daily life, the clinical therapy for upper limb rehabilitation training should be customized. The rehabilitation robots based on neural networks have been widely discussed to change therapy parameters according to patients' conditions. Owing to the difficulty of intelligent control training and lack of sufficient training set [16, 20, 21], rehabilitation robots based on intelligent control strategies have been still not widely used in clinical rehabilitation.

The objective of this article is to develop a new rehabilitation robot based on interaction force and displacement of end-effector to help patients to train in point-to-point line and circle tracking tasks. Besides, this article provides some experiments to verify the effectiveness of the robot.

2. Materials and Methods

2.1. Description of the EEULRobot System. Upper extremity compound movement robot rehabilitation platform (UECM) was an end-effector rehabilitation robot providing trainings in a fixed plane [22, 23], which can only deliver passive-guided therapy for the patients with line and circle tracking tasks in clinical rehabilitation. End-effector upper limb rehabilitation robot (EEULRobot), the improved version of (UECM), is developed with multiple

training modes for shoulder and elbow coordination for hemiplegic patients following a stroke. This new robot can train patients in multiple planes in order to imitate the activities of daily life, which is the improvement from UECM. When the deviation between actual movement and designed trajectory is larger than the threshold, or when the movement velocity is smaller than the threshold velocity which reflected patients' functional ability [24], training modes should be adjusted. The details of the adjustment are illustrated in the following section of control strategies, which will widen the robot application in clinical research.

Mechanical system of the EEULRobot is designed to mimic the human body structure, with two links similar to human upper arm and forearm. Besides, a handle and elbow support is implemented in the system, which is used to help patients hold their arms in normal posture.

EEULRobot is equipped with an adjustable height and inclination angle supporter actuated by a lift (LP2, LINAK, Denmark) as well as a height adjustable chair implemented by another lift (LB1, LINAK, Denmark). According to the patients' needs, the height of the supporter platform is in range of 700~1200 mm with the height of the designed chair in range of 350~750 mm. Besides, the planar inclination angle of the supporter platform is in range of -30° ~ 60° for different planar training. Two Maxon RE40 DC motors are used to drive the upper limb and forearm, respectively, to realize the planar movement of end-effector. Two planetary gear reducer with a ratio of 53:1 (Maxon GP42) are used in order to increase the output torque of motors as well as decrease the output rotation speed. During one training, the end-effector is moved on one plane, and the planar force, which is a two-dimensional force, is needed to calculate the torque of each motor. So the robot is also equipped with a two-dimensional force sensor (BaiSen Instrument, China) that

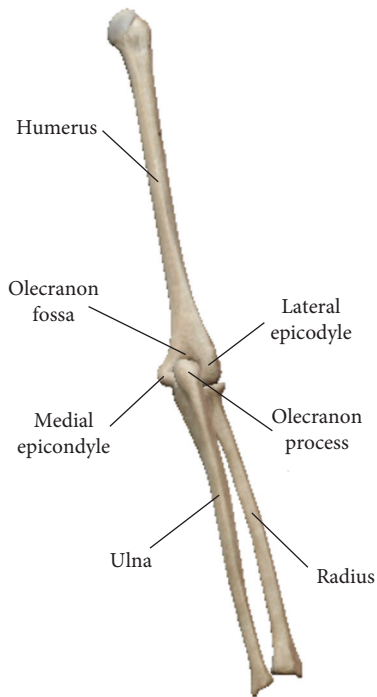


FIGURE 2: Posterior view of human upper limb. The humerus and ulna as well as radius form the elbow joint with their characteristic shape features: medial epicondyle, lateral epicondyle, olecranon fossa, and olecranon process.

measures the interaction force between the human and the robot. The isometric view of the EEULRebot system is shown in Figure 1.

Besides the adjustable supporter system and the driving system, the EEULRebot system also includes a visual feedback displayer as a biofeedback system. This displayer will show the designed trajectory and the actual movement of the end-effector in different colors to highlight the difference, which will remind patients to adjust their movement to decrease the deviation.

2.2. Kinematic Model. The EEULRebot system has two serial links similar to human upper arm and forearm, which will have two different postures for a certain end-effector position. But, while we apply some anatomical features in human upper limb, we will get a determined solution for the two serial links inverse kinematics. Our actual forearm consisting of ulna and radius is connected with our upper arm humerus, forming the elbow joint [25]. The olecranon fossa at humerus and the olecranon process at ulna are connected with each other as shown in Figure 2. This connection will limit the range of elbow extension and make the forearm usually in anterior of upper arm. Accordingly, it is reasonable to suppose that the forearm of EEULRebot should also be in one side of its upper arm during all the tasks. Then, we can get the determined inverse kinematic solution calculated as following process.

The kinematic model of EEULRebot, as shown in Figure 3. According to the previously mentioned characteristics that

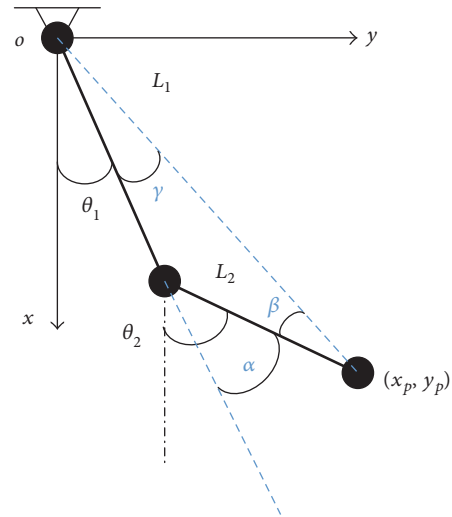


FIGURE 3: The kinematic model of EEULRebot. θ_1 and θ_2 refer to each motor rotation angle relative to the settled zero reference position ($\theta_1 = \theta_2 = 0$ while the two links are parallel to the x -axis). L_1 and L_2 mean the length of the EEULRebot upper arm and forearm. The end point position is (x_p, y_p) . α , β , and γ represent the angles between the segments and the reference lines.

the forearm is always in anterior of the upper arm during upper limb movements, we get the solution constraints in inverse kinematics: $-\pi/2 \leq \theta_1 \leq \pi/2, 0 \leq \theta_2 - \theta_1 \leq \pi$.

$$\begin{aligned} \alpha &= \theta_2 - \theta_1 = \cos^{-1} \frac{x_p^2 + y_p^2 - L_1^2 - L_2^2}{2 \times L_1 \times L_2}, \\ \beta &= \cos^{-1} \frac{L_1 \cos \alpha + L_2}{\sqrt{x_p^2 + y_p^2}}, \\ \gamma &= \alpha - \beta, \\ \theta_1 &= \cos^{-1} \frac{x_p}{\sqrt{x_p^2 + y_p^2}} - \gamma, \\ \theta_2 &= \theta_1 + \alpha. \end{aligned} \quad (1)$$

Then, the program is implemented in C++ software (Microsoft Visual C++ 6.0) and converse θ_1 and θ_2 to the steps of each motor for rotation function.

2.3. Dynamic Model. Since trainings in one training session are always on the supporting surface, which is a fixed plane during the training, the effect of gravitational potential energy can be ignored.

As shown in Figure 4, θ_1 , θ_2 , L_1 , and L_2 represent the same variables as they do in Figure 3. F_x and F_y are the external forces at the end-effector of EEULRebot. τ_1 and τ_2 represent the torque of each motor and m_u , m_f , and m_s , respectively, mean the mass of upper arm, forearm of EEULRebot, and the force sensor (since m_s is in the same magnitude with m_u and m_f , we must consider m_s during dynamic modeling). τ_1 and τ_2 are calculated according to Lagrange's formulation.

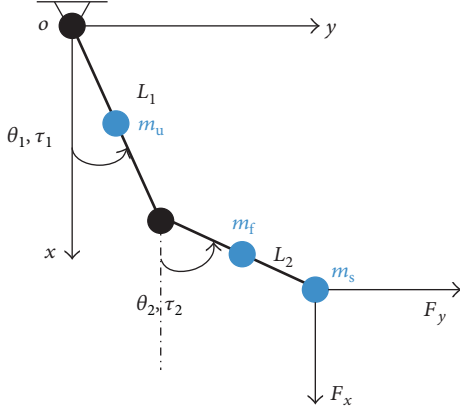


FIGURE 4: The dynamic model of EEULRebot.

Kinetic energy of upper limb is calculated as follows:

$$\begin{aligned}
 E_k = & \left(\frac{1}{6} m_u + \frac{1}{2} m_f + \frac{1}{2} m_s \right) L_1^2 \dot{\theta}_1^2 \\
 & + \left(\frac{1}{6} m_f + \frac{1}{2} m_s \right) L_2^2 \dot{\theta}_2^2 \\
 & + \left(\frac{1}{2} m_f + m_s \right) L_1 L_2 \dot{\theta}_1 \dot{\theta}_2 \cos(\theta_1 - \theta_2).
 \end{aligned} \quad (2)$$

We select the training plane as the potential energy zero, $E_p = 0$.

The Lagrange function is shown as follows:

$$\begin{aligned}
 L = E_k - E_p = & \left(\frac{1}{6} m_u + \frac{1}{2} m_f + \frac{1}{2} m_s \right) L_1^2 \dot{\theta}_1^2 \\
 & + \left(\frac{1}{6} m_f + \frac{1}{2} m_s \right) L_2^2 \dot{\theta}_2^2 \\
 & + \left(\frac{1}{2} m_f + m_s \right) L_1 L_2 \dot{\theta}_1 \dot{\theta}_2 \cos(\theta_1 - \theta_2).
 \end{aligned} \quad (3)$$

By Lagrange's formulation, the equivalent joint torques can be calculated as follows:

$$\begin{aligned}
 \tau_{1e} = & \frac{d}{dt} \left(\frac{\partial L}{\partial \dot{\theta}_1} \right) - \frac{\partial L}{\partial \theta_1}, \\
 \tau_{2e} = & \frac{d}{dt} \left(\frac{\partial L}{\partial \dot{\theta}_2} \right) - \frac{\partial L}{\partial \theta_2}.
 \end{aligned} \quad (4)$$

Since the movement of each motor is with small velocity, then, the equivalent joint torque caused by the Coriolis force and centrifugal force can be ignored and the calculation can be simplified as follows:

$$\begin{aligned}
 \tau_{1e} = & \left(\frac{1}{3} m_u + m_f + m_s \right) L_1^2 \ddot{\theta}_1 + \left(\frac{1}{2} m_f + m_s \right) L_1 L_2 \cos(\theta_1 - \theta_2) \ddot{\theta}_2, \\
 \tau_{2e} = & \left(\frac{1}{3} m_f + m_s \right) L_2^2 \ddot{\theta}_2 + \left(\frac{1}{2} m_f + m_s \right) L_1 L_2 \cos(\theta_1 - \theta_2) \ddot{\theta}_1.
 \end{aligned} \quad (5)$$

TABLE 1: The physical significance of all symbols in equations.

Symbols	Physical significance
θ_1	The motor angle of EEULRebot upper arm
θ_2	The motor angle of EEULRebot forearm
L_1	The length of EEULRebot upper arm
L_2	The length of EEULRebot forearm
m_u	The mass of EEULRebot upper arm
m_f	The mass of EEULRebot forearm
m_s	The mass of force sensor at the end-effector of EEULRebot
E_k	Kinetic energy
E_p	Potential energy
L	Mechanical energy
τ_{1e}	Resultant external torque of motor of EEULRebot upper arm
τ_{2e}	Resultant external torque of motor of EEULRebot forearm
J	The Jacobian matrix of the EEULRebot system
τ_e	Equivalent torque of external forces
F_x	The external force in x -axis
F_y	The external forces in y -axis
τ_1	Motor torque of EEULRebot upper arm
τ_2	Motor torque of EEULRebot forearm

The velocity Jacobian of the EEULRebot system can be described following

$$J = \begin{pmatrix} -L_1 \sin \theta_1 & -L_2 \sin \theta_2 \\ L_1 \cos \theta_1 & L_2 \cos \theta_2 \end{pmatrix}. \quad (6)$$

Equivalent torque of external forces is calculated following

$$\tau_e = J^T \begin{pmatrix} F_x \\ F_y \end{pmatrix}. \quad (7)$$

Then, the motor torques can be calculated as follows:

$$\begin{pmatrix} \tau_1 \\ \tau_2 \end{pmatrix} = \begin{pmatrix} \tau_{1e} \\ \tau_{2e} \end{pmatrix} - J^T \begin{pmatrix} F_x \\ F_y \end{pmatrix}. \quad (8)$$

The physical significance of all symbols in the equations is explained in Table 1.

2.4. Control Strategy. Hemiplegic patients need different training modes in different conditions [26, 27]. The passive-guided mode is needed while patients are lacking of voluntary movement in early stage after a stroke. When the movement ability is improved, the system can assist the patients to perform training tasks. When patients' abilities are recovered more, the patients will need some challenge in the training tasks [28]. All of these training modes should be included in the control system. Three training modes were implemented in EEULRebot control system: passive-guided

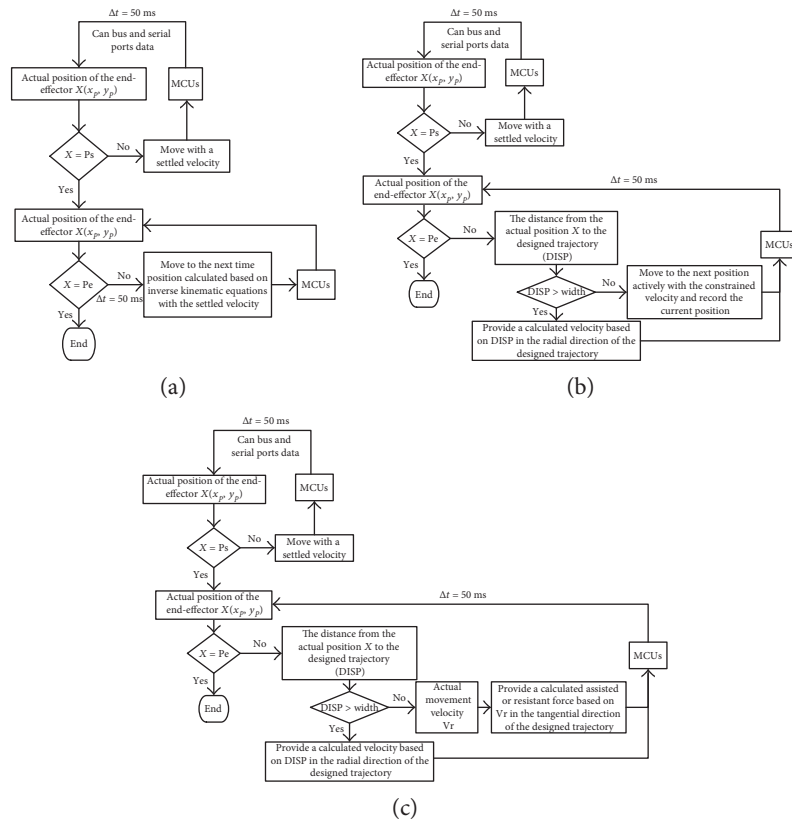


FIGURE 5: Three control modes of EEULRobot.

mode, active-constrained mode, and active assistant or resistant mode.

Reaching from one point to another point is a basic movement in upper limb movement [29] and tracking a circle is known as the basic movement involving shoulder and elbow joint coordination [30]. Therefore, EEULRobot chooses a point-to-point line tracking and a circle tracking as the training tasks. In order to maximize the range of motion but do not cause discomfort, the two endpoint should be selected by the patients' therapist according to patients' shoulder and elbow passive maximum degrees of freedom.

2.5. Passive-Guided Mode. During the passive-guided mode, it was the most important thing to move patients' hand in an accurate trajectory to inhibit patients' abnormal movement patterns during the tasks. In this mode, we designed a position loop control with a settled velocity to provide pulses to motor control units (MCUs) based on the inverse kinematic calculation from the current position to the next time position (Δt was set as 50 ms for the calculation of motor angles and for movement control information transformed from personal computer to MCUs). The control loop system was shown in Figure 5(a).

2.6. Active-Constrained Mode. Active-constrained mode meant a training mode that restricted patients' motion range at the end-effector. Firstly, we designed a motion range along the desired trajectory, called fault tolerance zone (FTZ). In

order to make the width of FTZ suitable for the specific patient, the patient should first perform the desired trajectory actively with no constraint. The default width of FTZ was set as 50 mm, and this width value would be updated according to the patient's performance. Once the maximum deviation from the active-with-no-constraint performance to the desired trajectory was smaller than 50 mm, the width should be decreased until it was smaller than the maximum deviation.

The active-constrained mode was designed based on a regional position and velocity loop as shown in Figure 5(b). Once the end-effector was outside of the trajectory and its FTZ, the EEULRobot would provide a helpful motion to move the end-effector back to the region. The helpful motion was designed as a straight line motion from the current point to the point on the desired trajectory, which point made the minimum distance from current point to the designed trajectory.

2.7. Active Assistant or Resistant Mode. Active assistant or resistant mode was provided for patients who had some voluntary movement ability less than or more than the tracking tasks required. Patients' voluntary movement ability was evaluated by their movement velocity. If the movement velocity was bigger than 50 mm/s, it meant the patient had more voluntary ability than the task required, vice versa [24]. It was also of great importance in this mode to detect the interaction force between EEULRobot and the patient to

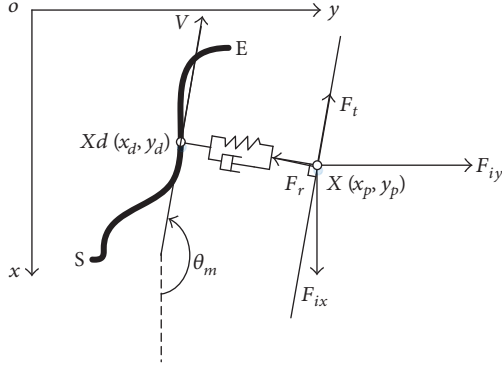


FIGURE 6: The illustration of impedance control strategy. The bold black curve was the defined trajectory (S and E, resp., represented the start and end point in the designed trajectory); $X(x_p, y_p)$ was the coordinate of the real position; $X_d(x_d, y_d)$ was the point on the designed trajectory determined by the position which produced the minimum distance from the real position $X(x_p, y_p)$. V represented the movement direction at the designed point $X_d(x_d, y_d)$ in the defined trajectory; θ_m represented the angle between v and the x -axis; F_t and F_r were, respectively, the required force. F_t was parallel to the direction of v , and F_r was perpendicular to F_t . F_t was the designed assistant or resistant force calculated based on the actual moment velocity, and F_r was the designed assisted resilience based on the absolute value of distance between X and X_d ; F_{ix} and F_{iy} were the interaction forces detected by the two-dimensional force sensor.

calculate the assistance or resistance. We designed this mode based on a regional position, velocity, and force loop control shown in Figure 5(c). The desired position and velocity were calculated by inverse kinematic analysis, and the desired force was calculated based on inverse dynamic analysis as well as the impedance-based control theory. Impedance control, proposed by Hogan in 1985, was designed to make the interaction environment between patients and the robot more harmonious [31]. The interaction environment was equivalent as a virtual mass-spring-damp system. The impedance control strategy can be illustrated in Figure 6.

The active assistant or resistant mode was developed based on the active-constrained mode, which was more complicated when the point was within the region of FTZ. If the current point was outside of the FTZ, EEULRebot should rotate the robot upper limb and forearm to provide a radial helpful force F_r to pull the end-effector back into the region of FTZ with $F_t = 0$. Besides, while the current point was within the region of FTZ, the active assistant or resistant mode should also provide an external force F_t in movement direction according to the movement velocity with $F_r = 0$. The movement velocity could be calculated based on the angular velocity of each motor and the theorem of composition of velocities. If the movement velocity was smaller than the velocity settled by the therapist, EEULRebot should provide a positive F_t as assistance to help the participant complete the task. The default velocity was set as 10 mm/s which was considered as a velocity that could produce a normal movement. While the movement velocity was bigger than the settled

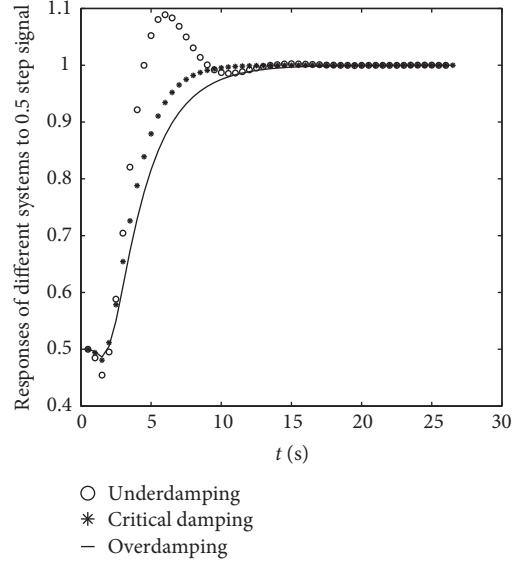


FIGURE 7: The system response to step signal with amplitude of 0.5 in the environment mass-spring-damp system with different damping coefficients. x : the time of response; y : response values to 0.5 step signal. The continuous black solid line was the response of overdamping system, and it had no overshoot and a stable value at the end.

velocity, EEULRebot should provide a negative F_t as resistance to increase the task difficulty for the participant.

The values of F_r and F_t can be calculated based on the impedance control strategy shown in (9)-(10). v_a meant the actual movement velocity, and v_s meant the settled velocity in the movement task.

$$F_r = \begin{cases} B(v_a - v_s) + K\Delta X & \text{(while points out of FTZ region)} \\ 0 & \text{(while points in region of FTZ),} \end{cases} \quad (9)$$

$$F_t = \begin{cases} 0 & \text{(while points out of FTZ region)} \\ B(v_a - v_s) & \text{(while points in region of FTZ).} \end{cases} \quad (10)$$

It can be found from Figure 7 that overdamping system was better than underdamping and critical damping systems with a stable response to the same step signal. Then, we chose $B = 2.5$ Ns/m and $K = 1$ N/m as a simple overdamping system to make the interaction environment a stable system.

3. Experiments and Results

3.1. Subjects. In order to demonstrate the usability of EEULRebot, we designed two experiments to test the system movement accuracy and the influence of different movement modes on subjects in passive-guided and active-constrained mode. Eleven healthy subjects (ages: 26.45 ± 9.37 , BMI: 22.61 ± 2.97) took part in both the experiments, and three patients (males, ages: 46 ± 16.52 , BMI: 25.34 ± 1.36) participated in the passive-guided mode experiment. But only one hemiplegic patient (65 years old, BMI = 23.78) participated in active-constrained mode experiment because other two

TABLE 2: Participants in the experiment groups and actions.

Experiments	Actions	Healthy subjects	Hemiplegic patients
Passive-guided mode experiment (PGE)	Line tracking and circle tracking task with robot at passive-guided mode	11	3
	Line tracking and circle tracking tasks actively without constraint (ALNC and ACNC)	11	1
Active-constrained mode experiment (ACE)	Line tracking and circle tracking tasks actively with constraint (AL and AC)	11	1

patients had no voluntary movement ability at the elbow extension. All the participants were provided with the informed consent form before the experiments; the experiments were approved by the Medical Ethics Committee of the Affiliated Hospital of National Research Center for Rehabilitation Technical Aids.

3.2. Experiment Process. Each subject was asked to sit in a chair with his/her trunk strapped to restrain his/her trunk moment. The experiment process included two experiments (shown in Table 2): passive-guided mode experiment (PGE) and active-constrained mode experiment (ACE). Participants should perform a line or a circle tracking task with EEULRebot at passive-guided mode during PGE, which asked patients to make no effort to move the end-effector. While during ACE, participants should perform the same task by themselves with constraint. In order to test whether the constraint worked well on the subjects, each participant was asked to perform the same task actively with no constraint at first during ACE. Each subject was asked to perform five trials in each task during both PGE and ACE to reduce the random error.

During PGE, the movement information was collected by the robot encoders. The movement information of robot end-effector was used to describe the accuracy of robot system. During ACE, participants' surface electromyographic signals (EMG) and the interaction force between the robot and participants were recorded. EMG signals of trapezius (TR), pectoralis major (PM), anterior, median and posterior deltoid (AD, MD, and PD), biceps brachii (BB), triceps brachii (TB), and brachioradialis (BR) were recorded by 8-channel Telemyo DTS (Noraxon, USA) with cutoff frequency of 1500 Hz and sample frequency of 1500 Hz. The interaction force was recorded by the two-dimensional force sensor with sample frequency of 5 Hz. The EMG analysis system and the force-recorded system were synchronized by a high level trigger signal with frequency of 100 Hz. EMG signals and the interaction force were used to explore the influence of the constraint on the participants.

3.3. Data Processing

3.3.1. Analysis of Movement Accuracy of Robot System. During PGE, the average distance between the actual point and the designed trajectory was calculated according to (11),

TABLE 3: The deviation of actual trajectory and designed trajectory during passive-guided mode movement.

Action	DISP _{aver} /mm (mean ± SD)	
	Healthy subjects (10 men)	Hemiplegic patients (3 men)
Passive-guided line tracking	0.51 ± 0.13	0.39 ± 0.01
Passive-guided circle tracking	0.53 ± 0.32	0.69 ± 0.52

which was used to describe the movement accuracy during passive-guided mode.

$$\text{DISP}_{\text{aver}} = \frac{\sum_{i=1}^N \text{DISP}_i}{N}. \quad (11)$$

In (11), DISP_i meant the distance from actual point i to the designed trajectory. N meant the number of actual points during the task.

3.3.2. Analysis of Influence of the Different Movement Modes on Healthy Subjects and Patients. The EMG and interaction force were used to explore the influence of the different control modes on the subjects. The raw EMG signals were rectified and reduced the electrocardiogram (ECG) in the commercial software (MR-XP 1.07 Master Edition). Then, the signals were filtered by a bidirectional Butterworth band-pass filter with cutoff values of 10 Hz and 500 Hz in the same software [32–34]. After filtering, the signals were smoothed by calculating the average with a window of 50 ms. The mean EMG (MEMG) in the task duration among 3 trials were averaged to describe each muscle energy in the task. MEMG were normalized by (12), thus making the MEMG comparable between different subjects and different movement modes (with constraint and with no constraint).

$$\text{MEMG}_{\text{normalized}} = \frac{\text{MEMG}_i}{\sum_{i=1}^n \text{MEMG}_i} \times 100\%. \quad (12)$$

MEMG_i meant the mean EMG of i muscle, $i = 1, 2, 3, \dots, 8$.

The interaction force and distance from the actual point to the designed trajectory among the task were smoothed and linear interpolation to 100 points and then averaged among 3 trials in the task for one subject performance. The changes among interaction force and distance were

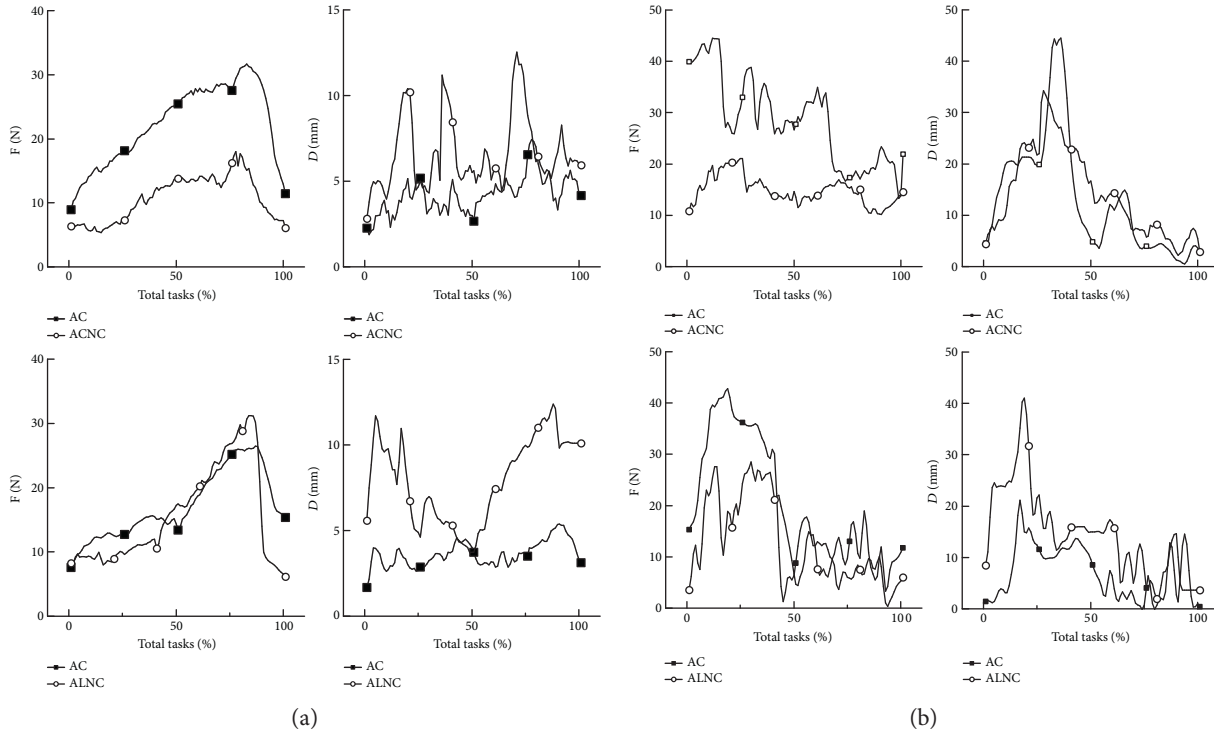


FIGURE 8: The interaction force and end-effector distance during ACE. (a) The average interaction force and end-effector distance of healthy subjects and (b) that of the hemiplegic patient. F : the interaction force; D : the distance; AC: active circle tracking task with constraint; AL: active line tracking task with constraint; ACNC: active circle tracking task with no constraint; ALNC: active line tracking task with no constraint.

compared between different movement modes to describe the influence.

4. Results and Discussion

4.1. Movement Accuracy of Robot System. The movement accuracy was calculated as the average distance from the actual point to the designed trajectory. The deviation of the passive-guided movement along a designed trajectory was less than 1 mm illustrated in Table 3. Besides, the deviation in patients was not significantly different with that in healthy subjects. The small deviation and difference among different subjects demonstrated the good movement accuracy of the robot system.

4.2. The Influence of Control Mode on Interaction Force and Movement Accuracy. The forces and displacement were the primary two external factors in human movement. The active movement with no constraint during the ACE was implemented as a comparison test with the active movement with constraint. A circle tracking task or a line tracking forward and backward was normalized by time to be a task with 100 points in the length of total time. The interaction force and distance among different control modes were, respectively, compared with each other (Figure 8).

It can be found that the active-constrained mode movement can bring in a large interaction force with the largest force twice of that in the no-constraint mode movement, especially in the latter part of the task for

healthy subjects and in the former part for the patient. Besides, a more accurate movement was achieved by the constrained mode, which can be demonstrated by the smaller distance in Figure 8.

The movement in ACE with constraint was more accurate, because once the end-effector was out of the fault tolerance zone (FTZ) the robot would rotate its arms to bring the end-effector back to the zone. And the movement of robot upper limb and forearm would also increase the interaction force between human and robot. Therefore, the bigger interaction force and the more accurate movement were consistent with each other in the ACE with constraint.

The visual biofeedback may be the factor that caused the big interaction force and the distance of end-effector in the latter part of tasks (the tracking from the farthest point to the nearest point) for healthy subjects. The sight of participants may be blocked by their body and the end-effector handle during the latter part, which revealed the importance of biofeedback in robot therapy and the necessity of the adjustable part in the robot structure. As for the hemiplegic patient, the biggest interaction force and distance were observed in the former part (the tracking from the nearest point to the farthest point). It can be explained by the stereotypic movement pattern between shoulder and elbow joints: shoulder abduction accompanied by elbow flexion [35, 36]. During the former part of tasks, patients should perform shoulder abduction and elbow extension, while the accompanied elbow flexion movement in patients increased the interaction force and the distance.

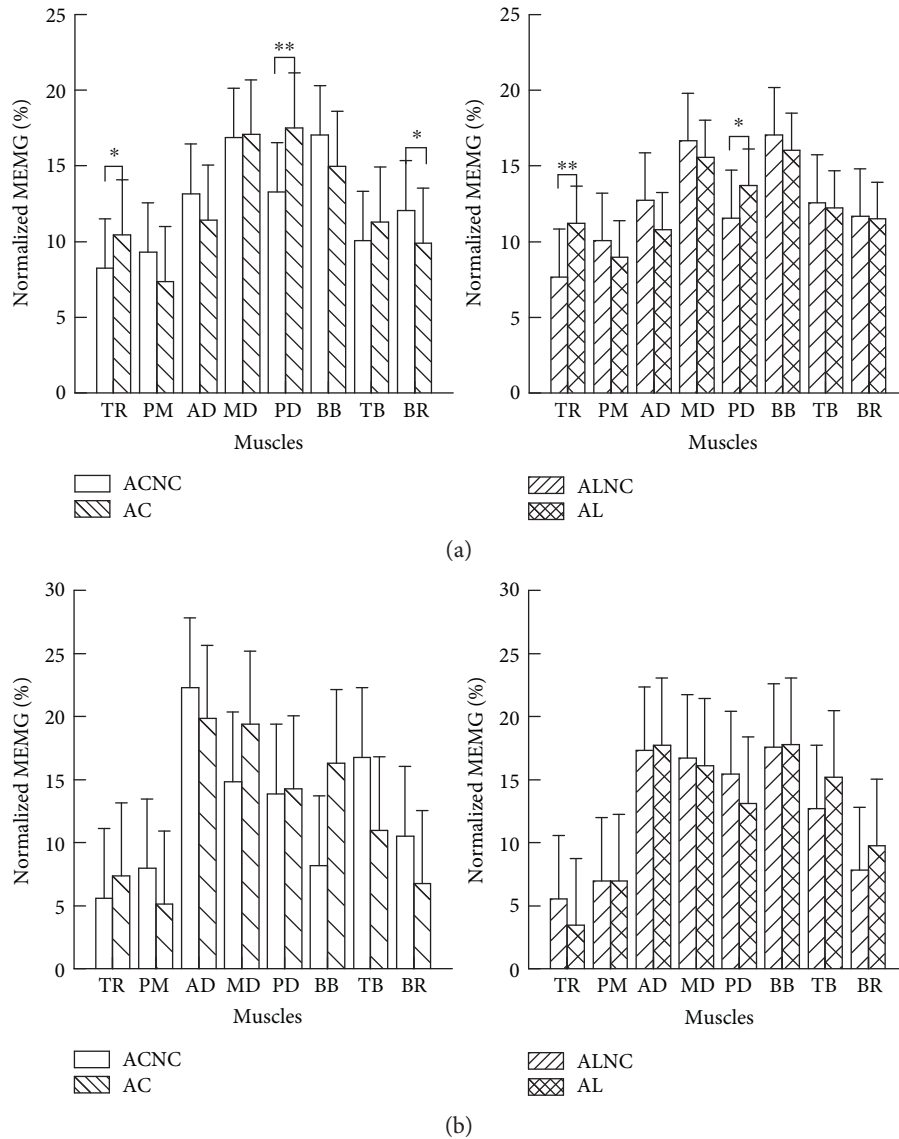


FIGURE 9: The normalized MEMG of the eight muscles among four actions during ACE. (a) Each muscle effort of healthy subjects during different tasks and (b) that of the only hemiplegic patient. $0.01 < p < 0.05$; $p < 0.01$. The abbreviations (AC, ACNC, AL, and ALNC) were in the same representation with that in Figure 8.

4.3. The Influence of Control Mode on Muscle Activation Distribution. The interaction force was the external factor between human and the robot, and the muscle strength and activation would be the internal factor. Therefore, the EMG of the eight muscles was recorded, which were involved in shoulder external rotation, flexion, and abduction as well as elbow flexion. The normalized mean EMG ($MEMG_{normalized}$) calculated according to (12) was used to describe each muscle effort to complete the task. Besides, several independent *t*-tests were used to analyze the difference of each muscle effort during tasks in healthy subjects. Statistical significance was set at $p < 0.05$.

The normalized MEMG of healthy subjects while completing the four tasks (active circle or line tracking with no constraint and with constraint (ACNC, AC, ALNR, and AL)) were shown in Figure 9(a). The effort of each muscle

contributing to complete a task was modified by the constraint. The normalized MEMG of TR and PD were significantly larger in tasks with constraint than that in tasks with no constraint both in circle tracking and in line tracking, while the normalized MEMG of PM, AD, BB, and BR were smaller.

The changes of muscle activation distribution in the hemiplegic patient were not the same with that in the healthy subject (founded in Figure 9). The changes of the normalized MEMG of most muscles except BB and TB in circle tracking tasks were the same with that in healthy subjects. However, the change trends of most muscles except MD during line tracking task in the hemiplegic patient were different with that in healthy subjects. The constraint mode had more activation of BB and less TB activation during circle tracking and had more BB and TB activation during line tracking, which

was the opposite change trends of the same muscles in healthy subjects. The different changes at elbow flexion and extension muscle group suggest hemiplegic subjects may have much lesion in elbow flexion and extension control ability [37].

Comparing the changes of muscle activation distribution between healthy subjects and patients, it indicated that the active-constrained mode movement can adjust the muscle activation distribution of hemiplegic patients similar to healthy subjects during circle tracking tasks, which suggested that hemiplegic patients innervated muscles in a similar way to healthy subjects. Besides, circle tracking was more variable than the line tracking in the changes of distance of end-effector (shown in Figure 8(b)), which suggested circle tracking had more variability than line tracking. More variability was beneficial for cerebellum development [38]. Moreover, the circle tracking would require more joint movements than line tracking [30, 38], which can contribute to the coordination of shoulder and elbow joints. All above, the circle tracking task in robot active-constrained mode should be a basic training to promote patients' recovery.

5. Conclusions

In this article, the new EEULRebot system was developed. The movement accuracy of the system at passive-guided proved the usability of the robot in participants' training. Besides, the influence of active-constrained mode on the participants' interaction force and their internal muscle activation distribution was explored, in which we designed the constraint correlated with the deviation of the actual point to designed trajectory. This study confirmed the constraint at end-effector modified the muscle activation distribution in the same trend in hemiplegic patients and healthy subjects in circle tracking, which suggested that the circle tracking may be a representative motion in rehabilitation training to improve the muscle activation pattern the same with healthy subjects.

The study has demonstrated the usability of passive-guided and active-constraint mode in the experiment. However, the number of the patients is too small. Therefore, we will enroll more hemiplegic patients to complete the experiment in the future. Besides, we will also do experiment on the active assistant or resistant mode to demonstrate its usability on patients.

Conflicts of Interest

The authors have no financial conflict of interest.

Acknowledgments

The study was supported by the National Science Foundation (Grant nos. 81272162 and U1613207). The authors are grateful to the subjects who participated in the investigation and to the National Research Center for Rehabilitation Technical Aids of China for the equipment support.

References

- [1] J. Sui, Y. Liu, R. Yang, and L. Ji, "A multiposture locomotor training device with force-field control," *Advances in Mechanical Engineering*, vol. 6, article 173518, 2014.
- [2] W. W. Liao, C. Y. Wu, Y. W. Hsieh, K. C. Lin, and W. Y. Chang, "Effects of robot-assisted upper limb rehabilitation on daily function and real-world arm activity in patients with chronic stroke: a randomized controlled trial," *Clinical Rehabilitation*, vol. 26, no. 2, pp. 111–120, 2012.
- [3] M. Sin, W. S. Kim, D. Park et al., "Electromyographic analysis of upper limb muscles during standardized isotonic and isokinetic robotic exercise of spastic elbow in patients with stroke," *Journal of Electromyography and Kinesiology*, vol. 24, no. 1, pp. 11–17, 2014.
- [4] I. Brunner, J. S. Skouen, H. Hofstad et al., "Virtual reality training for upper extremity in subacute stroke (VIRTUES): study protocol for a randomized controlled multicenter trial," *BMC Neurology*, vol. 14, no. 1, p. 186, 2014.
- [5] W. H. Miltner, H. Bauder, M. Sommer, C. Dettmers, and E. Taub, "Effects of constraint-induced movement therapy on patients with chronic motor deficits after stroke," *Stroke*, vol. 30, no. 3, pp. 586–592, 1999.
- [6] T. Nef, M. Mihelj, G. Colombo, and R. Riener, "ARMin - robot for rehabilitation of the upper extremities," in *Proceedings 2006 IEEE International Conference on Robotics and Automation (ICRA 2006)*, Orlando, FL, 2006.
- [7] J. A. Cozens, "Robotic assistance of an active upper limb exercise in neurologically impaired patients," *IEEE Transactions on Rehabilitation Engineering*, vol. 7, no. 2, pp. 254–256, 1999.
- [8] L. Dipietro, M. Ferraro, J. J. Palazzolo, H. I. Krebs, B. T. Volpe, and N. Hogan, "Customized interactive robotic treatment for stroke: EMG-triggered therapy," *IEEE Transactions on Neural Systems and Rehabilitation Engineering*, vol. 13, no. 3, pp. 325–334, 2005.
- [9] M. Mihelj, T. Nef, and R. Riener, "ARMin II - 7 DoF rehabilitation robot: mechanics and kinematics," in *Proceedings 2007 IEEE International Conference on Robotics and Automation*, Roma, 2007.
- [10] J. C. Fraile, J. Pérez-Turiel, E. Baeyens et al., "E2Rebot: a robotic platform for upper limb rehabilitation in patients with neuromotor disability," *Advances in Mechanical Engineering*, vol. 8, no. 8, 2016.
- [11] S. W. Tung, C. Guan, K. K. Ang et al., "Motor imagery BCI for upper limb stroke rehabilitation: an evaluation of the EEG recordings using coherence analysis," in *2013 35th Annual International Conference of the IEEE Engineering in Medicine and Biology Society (EMBC)*, Osaka, 2013.
- [12] R. Li, X. L. Hu, and K. Tong, "Combined electromyography (EMG)-driven system with functional electrical stimulation (FES) for poststroke rehabilitation," in *2008 2nd IEEE RAS & EMBS International Conference on Biomedical Robotics and Biomechanics*, Scottsdale, AZ, 2008.
- [13] X. L. Hu, K. Y. Tong, R. Song, X. J. Zheng, and W. W. Leung, "A comparison between electromyography-driven robot and passive motion device on wrist rehabilitation for chronic stroke," *Neurorehabilitation and Neural Repair*, vol. 23, no. 8, pp. 837–846, 2009.
- [14] S. H. Scott, "Kinesiological instrument for limb movements," Google Patents, 2000.

- [15] V. S. Huang and J. W. Krakauer, "Robotic neurorehabilitation: a computational motor learning perspective," *Journal of Neuroengineering and Rehabilitation*, vol. 6, no. 1, p. 5, 2009.
- [16] G. Xu and A. Song, "Adaptive impedance control based on dynamic recurrent fuzzy neural network for upper-limb rehabilitation robot," in *2009 IEEE International Conference on Control and Automation*, Christchurch, 2009.
- [17] E. Vergaro, M. Casadio, V. Squeri, P. Giannoni, P. Morasso, and V. Sanguineti, "Self-adaptive robot training of stroke survivors for continuous tracking movements," *Journal of Neuroengineering and Rehabilitation*, vol. 7, no. 1, p. 13, 2010.
- [18] M. Casadio, P. Morasso, V. Sanguineti, and P. Giannoni, "Impedance-controlled, minimally-assistive robotic training of severely impaired hemiparetic patients," in *The First IEEE/RAS-EMBS International Conference on Biomedical Robotics and Biomechatronics, 2006 (BioRob 2006)*, Pisa, 2006.
- [19] U. Demir, S. Kocaoglu, and E. Akdoğan, "Human impedance parameter estimation using artificial neural network for modelling physiotherapist motion," *Biocybernetics and Biomedical Engineering*, vol. 36, no. 2, pp. 318–326, 2016.
- [20] A. Song, L. Pan, G. Xu, and H. Li, "Adaptive motion control of arm rehabilitation robot based on impedance identification," *Robotica*, vol. 33, no. 09, pp. 1795–1812, 2015.
- [21] Z. Fang, "Intellectual control of upper limbs rehabilitation robot based on fuzzy neural network," Northeastern University, 2010.
- [22] Z. Yubo, W. Zixi, J. Linhong, and B. Sheng, "The clinical application of the upper extremity compound movements rehabilitation training robot," in *9th International Conference on Rehabilitation Robotics, 2005 (ICORR 2005)*, Chicago, IL, USA, 2005.
- [23] Y. C. Hu and L. H. Ji, "A multiple-motion rehabilitation training robot for hemiplegia upper limbs," *Machinery Design & Manufacture*, vol. 6, pp. 47–49, 2004.
- [24] I. Aprile, M. Rabuffetti, L. Padua, E. Di Sipio, C. Symbolotti, and M. Ferrarin, "Kinematic analysis of the upper limb motor strategies in stroke patients as a tool towards advanced neurorehabilitation strategies: a preliminary study," *BioMed Research International*, vol. 2014, Article ID 636123, 8 pages, 2014.
- [25] R. S. Behnke, *Kinetic Anatomy*, Human Kinetics, Champaign, 2006.
- [26] G. B. Prange, M. J. Jannink, C. G. Groothuis-Oudshoorn, H. J. Hermens, and I. J. MJ, "Systematic review of the effect of robot-aided therapy on recovery of the hemiparetic arm after stroke," *Journal of Rehabilitation Research and Development*, vol. 43, no. 2, p. 171, 2006.
- [27] G. Kwakkel, B. J. Kollen, and H. I. Krebs, "Effects of robot-assisted therapy on upper limb recovery after stroke: a systematic review," *Neurorehabilitation and Neural Repair*, vol. 22, no. 2, pp. 111–121, 2008.
- [28] B. T. Volpe, "Robotics and other devices in the treatment of patients recovering from stroke," *Current Neurology and Neuroscience Reports*, vol. 5, no. 6, pp. 465–470, 2005.
- [29] J. M. Wagner, C. E. Lang, S. A. Sahrman, D. F. Edwards, and A. W. Dromerick, "Sensorimotor impairments and reaching performance in subjects with poststroke hemiparesis during the first few months of recovery," *Physical Therapy*, vol. 87, no. 6, p. 751, 2007.
- [30] L. Dipietro, H. I. Krebs, S. E. Fasoli et al., "Changing motor synergies in chronic stroke," *Journal of Neurophysiology*, vol. 98, no. 2, pp. 757–768, 2007.
- [31] S. Part, "Impedance control: an approach to manipulation," *Journal of Dynamic Systems, Measurement, and Control*, vol. 107, p. 17, 1985.
- [32] S. K. Chen, M. T. Wu, C. H. Huang, J. H. Wu, L. Y. Guo, and W. L. Wu, "The analysis of upper limb movement and EMG activation during the snatch under various loading conditions," *Journal of Mechanics in Medicine and Biology*, vol. 13, no. 01, article 1350010, 2013.
- [33] I. Rogowski, D. Rouffet, F. Lambalot, O. Brosseau, and C. Hautier, "Trunk and upper limb muscle activation during flat and topspin forehand drives in young tennis players," *Journal of Applied Biomechanics*, vol. 27, no. 1, pp. 15–21, 2011.
- [34] P. Konrad, *The ABC of EMG: A Practical Introduction to Kinesiological Electromyography*, pp. 30–35, Noraxon USA, Scottsdale, AZ, 2005.
- [35] R. F. Beer, J. P. Dewald, and W. Z. Rymer, "Deficits in the coordination of multijoint arm movements in patients with hemiparesis: evidence for disturbed control of limb dynamics," *Experimental Brain Research*, vol. 131, no. 3, pp. 305–319, 2000.
- [36] J. Dewald and R. F. Beer, "Abnormal joint torque patterns in the paretic upper limb of subjects with hemiparesis," *Muscle & Nerve*, vol. 24, no. 2, pp. 273–283, 2001.
- [37] T. K. Koo, A. F. Mak, L. K. Hung, and J. P. Dewald, "Joint position dependence of weakness during maximum isometric voluntary contractions in subjects with hemiparesis," *Archives of Physical Medicine and Rehabilitation*, vol. 84, no. 9, pp. 1380–1386, 2003.
- [38] J. Bo, A. J. Bastian, J. L. Contreras-Vidal, F. A. Kagerer, and J. E. Clark, "Continuous and discontinuous drawing: high temporal variability exists only in discontinuous circling in young children," *Journal of Motor Behavior*, vol. 40, no. 5, pp. 391–399, 2008.

Research Article

The Effect of Arch Height and Material Hardness of Personalized Insole on Correction and Tissues of Flatfoot

Shonglun Su,^{1,2} Zhongjun Mo,^{1,2} Junchao Guo,^{1,2} and Yubo Fan^{1,2}

¹Key Laboratory for Biomechanics and Mechanobiology of Ministry of Education, School of Biological Science and Medical Engineering, Beihang University, Beijing 100086, China

²Beijing Key Laboratory of Rehabilitation Technical Aids for Old-Age Disability, Key Laboratory of Rehabilitation Technical Aids Analysis and Identification of the Ministry of Civil Affairs, National Research Centre for Rehabilitation Technical Aids, Beijing 100176, China

Correspondence should be addressed to Yubo Fan; yubofan@buaa.edu.cn

Received 5 March 2017; Revised 31 March 2017; Accepted 9 April 2017; Published 12 June 2017

Academic Editor: Rui Zhu

Copyright © 2017 Shonglun Su et al. This is an open access article distributed under the Creative Commons Attribution License, which permits unrestricted use, distribution, and reproduction in any medium, provided the original work is properly cited.

Flat foot is one of the common deformities in the youth population, seriously affecting the weight supporting and daily exercising. However, there is lacking of quantitative data relative to material selection and shape design of the personalized orthopedic insole. This study was to evaluate the biomechanical effects of material hardness and support height of personalized orthopedic insole on foot tissues, by *in vivo* experiment and finite element modeling. The correction of arch height increased with material hardness and support height. The peak plantar pressure increased with the material hardness, and these values by wearing insoles of 40° were apparently higher than the bare feet condition. Harder insole material results in higher stress in the joint and ligament stress than softer material. In the calcaneocuboid joint, the stress increased with the arch height of insoles. The material hardness did not apparently affect the stress in the ankle joints, but the support heights of insole did. In general, insole material and support design are positively affecting the correction of orthopedic insole, but negatively resulting in unreasonable stress on the stress in the joint and ligaments. There should be an integration of improving correction and reducing stress in foot tissues.

1. Introduction

The foot and ankle is a complex structure with stability and elasticity, consisting of 28 bones, more than 30 joints, and many intertwined ligaments and tendons [1]. It plays an important role in supporting the body weight. Foot deformity is a very common disease, not only causing pain but also seriously affecting people's health and daily activities [2]. Flatfoot is one of the common deformities, which has a high incidence rate in the Chinese youth population. During the growth period, the mild and moderate flattened feet will be corrected with the growth of soft tissue and bones. Severe flatfoot may result in ligament relaxation, muscle weakness, joint distortion, limb pain, ankle injury, ulcer, and other clinical symptoms, which need for conservative correction or surgical intervention [3, 4].

Clinically, correction of orthopedic insoles combined with manual reposition is one of the primary conservation therapies for flexible flatfoot of young patient [3, 4]. Orthopedic insoles have been revealed to be an effective treatment for flatfoot by elevating the arch height and recovering the body weight supporting and force transmission [5]. Due to the difference between individuals (soft tissue material properties, flatness, etc.), customized orthopedic insole needs to be produced. In the customization process, the insole shape design and material selection of the insole seriously depended on the experience of pedorthist, lack of quantitative theoretical support. Previous study showed that the custom-molded insole could reduce stress compared with the flat insole. The thickness, heel's height, and materials of proper insole could minimize the peak plantar stress and achieve uniform stress distribution [6]. The material and

arch height of insole in the sport shoes have a significant effect on biomechanical characteristics of the foot [7, 8]. Therefore, it is necessary to research the biomechanical effect of the design parameters of orthopedic insole, including the material and shape of support and the correction effect of foot arch height, and explore the influence on the foot tissues. Quantified assessment of the design parameters is a benefit to the future design of orthopedic insole to improve treatment effect and to reduce the adverse effects on the patient's foot tissues [9–12].

This study was to evaluate the effects of design parameters including material hardness and support arch height of personalized orthopedic insole on the correction of foot arch and plantar pressure distribution by *in vivo* experiments and to evaluate the biomechanical effects on the foot tissues, including stress distribution on joint cartilage and ligaments using finite element modeling.

2. Material and Methods

Based on a specific patient with flatfoot, this study was to evaluate the effect of design parameters including material hardness (Shore A, 30°, 35°, and 40°) and support arch height (27 mm, 30 mm, and 33 mm) of orthopedic insole on the correction effect of foot arch and plantar pressure distribution by *in vivo* experiment. In the second step, finite element modeling was adopted to evaluate the biomechanical effects on the foot tissues, including stress distribution on joint cartilage and ligaments.

2.1. Subject and Data Processing. A young subject (12 years old, 160 cm height, and 55 kg weight) with severe flatfoot participated this study. The participant was explained on the research purpose and signed the consent form. At first, a series of customized insole of the subject were achieved for the *in vivo* experiment. CT images including the whole foot and portion crus of the subject were obtained at 0.5 mm interval and 0.6 mm resolution using a CT scanner (Brilliance iCT, Philips, Netherlands) under a quasi-weight-bearing condition with bare feet, used in the geometrical modeling. The quasi-weight-bearing status (275 N per foot) was produced by a customized equipment that consisted of an adjustable frame and a plane pressure measuring system (Pedar, Novel, Germany). The images were also checked to ensure that the flatfoot does not exhibit any radiographic evidence of tissue deformity symptoms. The study plan was approved by the Ethical Committee of the corresponding institute.

2.2. Customized Insole of the Subject. The foot profile of the subject under weight-bearing and non-weight-bearing conditions was obtained as point contours using a 3D foot scanner (Infoot, I-Ware Laboratory Co. Ltd. JPN). An insole design software (GeBioM, Go_Tec Inc. GER) was used to develop the 3D geometrical model of customize insoles according to the participant's foot contours. The general thickness of the insole was designed as 7 mm. In clinical practice, the orthopedic insole is produced basing on non-weight-bearing condition, in which the arch shape was close to the

normal configuration. Since the arch height of the subject is about 23 mm in the non-weight-bearing condition, the initial total arch height was setting at 30 mm and ± 3 mm that were chosen for this parametric study and that were 27 mm (type I), 30 mm (type II), and 33 mm (type III) in sequence, as shown in Figure 1. All these settings were guided by a pedorthist and a therapist. Three kinds of materials, with different hardness (Shores A, 30°, 35°, and 40°), were chosen for its high popularity and sustainability for orthopedic insoles.

2.3. In Vivo Measurement. Wireless in-foot pressure measurement system (F-Scan, Novel Inc., US), which consists of 100 capacitive sensors, was used to test the plantar pressure by wearing the nine different orthopedic insoles (3 arch heights, 3 materials), as shown in Figure 1(a). In the meanwhile, the distance between the mark point on the navicular bone and ground was measured to evaluate the correction effect of different insoles, as shown in Figure 1(b), and to be used in the next FE modeling as the boundary loading conditions to explore the effect on the foot tissues.

2.4. Finite Element Modeling of Flatfoot. Medical image processing software (Mimics 10.1, Materialise Inc., Belgium) was used to segment the CT images to acquire the boundaries of each foot bone and skin surface to reconstruct the geometry models. Then, the geometries were imported into a reverse engineering software (Rapidform XOR3, INS Technology Inc., US) to edit the geometry with operations, such as smoothing and partition, and reconstruct the geometry as nurbs format. In total, the model included 28 bony structures, including tibia, fibia, talus, and calcaneus, as shown in Figure 2. The joint regions on the bone were extracted separately and rebuilt into solid blocks by thickening operation with a depth of 0.4 mm to reconstruct joint cartilages. Seventy-two major ligaments, deep fascia, superficial fascia, and nine major extrinsic muscle groups controlling foot movement were included and defined by connecting the corresponding anatomical attachment sites on the bones.

The FE package, ABAQUS 6.13 (Simulia Inc., US), was used for assembling the foot components, creating of the FE mesh, and implicit solver was employed for the subsequent analysis. The insertion points of the ligaments, the interface of skin, and the interfaces of the joint cartilage were fixed onto the corresponding regions on the bony structure by tie constraint formulation to assemble the foot components. The interaction among interfaces of joint cartilage was assigned with frictionless sliding contact formulation.

The material properties of each component of the foot tissues and insoles were selected from the literature and listed in Table 1 [13–18]. The element type of the foot tissues and insoles obtained by multimeshing techniques is listed in Table 1, together with the material properties. The element sizes for bone and skin were 2.5 and 1.5 mm, respectively, that resulted in a total of 94,522 nodes and 306,289 elements. Convergence within 3% in joint cartilage stress was achieved in bare feet weight-bearing condition, to ensure that the results were irrelevant to the mesh density [19, 20].

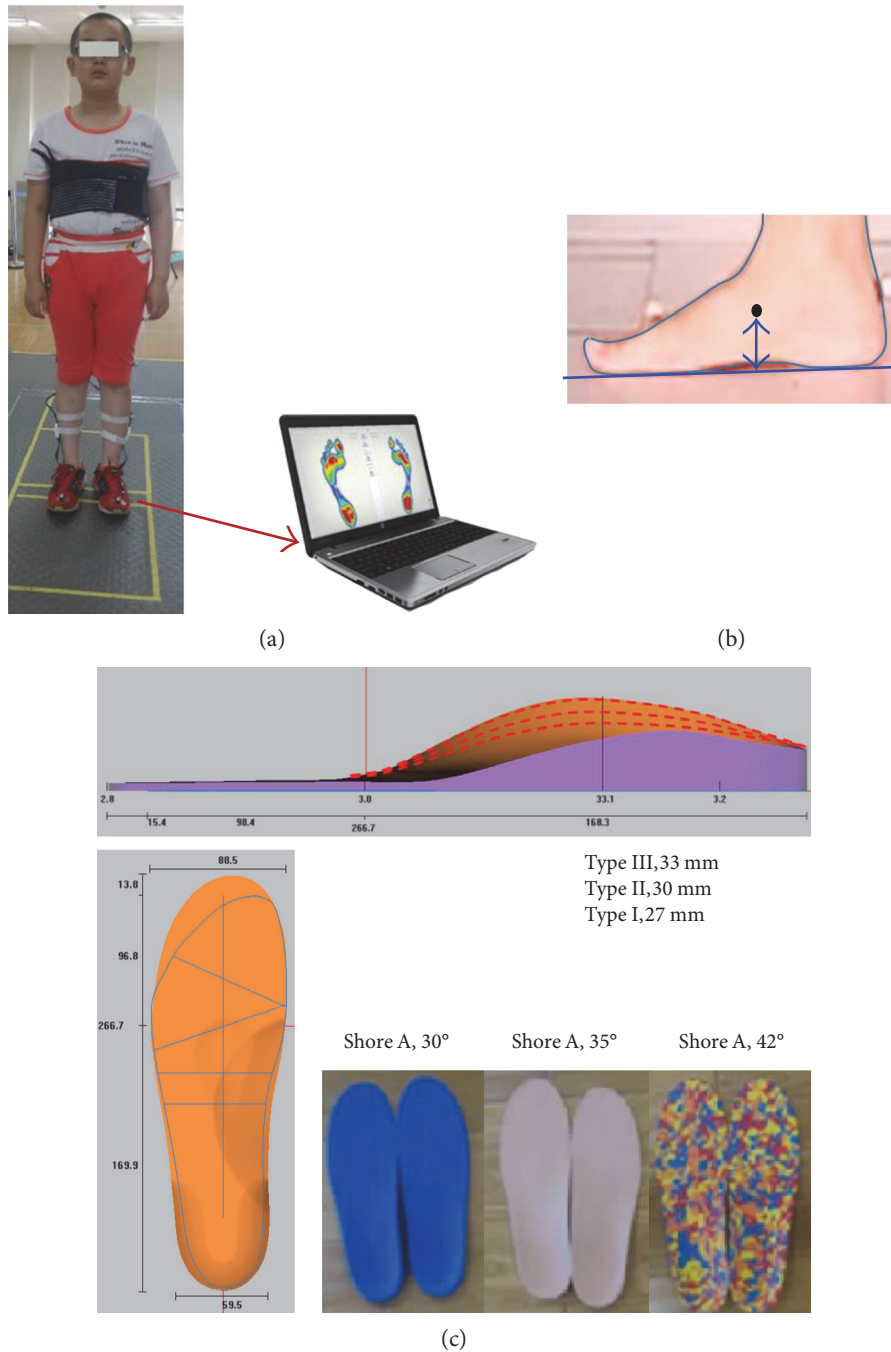


FIGURE 1: Illustration of in vivo measurement, (a) plantar pressure measurement, (b) displacement measurement of the navicular bone, and (c) insole material hardness and design sketch.

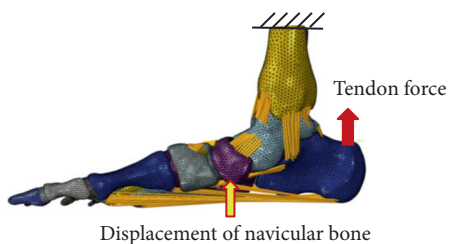


FIGURE 2: Finite element model of flatfoot and its components.

Prior to applying the correct loading on the navicular bone condition, the superior cross section surface of the tibia, fibula, and skin was fixed at the six degrees of freedom, and the initial tendon force of 375 N was properly adjusted until the foot was properly aligned relative to the insole [15–17]. In the second step, the displacement of the navicular bone achieved in the previously described in vivo experiment was applied on the reference point of the navicular bone in vertical direction by keeping the freedom in other direction to

TABLE 1: Material mechanical properties and element types of the FE model.

Component	Element type	Young's modulus E (MPa)	Poisson's ratio	Cross-sectional area (mm ²)
Bony structures	3D tetrahedra	7300	0.3	—
Soft tissue	3D tetrahedra	1.19	0.48	—
Plantar fascia	3D tetrahedra	350	0.35	290.7
Cartilage	3D tetrahedra	10	0.4	—
Ligaments	Tension-only truss	0~700	0.34	18.4~260
Skin	3D tetrahedra	1	0.4	—
Plantar support	3D hexahedron	21,0000	0.3	—

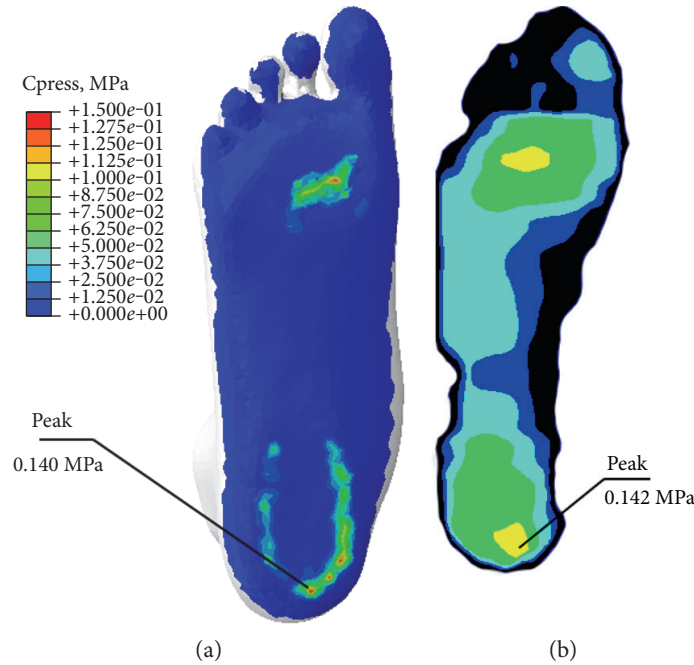


FIGURE 3: Plantar pressure distribution in (a) FE model and (b) F-Scan measurement.

allow coupling motion and to simulate the correcting effect of different orthopedic insoles.

2.5. Finite Element Model Validation. Validation is one of the important stages in finite element modeling. This flatfoot model was validated by comparing the plantar pressure in FE model and in vivo measurement, under weight-bearing with bare foot on a flat plane.

3. Results

Nine customize insoles (3 arch heights, 3 hardness materials) were manufactured. The height between the navicular bone and the ground and the plantar pressure by wearing the different customize insoles were achieved in the in vivo experiment. By the finite element modeling, the stress in the joint cartilage and ligaments was extracted.

3.1. Validation of Flatfoot Model. As shown in Figure 3, the plantar pressure distribution in FE model was similar with F-Scan data and the peak plantar pressure was 140.0 KPa

and 142 KPa in FE model and F-Scan measurement, respectively. It meant that the FE flatfoot could provide reasonable results in the present research purpose.

3.2. Correction in Foot Arch Height. In bare foot and weight-bearing condition, the distance between the navicular bone and the foot bottom (arch height) was about 16.6 mm. The displacement of the navicular bone in the vertical direction by wearing orthopedic insoles is shown in Figure 4. The foot arch height increased with the material hardness and arch shape of the insole. By wearing insoles made up by material with hardness of 30°, the arch height increased by 43%, 66%, and 83% with insoles of types I, II, and III, respectively. By wearing the insoles with material hardness of 35°, the arch height increased by 65%, 90%, and 103% with insoles of types I, II, and III, respectively. By wearing insoles with material hardness of 40°, the arch height increased by 80%, 97%, and 110% with insole of types I, II, and III, respectively.

3.3. Plantar Pressure Distribution. Plantar pressure is one of the most important parameters reflecting the interaction

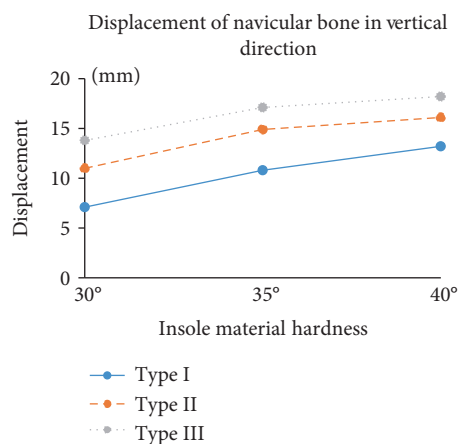


FIGURE 4: Displacement of the navicular bone in the vertical direction.

between the foot and insole. The peak plantar pressure and its distribution in the *in vivo* experiment are shown in Figure 5. In bare feet condition, the maximal plantar pressure was about 142 KPa. Regardless the insole shape, the peak plantar pressure increased with the material hardness. Regardless the material hardness, the maximal plantar pressure was not apparently increased by wearing types I and II insoles. However, the pressure was apparently increased by wearing type III insoles. By wearing insoles made up by the material hardness of 40°, regardless the shapes (types I, II, and III), the plantar pressure was higher than the bare feet condition.

3.4. Stress in the Primary Foot Joints. The maximal stress in the cartilage of the primary foot joints (talonavicular, calcaneocuboid, tibiotalar, and talofibular joints) is shown in Figure 6. In the joint of the middle foot (talonavicular joint and calcaneocuboid joint), the maximal stress increased with the material hardness. In the calcaneocuboid joint, the stress increased with the arch height of insoles. However, in the talonavicular joint, type II insole results in the greatest cartilage stress. The stress in the middle joint was relatively much lower than the ankle joints (tibiotalar joint and talofibular joint). The material hardness did not apparently affect the stress in the ankle joints, but the arch height of orthopedic insoles did.

3.5. Stress in the Primary Foot Ligaments. The maximal stress in the primary foot ligaments is shown in Figure 7. Unlike in the joint cartilage, the maximal stress in almost all the primary foot ligaments increased with the material hardness and arch height of the orthopedic insoles.

4. Discussion

Correction and protection of orthopedic insole is a widely used physical therapy for the treatment of adolescent flat feet [16, 21, 22]. However, the corrective effectivity is significantly related with the insole shapes and material hardness. An optimal design of personalized orthopedic insole could greatly improve the foot supporting function and prevent the occurrence of symptomatic complications. Previous

study showed that the custom-molded insole reduced maximum stress 40% more than the flat surface insole. In the increase of insole thickness, stress distribution becomes more uniform and maximum stress value decreases up to 10% [6].

It was reported that orthopedic insole could improve the patient's foot arch, hereby relieving foot pain, preventing inflammation of soft tissue and tendon sheath and other pathological features [7]. However, there is little knowledge about the changes in the internal skeleton and of medial longitudinal arch by wearing orthopedic insole. In this study, the influence of design parameters, including material hardness and support arch height of personalized orthopedic insole on the correction of foot arch and plantar pressure distribution, and the biomechanical effects on the foot tissues, including stress distribution on joint cartilage and ligaments, were quantitatively analyzed by *in vivo* experiment and finite element modeling. The results showed that the foot arch height increased with the material hardness and arch shape of the insole. The insole with harder material and higher scaffold of the medial longitudinal arch elevate higher foot arch [23–25]. By wearing the insole made up with the material of 40° and type III shape, the arch height was elevated up to twice of the initial bare foot weight-bearing condition.

Plantar pressure is one of the most important parameters reflecting the interaction between the foot and insole [5, 25, 26]. It was found that the hardness of the insole material will affect the plantar pressure distribution and the peak value, and affect the trajectory of plantar pressure center, and hereby affect trajectory of upper body gravity center [22]. Regardless the insole shape (types I, II, and III), the peak plantar pressure increased with the material hardness that means harder material results in higher plantar pressure. The peak plantar pressure was not apparently increased by wearing types I and II insoles, but apparently increased by wearing type III insoles. By wearing insoles made up by material with hardness of 40°, regardless the shapes (types I, II, and III), the plantar pressure was higher than the bare feet condition in which it was about 142 KPa.

Cartilage injury and joint dislocation are the primary reasons for foot pain in many patients [25]. Orthopedic insole is used to correct the foot arch height and relieve the pain. The purpose of correcting foot arch height is to redistribute the force transfer pattern in the joints to avoid further damaging of foot tissues. However, in the clinical practice, wearing orthopedic insoles is more painful than nonwearing condition in short-term follow-ups. It means that there is an effect on the foot tissues like the ligament and joints by wearing orthopedic insole, at least in short-term follow-ups. In the primary middle joints (talonavicular joint and calcaneocuboid joint), the maximal stress increased with the material hardness. In the calcaneocuboid joint, the stress increased with the arch height of insoles, meaning higher insole arch height results in greater joint stress. However, in the talonavicular joint, type II insole results in the greatest cartilage stress. Despite that, the stress in the middle joint was relatively much lower than that in the ankle joints (tibiotalar joint and talofibular joint), which are the primary structure transferring body weight to the foot. The material hardness did not apparently

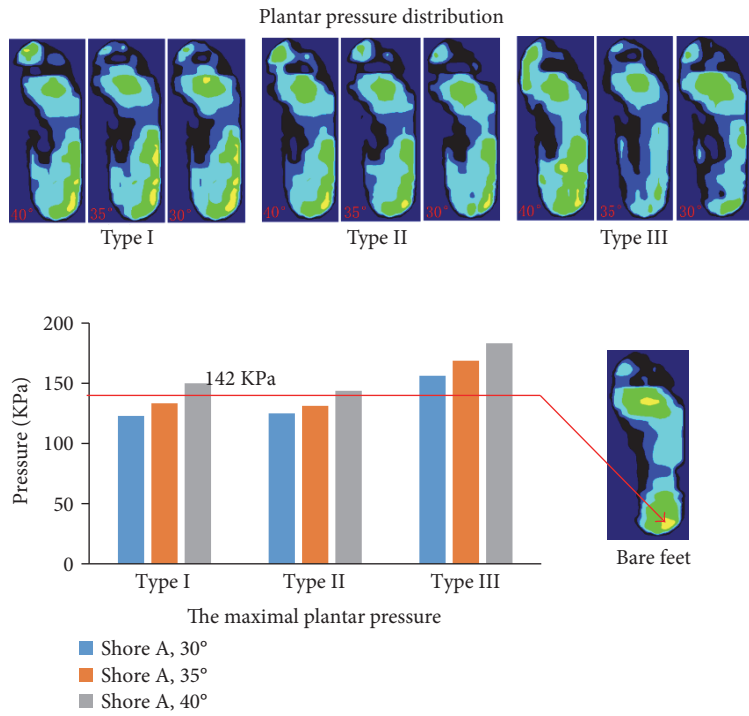


FIGURE 5: The maximal plantar pressures and pressure distribution in the in vivo measurement.

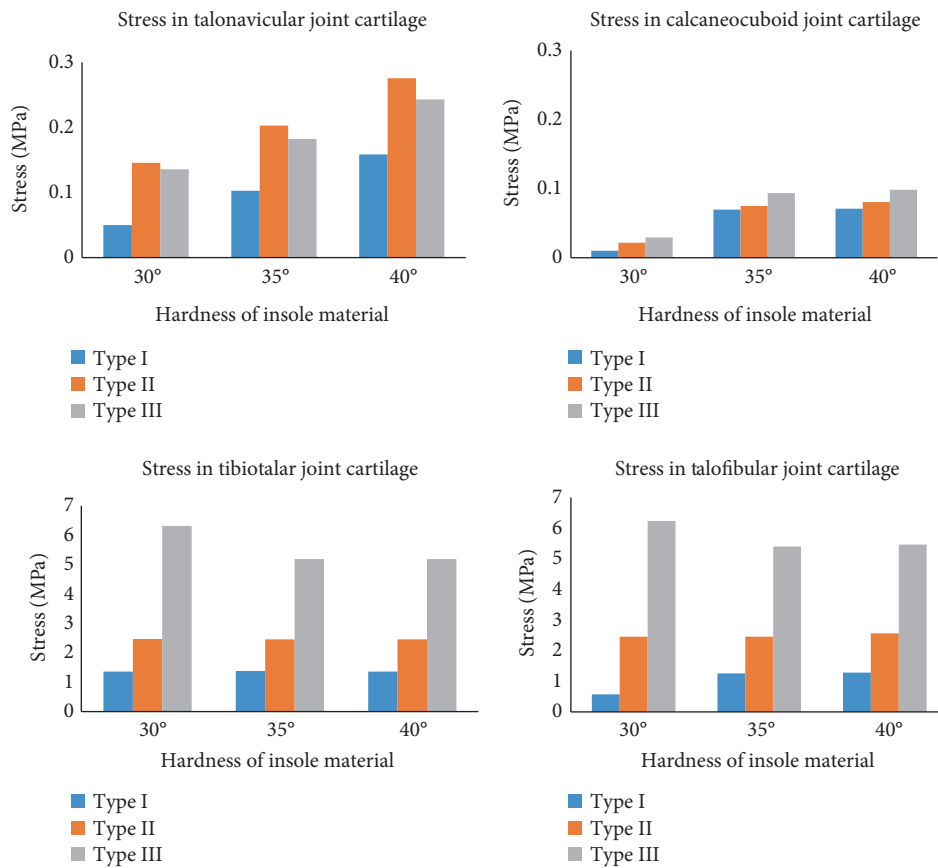


FIGURE 6: The maximal stress in joint cartilage in the finite element model.

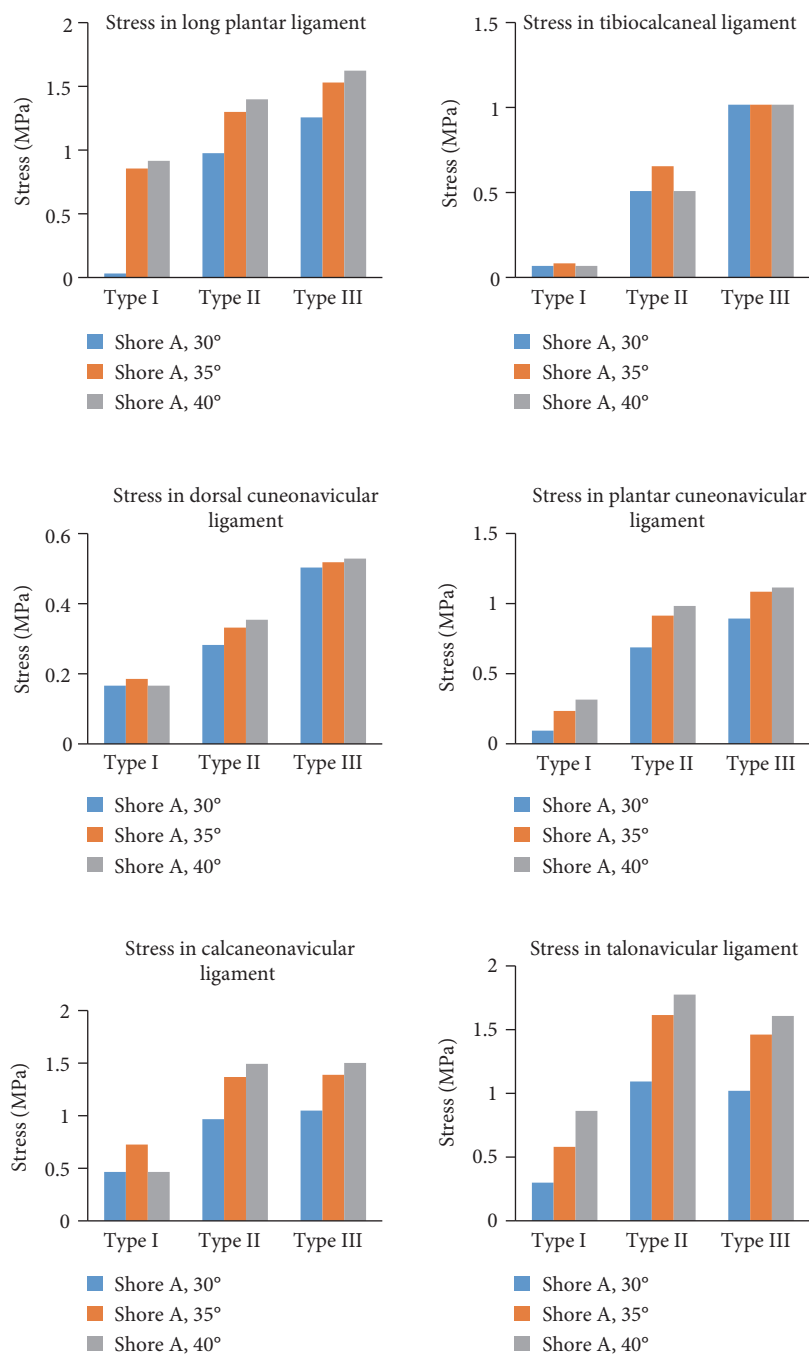


FIGURE 7: The maximal stress in the foot ligaments in the finite element model.

affect the stress in the ankle joints, but the arch height of orthopedic insoles did. However, the maximal stress in almost all the primary foot ligaments increased with the material hardness and arch height of the orthopedic insoles.

In a previous study, the authors found that by changing the material of the insole, the value of maximum stress remains nearly constant [6]. In this study, material hardness of 30°, 35°, and 40° and arch height of 27 mm, 30 mm, and 33 mm were chosen for analysis. The biomechanical effects on the flatfoot of the arch height (increase with 3 mm interval) were more sensitive than the material hardness (increase

with 5 intervals). For example, the average plantar pressure with type I, type II, and type III insoles was 10.4, 14.0, and 16.4 MPa (standard deviation: SD = 3.0 MPa), respectively, while the average plantar pressure with material hardness of 30°, 35°, and 40° was 10.6, 14.3, and 15.8 MPa (SD = 2.7 MPa). The average stress in dorsal cuneonavicular ligament was 0.17 MPa, 0.32 MPa, and 0.52 MPa (SD = 0.17 MPa) for insole shape, but 0.32 MPa, 0.35 MPa, and 0.35 MPa (SD = 0.018 MPa) for material hardness.

Several limitations of this study should be noted for the interpretations and applications of the predicted results.

The correction stage of flatfoot might influence the biomechanical evaluation eventually. However, the biomechanics was just evaluated for the first stage of orthopedic insole treatment. Evaluation of long-term effect should be done in the future. Since there were differences between individuals (degree of flatness, flexible of foot arch, material property, etc.), it is limited to apply the findings obtained from only one subject to all flatfoot. Fortunately, it was a self-comparison and parametric study, especially the FE foot model could represent patients with similar tissue geometry and arch height. Muscle forces play important role by keeping foot stability and providing stiffness. However, only tendon force was considered in the present study. The displacement of navicular bone based on the in vivo experiment was used as a displacement loading to simulate to corrective function of orthopedic insole, which might not reflect the interaction of insole and skin. In addition, the material property of the foot tissues which was simplified as linear formulation and achieved for the literature weakens the individual characters. However, as a parameterized study of material hardness and shape of insole, this simplification should induce a universal support of orthopedic insole design.

5. Conclusion

In general, insole material and support design are positively affecting the correction of orthopedic insole, but negatively resulting in unreasonable stress on the stress in the joint and ligaments. There should be an integration of improving correction and reducing stress in foot tissues.

Conflicts of Interest

There is no conflict of interest disclosure to be declared by the authors.

Authors' Contributions

Honglun Su and Zhongjun Mo contributed equally to this work.

Acknowledgments

This project was supported by the National Natural Science Foundation of China (nos. 11572029, 11421202, and 11602063), the National Key Research and Development Program in China (2016YFB1101101, 2016YFB1101105), and the 111 Project (no. B13003).

References

- [1] A. Kelikian and S. Sarrafian, *Sarrafian's Anatomy of the Foot and Ankle: Descriptive, Topographic, Functional*, Lippincott Williams & Wilkins, Philadelphia, PA, USA, 2011.
- [2] A. A. Buerk and M. C. Albert, "Advances in pediatric foot and ankle treatment," *Current Opinion in Orthopaedics*, vol. 12, no. 6, pp. 437–442, 2001.
- [3] G. S. Murley, H. B. Menz, and K. B. Landorf, "A protocol for classifying normal- and flat-arched foot posture for research studies using clinical and radiographic measurements," *Journal of Foot and Ankle Research*, vol. 2, no. 1, p. 22, 2009.
- [4] F. Hefti and R. Brunner, "Flexible arch of the foot," *Der Orthopäde*, vol. 28, no. 2, pp. 159–172, 1999.
- [5] J. S. Lee, K. B. Kim, J. O. Jeong, N. Y. Kwon, and S. M. Jeong, "Correlation of foot posture index with plantar pressure and radiographic measurements in pediatric flatfoot," *Annals of Rehabilitation Medicine*, vol. 39, no. 1, pp. 10–17, 2015.
- [6] A. Sarikhani, A. Motalebizadeh, S. Asiaei, and B. Kamali Doost Azad, "Studying maximum plantar stress per insole design using foot CT-Scan images of hyperelastic soft tissues," *Applied Bionics and Biomechanics*, vol. 2016, Article ID 8985690, 6 pages, 2016.
- [7] D. R. Bonanno, K. B. Landorf, and H. B. Menz, "Pressure-relieving properties of various shoe inserts in older people with plantar heel pain," *Gait & Posture*, vol. 33, no. 3, pp. 385–389, 2011.
- [8] Y. Han, D. Duan, K. Zhao, X. Wang, L. Ouyang, and G. Liu, "Investigation of the relationship between flatfoot and patellar subluxation in adolescents," *The Journal of Foot and Ankle Surgery*, vol. 56, no. 1, pp. 15–18, 2017.
- [9] S. E. Van Aman and L. C. Schon, "Subtalar Arthroereisis as adjunct treatment for type II posterior tibial tendon deficiency," *Techniques in Foot & Ankle Surgery*, vol. 5, no. 2, pp. 117–125, 2006.
- [10] Y. H. Kwak, K. B. Park, H. W. Park, and H. W. Kim, "Use of allograft in skeletally immature patients for calcaneal neck lengthening osteotomy," *Yonsei Medical Journal*, vol. 49, no. 1, pp. 79–83, 2008.
- [11] G. V. Viegas, "Reconstruction of the pediatric flexible planovalgus foot by using an Evans calcaneal osteotomy and augmentative medial split tibialis anterior tendon transfer," *The Journal of Foot and Ankle Surgery*, vol. 42, no. 4, pp. 199–207, 2003.
- [12] V. S. Mosca, "Calcaneal lengthening for valgus deformity of the hindfoot. Results in children who had severe, symptomatic flatfoot and skewfoot," *The Journal of Bone & Joint Surgery*, vol. 77, no. 4, pp. 500–512, 1995.
- [13] J. Guo, L. Wang, W. Chen, C. Du, Z. Mo, and Y. Fan, "Parametric study of orthopedic insole of valgus foot on partial foot amputation," *Computer Methods in Biomechanics and Biomedical Engineering*, vol. 19, no. 8, pp. 894–900, 2016.
- [14] J. Guo, L. Wang, Z. Mo, W. Chen, and Y. Fan, "Biomechanical analysis of suture locations of the distal plantar fascia in partial foot," *International Orthopaedics*, vol. 39, no. 12, pp. 2373–2380, 2015.
- [15] J. Guo, L. Wang, Z. Mo, W. Chen, and Y. Fan, "Biomechanical behavior of valgus foot in children with cerebral palsy: a comparative study," *Journal of Biomechanics*, vol. 48, no. 12, pp. 3170–3177, 2015.
- [16] J. Yu, J. T. Cheung, D. W. Wong, Y. Cong, and M. Zhang, "Biomechanical simulation of high-heeled shoe donning and walking," *Journal of Biomechanics*, vol. 46, no. 12, pp. 2067–2074, 2013.
- [17] J. Yu, J. T. Cheung, Y. Fan, Y. Zhang, A. K. Leung, and M. Zhang, "Development of a finite element model of female foot for high-heeled shoe design," *Clinical Biomechanics*, vol. 23, Supplement 1, pp. S31–S38, 2008.
- [18] J. T. Cheung and M. Zhang, "Parametric design of pressure-relieving foot orthosis using statistics-based finite element

- method," *Medical Engineering and Physics Medical Engineering and Physics*, vol. 30, no. 3, pp. 269–277, 2008.
- [19] Z. Mo, Q. Li, Z. Jia, J. Yang, D. W. Wong, and Y. Fan, "Biomechanical consideration of prosthesis selection in hybrid surgery for bi-level cervical disc degenerative diseases," *European Spine Journal*, vol. 26, no. 4, pp. 1181–1190, 2017.
- [20] Z. Mo, Y. Zhao, C. Du, Y. Sun, M. Zhang, and Y. Fan, "Does location of rotation center in artificial disc affect cervical biomechanics?" *Spine*, vol. 40, no. 8, pp. E469–E475, 2015.
- [21] E. Kim and J. S. Kim, "The effects of short foot exercises and arch support insoles on improvement in the medial longitudinal arch and dynamic balance of flexible flatfoot patients," *Journal of Physical Therapy Science*, vol. 28, no. 11, pp. 3136–3139, 2016.
- [22] B. Y. Tsung, M. Zhang, A. F. Mak, and M. W. Wong, "Effectiveness of insoles on plantar pressure redistribution," *Journal of Rehabilitation Research and Development*, vol. 41, no. 6A, pp. 767–774, 2004.
- [23] J. C. Gilmour and Y. Burns, "The measurement of the medial longitudinal arch in children," *Foot & Ankle International*, vol. 22, no. 6, pp. 493–498, 2001.
- [24] P. A. Ugolini and S. M. Raikin, "The accessory navicular," *Foot and Ankle Clinics the Navicular*, vol. 9, no. 1, pp. 165–180, 2004.
- [25] J. R. Kim, C. I. Park, Y. J. Moon, S. I. Wang, and K. S. Kwon, "Concomitant calcaneo-cuboid-cuneiform osteotomies and the modified Kidner procedure for severe flatfoot associated with symptomatic accessory navicular in children and adolescents," *Journal of Orthopaedic Surgery and Research*, vol. 9, no. 1, p. 131, 2014.
- [26] H. Elftman, "A cinematic study of the distribution of pressure in the human foot," *The Anatomical Record*, vol. 59, no. 4, pp. 481–491, 1934.

Research Article

Experimental Study on the Mechanical Properties of Porcine Cartilage with Microdefect under Rolling Load

Yu-tao Men,^{1,2} Xiao-ming Li,^{1,2} Ling Chen,^{1,2} and Hu Fu^{1,2}

¹Tianjin Key Laboratory of the Design and Intelligent Control of the Advanced Mechatronical System, Tianjin, China

²School of Mechanical Engineering, Tianjin University of Technology, Tianjin 300384, China

Correspondence should be addressed to Yu-tao Men; yutaomen@163.com

Received 28 March 2017; Accepted 8 May 2017; Published 12 June 2017

Academic Editor: Duo Wai-Chi Wong

Copyright © 2017 Yu-tao Men et al. This is an open access article distributed under the Creative Commons Attribution License, which permits unrestricted use, distribution, and reproduction in any medium, provided the original work is properly cited.

Objectives. To investigate the mechanical responses of microdefect articular cartilage under rolling load and find out the failure rule. **Methods.** Rolling load was applied to the porcine articular cartilage samples with rectangular notches of different depths. The displacement and strain near the notches were obtained by the noncontact digital image correlation technique. **Results.** The strain value and peak frequency around the notch increased; the maximum equivalent strain value could be observed at both bottom corners of the notch; the equivalent strain value first increased and then decreased at the points in the superficial and middle layers with the increase of rolling velocity; the points in the deep layer were less affected by rolling velocity; the equivalent strain value of the points in the superficial layer declined after rising with the increase of defect depth, while a decreased trend could be found for the points in the middle and deep layers. **Conclusions.** The shear strain, which rose with the increase in defect depth, was the main factor in cartilage destruction. The cartilage tended to be destructed firstly at the bottom corner of the defect. Rolling velocity showed significant effects on superficial and middle layers. Cartilage had the ability to resist destruction.

1. Introduction

The articular cartilage is an important part of the human bone joints, which plays critical roles in reducing vibration and bone protection in daily activities of the human body. Studies suggested that the articular cartilage has a quite complex composition and specific material properties like non-linearity and viscoelasticity [1]. The articular cartilage may be damaged to varying degrees due to excessive exercise or other sudden causes [2–4]. However, lots of patients present no symptom in the early stage of cartilage damage, and if let to accumulate, it could evolve into osteoarthritis which will then affect daily life [5, 6].

The articular cartilage can rarely be repaired if damaged; due to the absence of blood vessel, this usually results in osteoarthritis. Therefore, the study on mechanical properties of cartilage with the defect has started drawing attention in the scientific literature. Repeated load deformation can cause

fatigue wear, which alters the mechanical properties of the cartilage. Generally, the greater the surface roughness, the faster the wear is. Delamination damage is the major form of damage for a cartilage under a friction load [7]. Damage will change the mechanical properties of the cartilage [8], causing reduced rigidity [9, 10] or increased permeability [11] for instances. Cyclic loading experiment of cartilage showed that cyclic loading at 7–17 MPa could lead to cartilage cell death but not to damage on the surface structure [12]. By using α -chymotrypsin to label collagenous fibers, the cartilage was found to be deeply stained and marked fibrosis could be observed under acyclic load of 5 MPa for 20 minutes [13]. Gratz et al. [14] have explored changes in a notch angle in full-thickness-defected cartilage under a compressive load. It was found that the closed injury was more likely to slip than the open one. The experimental results of Stok and Oloyede [15, 16] showed that the crack propagation mechanism of the cartilage crack was quite different from the



FIGURE 1: (a) A tested cartilage sample; (b) the picture of making defects.

open mode of traditional fracture mechanics. Dabiri and Li [17] analyzed data from a knee joint model and found a gradually decreased osmotic pressure but an increased shear strain with the increase in cartilage degradation. Based on a 3-D ankle model, Hua et al. [18] observed that the peak stress values increased significantly as the articular cartilage defect area increased; joint functions will be remarkably affected when defect diameter exceeded 11 mm in the distal tibial articular cartilage. Hosseini et al. [19] showed the interactions between softening of bone matrix and damage of fibers. Numerical model also proved that the damage grew preferentially along the tangent direction of the fibers. Fibers played an important role in cartilage construct [20].

The distribution mode of collagen fibers in the cartilage plays a key role in the mechanical properties of cartilage. Based on the distribution and arrangement mode of the collagen fibers, the articular cartilage can be roughly divided into three layers [21]: superficial (tangential layer), middle (transitional layer), and deep layers (radiation). It was reported that changes in the displacement derived from different compressive levels; the loading velocity and the loading times gradually decreased from the surface to the deep layer [22]; and the superficial layer has a vital role in maintaining the biomechanical properties of the cartilage.

Previous studies have focused on the analysis of the mechanical properties of intact cartilage; however, various degrees of articular cartilage damages can be observed even in the early stage of osteoarthritis [23]. It often takes more than ten years or even decades from the initial damage to the loss of active ability. Therefore, it appears especially important to conduct researches on the mechanical properties of injured cartilage. According to the analysis of bone and joint mechanics, a rolling load is the major force among cartilage pressures [1]. In the present study, the noncontact digital image correlation (DIC) technique [24, 25] was used to study changes in the mechanical properties of the articular cartilage related with defect depth under rolling load, in order to summarize the mechanical properties of the injured cartilage. This study may provide a reliable reference for the prevention and the treatment of bone-joint diseases.

2. Materials and Methods

2.1. Sample Preparation. Fresh knee joint cartilage of the distal femoral end was obtained from a 6-month-old pig. Cartilage slices (length = 8 mm; height = 18 mm; thickness = 3 mm) were cut along the normal direction of the cartilage surface. The defect of cartilage was made of machine tools. The thickness of the circle blade was 0.5 mm, and the circle blade rotated with the main axis. The sample of the cartilage was fixed on the knife rest. The depth of notch was controlled by the feed of knife rest, and the feed precision is 0.1 mm. Notches with a width of 0.5 mm and a varying depth were prepared (Figure 1). Three different notch depths were obtained as follows: 0.2 ± 0.02 mm, 0.5 ± 0.02 mm, and 0.7 ± 0.02 mm which were reached into superficial layer, middle layer, and deep layer, respectively. For each notch depth, 6 samples were prepared and iron oxide nanoparticles, which were treated as pixels, were embedded on the side surface of the slices.

2.2. Experimental Device. Figure 2(a) shows the experimental apparatus which were composed of the mechanical loading system, the image acquisition system, the computer control system, and the image processing software.

Figure 2(b) shows the mechanical loading system including the rolling control device and the compression quantity adjusting device. The rolling control device was driven by a stepping motor, that is, the rotary motion was converted into a linear motion through the screw, then through the connecting rod to drive the cylindrical roller, to thus perform constant reciprocating rolling. The compression quantity adjusting device was regulated by the screw on both sides of the fixture portal frame. This system had a maximum rolling distance of 30 mm and a maximum rolling velocity of 10 mm/s. The diameter of the indenter was 40 mm, and the surface roughness was 0.05. A temperature-controlled liquid tank was implemented on this equipment to simulate in vivo environment.

The image acquisition system mainly consisted of a charge-coupled device (CCD) camera, which helped us

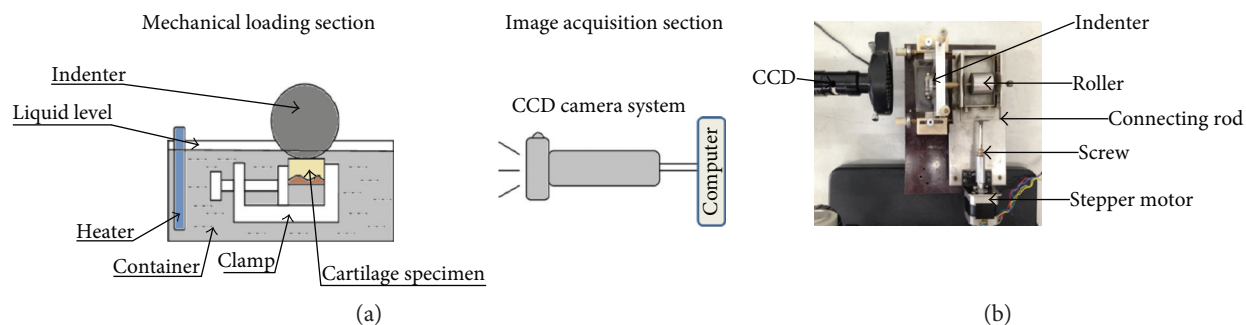


FIGURE 2: (a) Schematic diagram of the experimental apparatus; (b) the practicality of the experimental apparatus.

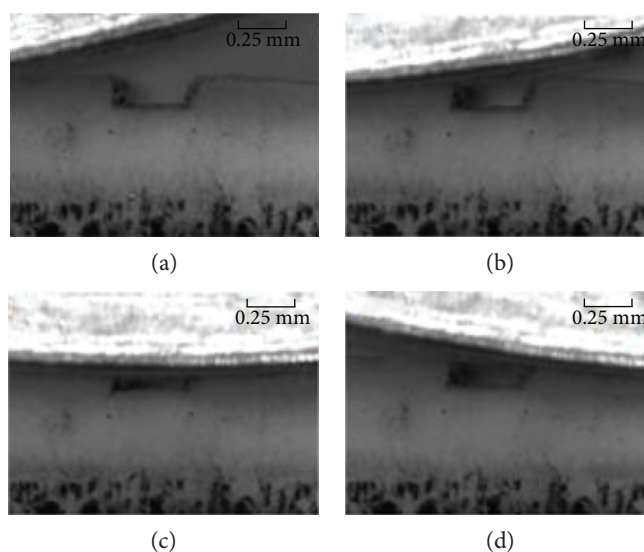


FIGURE 3: Images acquired by the CDD camera. From (a) to (d) represented image acquisition sequence.

obtain images with a 1376×1035 resolution. Images were then analyzed and postprocessed by an image processing software, producing data about the displacement and strain of the mark points of cartilage samples.

2.3. Experimental Methods. The cartilage samples were fixed on the fixture clamp of the portal frame and then placed in a saline tank. After that, saline was heated to 37°C so as to reduce the experimental errors. The indenter rolled onto the surface of the cartilage sample 50 times back and forth, with a compression quantity of 0.1 mm and a rolling velocity set as 1 mm/s, 2 mm/s, 4 mm/s, and 6 mm/s, respectively. Images were acquired continuously by the CCD camera with 2 frames/s frequency (Figure 3). Then, the displacement and strain fields were obtained after image processing.

3. Results

In order to facilitate the analysis of stress and strains near the notch, regions near the notch were divided by uniformed grid partition. The interval between two longitudinal lines was set at 0.125 mm. The selected horizontal lines were located 5%, 25%, 45%, 65%, and 85% away from the cartilage surface (Figure 4).

3.1. Effect of Defects on the Mechanical Properties of Cartilage.

The iron oxide nanoparticles as mark points and pixels were embedded on the side surface of the sample before the experiments. The speckle image of the sample including mark points in its load-free state was first acquired and used as the reference image. The continuous and instantaneous speckle images including the mark points were also obtained at the different stages of loading. The images in random half cycle that the roller rolled above the sample from the left to the right were selected from all the acquired images. Using the computer to identify the mark points and pixels, the displacements of mark points and pixels were calculated by comparing the coordinates of current pixel images with reference image. And then, the strain values were obtained according to the relationship between the displacement and strain.

Figure 5 shows the comparison between intact and injured (notch depth of 0.5 mm) cartilages under a compression quantity of 0.1 mm and a rolling velocity of 4 mm/s. The equivalent strain significantly decreased with the increase of the cartilage notch depth when the roller went through the surface of the cartilage from the left to the right. The cartilage strain values could be changed by defects. Injured cartilage had a larger strain value as well as a higher frequency of strain peak value than the intact cartilage. At the A3 point, which

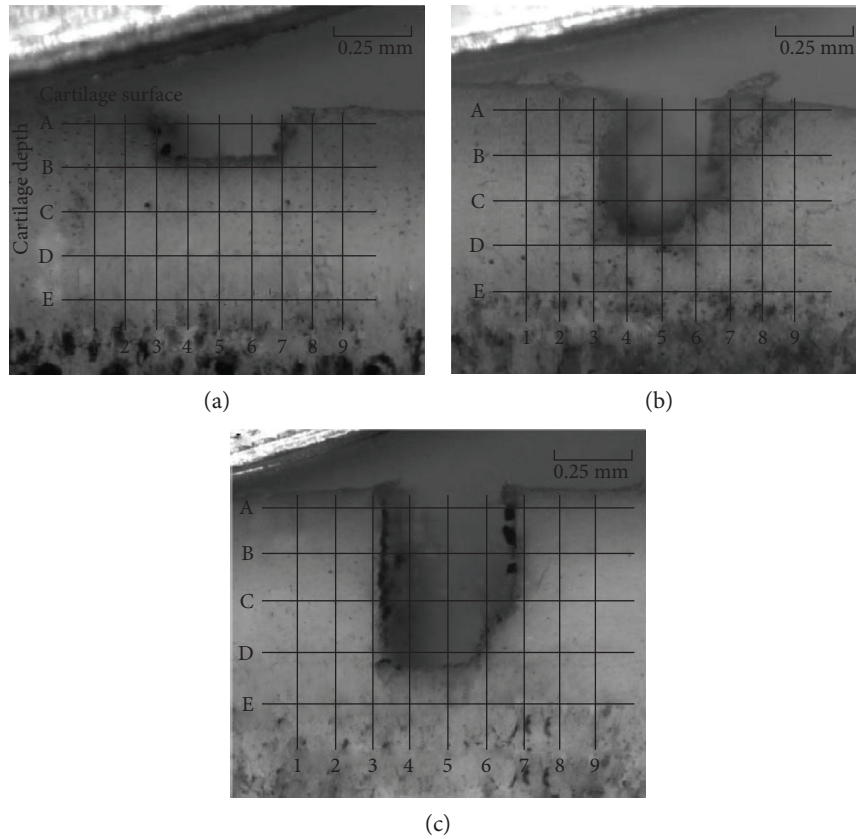


FIGURE 4: The position of the grid and the grid partition of the different notch depths. (a) Notch depth was 0.2 mm; (b) notch depth was 0.5 mm; and (c) notch depth was 0.7 mm.

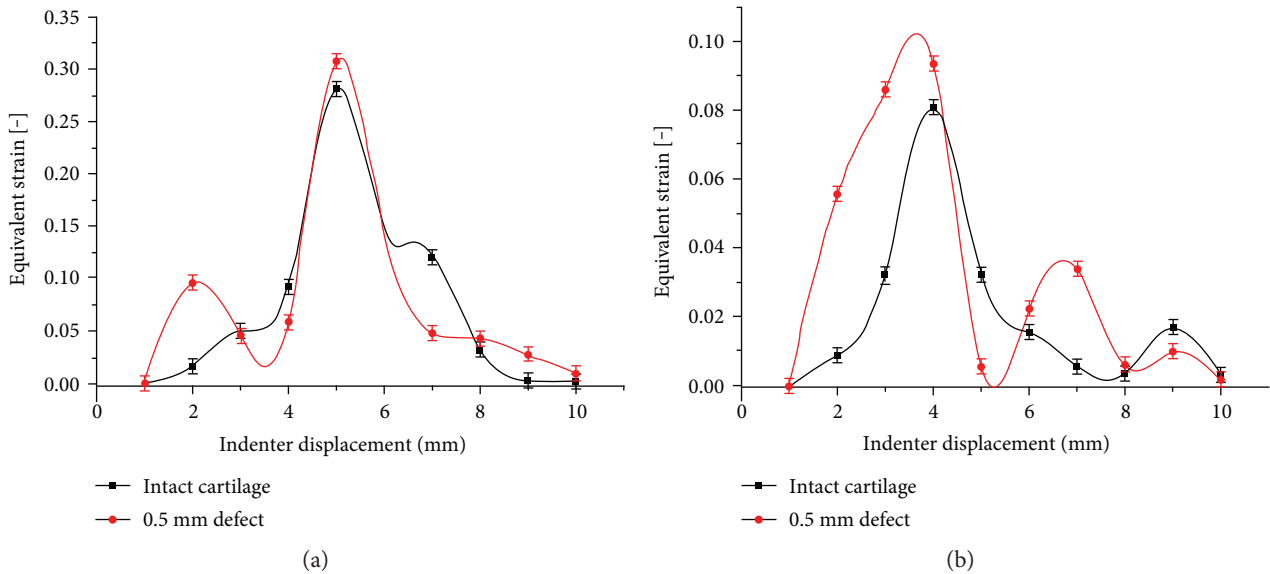


FIGURE 5: Comparison of the strain curves between intact and defective cartilages. (a) The strain curves at the A3 point; (b) the strain curves at the D3 point.

was in the superficial cartilage, the difference of the strain peak value accounted for 6% of the total strain value, while this represented 20% for the D3 point in the deep layer of the cartilage. Results showed that the defect had obvious effects on the mechanical properties of the cartilage.

3.2. Effect of Defect Depth on the Mechanical Properties of Cartilage. In this part, strain values were measured at each observation point around the notch with different depths under a compression quantity of 0.1 mm and a rolling velocity of 4 mm/s (Figure 6). The cartilage received a periodic

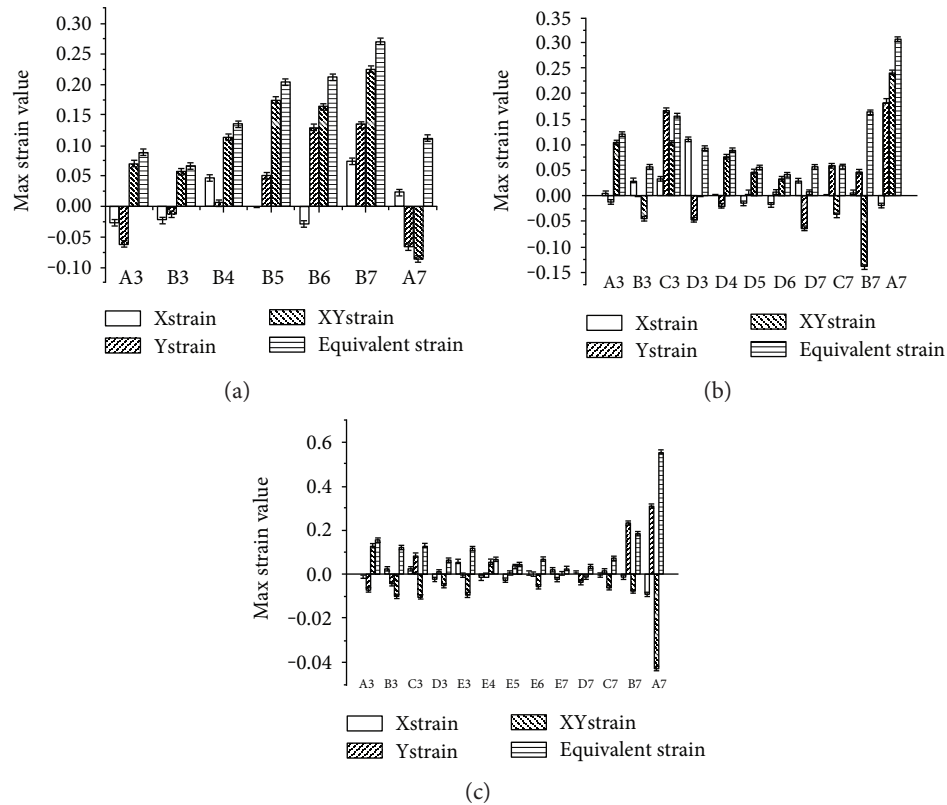


FIGURE 6: The strain values measured at the observation points around the notches. (a) Notch depth was 0.2 mm; (b) notch depth was 0.5 mm; and (c) notch depth was 0.7 mm.

load force when the reciprocating roller rolled over the surface of the cartilage, and we selected the maximum strains of the selected points in half cycle for further analysis. It was showed that a shearing strain played a dominant role in the strain value changes. For the cartilage with a notch depth of 0.2 mm (Figure 6(a)), the strain values of the defect's bottom points (B3–B7) gradually increased from the left to the right. Point B7, at the right bottom corner, had the maximum strain value of 0.27, which was 3 times that of the left bottom corner at point B3. For the cartilage with a notch depth of 0.5 mm (Figure 6(b)), the strain values of the bottom points (D3–D7) showed a fall-rise trend from the left to the right. The equivalent strain of the two bottom corners was twice that of the middle region points. For points C7, D7, and C3, the ϵ_y strain replaced the shearing strain as the dominate role, and the shearing strain direction changed at points B3 and B7. The strain values at the bottom of the notch (E3–E7) first decreased and then increased from the left to the right when the notch depth was 0.7 mm (Figure 7(c)). For the points at both sides of the notch (B3, C3, D3, A7, B7, and C7), their shearing strain directions changed, and the values gradually decreased with increase of the defect depth.

Figure 7 shows changes in the equivalent strain across the varying defect depth at points A3, C3, and D3 under a compression quantity of 0.1 mm and a rolling velocity of 4 mm/s. For each point, changes in the strain followed a periodic pattern; for the points in the middle and deep layers, the equivalent strain value significantly decreased with the

increase in the defect depth; at which the points were located near the superficial layer, the equivalent strain value was very small when damage was relatively small, and the maximum equivalent strain values could be observed with a notch depth of 0.5 mm.

3.3. Effect of Rolling Velocity on the Mechanical Properties of Defect Cartilage. Figure 8 illustrates the fluctuation curves of the equivalent strain at A3, C3, and D3 across different rolling velocities, with a notch depth of 0.5 mm and when the roller moved from the left to the right. For point A3, the minimum peak value was achieved at a rolling velocity of 2 mm/s. At 6 mm/s, the peak value became larger and a maximum of 0.30 was observed at 4 mm/s, which represented 1.5 times of the value measured at the rolling velocity of 2 mm/s.

For point C3, a single distinct peak could be found for the equivalent strain. Peak values presented an increasing trend and then a reduction with the increase in the rolling velocity. A maximum value of 0.16 was observed at a rolling velocity of 4 mm/s, which was 1.5 times of the value recorded at 2 mm/s.

In contrast, the case was rather complicated for point D3. There were two peaks with in half rolling period, and the peak frequency appeared enlarged with the increase in the rolling velocity. The first peak was located in the same position across the different rolling velocities, that is, when the indenter was right above the D3 point, while the second peak was located differently and decreased at velocities of 2 mm/s

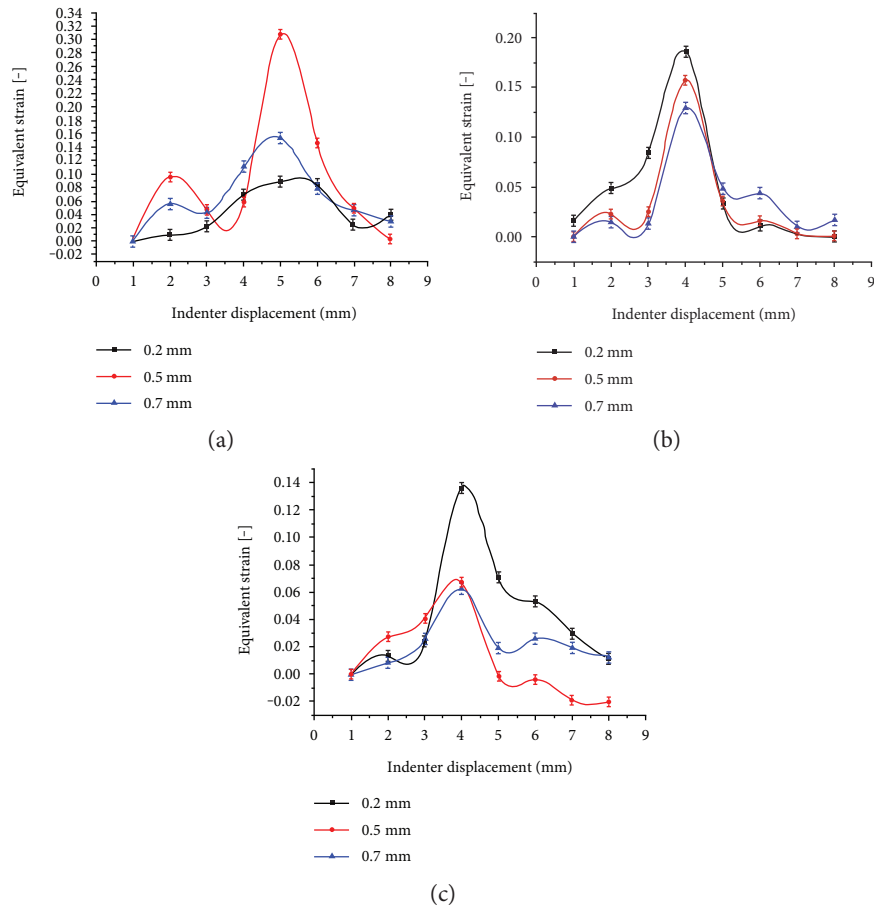


FIGURE 7: The strain curves measured at different points across the different notch depths. (a) Equivalent strain measured at point A3; (b) equivalent strain measured at point C3; and (c) equivalent strain measured at point D3.

and 4 mm/s. When rolling at a velocity of 6 mm/s, the second peak increased to 0.12.

4. Discussion

In this paper, we used the noncontact digital image correlation (DIC) technique to focus on the mechanical responses of cartilage with different defect depths under rolling load. As the distribution and content of the major components varied with defect depth, fibers inside the cartilage can be divided into three parts: superficial, middle, and deep layers (accounts for 5%, 45%, and 50% of the cartilage thickness, resp.). Collagen fibers in the superficial layer distribute densely and parallel with the articular surface, which has maximum moisture content and for which deformation can easily occur under normal stress. Collagen fibers in the middle layer are irregularly arranged with large interspaces and crisscross at a certain angle with joint surface, which has less moisture content and deforms slowly under normal stress. The deep layer fibers are nearly perpendicular to the articular surface and have the lowest water content and the smallest deformation under normal stress [26]. The method used in our study has the advantages of noncontact, low requirement for the experiment environment and light source, as well as high measurement accuracy, and allows full-field

measurement. It has thus been widely used in biomechanical studies [24, 25]. Due to high toughness and different distributions of fibers inside the cartilage, it was very difficult to obtain a smooth border when creating the defect, leading to certain errors in the measurement. In this paper, the left side, which was relatively smooth, was chosen for further analysis in order to reduce errors.

As can be seen from Figure 5, the peak values of the equivalent strain decreased gradually with the increase of the notch depth, which was consistent with the strain law obtained in intact cartilage experiments [22, 27]. When the indenter moved on a cartilage surface from the left to the right, each point was subjected to cyclic loading, leading to cartilage fatigue failure. When a defect existed, the cycle frequency enlarged and the strain value of each point increased around the defect. These results are consistent with those reported by Gratz et al. [14] and are likely due to the stress concentrations produced by the notch. Timely repairing of damaged cartilage can reduce strain value around the notch [28].

When notch is shallow, the maximum equivalent strain appeared at the bottom corner of the notch; with the increase of notch depth, the strain value rose quickly because the supporting structure became loose. Figure 6 showed that the shear strain increased significantly when the notch reached

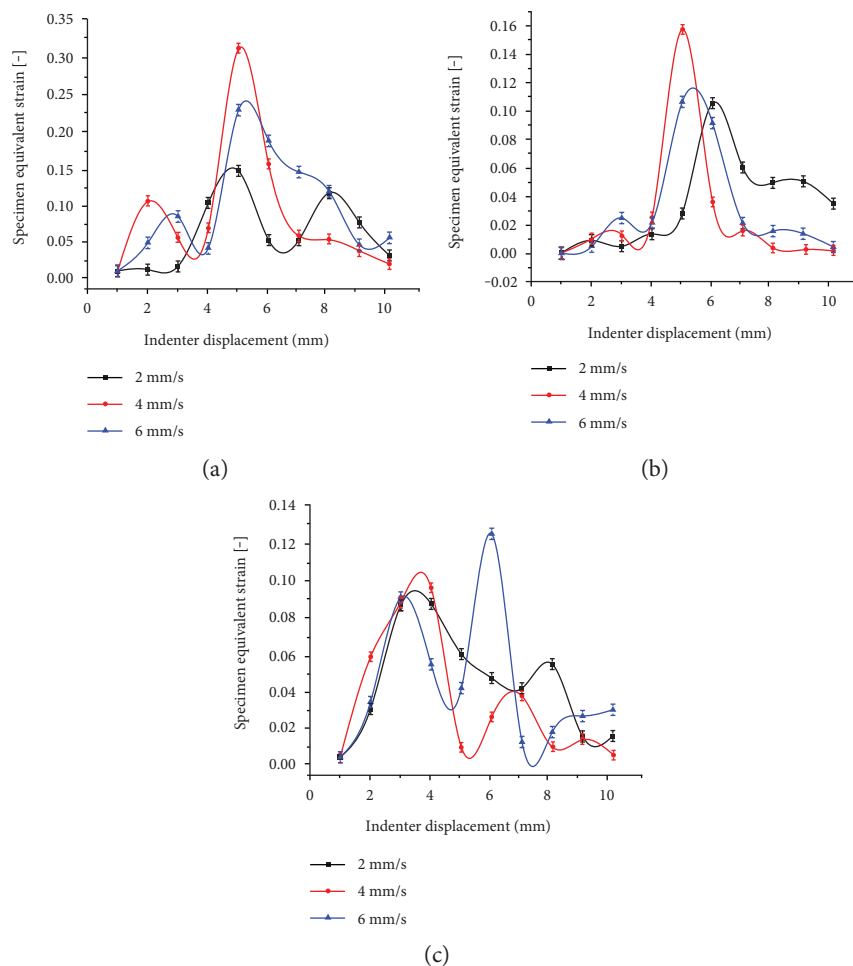


FIGURE 8: Variation trend curves of strain measured for dangerous points at different rolling velocities. (a) Equivalent strain measured at point A3; (b) equivalent strain measured at point C3; and (c) equivalent strain measured at point D3.

the deep layer, which is in agreement with the results of Dabiri and Li [17] obtained by using a knee joint model. This means that the shear strain of the cartilage increased gradually with cartilage degradation. It can be inferred that the shear strain is the key factor in cartilage destruction, and this destruction began from the bottom corner of the defect.

The positive and negative strain variations at points C3 and D3 existed in our study. These points were located in the vicinity of 50% of the cartilage height, which may be the interface between the middle and the deep layers. The distribution of cartilage fibers may vary in this position, resulting in different strain change rules compared with other points. This result indicated that fiber distribution has an important influence on the mechanical properties of cartilage [29, 30]. The interface between the middle and the deep layers will be easily destroyed when the notch will deepen.

Compared with the other points of the location, the points near the superficial layer showed different responses to the defect depth (Figure 7). Indeed, points located in the superficial layer had greater responses to the defect with a moderate depth, while deep points were sensitive to a small defect. This is considered to be determined by the fiber structure and the viscoelastic properties of the cartilage. Besides,

superficial layer has a higher water content, low modulus of elasticity as well as greater deformability. Accardi et al. [31] also confirmed that the fiber orientation of cartilage can resist the shear failure, which indicated that cartilage has a self-protective function against certain damage. This way, the destruction process can be significantly delayed.

The rolling velocity has a certain impact on the cartilage strain. It was reported that the friction coefficient increased first then became lower with the increase in the rolling velocity [32–34], leading to a rising and falling cartilage strain. This may be due to the cartilage viscoelasticity, which ensures that water can be continuously extruded under loading, causing changes in the friction coefficient and the strain values.

The main problem is that the experimental model of defect cartilage was a plane model using digital correlation technology to investigate mechanical properties of defect cartilage. The difference between experimental model and the cartilage model in vivo is that the confining pressure conditions could not be considered. However, the authors think that it is possible to obtain the confining pressure condition of the experimental model by using the method both numerical simulation and experiment. The displacement field and stress strain field of the model of integral cartilage and femur

could be obtained by using the numerical simulation method, then the plane model of the experiment was taken into account from the integral numerical model, and the boundary condition was applied to the cutting surface of the plane model base on the results of the integral cartilage and femur. Modified boundary conditions decreased the error between the strains of the experiment and strains of the numerical simulation. The confining pressure conditions could be obtained by the numerical simulation. The confining pressure conditions could be used to conduct the experimental defect cartilage model.

In addition, the analyzed images were from the random half cycle in this paper. Due to the viscoelastic properties of the cartilage, its strain is correlative with rolling number, which could result in experimental errors. As a result of the limitation of cartilage samples taken from the position, the experimental samples from different pig femoral cartilages could also cause error. The physical load of the knee joint involves rolling, sliding, and a combination of rolling and sliding. This paper focused on the defect cartilage subjected to single load such as rolling, and the research work will be carried out in the future to understand the mechanical properties of the defect cartilage under other loads.

5. Conclusion

In this paper, we used a noncontact DIC technique to measure the displacement and the strain fields near the notch of a defected cartilage under rolling load. Based on our study, we can conclude that the cartilage damage may increase the strain values and strain peak frequency around the defect. The shear strain, which serves as the main factor causing cartilage destruction, increased with the increase in the defect depth. The cartilage would be destructed firstly at the bottom corner of the defect, and when the defect reached the certain depth, it might be destroyed along the interface between the middle and deep layers. The rolling velocity showed a significant effect on the superficial and middle layers. The equivalent strain increased first and then decreased with the increase in the rolling velocity. Changes were not obvious in the deep layer except for the rising strain peak frequency. The special structure of the cartilage exhibited a self-protective function against destruction, which may slow down this destruction process. Our results can provide a basis for the clinical treatment of osteoarthritis and cartilage repair. It is also of great significance for the mechanical analysis of artificial cartilage.

Conflicts of Interest

The authors declared that they have no conflicts of interest to this work.

Acknowledgments

The project was supported by the National Natural Science Foundation of China (no. 11402171 and no. 11672208) and was partly supported by the National Natural Science Key Foundation of China (no. 11432016).

References

- [1] X. Wei, *Articular Cartilage*, Science press, Beijing, 2007.
- [2] N. Chen and K. Hu, "The research progress of articular cartilage injury," *Chinese Journal of Traditional Medicine Traumatology and Orthopedics*, vol. 3, no. 6, pp. 57–60, 1995.
- [3] Q. Gong, "Current research situation of arthroidal cartilage injury and repair," *Journal of Clinical Rehabilitative Tissue Engineering Research*, vol. 14, no. 24, pp. 4491–4494, 2010.
- [4] A. C. Luke, C. Stehling, R. Stahl, X. Li, and T. Kay, "High-field magnetic resonance imaging assessment of articular cartilage before and after marathon running: does long-distance running lead to cartilage damage?" *American Journal of Sports Medicine*, vol. 38, no. 11, pp. 2273–2280, 2010.
- [5] T. F. Moyad, "Cartilage injuries in the adult knee: evaluation and management," *Original Article*, vol. 2, no. 3, pp. 226–236, 2011.
- [6] K. Yin, X. Wei, J. Ding, and J. Lv, "Relationship between synovitis and articular cartilage injury," *Chinese Remedies and Clinics*, vol. 13, no. 12, pp. 1555–1557, 2013.
- [7] S. R. Oungoulian, K. M. Durney, B. K. Jones, C. S. Ahmad, C. T. Hung, and G. A. Ateshian, "Wear and damage of articular cartilage with friction against orthopedic implant materials," *Journal of Biomechanics*, vol. 48, no. 10, pp. 1957–1964, 2015.
- [8] W. Wilson, C. van Burken, C. van Donkelaar, P. Buma, B. van Rietbergen, and R. Huiskes, "Causes of mechanically induced collagen damage in articular cartilage," *Journal of Orthopaedic Research*, vol. 24, no. 2, pp. 220–228, 2006.
- [9] F. Guilak, A. Ratcliffe, N. Lane, M. P. Rosenwasser, and V. C. Mow, "Mechanical and biomechanical changes in the superficial zone of articular cartilage in a canine model of osteoarthritis," *Journal of Orthopaedic Research*, vol. 12, no. 4, pp. 474–484, 1994.
- [10] T. McCormack and J. M. Mansour, "Reduction in tensile strength of cartilage precedes surface damage under repeated compressive loading in vitro," *Journal of Biomechanics*, vol. 31, no. 1, pp. 55–61, 1998.
- [11] M. A. Leroux and L. A. Setton, "Experimental and biphasic FEM determinations of the material properties and hydraulic permeability of the meniscus in tension," *Journal of Biomechanical Engineering*, vol. 124, no. 124, pp. 315–321, 2002.
- [12] P. G. Alexander, Y. Song, J. M. Taboas et al., "Development of a spring-loaded impact device to deliver injurious mechanical impacts to the articular cartilage surface," *Cartilage*, vol. 4, no. 1, pp. 52–62, 2013.
- [13] C. T. Chen, N. Burtonwurster, G. Lust, R. A. Bank, and J. M. Tekoppele, "Compositional and metabolic changes in damaged cartilage are peak-stress, stress-rate, and loading-duration dependent," *Journal of Orthopaedic Research Official Publication of the Orthopaedic Research Society*, vol. 17, no. 6, pp. 870–879, 1999.
- [14] K. R. Gratz, B. L. Wong, W. C. Bae, and R. L. Sah, "The effects of focal articular defects on cartilage contact mechanics," *Journal of Orthopaedic Research*, vol. 27, no. 5, pp. 584–592, 2009.
- [15] K. Stok and A. Oloyede, "Conceptual fracture parameters for articular cartilage," *Clinical Biomechanics*, vol. 22, no. 6, p. 725, 2007.
- [16] K. Stok and A. Oloyede, "A qualitative analysis of crack propagation in articular cartilage at varying rates of tensile loading," *Connective Tissue Research*, vol. 44, no. 2, p. 109, 2003.

- [17] Y. Dabiri and L. P. Li, "Altered knee joint mechanics in simple compression associated with early cartilage degeneration," *Computational and Mathematical Methods in Medicine*, vol. 2013, no. 1, Article ID 862903, 2013.
- [18] H. Yu, S. Li, C. Zhao, and J. Yan, "Finite element model of distal tibial articular surface defect: biomechanical analysis," *Chinese Journal of Tissue Engineering Research*, vol. 17, no. 43, pp. 7571–7580, 2013.
- [19] S. M. Hosseini, W. Wilson, K. Ito, and C. C. van Donkelaar, "A numerical model to study mechanically induced initiation and progression of damage in articular cartilage," *Osteoarthritis and Cartilage*, vol. 22, no. 1, pp. 95–103, 2014.
- [20] Y. Men, Y. Jiang, L. Chen, C. Zhang, and J. Ye, "On mechanical mechanism of damage evolution in articular cartilage," *Materials Science and Engineering C*, vol. 78, pp. 79–87, 2017.
- [21] Y. Lu, X. Ding, C. He, Q. Zhou, and D. Lianjun, "Articular cartilage of the knee: laminar appearance in MR imaging with histological findings," *Chinese Journal of Medical Imaging Technology*, vol. 22, no. 12, pp. 1799–1802, 2006.
- [22] C.-Q. Zhang, L.-L. Gao, L.-M. Dong, and H.-Y. Liu, "Depth-dependent normal strain of articular cartilage under sliding load by the optimized digital image correlation technique," *Materials Science and Engineering: C*, vol. 32, no. 8, pp. 2390–2395, 2012.
- [23] F. Richard, M. Villars, and S. Thibaud, "Viscoelastic modeling and quantitative experimental characterization of normal and osteoarthritic human articular cartilage using indentation," *Journal of the Mechanical Behavior of Biomedical Materials*, vol. 24, no. 25, p. 41, 2013.
- [24] H. Wang, Y. Kang, and H. Xie, "Advance in digital speckle correlation method and its application," *Advances in Mechanics*, vol. 35, no. 2, pp. 195–203, 2005.
- [25] D. Zhang, "Digital image correlation: theory and applications," *Journal of Medical Biomechanics*, vol. 24, no. 2, pp. 85–88, 2009.
- [26] T. J. Klein, J. Malda, R. L. Sah, and D. W. Huttmacher, "Tissue engineering of articular cartilage with biomimetic zones," *Tissue Engineering Part B Reviews*, vol. 15, no. 2, pp. 143–157, 2009.
- [27] L. Gao, C. Zhang, Y. Yang, J. Shi, and Y. Jia, "Depth-dependent strain fields of articular cartilage under rolling load by the optimized digital image correlation technique," *Materials Science and Engineering C*, vol. 33, pp. 2317–2322, 2013.
- [28] G. N. Duda, Z. M. Maldonado, P. Klein, M. O. W. Heller, J. Burns, and H. Bail, "On the influence of mechanical conditions in osteochondral defect healing," *Journal of Biomechanics*, vol. 38, no. 4, pp. 843–851, 2005.
- [29] A. Thambyah, J. Y. Zhao, S. L. Beville, and N. D. Broom, "Macro-, micro- and ultrastructural investigation of how degeneration influences the response of cartilage to loading," *Journal of the Mechanical Behavior of Biomedical Materials*, vol. 5, no. 1, pp. 206–215, 2012.
- [30] M. A. Accardi, S. D. McCullen, A. Callanan et al., "Effects of fiber orientation on the frictional properties and damage of regenerative articular cartilage surfaces," *Tissue Engineering Part A*, vol. 19, no. 19–20, pp. 2300–2309, 2013.
- [31] M. A. Accardi, D. Dini, and P. M. Cann, "Experimental and numerical investigation of the behaviour of articular cartilage under shear loading—interstitial fluid pressurisation and lubrication mechanisms," *Tribology International*, vol. 44, no. 5, pp. 565–578, 2011.
- [32] A. C. Cilingir, "Effect of rotational and sliding motions on friction and degeneration of articular cartilage under dry and wet friction," *Journal of Bionic Engineering*, vol. 12, no. 3, pp. 464–472, 2015.
- [33] F. Li, A. Wang, and C. Wang, "Tribological behavior of articular cartilage against medical stainless steel," *Tribology*, vol. 36, no. 1, pp. 42–47, 2016.
- [34] M. H. Naka, K. Hattori, and K. Ikeuchi, "Evaluation of the superficial characteristics of articular cartilage using evanescent waves in the friction tests with intermittent sliding and loading," *Journal of Biomechanics*, vol. 39, no. 12, pp. 2164–2170, 2006.

Research Article

User-Centric Feedback for the Development and Review of a Unique Robotic Glove Prototype to Be Used in Therapy

Stuart James Biggar,¹ Wei Yao,¹ Lizhen Wang,² and Yubo Fan²

¹Biomedical Engineering, University of Strathclyde, Wolfson Centre, 106 Rottenrow East, Glasgow G76 0HD, UK

²School of Biological Science and Medical Engineering, Beihang University, Xueyuan Road No. 37, Haidian District, Beijing 100191, China

Correspondence should be addressed to Wei Yao; w.yao@strath.ac.uk and Yubo Fan; yubofan@buaa.edu.cn

Received 12 January 2017; Revised 20 March 2017; Accepted 27 April 2017; Published 4 June 2017

Academic Editor: Jesús Favela Vara

Copyright © 2017 Stuart James Biggar et al. This is an open access article distributed under the Creative Commons Attribution License, which permits unrestricted use, distribution, and reproduction in any medium, provided the original work is properly cited.

Disability can be a great impediment to daily living in later life and is often the result of illness or trauma. Modern thoughts on treatment are orientated towards the use of robotics; however, these are often designed without consultation with the user. This paper used a 5-point questionnaire to ask former therapy patients what they felt needed further improvements from potential robotics and what features of such a system were the most important. Significant emphasis was placed on helping them to grasp ($M=4.63$) as well as having a functional use. They also desired a system with clearly distinguished ($M=4.22$) and easy to operate controls ($M=4.44$) whilst allowing them some freedom to move around independently ($M=4.44$). This provided the rationale for a prototype dual-layered vacuum glove that was sampled by healthcare staff to provide feedback that forms the basis for future improvements.

1. Introduction

Improvements in technology have had a positive impact in many countries by increasing life expectancy. The downside of this is that it increases their chances of exposure to degenerative conditions; when this is coupled with poor lifestyle choices, it increases the possibility of impairment to their standard of living through disability [1, 2]. Increases in patient numbers means that health services must evaluate how best to adapt as the availability of staff to provide this therapy is reduced in both numbers and time [3, 4]. To bridge this gap, robotic systems can be utilized to enable therapy workers to attend to the needs of a greater number of patients. There are also potential benefits if the patient could use it in their own home to maximise exposure and the associated increase in exercise compliance [5, 6].

The first step in this process is to develop systems that work in conjunction with the therapists to help the patients to increase their recovery. The issue is that traditionally these devices will be developed to solve a problem that has been highlighted by the researcher, such as assisting mobility in

structurally complicated joints like the shoulder [7] or the integration of design features for user feedback and control [8, 9], rather than a system that is developed in consultation with the patients. Whilst the designs perform their intended purpose, they can be large, bulky units that are not practical for a patient to take home, such as Dampace [10], while EMG controlled systems may also be challenging to set up and operate at home on their own due to a large number of electrodes requiring positioning to function [11]. Whilst a larger mechanism may be required for the shoulder due to its complexity, for hand-centric therapy, mechanical designs must accommodate the varied sizes of the fingers and be adaptable to this range and the changes in mechanical performance that result; an example of this is the adjustable iHandRehab system [12] that offers both active and passive control of the index finger and thumb. The design had a worn hand component that the user would interact with, along with a larger controller and actuator unit that is not worn; assessing the mobility of this device showed it to be achieving at least 86% of the maximal rotation in each joint of the thumb and 71.5% for the index finger. Smaller glove designs

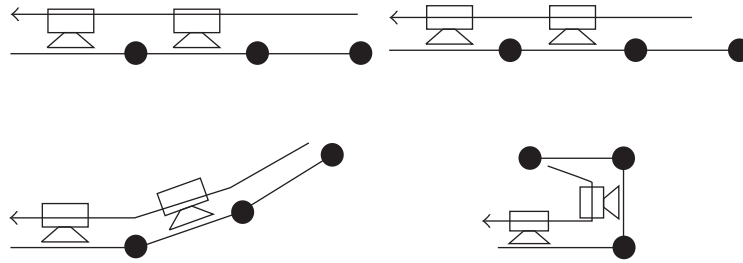


FIGURE 1: Illustration of process of finger rotation for glove design.

that are completely wearable have also begun to be developed, with examples such as the J-Glove and X-Glove [13, 14]. They are cable-driven designs that are portable and can be completely worn by the patient, although the results have not produced a significant improvement in patient outcomes, along with the design exposing the mechanism that enables its operation which may compromise the motion of the hand.

As a developing field, it is important to quantify the needs of the end user to ensure that the devices are used by patients. The best way to identify which areas patients are most in need of further support in their treatment is through discussion, although this lacks the formal structure to score the findings and assess trends. Pairing this with a questionnaire allowed for the formation of results in the assessment method Quality Function Deployment (QFD). This model originates in Japan and provides a reasoned process for how decisions can be reached by placing the needs of the user at the centre. The process begins with the product planning stage that highlights the design requirements and progresses to the characteristics of the parts to be used before outlining the planning and production phases for mass development. As a prototype is being developed in this study, only the initial phases are required. QFD has a pedigree of use in healthcare, such as diagnostic devices [15], cochlear implants [16], and power wheelchairs [17]. The purpose of this research was to consult with patients and use QFD to shape the design of a low-cost device that patients could use at home as both an assistive tool and as a therapy aid and to review it with therapy workers.

2. Method

The study consulted with former patients in central Scotland who were only eligible if their upper limb had been previously impaired and they had completed their prescribed therapy. The study discussed their experiences with this therapy to find out what they felt was and was not successful in their recovery. This was done through the combined use of a questionnaire and a follow-up interview to gather a mixture of qualitative and quantitative data to give the design features a weighted relevance to each other.

The questionnaire asked about five separate categories that had been highlighted to feature in the design (joint motion, function, control, wearability, and a combination of remaining aesthetic and practical features). These five categories had five criteria each of their own; the participants were asked to rank these criteria by importance in their opinion (five was to be considered the most important and one

the least). To clarify this data, they were also asked to rank the whole categories to differentiate between criteria given the same rank across categories. Whilst the intention is to integrate as many of the 25 criteria into the design as possible, when these features clashed, the emphasis was placed towards the highest ranking criteria.

The initial data collection from the questionnaire was distributed to interested parties via physical activity groups, with participants being provided a copy of the studies paperwork and a stamped addressed envelope to return the questionnaire as well as the opt-in form for the interview. The interview was framed around their questionnaire responses, asking why the highest ranked features were the most important and why the lesser ones were not, using these points as a springboard for discussion over the merits of the features in the categories. Discussion of connections between the criteria that are in differing categories was encouraged to form a dialogue over the integration of functional needs in the overall design and allow the relationships to be quantified in the QFD design matrix.

The information gathered in the matrix was used to create a design that developed into a prototype that was tested to get an indication of its performance in relation to its objectives. This prototype used a double-layered glove design that would grip tightly to the wearer by creating a vacuum within it, with suction cups being distributed on the inner layer. This resulted in the creation of fixed points within the glove that a cable could be threaded through to drive motion of the fingers (Figure 1); using these fixed points also results in the outer layer being used as a cover for the cables that prevents them from being impeded or damaged when items are grasped. The initially developed prototype was designed to assist with grasping, as this was highlighted as the main need of the former patients, but the principle could be reapplied to control finger extension, and the addition of a spring component would allow for both to be possible.

The use of the vacuum enables the skeleton of the wearer to be used as the frame for motion instead of an exoskeletal body, making it lighter than a metal frame and allows the device to be able to fit multiple wearers without needing components that are adjustable to fit each wearer due to variations in the length and width of their fingers. To further reduce the weight applied to the hand, the actuation system was placed on a separate unit on the forearm which would house the motors' mechanism and provide a set base for operation by attaching to the cables in the glove. The vacuum's outer layer also provides an additional protection to the cables from impact that is not provided to the exposed



FIGURE 2: Photograph of developed prototype glove.

cables in previous designs [13, 14]. Whilst the creation of a vacuum can be loud and distracting, the aesthetic factors appearance and noise were amongst the lowest scoring criteria in the total study (1.78 and 1.56/5, resp.); consequently, they could be considered tolerable for the initial design.

Applying the design matrix in conjunction with the design principles discussed resulted in the production of a functional prototype for user testing (Figure 2). The prototype replicated a pinch grasp with the cable-driven system and was a low-cost model using parts that were predominantly sourced locally. The layers were two brands of rubber gloves, with a braided fishing line used for the inner cable. Suction cups made from elastosil were threaded through the inner layer and were used as fixed points to connect the cable from the fingers to the motor. Activating the motors would shorten the length of the cable, creating rotation at the finger joints that would allow for replication of the motion of finger flexion. These motors were secured to a sports shin guard that provided a secure base on the forearm to distribute the weight and make the device easier to don and doff.

To control the device, a balance needed to be found between the number of commands that could be controlled and the ease with which those commands can be made; from the discussion, the prominent response was that it would be preferable to give the device fewer control options to lessen the effort required by the patient. Consequently, the motors that drive finger motion were controlled by a switch; this would be useable with orthopaedic injury population but would need to be revised in the future to make a device that was compatible with neurological conditions. The prototype structure has been trialled for its performance previously [18].

Feedback was gathered from rehabilitation workers at the National Research Center for Rehabilitation Technical Aids in Beijing to get feedback from those who would be prescribing future devices to patients. They were asked to use their experience to provide feedback on how practical the device would be to use in treatment with their current patients and to provide input for future improvements to the design. 15 staff members (five rehabilitation doctors, four physical therapists, one occupational therapist, one orthopaedic surgeon, three orthotists, and one prosthetist) with an average experience of 6.4 years ($SD=5.25$) in their role volunteered to sample the device and provide feedback on its function. They were given an opportunity to put on and try out the prototype to grasp and release large and small everyday items available in the department before discussing what they felt

were the positives and negatives of the prototype; these included a pen, a telephone handset, a bottle of water, a watch, and a plastic tube. It was rated on the same five-point scale as was used with the unimpaired volunteers, and the average scores can be viewed in Figure 3. Each component of the study was approved by the local ethics committee and complied with the Declaration of Helsinki, with informed consent being received from the participants.

3. Results

37 former patients were approached at local physical activity groups to participate in the study, of which 13 responded to the questionnaire (response rate of 35.14%) with nine of those providing sufficient detail to be included in the study and eight of them agreeing to participate in the interview. The findings of the experimental process are shown in the matrix Table 1, where the results are firstly separated by their category and then further divided into their respective criteria. The results of the questionnaire are visible in the importance column and the relationship between the needs of the user and the critical functions having been made from the content of the interview discussions. The strength of the relationship is measured as a scale of 1, 3, and 9 where 1 indicates a weak relationship whilst 9 indicates a strong one. The rating of this relationship was judged based on the interview discussions conducted after the questionnaire, resulting from direct questioning, for example, how they felt that the discussed factors would impact on the level of control available to them, with the likelihood influencing the score assigned between the factors. An example of this is the wearability factors of comfort, weight, and stability all having a strong association with the idea of being easy to fit; therefore, to achieve this design requirement, all of the factors should be considered.

As illustrated in Table 2, a two tailed t -test was conducted to ascertain which criteria were significantly more important to the participants; however, the sample size means that the results may require scepticism. The t -test was used as the traditional means of assessing small data samples; Spearman's rho and Pearson's correlation require the data being assessed to be independent variables, where the ranking data gathered in this study is not. The t -test can still illustrate differences in the data however tends to produce more pronounced results; for example, hand grasping was thought to be most in need of further assistance post therapy in comparison to lifting ($r = .035$), rotation of the forearm ($r = .00039$), or reaching ($r = .000015$), whilst there was no significant difference to releasing ($r = .1211$). Additionally, in giving the user a sense of control over any possible system, it is important to ensure that the actions can be easily differentiated from one another ($M=4.22$, $SD=.667$) as well as requiring as not requiring too much effort to operate ($M=4.44$, $SD=.726$) to minimise fatigue. These results were utilised to design a wearable device that could be used for hand grasping by those with impaired mobility of their hand. A first-generation prototype was developed as can be seen in Figure 2 and was used for the sample testing.

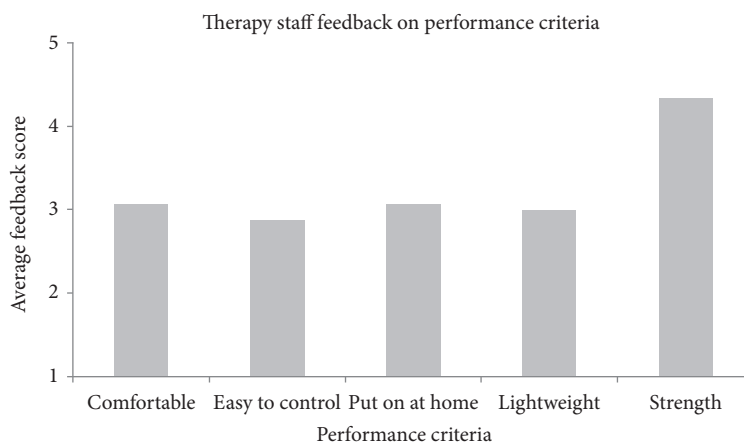


FIGURE 3: Graph of feedback scores for rehabilitation worker discussion.

Feedback on the prototype was provided by the rehabilitation workers, and the average score from their feedback can be viewed in Figure 3. They were asked to use their experience to consider how the device would perform with their patients. The workers believed that the prototype offered sufficient grip strength to be used as an assistive tool by patients ($M = 4.33$, $SD = .617$), although they had concerns about the comfort of the design and the level of control offered by the prototype ($M = 3.07$, $SD = .799$ and $M = 2.87$, $SD = .64$, resp.), the feedback from which will be used to improve the design in the future.

4. Discussion

The questionnaire showed that the most prevalent, but not significant, area of dissatisfaction with therapy was in the level of recovery achieved by the fingers ($M = 3.78$, $SD = 1.481$), in particular the act of grasping ($M = 4.63$, $SD = .744$), which aside from its related action of releasing was considered to be significantly more difficult than the arm-orientated actions of tilting and reaching ($r = .0004$ and $.00001$, resp.) with a difference to lifting being noticeable at the 95% confidence interval ($r = .0355$); therefore, it was best to focus the design on helping this action. Discussion with the former patients also made it clear that they were primarily hoping for a device that was able to assist them in the performance of tasks at home, although this perspective may come from the volunteers being at an advanced stage of their therapy. Consequently, ensuring that the designed prototype could perform this action was the key outcome of the design stage.

Having defined the central activity of the device, consideration must be given to the method of control. In the opinion of these former patients, the most important factors to giving them control over the device would be to minimise the effort required to make commands as well as how easily they can differentiate between them ($M = 4.44$, $SD = .726$ and $M = 4.22$, $SD = .667$, resp.). To accommodate these criteria, the options for control would need to be minimised as increased movement options will cause a conflation of the commands and reduce the control offered to the user.

Therefore, to best meet the dominant functional and control criteria, the motion of the fingers should be limited to flexion and extension axis for control of grasping, as this motion can be controlled by a linear system such as a switch.

When designing a device that can be used at home by patients, how comfortable the device is to wear is a core consideration that should be considered alongside its function and control. The system's weight was deemed an important factor in how wearable any device is ($M = 4$, $SD = .866$) and has an association with its lifespan and ease of fitting; these factors are also important for giving the wearer freedom to move around as well as the setup time. Minimising the weight can also help meet the patients' needs in other factors, and it is also important to consider how comfortable any design is ($M = 3.67$, $SD = 1.581$); both of these factors scored higher in their category than the other features, but not significantly, but the ideas have been successfully applied in the past with the lower limb soft exosuit [19]. Less emphasis was placed on the stability of the components, although this may result in inconsistency in the device's performance. With upper limb disability of patients, particularly if their injury also weakens their shoulder, it becomes increasingly important to make the device as lightweight as possible to enable them to utilise it as they are moving.

Beyond these factors, the most prominent design considerations were that the participants hoped to retain the freedom of movement whilst using the device as well as ensuring their safety ($M = 4.44$, $SD = .527$ and $M = 4.33$, $SD = .707$, resp., with significant differences between these 2 factors and those remaining in the category at a 95% confidence interval). Some previous designs of therapeutic devices require to be fixed in position to operate [20, 21], which whilst beneficial to recovery do not allow for use in an assistive capacity. The main anomaly from this result is that the respondents placed the importance of functionality over their own safety which may be due to a combination of factors: firstly, the volunteers for this study were at an advanced stage of recovery than patients who would be using the device are and this may distort their expectations for what can be achieved; additionally, it is possible that the participants were unaware of the risks that may occur in terms of further

TABLE 1: First design matrix table connecting the user's needs to the critical functions of the product.

Category	Design criteria	Importance (ranking of 1-5)	Range of motion	Ease of control	Consistency of response	Independence	Long life	Ease of fitting	User protection	Low cost	How much?
Joint motion Category importance: 4	Shoulder	2.56	9	3	9	9	9	3	3	3	5 dof
	Elbow	2.89	9	3	9	9	3	3	3	9	2 dof
	Wrist	2.67	9	3	9	9	3	3	3	3	3 dof
	Fingers	3.78	9	3	9	9	9	3	3	9	4 dof
	Thumb opposability	3.11	9	3	9	9	9	3	3	9	3 dof
Function Category importance: 4.78	Grasping	4.63	3	9	9	9	9	3	3	9	Clinical evaluation
	Lifting	3	9	9	9	9	9	3	9	3	Clinical evaluation
	Releasing	3.63	3	9	9	9	9	3	1	9	Clinical evaluation
	Tilting/rotation	2.25	9	9	9	9	3	3	3	3	Clinical evaluation
	Reaching	1.5	9	9	9	9	9	3	1	3	Clinical evaluation
Interaction /control Category importance: 2.67	Ease of selection	4.22	9	9	9	9	9	9	3	3	Testing
	Starting motion	2.56	3	9	9	9	3	1	3	9	Testing
	Stopping motion	1.44	3	9	9	9	3	1	9	9	Testing
	Effort	4.44	3	9	9	9	9	1	3	3	Clinical evaluation
	Feedback	2.33	1	1	9	9	3	1	9	3	Haptic devices
Wearability Category importance: 2.22	Comfort	3.67	3	1	3	3	9	9	3	3	User feedback
	Weight	4	3	3	1	9	9	9	9	3	<1 kg
	Stability	2.33	9	1	3	3	9	9	9	3	Clinical evaluation
	Tightness at joints (fit 1)	2.33	3	1	3	3	9	9	3	9	Clinical evaluation
	Tightness at muscles (fit 2)	2.67	3	1	3	3	9	9	3	9	Clinical evaluation
Other Category importance: 1.33	Setup	2.89	3	3	1	9	9	9	9	9	Market analysis
	Appearance	1.78	9	1	1	3	9	1	1	3	User feedback
	Noise	1.56	1	1	1	3	9	1	1	3	User feedback
	Freedom	4.44	9	9	9	9	9	9	9	3	Clinical evaluation
	User safety	4.33	9	9	9	9	9	9	9	9	Clinical evaluation

The matrix depicts the strength of relationship between factors on a 3-point scale where 1 is a weak correlation and 9 is a strong correlation. The relationship strength was taken from the participant interviews after the questionnaire. dof stands for degrees of freedom.

TABLE 2: Two tailed t -test of questionnaire scores.

	Importance	Joint motion	Function	Interaction	Wearability	Other
Joint motion	4	N/A	.06528478	.02850921	.00058196*	.00001529*
Function	4.78	.06528478	N/A	.00032041*	.00006532*	.00000005*
Interaction	2.67	.02850921	.00032041*	N/A	.44681333	.01142455
Wearability	2.22	.00058196*	.00006532*	.44681333	N/A	.05160895
Other	1.33	.00001529*	.00000005*	.01142455	.05160895	N/A
Joint motion		Shoulder	Elbow	Wrist	Fingers	Thumb
Shoulder	2.56	N/A	.63053608	.89606922	.23611504	.50770165
Elbow	2.89	.63053608	N/A	.75992297	.29290489	.75314164
Wrist	2.67	.89606922	.75992297	N/A	.14911670	.57763523
Fingers	3.78	.23611504	.29290489	.14911670	N/A	.28153692
Opposable thumb	3.11	.50770165	.75314164	.57763523	.28153692	N/A
Function		Grasping	Lifting	Releasing	Tilting/rotation	Reaching
Grasping	4.625	N/A	.03542516	.12112229	.00039143*	.00001463*
Lifting	3	.03542516	N/A	.40509395	.22160142	.02628739
Releasing	3.625	.12112229	.40509395	N/A	.05434357	.00612321*
Tilting/rotation	2.25	.00039143*	.22160142	.05434357	N/A	.19702207
Reaching	1.5	.00001463*	.02628739	.00612321*	.19702207	N/A
Interaction		EoS	Start	Stop	Effort	Feedback
Ease of selection	4.22	N/A	.00352202*	.00002641*	.59426402*	.00454422*
Starting motion	2.56	.00352202*	N/A	.04035065	.00066491*	.71883630
Stopping motion	1.44	.00002641*	.04035065	N/A	.00000636*	.15355473
Effort	4.44	.59426402	.00066491*	.00000636*	N/A	.00707767*
Feedback	2.33	.00454422*	.71883630	.15355473	.00707767*	N/A
Wearability		Comfort	Weight	Stability	Fit 1	Fit 2
Comfort	3.67	N/A	.56319426	.14111328	.10378649	.30520137
Weight	4	.56319426	N/A	.02416573	.00539088*	.09607159
Stability	2.33	.14111328	.02416573	N/A	1.00000000	.61954375
Fit 1—joints	2.33	.10378649	.00539088*	1.00000000	N/A	.63053608
Fit 2—muscles	2.67	.30520137	.09607159	.61954375	.63053608	N/A
Other		Setup	App	Noise	Freedom	Safety
Setup	2.89	N/A	.06188556	.02220390	.00542273*	.02602469
Appearance	1.78	.06188556	N/A	.59426402	.00004367*	.00000049*
Noise	1.56	.02220390	.59426402	N/A	.00000391*	.00012037*
Freedom	4.44	.00542273*	.00004367*	.00000391*	N/A	.75992297
User safety	4.33	.02602469	.00000049*	.00012037*	.75992297	N/A

The table shows the value of a 2-tailed t -test comparing the factors of the questionnaire within their category. A significant relationship ($p \leq .01$) is denoted with *. EoS is ease of selection.

damage if the device is not properly designed, which is partly supported by over half of the volunteers considering the mobility allowed to be more important than the protections it provides them, but due to the importance of protecting the patient in therapy, this factor should remain a key consideration.

This provided the basis for the design that was outlined previously to develop a prototype that could be used for preliminary sampling to improve further. When sampling the device, the rehabilitation workers were able to securely grasp the objects and were then able to use them, as intended, such as the telephone and the pen for writing. The only exception to this was grasping a bottle of water, where the material

compresses under the pressure exerted by the device, making the grasp unstable. The rehabilitative workers scored the strength of the device at $M = 4.33$, $SD = 0.617$; the scoring of this factor would suggest that the principle of design is viable for use with a patient population as an assistive tool for daily living, but will require further refinement in other areas of design.

The comfort of the device was considered to be another area that required improvement in the opinion of the rehabilitation professionals ($M = 3.067$, $SD = .799$). These areas were firstly that there is a temperature buildup that occurs over prolonged wearing, and this resulted in sweating that made removing the rubber gloves more challenging. Secondly, the size and weight of the forearm unit was considered to be

too large, although this issue was reported by the smallest volunteers, suggesting that the size issue may be remedied by appropriately scaling the component to the wearer, although reductions must be made to the total weight of 525 grams before it could be considered suitable for patient use. This is 125 grams heavier than the similarly sized Saebot-Flex. Reductions in the weight of these components are possible in future iterations of the design to make it more comfortable to wear, and this can be achieved by optimising the components distributed on the forearm.

The ease of control that the prototype offers to the patients was also considered to require improvements by the rehabilitation workers ($M=2.867$, $SD=.64$). This was due to their expressed concern that patient's may overfocus on managing the cable mechanism rather than observing the motion of their fingers; this may result in the fingers being overstrained and risks harming them, a flaw that could be amended with the addition of an automatic brake. There were also concerns raised about the 3 control switches used to operate the fingers, firstly that the number of switches may be confusing for a patient who has also experienced a mental injury and secondly that they may be too stiff for a weakened patient to operate. The switches could be replaced in future designs with alternatives that enable a singular control for activity, or allow the patient to operate it with a mechanism that supports neurorehabilitative recovery. The variety of control mechanisms used with the J-Glove [13] shows the possibilities for control that can be achieved without burdening the patient.

5. Conclusion

This study has developed a low-cost robotic prototype intended for disability patients that can be used for rehabilitation as well as being used as an assistive tool at home. It was designed in accordance with the stated requirements of former therapy patients from a combined questionnaire and interview that was then integrated into a matrix and used to build a working prototype. This prototype was sampled with a group of medical workers to gather their feedback on what the strengths and weaknesses of the design were and to discuss further refinements that could be made to the prototype to improve it in the future.

Conflicts of Interest

There are no conflicts of interest raised in this paper.

Acknowledgments

The authors would like to thank the charity Different Strokes for assisting with access to the volunteers for the consultation in this study.

References

- [1] Department for Work and Pensions, *Family Resources Survey 2012/13*, 2014, December 2016, https://www.gov.uk/government/uploads/system/uploads/attachment_data/file/325491/family-resources-survey-statistics-2012-2013.pdf.
- [2] World Health Organization, *Disability and Health Factsheet*, October 2016, <http://www.who.int/mediacentre/factsheets/fs352/en/>.
- [3] Health & Social Care Information Centre, *Personal Social Services: Staff of Social Services Departments, England*, 2015, <http://content.digital.nhs.uk/catalogue/PUB19985/pss-staff-eng-15-rpt.pdf>.
- [4] M. N. Orlin, N. A. Cicirello, A. E. O'Donnell, and A. K. Doty, "The continuum of care for individuals with lifelong disabilities: role of the physical therapist," *Physical Therapy*, vol. 94, no. 7, pp. 1043–1053, 2014.
- [5] K. M. Murphy, L. Rasmussen, S. L. Hervey-Jumper, D. Justice, V. S. Nelson, and L. J. S. Yang, "An assessment of the compliance and utility of a home exercise DVD for caregivers of children and adolescents with brachial plexus palsy: a pilot study," *PM&R*, vol. 4, no. 3, pp. 190–197, 2012.
- [6] S. H. Brown, R. Napier, V. S. Nelson, and L. J. S. Yang, "Home-based movement therapy in neonatal brachial plexus palsy: a case study," *Journal of Hand Therapy*, vol. 28, no. 3, pp. 307–313, 2015.
- [7] C. Carignan and M. Liszka, "Design of an arm exoskeleton with scapula motion for shoulder rehabilitation," *12th International Conference on Advanced Robotics*, pp. 524–531, IEEE, NY, 2005.
- [8] A. Gupta and M. K. O'Malley, "Design of a haptic arm exoskeleton for training and rehabilitation," *IEEE/ASME Transactions on Mechatronics*, vol. 11, no. 3, pp. 280–289, 2006.
- [9] O. A. Daud, F. Biral, R. Oboe, and L. Piron, "A general framework for a rehabilitative oriented haptic interface," *11th IEEE International Workshop on Advanced Motion Control*, IEEE, NY, 2010.
- [10] A. H. A. Steinen, E. E. G. Hekman, F. C. T. van der Helm et al., "Dampace: dynamic force-coordination trainer for the upper extremities," *IEEE 10th International Conference on Rehabilitation Robotics*, pp. 820–826, IEEE, NY, 2007.
- [11] K. Kiguchi and Y. Hayashi, "An EMG-based control for an upper-limb power-assist exoskeleton robot," *IEEE Transactions on Systems, Man, and Cybernetics. Part B, Cybernetics*, vol. 42, no. 4, pp. 1064–1071, 2012.
- [12] J. Li, R. Zheng, Y. Zhang, and J. Yao, "iHandRehab: an interactive hand exoskeleton for active and passive rehabilitation," *IEEE International Conference on Rehabilitation Robotics*, IEEE, NY, 2011.
- [13] J. M. Ochoa, Y. Jia, D. Narasimhan, and D. G. Kamper, "Development of a portable actuated orthotic glove to facilitate gross extension of their digits for therapeutic training after stroke," *Annual International Conference of the IEEE Engineering in Medicine and Biology Society*, pp. 6918–6921, IEEE, NY, 2009.
- [14] K. M. Triandafilou, J. Ochoa, X. Kang, H. C. Fischer, M. E. Stykov, and D. G. Kamper, "Transient impact of prolonged versus repetitive stretch on hand motor control in chronic stroke," *Topics in Rehabilitation*, vol. 18, no. 4, pp. 316–324, 2011.
- [15] S. Asfour, E. Iakovou, and G. A. Cortes, "A synthesis of quality function deployment and robust design and its application in the medical device industry," *Quality Engineering*, vol. 12, no. 1, pp. 37–45, 1999.
- [16] T. J. Kriewall and G. P. Widin, "An application of quality function deployment to medical device development," *Medical Instrument Design*, pp. 23–36, IEEE, NY, 1991.

- [17] K. H. Tsai, C. Y. Yeh, H. C. Lo, C. T. Li, C. P. Cheng, and G. L. Chang, "Application of quality function deployment in design of mobile assistive devices," *Journal of Medical and Biological Engineering*, vol. 28, no. 2, pp. 87–93, 2008.
- [18] S. Biggar and W. Yao, "Design and evaluation of a soft and wearable robotic glove for hand rehabilitation," *IEEE Transactions on Neural Systems and Rehabilitation Engineering*, vol. 24, no. 10, pp. 1071–1080, 2016.
- [19] A. T. Asbeck, R. J. Dyer, A. F. Larusson, and C. J. Walsh, "Biologically-inspired soft exosuit," *IEEE International Conference on Rehabilitation Robotics*, IEEE, NY, 2013.
- [20] C. N. Schabowsky, S. B. Godfrey, R. J. Holley, and P. S. Lum, "Development and pilot testing of HEXORR: hand EXOskeleton rehabilitation robot," *Journal of Neuroengineering and Rehabilitation*, vol. 7, no. 1, p. 36, 2010.
- [21] X. Tu, J. He, Y. Wen et al., "Cooperation of electrically stimulated muscle and pneumatic muscle to realize RUPERT bi-directional motion for grasping," *Annual International Conference of the IEEE Engineering in Medicine and Biology Society*, pp. 4103–4106, IEEE, NY, 2014.

Research Article

Effects of Scan Resolutions and Element Sizes on Bovine Vertebral Mechanical Parameters from Quantitative Computed Tomography-Based Finite Element Analysis

Meng Zhang,¹ Jiazi Gao,¹ Xu Huang,² He Gong,¹ Min Zhang,¹ and Bei Liu¹

¹Department of Engineering Mechanics, Nanling Campus, Jilin University, Changchun 130025, China

²Department of Radiology, The First Hospital of Jilin University, Changchun 130021, China

Correspondence should be addressed to He Gong; gonghe@jlu.edu.cn

Received 26 February 2017; Accepted 2 April 2017; Published 1 June 2017

Academic Editor: Wei Yao

Copyright © 2017 Meng Zhang et al. This is an open access article distributed under the Creative Commons Attribution License, which permits unrestricted use, distribution, and reproduction in any medium, provided the original work is properly cited.

Quantitative computed tomography-based finite element analysis (QCT/FEA) has been developed to predict vertebral strength. However, QCT/FEA models may be different with scan resolutions and element sizes. The aim of this study was to explore the effects of scan resolutions and element sizes on QCT/FEA outcomes. Nine bovine vertebral bodies were scanned using the clinical CT scanner and reconstructed from datasets with the two-slice thickness, that is, 0.6 mm (PA resolution) and 1 mm (PB resolution). There were significantly linear correlations between the predicted and measured principal strains ($R^2 > 0.7$, $P < 0.0001$), and the predicted vertebral strength and stiffness were modestly correlated with the experimental values ($R^2 > 0.6$, $P < 0.05$). Two different resolutions and six different element sizes were combined in pairs, and finite element (FE) models of bovine vertebral cancellous bones in the 12 cases were obtained. It showed that the mechanical parameters of FE models with the PB resolution were similar to those with the PA resolution. The computational accuracy of FE models with the element sizes of $0.41 \times 0.41 \times 0.6 \text{ mm}^3$ and $0.41 \times 0.41 \times 1 \text{ mm}^3$ was higher by comparing the apparent elastic modulus and yield strength. Therefore, scan resolution and element size should be chosen optimally to improve the accuracy of QCT/FEA.

1. Introduction

Osteoporosis (OP) is a common disease in aging population characterized by reduced bone mass and compromised bone strength. It is well known that the elderly have been seriously affected by bone-related diseases resulting from OP, which even endanger their health [1]. The lumbar spine has the highest risk of developing disease among all joints, and vertebral body compressive fracture is one of the major complications of OP, which tends to occur in minor injury [2, 3]. Dual-energy radiograph absorptiometry (DXA) is widely used to measure bone mineral density (BMD) in clinics, which represents bone strength to assess the risk of OP and fracture. However, it was shown that DXA-measured BMD accounts for only 50%–70% of the variation

in lumbar vertebral body strength [4, 5]. Nowadays, with the development of computer technology and biomechanics, quantitative computed tomography-based finite element analysis (QCT/FEA) is a promising tool for assessing strength and stiffness because it can take into account accurate vertebral geometry, architecture, and the heterogeneous distribution of bone material properties according to grey-scale values in images [6, 7]. For lumbar vertebral body, QCT/FEA is more accurate than quantitative computed tomography- (QCT-) measured BMD for strength assessment in clinics [7].

Recent study showed that strength evaluated from general finite element (FE) models was not significantly correlated with experimental strength ($R^2 = 0.01$, $P = 0.71$) [8], because significant difference in macro morphology and

microstructure of vertebral body does exist between patients. Subject-specific QCT-based nonlinear FE modeling is a valuable tool, in which subtle geometric and densitometric differences among patients are considered, and it can also reflect the real mechanical behavior of specimens under different boundary and loading conditions. Consequently, human vertebral strength and stiffness predicted from QCT/FEA models according to relevant data were much better than BMD measurement [7, 9–12]. Previously, QCT/FEA subject-specific femur models were constructed to predict principal strains at multiple locations, and the modulus-density relationship, which was obtained from the femur specimens, was used. The result indicated a strong correlation between the predicted strains and the experimental data [13]. Specimen-specific nonlinear FE models of lumbar vertebral bodies after vertebroplasty were constructed to predict vertebral fracture load and stiffness, and it was shown that QCT/FEA could predict the strength of vertebral body effectively [14]. It was demonstrated that subject-specific FE models based on low-dose imaging are able to predict the strength of vertebral body, and failure loads evaluated from these models were significantly correlated with experimental data [8]. QCT/FEA techniques not only can be used to reflect the real mechanical properties of single vertebral body but also can predict the mechanical properties of whole lumbar spine by constructing the specimen-specific lumbar spine model [15].

QCT scan is the basis of specimen-specific finite element analysis (FEA), and the scan resolution is extremely important. Too low-resolution setting will induce the image distortion and erroneous analysis results; and too high-resolution setting will increase the absorbed dose of the patients and the time of computation [16]. Different QCT scan protocols will change the scan resolution and voxel size, which consequently will influence the FE modeling and FEA outcomes [17–19]. The most important QCT scanning parameters affecting image quality are current time [mAs], voltage [kVp], scan resolution, reconstruction algorithms, scanner type, and table height [20]. A previous study demonstrated that the most relevant parameters for strength prediction of vertebral body were scan current and reconstruction kernel by changing different scanning and postprocessing settings, which have great influence on the strength prediction of vertebral bodies. The stronger scan current and the sharper reconstruction kernel mean the higher scan resolution, resulting in higher volumetric BMD estimation with the same CT values (in Hounsfield unit) [20]. The strength and stiffness of normal and osteoporotic femurs predicted from high- (experimental setting) and low- (clinical setting) resolution scans were significantly different [21]. The apparent BMD, the elastic modulus, and the yield strength of human vertebral cancellous bone showed significant differences between the standard scan protocol and the low-dose protocol; besides, those from the two protocol groups were highly linearly correlated [22].

Clinical QCT scan resolution is controlled by two independent settings, that is, in-plane resolution and slice

thickness [23]. In-plane resolution, slice thickness, and the scan status of specimen (in situ/in vitro) influence image voxel size, which will affect subsequent prediction [24, 25]. Although a large number of studies have shown that QCT images with different quality will affect the results of FEA, but the relationship between scan resolution and element size needs further investigation. Little is known about the differences predicted from the models with different element sizes reconstructed by using high- and low-resolution scans. Therefore, the aims of this study were as follows:

- (1) To construct the subject-specific bovine vertebral body models by using QCT/FEA method and verify them by compressive mechanical tests.
- (2) To investigate the influences of two different QCT scan resolutions (0.6 mm slice thickness and 1 mm slice thickness) on the QCT/FEA outcomes of bovine vertebral body.
- (3) To explore the influences of two different QCT scan resolutions and six different element sizes on the QCT/FEA outcomes of bovine vertebral cancellous bone.

2. Materials and Methods

2.1. Specimen Preparation and QCT Scanning. Nine lumbar vertebrae were disarticulated from two bovine fresh cadavers without any pre-existing fractures or pathologies that are known to affect bone quality. Then, the surrounding soft tissues and intervertebral disc materials of both vertebral endplates were removed by using scalpels. The posterior elements of each vertebra were transected at the pedicles using the low-speed diamond saw (SYJ-150, Shenyang Kejing Machinery Manufactory Ltd., Shenyang, China). After these procedures, nine bovine vertebral body specimens were obtained. To ensure that the uniaxial compressive mechanical test is performed under a stable loading condition, the upper and lower surfaces of vertebral body should keep plano-parallel and perpendicular to the axis of the mechanical testing machine. The upper and lower surfaces of specimens were trimmed in parallel surfaces by using the polishing machine (PG-1A, Shanghai Metallurgical Machinery Manufactory Ltd., Shanghai, China).

After the preparation of the specimens, they were wrapped in saline-soaked gauze and stored at -20°C before compressive mechanical test [10, 11, 18]. The specimens were thawed to the room temperature only before compressive mechanical test to minimize the effect on the mechanical properties of the bone, and both QCT scanning and mechanical testing were conducted within 8 h with no refreezing [11]. The vertebral bodies were scanned on the clinical CT scanner (Somatom Sensation 64, Siemens, Munich, Germany: 120 kV, 260 mAs, 0.41×0.41 mm/pixel resolution, 1.5 mm slice thickness), and the scanning range should cover the entire

specimens. The datasets from the standard protocol were reconstructed with voxel size of $0.41 \times 0.41 \times 1 \text{ mm}^3$, and those from the high resolution protocol were reconstructed with voxel size of $0.41 \times 0.41 \times 0.6 \text{ mm}^3$. After these procedures, FE models were constructed from the two resolutions: 0.6 mm slice thickness (PA resolution) and 1 mm slice thickness (PB resolution).

2.2. Mechanical Testing. Each specimen was kept in saline-soaked gauze for at least 1 h before testing to make sure specimens maintain the normal physiological state [10]. Rosette strain gauges were located at the anterior, left, right, and posterior surfaces of the vertebral body. The area for strain measurement was prepared using a validated procedure [26]: careful cleaning and degreasing with ethanol and acetone, then bonding the four rectangular rosette strain gauges (ZF120-05CA (13)-01Q30-P1K, AVIC Limited by Share Ltd., Shanxi, China) with 502 glue. And then the wires of strain gauges were connected to the strain indicator (DH5922 dynamic signal test and analysis system, Donghua Testing Technology Ltd., Jiangsu, China) in a quarter bridge arrangement. Strains were recorded at a sampling rate of 2 kHz during the whole loading time and stored by the strain indicator, and then the maximum principal strains and minimum principal strains were collected from the four rosette strain gauges. Each specimen was carefully positioned in the working table, and then the uniaxial compressive mechanical test was performed at the room temperature by using the electronic universal testing machine (CSS-44100, Changchun Testing Machine Research Institute, Changchun, China). Unloading-reloading cycles were repeated five times before the test recording under a compressive preload of 2000 N to reduce the viscoelastic effect [27, 28]. After preconditioning, specimens were destructively tested in displacement-control at 1 mm/min on the upper surface until the ultimate force was achieved [29, 30]. Load and displacement data were digitally recorded at a sampling rate of 50 Hz.

2.3. QCT/FEA Modeling

2.3.1. Establishment of Bovine Vertebral Body QCT/FEA Models. The QCT consecutive images with DICOM format were imported and reconstructed to three-dimensional (3D) model of bovine vertebral body in Mimics 17.0 software (Materialise, Leuven, Belgium), and then each QCT voxel was converted directly into an 8-node linear brick element (C3D8). After these procedures, vertebral body QCT/FEA models from the two protocol groups (PA and PB resolutions) were constructed. Then, 150 kinds of material properties were assigned according to the relationship between image greyscale value and density. The mechanical properties of bovine vertebral materials in the QCT/FEA models were set to be transversely anisotropic. The proposed empirical relationships between elastic modulus (E), Poisson's ratio (ν), shear modulus (G), yield stress (σ), and the QCT-derived BMD for trabecular bone were as follows [31]:

$$\begin{aligned}
 E_z(\text{MPa}) &= -34.7 + 3230 \times \text{BMD}_{\text{QCT}}(\text{g}/\text{cm}^3); \\
 &\text{BMD}_{\text{QCT}} \geq 0.0527, \\
 E_z(\text{MPa}) &= 2980 \times \text{BMD}_{\text{QCT}}^{1.05}(\text{g}/\text{cm}^3); \\
 &\text{BMD}_{\text{QCT}} < 0.0527, \\
 E_x &= E_y = 0.333E_z, \\
 G_{xy} &= 0.121E_z, \\
 G_{xz} &= G_{yz} = 0.157E_z, \\
 \nu_{xy} &= 0.381, \\
 \nu_{xz} &= \nu_{yz} = 0.104, \\
 \sigma_{ys}(\text{MPa}) &= -0.75 + 24.9 \times \text{BMD}_{\text{QCT}}(\text{g}/\text{cm}^3); \\
 &\text{BMD}_{\text{QCT}} \geq 0.06, \\
 \sigma_{ys}(\text{MPa}) &= 37.4 \times \text{BMD}_{\text{QCT}}^{1.39}(\text{g}/\text{cm}^3); \\
 &\text{BMD}_{\text{QCT}} < 0.06.
 \end{aligned} \tag{1}$$

The ultimate stress of each vertebral material in QCT/FEA models was considered 1.2 times of its yield stress [17, 32], and the ultimate strain of all vertebral materials was set as 0.0145 [33, 34].

After assignment of material properties, QCT/FEA models were imported into ABAQUS 6.14 software (Simulia, Providence, RI) to conducted standard/static analysis. The boundary conditions for the QCT/FEA models were prescribed to match constrains from experimental testing. In order to ensure that compressive load with uniform distribution was applied on the upper surface of vertebral body, all the nodes on the lower surface of the QCT/FEA model were completely restrained, and a 1.5% compressive strain along the vertebral upper-lower direction was uniformly applied on the nodes of upper surface of the QCT/FEA model. The QCT/FEA process of bovine vertebral bodies was shown in Figure 1. The image registration method was used to identify the four gauge attachment sites on each vertebral body QCT/FEA model [9], and the maximum principal strains and the minimum principal strains evaluated from QCT/FEA models were obtained. The predicted principal strains were compared with the experimental principal strains to validate the QCT/FEA models. Vertebral strength was defined as the ultimate load in the whole bone force-displacement curve, and stiffness was measured as the slope of the linear portion of the force-displacement curve [11].

2.3.2. Establishment of Bovine Vertebral Cancellous FE Models. The QCT datasets from the two resolutions (PA and PB resolutions) were imported into Mimics software, where cuboid volume of interest (VOI) with the size of $14 \times 13 \times 25 \text{ mm}^3$ were cropped from the center of the vertebral bodies by using the crop mask function in Mimics. The VOI size was chosen to cover the largest possible trabecular

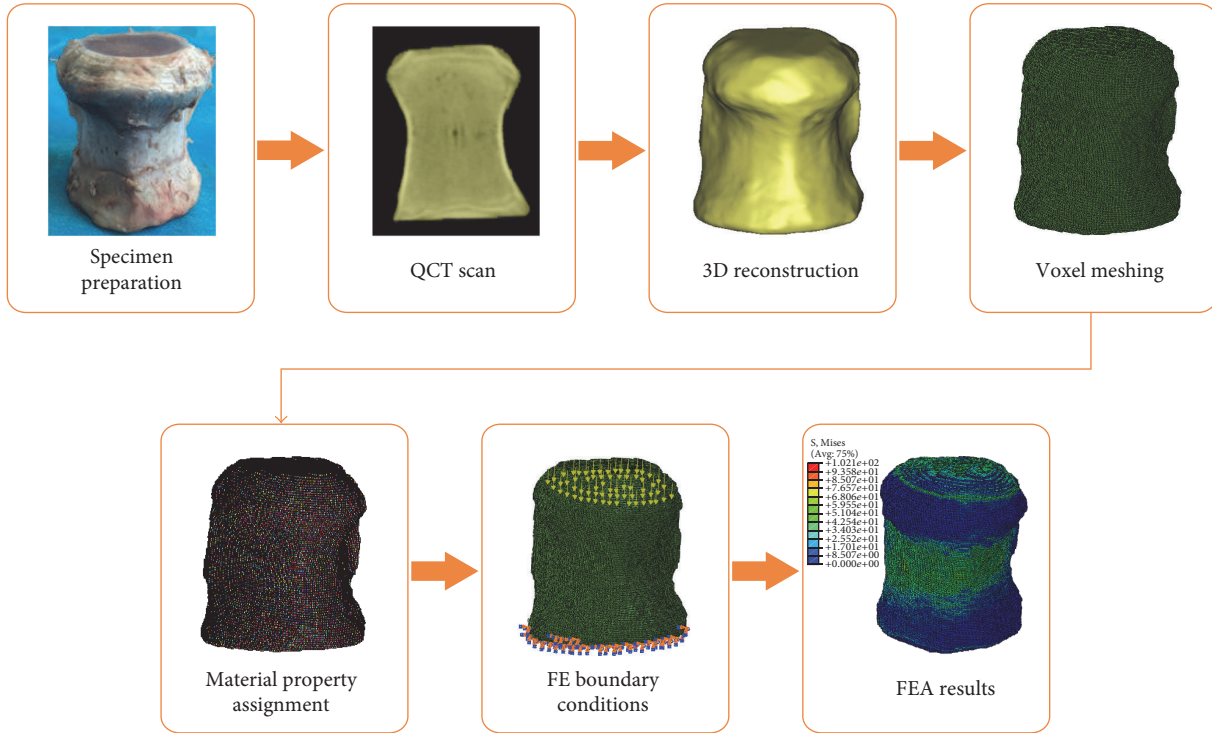


FIGURE 1: The QCT/FEA process of bovine vertebral bodies.

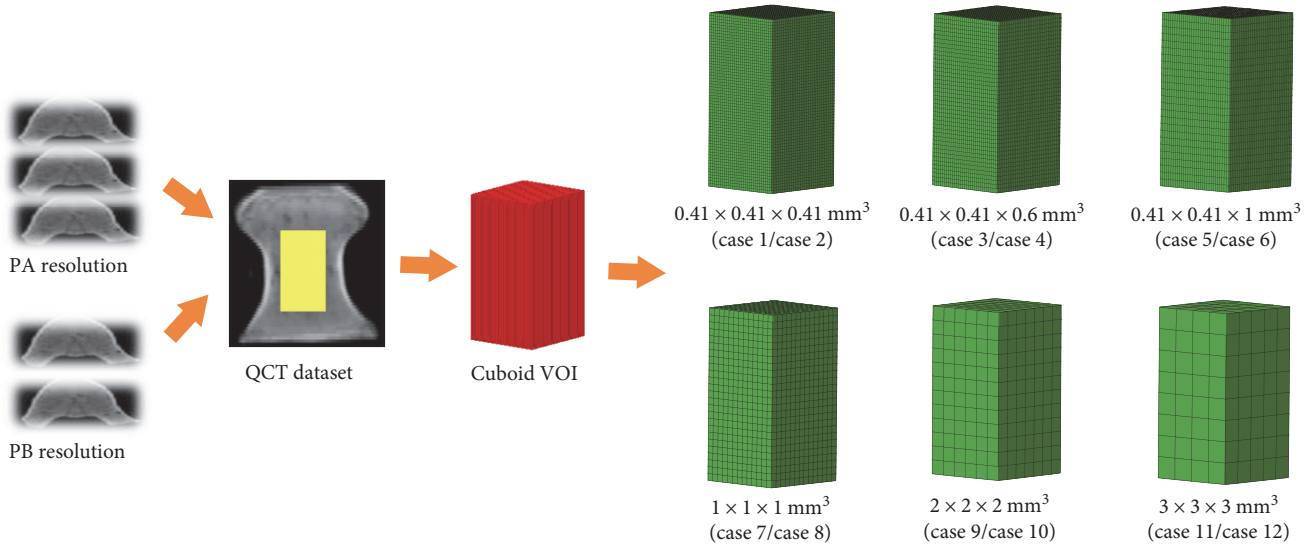


FIGURE 2: Generation of bovine vertebral cancellous FE model from QCT dataset and illustration of the FE models in the 12 cases.

region within a vertebral body. The FE models were constructed with hexagonal structural mesh by using HyperMesh 13.0 software (Altair Engineering Inc., Troy, MI), and C3D8 elements were used. The FE models were shown in Figure 2. These FE models were meshed with six kinds of element sizes: $0.41 \times 0.41 \times 0.41 \text{ mm}^3$ (m1), $0.41 \times 0.41 \times 0.6 \text{ mm}^3$ (m2), $0.41 \times 0.41 \times 1 \text{ mm}^3$ (m3), $1 \times 1 \times 1 \text{ mm}^3$ (m4), $2 \times 2 \times 2 \text{ mm}^3$ (m5), and $3 \times 3 \times 3 \text{ mm}^3$ (m6), and the material properties were assigned in Mimics, then they were imported into ABAQUS to conducted standard/static analysis. The lower surface of each FE model was completely restrained,

and 5000 N loading was applied on the upper surface. Two different resolutions and six different element sizes were combined in pairs and then 12 cases were obtained: PA/PB-m1 (case 1/case 2), PA/PB-m2 (case 3/case 4), PA/PB-m3 (case 5/case 6), PA/PB-m4 (case 7/case 8), PA/PB-m5 (case 9/case 10), and PA/PB-m6 (case 11/case 12). The bovine vertebral cancellous FE models in different cases (i.e., case 1 to case 12) were shown in Figure 2. The stress-strain curve was obtained from the axial compressive simulation. The apparent elastic modulus was calculated from the linear portion of the stress-strain curve, and the apparent

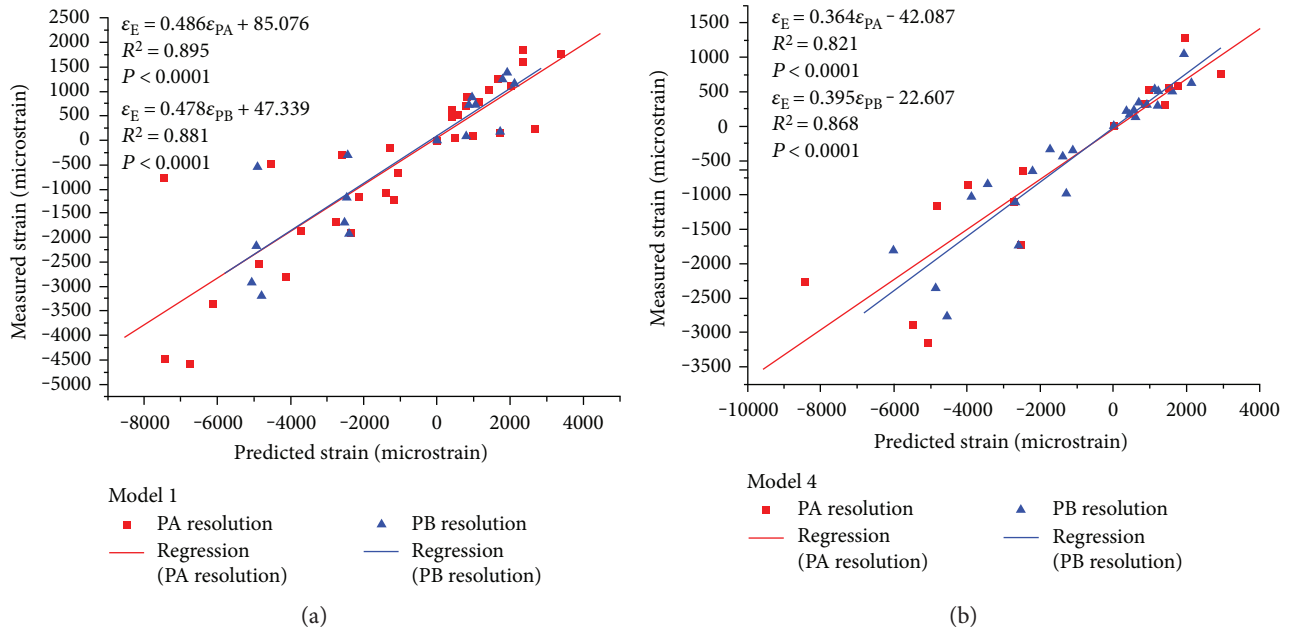


FIGURE 3: The linear regressions of two bovine vertebral bodies (model 1 and model 4) for principal strains estimated from the two resolution models as predictors of experimental principal strains.

yield strength was defined at the apparent 0.2% offset yield point in the stress-strain curve [35].

2.4. Statistical Analysis. Linear regression models of nine bovine vertebral bodies were developed, in which principal strains estimated from the two resolution models were used as predictors for experimentally measured principal strains; regression equations were fitted for vertebral strength and stiffness estimated from QCT/FEA model with the PB resolution as predictors of those estimated from QCT/FEA model with the PA resolution; regression equations were also fitted for vertebral strength and stiffness estimated from the two resolution models as predictors of those obtained from compressive mechanical test. Then the Bland-Altman plots for strength and stiffness were used to evaluate significance of mean differences between the two resolution settings by using Prism software (GraphPad Software, San Diego, California, USA). Paired *t*-test was performed to compare the differences between principal strains predicted from the two resolution models and those measured in the compressive mechanical testing by using SPSS 19.0 software (BM Inc., Chicago, USA).

3. Results

3.1. Comparison of the Mechanical Parameters of Each Bovine Vertebral Body between QCT/FEA Models and Compressive Mechanical Tests

3.1.1. Validation of QCT/FEA Models. The results of two bovine vertebral bodies (model 1 and model 4) were selected as examples, and the linear regression models were developed to assess the correlations between principal strains predicted from the two resolution models and experimental principal strains (Figure 3). The results of the other models were

similar. The linear regression equations and the correlation coefficients of nine bovine vertebral bodies were summarized in Table 1, in which $\varepsilon_{PA}[\mu\epsilon]$ represents the principal strains predicted from QCT/FEA models with the PA resolution, $\varepsilon_{PB}[\mu\epsilon]$ represents the principal strains predicted from QCT/FEA models with the PB resolution, and $\varepsilon_E[\mu\epsilon]$ represents the principal strains measured in compressive mechanical testing. All correlations were statistically significant ($P < 0.0001$).

There were modestly positive correlations between the predicted principal strains and the experimental principal strains with $R^2 > 0.7$. The linear regression equations of two resolution models for each vertebral body were similar, and the slope and intercept of equation for the PA resolution were not significantly different from those for the PB resolution.

Paired *t*-test showed that there were significant linear correlations between the predicted principal strains and the experimental principal strains ($P < 0.05$). The paired sample correlations of the nine vertebral bodies were summarized in Table 2, in which $C_{PA\&E}$ represents the paired sample correlations between principal strains predicted from QCT/FEA models with the PA resolution and experimental principal strains, and $C_{PB\&E}$ represents the paired sample correlations between principal strains predicted from QCT/FEA models with the PB resolution and experimental principal strains. The average $C_{PA\&E}$ of the nine vertebral bodies was 0.893, and the average $C_{PB\&E}$ of the nine vertebral bodies was 0.889. The experimental principal strains showed stronger linear correlation to the principal strains predicted from QCT/FEA models with the PA resolution than to those predicted from QCT/FEA models with the PB resolution. However, the differences between $C_{PA\&E}$ and $C_{PB\&E}$ of nine vertebral bodies were less than

TABLE 1: Linear regression equations of nine bovine vertebral bodies for principal strains estimated from the two resolution models as predictors of experimental principal strains and the correlation coefficients.

Model number	PA resolution	Correlation coefficient (R^2)	PB resolution	Correlation coefficient (R^2)
Model 1	$\epsilon_E = 0.486\epsilon_{PA} + 85.076$	0.895	$\epsilon_E = 0.478\epsilon_{PB} + 47.339$	0.881
Model 2	$\epsilon_E = 0.506\epsilon_{PA} + 125.856$	0.750	$\epsilon_E = 0.501\epsilon_{PB} + 98.883$	0.740
Model 3	$\epsilon_E = 0.310\epsilon_{PA} + 262.288$	0.746	$\epsilon_E = 0.300\epsilon_{PB} + 252.966$	0.708
Model 4	$\epsilon_E = 0.364\epsilon_{PA} - 42.087$	0.821	$\epsilon_E = 0.395\epsilon_{PB} - 22.607$	0.868
Model 5	$\epsilon_E = 0.531\epsilon_{PA} - 164.905$	0.935	$\epsilon_E = 0.504\epsilon_{PB} - 103.602$	0.915
Model 6	$\epsilon_E = 0.577\epsilon_{PA} + 31.739$	0.804	$\epsilon_E = 0.521\epsilon_{PB} + 37.728$	0.804
Model 7	$\epsilon_E = 0.961\epsilon_{PA} + 356.185$	0.961	$\epsilon_E = 0.828\epsilon_{PB} + 345.191$	0.853
Model 8	$\epsilon_E = 0.276\epsilon_{PA} + 118.171$	0.766	$\epsilon_E = 0.275\epsilon_{PB} + 117.932$	0.766
Model 9	$\epsilon_E = 0.252\epsilon_{PA} + 138.514$	0.702	$\epsilon_E = 0.262\epsilon_{PB} + 150.531$	0.701

TABLE 2: Paired sample correlations between predicted (PA and PB resolutions) and measured principal strains of nine bovine vertebral bodies.

Model number	$C_{PA\&E}$	$C_{PB\&E}$
Model 1	0.881	0.895
Model 2	0.866	0.860
Model 3	0.864	0.842
Model 4	0.906	0.932
Model 5	0.967	0.957
Model 6	0.897	0.883
Model 7	0.940	0.924
Model 8	0.875	0.875
Model 9	0.838	0.832

0.026, and it showed that the computational cost of QCT/FEA model with the PB resolution was less than that with the PA resolution given that the computational accuracy was met.

3.1.2. Correlation Analysis of the Mechanical Parameters Derived from the Two Resolution Models. The results of two bovine vertebral body QCT/FEA models (model 2 and model 5) were selected as examples, and the force-displacement curves and the von Mises stress distributions of the two resolution models were shown in Figure 4. The results of the other models were similar. Figure 4 showed that the von Mises stress distributions predicted from the two resolution models were similar, and the force-displacement curves obtained from the two resolution models were also similar. Combining these results with the results of principal strains showed above, it showed that the mechanical parameters of bovine vertebral body QCT/FEA models reconstructed from the two resolution scans were almost the same.

The strength and stiffness of nine vertebral body QCT/FEA models were predicted from the load-displacement curves of the two resolution models, and the linear regression models were developed. All correlations were statistically significant ($P < 0.0001$). For strength, the regression equation using the values estimated from QCT/FEA models with the PB resolution (S_{PB} , [N]) as predictors for those estimated

from QCT/FEA models with the PA resolution (S_{PA} , [N]) was as follows:

$$S_{PA} = 1.018S_{PB} - 1081.531. \quad (2)$$

A correlation coefficient of $R^2 = 0.992$ was obtained (Figure 5(a)).

Similarly, for stiffness, the linear regression equation using the values estimated from QCT/FEA models with the PB resolution (K_{PB} , [N/mm]) as predictors for those estimated from QCT/FEA models with the PA resolution (K_{PA} , [N/mm]) was as follows:

$$K_{PA} = 0.976K_{PB} + 1890.301. \quad (3)$$

A correlation coefficient of $R^2 = 0.962$ was obtained (Figure 5(b)).

The Bland-Altman plots for strength showed that there was a consistent bias of around 201.100 N between the strength predicted from the two resolution models of nine vertebral bodies (Figure 5(c)). Only one specimen was outside 95% confidence limits for the difference, and the other specimens were centrally distributed around the mean difference of 201.100 N and x -axis. The Bland-Altman plots for stiffness showed there was a consistent bias of around 886.900 N/mm between the stiffness predicted from the two resolution models of nine vertebral bodies (Figure 5(d)). All specimens were inside 95% confidence limits for the difference.

3.1.3. Correlation Analysis of Mechanical Parameters Derived from QCT/FEA Models and Compressive Mechanical Tests.

The strength and stiffness of the nine bovine vertebral bodies were estimated from the load-displacement curves from the compressive mechanical tests, and then the linear regression models were developed to assess the correlations between the mechanical parameters predicted from the two resolution models and those obtained from the compressive mechanical tests. For strength, the values predicted from the two resolution models were correlated to the experimental strength (S_E , [N]) through linear regression equations as follows:

$$\begin{aligned} S_E &= 0.980S_{PA} - 22224, \\ S_E &= 0.970S_{PB} - 21842. \end{aligned} \quad (4)$$

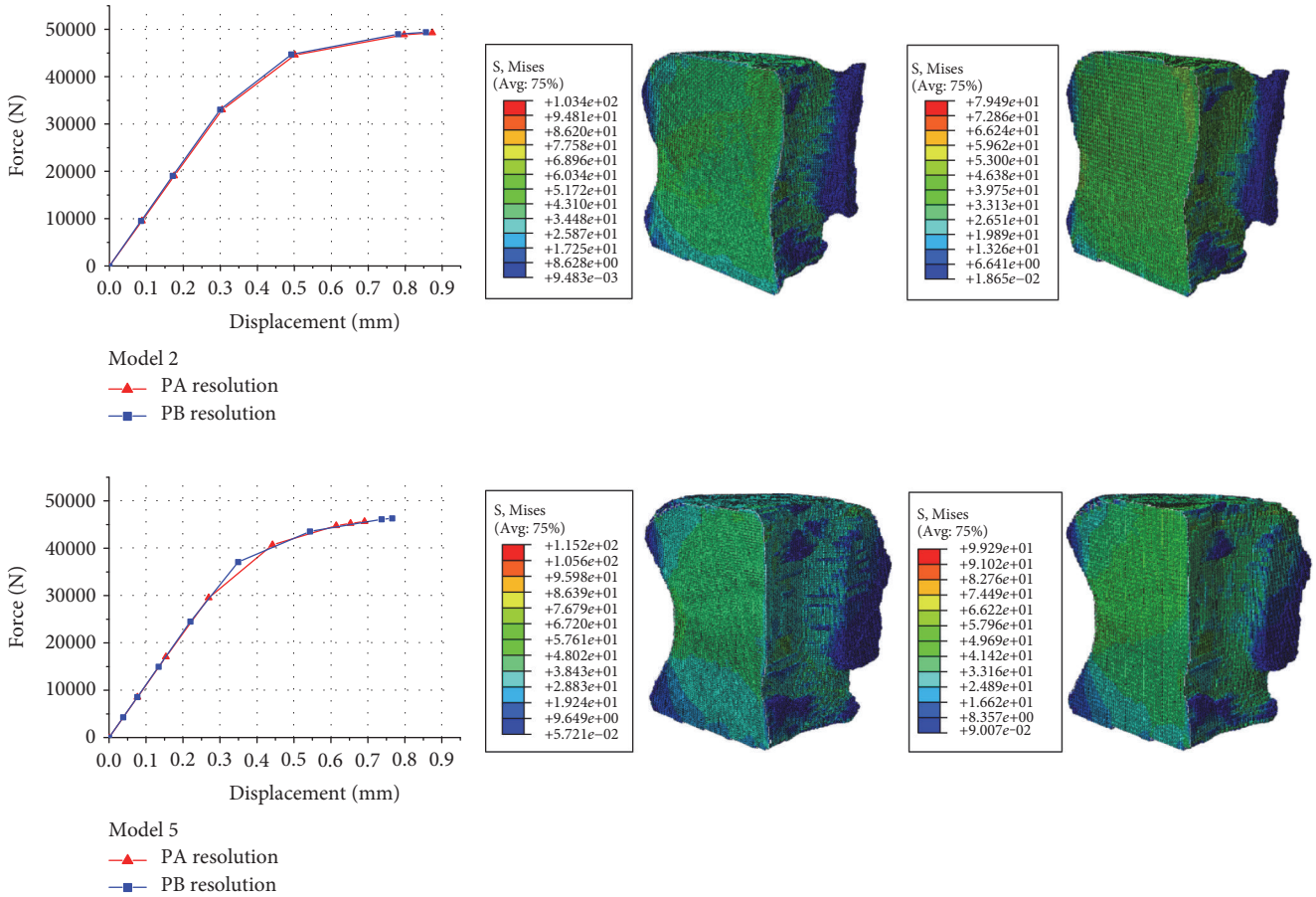


FIGURE 4: The results of two bovine vertebral body QCT/FEA models (model 2 and model 5): load-displacement curves from the two resolution models (left column), von Mises stress distributions from QCT/FEA models with the PA resolution (middle column), and von Mises stress distributions from QCT/FEA models with the PB resolution (right column).

The correlation coefficients of $R^2 = 0.680$ and $R^2 = 0.635$ were obtained (Figure 6(a)).

For stiffness, the values predicted from the two resolution models were correlated to the experimental stiffness (K_E , [N/mm]) through linear regression equations as follows:

$$\begin{aligned} K_E &= 0.156K_{PA} - 4032.400, \\ K_E &= 0.157K_{PB} - 4326.200. \end{aligned} \quad (5)$$

The correlation coefficients of $R^2 = 0.766$ and $R^2 = 0.787$ were obtained (Figure 6(b)).

3.2. Comparison of the Mechanical Parameters of Bovine Vertebral Cancellous Bone from FE Models

3.2.1. von Mises Stress Distribution. One bovine vertebral cancellous FE model (model 3) was selected as an example, and the von Mises stress distributions of the 12 cases were shown in Figure 7. The results of the other models were similar. As shown in Figure 7, (1) the variation trends of von Mises stresses of each vertebral cancellous FE model in the 12 cases were similar; besides, as the enlargement of element size, the stress ranges predicted from FE models were decreased gradually, and the continuity of stress distributions became poor. (2) The stress

ranges predicted from case 3/case4 to case 5/case 6 were similar. There were very little differences in the maximum stresses predicted from these four cases and those predicted from the other FE models, but there were marked differences in the minimum stresses predicted from these four cases and those predicted from the other FE models. (3) The von Mises stress distributions predicted from the two resolution models with the same element size were similar, and it showed that the mechanical parameters of bovine vertebral cancellous FE models with the same element size reconstructed from the two resolution scans were almost the same.

3.2.2. Stress-Strain Curve. The results of two bovine vertebral cancellous FE models (model 1 and model 3) were selected as examples, and the stress-strain curves of these models in the 12 cases were shown in Figure 8. The results of the other models were similar.

The stress-strain curves of vertebral cancellous FE models showed the following:

- (1) There were differences within the stress-strain curves predicted from the FE models with different element sizes reconstructed by using the same resolution scan, which showed that element size may affect the mechanical parameters of FE models. The slopes of

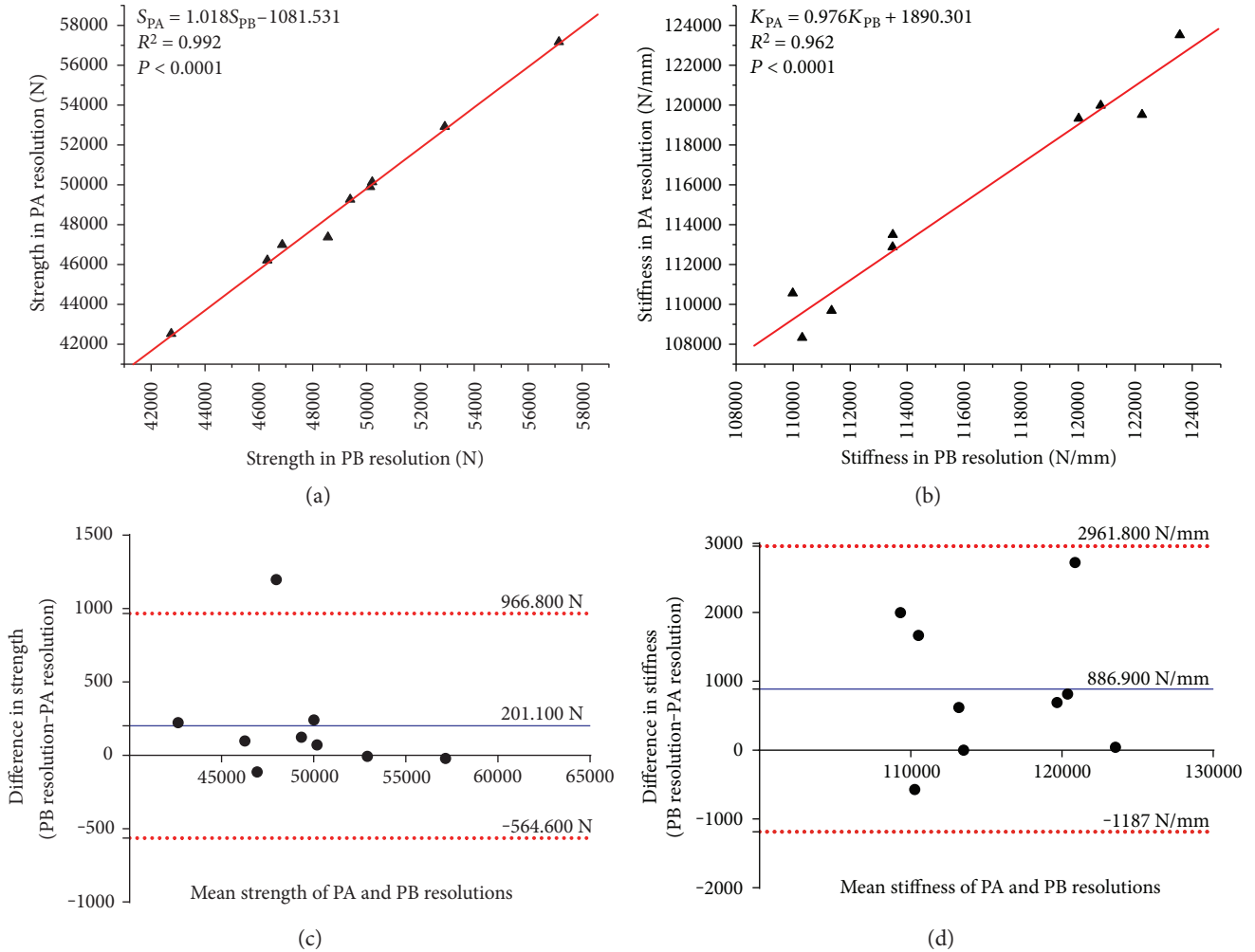


FIGURE 5: Correlation and consistent analysis between the two resolution models of nine bovine vertebral bodies for strength and stiffness. (a) Linear regression using the estimated strength of QCT/FEA models with the PB resolution as predictors for those with the PA resolution. (b) Linear regression using the estimated stiffness of QCT/FEA models with the PB resolution as predictors for those with the PA resolution. (c) Bland-Altman plot for strength. (d) Bland-Altman plot for stiffness.

linear portion of stress-strain curves predicted from FE models with the element sizes of $0.41 \times 0.41 \times 0.41 \text{ mm}^3$, $0.41 \times 0.41 \times 0.6 \text{ mm}^3$, and $0.41 \times 0.41 \times 1 \text{ mm}^3$ (case 1/case 2, case 3/case 4, and case 5/case 6) were almost the same. However, there were significant differences within the ultimate stresses predicted from these FE models. The ultimate stresses of case 1/case 2 were the lowest, and those of case 5/case 6 were the highest. The slopes of linear portion of stress-strain curves predicted from FE models with the element sizes of $1 \times 1 \times 1 \text{ mm}^3$, $2 \times 2 \times 2 \text{ mm}^3$, and $3 \times 3 \times 3 \text{ mm}^3$ (case 7/case 8, case 9/case 10, and case 11/case 12) were much less than those predicted from the first six cases (case 1/case 2, case 3/case 4, and case 5/case 6). The larger was the element size, the less was the slope of linear portion of the stress-strain curve. The variation trend of the ultimate stresses predicted from these FE models was similar to those predicted from the first six cases. The smaller was the element size, the less was the

ultimate stress in the stress-strain curve. For all 12 cases, the ultimate stresses predicted from the FE models with element size of $0.41 \times 0.41 \times 1 \text{ mm}^3$ (case 5/case 6) were the highest.

- (2) The stress-strain curves predicted from the two resolution models with the same element size were similar, and the stress-strain curves of FE models with the PA resolution were almost coincided with those with the PB resolution. It demonstrated that the mechanical parameters predicted from the two resolution models with same element size were almost the same. The simulation results of vertebral cancellous FE models were similar, as long as the two resolution models were meshed with the same element size, no matter whether the element size was larger than the image voxel size, or less than the image voxel size.

3.2.3. *Apparent Elastic Modulus and Yield Strength.* The results of two bovine vertebral cancellous FE models

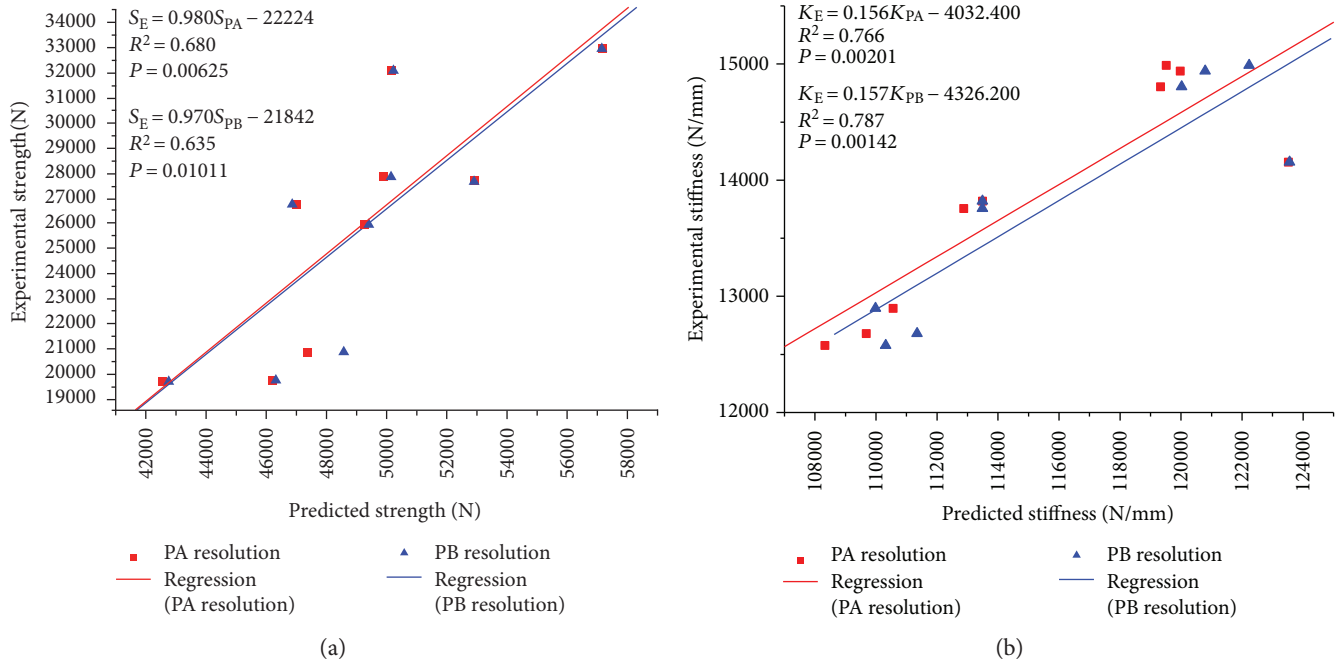


FIGURE 6: Linear regressions of nine bovine vertebral bodies for strength and stiffness estimated from the two resolution models as predictors of experimentally measured values. (a) Strength. (b) Stiffness.

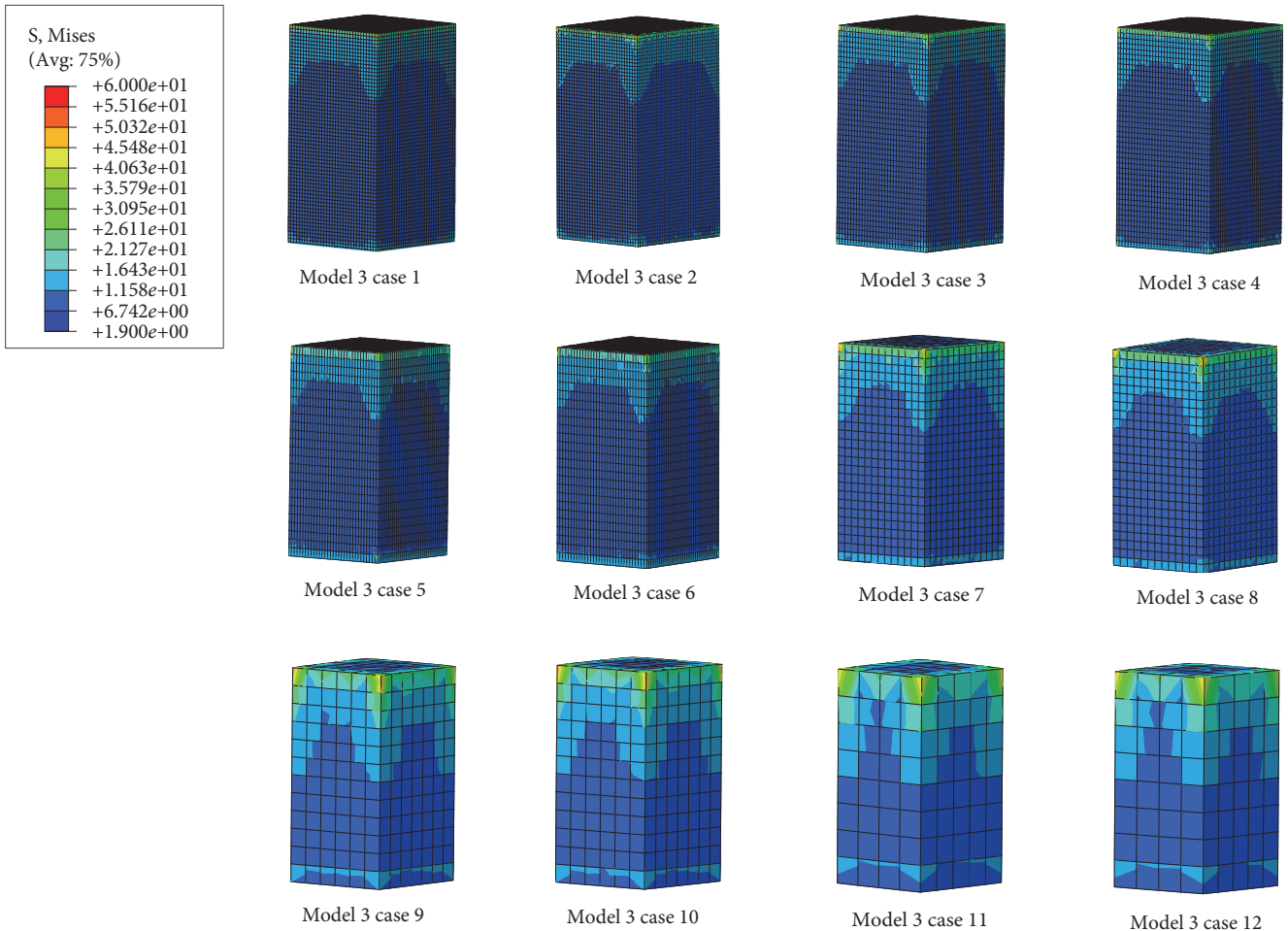


FIGURE 7: The von Mises stress distributions of the bovine vertebral cancellous FE model (model 3) in the 12 cases.

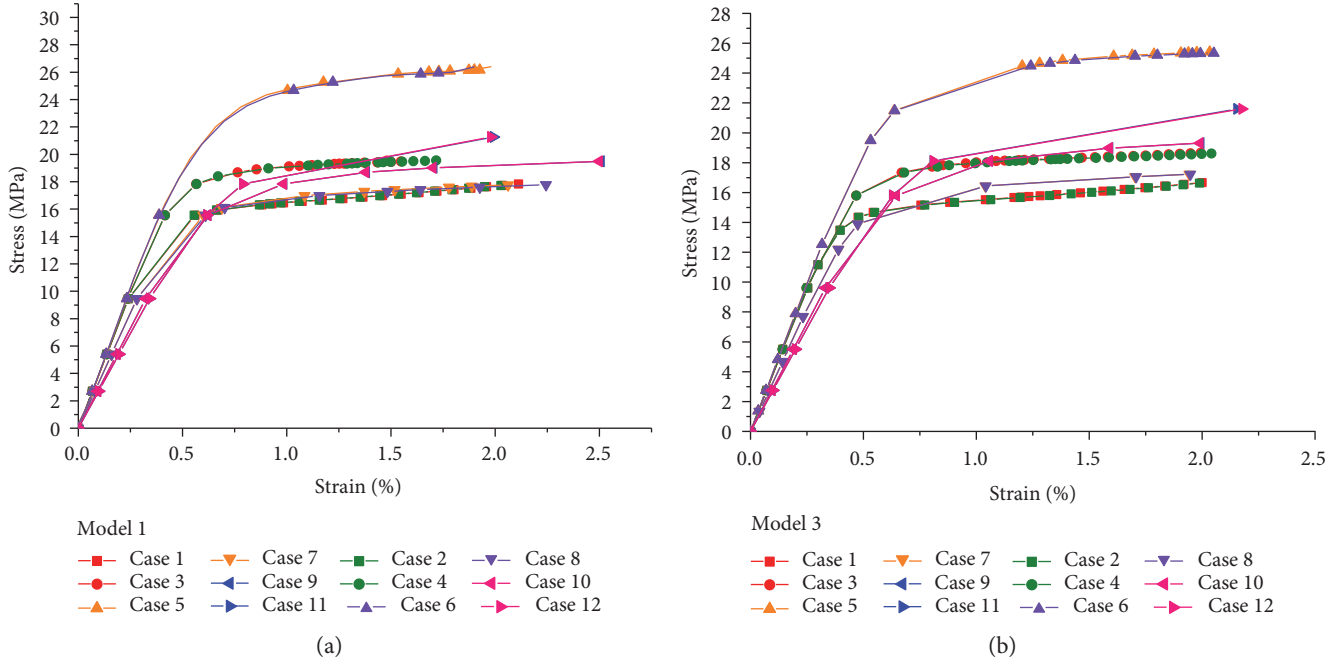


FIGURE 8: The stress-strain curves of two bovine vertebral cancellous FE models (model 1 and model 3) in the 12 cases.

TABLE 3: The apparent elastic modulus and yield strength of two bovine vertebral cancellous FE models (model 1 and model 3) in the 12 cases.

Model 1	Apparent elastic modulus (MPa)	Apparent yield strength (MPa)	Model 3	Apparent elastic modulus (MPa)	Apparent yield strength (MPa)
Case 1	3941.227	16.042	Case 1	3805.429	14.777
Case 2	3940.671	15.937	Case 2	3805.430	14.757
Case 3	4001.609	18.245	Case 3	3880.540	17.130
Case 4	4000.812	18.336	Case 4	3878.778	17.038
Case 5	4043.559	20.168	Case 5	3956.389	22.138
Case 6	4051.587	19.810	Case 6	3955.478	22.085
Case 7	3376.930	15.687	Case 7	3311.664	14.633
Case 8	3374.061	15.683	Case 8	3310.961	14.659
Case 9	2924.677	16.428	Case 9	2898.350	16.494
Case 10	2923.354	16.436	Case 10	2898.350	16.492
Case 11	2769.774	17.990	Case 11	2762.848	18.248
Case 12	2769.711	18.011	Case 12	2762.162	18.242

(model 1 and model 3) were selected as examples, and the apparent elastic modulus and yield strength of these models in the 12 cases were obtained from the stress-strain curves (Table 3). The results of the other models were similar.

The apparent elastic modulus of vertebral cancellous FE models showed the following:

- (1) The apparent elastic moduli predicted from the FE models reconstructed from the same resolution scan with the element sizes of $0.41 \times 0.41 \times 0.41 \text{ mm}^3$, $0.41 \times 0.41 \times 0.6 \text{ mm}^3$, and $0.41 \times 0.41 \times 1 \text{ mm}^3$ (case 1/case 2, case 3/case 4, and case 5/case 6) were almost

the same. For case 1/case 2, the apparent elastic moduli were the lowest, and for case 5/case 6, the apparent elastic moduli were the highest. The apparent elastic moduli of the last six cases (case 7/case 8, case 9/case 10, and case 11/case 12) were less than those of the first six cases, and they were different from each other. It showed that the sizes of cross section and longitudinal thickness of each element (in correspondence with in-plane resolution and slice thickness of QCT scan resolution setting) can affect the apparent elastic moduli predicted from FE models. For all apparent elastic moduli of the last six cases, the values of case 7/case 8 were the highest, and those of case 11/case 12 were the lowest.

- (2) The apparent elastic moduli predicted from the two resolution models with the same element size were almost the same. According to the apparent elastic moduli in the 12 cases of each vertebral cancellous FE model, the maximum difference within the apparent elastic moduli predicted from the two resolution models was 17.312 MPa (case 11 versus case 12 for model 5), the minimum difference was 0 MPa (case 9 versus case 10 for model 3; case 5 versus case 6 for model 5), and the other differences were less than 11.400 MPa.

The apparent yield strength of vertebral cancellous FE models showed the following:

- (1) The apparent yield strengths of case 5/case 6 were the highest, and those of case 7/case 8 were the lowest.
- (2) The apparent yield strengths of the first and last six cases reconstructed from the same resolution scan were increased with the enlargement of element size, but the increase of apparent yield strengths for the first and last six cases were discontinuous. It showed that the sizes of cross section and longitudinal thickness of each element (in correspondence with in-plane resolution and slice thickness of QCT scan resolution setting) can affect the apparent yield strengths predicted from FE models.
- (3) The apparent yield strengths predicted from the two resolution models with the same element size were similar. According to the apparent yield strengths in the 12 cases of each vertebral cancellous FE model, the maximum difference within the apparent yield strengths predicted from the two resolution models was 1.437 MPa (case 7 versus case 8 for model 2), and the other differences were less than 0.100 MPa.

In conclusion, the computational accuracy of bovine vertebral cancellous FE models with the element sizes of $0.41 \times 0.41 \times 0.6 \text{ mm}^3$ (case 3/case 4) and $0.41 \times 0.41 \times 1 \text{ mm}^3$ (case 5/case 6) were higher than those of the other FE models.

4. Discussion

In this study, subject-specific QCT/FEA models of nine bovine vertebral bodies were constructed. There were modestly significant positive correlations between the predicted principal strains and the experimentally measured principal strains. The model validation illustrated that our QCT/FEA models were well validated and can be used to explore the effects of scan resolutions and element sizes on mechanical parameters of QCT/FEA models. The correlations between predicted (PA and PB resolutions) and experimentally measured results were investigated in our study by developing the linear regression models, in which vertebral strength and stiffness estimated from the two resolution models were used as predictors of values obtained

from the compressive mechanical tests. The errors of the exterior material property distributions of QCT/FEA models reconstructed from in vitro datasets are larger than those reconstructed from in situ datasets, which would consequently influence the apparent elastic modulus and yield strength predicted from FE models [24, 25]. In order to minimize this limitation and for the convenience to explore the effects of scan resolutions and element sizes on the QCT/FEA outcomes, FE model with cuboid VOI from the vertebral body center was used instead of a whole vertebral body model. Two different scan resolutions and six different element sizes were combined in pairs to compare the mechanical parameters derived from FE models in the 12 cases.

Subject-specific nonlinear QCT/FEA modeling of lumbar vertebral bodies has recently gained increasing interest in assessing the risks of OP and vertebral fracture. It was shown that this technique could reflect the real mechanical behavior of vertebral bodies and may be able to provide better predictions of strength levels and failure patterns than BMD measurement for the human lumbar spine [6, 17, 36]. The previous study showed that there was a significant linear correlation between the predicted minimum principal strains and the measured values ($R^2 = 0.838$, $P < 0.0001$) [9], which were consistent with our results (Table 1). It illustrated that our QCT/FEA models were well validated. Vertebral strength and stiffness predicted from the QCT/FEA models have generally shown modestly linear correlations ($R^2 \geq 0.685$) with the in vitro measurements of strength and stiffness [17, 18]. As shown in Figure 6, vertebral strength and stiffness estimated from the two resolution models were modestly correlated with those obtained from the compressive mechanical tests ($R^2 \geq 0.635$), which were similar to the previous results.

The standard slice thickness used in clinics is 1 mm, and it was proven that the QCT/FEA model with this resolution could provide a high-quality estimation of vertebral strength [30, 37]. From the von Mises stress distribution, strength and stiffness derived from FE models with the same element size of the vertebral bodies and the vertebral cancellous bones (Figures 4, 5, 7, and 8), it was shown that the mechanical parameters of FE models reconstructed from QCT datasets with 1 mm slice thickness were close to those reconstructed from QCT datasets with 0.6 mm slice thickness. These results suggested that the computational accuracy of the FE models reconstructed from QCT datasets with 1 mm slice thickness was satisfactory, and the computational cost of these FE models was relatively lower. However, the smaller QCT voxels require the higher scan resolution and allow for a more detailed representation of the geometry and material properties of FE models [16]. In terms of the paired sample correlations between principal strains predicted from the two resolution models and experimental principal strains, we found that the average $C_{PA\&E}$ of the nine vertebral bodies was higher than the average $C_{PB\&E}$, but the differences between $C_{PA\&E}$ and $C_{PB\&E}$ of each specimen

were little (Table 2). These results demonstrated that the QCT/FEA models reconstructed from the datasets with 1 mm slice thickness may be accurate enough to reflect the real mechanical properties of vertebral bodies. Therefore, the scan resolution of 1 mm slice thickness is recommended by comprehensively considering radiation doses and computational costs of FE models.

Element size is a crucial factor that can significantly affect the numerical convergence characteristics and computational accuracy of FE models [23, 38, 39]. The mechanical parameters of FE models reconstructed from the higher resolution scans with smaller element sizes are similar; however, when the element sizes are much larger than the image voxel sizes, it will not only lead to coarser models and surface serration but also change the material distributions of FE models, which will finally affect the predicted results. The FE models with element sizes of $0.25 \times 0.25 \times 1 \text{ mm}^3$, $0.5 \times 0.5 \times 1 \text{ mm}^3$, and $1 \times 1 \times 1 \text{ mm}^3$ were constructed based on QCT datasets with $0.25 \times 0.25 \text{ mm}$ /pixel resolution and 1 mm slice thickness, and the load-displacement curves obtained from these three FE models were almost coincided with each other [11]. The voxel models created from the QCT datasets with slice thickness greater than 1.25 mm will result in a loss of fidelity of the representative anatomical characteristics of bone structures [40]. It was demonstrated that voxel size has a significant effect on the simulated biomechanical behavior, that is, larger voxel size results in greatly reduced maximum principal strains [41]. In this study, the apparent elastic moduli predicted from the FE models reconstructed from the same resolution scan with the element sizes of $0.41 \times 0.41 \times 0.41 \text{ mm}^3$, $0.41 \times 0.41 \times 0.6 \text{ mm}^3$, and $0.41 \times 0.41 \times 1 \text{ mm}^3$ were almost the same; but the apparent elastic moduli were significant decreased when element sizes were larger than $1 \times 1 \times 1 \text{ mm}^3$; the computational errors will rise to more than 60% when element sizes were larger than $2 \times 2 \times 2 \text{ mm}^3$ (Table 3). It is recommended that the element sizes should be less than $2 \times 2 \times 2 \text{ mm}^3$ in order to improve the computational accuracy of FE models. The apparent elastic moduli and yield strengths of FE models with element size of $0.41 \times 0.41 \times 0.6 \text{ mm}^3$ reconstructed from the low-resolution scans (1 mm slice thickness) were similar with those reconstructed from the high-resolution scans (0.6 mm slice thickness). It was suggested that the smaller element sizes can make up for the “defect” of low resolutions when controlling the scan resolutions within a certain range.

The sensitivities of the FEA results to QCT scan resolutions (i.e., in-plane resolution and slice thickness) were different, and it means that the sizes of cross section and longitudinal thickness of each element have different effect on the mechanical parameters of FE models [23]. Four different in-plane resolutions (1 mm, 2 mm, 3 mm, and 4 mm) and two different slice thicknesses (1.5 mm and 3 mm) were combined in pairs, and it was shown that in-plane resolution and slice thickness had significant effects on stiffness of FE

models. Analysis of covariance indicated that the predicted stiffness was highly correlated with in-plane resolution ($P < 0.0001$) and moderate correlated with slice thickness ($P = 0.0036$) [23]. The linear regression equations of vertebral cancellous FE models in the specific cases (case 1/case 2, case 5/case 6, and case 7/case 8) were developed for in-plane resolution and slice thickness as predictors of apparent elastic modulus, and the correlation analysis indicated that apparent elastic modulus was highly correlated with in-plane resolution ($R^2 = 0.880$, $P < 0.0001$) and weakly correlated with slice thickness ($R^2 = 0.106$, $P = 0.1618$). It was demonstrated that in-plane resolution has more significant effects on mechanical parameters of FE models than slice thickness. In conclusion, the optimal selection of in-plane resolution may be more important than slice thickness for increasing the computational accuracy of the FE model.

A few limitations in the study were summarized as follows:

- (1) The material properties have great influence on the computational accuracy of subject-specific FE models for human bones, and different density-elasticity relationship will consequently change the mechanical parameters of FE models [34, 42]. A specific density-elasticity relationship, which was obtained from the human vertebral body samples, was used [31]. The material properties are different as the bovine vertebral bodies in this study, which may cause differences between FE-derived and experimentally measured results. Although all correlations of linear regression equations for the principal strain, strength and stiffness predicted from the QCT/FEA models as predictors of those obtained from the compressive mechanical tests were significant, and the slopes and intercepts of these linear regression equations were markedly different from those of the diagonal line of $y = x$.
- (2) The ranges of QCT scan resolutions used (0.6 mm slice thickness and 1 mm slice thickness) were limited, and there were no significant differences in the mechanical parameters derived from the two resolution models of bovine vertebral bodies and vertebral cancellous bones. However, recent studies showed that the scan resolution is the key parameter in determining the geometries and mechanical properties of FE models [41, 43]. Taken together, it suggested that the range of scan resolutions in this study was too small, and this limitation could be solved by choosing a wider range of scan resolutions.

In summary, this study showed that QCT/FEA models created from the two resolution scans with six different element sizes would give various predicted results, and it revealed that QCT scan resolutions and element sizes had different influences on FEA outcomes. This study provides theoretical basis for selection of clinical scan resolutions

and element sizes. The optimal selection of the scan resolutions and element sizes could improve the accuracy of predictions for vertebral strength and lay a good foundation for assessing the risk of OP and clinical fracture.

5. Conclusions

The mechanical parameters of FE models with the same element size reconstructed from the QCT datasets with 0.6 mm slice thickness and those reconstructed from the QCT datasets with 1 mm slice thickness were almost the same. The computational accuracy of the FE models reconstructed from QCT datasets with 1 mm slice thickness was satisfactory, and the computational cost of these FE models was relatively lower. The apparent elastic modulus and yield strength of the FE models reconstructed from the same resolution scan with the element sizes larger than $0.41 \times 0.41 \times 1 \text{ mm}^3$ were significant different from those of the FE models with the element sizes less than $0.41 \times 0.41 \times 1 \text{ mm}^3$. In conclusion, it is recommended that FE models with the element size of $0.41 \times 0.41 \times 1 \text{ mm}^3$ reconstructed from the QCT datasets with 1 mm slice thickness could be utilized to predict the mechanical parameters of vertebral bodies; meanwhile, FE models with the element size of $0.41 \times 0.41 \times 0.6 \text{ mm}^3$ are recommended for increasing the computational accuracy.

Conflicts of Interest

The authors declare that there is no conflict of interests regarding the publication of this paper.

Acknowledgments

This work is supported by the National Natural Science Foundation of China (nos. 81471753, 11432016, and 11322223), the Science and Technology Development Plan Projects of Jilin Province (nos. 20160101297JC, 20170519008JH, and 20170520093JH), and the China Postdoctoral Science Foundation (2016M591477).

References

- [1] L. Si, T. M. Winzenberg, M. Chen, Q. Jiang, and A. J. Palmer, "Residual lifetime and 10 year absolute risks of osteoporotic fractures in Chinese men and women," *Current Medical Research and Opinion*, vol. 31, no. 6, pp. 1149–1156, 2015.
- [2] C. L. Benhamou, "Effects of osteoporosis medications on bone quality," *Joint, Bone, Spine*, vol. 74, no. 1, pp. 39–47, 2007.
- [3] T. Sone, T. Tomomitsu, M. Miyake, N. Takeda, and M. Fukunaga, "Age-related changes in vertebral height ratios and vertebral fracture," *Osteoporosis International*, vol. 7, no. 2, pp. 113–118, 1997.
- [4] E. M. Lochmüller, D. Bürklein, V. Kuhn et al., "Mechanical strength of the thoracolumbar spine in the elderly: prediction from in situ dual-energy X-ray absorptiometry, quantitative computed tomography (QCT), upper and lower limb peripheral QCT, and quantitative ultrasound," *Bone*, vol. 31, no. 1, pp. 77–84, 2002.
- [5] P. Ammann and R. Rizzoli, "Bone strength and its determinants," *Osteoporosis International*, vol. 14, Supplement 3, pp. S13–S18, 2003.
- [6] T. Matsumoto, I. Ohnishi, M. Bessho, K. Imai, S. Ohashi, and K. Nakamura, "Prediction of vertebral strength under loading conditions occurring in activities of daily living using a computed tomography-based nonlinear finite element method," *Spine*, vol. 34, no. 14, pp. 1464–1469, 2009.
- [7] E. Dall'Ara, D. Pahr, P. Varga, F. Kainberger, and P. Zysset, "QCT-based finite element models predict human vertebral strength in vitro significantly better than simulated DEXA," *Osteoporosis International*, vol. 23, no. 2, pp. 563–572, 2012.
- [8] B. E. Sapin-De, E. Jolivet, C. Travert, D. Mitton, and W. Skalli, "Prediction of the vertebral strength using a finite element model derived from low-dose biplanar imaging: benefits of subject-specific material properties," *Spine*, vol. 37, no. 3, pp. E156–E162, 2012.
- [9] K. Imai, I. Ohnishi, M. Bessho, and K. Nakamura, "Nonlinear finite element model predicts vertebral bone strength and fracture site," *Spine*, vol. 31, no. 16, pp. 1789–1794, 2006.
- [10] E. Dall'Ara, R. Schmidt, D. Pahr et al., "A nonlinear finite element model validation study based on a novel experimental technique for inducing anterior wedge-shape fractures in human vertebral bodies in vitro," *Journal of Biomechanics*, vol. 43, no. 12, pp. 2374–2380, 2010.
- [11] A. Zeinali, B. Hashemi, and S. Akhlaghpour, "Noninvasive prediction of vertebral body compressive strength using nonlinear finite element method and an image based technique," *Physica Medica*, vol. 26, no. 2, pp. 88–97, 2010.
- [12] M. J. Silva, T. M. Keaveny, and W. C. Hayes, "Computed tomography-based finite element analysis predicts failure loads and fracture patterns for vertebral sections," *Journal of Orthopaedic Research*, vol. 16, no. 3, pp. 300–308, 1998.
- [13] F. Taddei, L. Cristofolini, S. Martelli, H. S. Gill, and M. Viceconti, "Subject-specific finite element models of long bones: an in vitro evaluation of the overall accuracy," *Journal of Biomechanics*, vol. 39, no. 13, pp. 2457–2467, 2006.
- [14] Y. Matsuura, H. Giambini, Y. Ogawa et al., "Specimen-specific nonlinear finite element modeling to predict vertebrae fracture loads after vertebroplasty," *Spine*, vol. 39, no. 22, pp. E1291–E1296, 2014.
- [15] J. Q. Campbell, D. J. Coombs, M. Rao, P. J. Rullkoetter, and A. J. Petrella, "Automated finite element meshing of the lumbar spine: verification and validation with 18 specimen-specific models," *Journal of Biomechanics*, vol. 49, no. 13, pp. 2669–2676, 2016.
- [16] P. Suetens, *Fundamentals of Medical Imaging*, Cambridge University Press, New York, NY, USA, 2nd edition, 2009.
- [17] R. P. Crawford, C. E. Cann, and T. M. Keaveny, "Finite element models predict in vitro vertebral body compressive strength better than quantitative computed tomography," *Bone*, vol. 33, no. 4, pp. 744–750, 2003.
- [18] D. H. Pahr, J. Schwiedrzik, E. Dall'Ara, and P. K. Zysset, "Clinical versus pre-clinical FE models for vertebral body strength predictions," *Journal of the Mechanical Behavior of Biomedical Materials*, vol. 33, no. 7, pp. 76–83, 2014.
- [19] J. Paul, B. Krauss, R. Banckwitz, W. Maentele, R. W. Bauer, and T. J. Vogl, "Relationships of clinical protocols and reconstruction kernels with image quality and radiation dose in a 128-slice CT scanner: study with an anthropomorphic and water phantom," *European Journal of Radiology*, vol. 81, no. 5, pp. e669–e703, 2012.
- [20] H. Giambini, D. D. Dan, A. Nassr, M. J. Yaszemski, and C. Zhao, "Quantitative computed tomography protocols affect

- material mapping and quantitative computed tomography-based finite-element analysis predicted stiffness,” *Journal of Biomechanical Engineering*, vol. 138, no. 9, pp. 091003-1–091003-7, 2016.
- [21] D. Dragomir-Daescu, C. Salas, S. Uthamaraj, and T. Rossman, “Quantitative computed tomography-based finite element analysis predictions of femoral strength and stiffness depend on computed tomography settings,” *Journal of Biomechanics*, vol. 48, no. 1, pp. 153–161, 2015.
- [22] Y. Lu, K. Engelke, K. Püschel, M. M. Morlock, and G. Huber, “Influence of 3D QCT scan protocol on the QCT-based finite element models of human vertebral cancellous bone,” *Medical Engineering & Physics*, vol. 36, no. 8, pp. 1069–1073, 2014.
- [23] R. P. Crawford, W. S. Rosenberg, and T. M. Keaveny, “Quantitative computed tomography-based finite element models of the human lumbar vertebral body: effect of element size on stiffness, damage, and fracture strength predictions,” *Journal of Biomechanical Engineering*, vol. 125, no. 4, pp. 434–438, 2003.
- [24] Y. Lu, K. Engelke, C. C. Glueer, M. M. Morlock, and G. Huber, “The effect of in situ/in vitro three-dimensional quantitative computed tomography image voxel size on the finite element model of human vertebral cancellous bone,” *Proceedings of the Institution of Mechanical Engineers Part H: Journal of Engineering in Medicine*, vol. 228, no. 11, pp. 1208–1213, 2014.
- [25] Y. Lu, “Influence of the specimen scan condition on the finite element voxel model of human vertebral cancellous bone,” *Computer Methods in Biomechanics and Biomedical Engineering: Imaging & Visualization*, vol. 3, no. 3, pp. 172–176, 2015.
- [26] E. Schileo, F. Taddei, A. Malandrino, L. Cristofolini, and M. Viceconti, “Subject-specific finite element models can accurately predict strain levels in long bones,” *Journal of Biomechanics*, vol. 40, no. 13, pp. 2982–2989, 2007.
- [27] H. J. Wilke, K. Wenger, and L. Claes, “Testing criteria for spinal implants: recommendations for the standardization of in vitro stability testing of spinal implants,” *European Spine Journal*, vol. 7, no. 2, pp. 148–154, 1998.
- [28] D. L. Kopperdahl, J. L. Pearlman, and T. M. Keaveny, “Biomechanical consequences of an isolated overload on the human vertebral body,” *Journal of Orthopaedic Research*, vol. 18, no. 5, pp. 685–690, 2000.
- [29] J. M. Buckley, C. C. Kuo, and L. C. Cheng, “Relative strength of thoracic vertebrae in axial compression versus flexion,” *The Spine Journal*, vol. 9, no. 6, pp. 478–485, 2009.
- [30] J. M. Buckley, K. Loo, and J. Motherway, “Comparison of quantitative computed tomography-based measures in predicting vertebral compressive strength,” *Bone*, vol. 40, no. 3, pp. 767–774, 2007.
- [31] D. L. Kopperdahl, E. F. Morgan, and T. M. Keaveny, “Quantitative computed tomography estimates of the mechanical properties of human vertebral trabecular bone,” *Journal of Orthopaedic Research*, vol. 20, no. 4, pp. 801–805, 2002.
- [32] E. Morgan and T. Keaveny, “Dependence of yield strain of human trabecular bone on anatomic site,” *Journal of Biomechanics*, vol. 34, no. 34, pp. 569–577, 2001.
- [33] D. L. Kopperdahl and T. M. Keaveny, “Yield strain behavior of trabecular bone,” *Journal of Biomechanics*, vol. 31, no. 7, pp. 601–608, 1998.
- [34] E. F. Morgan, H. H. Bayraktar, and T. M. Keaveny, “Trabecular bone modulus-density relationships depend on anatomic site,” *Journal of Biomechanics*, vol. 36, no. 7, pp. 897–904, 2003.
- [35] G. L. Niebur, M. J. Feldstein, J. C. Yuen, T. J. Chen, and T. M. Keaveny, “High-resolution finite element models with tissue strength asymmetry accurately predict failure of trabecular bone,” *Journal of Biomechanics*, vol. 33, no. 12, pp. 1575–1583, 2000.
- [36] M. A. K. Liebschner, D. L. Kopperdahl, W. S. Rosenberg, and T. M. Keaveny, “Finite element modeling of the human thoracolumbar spine,” *Spine*, vol. 28, no. 6, pp. 559–565, 2003.
- [37] M. Mirzaei, A. Zeinali, A. Razmjoo, and M. Nazemi, “On prediction of the strength levels and failure patterns of human vertebrae using quantitative computed tomography (QCT)-based finite element method,” *Journal of Biomechanics*, vol. 42, no. 11, pp. 1584–1591, 2009.
- [38] J. H. Keyak and H. B. Skinner, “Three-dimensional finite element modelling of bone: effects of element size,” *Journal of Biomedical Engineering*, vol. 14, no. 6, pp. 483–489, 1992.
- [39] W. Tjong, G. J. Kazakia, A. J. Burghardt, and S. Majumdar, “The effect of voxel size on high-resolution peripheral computed tomography measurements of trabecular and cortical bone microstructure,” *Medical Physics*, vol. 39, no. 4, pp. 1893–1903, 2012.
- [40] J. M. Ford and S. J. Decker, “Computed tomography slice thickness and its effects on three-dimensional reconstruction of anatomical structures,” *Journal of Forensic Radiology and Imaging*, vol. 4, pp. 43–46, 2015.
- [41] A. Maloul, J. Fialkov, and C. Whyne, “The impact of voxel size-based inaccuracies on the mechanical behavior of thin bone structures,” *Annals of Biomedical Engineering*, vol. 39, no. 3, pp. 1092–1100, 2011.
- [42] E. Schileo, E. Dall’Ara, F. Taddei et al., “An accurate estimation of bone density improves the accuracy of subject-specific finite element models,” *Journal of Biomechanics*, vol. 41, no. 11, pp. 2483–2491, 2008.
- [43] Y. N. Yeni, G. T. Christopherson, X. N. Dong, D. G. Kim, and D. P. Fyhrie, “Effect of microcomputed tomography voxel size on the finite element model accuracy for human cancellous bone,” *Journal of Biomechanical Engineering*, vol. 127, no. 1, pp. 1–8, 2005.

Research Article

Comparison of Morphologic Parameters of Temporomandibular Joint for Asymptomatic Subjects Using the Two-Dimensional and Three-Dimensional Measuring Methods

Yuanli Zhang, Xianchao Xu, and Zhan Liu

Provincial Key Lab for Biomechanical Engineering, Sichuan University, Chengdu 610065, China

Correspondence should be addressed to Zhan Liu; bmeliuzhan@163.com

Received 28 February 2017; Accepted 4 April 2017; Published 2 May 2017

Academic Editor: Lizhen Wang

Copyright © 2017 Yuanli Zhang et al. This is an open access article distributed under the Creative Commons Attribution License, which permits unrestricted use, distribution, and reproduction in any medium, provided the original work is properly cited.

The differences of temporomandibular joint (TMJ) morphologic parameters by using two-dimensional (2D) and three-dimensional (3D) measuring methods were compared. Ten asymptomatic subjects (26.75 ± 4.89 years) were randomly recruited. The 3D models of the maxilla, mandible, and teeth were reconstructed according to cone-beam computed tomography (CBCT) image data. The morphologic parameters of TMJs were measured by the 2D CBCT measuring method (group A) and the 3D reconstruction model measuring method (group B), respectively. The morphologic parameters in each group were assessed by paired samples *t*-test, and the statistical significance was achieved when $p < 0.05$. The horizontal condylar angle (HCA), sagittal ramus angle (SRA), medial joint space (MJS), lateral joint space (LJS), superior joint space (SJS), and anterior joint space (AJS) in group A were significantly smaller than those in group B ($p < 0.05$). The HCA on the left side was significantly smaller than that on the right side in group A ($p < 0.05$). However, all the morphologic parameters in group B were not significantly different between left and right sides. In conclusion, there were significant differences for the morphologic parameters of TMJ measured on 2D CBCT and 3D models. 3D measuring method should be used for the detection of TMJ morphology in clinical practice.

1. Introduction

Temporomandibular joints (TMJs) are a pair of complex and highly mobile joints. TMJs are the most active joints in the human body with more than 2000 movements each day during chewing, biting, swallowing, talking, and snoring [1]. Dupuy-Bonafe et al. indicated that the morphologic examination of the TMJ has important applications in the domain of TMJ pathology [2]. Therefore, the reasonable measurement of TMJ morphologic parameters will help us to better understand the structure and function of TMJ.

Due to the complexity of the skull base and TMJ components, many studies have investigated the TMJ morphologic parameters using different types of imaging techniques. Conventional X-rays were first used to assess the morphology of mandibular condyle and articular eminence [3]. Subsequently, the lateral cephalogram was used to determine the selection criteria for ordering a corrected lateral

tomogram of the TMJ [4], to investigate the possible association between the joint structure and condylar position and craniofacial morphology [5], and to measure the TMJ positions of Malays and Chinese with facial asymmetry for assessing its impact on the temporomandibular disorders [6]. After that, computed tomography (CT) images were widely used for the morphologic detection of TMJ [2, 7, 8]. In recent years, the micro-CT, panoramic radiography (PR), cone-beam computed tomography (CBCT), and magnetic resonance imaging (MRI) were used for research of TMJ morphology [9–14]. In Zhao et al.'s study, micro-CT images were used to observe morphologic changes of the TMJ condyle under mandibular deviation continuously in an animal model [9]. PR images were used to diagnose the condylar bone defects in 5 dried human skulls [10]. CBCT images were used to analyze the facial morphologic characteristics of female patients with skeletal class II deformity [11] and to examine the relationship between the thickness of the glenoid

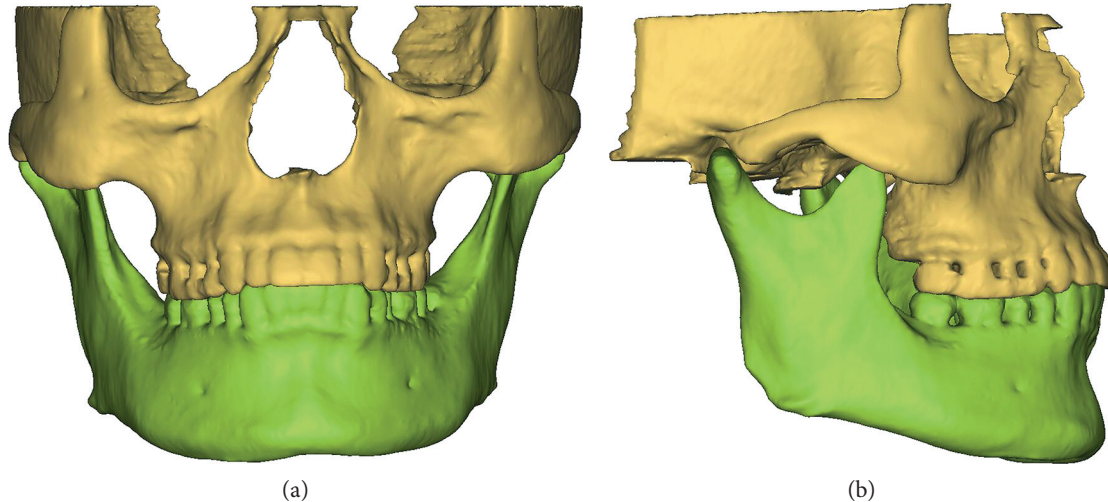


FIGURE 1: The 3D model of an asymptomatic subject: (a) front view and (b) lateral view.

fossa roof and condyle morphology [12]. MRI images were used to evaluate the change of morphologic symmetry of TMJ during natural course of teen-age unilateral anterior disc displacement [13]. Meanwhile, the three-dimensional (3D) models were also used to investigate the condylar morphology and TMJ osteoarthritis [15–17].

Most of the related studies have been limited to two-dimensional (2D) measuring method to assess the TMJ morphologic parameters. However, these results measured by 2D method do not show the spatial position of the structures in TMJ. The 3D measuring method was used to assess the morphology of condyle, but other TMJ structures, such as glenoid fossa and articular eminence, were not included in the previous studies. Furthermore, the comparisons between the TMJ morphologic parameters measured by 2D and 3D methods have not been studied. The aim of this study was to compare the differences of TMJ morphologic parameters using 2D CBCT and 3D model measuring methods. This work has been presented as a poster at the ORS 2017 Annual Meeting, and it was considered as a valuable research by the experts.

2. Materials and Methods

2.1. Subjects and Data Acquisition. This study consisted of 10 asymptomatic subjects (4 females and 6 males, 26.75 ± 4.89 years old). The subjects were randomly identified and recruited by a dentist in the Affiliated Hospital of Stomatology, Chongqing Medical University from January 2015 to January 2016. This study was approved by the Affiliated Hospital of Stomatology of Chongqing Medical University Institutional Review Board, and all participants signed an informed consent agreement. The inclusion criteria of asymptomatic subjects were as follows: healthy physical condition, no TMJ disorder symptoms, no degenerative joint disease, and facial symmetry with no prior TMJ-related procedures.

CBCT data for all subjects were collected at the Affiliated Hospital of Stomatology, Chongqing Medical University. The maxilla and mandible were scanned using a CBCT machine (KaVo 3D eXam, Germany) with a complete head

view. All images were taken following a standardized protocol for patient positioning and exposure parameter setting (120 kVp, 3–8 mA, 20 sec, and 0.4 mm voxel resolution). The resolution of cross-sectional images was 400 pixels \times 400 pixels, and the pixel size was 0.4 mm. The CBCT scans consisted of a total amount of 290 to 330 images with the slice thicknesses of 0.4 mm. The CBCT images were reformatted into Digital Imaging and Communications in Medicine (DICOM) format.

2.2. 3D Modeling. According to the Hounsfield units (HU), the cortical bone, cancellous bone, and teeth were separated in MIMICS (Materialise, Leuven, Belgium), respectively. The boundaries of the regions of the maxilla, mandible, and teeth were accurately distinguished on each slice of CBCT images. Subsequently, the 3D models of the maxilla, mandible, and teeth were reconstructed in MIMICS for the 10 asymptomatic subjects (Figure 1).

2.3. TMJ Morphologic Analysis. Based on previous research [18, 19], the horizontal condylar angle (HCA), coronal condylar angle (CCA), sagittal ramus angle (SRA), coronal condylar width (CCW), medial joint space (MJS), lateral joint space (LJS), superior joint space (SJS), anterior joint space (AJS), and posterior joint space (PJS) were selected to investigate the morphology of TMJ. The above nine morphologic parameters were measured in the 2D CBCT images and 3D models of all the subjects, respectively.

The HCA was measured in the horizontal view (parallel to the Frankfurt horizontal (FH) plane):

- (1) HCA: the angle between the condylar long axis (the line between the most medial and lateral points) and the RL line (the line between the most anterior points of the bilateral auricles) [19], as shown in Figure 2

The CCA, CCW, MJS, SJS, and LJS were measured in the coronal view (Figure 3).

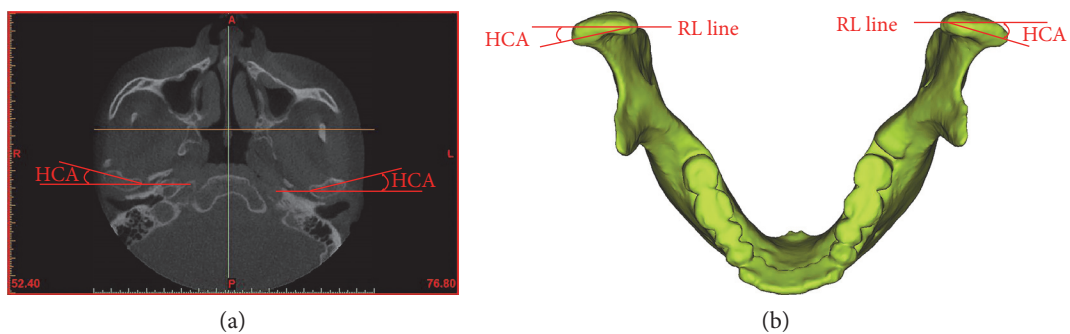


FIGURE 2: Measurements of the HCA in the horizontal view: (a) on the CBCT images and (b) in the 3D models. HCA: horizontal condylar angle.

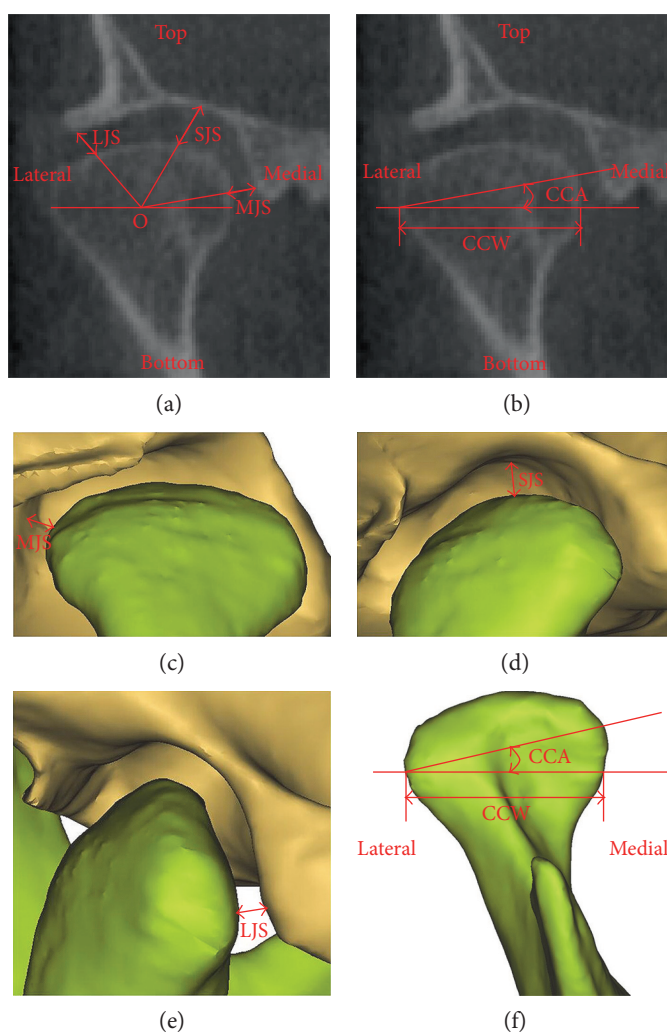


FIGURE 3: Measurements of the MJS, SJS, LJS, CCA, and CCW in the coronal view: (a and b) on the CBCT images and (c, d, e, and f) in the 3D models. The point O is the midpoint of CCW in part (a). CCA: coronal condylar angle; CCW: coronal condylar width; MJS: medial joint space; LJS: lateral joint space; SJS: superior joint space.

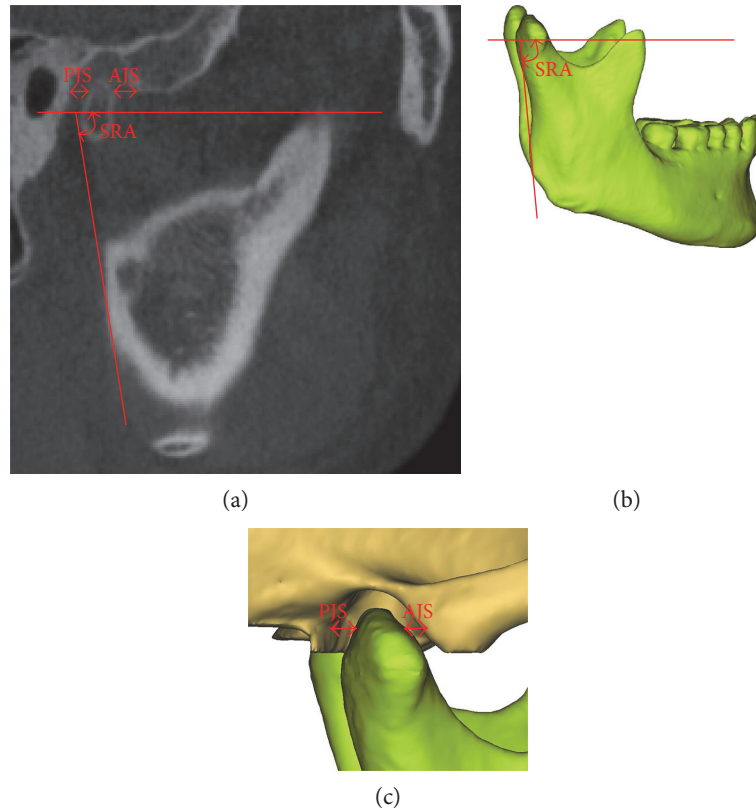


FIGURE 4: Measurements of the SRA, PJS, and AJS in the sagittal view: (a) on the CBCT images and (b and c) in the 3D models. SRA: sagittal ramus angle; AJS: anterior joint space; PJS: posterior joint space.

- (2) CCA: the angle between the FH plane and the condylar long axis
- (3) CCW: the length of a line segment paralleled to the FH plane and passed through the most lateral point of the condyle
- (4) MJS: the distance between the most medial point of the condyle and the articular fossa
- (5) SJS: the distance between the most superior point of the condyle and the articular fossa
- (6) LJS: the distance between the most lateral point of the condyle and the articular fossa

The SRA, PJS, and AJS were measured in the sagittal view (Figure 4).

- (7) SRA: the angle between the FH plane and the tangential line to the posterior outline of mandibular ramus
- (8) PJS: the distance paralleled to the FH plane between the posterior points of the condyle and the articular eminence outline
- (9) AJS: the distance paralleled to the FH plane between the anterior points of the condyle and the articular fossa outline.

In this study, the nine morphologic parameters for each model were re-evaluated thrice within a one-week interval

by three authors of this study using 2D and 3D measuring methods, respectively. The correlation coefficients of the results in each measurement were greater than 0.95. Therefore, the repeatability of the measurements was acceptable in this study.

2.4. Statistical Analysis. The morphologic differences of TMJ between 2D and 3D measuring methods were analyzed using paired samples *t*-test. In addition, the comparisons were performed in the following: (1) between the 2D measuring results (group A) and 3D measuring results (group B) of the nine morphologic parameters and (2) between the left TMJ and right TMJ in groups A and B, respectively. SPSS 20.0 (SPSS Inc., Chicago, IL) was used for the analysis. The statistical significance was achieved when $p < 0.05$.

3. Results

The angles (HCA and SRA) and the joint spaces (MJS, LJS, SJS, and AJS) were found to be statistically significant between the groups A and B (Table 1). The HCA in group B was significantly larger than that in group A ($p < 0.05$). However, there was no significant difference for CCA between groups A and B ($p > 0.05$). The SRA in group B was significantly higher than that in group A ($p < 0.05$). Meanwhile, the MJS, LJS, and SJS in group B were highly significantly greater than those in group A ($p < 0.01$). The AJS in group B was also significantly greater than that in group A ($p < 0.05$). Although there were no significant differences

TABLE 1: Mean and standard deviation of the morphologic parameters for the ten asymptomatic subjects measured in 2D CBCT (group A) and 3D model (group B).

Morphologic parameters	Group A (<i>n</i> = 10)	Group B (<i>n</i> = 10)	<i>p</i> value
HCA (°)	12.19 ± 0.57	12.72 ± 0.23	0.034*
CCA (°)	12.61 ± 0.39	12.93 ± 0.59	0.123
SRA (°)	76.68 ± 3.54	80.37 ± 1.23	0.012*
CCW (mm)	18.21 ± 2.23	18.54 ± 2.12	0.607
MJS (mm)	2.30 ± 0.20	2.81 ± 0.35	0.002**
LJS (mm)	2.57 ± 0.19	3.03 ± 0.53	0.007**
SJS (mm)	2.05 ± 0.12	2.27 ± 0.18	0.001**
AJS (mm)	2.47 ± 0.24	2.77 ± 0.43	0.039*
PJS (mm)	2.53 ± 0.47	2.62 ± 0.66	0.601

Note: $p > 0.05$, not significant. *Statistically significant difference between group A and group B by paired samples *t*-test ($p < 0.05$). **Highly statistically significant difference between group A and group B by paired samples *t*-test ($p < 0.01$). HCA: horizontal condylar angle; CCA: coronal condylar angle; SRA: sagittal ramus angle; CCW: coronal condylar width; MJS: medial joint space; LJS: lateral joint space; SJS: superior joint space; AJS: anterior joint space; PJS: posterior joint space; 2D: two-dimensional; 3D: three-dimensional.

for CCW and PJS between the groups A and B, the mean values of CCW and PJS in group B were still larger than those in group A (Table 1).

The morphologic differences of TMJ between the left and right sides were compared in group A and group B, respectively. The results showed that the HCA on the left side was significantly smaller than that on the right side in group A ($p < 0.05$). There was no significant difference for other morphologic parameters between the left TMJ and right TMJ in group A ($p > 0.05$). However, there was no significant difference for all the nine morphologic parameters between the left and right sides in group B (Table 2).

4. Discussion

The morphologic parameters of TMJ obtained from the medical images were the projection of the actual morphology of TMJ in a certain plane, such as horizontal plane, coronal plane, and sagittal plane. Therefore, these morphologic parameters measured by the medical images (2D method) did not show the spatial position relation of the structures in the TMJs. At present, a few stomatology hospitals are trying to establish the 3D measurement standard of the morphologic parameters of TMJ. However, the differences of the morphologic parameters of TMJ between the 2D and 3D measuring methods are still unclear. In this study, the TMJ morphology was evaluated by 2D and 3D measuring methods in asymptomatic subjects. The results indicated that there were significant differences between the two methods.

The joint space (MJS, LJS, SJS, AJS, and PJS) of TMJ would determine the disc position in the TMJ [20]. The condylar angle (HCA and CCA) could be an aetiological factor for disc displacement and degenerative joint disease [19–21]. The ramus angle (SRA) would determine the symmetry of mandible [19, 20]. Meanwhile, the AJS, PJS,

MJS, LJS, SJS, and CCW were the frequently used parameters in clinics to examine the morphology of TMJ. Therefore, the above nine morphologic parameters were used to investigate the TMJ morphology in this study. The 2D CBCT measuring method has been validated in the related studies [18, 19, 22–24]. The 3D measuring method also has been used to evaluate the condylar morphology [15, 17, 25]. The mean values of CCA were 11.9° and 12.7° on the left and right sides measured in 2D CBCT from Ueki et al.'s study [19]. In this study, the mean angles of CCA were 12.48 ± 0.55° and 12.73 ± 0.51° on the left and right sides, respectively. The mean distances of SJS and PJS were 1.8 mm and 2.5 mm measured in 2D CBCT, respectively, from Ueki et al. [19]. In this study, the mean distances of SJS and PJS were 2.05 ± 0.12 mm and 2.53 ± 0.47 mm, respectively. The mean value of CCW was 18.21 ± 2.23 mm measured in 2D CBCT in this study, close to Al-koshab et al.'s results of 17.80 mm [26]. In Martins et al.'s study [27], the mean values of MJS and SJS for asymptomatic subjects were 2.94 mm and 2.55 mm measured in 3D models, respectively. In this study, the mean values of MJS and SJS were 2.81 ± 0.35 mm and 2.27 ± 0.18 mm measured in 3D models, respectively. Other morphologic parameters of TMJ measured in this study were also similar to previous studies [18, 28–30]. Therefore, the results were accurate in this study.

The transverse dimension of condyloid process was 19.5 ± 2.4 mm measured in the Chinese skull specimens [31]. In this study, the CCW was 18.54 ± 2.12 mm and the CCA was 12.93 ± 0.59° in 3D models, so the transverse dimension of condyloid process was 19.11 mm in 3D models, and it was 98.00% of the actual value. However, the CCW was 18.21 ± 2.23 mm and the CCA was 12.61 ± 0.39° in 2D CBCT, so the transverse dimension of condyloid process was 18.58 mm in 2D CBCT, and it was 95.28% of the actual value. Meanwhile, the angle of the long axis of bilateral condyle was 145°–160° measured in the Chinese skull specimens [32], that is to say, the average HCA was 13.75°. In this study, the HCA was 12.72 ± 0.23° in 3D models, and it was 92.51% of the actual value. However, the HCA was 12.19 ± 0.57° in 2D CBCT, and it was 88.65% of the actual value. Therefore, the morphologic parameters of TMJ in 3D models were more accurate than those in the 2D CBCT, and then the morphologic parameters of TMJ measured in 3D models could represent the actual morphology of TMJ to some extent.

The results in Table 1 showed that the nine morphologic parameters of TMJ in group A were smaller than those in group B. The results suggested that the angles and distances measured by 2D method were smaller than those measured by 3D method. This finding also indicated that the 2D method may underestimate the size of TMJ morphologic parameters. These smaller results measured by 2D method may be caused by the projective values that were less than the actual values. The degree of motion of the cervical spine during CT imaging could also affect the projection of the TMJ morphologic parameters in the 2D image. In addition, CBCT images can only show the morphology and position of TMJ in horizontal, coronal, and sagittal planes. Clinicians need to combine the 2D images and their clinic experience to diagnose the TMJs. However, 3D reconstructed models can

TABLE 2: Mean and standard deviation of the morphologic parameters for the ten asymptomatic subjects on the left and right TMJs.

Morphologic parameters	Group A ($n = 10$)		p value	Group B ($n = 10$)		p value
	Left TMJ	Right TMJ		Left TMJ	Right TMJ	
HCA ($^{\circ}$)	11.91 \pm 0.55	12.46 \pm 0.74	*	12.57 \pm 0.37	12.87 \pm 0.31	NS
CCA ($^{\circ}$)	12.48 \pm 0.55	12.73 \pm 0.51	NS	12.91 \pm 0.63	12.95 \pm 0.60	NS
SRA ($^{\circ}$)	76.65 \pm 3.28	76.70 \pm 3.86	NS	80.11 \pm 1.52	80.62 \pm 1.30	NS
CCW (mm)	18.54 \pm 2.56	17.88 \pm 2.04	NS	18.69 \pm 2.05	18.39 \pm 2.28	NS
MJS (mm)	2.27 \pm 0.28	2.32 \pm 0.21	NS	2.84 \pm 0.50	2.78 \pm 0.46	NS
LJS (mm)	2.54 \pm 0.24	2.59 \pm 0.19	NS	3.09 \pm 0.77	2.96 \pm 0.47	NS
SJS (mm)	2.03 \pm 0.14	2.07 \pm 0.15	NS	2.26 \pm 0.19	2.28 \pm 0.18	NS
AJS (mm)	2.55 \pm 0.56	2.39 \pm 0.35	NS	2.64 \pm 0.65	2.90 \pm 0.48	NS
PJS (mm)	2.49 \pm 0.44	2.57 \pm 0.54	NS	2.55 \pm 0.82	2.68 \pm 0.61	NS

Note: NS: not significant ($p > 0.05$). *Statistically significant difference between the left and right TMJs by paired samples t -test ($p < 0.05$). HCA: horizontal condylar angle; CCA: coronal condylar angle; SRA: sagittal ramus angle; CCW: coronal condylar width; MJS: medial joint space; LJS: lateral joint space; SJS: superior joint space; AJS: anterior joint space; PJS: posterior joint space.

accurately provide the stereoscopic structure and spatial anatomical location of TMJ, which can better help clinicians to diagnose the morphology of TMJs along with the symptom and sign. The HCA, SRA, MJS, LJS, SJS, and AJS in group A were significantly smaller than those in group B, consistent with Zhang et al.'s study [18]. In particular, the values of MJS, LJS, and SJS measured in 2D CBCT were 81.85%, 84.82%, and 90.31% of those measured in 3D models, respectively. The significant difference in 2D image measurement could lead to the misdiagnosis of TMJ. The CCA, CCW, and PJS measured by 2D method were also a little smaller than those measured by 3D method. Due to the small projective angles, the projective values of CCA, CCW, and PJS were close to their actual values. In summary, there were significant differences in the results of the morphologic parameters of TMJ between 2D and 3D measurements. In addition, 3D reconstructed model can show the stereoscopic structure and spatial position of TMJ and would better help clinicians to accurately diagnose the morphology of TMJ, in accordance with Cevidanes and Al-Saleh et al.'s studies [15–17].

There was significant difference for HCA between the left and right sides in group A. However, all the subjects in this study were asymptomatic and symmetric, in accordance with the 3D measured results in this study. This finding suggested that the HCA measured in 2D CBCT was not consistent with the actual situation. The asymmetric parameter of TMJ measured in 2D image may be caused by the subjects' deflected scanning body position. The 3D reconstructed models of TMJ are not affected by the subjects' scanning body position. Therefore, some parameters of TMJ morphology measured by 2D measuring method were inaccurate to some extent. Moreover, the biased results measured in 2D image may lead to the misdiagnosis of TMJ morphology for clinicians. There were no significant differences for all the nine morphologic parameters of TMJ between the left and right sides in group B. The results were consistent with the fact of the ten asymptomatic subjects recruited in this study. Generally, we believe that the morphologic parameters measured in the 3D reconstructed models can represent the actual morphology of TMJ. Therefore, the values of TMJ morphology measured by 3D measuring method were more accurate than those measured

by 2D method. 3D measuring method should be used for the detection of TMJ morphology in clinical practice.

One major limitation of the current study is that the sample size is a little small. Certainly, a multicentric study with a larger sample should be necessary to confirm our findings.

5. Conclusions

There were significant differences for the morphologic parameters of TMJ measured in 2D CBCT images and 3D reconstructed models. In addition, the 3D reconstructed model could show the actual stereoscopic structure and spatial position of TMJ, so the 3D measuring method is more accurate for clinicians to investigate the morphology of TMJ.

Conflicts of Interest

The authors declare that there is no conflict of interests regarding the publication of this paper.

Acknowledgments

This study was supported by the National Natural Science Foundation of China under Grant nos. 31670963 and 11202143.

References

- [1] N. Mahdian, T. Dostalova, J. Danek et al., "3D reconstruction of TMJ after resection of the cyst and the stress-strain analyses," *Computer Methods and Programs in Biomedicine*, vol. 110, no. 3, pp. 279–289, 2013.
- [2] I. Dupuy-Bonafe, P. Otal, S. Montal, A. Bonafe, and I. L. Maldonado, "Biometry of the temporomandibular joint using computerized tomography," *Surgical and Radiologic Anatomy*, vol. 36, no. 9, pp. 933–939, 2014.
- [3] T. Kawashima, S. Abe, M. Okada, E. Kawada, C. Saitoh, and Y. Ide, "Internal structure of the temporomandibular joint and the circumferential bone: comparison between dentulous and edentulous specimens," *The Bulletin of Tokyo Dental College*, vol. 38, no. 2, pp. 87–93, 1997.

- [4] L. S. Luke, P. Lee, K. A. Atchison, and S. C. White, "Orthodontic residents' indications for use of the lateral TMJ tomogram and the posteroanterior cephalogram," *Journal of Dental Education*, vol. 61, no. 1, pp. 29–36, 1997.
- [5] K. Kikuchi, S. Takeuchi, E. Tanaka, T. Shibaguchi, and K. Tanne, "Association between condylar position, joint morphology and craniofacial morphology in orthodontic patients without temporomandibular joint disorders," *Journal of Oral Rehabilitation*, vol. 30, no. 11, pp. 1070–1075, 2003.
- [6] N. Rakesh, B. K. Y. Devi, D. J. Patil, and R. Nagi, "Assessment of cervical spine postural disorders in patients with temporomandibular dysfunction: a radiographic evaluation," *Oral Radiology*, vol. 30, no. 1, pp. 38–44, 2014.
- [7] T. A. Rehman, S. Gibikote, N. Ilango, J. Thaj, R. Sarawagi, and A. Gupta, "Bifid mandibular condyle with associated temporomandibular joint ankylosis: a computed tomography study of the patterns and morphological variations," *Dentomaxillofacial Radiology*, vol. 38, no. 4, pp. 239–244, 2009.
- [8] S. Minagi, T. Sato, K. Kishi, N. Natsuaki, and Y. Akamatsu, "Comparative study of the temporomandibular joint space in maximum intercuspation and canine edge-to-edge positions in deep bite and non-deep bite subjects," *Journal of Oral Rehabilitation*, vol. 27, no. 6, pp. 517–521, 2000.
- [9] C. Zhao, H. Kurita, K. Kurashina, A. Hosoya, Y. Arai, and H. Nakamura, "Temporomandibular joint response to mandibular deviation in rabbits detected by 3D micro-CT imaging," *Archives of Oral Biology*, vol. 55, no. 12, pp. 929–937, 2010.
- [10] F. Salemi, A. Shokri, H. Mortazavi, and M. Baharvand, "Diagnosis of simulated condylar bone defects using panoramic radiography, spiral tomography and cone-beam computed tomography: a comparison study," *Journal of Clinical and Experimental Dentistry*, vol. 7, no. 1, pp. e34–e39, 2015.
- [11] S. Chen, J. Lei, K.-Y. Fu, X. Wang, and B. Yi, "Cephalometric analysis of the facial skeletal morphology of female patients exhibiting skeletal class II deformity with and without temporomandibular joint osteoarthritis," *PloS One*, vol. 10, no. 10, article e0139743, 2015.
- [12] K. Ejima, D. Schulze, A. Stippig, K. Matsumoto, D. Rottke, and K. Honda, "Relationship between the thickness of the roof of glenoid fossa, condyle morphology and remaining teeth in asymptomatic European patients based on cone beam CT data sets," *Dentomaxillofacial Radiology*, vol. 42, no. 3, article 90929410, 2013.
- [13] Q. Y. Xie, C. Yang, D. M. He et al., "Will unilateral temporomandibular joint anterior disc displacement in teenagers lead to asymmetry of condyle and mandible? A longitudinal study," *Journal of Cranio-Maxillofacial Surgery*, vol. 44, no. 5, pp. 590–596, 2016.
- [14] C. Chien-Chih, L. Cheng-Chung, C. Yunn-Jy, L. Tung-Wu, and H. Chun-Yu, "Accuracy assessment of marker-cluster registration method for measuring temporomandibular kinematics using cone-beam computed tomography with fluoroscopy," *Journal of Medical and Biological Engineering*, vol. 33, no. 5, pp. 443–448, 2013.
- [15] L. H. S. Cevidanes, D. Walker, J. Schilling et al., "3D osteoarthritic changes in TMJ condylar morphology correlates with specific systemic and local biomarkers of disease," *Osteoarthritis and Cartilage*, vol. 22, no. 10, pp. 1657–1667, 2014.
- [16] L. H. S. Cevidanes, L. R. Gomes, B. T. Jung et al., "3D superimposition and understanding temporomandibular joint arthritis," *Orthodontics & Craniofacial Research*, vol. 18, Supplement 1, pp. 18–28, 2015.
- [17] M. A. Q. Al-Saleh, N. Alsufyani, C. Flores-Mir, B. Nebbe, and P. W. Major, "Changes in temporomandibular joint morphology in class II patients treated with fixed mandibular repositioning and evaluated through 3D imaging: a systematic review," *Orthodontics & Craniofacial Research*, vol. 18, no. 4, pp. 185–201, 2015.
- [18] Y. L. Zhang, J. L. Song, X. C. Xu et al., "Morphologic analysis of the temporomandibular joint between patients with facial asymmetry and asymptomatic subjects by 2D and 3D evaluation a preliminary study," *Medicine*, vol. 95, no. 13, article e3052, 2016.
- [19] K. Ueki, A. Moroi, M. Sotobori et al., "Changes in temporomandibular joint and ramus after sagittal split ramus osteotomy in mandibular prognathism patients with and without asymmetry," *Journal of Cranio-Maxillofacial Surgery*, vol. 40, no. 8, pp. 821–827, 2012.
- [20] K. Ueki, K. Nakagawa, S. Takatsuka et al., "Temporomandibular joint morphology and disc position in skeletal class III patients," *Journal of Cranio-Maxillofacial Surgery*, vol. 28, no. 6, pp. 362–368, 2000.
- [21] J. F. Sanroman, J. M. G. Gonzalez, and J. A. del Hoyo, "Relationship between condylar position, dentofacial deformity and temporomandibular joint dysfunction: an MRI and CT prospective study," *Journal of Cranio-Maxillofacial Surgery*, vol. 26, no. 1, pp. 35–42, 1998.
- [22] L. H. S. Cevidanes, A. K. Hajati, B. Paniagua et al., "Quantification of condylar resorption in temporomandibular joint osteoarthritis," *Oral Surgery Oral Medicine Oral Pathology Oral Radiology and Endodontology*, vol. 110, no. 1, pp. 110–117, 2010.
- [23] K. Ueki, K. Degerliyurt, Y. Hashiba, K. Marukawa, K. Nakagawa, and E. Yamamoto, "Horizontal changes in the condylar head after sagittal split ramus osteotomy with bent plate fixation," *Oral Surgery Oral Medicine Oral Pathology Oral Radiology and Endodontology*, vol. 106, no. 5, pp. 656–661, 2008.
- [24] M. O. Borahan, M. Mayil, and F. N. Pekiner, "Using cone beam computed tomography to examine the prevalence of condylar bony changes in a Turkish subpopulation," *Nigerian Journal of Clinical Practice*, vol. 19, no. 2, pp. 259–266, 2016.
- [25] T. Xi, B. van Loon, P. Fudalej, S. Berge, G. Swennen, and T. Maal, "Validation of a novel semi-automated method for three-dimensional surface rendering of condyles using cone beam computed tomography data," *International Journal of Oral and Maxillofacial Surgery*, vol. 42, no. 8, pp. 1023–1029, 2013.
- [26] M. Al-koshab, P. Nambiar, and J. John, "Assessment of condyle and glenoid fossa morphology using CBCT in South-East Asians," *PloS One*, vol. 10, no. 3, article e0121682, 2015.
- [27] E. Martins, J.-C. Silva, C. A. Pires, M.-J.-F. Ponces-Ramalhao, and J.-D. Lopes, "Coronal joint spaces of the temporomandibular joint: systematic review and meta-analysis," *Journal of Clinical and Experimental Dentistry*, vol. 7, no. 3, pp. e435–e440, 2015.
- [28] L. R. Gomes, M. Gomes, B. Jung et al., "Diagnostic index of three-dimensional osteoarthritic changes in temporomandibular joint condylar morphology," *Journal of Medical Imaging*, vol. 2, no. 3, article 034501, 2015.
- [29] C.-C. Chen, C.-C. Lin, T.-W. Lu, H. Chiang, and Y.-J. Chen, "Feasibility of differential quantification of 3D temporomandibular kinematics during various oral activities using a cone-beam computed tomography-based 3D fluoroscopic

- method,” *Journal of Dental Sciences*, vol. 8, no. 2, pp. 151–159, 2013.
- [30] L.-Z. Zhang, S.-S. Meng, D.-M. He et al., “Three-dimensional measurement and cluster analysis for determining the size ranges of Chinese temporomandibular joint replacement prosthesis,” *Medicine*, vol. 95, no. 8, article e2897, 2016.
- [31] J. He, M. Wang, and C. Lu, “Relative analysis on the anatomic parameters of condyoid process of mandible and glenoid fossa of TMJ,” *Chinese Journal of Conservative Dentistry*, vol. 13, no. 12, pp. 669–671, 2003.
- [32] F. Li, Q. Wang, F. X. Xia, and M. Zhang, “TMJ form comparison among subjects with different occasions: an MRI survey,” *Journal of Dental Research*, vol. 79, Supplement 1, pp. 494–494, 2000.